Can Europe stop its silent hepatitis E epidemic? *p. 862*

Paying with time rather than money *pp. 864 & 889*

A protein receptor for norovirus *p. 933*

Science

$15
26 AUGUST 2016
sciencemag.org

AAAS

WEATHER BOMB

Detecting seismic waves from distant storms *pp. 869 & 919*

CONTENTS

26 AUGUST 2016 • VOLUME 353 • ISSUE 6302

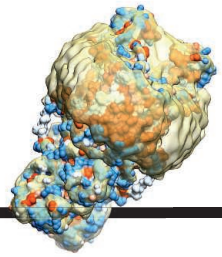

887
A receptor for retinol

853

NEWS

IN BRIEF

850 News at a glance

IN DEPTH

852 **ANTHROPOCENE PINNED TO POSTWAR PERIOD**
Geologists vote to seek a "golden spike," but push for formal acceptance faces skepticism *By P. Voosen*

853 **NASA FLIES INTO NAMIBIA'S CLOUD LABORATORY**
Commingling smoke and fog pose thorny climate puzzles *By E. Hand*

855 **CHOLESTEROL SCREENING FOR KIDS SPARKS DEBATE (AGAIN)**
Evidence for universal testing is insufficient, task force says
By J. Couzin-Frankel

856 **RESEARCH WATCHDOG'S NEW LEADER FACES STAFF REVOLT**
ORI head tries to chart future course, but staff warn of "tensions and conflict" in letters to her superiors
By J. Kaiser

857 **THE EXOPLANET NEXT DOOR**
Earth-like planet found 4 light-years away around Proxima Centauri, the closest star
By D. Clery

FEATURES

858 **THE CARBON ACCOUNTANT**
Richard Heede pins much of the responsibility for climate change on just 90 companies. Others say that's a cop-out *By D. Starr*

862 **EUROPE'S NEW HEPATITIS PROBLEM**
Many get infected with hepatitis E, and a few get very sick. How can the virus be stopped?
By K. Kupferschmidt

INSIGHTS

PERSPECTIVES

864 **HASSLES VERSUS PRICES**
How can subsidized health products best target those who value them?
By B. A. Olken
▸ RESEARCH ARTICLE P. 889

866 **BUILDING MOLECULAR COMPLEXITY FROM SCRATCH**
The Pauson-Khand cycloaddition reaction builds the tetracyclic core of (+)-ryanodol *By X. Verdaguer*
▸ REPORT P. 912

867 **DO YOU SPEAK LION?**
To be effective, conservation decisions must be transparent and based on diverse views *By W. M. Adams*

869 **"WEATHER BOMB" INDUCED SEISMIC SIGNALS**
Seismic waves generated by intense storms can reveal details of Earth's interior
By P. Gerstoft and P. D. Bromirski
▸ REPORT P. 919

870 **PROLINE HYDROXYLATION LINKED TO AKT ACTIVATION**
Oxygen-sensing enzymes regulate the Akt kinase
By M. Voulgarelis and P. N. Tsichlis
▸ REPORT P. 929

872 **A PATH TOWARD UNDERSTANDING NEURODEGENERATION**
A focus on cell biology may accelerate progress in disease prevention and cures *By K. S. Kosik* et al.

POLICY FORUM

874 **ACHIEVING GLOBAL TARGETS FOR ANTIMICROBIAL RESISTANCE**
The UN should promote targets, funding, and governance
By R. Laxminarayan et al.

BOOKS *ET AL.*

876 **THE FUTURE OF THREE-DIMENSIONAL THINKING**
A new holographic platform holds promise for enhancing education, research, and collaboration
By M. A. Hoffman

877 **NAVIGATING TODAY'S JOB MARKET**
A step-by-step guide offers practical science career advice
By T. A. Dellibovi-Ragheb

877 **BUILDING STAR TREK**
By B. Jasny

Downloaded from http://science.sciencemag.org/ on September 3, 2016

Published by AAAS

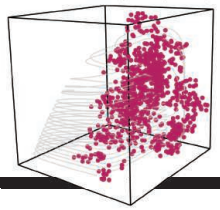

922
Forecasting for complex ecosystems

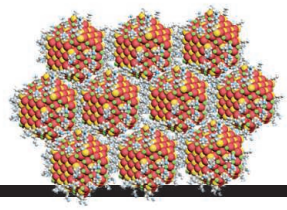

885
Wiring up colloidal devices

LETTERS

878 **REDUCING THE RISK OF ANOTHER ALISO CANYON**
By B. R. Knudsen

878 **NSF VALUES MID-SCALE INFRASTRUCTURE**
By F. Crim and J. Kurose

879 **ERRATA**

879 **ONLINE BUZZ: SIX-WORD STORIES**

RESEARCH

IN BRIEF

882 From *Science* and other journals

REVIEW

885 **MATERIALS SCIENCE**
Building devices from colloidal quantum dots *C. R. Kagan* et al.
REVIEW SUMMARY; FOR FULL TEXT: dx.doi.org/10.1126/science.aac5523
▸ PODCAST

RESEARCH ARTICLES

886 **PHOTOSYNTHESIS**
Light-dependent chlorophyll f synthase is a highly divergent paralog of PsbA of photosystem II *M.-Y. Ho* et al.
RESEARCH ARTICLE SUMMARY; FOR FULL TEXT: dx.doi.org/10.1126/science.aaf9178

887 **STRUCTURAL BIOLOGY**
Structure of the STRA6 receptor for retinol uptake *Y. Chen* et al.
RESEARCH ARTICLE SUMMARY; FOR FULL TEXT: dx.doi.org/10.1126/science.aad8266

888 **ACTINIDE CHEMISTRY**
Characterization of berkelium(III) dipicolinate and borate compounds in solution and the solid state *M. A. Silver* et al.
RESEARCH ARTICLE SUMMARY; FOR FULL TEXT: dx.doi.org/10.1126/science.aaf3762

889 **HEALTH ECONOMICS**
Targeting health subsidies through a nonprice mechanism: A randomized controlled trial in Kenya *P. Dupas* et al.
▸ PERSPECTIVE P. 864

STRUCTURAL BIOLOGY
895 Structure of a yeast catalytic step I spliceosome at 3.4 Å resolution *R. Wan* et al.
904 Structure of a yeast activated spliceosome at 3.5 Å resolution *C. Yan* et al.
▸ RESEARCH ARTICLE BY R. RAUHUT *ET AL.* 10.1126/science.aag1906

REPORTS

912 **ORGANIC SYNTHESIS**
A 15-step synthesis of (+)-ryanodol *K. V. Chuang* et al.
▸ PERSPECTIVE P. 866

916 **ULTRAFAST DYNAMICS**
Attosecond dynamical Franz-Keldysh effect in polycrystalline diamond *M. Lucchini* et al.

919 **GEOPHYSICS**
Teleseismic *S* wave microseisms *K. Nishida and R. Takagi*
▸ PERSPECTIVE P. 869

922 **TIME SERIES ANALYSIS**
Information leverage in interconnected ecosystems: Overcoming the curse of dimensionality *H. Ye and G. Sugihara*

925 **SINGLE-CELL GENOMICS**
Div-Seq: Single-nucleus RNA-Seq reveals dynamics of rare adult newborn neurons *N. Habib* et al.

929 **SIGNAL TRANSDUCTION**
pVHL suppresses kinase activity of Akt in a proline-hydroxylation–dependent manner *J. Guo* et al.
▸ PERSPECTIVE P. 870

933 **VIROLOGY**
Discovery of a proteinaceous cellular receptor for a norovirus *R. C. Orchard* et al.
▸ RESEARCH ARTICLE BY K. ETTAYEBI *ET AL.* 10.1126/science.aaf5211

DEPARTMENTS

849 **EDITORIAL**
Benefits of steady growth
By Jeremy Berg

954 **WORKING LIFE**
Adaptability in life and work
By Amit Kumar

ON THE COVER

A low-pressure system swirls off the coast of Greenland. A seismic array in Japan is now being used to detect seismic waves generated by ocean swell from a more powerful system known as a "weather bomb" in North Atlantic waters. The ability to collect precise seismic source locations of distant storms may provide a new approach for exploring Earth's interior. See pages 869 and 919. *Photo: Jacques Descloitres, MODIS Rapid Response Team, NASA/GSFC*

Science Staff 846
AAAS News & Notes 880
New Products 937
Science Careers 938

SCIENCE (ISSN 0036-8075) is published weekly on Friday, except the last week in December, by the American Association for the Advancement of Science, 1200 New York Avenue, NW, Washington, DC 20005. Periodicals mail postage (publication No. 484460) paid at Washington, DC, and additional mailing offices. Copyright © 2016 by the American Association for the Advancement of Science. The title SCIENCE is a registered trademark of the AAAS. Domestic individual membership and subscription (51 issues): $165 ($74 allocated to subscription). Domestic institutional subscription (51 issues): $1522; Foreign postage extra: Mexico, Caribbean (surface mail) $55; other countries (air assist delivery) $89. First class, airmail, student, and emeritus rates on request. Canadian rates with GST available upon request, GST #1254 88122. Publications Mail Agreement Number 1069624. **Printed in the U.S.A.**
Change of address: Allow 4 weeks, giving old and new addresses and 8-digit account number. **Postmaster:** Send change of address to AAAS, P.O. Box 96178, Washington, DC 20090–6178. **Single-copy sales:** $15.00 current issue, $20.00 back issue prepaid includes surface postage; bulk rates on request. **Authorization to photocopy** material for internal or personal use under circumstances not falling within the fair use provisions of the Copyright Act is granted by AAAS to libraries and other users registered with the Copyright Clearance Center (CCC) Transactional Reporting Service, provided that $35.00 per article is paid directly to CCC, 222 Rosewood Drive, Danvers, MA 01923. The identification code for *Science* is 0036-8075. *Science* is indexed in the *Reader's Guide to Periodical Literature* and in several specialized indexes.

Downloaded from http://science.sciencemag.org/ on September 3, 2016

Published by AAAS

Science
AAAS
1200 New York Avenue, NW, Washington, DC 20005
Clarendon House, Clarendon Road, Cambridge, UK CB2 8FH

Editor-in-Chief Jeremy Berg
Executive Editor Monica M. Bradford **News Editor** Tim Appenzeller
Deputy Editors Lisa D. Chong, Andrew M. Sugden(UK), Valda J. Vinson, Jake S. Yeston

Research and Insights

DEPUTY EDITOR, EMERITUS Barbara R. Jasny **SR. EDITORS** Caroline Ash(UK), Gilbert J. Chin, Julia Fahrenkamp-Uppenbrink(UK), Pamela J. Hines, Stella M. Hurtley(UK), Paula A. Kiberstis, Marc S. Lavine(Canada), Kristen L. Mueller, Ian S. Osborne(UK), Beverly A. Purnell, L. Bryan Ray, Guy Riddihough, H. Jesse Smith, Jelena Stajic, Peter Stern(UK), Phillip D. Szuromi, Sacha Vignieri, Brad Wible, Nicholas S. Wigginton, Laura M. Zahn **ASSOCIATE EDITORS** Brent Grocholski, Keith T. Smith **ASSOCIATE BOOK REVIEW EDITOR** Valerie B. Thompson **LETTERS EDITOR** Jennifer Sills **LEAD CONTENT PRODUCTION EDITORS** Harry Jach, Lauren Kmec **CONTENT PRODUCTION EDITORS** Jeffrey E. Cook, Chris Filiatreau, Cynthia Howe, Barbara P. Ordway, Catherine Wolner **SR. EDITORIAL COORDINATORS** Carolyn Kyle, Beverly Shields **EDITORIAL COORDINATORS** Aneera Dobbins, Joi S. Granger, Jeffrey Hearn, Lisa Johnson, Maryrose Madrid, Anita Wynn **PUBLICATIONS ASSISTANTS** Nida Masiulis, Dona Mathieu, Le-Toya Mayne Flood, Shannon McMahon, Scott Miller, Jerry Richardson, Alice Whaley(UK), Brian White **EXECUTIVE ASSISTANT** Anna Bashkirova **ADMINISTRATIVE SUPPORT** Janet Clements(UK), Lizanne Newton(UK)

News

NEWS MANAGING EDITOR John Travis **INTERNATIONAL EDITOR** Richard Stone **DEPUTY NEWS EDITORS** Elizabeth Culotta, David Grimm, Eric Hand David Malakoff, Leslie Roberts **CONTRIBUING EDITOR** Martin Enserink(Europe) **SR. CORRESPONDENTS** Daniel Clery(UK), Jeffrey Mervis, Elizabeth Pennisi **NEWS WRITERS** Adrian Cho, Jon Cohen, Jennifer Couzin-Frankel, Carolyn Gramling, Jocelyn Kaiser, Catherine Matacic, Kelly Servick, Robert F. Service, Erik Stokstad(Cambridge, UK) **INTERNS** Jessica Boddy, Ben Panko **CONTRIBUTING CORRESPONDENTS** John Bohannon, Warren Cornwall, Ann Gibbons, Mara Hvistendahl, Sam Kean, Eli Kintisch, Kai Kupferschmidt(Berlin), Andrew Lawler, Mitch Leslie, Charles C. Mann, Eliot Marshall, Virginia Morell, Dennis Normile(Shanghai), Heather Pringle, Tania Rabesandratana(London), Emily Underwood, Gretchen Vogel(Berlin), Lizzie Wade(Mexico City) **CAREERS** Donisha Adams, Rachel Bernstein(Editor), Maggie Kuo **COPY EDITORS** Julia Cole, Dorie Chevlen, Jennifer Levin (Chief) **ADMINISTRATIVE SUPPORT** Jessica Adams

Executive Publisher Rush D. Holt
Publisher Bill Moran **Chief Digital Media Officer** Rob Covey

BUSINESS OPERATIONS AND PORTFOLIO MANAGEMENT DIRECTOR Sarah Whalen **PRODUCT DEVELOPMENT DIRECTOR** Will Schweitzer **PRODUCT DEVELOPMENT ASSOCIATE** Hannah Heckner **BUSINESS SYSTEMS AND FINANCIAL ANALYSIS DIRECTOR** Randy Yi **SENIOR SYSTEMS ANALYST** Nicole Mehmedovich **DIRECTOR, BUSINESS OPERATIONS & ANALYSIS** Eric Knott **MANAGER, BUSINESS OPERATIONS** Jessica Tierney **SENIOR BUSINESS ANALYST** Cory Lipman **BUSINESS ANALYSTS** David Garrison, Michael Hardesty Meron Kebede, Sandy Kim **FINANCIAL ANALYST** Drew Sher **DIRECTOR, COPYRIGHTS LICENSING SPECIAL PROJECTS** Emilie David **PERMISSIONS ASSOCIATE** Elizabeth Sandler **RIGHTS, CONTRACTS, AND LICENSING ASSOCIATE** Lili Kiser **RIGHTS & PERMISSIONS ASSISTANT** Alexander Lee

MARKETING DIRECTOR Elise Swinehart **ASSOCIATE MARKETING DIRECTOR** Stacey Burke Bowers **MARKETING ASSOCIATE** Steven Goodman **CREATIVE DIRECTOR** Scott Rodgerson **SENIOR ART ASSOCIATES** Paula Fry **ART ASSOCIATE** Kim Huynh

FULFILLMENT SYSTEMS AND OPERATIONS membership@aaas.org **MANAGER, MEMBER SERVICES** Pat Butler **SPECIALISTS** Terrance Morrison, Latasha Russell **MANAGER, DATA ENTRY** Mickie Napoleoni **DATA ENTRY SPECIALISTS** Brenden Aquilino, Fiona Giblin **MARKETING ASSOCIATE** Isa Sesay-Bah

PUBLISHER RELATIONS, EASTERN REGION Keith Layson **PUBLISHER RELATIONS, WESTERN REGION** Ryan Rexroth **SALES RESEARCH COORDINATOR** Aiesha Marshall **ASSOCIATE DIRECTOR, INSTITUTIONAL LICENSING OPERATIONS** Iquo Edim **SENIOR OPERATIONS ANALYST** Lana Guz **MANAGER, AGENT RELATIONS & CUSTOMER SUCCESS** Judy Lillibridge

WEB TECHNOLOGIES PORTFOLIO MANAGER Trista Smith **TECHNICAL MANAGER** Chris Coleman **PROJECT MANAGER** Nick Fletcher **DEVELOPERS** Ryan Jensen, Jimmy Marks, Brandon Morrison **BUSINESS ANALYST** Christina Wofford

DIGITAL MEDIA DIRECTOR OF ANALYTICS Enrique Gonzales **DIGITAL REPORTING ANALYST** Eric Hossinger **SR. MULTIMEDIA PRODUCER** Sarah Crespi **MANAGING DIGITAL PRODUCER** Alison Crawford **PRODUCER** Liana Birke **VIDEO PRODUCER** Chris Burns, Nguyên Khôi Nguyễn **DIGITAL SOCIAL MEDIA PRODUCER** Brice Russ

DIRECTOR OF OPERATIONS PRINT AND ONLINE Lizabeth Harman **DIGITAL/PRINT STRATEGY MANAGER** Jason Hillman **QUALITY TECHNICAL MANAGER** Marcus Spiegler **PROJECT ACCOUNT MANAGER** Tara Kelly **DIGITAL PRODUCTION MANAGER** Lisa Stanford **ASSISTANT MANAGER DIGITAL/PRINT** Rebecca Doshi **SENIOR CONTENT SPECIALISTS** Steve Forrester, Antoinette Hodal, Lori Murphy, Anthony Rosen **CONTENT SPECIALISTS** Jacob Hedrick, Kimberley Oster **ADVERTISING OPERATIONS SPECIALIST** Ashley Jeter

DESIGN DIRECTOR Beth Rakouskas **DESIGN EDITOR** Marcy Atarod **SENIOR DESIGNERS** Garvin Grullón, Chrystal Smith **GRAPHICS MANAGING EDITOR** Alberto Cuadra **SENIOR SCIENTIFIC ILLUSTRATORS** Chris Bickel, Katharine Sutliff **SCIENTIFIC ILLUSTRATOR** Valerie Altounian **INTERACTIVE GRAPHICS EDITOR** Jia You **SENIOR GRAPHICS SPECIALISTS** Holly Bishop, Nathalie Cary **PHOTOGRAPHY MANAGING EDITOR** William Douthitt **SENIOR PHOTO EDITOR** Christy Steele **PHOTO EDITOR** Emily Petersen

DIRECTOR, GLOBAL COLLABORATION, CUSTOM PUBLICATIONS, ADVERTISING Bill Moran **EDITOR, CUSTOM PUBLISHING** Sean Sanders: 202-326-6430 **ADVERTISING MARKETING MANAGER** Justin Sawyers: 202-326-7061 science_advertising@aaas.org **ADVERTISING SUPPORT MANAGER** Karen Foote: 202-326-6740 **ADVERTISING PRODUCTION OPERATIONS MANAGER** Deborah Tompkins **SR. PRODUCTION SPECIALIST/GRAPHIC DESIGNER** Amy Hardcastle **SR. TRAFFIC ASSOCIATE** Christine Hall **SALES COORDINATOR** Shirley Young **ASSOCIATE DIRECTOR, COLLABORATION, CUSTOM PUBLICATIONS/CHINA/TAIWAN/KOREA/SINGAPORE** Ruolei Wu: +86-186 0082 9345, rwu@aaas.org **COLLABORATION/CUSTOM PUBLICATIONS/JAPAN** Adarsh Sandhu + 81532-81-5142 asandhu@aaas.org **EAST COAST/E. CANADA** Laurie Faraday: 508-747-9395, FAX 617-507-8189 **WEST COAST/W. CANADA** Lynne Stickrod: 415-931-9782, FAX 415-520-6940 **MIDWEST** Jeffrey Dembksi: 847-498-4520 x3005, Steven Loerch: 847-498-4520 x3006 **UK EUROPE/ASIA** Roger Goncalves: TEL/FAX +41 43 243 1358 **JAPAN** Katsuyoshi Fukamizu(Tokyo): +81-3-3219-5777 kfukamizu@aaas.org **CHINA/TAIWAN** Ruolei Wu: +86-186 0082 9345, rwu@aaas.org

WORLDWIDE ASSOCIATE DIRECTOR OF SCIENCE CAREERS Tracy Holmes: +44 (0) 1223 326525, FAX +44 (0) 1223 326532 tholmes@science-int.co.uk **CLASSIFIED** advertise@sciencecareers.org **U.S. SALES** Tina Burks: 202-326-6577, Nancy Toema: 202-326-6578 **EUROPE/ROW SALES** Sarah Lelarge **SALES ASSISTANT** Kelly Grace **JAPAN** Hiroyuki Mashiki(Kyoto): +81-75-823-1109 hmashiki@aaas.org **CHINA/TAIWAN** Ruolei Wu: +86-186 0082 9345 rwu@aaas.org **MARKETING MANAGER** Allison Pritchard **MARKETING ASSOCIATE** Aimee Aponte

AAAS BOARD OF DIRECTORS, CHAIR Geraldine L. Richmond **PRESIDENT** Barbara A. Schaal **PRESIDENT-ELECT** Susan Hockfield **TREASURER** David Evans Shaw **CHIEF EXECUTIVE OFFICER** Rush D. Holt **BOARD** Cynthia M. Beall, May R. Berenbaum, Carlos J. Bustamante, Stephen P.A. Fodor, Claire M. Fraser, Michael S. Gazzaniga, Laura H. Greene, Elizabeth Loftus, Mercedes Pascual

SUBSCRIPTION SERVICES For change of address, missing issues, new orders and renewals, and payment questions: 866-434-AAAS (2227) or 202-326-6417, FAX 202-842-1065. Mailing addresses: AAAS, P.O. Box 96178, Washington, DC 20090-6178 or AAAS Member Services, 1200 New York Avenue, NW, Washington, DC 20005

INSTITUTIONAL SITE LICENSES 202-326-6730 **REPRINTS:** Author Inquiries 800-635-7181 **COMMERCIAL INQUIRIES** 803-359-4578 **PERMISSIONS** 202-326-6765, permissions@aaas.org **AAAS Member Services** 202-326-6417 or http://membercentral.aaas.org/discounts

Science serves as a forum for discussion of important issues related to the advancement of science by publishing material on which a consensus has been reached as well as including the presentation of minority of conflicting points of view. Accordingly, all articles published in *Science*—including editorials, news and comment, and book reviews—are signed and reflect the individual views of the authors and not official points of view adopted by AAAS or the institutions with which the authors are affiliated.

INFORMATION FOR AUTHORS See pages 624 and 625 of the 5 February 2016 issue or access www.sciencemag.org/authors/science-information-authors

SENIOR EDITORIAL BOARD
Gary King, *Harvard University,* **Susan M. Rosenberg,** *Baylor College of Medicine,*
Ali Shilatifard, *Northwestern University Feinberg School of Medicine*

BOARD OF REVIEWING EDITORS (Statistics board members indicated with **(S)**)

Adriano Aguzzi, *U. Hospital Zürich*
Takuzo Aida, *U. of Tokyo*
Leslie Aiello, *Wenner-Gren Foundation*
Judith Allen, *U. of Edinburgh*
Sonia Altizer, *U. of Georgia*
Sebastian Amigorena, *Institut Curie*
Kathryn Anderson, *Memorial Sloan-Kettering Cancer Center*
Meinrat O. Andreae, *Max-Planck Inst. Mainz*
Paola Arlotta, *Harvard U.*
Johan Auwerx, *EPFL*
David Awschalom, *U. of Chicago*
Clare Baker, *University of Cambridge*
Nenad Ban, *ETH Zurich*
Jordi Bascompte, *University of Zurich*
Franz Bauer, *Pontificia Universidad Católica de Chile*
Ray H. Baughman, *U. of Texas, Dallas*
David Baum, *U. of Wisconsin*
Carlo Beenakker, *Leiden U.*
Kamran Behnia, *ESPCI-ParisTech*
Yasmine Belkaid, *NIAID, NIH*
Philip Benfey, *Duke U.*
May Berenbaum, *U. of Illinois*
Gabriele Bergers, *U. of California, San Francisco*
Bradley Bernstein, *Massachusettes General Hospital*
Peer Bork, *EMBL*
Bernard Bourdon, *Ecole Normale Supérieure de Lyon*
Chris Bowler, *École Normale Supérieure*
Ian Boyd, *U. of St. Andrews*
Emily Brodsky, *U. of California, Santa Cruz*
Ron Brookmeyer, *U. of California Los Angeles* **(S)**
Christian Büchel, *U. Hamburg-Eppendorf*
Joseph A. Burns, *Cornell U.*
Carter Tribley Butts, *U. of California, Irvine*
Gyorgy Buzsaki, *New York U. School of Medicine*
Blanche Capel, *Duke U.*
Mats Carlsson, *U. of Oslo*
Ib Chorkendorff, *U. of Denmark*
David Clapham, *Children's Hospital Boston*
Joel Cohen, *Rockefeller U., Columbia U.*
James J. Collins, *MIT*
Robert Cook-Deegan, *Duke U.*
Lisa Coussens, *Oregon Health & Science U.*
Alan Cowman, *Walter & Eliza Hall Inst.*
Robert H. Crabtree, *Yale U.*
Roberta Croce, *Vrije Universiteit*
Janet Currie, *Princeton U.*
Jeff L. Dangl, *U. of North Carolina*
Tom Daniel, *U. of Washington*
Frans de Waal, *Emory U.*
Stanislas Dehaene, *Collège de France*
Robert Desimone, *MIT*
Claude Desplan, *New York U.*
Dennis Discher, *U. of Pennsylvania*
Gerald W. Dorn II, *Washington U. School of Medicine*
Jennifer A. Doudna, *U. of California, Berkeley*
Bruce Dunn, *U. of California, Los Angeles*
William Dunphy, *Caltech*
Christopher Dye, *WHO*
Todd Ehlers, *U. of Tuebingen*
David Ehrhardt, *Carnegie Inst. of Washington*
Tim Elston, *U. of North Carolina at Chapel Hill*
Jennifer Elisseeff, *U. of N*
Gerhard Ertl, *Fritz-Haber-Institut, Berlin*
Barry Everitt, *U. of Cambridge*
Ernst Fehr, *Johns Hopkins U.*
Anne C. Ferguson-Smith, *U. of Cambridge*
Michael Feuer, *The George Washington U.*
Toren Finkel, *NHLBI, NIH*
Kate Fitzgerald, *U. of Massachusetts*
Peter Fratzl, *Max-Planck Inst.*
Elaine Fuchs, *Rockefeller U.*
Daniel Geschwind, *UCLA*
Karl-Heinz Glassmeier, *TU Braunschweig*
Ramon Gonzalez, *Rice U.*
Julia R. Greer, *Caltech*
Elizabeth Grove, *U. of Chicago*
Nicolas Gruber, *ETH Zurich*
Kip Guy, *St. Jude's Children's Research Hospital*
Taekjip Ha, *U. of Illinois at Urbana-Champaign*
Wolf-Dietrich Hardt, *ETH Zurich*
Christian Haass, *Ludwig Maximilians U.*
Sharon Hammes-Schiffer, *U. of Illinois at Urbana–Champaign*
Michael Hasselmo, *Boston U.*
Martin Heimann, *Max-Planck Inst. Jena*
Yka Helariutta, *U. of Cambridge*
James A. Hendler, *Rensselaer Polytechnic Inst.*
Janet G. Hering, *Swiss Fed. Inst. of Aquatic Science & Technology*
Kai-Uwe Hinrichs, *U. of Bremen*
David Hodell, *U. of Cambridge*
Lora Hooper, *UT Southwestern Medical Ctr. at Dallas*
Tamas Horvath, *Yale University*
Raymond Huey, *U. of Washington*
Fred Hughson, *Princeton U.*
Auke Ijspeert, *EPFL Lausanne*
Stephen Jackson, *USGS and U. of Arizona*
Steven Jacobsen, *U. of California, Los Angeles*
Kai Johnsson, *EPFL Lausanne*
Peter Jonas, *Inst. of Science & Technology (IST) Austria*
Matt Kaeberlein, *U. of Washington*
William Kaelin Jr., *Dana-Farber Cancer Inst.*
Daniel Kahne, *Harvard U.*
Daniel Kammen, *U. of California, Berkeley*
Abby Kavner, *U. of California, Los Angeles*
Hitoshi Kawakatsu, *U. of Tokyo*
Masashi Kawasaki, *U. of Tokyo*
V. Narry Kim, *Seoul National U.*
Robert Kingston, *Harvard Medical School*
Etienne Koechlin, *Ecole Normale Suprieure*
Alexander Kolodkin, *Johns Hopkins U.*
Thomas Langer, *U. of Cologne*
Mitchell A. Lazar, *U. of Pennsylvania*
David Lazer, *Harvard U.*
Thomas Lecuit, *IBDM*
Virginia Lee, *U. of Pennsylvania*
Stanley Lemon, *U. of North Carolina at Chapel Hill*
Ottoline Leyser, *Cambridge U.*
Wendell Lim, *U.C. San Francisco*
Marcia C. Linn, *U. of California, Berkeley*
Jianguo Liu, *Michigan State U.*
Luis Liz-Marzan, *CIC biomaGUNE*
Jonathan Losos, *Harvard U.*
Ke Lu, *Chinese Acad. of Sciences*
Christian Lüscher, *U. of Geneva*
Laura Machesky, *CRUK Beatson Inst. for Cancer Research*
Anne Magurran, *U. of St. Andrews*
Oscar Marin, *CSIC & U. Miguel Hernández*
Charles Marshall, *U. of California, Berkeley*
C. Robertson McClung, *Dartmouth College*
Rodrigo Medellin, *U. of Mexico*
Graham Medley, *U. of Warwick*
Tom Misteli, *NCI*
Yasushi Miyashita, *U. of Tokyo*
Mary Ann Moran, *U. of Georgia*
Richard Morris, *U. of Edinburgh*
Alison Motsinger-Reif, *NC State U.* **(S)**
Thomas Murray, *The Hastings Center*
Daniel Neumark, *U. of California, Berkeley*
Kitty Nijmeijer, *U. of Twente*
Helga Nowotny, *European Research Advisory Board*
Ben Olken, *MIT*
Rachel O'Reilly, *Warwick U.*
Joe Orenstein, *U. of California Berkeley & Lawrence Berkeley National Lab*
Harry Orr, *U. of Minnesota*
Pilar Ossorio, *U. of Wisconsin*
Andrew Oswald, *U. of Warwick*
Isabella Pagano, *Istituto Nazionale di Astrofisica*
Margaret Palmer, *U. of Maryland*
Steve Palumbi, *Stanford U.*
Jane Parker, *Max-Planck Inst. of Plant Breeding Research*
Giovanni Parmigiani, *Dana-Farber Cancer Inst.* **(S)**
John H. J. Petrini, *Memorial Sloan-Kettering Cancer Center*
Samuel Pfaff, *Salk Institute for Biological Studies*
Joshua Plotkin, *U. of Pennsylvania*
Albert Polman, *FOM Institute AMOLF*
Philippe Poulin, *CNRS*
Jonathan Pritchard, *Stanford U.*
Wim van der Putten, *Netherlands Institute of Ecology*
David Randall, *Colorado State U.*
Felix Rey, *Institut Pasteur*
Trevor Robbins, *U. of Cambridge*
Jim Roberts, *Fred Hutchinson Cancer Research Ctr.*
Amy Rosenzweig, *Northwestern University*
Mike Ryan, *U. of Texas, Austin*
Mitinori Saitou, *Kyoto U.*
Shimon Sakaguchi, *Kyoto U.*
Miquel Salmeron, *Lawrence Berkeley National Lab*
Jürgen Sandkühler, *Medical U. of Vienna*
Alexander Schier, *Harvard U.*
Vladimir Shalaev, *Purdue U.*
Robert Siliciano, *Johns Hopkins School of Medicine*
Denis Simon, *Arizona State U.*
Uri Simonsohn, *U. of Pennsylvania*
Alison Smith, *John Innes Centre*
Richard Smith, *U. of North Carolina* **(S)**
John Speakman, *U. of Aberdeen*
Allan C. Spradling, *Carnegie Institution of Washington*
Jonathan Sprent, *Garvan Inst. of Medical Research*
Eric Steig, *U. of Washington*
Paula Stephan, *Georgia State U. and National Bureau of Economic Research*
Molly Stevens, *Imperial College London*
V. S. Subrahmanian, *U. of Maryland*
Ira Tabas, *Columbia U.*
Sarah Teichmann, *Cambridge U.*
John Thomas, *North Carolina State U.*
Shubha Tole, *Tata Institute of Fundamental Research*
Christopher Tyler-Smith, *The Wellcome Trust Sanger Inst.*
Herbert Virgin, *Washington U.*
Bert Vogelstein, *Johns Hopkins U.*
Cynthia Volkert, *U. of Göttingen*
David Wallach, *Weizmann Inst. of Science*
Ian Walmsley, *U. of Oxford*
Jane-Ling Wang, *U. of California, Davis* **(S)**
David Waxman, *Fudan U.*
Jonathan Weissman, *U. of California, San Francisco*
Chris Wikle, *U. of Missouri* **(S)**
Ian A. Wilson, *The Scripps Res. Inst.* **(S)**
Timothy D. Wilson, *U. of Virginia*
Rosemary Wyse, *Johns Hopkins U.*
Jan Zaanen, *Leiden U.*
Kenneth Zaret, *U. of Pennsylvania School of Medicine*
Jonathan Zehr, *U. of California, Santa Cruz*
Len Zon, *Children's Hospital Boston*
Maria Zuber, *MIT*

BOOK REVIEW BOARD
David Bloom, *Harvard U.,* **Samuel Bowring,** *MIT,* **Angela Creager,** *Princeton U.,*
Richard Shweder, *U. of Chicago,* **Ed Wasserman,** *DuPont*

EDITORIAL

Benefits of steady growth

When the United States Congress returns from an August recess, it must take up appropriations bills, including those that fund science agencies. These bills will only focus on one fiscal year. Yet, almost all scientific projects require years to yield substantial progress. This timeline may favor longer-term budget allocation and other policy adjustments.

Science-funding agencies typically make multiyear grants, with averages of approximately 3 years for the U.S. National Science Foundation (NSF) and 4 years for the U.S. National Institutes of Health (NIH). For the NIH and, to a lesser extent, NSF, these grants are paid out over consecutive years. Thus, when an agency makes an award, it often takes on a "mortgage" for funding the grant in future years. This approach allows agencies to monitor research efforts effectively through progress reports. However, multiyear funding means that the likelihood that applications submitted in subsequent years will be funded (often measured by "success rates" or "funding rates") will depend largely on decisions made in previous years. Transitions from years with relatively generous appropriations (in which many new grants can be awarded) to those with limited appropriations can result in large drops in success rates.

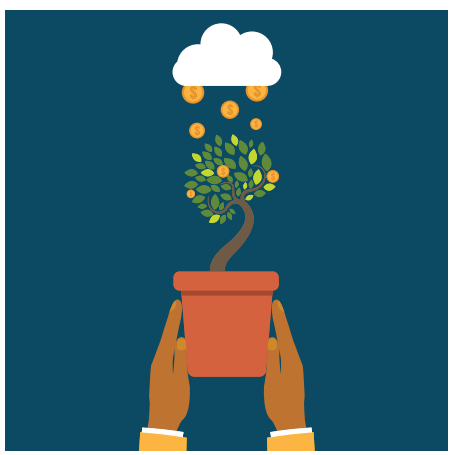

"...ground-breaking research may be missed for arbitrary reasons of timing."

Such fluctuations have important consequences. Outstanding applications that would have been funded one year go unsupported the next year, so that potentially ground-breaking research may be missed for arbitrary reasons of timing. Low success rates result in scientists spending more time writing and reviewing proposals instead of conducting research. Investigators, particularly those at vulnerable career stages, can become demoralized by the apparently capricious nature of funding decisions.

I have constructed a quantitative model that estimates grant success rates based on past appropriation levels, described in *Sciencehound* (http://blogs.sciencemag.org/sciencehound/2016/08/26/modeling-success-rates). The first component of the model estimates the number of grants that can be awarded annually based on the appropriations history. Remarkably, a simple model that captures only the essential features of multiyear funding reproduces year-to-year patterns quite well. The second component estimates the number of grant applications reviewed each year, based on the observation that increases in agency appropriations usually result in increases in subsequent application numbers with a 1- to 2-year lag.

The NIH budget doubled from 1998 through 2003 but has been nearly flat ever since. The model, applied from 1990 to 2015, reproduces the drop in the success rate (from approximately 30 to 20%) that occurred over the 2 years after the doubling. The success of the model supports the hypothesis that basic features of grant-funding processes were responsible for this drop rather than changes in NIH policies.

A benefit of these models is that consequences of potential alternative appropriation scenarios can be examined in quantitative terms. Suppose that Congress had increased the NIH appropriation from 1998 to 2015 at a constant rate instead of the "boom" of the doubling and the "bust" of the flat funding, with the same overall constant dollar investment. The model suggests that this would have resulted in 2.4-fold smaller fluctuations in success rates and a decrease of nearly 35,000 unsuccessful grant applications. Thus, with a more stable funding stream, the system would have been more equitable on a year-to-year basis, and an average of 1300 fewer applications would have needed to be written and peer-reviewed per year to support the same amount of research.

Scientists and other advocates often call for steady increases in science budgets, arguing that growth at the rate of inflation is necessary to maintain research activity and that predictable budgets allow longer-term planning. These are important arguments, but they apply to many sectors. The multiyear nature of science funding provides an additional compelling argument for the implementation of longer-term science budget planning by the scientific community and the government.

–Jeremy Berg

Editor-in-Chief, Science *Journals. Email: jberg@aaas.org*

Downloaded from http://science.sciencemag.org/ on September 3, 2016

CREDITS: (INSET) ANDSIM/ISTOCKPHOTO.COM; (TOP RIGHT) TERRY CLARK

10.1126/science.aai8237

Published by AAAS

NEWS

> “D.A. was a force of nature who, until relatively recently, seemed invulnerable. Public health has lost a hero.”
>
> **Michael J. Klag, dean of the Johns Hopkins Bloomberg School of Public Health** in Baltimore, Maryland, posting on Facebook about the death last week of Donald Ainslie (“D.A.”) Henderson, who led the successful global campaign to eradicate smallpox from 1966 to 1977.

IN BRIEF

Peru’s mysterious dog mummies

Archaeological excavations in Lima’s zoo have revealed more than 100 well-preserved dogs.

Like much of Lima, Peru’s capital city, the Parque de las Leyendas zoo is built atop layers of settlements that stretch back millennia. In 2012, a team led by archaeologist Karina Venegas Gutiérrez of the zoo’s Division of Archaeology unearthed something strange there: the remains of more than 100 dogs, resting alongside a similar number of humans. The dogs had been arranged in peaceful, sleeplike postures and were wrapped in textiles for burial, just as most humans were at that time. However, many of the humans sustained violent injuries such as skull fractures and broken limbs just before death. Nearby ceramics and other artifacts suggest both dogs and humans were buried around 1000 C.E., a transitional time for Peru’s coastal societies, as the agricultural society of Ychsma moved into regions previously occupied by the Lima culture. The dogs may have been part of a ritual sacrifice, perhaps carried out hastily after a traumatic event, Venegas Gutiérrez said last week at the World Congress on Mummy Studies in Lima. “Maybe the dogs were offered to the humans after a mass death of some kind,” she said. As for who may have killed these people and why, she still can’t say. http://bit.ly/Perudogmummies

AROUND THE WORLD

U.N. makes U-turn on cholera

NEW YORK CITY | The United Nations has finally acknowledged that it bears responsibility for triggering a cholera outbreak in Haiti in 2010 that sickened at least 700,000 people and killed more than 9000. In a 19 August statement, U.N. Secretary-General Ban Ki-moon said he “deeply regrets the terrible suffering” the outbreak has caused and acknowledged the United Nations’s “moral responsibility” to make amends. U.N. peacekeepers from Nepal operated a camp with poor sanitation close to where the first cholera cases in Haiti occurred, and genome studies have shown that the Haiti strain is virtually identical to one circulating in Nepal at the time; a panel appointed by Ban in 2011 called the evidence for a link “overwhelming.” But until last week, the United Nations had denied any responsibility. Although a federal appeals court on 18 August upheld the United Nations’s legal immunity from a lawsuit started by Haitian victims, Ban promised to provide “material assistance and support” and to intensify efforts to end the epidemic.

Flawed voting mars election

BETHESDA, MARYLAND | Members of the Society of Biological Inorganic Chemistry (SBIC) are reacting with puzzlement and shock after learning that the results of a recent online leadership election have been thrown out because of voting irregularities. Counting revealed far more votes than there are members of the organization, according to an internal newsletter sent to SBIC members last week. One candidate received four times the number of votes as there are members of the group, it noted. The cause of the flawed voting isn’t clear, but “the results appear to have been manipulated,” Michael Hannon, president-elect of SBIC and the chair of chemical biology at the University of Birmingham in the United Kingdom, wrote in the 9 August newsletter. SBIC has asked the Federation of American Societies for Experimental Biology, which carried out the elections on behalf of the society, to arrange a new election that is run in a “more secure” fashion,

PHOTO: LUCKEZ OLMOS

Downloaded from http://science.sciencemag.org/ on September 3, 2016

Published by AAAS

A pneumatic network (pink) can flex the arms of the soft-bodied octobot.

Gas-powered robot is the squishiest yet

Octopuses are known escape artists, able to squeeze and squish themselves into and around a wide range of obstacles. Now, in an ode to these clever cephalopods, Harvard University scientists have created the first completely soft-bodied robot, dubbed the "octobot." "For the soft robotics community, the octopus has always kind of been an inspiration," says the project's leader, Harvard bioengineer Jennifer Lewis. The palm-sized octobot's exterior is made of silicone, "like bathroom caulking," Lewis says. Whereas other soft robots have had at least a few hard parts, such as batteries or wires, the octobot has none. It contains a small reservoir of hydrogen peroxide that it uses as fuel: When the hydrogen peroxide washes over flecks of platinum embedded within the octobot's silicone body, the resulting chemical reaction produces gas that inflates and flexes the robot's arms. As described this week in *Nature*, the gas flows through a series of 3D-printed pneumatic chambers in its eight arms; their flexing propels it through water. Right now, the octobot's fuel lasts between 4 and 8 minutes and it can't steer in any particular direction. But as the field of soft robotics advances, Lewis envisions these robots being used for oceanic search and rescue, climate sensing, and military applications.

using a unique link identifier that enables just one vote per individual. **http://bit.ly/SBICvote**

Silver lining in ministry purge?

MOSCOW | Continuing a summer of upheavals for Russian science, on 19 August President Vladimir Putin fired his science minister and replaced him with historian Olga Vasilyeva, known for her admiration for Soviet dictator Joseph Stalin. The move startled many scientists, but some see it as a ray of hope for the Russian Academy of Sciences (RAS), which is undergoing a painful downsizing in which dozens of academy institutes are expected to merge, and thousands of scientists will likely lose their jobs. Ousted Science Minister Dmitry Livanov was an architect of the reforms; he had long pressed for strengthening science in the universities at the academy's expense. Vasilyeva, who was head of the religious studies department of the Russian Presidential Academy of National Economy and Public Administration and worked in Putin's executive office, told daily newspaper *Kommersant* that her first order of business is to scrutinize the ongoing reforms. RAS President Vladimir Fortov told reporters on 20 August that he welcomed her appointment; her experience in the executive office will help "build a constructive dialogue" between scientists and bureaucrats, he said. **http://bit.ly/Russiaminister**

Olga Vasilyeva

Nanopore lawsuit settled

WASHINGTON, D.C. | In March, genetic sequencing giant Illumina Inc. sued Oxford Nanopore Technologies for patent infringement (*Science*, 4 March, p. 1010). Illumina claimed that Oxford's sequencing platforms rely on its patented *Mycobacterium smegmatis* porin (Msp) protein. Last week, the two companies reached a settlement, according to a U.S. International Trade Commission document dated 18 August. Oxford has agreed not to import or sell any product containing a pore with an amino acid sequence at least 68% similar to Msp and to destroy any inventory of such products. The document explicitly states that the restriction doesn't affect Oxford's ability to use CsgG, a different pore that the company unveiled shortly after the suit was filed, and which underlies its newest line of sequencers. Whether Oxford ever did rely on Msp is still a mystery.

NEWSMAKERS

Bloomberg a WHO ambassador

The World Health Organization (WHO) has named former New York City mayor, businessman, and philanthropist **Michael Bloomberg** as global ambassador for noncommunicable diseases—a position that comes without a salary or expense account but that allows Bloomberg to draw more attention to issues he cares about deeply. Some 16 million people die before turning 70 from problems such as heart disease, stroke, cancer, diabetes, and chronic respiratory ailments, according to WHO, and another 1.25 million perish in traffic. The $4.3 billion that Bloomberg has donated to charity so far includes a $600 million initiative to reduce tobacco use and programs aimed at obesity, road safety, and maternal health. Bloomberg also focused on public health during his time as mayor from 2002 until 2013. A ban on supersize sodas that he introduced in 2012 was struck down 2 years later by New York's Court of Appeals.

PHOTOS: (TOP TO BOTTOM) LORI SANDERS/RYAN TRUBY/MICHAEL WEHNER/ROBERT WOOD/JENNIFER LEWIS; MOSCOW STATE HUMANITARIAN-ECONOMIC INSTITUTE PRESS OFFICE/TASS/NEWSCOM

Downloaded from http://science.sciencemag.org/ on September 3, 2016

Published by AAAS

PHOTO: SCIENCE SOURCE

STRATIGRAPHY

Anthropocene pinned to postwar period

Geologists vote to seek a "golden spike," but push for formal acceptance faces skepticism

By **Paul Voosen**

Just after World War II, when the atomic bombs fell and our thirst for coal and oil became a full-blown addiction, Earth entered the Anthropocene, a new geologic time when humanity's environmental reach left a mark in sediments worldwide. That's the majority conclusion of the Anthropocene Working Group, a collection of researchers that has spent the past 7 years quietly studying whether the term, already popular, should be submitted as a formal span of geologic time.

After tallying votes this month, the group has decided to propose the postwar boom of the late 1940s and early 1950s as the Anthropocene's start date. The group will ask the International Commission on Stratigraphy (ICS), the bureaucracy that governs geologic time, to recognize the Anthropocene as a series, the stratigraphic equivalent of an epoch, on par with the Holocene and Pleistocene that preceded it. Colin Waters, the group's secretary and a geologist at the British Geological Survey in Keyworth, will reveal the group's recommendations on 29 August at the International Geological Congress in Cape Town, South Africa.

The group won't submit a formal proposal yet. To do so, it must gather multiple cores of sediment from around the planet and show that they contain a sharp transition in geochemical tracers that is likely to persist as a permanent part of the rock record; the core with the best example of the transition would then serve as a "golden spike," marking the Anthropocene's start. These cores could come from lakebeds, ocean floors, ice sheets—or even corals or tree rings. But they must capture the "Great Acceleration": the postwar period when fossil fuel combustion took off, says Jan Zalasiewicz, a geologist at the University of Leicester in the United Kingdom who convened the group. "We'll go and get our hands dirty, beginning to look for sections that we can formally propose."

> ***"I feel like a lighthouse with a huge tsunami wave coming at it."***
>
> **Stan Finney**, chair of the International Commission on Stratigraphy

Those sections will have to be rich with multiple signatures, as the Anthropocene proposal faces deep skepticism from stratigraphers. "The voting members of the International Commission on Stratigraphy look at these things critically," says Stan Finney, chair of ICS and a geologist at California State University, Long Beach.

He and other stratigraphers doubt that their standards can be properly applied to decades-old mud and silt rather than the solid rock that records older stratigraphic boundaries. They question the value of the Anthropocene for their science, which seeks to draw coherent chronologies out of sedimentary rocks. Some also resent the role that scientists from other disciplines such as climate science have played in driving the proposal and see it as a political statement.

Should ICS decide against the Anthropocene, some stratigraphers fear, they could be swamped with bad press. "I feel like a lighthouse with a huge tsunami wave coming at it," Finney says. Phil Gibbard, a stratigrapher at the University of Cambridge in the United Kingdom and a working group member who voted against the proposal, also worries about a backlash. "We're nervous," he says.

The working group, a mix of 35 geologists, climate scientists, archaeologists, and others, considered multiple dates. There were votes for an early start to the Anthropocene, 7000 years ago, when humanity began converting forests en masse to pastures and cropland, perhaps causing carbon dioxide (CO_2) to spike, and also for 3000 years ago, when lead smelting tainted the ground. More recently, they considered 1610, when pollen from the New World appeared in Europe, and the early 1800s, the start of the Industrial Revolution. But the most votes went to the Great Acceleration.

Downloaded from http://science.sciencemag.org/ on September 3, 2016

Published by AAAS

Plutonium from atomic weapons testing, found in soil beginning in 1951, could mark the Anthropocene.

The group's decision to go for a single, recent start date for the Anthropocene disappoints Bill Ruddiman, an emeritus professor of environmental science at the University of Virginia in Charlottesville. "It is a mistake to formalize the term by rigidly affixing it to a single time," he says, "especially one that misses most of the history of the major transformation of Earth's surface." Many archaeologists also favor the 7000-year-old date, when early humans began to alter the planet's surface. But the working group was looking for a signature of global, human-driven change that would wind up in the rock record, not the first traces of human influence on the local landscape.

In a study published in *Science* earlier this year, the working group highlighted their most likely proxies. Materials that rose to mass use in the 1950s, such as plastics and elemental aluminum, are prime targets. Plutonium from atmospheric nuclear testing, first visible in the soil in 1951, will linger in sediments globally for the next 100,000 years as it decays into uranium and then lead. But perhaps the most promising proxy comes from recent work that has shown, across 71 lakebeds worldwide, a 1950s spike in fly ash residue from the high-temperature combustion of coal and oil. "This is a permanent signal," Waters says. "These particles will not be degrading." He adds that the ash is directly tied to the human-driven increase in CO_2 that sparked the notion of the Anthropocene in the first place.

Until this year, the group had not sought a golden spike; instead, they favored defining the Anthropocene simply by a starting date, a method stratigraphers have only used for units of time within the Precambrian, more than 540 million years ago, when clear dividing signals have been impossible to find in the rock. But several ICS members, including Finney, made it clear a golden spike would be necessary for any chance of approval.

The group's proposal may not satisfy him. But Waters hopes the ICS will consider the chosen golden spike on its merits. "Just because it's thin and short duration, the fact that it's very sizable is the most important thing," he says.

Zalasiewicz adds that the marks of the Great Acceleration will endure, even if somehow humanity reverses global warming and gives half the planet over to conservation. And if humanity doesn't change course, then future stratigraphers might need to elevate the Anthropocene's rank in the geological hierarchy, he says. "An epoch would be thinking too small." ■

PHOTO: BUENA VISTA IMAGES

ATMOSPHERIC SCIENCE

NASA flies into Namibia's cloud laboratory

Commingling smoke and fog pose thorny climate puzzles

By **Eric Hand**

Off the coast of Namibia, for several months a year, a layer of smoke drifts over a persistent deck of low clouds. It's the perfect place to investigate the thorniest problem in all of climate science: how haze and clouds interact to influence global warming, either boosting or moderating it. Now, after weeks of delay, an airborne research campaign is getting started in this diaphanous natural laboratory.

The smoke, from fires deep in Africa, is nearly invisible to satellites in space, and because the southeast Atlantic Ocean has few islands, the layers are hard to study from below. But flying directly into them from Namibia has posed its own hurdles—bureaucratic ones, which NASA has now cleared. On 29 August, research planes will begin nearly a month of flights into the heart of the smoke and clouds, taking off every other day from Walvis Bay, Namibia, with plans to return in 2017 and 2018.

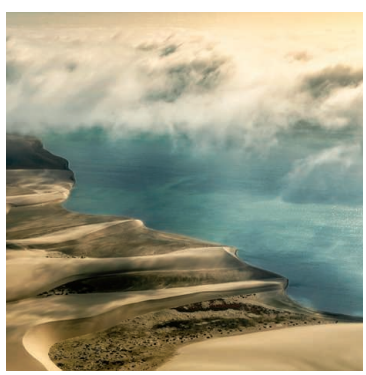

Like California and Chile, Namibia has a persistent bank of coastal fog.

Complementary efforts from France and the United Kingdom would have expanded the sampling area but were postponed when the teams couldn't get diplomatic clearances from Namibia. NASA itself almost canceled this season's flights before getting permission last week. Mission leaders were relieved and eager to begin their studies of cloud and haze effects, which "constitute the largest uncertainties in our models of future climate—that's no exaggeration," says Jens Redemann, an atmospheric scientist at NASA's Ames Research Center in Mountain View, California, and the principal investigator for ObseRvations of Aerosols above CLouds and their IntEractionS (ORACLES).

Like Chile and California, Namibia has a near-constant coastal fog: a bank of low-lying, relatively thin stratocumulus clouds sitting just offshore. It also has a supply of smoke from the natural and human-caused fires that whip across the savannas of southern Africa. In August, the prevailing winds shift and, for about 3 months, blow the smoke out to sea and above the cloud deck. Near shore, the clouds and smoke stay separated in tidy layers, but farther west the smoke settles and mixes with the clouds. This gives scientists an ideal laboratory to observe the varied and complex interactions of the clouds and smoke and their climate effects (see graphic, p. 854).

Atmospheric scientists already have a decent handle on how clouds and smoke work on their own. For instance, bright, white clouds reflect light to space, cooling the planet. Aerosols can also have a cooling effect, if they are bright, like the sulfate particles emitted by volcanoes. Sooty black carbon, on the other hand, tends to absorb light and heat the planet. Although scientists don't know exactly how the African smoke evolves chemically as it drifts over the ocean, they think that because it originates from burning vegetation, it contains a lot of brown carbon. That would put its brightness somewhere between that of soot and sulfate—able to both trap and reflect heat.

Things get more complicated when clouds and smoke overlap. When the African smoke blows over the top of the white cloud deck, it absorbs some of the heat that the clouds would have reflected, which turns up the thermostat. But at breaks in the cloud deck, smoke has the opposite effect: It is brighter than the dark ocean surface, reflecting solar radiation and reducing warming.

Smoke particles also influence clouds. By absorbing heat, aerosols can evaporate nearby cloud droplets—making the cloud less reflective and compounding the heating effect. On the other hand, by warming the atmosphere, aerosols can stabilize the air and protect clouds from drying out and thinning. Still other effects—which primarily promote cooling—occur when the aerosols begin mixing into a cloud. The aerosols create additional seeds around which water vapor can

Downloaded from http://science.sciencemag.org/ on September 3, 2016

Published by AAAS

condense, boosting the number of cloud droplets and making the cloud more reflective. Because the added droplets are smaller, they are less likely to be rained out, which enhances cloud longevity.

The smoke is virtually invisible against a bright cloud, which handicaps satellites looking down from above. So the $30 million ORACLES mission will fly straight into the mix. The mission's workhorse is NASA's P-3, a low-flying turboprop originally developed by the U.S. Navy to hunt for submarines. Flying at altitudes between 4 and 6 kilometers, it will carry instruments that look up and down and sample the air directly. Flight paths will vary, with lots of turns and sudden changes in altitude. The pilots love it, Redemann says, but the scientists—not so much. "It's not rare that multiple people vomit."

Some flights will try to stay on a particular line of latitude or longitude, no matter what the clouds and smoke are doing that day, because climate modelers need data collected along a transect. Others will be flights of opportunity, following the weather. One such plan is a flight to Ascension Island, 1600 kilometers off the African coast, that will seek to follow the smoke layer westward to see how it changes chemically with time.

ORACLES will also deploy a camera-carrying ER-2—a variant of the venerable U-2 spy plane—that will cruise at an altitude of 20 kilometers, providing contextual images. "It's our personal satellite," Redemann says. Meanwhile, a battery of sensors and radars is watching from the ground, on Ascension Island. Part of a separate experiment run by the U.S. Department of Energy called Layered Atlantic Smoke Interactions with Clouds (LASIC), the ground station recently captured samples of the downwind smoke to see how its properties changed during its drift westward. "It was both exciting and a relief," says Paquita Zuidema, an atmospheric scientist at the University of Miami in Coral Gables, Florida, and LASIC lead scientist. "You'd hate to think that the smoke is just blowing by you overhead, without being able to take direct measurements."

What the ORACLES team learns should sharpen forecasts of regional climate change. Climate models suggest that, in a hotter future, weather patterns will shift and southern Africa will become dryer. But that prediction might not hold if African nations tamp down fires in order to limit smoke, a health hazard. Eliminating aerosols could reduce their tendency to evaporate rain clouds, and the region could get wetter, says Rob Wood, ORACLES deputy principal investigator and an atmospheric scientist at the University of Washington, Seattle. "There's a potential for [the effect] to mitigate the greenhouse gas changes in precipitation," he says.

The team also hopes to shrink broader uncertainties about clouds and aerosols. In a recent study, for instance, well-respected climate models were shown to have completely opposing estimates for the overall effect of the clouds and smoke in the southeast Atlantic: Some found net warming, whereas others found cooling.

When ORACLES scientists return to Namibia next August, they hope to be joined by French and U.K. researchers, who postponed their missions for at least a year when they didn't get diplomatic clearances. Researchers with the U.K. mission, called CLARIFY (Cloud-Aerosol-Radiation Interactions and Forcing for Year 2016), initially looked at relocating its research aircraft to Ascension Island, but they couldn't make the switch work logistically. "Everybody is quite frustrated," says Steven Abel, a CLARIFY principal investigator with the U.K. Met Office in Exeter.

NASA, too, ran into obstacles. Namibia gained its independence in 1990 from South Africa, after a long struggle led by a Socialist Party supported by Cuba and the Soviet Union—enemies of the United States at the time. Some suspected that Namibia's defense ministry harbored lingering suspicions of the United States that slowed approval of the project. "I have to assume it's discomfort with having an ex–high-altitude spy plane and an ex–submarine hunter placed in their country," Zuidema says.

Bob Swap, an ORACLES program scientist in Washington, D.C., spent the month of July in Namibia shuttling between ministries and trying to rally support. "You camp out and you're on their time schedule not yours, and you're showing respect," he says. Eventually, ORACLES got on the agenda of a presidential cabinet meeting on 16 August. The bureaucratic skies cleared; visas for the mission scientists and flight permits for the aircraft were proffered days later. ■

Noses in the air

This month, NASA aircraft will begin studying a natural atmospheric laboratory off the coast of Namibia, where a layer of smoke wafts over a low cloud deck.

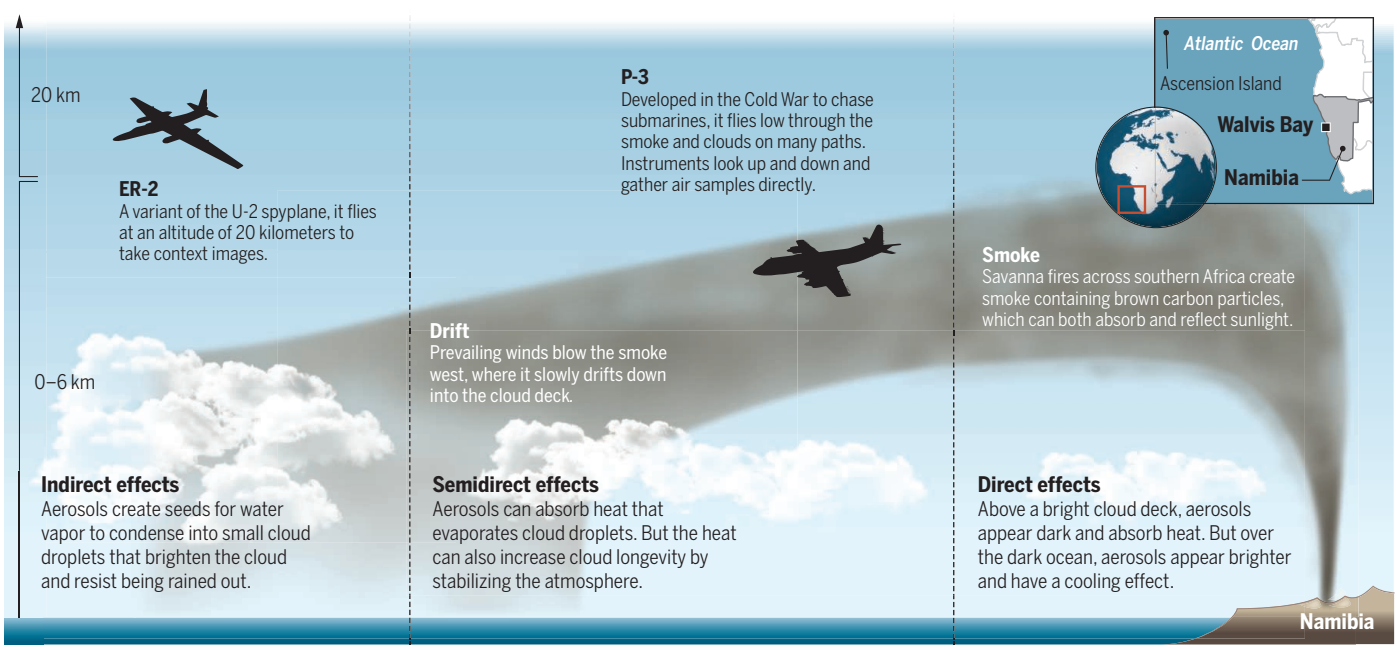

GRAPHIC: C. BICKEL/*SCIENCE* ADAPTED FROM NASA/ORACLES

Downloaded from http://science.sciencemag.org/ on September 3, 2016

Published by AAAS

PHOTO: CHOJA/ISTOCKPHOTO.COM

The American Academy of Pediatrics suggests that all 9- to 11-year-olds get a blood test for cholesterol.

CHILDREN'S HEALTH

Cholesterol screening for kids sparks debate (again)

Evidence for universal testing is insufficient, task force says

By **Jennifer Couzin-Frankel**

A long-simmering dispute over whether every school-age child in the United States should be tested for high cholesterol erupted again earlier this month, after a national task force said there is insufficient evidence for such screening. Nearly 5 years ago the American Academy of Pediatrics (AAP) endorsed National Heart, Lung, and Blood Institute recommendations that pediatricians draw blood from all 9- to 11-year-olds and test their cholesterol levels. Those with very high low-density lipoprotein (LDL), sometimes called "bad" cholesterol, would qualify for statin drugs, AAP suggested; lifestyle changes could be offered to children whose LDL is on the high end—those in the 90th percentile or above, with an LDL of more than 130.

In strongly worded comments, several physicians welcomed the August conclusions of the U.S. Preventive Services Task Force and upbraided AAP for a position whose health benefits they consider inadequate to justify the medical risks and financial costs of cholesterol screening in all kids. "We're treating a risk factor. We're not treating a disease," says Peter Belamarich, a pediatrician at Montefiore Medical Center in New York City with expertise in lipid disorders. "We are under an extraordinarily high burden to show that we are not harming people" with interventions.

AAP representatives say they stand by screening, although they acknowledge the uncertainties. "I believe the full set of evidence … weighs towards benefit" of universal screening, Sarah De Ferranti, a member of the AAP Committee on Nutrition and director of preventive cardiology at Boston Children's Hospital, told *Science* in an email. But many doctors seem to side with the skeptics. In a survey published in 2014 in *The Journal of Pediatrics*, only 16% of 548 primary pediatric providers in Minnesota were screening all of their young patients.

The screening question braids together some of the toughest subjects in medicine, including how or whether to set guidelines with incomplete scientific evidence, and when to give drugs to treat a risk factor whose effects, if they manifest, are probably decades off. "We're not saying that [AAP's] position is wrong," says David Grossman, a vice chair of the task force and a pediatrician at the Group Health Research Institute in Seattle, Washington. "We're saying we just don't know."

When the task force turned to published studies, it immediately hit a roadblock, Grossman explains. "In children, it's really, really difficult to find screening trials," he says. So the group sought indirect evidence about whether childhood cholesterol screening and treatment with either statins or lifestyle modifications could stave off later cardiovascular disease.

What little evidence the task force could find was mixed. Thirteen trials of statins in children showed that, as in adults, they markedly reduce LDL. But there were also hints that some children with high LDL who went untreated had normal LDL as adults. Furthermore, there are virtually no data on the long-term effects of statins in children, whose developing bodies may respond differently than adults to long-term use.

Some doctors also worry that following the current AAP guidelines may cause unnecessary heartache. Thomas Newman, a pediatrician and epidemiologist at the University of California, San Francisco, and an outspoken critic of the AAP position, shares the story of a teenaged athlete whose pediatrician offered testing. The teen just assumed he would score well. To the boy's shock, he had elevated LDL. A strict diet failed to normalize it, which isn't unusual, Newman says. The teenager grew depressed. "He was invited to go eat hot dogs on the beach," Newman recalls, "and said, 'I can't do that.'"

De Ferranti agrees the issue is complex, but argues that the benefits of a healthy diet and exercise are well documented—and this is how the vast majority of children with high cholesterol would be treated.

Still, the chair of the expert panel says that in retrospect, the group's 2011 recommendation should have placed more emphasis on the highest risk children. "As I went out and talked about those guidelines, it became clearer and clearer to me that we hadn't presented it in the right way," says Stephen Daniels, pediatrician-in-chief at Children's Hospital Colorado in Denver. Although he supports reinforcing a healthy lifestyle for kids with modestly elevated LDL, Daniels now believes screening should be mainly used to identify and treat the small subset of children whose genetics cause very high LDL levels, often more than 190 mg/dl. About one in every 250 people has the genetic condition, known as familial hypercholesterolemia (FH), which can lead to premature heart attacks.

Even there, the knowledge gap looms: There is "inadequate evidence" for universal FH screening as well, the Preventive Services Task Force concludes. It suggested that no one knows whether an extra decade of statins helps these children more than it hurts them.

There's one point on which both sides agree: Doctors need more evidence, particularly studies that track kids with high cholesterol whose families select different treatment approaches. "We have an obligation" to conduct these studies, Belamarich says. ■

Downloaded from http://science.sciencemag.org/ on September 3, 2016

Published by AAAS

Kathryn Partin, new head of the Office of Research Integrity, is clashing with staff.

SCIENTIFIC MISCONDUCT

Research watchdog's new leader faces staff revolt

ORI head tries to chart future course, but staff warn of "tensions and conflict" in letters to her superiors

By **Jocelyn Kaiser**

The Office of Research Integrity (ORI) in Rockville, Maryland, which guards against misconduct in biomedical research, usually attracts attention with its findings, not its internal workings. But 2 years ago, its director, David Wright, quit in a public huff, complaining that ORI was hobbled by a dysfunctional federal bureaucracy. Now, his successor is encountering her own rough waters, *Science* has learned.

Kathryn Partin, who took the helm of ORI in December 2015, has launched a top-to-bottom review of the office, which has been criticized for moving too slowly and meting out sanctions that lack teeth. She has also brought in an investigator from the National Science Foundation (NSF) as her acting deputy director, a possible sign that she wishes to expand ORI's powers to mirror those of the research integrity division within NSF's Office of Inspector General, which can issue subpoenas, for example (see table, right). But in one of several letters of protest to Partin's superiors at the Department of Health and Human Services (HHS), many of ORI's investigative staff recently expressed "profound concern about the tone and direction" she has taken. They contend that Partin does not fully understand ORI's regulatory constraints and is unjustifiably seeking to replace ORI's two division directors, whose departure, they write, would be a "disaster." John Dahlberg, who before retiring last year was ORI's deputy director, says that his former office "seems to be falling apart."

Whether the quarrel is more than a new boss challenging an old guard resistant to change is hard to resolve. Partin and her superiors have declined to comment on the staff turmoil or on specific plans for change. "We are focused on examining all of our processes, and all of the ways we can support institutions in their investigations," the former neuroscientist told *Science* in her first interview since taking over. (Partin provided written responses to emailed questions; an edited transcript of the interview is online at http://bit.ly/ORIhead.)

ORI was created 24 years ago to police research misconduct among scientists funded by the National Institutes of Health (NIH) and other HHS agencies. The office's 13-person investigative division currently relies mainly on probes by researchers' home institutions to produce about a dozen research misconduct findings a year. An education division runs research integrity teaching programs and helps organize well-regarded "boot camps" for university research integrity officers (RIOs). A model for science agencies in other countries, ORI is "by far the most important research integrity program in the world," says Nicholas Steneck of the University of Michigan, Ann Arbor, a research ethics expert who has worked closely with ORI.

The penalties ORI delivers usually don't go beyond a negotiated ban on seeking federal grant funds for a few years. That publicly announced debarment effectively ends most research careers, one ORI investigator stressed to *Science*. Partin appears to support that approach. "I believe that our current model of very aggressive notification to the public, journals, and funding offices of our findings of research misconduct has merit."

Others think ORI's sanctions are too light. In one recent misconduct case involving an AIDS vaccine researcher who accepted a 3-year funding ban, Senator Charles Grassley (R–IA) complained that ORI or HHS should have taken stronger actions. After his intervention, federal prosecutors took on the case and won a lengthy jail term for the scientist, along with an order that he pay back $7.2 million in grant money (*Science*, 10 July 2015, p. 122).

ORI's new head spent 20 years at Colorado State University (CSU), Fort Collins, where she served as CSU's RIO and oversaw research ethics education. While she was there, NSF found that a CSU plant scientist had published fabricated data with a postdoc, resulting in many retracted papers. "I learned how devastating findings of research misconduct are—to the individual, the department, and the

A tale of two offices

The offices that monitor research integrity for projects funded by the National Science Foundation (NSF) or the National Institutes of Health work differently.

OFFICE OF RESEARCH INTEGRITY	NSF INSPECTOR GENERAL
Often negotiates voluntary exclusions from seeking federal funding.	Can recommend debarment or other sanctions by NSF.
Oversees institutions' investigations.	Can conduct independent investigations.
No subpoena authority.	Can subpoena, issue search warrants.
Publishes findings in *Federal Register* with names.	Publishes case summaries but names redacted.
No plagiarism findings since 2013.	Plagiarism makes up 81% of findings of research misconduct.

Downloaded from http://science.sciencemag.org/ on September 3, 2016

CREDITS: (PHOTO) WILLIAM A. COTTON/CSU PHOTOGRAPHY; (DATA) HHS/ORI; NSF

Published by AAAS

whole institution," Partin says.

At ORI, Partin says she has gathered input about what her office could do better. The research community wants faster case closure, more guidance on handling retractions, and more data on misconduct trends, she says. Partin has also named Scott Moore, an investigative scientist and attorney who works at NSF's Office of Inspector General in Arlington, Virginia, as her acting deputy. The objective is "not for ORI to become more like NSF, but rather to allow both organizations to benefit from sharing information about processes and procedures," she says.

Partin may be looking to NSF for ideas about how to handle charges of plagiarism. Although 81% of NSF's research misconduct findings involve plagiarism, ORI has left most plagiarism allegations to institutions to handle. ORI's policy in this area "deserves a fresh look," Partin says. Some research integrity experts who spoke with *Science* agreed. But expanding ORI's purview would mean a much larger caseload for an already overwhelmed staff, warns Wright, now at Michigan State University in East Lansing.

In Wright's view, ORI should have subpoena power and should sometimes conduct its own investigations. Partin, however, remains publicly noncommittal on those issues. "If it … becomes clear that ensuring integrity … warrants a change in the rules, then the only responsible thing for ORI to do is to initiate that conversation," she says.

ORI's $8.6 million budget would likely need a boost to make use of any expanded powers—and changing its authority would not be for the faint of heart. "It would be a cold day in hell before most of the major research groups would recommend bolstering and strengthening ORI," Steneck says. Partin says she realizes agency rulemaking is a "long and difficult process." But, she adds, "In the short term, there is much we can do without going that route."

Partin may need to resolve the friction within ORI first. A 10 May letter from six of the office's scientist-investigators complains that Partin has "apparently concluded that she cannot work with" either division director. The letter also takes her to task for "lack of transparency"—noting in particular Moore's arrival. "Tensions and conflict" are "tearing this office apart," the letter says.

ORI watchers say that whatever changes Partin makes, she should aim for stability within the staff, which has the unusual blend of science and legal expertise needed to deal with research misconduct and has formed long-running relationships with universities. "ORI needs strong leadership at all levels and staff continuity. The public would not be well-served if research were to lose its conscience," Steneck says. ■

ASTRONOMY

The exoplanet next door

Earth-like planet found 4 light-years away around Proxima Centauri, the closest star

By **Daniel Clery**

Say hello to our nearest neighbor.

After years of scrutinizing the closest star to Earth, a red dwarf known as Proxima Centauri, astronomers have finally found evidence for a planet, slightly bigger than Earth, well within the star's habitable zone—the range of orbits in which liquid water could exist on its surface.

Researchers have already found hundreds of similarly sized planets, and many appear to be far better candidates for hosting life than the one around Proxima Centauri, called Proxima b. But researchers are excited because the planet, just 4.25 light-years away, may be within reach of telescopes and techniques that could reveal more about its composition and atmosphere than that of any other exoplanet discovered to date. "This is the best planet we have [for study] right now, no question," says planetary scientist Sara Seager of the Massachusetts Institute of Technology in Cambridge.

Rumors had been circulating for weeks about the discovery, announced on 24 August in *Nature*. The planet was found using the radial velocity method: Telescopes scrutinize a star's light to see whether its frequency is periodically stretched and squeezed by movement of the star as it is tugged away from and toward us by an orbiting planet. The task was especially difficult for Proxima Centauri, because it tends to flare up dramatically, obscuring the planet-induced signal.

In recent years, a number of groups had found inconclusive hints of a planet around the star. "We designed an experiment to confirm what we suspected was there," says team leader Guillem Anglada-Escudé of Queen Mary University of London, who used the European Southern Observatory's High Accuracy Radial velocity Planet Searcher (HARPS) spectrograph on a 3.6-meter telescope in Chile. Their Pale Red Dot campaign, carried out on HARPS from January to the end of March, revealed a planet 1.3 times the mass of Earth orbiting the star every 11.2 days. "This solidifies our view that rocky planets are everywhere, ubiquitous, around all kinds of stars," says astrophysicist Nikku Madhusudhan of the University of Cambridge in the United Kingdom.

The red dwarf's dimness means that liquid water could exist on Proxima b even though it orbits at just 5% of the Earth-sun distance. Apart from that, it has little to recommend it for life. It's probably tidally locked, meaning that it always presents the same face to the star and has a hot side and a cold side, although a circulating atmosphere could moderate temperatures. During stellar flare-ups, it is probably blasted with intense ultraviolet light and x-rays, along with particles—unless it has a protective magnetic field like Earth's. Nevertheless, Anglada-Escudé says, there is "a reasonable range of parameters that could make it a comfortable planet."

Water could exist on Proxima b, but the planet's surface (imagined here) may be blasted by radiation from its flaring red sun.

Astronomers are now studying the star to see whether Proxima b's orbit takes it in front of the star as viewed from Earth. If it does, then the spectrum of starlight passing through its atmosphere could reveal volumes about its structure and composition. "That would be amazing. A dream come true," Seager says. Next decade, a generation of extremely large telescopes may be able to image it—our first direct look at another potentially habitable world.

And if sending a probe across the trillions of kilometers of space to visit a nearby star system ever becomes feasible, engineers have their first target. ■

IMAGE: ESO/M. KORNMESSER

Downloaded from http://science.sciencemag.org/ on September 3, 2016

Published by AAAS

PHOTO: NOAH BERGER

Downloaded from http://science.sciencemag.org/ on September 3, 2016

THE CARBON ACCOUNTANT

Richard Heede pins much of the responsibility for climate change on just 90 companies. Others say that's a cop-out

By **Douglas Starr**

Last month, geographer Richard Heede received a subpoena from Representative Lamar Smith (R–TX), chairman of the House of Representatives Committee on Science, Space, and Technology. Smith, a climate change doubter, became concerned when the attorneys general of several states launched investigations into whether ExxonMobil had committed fraud by sowing doubts about climate change even as its own scientists knew it was taking place. The congressman suspected a conspiracy between the attorneys general and environmental advocates, and he wanted to see all the communications among them. Predictably, his targets included advocacy organizations such as Greenpeace, 350.org, and the Union of Concerned Scientists. They also included Heede, who works on his own aboard a rented houseboat on San Francisco Bay in California.

Heede is less well known than his fellow recipients, but his work is no less threatening to the fossil fuel industry. Heede (pronounced "Heedie") has compiled a massive database quantifying who has been responsible for taking carbon out of the ground and putting it into the atmosphere. Working alone, with uncertain funding, he spent years piecing together the annual production of every major fossil fuel company since the Industrial Revolution and converting it to carbon emissions.

The results showed that nearly two-thirds of the major industrial greenhouse gas emissions (from fossil fuel use, methane leaks, and cement manufacture) originated in just 90 companies around the world, which either emitted the carbon themselves or supplied carbon ultimately released by consumers and industry. As Heede told *The Guardian* newspaper, you could take all the decision-makers and CEOs of these companies and fit them on a couple Greyhound buses.

The study provoked controversy when it was published in 2013, with some complaining that it unfairly held the fossil fuel industry responsible for the lifestyle choices made by billions of consumers. "It's a cop-out to blame the producers of products that we have demanded, and benefited from, for more than a century," wrote Severin Borenstein, a business and public policy

Published by AAAS

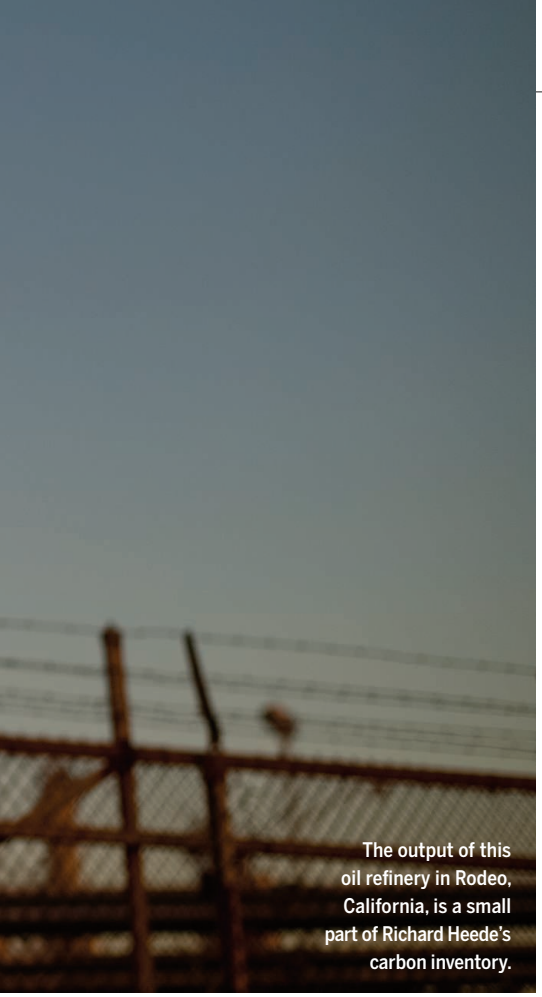

The output of this oil refinery in Rodeo, California, is a small part of Richard Heede's carbon inventory.

expert at the University of California (UC), Berkeley, in a blog post.

Others, however, saw the study as a turning point in the debate about apportioning responsibility for climate change. With traditional environmental issues, such as river pollution or toxic waste, it has always been possible to identify perpetrators who could be targeted for regulation or enforcement. But greenhouse gases are emitted everywhere, in every process that involves combustion. "For decades there's been a persistent myth that everyone is responsible, and if everyone is responsible then no one is responsible," says Carroll Muffett, president and CEO of the Center for International Environmental Law in Washington, D.C., who also serves on the board of a nonprofit that Heede co-founded. "Rick's work for the first time identifies a discrete class of defendants."

Heede's carbon accounting is already opening a new chapter in climate change litigation and policy, helping equip plaintiffs who believe they have suffered damages from climate change to claim compensation. "Rick's work really helps connect the dots," says Marco Simons, general counsel of EarthRights International, a Washington, D.C.–based legal group that defends the rights of the poor. "He hasn't sought out the spotlight, but I think his work is tremendously important."

HEEDE TALLIES CARBON OBSESSIVELY. When we discussed my plans to fly out from Boston to Sausalito, California, where his houseboat is anchored, he did a quick calculation and told me that my share of the flights would add 716 kilograms of carbon to the atmosphere. "And if you'd driven an average car the trip would be 1.78 tons of CO_2 [carbon dioxide]" he added, apparently riffing on his own compulsiveness. During my visit I noticed that when he boiled water to make noodles for lunch he put a frying pan on the pot instead of a lid—to preheat the pan so it would use a tiny bit less fuel to heat up the stir-fry. "It's a practice of mine to figure out how I can minimize energy use."

He was born in Norway into a long line of watchmakers, which may contribute to his own meticulousness. At 15, he and his parents immigrated to the United States. His father was a consulting engineer, but the younger Heede wasn't keen on "fixing problems that should not have been created in the first place"—which, he admits, is exactly what he's doing these days.

Heede has spent most of his life in Colorado, and he has the solid build and weathered face of someone who has spent lots of time in the mountains. He earned undergraduate and master's degrees in geography at the University of Colorado, Boulder, and then joined forces with Amory Lovins, the soft-energy guru who co-founded the Rocky Mountain Institute in Boulder. Ronald Reagan had just been elected president, and his administration moved to gut subsidies for alternative energy sources, claiming that they were not economically competitive. Heede tested that assertion, analyzing the federal budget to find the hidden subsidies to the coal and oil industries, even including the cost of treating workers who developed black lung disease from coal mining.

Contrary to Reagan administration claims, Heede showed that the vast bulk of federal energy subsidies went to conventional energy sources. He wrote a report, testified to Congress, and wrote an opinion piece in *The Wall Street Journal*. "I don't recall getting any calls as a result," he says. It was an early taste of working in obscurity.

In 2003, he left the Rocky Mountain Institute to form Climate Mitigation Services, a consulting firm specializing in surveying and mitigating greenhouse gas emissions. One of his early clients was Aspen, Colorado, a rich and progressive ski town whose leaders wanted to act decisively to reduce emissions. They hired Heede to do a baseline greenhouse gas inventory with the broadest possible scope—including not only activities within the city, but the cars and airplanes that annually brought in hundreds of thousands of tourists … in short, Heede recalls, "everything that uses energy as a result of Aspen's existence."

The exercise raised fascinating questions, Heede says: "What is a community, and what is a boundary? There's leakage everywhere: airplanes, trucks, cars, visitors. How do you quantify that stuff?"

Heede interviewed airport managers and checked their logs to find out which aircraft served the more than 178,000 annual passengers, calculating fuel consumption and emissions for each flight. Standing at the main bridge into Aspen for hours at a time, he categorized the cars that went by—sedans, SUVs, trucks, vans. Then, he used his records to estimate emissions from the 13,000 vehicles tabulated by an automated counter each day. In the end, he determined that in 2004, Aspen was responsible for more than 840,000 tons of carbon emissions—"roughly equivalent to a large, diesel-powered aircraft carrier running flank speed at all times." This and subsequent reports enabled the city to reduce its emissions despite a growing population and economy.

Aspen was an early test of Heede's ability to gather information and see beyond obvious boundaries—the invisible ripples from every project that affect the infinitely interconnected atmosphere. In the early 2000s, for example, an Australian firm proposed building a liquefied natural gas terminal off the California coast. It seemed a good way to transition to a low-carbon "bridge" fuel. But, Heede says, "They hadn't done any work on life cycle emissions." When he tallied all the direct and indirect emissions—from the gas extraction in Australia to distribution in California—he found that the project would have produced nearly a third more carbon than anticipated. His analysis helped persuade California officials to vote it down.

Later, he tackled targets that produce bigger but more diffuse ripples. Several U.S. cities and environmental groups were suing the Export-Import Bank of the United States and the Overseas Private Investment Corporation, alleging the institutions were financing projects that would damage Earth's climate. The plaintiffs retained Heede to analyze the carbon emissions resulting from the banks' loans and investments around the world, from a gas project in Central Africa to a coal mine in Poland. He found that the projects were directly and indirectly emitting nearly 2 billion metric tons of CO_2 per year—almost 8% of the world's emissions. The plaintiffs won: The banks agreed to conduct environmental impact statements, create carbon-sensitive policies, and increase their financing of renewable energy projects.

Meanwhile, a new idea was coalescing in the environmental law community. For years, attorneys had litigated so-called

Downloaded from http://science.sciencemag.org/ on September 3, 2016

Published by AAAS

Holding carbon producers accountable

Analyzing the amount of carbon that the fossil fuel and cement industries have extracted from the ground, Heede found that more than 60% of emissions since the Industrial Revolution can be traced to the "carbon majors"—companies producing at least 8 million tons of carbon a year.

Cumulative emissions (million metric tons of CO_2)

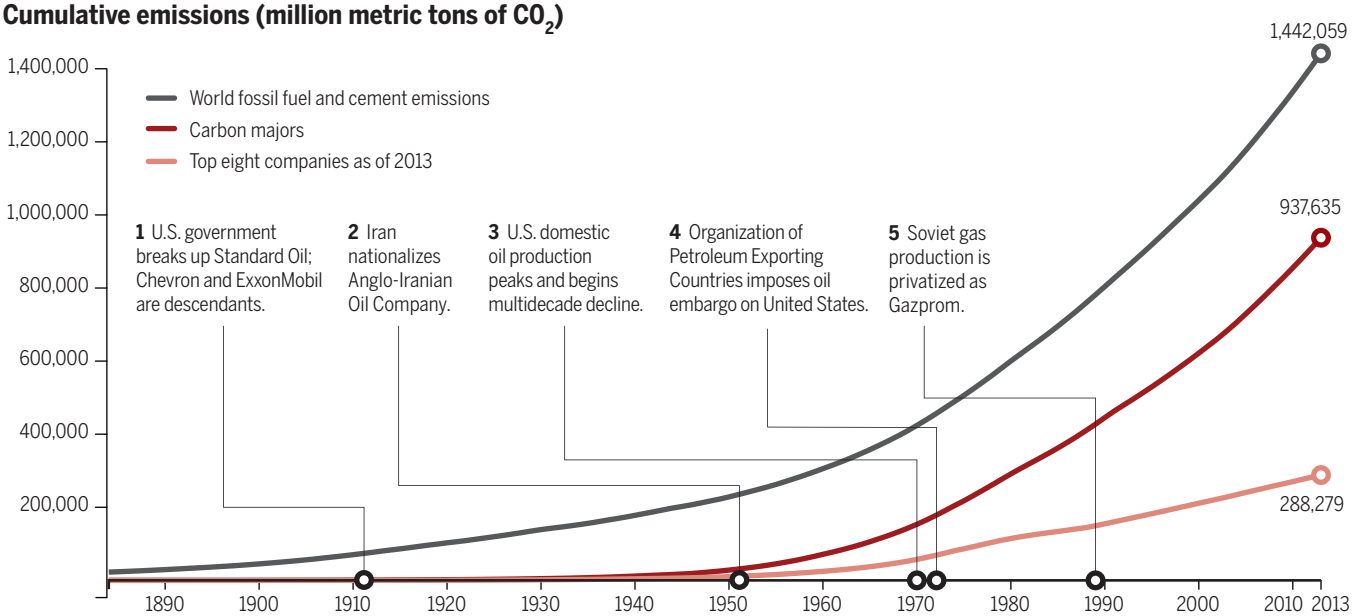

Topping the chart

The eight top fossil fuel companies have experienced name changes and production peaks and drops (see numbered events). But by tracking production and emissions throughout their histories, Heede was able to calculate their contribution to the world's cumulative greenhouse gas emissions.

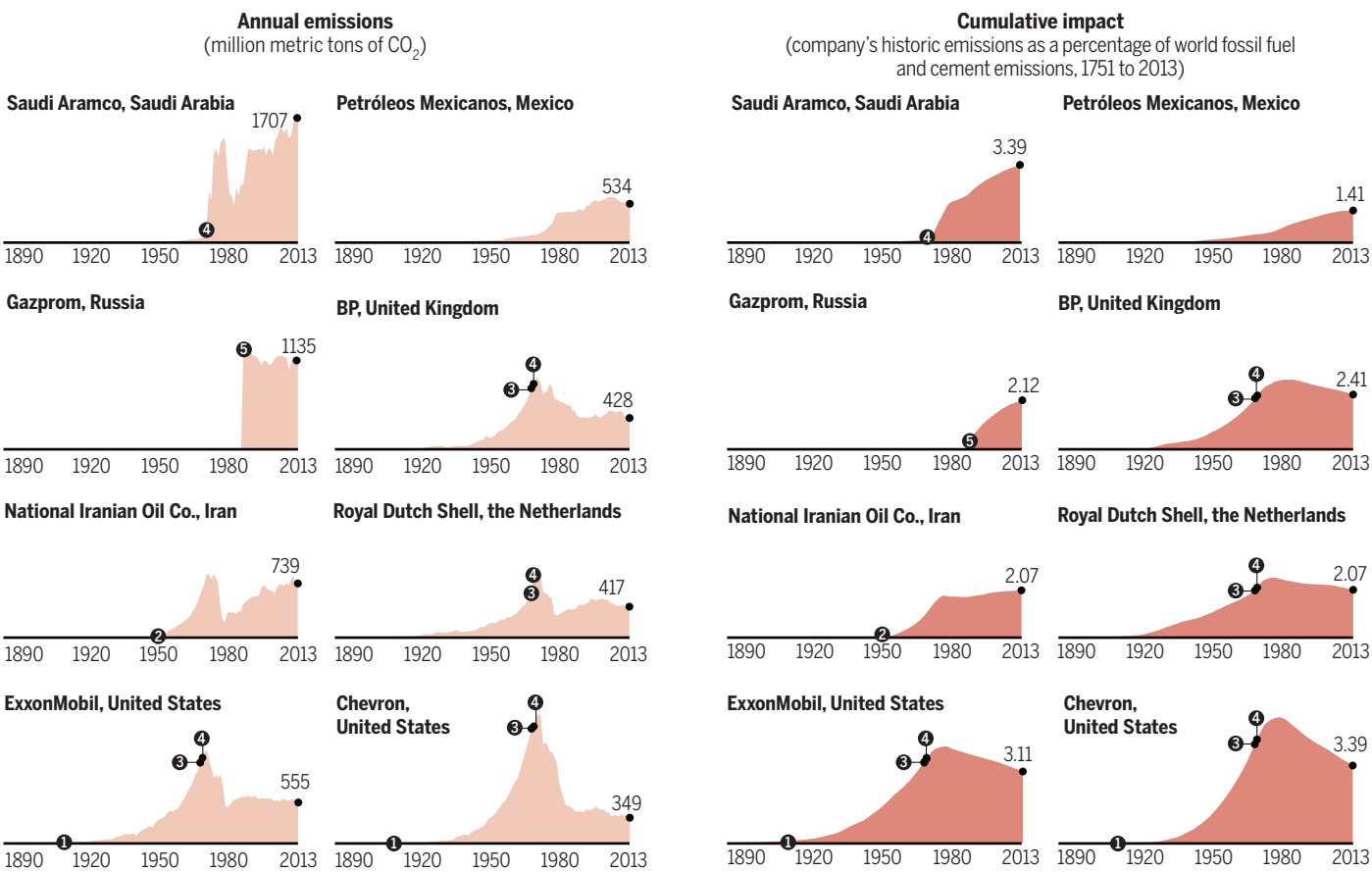

Downloaded from http://science.sciencemag.org/ on September 3, 2016

CREDITS: (GRAPHIC) J. YOU/SCIENCE; (DATA) RICHARD HEEDE

Published by AAAS

environmental justice cases to redress the fact that poor people disproportionally suffer from pollution. By the early 2000s, it was becoming clear that the poor will also face the heaviest impacts of climate change. But how do you structure a liability case when the entire world takes part in the carbon economy? Can a Pacific Islander whose town has been flooded sue 7 billion people? Searching for more specific culprits, Peter Roderick, head of the Climate Justice Programme for Greenpeace International in London, commissioned Heede to study ExxonMobil and quantify total greenhouse emissions across its history.

He would have to follow a tangled corporate path. Founded as Standard Oil by John D. Rockefeller in 1870, the company became one of the world's largest multinationals until 1911, when the Supreme Court split it into several "baby Standards." Decades later, two of the largest of those firms merged to form ExxonMobil. Heede tracked down production figures in annual reports scattered among university archives on two continents, supplemented by court documents, news reports, and academic and industry papers. Then he converted production volumes to CO_2 and methane. He included direct emissions, for instance from the fuels used to run the company's operations, and indirect emissions released by the combustion of its products.

After 15 months of research, Heede concluded that ExxonMobil and its precursors had directly or indirectly emitted 20.3 billion metric tons of CO_2 and 199 million metric tons of methane. Friends of the Earth calculated that the quantity represented between 4.7% and 5.3% of humanity's industrial greenhouse gas emissions since 1882.

"I thought, 'This is exactly the kind of thing I had in mind,'" Roderick recalls. "But I knew it was just a small part of the big picture."

Roderick commissioned Heede to look at the entire fossil fuel industry. To make the project manageable, they limited it to companies that produced at least 8 million tons of carbon per year, the so-called "carbon majors." The research took 8 years. Money from the original grant ran out, and after the crash of 2008 Heede's consulting business collapsed. He maxed out his credit card, borrowed against his Colorado house, and scraped by, enlisting graduate students in several countries to photocopy and send him papers, which he checked and double-checked with a watchmaker's precision. He filled shelves with binders of information and spent thousands of hours entering it into spreadsheets, working alone, often until midnight. "I take pleasure in that kind of stuff," Heede says. "I like to pay attention to detail."

SITTING AT DUAL MONITORS in the captain's cabin of his houseboat, Heede takes me on a tour of his data set, a seemingly endless series of color-coded and cross-indexed spreadsheets. Each sheet lists hundreds of entries, with columns showing the year and total production volumes for products such as crude oil, natural gas, and varieties of coal. Clicking on a company's name opens additional spreadsheets with the company's year-by-year production, plus screenshots of its annual reports for verification. Color-coded flowcharts display the evolution of companies as they separated or merged. The flowcharts from Russia are particularly ornate, as they incorporate the transformation of companies after the fall of the Soviet Union. (Heede got production data for the Soviet companies from Central Intelligence Agency analyses and the International Energy Agency.) Detailed annotations reveal his methods and calculations. The structure of these charts, so layered and interlocking, seems almost medieval in its complexity, and Heede seems monklike in his devotion to compiling it.

The result, peer reviewed and published in *Climatic Change*, showed that just 90 companies contributed 63% of the greenhouse gases emitted globally between 1751 and 2010. Half of those emissions took place after 1988—the year James Hansen of NASA testified to Congress that there was no longer any doubt that global warming had begun.

> ***"Frankly, we're all the users and therefore we're all guilty."***
>
> **David Victor**, University of California, San Diego

The data "just blew me away," says Naomi Oreskes, a science historian at Harvard University and co-author of the book *Merchants of Doubt*, which compares the fossil fuel industry to the tobacco industry in its efforts to raise doubts about science. "Everyone talks about this as a problem since the Industrial Revolution, but I now think that's incorrect," she says. Heede has shown that the roots of the problem are more recent and easier to trace. In 2011, Oreskes joined Heede in creating the Climate Accountability Institute, a nonprofit devoted to quantifying the contribution of fossil fuel companies to climate change and investigating their alleged attempts to obfuscate the science.

Other people criticize the work as oversimplified and naïve. David Victor, a political scientist and energy policy specialist at UC San Diego and a co-author of the 2015 Intergovernmental Panel on Climate Change report, doesn't question Heede's numbers but says his approach is wrongheaded. "It's part of a larger narrative of trying to create villains; to draw lines between producers as responsible for the problem and everyone else as victims. Frankly, we're all the users and therefore we're all guilty. To create a narrative that involves corporate guilt as opposed to problem-solving is not going to solve anything."

Heede concedes that the responsibility is shared. "I as a consumer bear some responsibility for my own car, etcetera. But we're living an illusion if we think we're making choices, because the infrastructure pretty much makes those choices for us." He focused on fossil fuel companies, he says, because unlike industries that produce greenhouse gases as a byproduct (such as the automobile industry, which has adhered to increasingly strict mileage standards), the mission of fossil fuel companies is to pull carbon out of the ground and put it into commerce.

His data, together with an emerging line of research that uses computer models to discern how likely it is that a given storm, flood, or heat wave was related to human-caused emissions, are now driving efforts to allocate responsibility for climate change. Last year, for instance, several nongovernmental organizations in the Philippines filed a petition with that nation's Commission on Human Rights. It asks the "carbon majors" to take remedial actions on behalf of typhoon survivors in the islands, which suffer devastating storms that may have worsened as a result of climate change. "Heede's report is one of the bedrock pieces of science and research that helped form our campaign," says Kristin Casper, litigation counsel for Greenpeace's Global Climate Justice and Liability Project in Toronto, Canada. In late July, the commission sent orders to 47 of the world's largest investor-owned fossil fuel companies, asking them to respond to the human rights charges in the petition. Similar actions and lawsuits are proceeding in several other countries.

Now, Heede is extending his carbon accounting into the future, quantifying the potential carbon release from future fossil fuel exploration. Like the other recipients of Representative Smith's subpoena, he has no intention of complying with what he calls a "campaign to intimidate us and stop scientific research." At the same time, he confesses an admiration for the fossil fuel industry, which has made "fantastic efforts to find resources for the betterment of humanity," often in the harshest environments. They've done such a good job that we haven't paused to reflect on the unintended consequences, he says. "And now we have to cope with the result." ■

Douglas Starr is co-director of the program in science journalism at Boston University.

Downloaded from http://science.sciencemag.org/ on September 3, 2016

Published by AAAS

A pig liver sausage named figatellu (left) has been linked to hepatitis E infections.

PHOTO: HEMIS/ALAMY STOCK PHOTO

EUROPE'S NEW HEPATITIS PROBLEM

Many get infected with hepatitis E, and a few get very sick. How can the virus be stopped?

By **Kai Kupferschmidt**

Almost immediately after Holger Stadler* received a new heart, his body began to reject it. To save the 58-year-old retired plumber from northern Germany, doctors replaced his blood plasma with donated plasma lacking the antibodies that targeted the donor organ. It worked—but 3 years later, it's clear that Stadler received something else in the bargain: the hepatitis E virus (HEV).

It's a pathogen that most people get rid of easily without even getting sick. But Stadler is taking drugs that dampen his immune system to prevent another rejection of his heart. As a result, he can't clear the virus; it has been quietly replicating in his liver ever since. "If that is not resolved, it leads to liver fibrosis, then liver cirrhosis, then death," Sven Pischke, his doctor at the University Medical Center Hamburg-Eppendorf, says matter-of-factly. "That was a shock, of course," Stadler says.

Patients like him are a new challenge for European physicians. Until a few years ago, no one even knew they existed. Hepatitis E was seen as an exotic disease that travelers from India or Africa sometimes brought home. Now, it's clear that there's a silent epidemic of the virus at home, with an estimated 300,000 people infected annually in Germany alone. Most appear to catch it from eating pork, with blood and plasma transfusions playing a smaller role. The virus occurs in other developed countries as well—including the United States, Japan, and Australia—though infections appear to be much rarer there.

Scientists are still scrambling to understand the epidemiology of hepatitis E, but they know that in Europe, infection rates rival those for other major hepatitis pathogens (A, B, and C). Two questions are looming large: Should blood donations be screened for the virus? And what can be done to eliminate it from swine herds?

RESEARCHERS SUSPECTED a new form of hepatitis in 1978, when hundreds of people in Jammu and Kashmir, in northern India, got sick—and four men and six pregnant women died—from what appeared to be a waterborne hepatitis virus. Similar but larger outbreaks followed in India, Pakistan, and China, killing thousands of people, many of them pregnant women. It wasn't until 1983 that Russian scientist Mikhail Balayan isolated the virus from his own stool after a gutsy self-experiment: He drank a cocktail of yogurt and stool samples from Soviet soldiers infected in Afghanistan. Hepatitis E became known as an important waterborne pathogen in Asia and Africa; two strains, named genotype 1 and 2, together kill an estimated 58,000 people per year.

But in 1997, scientists discovered that pigs in the U.S. Midwest carried a new strain of the virus, which they named genotype 3. It was soon identified in European pigs as well, and surveys showed that many Europeans had antibodies to it, a sign they had been infected at some point in their lives. Genotype 3 was very different from its relatives: Pork, not dirty water, appeared to be its main transmission route, and it seemed not to cause any symptoms. "Hepatitis E does not exist," says Hans Zaaijer, who heads the department of bloodborne infections at Sanquin, a nonprofit blood transfusion service in Amsterdam.

Downloaded from http://science.sciencemag.org/ on September 3, 2016

Published by AAAS

"These are two completely distinct diseases." (It's not clear whether genotype 3 might also spread in developing countries, hiding in the shadow of its more obvious relatives.)

Alas, the new strain wasn't as innocuous as it seemed. In 2008, French researchers reported that in a group of 300 recent transplant patients, 14 had an acute hepatitis E infection. Six got rid of the virus quickly, but eight couldn't seem to shake it. At Hannover Medical School in Germany, hepatitis specialist Heiner Wedemeyer couldn't believe it at first. "We are one of the largest transplantation centers in Europe," he remembers thinking. "We would have seen that." But when he started screening patients he soon found some that were chronically infected with hepatitis E, as did other clinics all over Europe. Patients had one thing in common: a weakened immune system.

There's not much doctors can do to help them. For transplant patients, one option is lowering the doses of immunosuppressive drugs to allow the immune system to regenerate, but this increases the risk of organ rejection. Doctors also use ribavirin, a drug approved for hepatitis C and several other viral infections. But there hasn't been a controlled trial yet, and ribavirin has serious side effects.

These patients are the visible part of a much wider epidemic. Surveys have shown that 17% of adults in Germany have antibodies against the virus, meaning they became infected at some point; so do 14% in Austria, 4% in southern Italy, and 27% in the Netherlands. One Dutch study found that antibody levels in people aged 18 to 21 dropped from almost 20% in 1995 to less than 5% in 2000, then rose again to 13% in 2011, which suggests the infection is re-emerging, says Zaaijer, a co-author on the study.

Blood and blood products account for at least some of the new infections. One study suggested that 1200 blood components containing the virus are transfused each year in the United Kingdom, and roughly one in a thousand blood donors in the Netherlands carries the virus. (By contrast, a recent U.S. study found the virus's genetic material in just one donor per 9500.)

A much bigger risk factor is the consumption of sausages and other pork products. Hepatitis E has been shown to be ubiquitous in swine herds in many European countries. Most animals become infected without getting sick between 3 and 6 months after birth, when antibodies inherited from their mothers start to wane. And there's strong evidence that the virus is passed on to humans through pork. In one study, Wim van der Poel, a veterinary virologist at Wageningen University and Research Centre in the Netherlands, analyzed hepatitis E sequences found in Dutch blood donors between 2010 and 2015. "When we looked for the closest sequence ever found, [it] was always a swine sequence from the same region," he says.

What's unclear is which pork products carry the highest risk. In one region in the south of France, infections have been linked to consumption of figatellu, a pig liver sausage that's often eaten raw. Scientists are still trying to pinpoint which other products contain the virus. It's difficult to culture the virus from meat products, and looking directly for viral RNA is technically complicated; moreover, finding RNA does not mean the food contains intact virus that can infect a consumer. Meanwhile, some studies have also shown a risk from eating shellfish or fruit.

In the United States, in contrast, hepatitis E "is very rare even in transplant patients and the immunosuppressed," says Jay Hoofnagle of the National Institute of Diabetes and Digestive and Kidney Diseases in Bethesda, Maryland. One theory is that U.S. residents eat less raw or undercooked pork. Another theory: Pigs in Europe may suffer from immune deficiencies because of some other infection. "An HIV-like agent may cause pigs or wild boar to develop chronic HEV infection," Hoofnagle says.

WITH SO MANY UNKNOWNS, controlling this silent epidemic is a challenge. Ireland already screens blood products for hepatitis E, and other countries are debating doing so. Like everything else involving the blood supply, "it's a touchy subject," Pischke says. Screening is costly and may not make sense for the general population, which has little to fear from HEV, says Rainer Seitz, head of transfusion medicine at the Paul Ehrlich Institute in Langen, Germany, a federal institute responsible for blood safety. But he supports screening blood products before use in immunocompromised patients. The virus's apparent ubiquity in pork products and elsewhere in the environment also makes general blood screening questionable, Zaaijer says. "It's like screening donors for flu in times of flu. The blood is safe, but the air isn't," he says. It's far more important to make food and water free of hepatitis E, he adds.

One way to do that would be to vaccinate pigs. A human vaccine has already been approved in China, and scientists think a swine vaccine is feasible as well. But getting pig farmers to adopt it would be difficult, Van der Poel predicts, because their animals don't get sick. And you'd have to be careful to vaccinate every last animal in a herd, Zaaijer adds; otherwise, the virus might just spread slowly, meaning that animals would get infected later in life, closer to slaughter, which might increase the risk in meat.

Reimar Johne, who studies hepatitis E at the Federal Institute for Risk Assessment in Berlin, is trying to find out how the virus can be inactivated in food. Twenty minutes at 70°C destroys it, but what about drying, smoking, or curing meat? To find out, Johne has started to make sausages in the lab himself. After adding a strain of hepatitis E, he can process the meat any way he wants and check whether viable virus survives. "It's a bit artificial," he says. "But for the moment, it's all we have." ■

**Holger Stadler's name has been changed at his request.*

The two faces of hepatitis E

Genotype 3 primarily spreads through pork and causes "silent epidemics" in developed countries, as does genotype 4. Genotypes 1 and 2 spread through dirty water and cause outbreaks, often with many deaths, in the developing world.

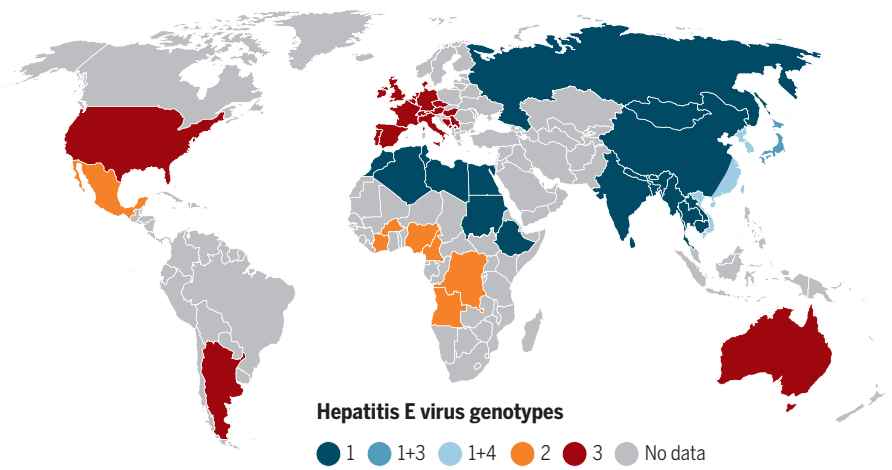

MAP: ADAPTED BY A. CUADRA/SCIENCE FROM Z. HUSSAIN, *GENOMIC HETEROGENEITY OF HEPATITIS VIRUSES (A-E): ROLE IN CLINICAL IMPLICATIONS AND TREATMENT*, PRACTICAL MANAGEMENT OF CHRONIC VIRAL HEPATITIS (29 MAY 2013)

Downloaded from http://science.sciencemag.org/ on September 3, 2016

Published by AAAS

Downloaded from http://science.sciencemag.org/ on September 3, 2016

ECONOMICS

Hassles versus prices

How can subsidized health products best target those who value them?

By **Benjamin A. Olken**

Suppose that a government or NGO has a valuable health product, such as bed nets to prevent infection by malarial mosquitoes or hand soap to prevent the spread of disease. It wants to distribute this product to those who need it, but not everyone needs or will use the product. Thus, if the organization gives the product away for free, a substantial amount may be wasted. On page 889 of this issue, Dupas *et al.* show that introducing small hassles, such as visiting a store each month to redeem a voucher, can be a much more effective way of reducing wastage than charging for the product (*1*).

Many organizations and governments charge a price even for heavily subsidized goods to screen out those who would not use the product. The idea is that those who would not use a product value it less and would not buy it once it is priced. However, if the product is needed most by the poor, those who need it the most may no longer be able to afford it. Several studies have found that raising prices for these types of goods substantially reduces take-up but does not dramatically change usage rates among those who obtain the product (*2*–*6*). In short, charging a price screens out people not just based on how much they will use the product but also based on income.

Dupas *et al.* aimed to find an alternative way to eliminate wastage without charging a monetary price and thus discourag-

Department of Economics, Massachusetts Institute of Technology, Cambridge, MA 02139, USA. Email: bolken@mit.edu

PHOTO: DANITA DELIMONT/ALAMY STOCK PHOTO

Published by AAAS

ing the very poor. In their experiment, they compare three mechanisms for distributing a chlorine solution for treating household drinking water in Kenya: giving the chlorine away for free door-to-door to those who want it, offering people at their doorstep the option to buy chlorine at 50% off the retail price, or giving them a voucher that can be redeemed each month for free chlorine at a nearby shop. The key idea of the third mechanism is that going to the shop is a small hassle, costing time (scarce for both poor and rich) rather than money (particularly scarce for the poor).

Rural populations in many African countries do not have access to safe drinking water. A study in Kenya shows that giving out free water treatment vouchers helps to reach those households that need or will use the water treatment.

PHOTO: OLIVIER ASSELIN/ALAMY STOCK PHOTO

The experimental findings show that this type of small hassle can work. Requiring households to redeem the vouchers every month reduces the amount of chlorine given out by 60 percentage points compared with the free distribution group. Yet, the share of households actually using the chlorine falls by only 1 percentage point: 32.9% of households in the voucher group had water that tested positive for chlorine, compared with 33.9% in the free distribution group. Vouchers dramatically reduce wastage with only minor reductions in usage.

Charging a price, by contrast, screens out more households that would have used the product. Only 12.4% of households offered chlorine at 50% off the retail cost had water that tested positive for chlorine. Poorer households that may have used the chlorine under the voucher or free distribution treatment were screened out by the price.

The idea that time costs can be used to help target the poor is not limited to subsidized health products. The basic idea is that, whereas money is particularly scarce for the poor, time is not, and so time costs can be used to screen (*7*). This does not imply that the poor do not value their time—of course they do—but rather that the relative trade-off of time versus money is different for the poor, precisely because money is relatively scarcer than time for the poor.

For example, in an experiment in Indonesia, my coauthors and I found that in villages where people had to come to a government office to apply to be screened for a cash transfer program, the resulting group of program recipients was poorer on average than in villages where government representatives screened all potential recipients at home (*8*). The logic in that case was slightly different than in Dupas *et al.*'s study, but the result was the same. In the Indonesia transfer program, middle-class people knew that they were unlikely to pass the screening test, whereas poor people thought they would be likely to pass. When faced with a hassle cost—having to go to a government office and wait to be screened—those who do not expect to get the benefits, the middle class, self-select themselves out. But if the government comes to your house to give you the screening test at your doorstep, the cost of being screened is essentially zero, so even the middle class figure they might as well try—and since the formula is imperfect, some may wrongly qualify for benefits.

Other types of government benefit programs similarly use time costs to try to select just the poor for assistance. Workfare programs, such as the Works Progress Administration (WPA) in the United States during the Great Depression or the Mahatma Gandhi National Rural Employment Guarantee Act (MGNREGA) in India today, are based on a similar idea. These programs guarantee low-paying, manual labor–based employment to anyone who needs it. The unemployed can access these government benefits by working. But people with another job cannot take up the program, because they need to spend that time working elsewhere. And, indeed, the poor and those who have the most difficult time finding regular work are the ones who disproportionately take up these programs (*9*, *10*).

The key innovation of Dupas *et al.*'s study is to show that these same ideas—making people spend some time to claim a benefit—can be used for a different purpose, namely to target subsidized health products to those who need them. It is important, of course, that the time the poor spend on claiming benefits is not so onerous that it outweighs the benefits from better screening. But when this can be done, it is an important way of screening that, in contrast to prices, does not cut off those who may need the products the most. ■

REFERENCES

1. P. Dupas, V. Hoffmann, M. Kremer, A. P. Zwane, *Science* **353**, 889 (2016).
2. J. Cohen, P. Dupas, *Q. J. Econ.* **125**, 1 (2010).
3. N. Ashraf, J. Berry, J. M. Shapiro, *Am. Econ. Rev.* **100**, 2383 (2010).
4. J. Berry, G. Fischer, R. P. Guiteras, "Eliciting and utilizing willingness to pay: Evidence from field trials in Northern Ghana," 2015, see http://personal.lse.ac.uk/fischerg/Assets/BFG-EUWTP.pdf.
5. Abdul Latif Jameel Poverty Action Lab (JPAL), "The price is wrong," April 2011, www.povertyactionlab.org/publication/the-price-is-wrong.
6. P. Dupas, *Science* **345**, 1279 (2014).
7. A. L. Nichols, R. J. Zeckhauser, *Am. Econ. Rev.* **72**, 372 (1982).
8. V. Alatas *et al.*, *J. Polit. Econ.* **124**, 371 (2016).
9. P. Dutta, R. Murgai, M. Ravallion, D. P. Van de Walle, "Does India's employment guarantee scheme guarantee employment?" *World Bank Policy Research Working Paper*, no. 6003, 2012.
10. R. A. Margo, *J. Econ. Hist.* **51**, 333 (1991).

10.1126/science.aah5055

Downloaded from http://science.sciencemag.org/ on September 3, 2016

Published by AAAS

ORGANIC SYNTHESIS

Building molecular complexity from scratch

The Pauson-Khand cycloaddition reaction builds the tetracyclic core of (+)-ryanodol

By **Xavier Verdaguer**

Cycloaddition reactions convert simple unsaturated components into cyclic products. Because cyclic molecules are intrinsically more complex than linear ones, cycloaddition reactions are ideally suited for building molecular complexity that characterizes many natural products used as pharmaceuticals. The equivalent to the Diels-Alder reaction for forming six-membered rings in the construction of five-membered rings is the Pauson-Khand reaction, a [2+2+1] cycloaddition reaction between an alkene, an alkyne, and carbon monoxide. On page 912 of this issue, Chuang *et al.* (*1*) have used a rhodium-catalyzed Pauson-Khand reaction to assemble the tetracyclic core of (+)-ryanodol in an elegant 15-step synthesis.

Institute for Research and Biomedicine (IRB Barcelona), Barcelona Institute of Science and Technology, Baldiri Reixac 10, 08028 Barcelona, Spain. Departament de Química Inorgànica i Orgànica, Secció Orgànica, Universitat de Barcelona, Martí i Franquès 1, 08028 Barcelona, Spain. Email: xavier.verdaguer@irbbarcelona.org

The Pauson-Khand reaction represented a second chance for Peter Pauson to be remembered in the chemistry community. He first came to prominence as the discoverer of ferrocene (*2*, *3*). When he visited my department in the early 1990s, he always spoke about the "Khand" reaction, referring to his postdoctoral associate Ihsan U. Khand, who discovered in the 1970s what we call now the Pauson-Khand reaction while working with alkyne cobalt complexes and strained alkenes (*4*).

The Pauson-Khand reaction (*5*) generates three new carbon bonds as it forms a cyclopentenone in one step. The Pauson-Khand reaction is a metal-promoted or -catalyzed process. Cobalt is the most widely used metal for this transformation, but other metals—such as rhodium, iridium, titanium, iron, and palladium—were reported to do the job. When a substituted alkene is used, a chiral cyclopentenone arises, thus allowing the development of enantioselective cyclizations.

Complex molecules isolated from the plant or the animal kingdoms that show useful pharmaceutical activity usually need to be made synthetically to meet demand. Synthetic chemists quickly realized the potential of the Khand and Pauson cycloaddition process and embraced it in natural product synthesis. The most widely used variant is the intramolecular version of the process, in which the alkyne and alkene units are linked, as in the synthesis of propindilactone G reported (see the figure) (*6*). In the intramolecular Pauson-Khand reaction, two rings are generated (highlighted in red). The chirality of the new ring system is substrate-dependent and is dictated by the chirality of the starting material. The intramolecular process is reliable for the synthesis of [3.3.0] and [3.4.0] bicyclic systems, and great advances have been made in the development of catalytic enantioselective processes (*7*).

In contrast, the intermolecular version of the Pauson-Khand reaction is underdeveloped and lags behind in its applications in the synthesis of natural products, mainly for two reasons. First, only strained alkenes react efficiently in the intramolecular process. Second, in practice, only cobalt carbonyl

Making five-membered rings

The Pauson-Khand reaction is the cycloaddition between an alkyne (blue), an alkene (green), and carbon monoxide. For the intermolecular reaction, a cyclopentenone (red) is generated (axinellamines A and B). For the intramolecular reaction, a fused bicyclic system (red) is formed (propindilactone G and ryanodol). Boc, *tert*-butyloxycarbonyl; NMO, *N*-methylmorpholine-*N*-oxide; DCM, dichloromethane; Ar, aryl; Me, methyl.

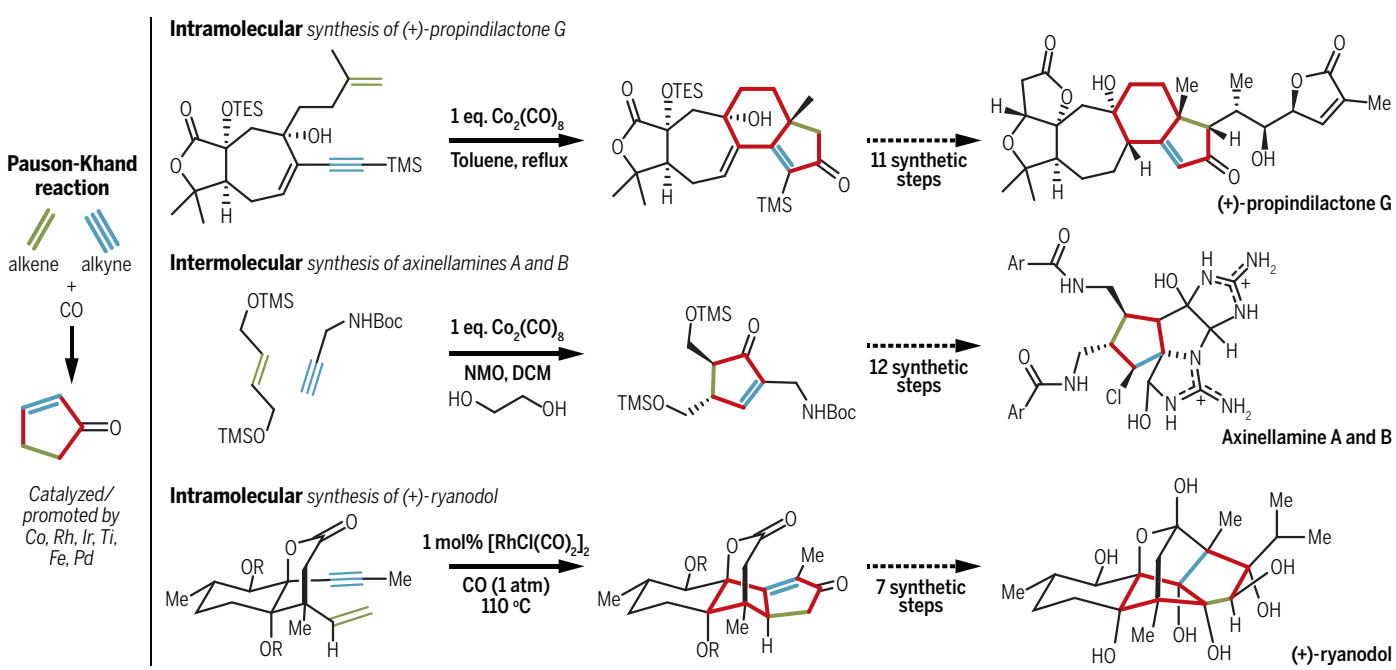

GRAPHIC: V. ALTOUNIAN/*SCIENCE*

Downloaded from http://science.sciencemag.org/ on September 3, 2016

Published by AAAS

complexes are suitable promoters for this process. Cobalt-alkyne complexes bearing chiral ligands have been used stoichiometrically in the reaction with norbornadiene in the asymmetric synthesis of carbanucleosides and 13-epi-12-oxo-phytodienoic (*8, 9*). However, efforts to turn this into a catalytic method have had limited success (*10*).

An encouraging result with respect to widening the scope of olefins used in the intermolecular reaction can be found in the racemic synthesis of axinellamines 1 and 2 (see the figure). Su *et al*. described the intermolecular Pauson-Khand reaction of a nonstrained symmetrically substituted *E*-olefin to build a cyclopentenone at the first step of the synthesis (*11*). After 12 steps, this cyclopentenone was elaborated to yield the natural product.

The synthesis of anxinellamines reflects the versatility of the cyclopentenone core. The α,β-unsaturated carbonyl can undergo multiple transformations, such as the classical 1,4- and 1,2-additions. In the synthesis of (+)-ryanodol, Chuang *et al*. present a stunning transformation of a cyclopentenone, in that a simple oxidation with SeO_2 provides a rearranged dihydroxy enone with all the hydroxyl groups in place with the right configuration. This single transformation and the Pauson-Khand cyclization are the key steps in the synthesis and allow for concise synthesis.

We can expect catalytic methods such as that used to synthesize (+)-ryanodol to become a general trend when performing an intramolecular cyclization. The biggest challenges, however, lay ahead for the intermolecular version. In this context, it would be desirable to increase the range of olefins that can be cyclized efficiently. Also, the development of catalytic enantioselective methods is underdeveloped. Advances in this direction will probably derive from ligand engineering efforts to increase the reactivity toward the alkene fragment. The cyclization discovered by Khand and Pauson will continue to find exciting applications in the synthesis of complex natural products, and developments are expected to further increase the potential of this fascinating reaction. ■

REFERENCES

1. K. V. Chuang *et al.*, *Science* **353**, 912 (2016).
2. H. Werner, *Angew. Chem. Int. Ed.* **53**, 3309 (2014).
3. J. I. Seeman, S. Cantrill, *Nat. Chem.* **8**, 193 (2016).
4. I. U. Khand *et al.*, *J. Chem. Soc. Perkin Trans.* **1**, 977 (1973).
5. R. Rios, *The Pauson-Khand Reaction: Scope, Variations and Applications* (Wiley, 2012).
6. L. You *et al.*, *J. Am. Chem. Soc.* **137**, 10120 (2015).
7. T. Shibata, *Adv. Synth. Catal.* **348**, 2328 (2006).
8. A. Vázquez-Romero *et al.*, *Org. Lett.* **10**, 4509 (2008).
9. N. Aiguabella *et al.*, *Org. Lett.* **15**, 2696 (2013).
10. S. Orgué *et al.*, *Org. Lett.* **17**, 250 (2015).
11. S. Su *et al.*, *J. Am. Chem. Soc.* **133**, 13922 (2011).

10.1162/science.aah5871

CONSERVATION

Do you speak lion?

To be effective, conservation decisions must be transparent and based on diverse views

By **W. M. Adams**

Problems in biodiversity conservation tend to be highly complex, encompassing both biological and social systems and their interactions (*1*). Many have argued for multidisciplinary research in conservation, particularly a more effective engagement of the human sciences (*2*). But even when multidisciplinary, research may not be able to deliver the insights needed to solve a conservation problem. Recent studies help to elucidate these challenges and show how research can be effective in underpinning conservation decisions (*2*–*5*).

A typical example of a complex conservation problem is crop raiding by wild elephants in countries such as Kenya. Efforts to address crop raiding in Laikipia, Kenya, have included study of elephant ecology and movement, development of on-farm deterrence techniques, and research with the local community (*6*). An 80-km electric fence constructed in 2007 raised hopes that a more permanent solution to the problem had been found, but the fence was poorly maintained and repeatedly broken and crossed by elephants (*7*). Elephants learned how to break the fence and taught each other how to do so, and no local actor was willing to maintain the fence. Smallholders welcomed the protection against crop raiding, but also wanted to cross the fence to water their cattle. Ranch managers welcomed elephants and hoped that an official boundary fence would help secure their land rights, but were reluctant to pay to maintain the fence and did not trust smallholders enough to permit access to their land to maintain it. Pastoralists whose animals were denied passage opposed the fence (*7*). The fence is now being rebuilt to a new design, with improved monitoring and management protocols in place; it remains to be seen whether the new system is more effective.

"The complexities of social-ecological systems and the contested politics of conservation decisions place great demands on expertise."

Department of Geography, University of Cambridge, Downing Place, Cambridge CB2 3EN, UK. Email: wa12@cam.ac.uk

EXPERTS AND EXPERTISE

Faced with such complexity, conservation decisions increasingly rely on the knowledge and advice of experts, particularly scientists. However, confronted with complex social-ecological systems, experts may vary markedly in their ideas and conclusions. For example, Stier *et al*. recently analyzed expert perceptions of ecosystem interactions in the Northeast Pacific Ocean (*5*). They invited individual experts to describe the number, direction, and strength of food web interactions connected directly or indirectly to populations of Pacific herring (*Clupea pallasii*), a fish of ecological, cultural, and economic importance. They then used fuzzy cognitive maps to compare each expert's understanding of the herring ecosystem. Individual experts had different perceptions of the number of ecological connections, the influence of focal functional groups, and their interaction strengths in the herring food web. These differences in perceptions affected expert responses to hypothetical scenarios in which either herring predators or prey increased.

Protocols for evidence-based conservation suggest ways to capture and clarify expertise—for example, through a hierarchical approach of progressive synthesis through scientific investigations, systematic reviews, summaries, and decision-support systems (*8*). However, Stier *et al*.'s study shows how experts can differ in their understanding of the interaction of natural and social systems, or in the knowledge they draw on (scientific, local, or traditional ecological knowledge and/or practical experience). Differences in expert views did not reflect conventional knowledge categories such as local, scientific, and traditional (*5*). This would make it difficult to construct a representative panel of experts based on their backgrounds. In these circumstances, three things can contribute to making expertise an effective basis for conservation: transdisciplinarity, diversity, and transparency.

TRANSDISCIPLINARITY

It is almost a truism in conservation that complex contemporary problems demand an interdisciplinary approach (*9*). Yet interdis-

Downloaded from http://science.sciencemag.org/ on September 3, 2016

Published by AAAS

Pacific herring school within giant kelp off Catalina Island, California. In a recent study, Stier *et al*. (*5*) found that experts differed widely in their perceptions of food web interactions involving Pacific herring. This diversity of knowledge must be taken into account in conservation decisions.

ciplinary projects pose substantial demands on the people involved (*10*), exposing them to unfamiliar facts and arguments and to different ontologies and epistemologies (*11*). Early-career researchers involved in work outside their discipline (in fields with different conventions) may worry about implications for future careers. Moreover, empirical research on funding by the Australian Research Council's Discovery Programme shows that more interdisciplinary proposals are less likely to be funded (*12*). Interdisciplinary research can seem like an impractical and risky idea.

To overcome these problems, conservation research, like other fields, must overcome the constraints of specialization and the compartmentalization of knowledge and seek transdisciplinarity; that is, learning that operates independently of disciplinary boundaries (*13*). The challenge for conservation education and training, both in formal university courses and in professional and lifelong learning, is to create conservationists who are unconstrained by the disciplinary boundaries familiar to academic researchers. Conservationists must become accustomed to the ways in which diverse disciplines think, talk, and write, and must recognize each discipline's strengths and weaknesses (*2*).

DIVERSITY OF KNOWLEDGE

Successful responses to complex problems also require openness to diverse inputs, discussion, and dissent, and a willingness to entertain competing and creative options and to disrupt existing behaviors. Such "participatory" openness is commonly proposed, but is hard to deliver in the face of budget and time constraints. Game *et al*. stress the need to harness creativity in planning and suggest that conservationists should learn from new thinking in military planning. The latter emphasizes distributed leadership and a decentralized approach to strategic analysis that includes listening to people outside the established decision-making hierarchy (*1*).

One type of knowledge about social-ecological systems is informal and local (*14*). Such knowledge is embedded in cultural practice and place, and often reflects observation of system dynamics over long periods of time. As Stier *et al*. show in their study of the Pacific herring food web, the insights of local, indigenous, and scientific experts overlapped. Indeed, these categories are not discrete. The authors suggest that uncertainty would be best reduced by embracing a diversity of knowledge and encouraging dialogue about alternative management actions (*5*). Nursey-Bray *et al*. have argued that the terms "scientific knowledge" and "local knowledge" imply a crude and unhelpful binary distinction in the context of coastal zone management. Both local and scientific expertise have contributions to make to coastal planning, both in terms of understanding system change and in building mutual trust: Effective coastal management demands fluidity of response, and this is often best enabled by local innovation and commitment (*4*).

TRANSPARENCY

The third challenge is to make the process of reaching conservation decisions more transparent. Individual experts often disagree; their knowledge may be substantial but not necessarily objective, and uncertainties may be created by the challenges of knowledge integration, not least among different disciplines. The chain of reasoning that underpins expert views is an essential element in their legitimacy and usefulness (*5*).

One practical strategy is to publish the evidence used to reach conservation decisions to provide an evidence audit trail that can be followed and understood by later planners, and by anyone skeptical of the validity of the decisions made, for example, stakeholders suspicious of scientific methods or analysis (*3*).

SPEAKING LION

Conservation decisions affect numerous stakeholders, and conflicts are all too common. The complexities of social-ecological systems and the contested politics of conservation decisions place great demands on expertise. Conservation success could be improved by effective interdisciplinarity, openness to new and contrasting ideas, and a commitment to transparency to encourage dialogue about alternative management actions.

Such a transition will not be easy. Interdisciplinary collaboration is profoundly challenging, and opening up expert decision systems to local and indigenous knowledge is difficult to achieve in practice. For example, critics note the continuing underrepresentation of the humanities and social sciences in the work of the Intergovernmental Platform on Biodiversity and Ecosystem Services (IPBES) (*15*).

Wittgenstein famously observed that "if a lion could speak, we couldn't understand it" (*16*). But communication between disciplines and between experts and the public surely offers a lesser challenge. Such conversations will never be easy, but it is important to get them right. ■

REFERENCES

1. E. T. Game, E. Meijaard, D. Sheil, E. McDonald-Madden, *Conserv. Lett.* **7**, 271 (2014).
2. S. P. Pooley, J. A. Mendelson, E. J. Milner-Gulland, *Conserv. Biol.* **28**, 22 (2013).
3. L. V. Dicks *et al*., *Conserv. Lett.* **7**, 119 (2014).
4. M. J. Nursey-Bray *et al*., *Environ. Sci. Policy* **38**, 107 (2014).
5. C. Stier *et al*., *Conserv. Lett.* 10.1111/conl.12245 (2016).
6. M. D. Graham, B. Notter, W. M. Adams, P. C. Lee, T. N. Ochieng, *System. Biodivers.* **8**, 435 (2010).
7. L. A. Evans, W. M. Adams, *Land Use Policy* **51**, 215 (2015).
8. L. V. Dicks, J. Walsh, W. J. Sutherland, *Trends Ecol. Evol.* **29**, 607 (2014).
9. H. Ledford, *Nature* **525**, 308 (2015).
10. A. Viseu, *Nature* **525**, 291 (2015).
11. K. Moon, D. Blackman, *Conserv. Biol.* **28**, 67 (2014).
12. L. Bromham, R. Dinnage, X. Hua, *Nature* **534**, 684 (2016).
13. J. H. Bernstein, *J. Res. Practice* **11**, Article R1 (2015).
14. J. Mistry, A. Berardi, *Science* **352**, 1274 (2016).
15. K. Reuter, M. Timpte, C. Nesshöver, *Nature* **531**, 173 (2016).
16. L. Wittgenstein, *Philosophical Investigations* (Blackwell, 1953).

10.1126/science.aaf8056

PHOTO: NATIONAL GEOGRAPHIC CREATIVE/ALAMY STOCK PHOTO

Downloaded from http://science.sciencemag.org/ on September 3, 2016

Published by AAAS

GEOPHYSICS

"Weather bomb" induced seismic signals

Seismic waves generated by intense storms can reveal details of Earth's interior

By **Peter Gerstoft** *and* **Peter D. Bromirski**

The atmosphere-ocean system interacts with the solid Earth to produce seismic signals called microseisms, which are observed globally. This interaction results from large-scale, slowly moving extratropical storms but also from smaller, intense weather systems such as tropical cyclones (called hurricanes in the Atlantic and eastern Pacific, and typhoons in the western Pacific). These are smaller storms, often travel much faster, and have steeper atmospheric pressure gradients that produce very strong winds. All storm systems generate various types of microseisms, which have been studied extensively. A special case of fast-developing, small, extratropical storms in which the central pressure intensifies rapidly, dropping by more than 1 mbar/hour for 24 hours, is called a "weather bomb" (*1*). On page 919 of this issue, Nishida and Takagi (*2*) report on the detection of previously unobserved *S* wave microseisms generated under a weather bomb between Greenland and Iceland.

A small fraction of the gravity-wave energy generated by storms interacts with the seafloor and couples into wave-generated seismic surface and body waves, called microseisms. Microseisms are a multicomponent physics problem: Atmospheric pressure gradients produce winds over the ocean that generate ocean gravity wave systems; when these wave systems interact either with themselves or with other systems, signals at nearly double the ocean wave frequency are generated. This energy propagates as standing waves to the seafloor; at the seafloor, this acoustic wave energy is coupled into seismic energy, which then propagates to the seismic stations.

Seismic stations on land and on the seafloor are primarily used to record earthquake signals resulting from episodic fracturing of Earth's crust and operate continuously in order to capture these events. Thus, seismic stations also record the constantly occurring background microseismic noise. Although the contribution from individual ocean waves produces little by way of microseisms, groups of waves in combination generate seismic surface waves that can be analyzed in a statistical manner (*3*).

The spectrum of ocean wave–induced seismicity contains three peaks. The most energetic peak is at twice the frequency (0.08 to 0.34 Hz) of ocean surface waves. Standing waves at nearly double the frequency of the incident wave field result from the interaction of nearly opposing waves of the same frequency (*3*). The double-frequency (DF) standing waves have small wave numbers compared with ocean surface waves and thus couple efficiently to microseismic modes.

The third peak, the Earth's seismic "hum" (*4*), is centered at frequencies (0.002 to 0.03 Hz) much lower than those of ocean surface gravity waves and is predominantly generated by infragravity waves and interactions of ocean waves in near-coastal waters.

Ocean surface waves can be described by sinusoidal wave motions at a spread of frequencies and directions. When two ocean surface wave systems interact, they create quadratic source terms that produce propagating acoustic waves at the sum and difference frequencies of the wave systems, corresponding to DF microseisms and hum

Storms making waves

Pelagic *P* wave microseism sources trailing Super Typhoon Ioke, 22 August to 7 September 2006 (*12*). The best track of Ioke (from National Hurricane Center), in blue, tracks Ioke-generated *P* wave sources (red) using the Southern California Seismic Network (SCSN). Locations of *P* wave sources (red hexagons) and storm centers (blue circles) are marked every second day. (**Inset**) Ocean wave-wave interactions are strongest in the wake of Ioke, generating acoustic waves in the ocean that couple into seismic *P* waves at the seafloor. The *P* waves penetrate 2000 km into the earth and reach California 8000 km away, where they are observed at 150 seismic-stations of the SCSN network, allowing source localization with array processing.

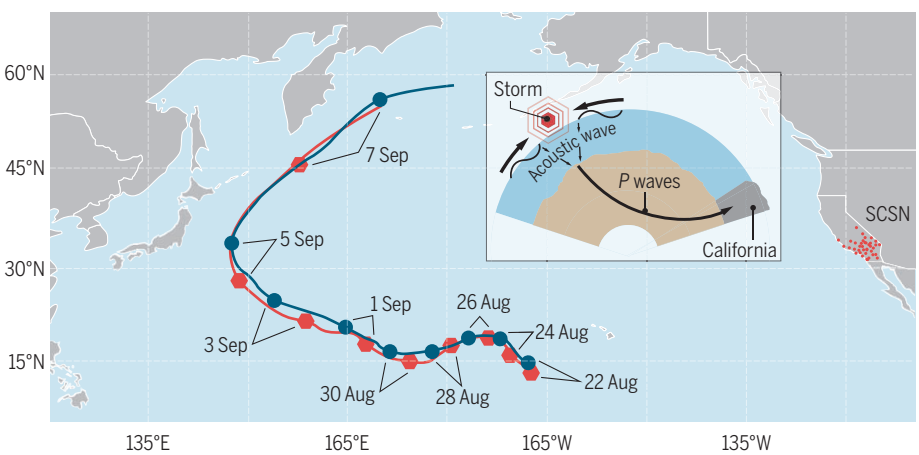

The second most energetic peak is the primary microseism peak, centered at the frequency (0.04 to 0.17 Hz) of ocean surface waves, results from the direct interaction of ocean waves with the seabed. Although ocean surface waves have much larger wave numbers than seismic modes, in environments with varying ocean depth in which the ocean wave spectrum varies spatially, nonlinear processes produce low-wave-number fluctuations that excite primary microseisms (*3*). Because ocean waves decay exponentially with depth, this generation process is limited to shallow water.

microseisms, respectively (*5*). DF microseisms are reasonably well-modeled by using ocean wave hindcasts (*6*). Microseisms are strongest when the wave systems are directly opposing because the pressure excitation produced by these interactions propagates nearly unattenuated to the ocean bottom.

The dominant seismic waves from DF wave interactions are surface-propagating Rayleigh waves. Although these waves are generated throughout ocean basins, the dominant contribution to the signal observed on land is generated in coastal re-

Scripps Institute of Oceanography, University of California, San Diego, La Jolla, CA 92093, USA. Email: gerstoft@ucsd.edu

GRAPHIC: ADAPTED FROM GERSTOFT *ET AL.* BY C. BICKEL/*SCIENCE* AND V. ALTOUNIAN/*SCIENCE*

Downloaded from http://science.sciencemag.org/ on September 3, 2016

Published by AAAS

gions. Surface wave microseisms from the deep ocean are generally not observed on land (*7*). However, microseismic body waves penetrate the deep Earth structure and can be observed at distant land seismic stations, with compressional *P* waves predominant (*8*). The recent observation of microseismic *S* waves by Nishida and Takagi and by Liu *et al.* (*9*) gives seismologists a new tool with which to study Earth's deeper structure.

Seismic arrays provide an opportunity to study microseism source locations and propagation characteristics. For surface waves, only the back-azimuth to their generation region can be determined. However, for seismic body waves, both back azimuth and range to the generation region can be obtained, giving additional information on propagation paths and crustal structure between the source and the receivers. These attributes of *P* wave microseisms allowed estimates of cyclone locations by using the Large Aperture Seismic Array in Montana installed in the 1960s for nuclear monitoring (*8*). In the 2000s, the transformative USArray has enabled more observations of microseism *P* wave body waves (*10*). The observed *P* waves can be linked to specific storms, such as waves from Hurricane Katrina hitting the coast near New Orleans in 2005 (*11*), and allowed the tracking of Super Typhoon Ioke across the Pacific (*12*) (see the figure) and Hurricane Sandy along the New England coast in 2012 (*13*).

By cross-correlating microseismic *P* waves, it is possible to determine the fine layer structure of the mantle-layer transition zone (*14*). Because *S* waves have shorter wavelengths than those of *P* waves and are more sensitive to state changes related to temperature and Earth composition, array processing of microseismic *S* waves (*2*, *9*) has the potential to add to our understanding of the deeper crust and upper mantle structure. ■

REFERENCES

1. F. Sanders, J. R. Gyakum, *Mon. Weather Rev.* **108**, 1589 (1980).
2. K. Nishida, R. Takagi, *Science* **353**, 919 (2016).
3. K. Hasselmann, *Rev. Geophys.* **1**, 177 (1963).
4. K. Nishida, *Annu. Rev. Earth Planet. Sci.* **41**, 719 (2013).
5. J. Traer, P. Gerstoft, *J. Geophys. Res.* **119**, 3317 (2014).
6. F. Ardhuin *et al.*, *J. Geophys. Res.* 10.1029/2011JC006952 (2011).
7. P. D. Bromirski, R. A. Stephen, P. Gerstoft, *J. Geophys. Res.* **118**, 3610 (2013).
8. R. A. Haubrich, K. McCamy, *Rev. Geophys.* **7**, 539 (1969).
9. Q. Liu *et al.*, *Earth Planet. Sci. Lett.* **449**, 39 (2016).
10. F. Landes *et al.*, *J. Geophys. Res.* 10.1029/2009JB006918 (2010).
11. P. Gerstoft, M. C. Fehler, K. G. Sabra, *Geophys. Res. Lett.* **33**, L17308 (2006).
12. J. Zhang, P. Gerstoft, P. D. Bromirski, *Geophys. Res. Lett.* **37**, L15301 (2010).
13. O. Sufri *et al.*, *Earth Planet. Sci. Lett.* **402**, 324 (2014).
14. P. Poli *et al.*, *Science* **338**, 1063 (2012).

10.1126/science.aag1616

CELL SIGNALING

Proline hydroxylation linked to Akt activation

Oxygen-sensing enzymes regulate the Akt kinase

By **Michael Voulgarelis** *and* **Philip N. Tsichlis**

Prolyl hydroxylases are oxygen-sensing enzymes that regulate the abundance of hypoxia-inducible factors (HIF)1α and HIF2α, which control the cellular response to oxygen deprivation (hypoxia). Three prolyl hydroxylases target the HIFα molecules, EglN1 (PHD2), EglN2 (PHD1), and EglN3 (PHD3) (*1*). All three are widely expressed iron (Fe^{++}) and α-ketoglutarate–dependent dioxygenases. When the oxygen tension is normal, they hydroxylate HIF1α and HIF2α. Hydroxylated HIFα molecules are recognized and ubiquitinated by an E3 ubiquitin ligase complex containing the von Hippel-Lindau tumor–suppressor protein pVHL (*1*), leading to their proteasomal degradation. Inactivation of prolyl hydroxylases during hypoxia results in the stabilization of HIFα molecules. On page 929 of this issue, Guo *et al.* present evidence that a prolyl hydroxylation–dependent pathway also plays an important role in the regulation of the Akt kinase, which in turn is a key player in oncogenesis (*2*).

"...inhibition of Akt may be therapeutically beneficial in pVHL-null and other tumors with mutations interfering with Akt hydroxylation."

Akt, also known as protein kinase B (PKB), is a member of the AGC family of serine-threonine protein kinases (*3*). There are three closely related Akt isoforms (Akt1/PKBα, Akt2/PKBβ, and Akt3/PKBγ). Activation of Akt, which in the absence of activation signals is catalytically-inactive, is phosphoinositide 3-kinase (PI3K)–dependent (*4*). PI3K generates D3-phosphorylated phosphoinositides at the cell membrane. Binding to these phosphoinositides results in the recruitment of Akt to the cell membrane, where it is phosphorylated at multiple sites by other membrane-associated kinases (*4*, *5*). Phosphorylation plays a critical role in Akt activation. One of the two main sites of Akt phosphorylation, Thr^{308}, is dephosphorylated by protein phosphatase 2A (PP2A) (*6*). PP2A is a multimeric phosphatase composed of a scaffold A subunit, a catalytic C subunit, and one of 26 regulatory/targeting B subunits. Access of PP2A to the phosphorylated Thr^{308} site is modulated by intramolecular interactions in the Akt catalytic cleft and by phosphorylation of the B55 subunit (*7*). It can also be modulated by Akt-interacting proteins. It is not known whether these interacting proteins simply join phosphorylated Akt with the phosphatase, or also modulate the intramolecular interactions that control accessibility of the phosphatase to phosphorylated Thr^{308}. Other modifications contributing to the activation of Akt include acetylation, glycosylation, oxidation, ubiquitination, and SUMOylation (*5*). Guo *et al.* now add proline hydroxylation to this list.

There are two types of mutations in the tumor-suppressor gene *pVHL* that are associated with cancer (*8*). Type 1 mutations result in deletion or truncation, and when truncated, the pVHL protein becomes misfolded and inactive. The loss of pVHL function results in the up-regulation of HIFα, high risk of renal cell carcinoma, and low risk of pheochromocytoma. Earlier studies had shown that, in addition to upregulating HIFα, type 1 mutations also activate Akt (*9*). Guo *et al.* confirmed this finding and also showed that HIFα induction is not required for the activation of Akt in pVHL-null tumors. Because pVHL is recruited to its targets by proline hydroxylation, the authors proceeded to show that EglN1, one of the three prolyl hydroxylases that target HIFα molecules, also binds and hydroxylates phosphorylated Akt (Akt1 and Akt2, but not Akt3) at four proline sites. Hydroxylation of two of these sites (Pro^{125} and Pro^{313}) promotes Akt binding to pVHL. The latter molecule also interacts with PP2A, which dephosphorylates the Thr^{308} site, resulting in Akt inactivation. Consistent with this, genetic or pharmacological inhibition of EglN1, and type 1 pVHL mutations, re-

Molecular Oncology Research Institute, Tufts Medical Center, Boston, MA 02111, USA. Email: ptsichlis@tuftsmedicalcenter.org

Downloaded from http://science.sciencemag.org/ on September 3, 2016

Published by AAAS

Shutting down Akt

Upon growth factor stimulation, Akt is recruited to the cell membrane by the actions of PI3K, where it is activated by phosphorylation (P) by other membrane-associated kinases such as 3-phosphoinositide–dependent protein kinase-1 (PDK1). Phosphorylated Akt1 and Akt2, but not Akt3, undergo proline hydroxylation (OH) by the prolyl hydroxylase EglN1 under conditions of normal oxygen tension. Hydroxylated Akt interacts with, and is dephosphorylated by, pVHL-associated PP2A, leading to Akt inactivation. Ptdins(4,5), phosphatidylinositol 4,5-bisphosphate; Ptdins(3,4,5), phosphatidylinositol 3,4,5-triphosphate; mTORC2, mTOR complex 2.

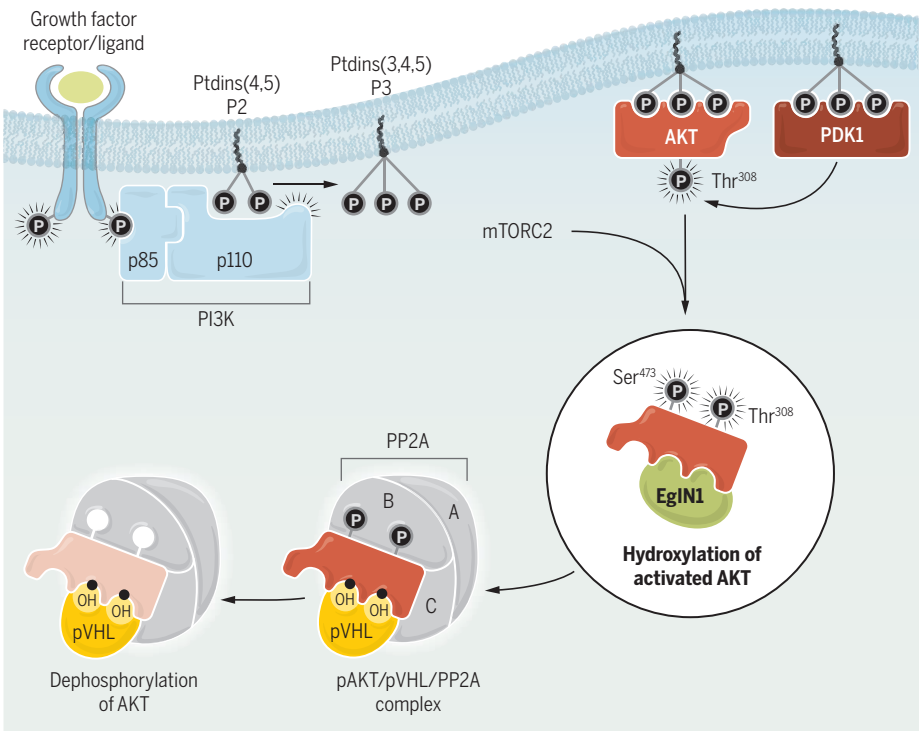

GRAPHIC: K. SUTLIFF/*SCIENCE*

sult in Akt activation by interfering with Akt dephosphorylation (see the figure).

The pathway of Akt deregulation described above may be activated in human cancer by several mechanisms. Although rare, mutations that alter the Akt hydroxylation sites (G311D in Akt1 and P127N in Akt2) do occur and are associated with Akt activation. It remains to be determined whether other Akt mutations also interfere with the hydroxylation and subsequent dephosphorylation of Akt. In addition, hypoxia, which is common in human cancer, results in the inactivation of EglN1, and this should interfere with proline hydroxylation and dephosphorylation of Akt. Mutations in pVHL, which are common in certain forms of human cancer, may also activate Akt by preventing its dephosphorylation. Other cancer-associated loss-of-function mutations targeting genes encoding enzymes involved in the Krebs cycle, such as succinate dehydrogenase and fumarate hydratase, result in the accumulation of succinate and fumarate, which inhibit the activity of EglN1 by competing with α-ketoglutarate (*1*). Also, regulation of Akt via proline hydroxylation may be under the control of additional signals that control the activity of EglN1 and the hydroxylation of Akt, or the expression of pVHL and its interaction with hydroxylated Akt.

EglN1 and other prolyl hydroxylases are activated by the metabolite D-2-hydroxyglutarate. An increase in D-2-hydroxyglutarate levels is caused by mutations in isocitrate dehydrogenase 1 (IDH1), which are commonly observed in diffuse gliomas and glioblastomas (*10*). According to the results of Guo *et al.*, this would inhibit Akt by activating EglN1, which is consistent with clinical observations showing that patients with IDH1 mutations tend to harbor lower-grade tumors and have a better prognosis (*11*). If the better prognosis of these patients is due to the inactivation of Akt, one would expect that the beneficial effect of the mutation would be more pronounced in patients with Akt1 and Akt2 rather than Akt3-expressing tumors. The observations in glial tumors are in sharp contrast to observations in acute myelogenous leukemia (AML) with normal cytogenetics and mutations in IDH1/IDH2, which also produce D-2-hydroxyglutarate. Despite the fact that D-2-hydroxyglutarate should inhibit Akt, the IDH2 mutations in AML are associated with bad prognosis, and the inhibition of the mutated IDH2 is therapeutically beneficial (*12*). It is not known why these mutations exert opposite effects in glial tumors and AML. Perhaps the pathway of Akt regulation by hydroxylation is active in glial but not in hematopoietic cells. Alternatively, Akt may be activated in AML by other pathways that supersede its inhibition by D-2-hydroxyglutarate.

Although not the focus of Guo *et al.*, hydroxylation of Akt should play an important role in the activation of Akt1 and Akt2 during hypoxia. Other mechanisms contributing to Akt activation in hypoxia include the down-regulation of phosphatase and tensin homolog (PTEN) by miR-21, which is induced by Akt2 and the inactivation of PTEN by hypoxia-induced reactive oxygen species (*13*, *14*). In addition, Akt may be activated via a feedback loop that is induced by inactivation of mechanistic target of rapamycin (mTOR) via HIF-induced expression of regulated in development and DNA damage responses 1 (REDD1) (*15*). The relative contribution of these pathways to Akt activation during hypoxia in different cell types remains to be determined.

The data of Guo *et al.* suggest that inhibition of Akt may be therapeutically beneficial in pVHL-null and other tumors with mutations interfering with Akt hydroxylation. It will be interesting to determine how efficiently currently available inhibitors interfere with Akt activation via this pathway. ■

REFERENCES AND NOTES

1. K. L. Gorres, R. T. Raines, *Crit. Rev. Biochem. Molec. Biol.* **45**, 106 (2010).
2. J. Guo *et al.*, *Science* **353**, 929 (2016).
3. A. Bellacosa, J. R. Testa, S. P. Staal, P. N. Tsichlis, *Science* **254**, 274 (1991).
4. T. F. Franke *et al.*, *Cell* **81**, 727 (1995).
5. G. Risso, M. Blaustein, B. Pozzi, P. Mammi, A. Srebrow, *Biochem. J.* **468**, 203 (2015).
6. S. Sato, N. Fujita, T. Tsuruo, *Proc. Natl. Acad. Sci. U.S.A.* **97**, 10832 (2000).
7. T. O. Chan *et al.*, *Proc. Natl. Acad. Sci. U.S.A.* **108**, E1120 (2011).
8. W. Y. Kim, W. G. Kaelin, *J. Clin. Oncol.* **22**, 4991 (2004).
9. J. An, M. B. Retting, *Mol. Cell Biol.* **25**, 7546 (2005).
10. P. Koivunen *et al.*, *Nature* **483**, 484 (2012).
11. P. F. Wang *et al.*, *Oncotarget* **2016** 10.18632/oncotarget.8918 (2016).
12. B. F. Clem, J. O'Neal, A. C. Klarer, S. Telang, J. Chesney, *Q. J. Med.* **109**, 367 (2016).
13. C. Polytarchou *et al.*, *Cancer Res.* **71**, 4720 (2011).
14. H. Pelicano *et al.*, *J. Cell Biol.* **175**, 913 (2006).
15. J. Brugarolas *et al.*, *Genes Dev.* **18**, 2893 (2004).

ACKNOWLEDGMENTS

Akt-related studies in the PNT laboratory are supported by National Institutes of Health grants R01CA186729 and R01CA198117.

10.1126/science.aah6254

Downloaded from http://science.sciencemag.org/ on September 3, 2016

Published by AAAS

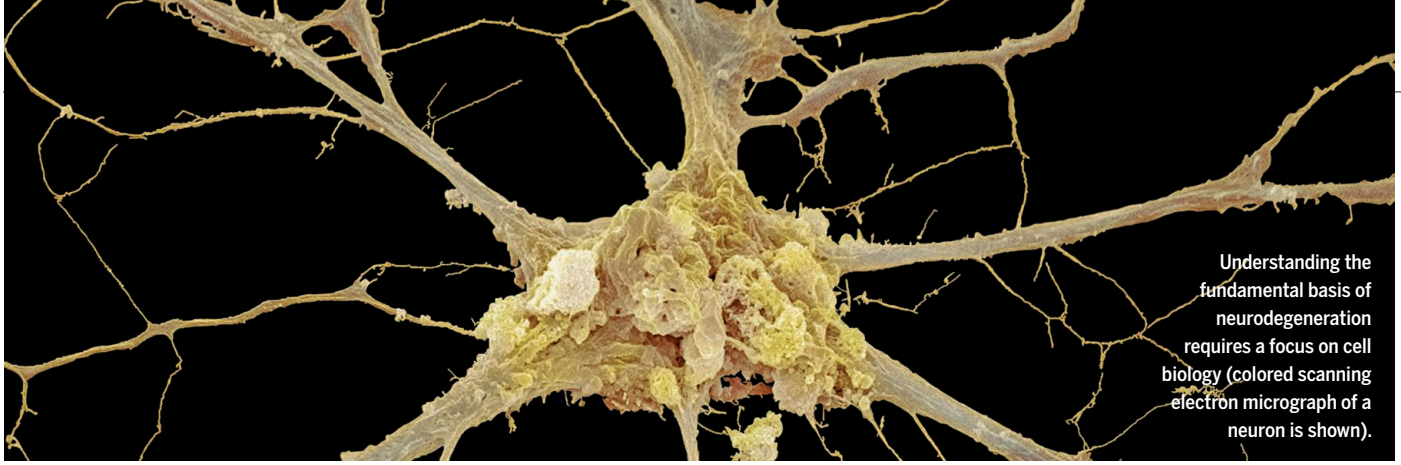

Understanding the fundamental basis of neurodegeneration requires a focus on cell biology (colored scanning electron micrograph of a neuron is shown).

PHOTO: SPL/SCIENCE SOURCE

NEUROSCIENCE

A path toward understanding neurodegeneration

A focus on cell biology may accelerate progress in disease prevention and cures

By **K. S. Kosik,[1] T. J. Sejnowski,[2,3] M. E. Raichle,[4] A. Ciechanover,[5] D. Baltimore[6]**

The specter of neurodegenerative disease, particularly Alzheimer's disease, haunts the developed world and exacts a poorly documented toll on underdeveloped countries. With so little progress made toward finding a cure—or, better, a prevention—it is time to rethink the path to progress. This requires a change in perspective on the type of research that will make a difference. The lesson learned from cancer research is that a new commitment means rethinking the fundamental approach to the disease. Cancer research moved from taking potshots with, usually, cytotoxic drugs to a bottom-up, mechanism-based approach in which newly acquired genetic knowledge played the largest role. Today, that effort has produced a platform of knowledge from which academia and industry are drawing. For neurodegenerative disease, the genetic approach remains valid but the problem must concurrently be approached from a complementary, robust cell biological perspective, focusing on the cellular cascade of events that lead to neuronal cell death.

BUILDING ON INSIGHTS

If cell biology is the core discipline from which progress in neurodegeneration will emerge, then the research path forward needs to build on insights over the past two decades that have converged upon core cellular dysfunctions related to the disease. These include controls over protein folding, trafficking, and degradation; specific cell-type vulnerabilities; activation of aberrant signaling pathways that lead to cell death; and the interface of genomics and brain imaging with cellular-level resolution. For example, relevant cellular work is emerging from biophysical methods with high spatial and temporal resolution in vivo (*1*). This has revealed protein conformations with a liquid-liquid phase separation into protein-rich droplets that potentially link RNA granules and pathological inclusions (*2*). New information will emerge from identifying cell type–specific proteostasis networks that involve the unfolded protein response, the ubiquitin-proteasome system, and autophagy (*3*). Among several incipient clues are mutations that inactivate the ubiquitination and destruction of faulty or damaged mitochondria. Inhibiting this removal (by "mitophagy") results in Parkinson's disease (*4*). These early leads position the field of neurodegenerative disease squarely upon a deeper cellular basis and support investigative cell biology as a worthy strategy for formulating translational end points and rapid progress. Answers to why cells die (leading to neurodegeneration) will be as revealing as discoveries in the cancer field that explain why cells proliferate.

In the cancer field, critical insights emerged not from taking a shortcut toward therapy, but from a deep knowledge of genes and cells. In the field of neurodegeneration, there are unfortunate repeats of some of the same mistakes made earlier in the cancer field. In the United States, funding to acquire basic knowledge should not be siphoned off to support expensive, and at times risky, clinical trials based on inadequate knowledge. The shift from basic to applied research in the field of neurodegeneration was apparent at the U.S. National Institute of Neurological Disorders and Stroke (NINDS) (*5*), where, from 1997 to 2012, basic research funding by the agency declined from 87 to 71%, with support for the most basic research falling from 52 to 27% of the competing budget.

The impetus for presenting this proposal for cell biology as the foundational science for understanding neurodegeneration arose from a series of five salons held at sites around the United States in 2015 (see supplementary materials). The goal was to take a fresh and objective measure of neurodegeneration research from an informed group of scientists outside the field. To achieve this goal, the selected participants were deeply knowledgeable of the basic science topics faced by the neurodegeneration field, but for the most part had not been immersed in the field. This setting created lively discussions about the multifaceted nature of neurodegeneration, but held to the common theme of how a sustained basic cell science effort could lead to progress in the field.

THE FUNDING PATH

The need for a larger research effort on neurodegenerative disease is evident from the aging of the population and consequent epidemic prevalence of Alzheimer's disease. Hopefully, the next few years will see a large influx of dedicated funds from government and private sources in the United States. Indeed, the Bypass Budget Proposal for Fiscal Year 2017 (*6*) for Alzheimer's disease suggests this. What is also needed is clear guidance as to how funds can be spent with a substantial likelihood of success. When cancer research matured to the point that it could absorb

[1]*Department of Molecular, Cellular, and Developmental Biology, Neuroscience Research Institute, University of California, Santa Barbara, Santa Barbara, CA 93106, USA.* [2]*Howard Hughes Medical Institute at the Salk Institute for Biological Studies, La Jolla, CA 92037, USA.* [3]*Division of Biological Sciences, University of California, San Diego, La Jolla, CA 92093, USA.* [4]*Mallinckrodt Institute of Radiology, Department of Neurology, Department of Biomedical Engineering, Department of Anatomy and Neurobiology, Washington University in St. Louis, St. Louis, MO 63110, USA.* [5]*Cancer and Vascular Biology Research Center, Faculty of Medicine, Technion–Israel Institute of Technology, Haifa 31096, Israel.* [6]*Division of Biology and Biological Engineering, California Institute of Technology, Pasadena, CA 91125, USA. Email: kosik@lifesci.ucsb.edu; baltimo@caltech.edu*

Downloaded from http://science.sciencemag.org/ on September 3, 2016

Published by AAAS

funding in a productive way, and the U.S. "War on Cancer" was declared (1971), much of the money was well spent. However, considerable funds supported trendy work, such as the fruitless search for virus-induced human cancer. Savvy gatekeepers are needed who can funnel funds in promising directions. Here, however, lie challenges. Peer review is the long-standing decision-making mechanism for evaluating science, but when any field is dominated by a few long-held ideas and strong personalities, such a process may not be the best approach. Thus, attracting basic cell biologists to the study of neurodegenerative disease will bring fresh ideas and insights. Also, collaborative large-scale efforts that require seeding by philanthropic donors, who are often less risk averse than government agencies, must operate in the context of advisers with open minds.

Funding comes with the question of establishing large-scale programs versus individual investigator-initiated grants. This debate is not an either-or matter, and there are intermediate blends of these tactics. What is important overall is to avoid setting unrealistic goals and timetables, which works against developing evidence for unobvious hypotheses. The many unknowns that neurodegeneration research faces make precise timetables unrealistic—another lesson learned from the effort put toward cancer research. The most remarkable discoveries come with a sense of surprise. The success of curiosity-driven science is a testimony to this path. A recent example is the development of gene editing tools such as clustered regularly interspaced short palindromic repeats (CRISPR) from a unique form of adaptive immunity in bacteria.

A CELL SCIENCE ENTERPRISE

Hand-in-hand with a defined scientific mission, the organization of a research enterprise with a cell science focus is critical to its success. An effective structure of a research entity that targets neurodegeneration will share many elements with other large biomedical entities. "Centers without walls" through the U.S. National Institutes of Health (NIH) represents a reasonable model for creating research entities. Its widely applicable core principles of cooperation, collaboration, and collegiality need to be balanced by the recognition of, and reward for, individual contributions and the freedom to engage in lively debate. The scientific effort should be inclusive of women and minorities, and without regard for national barriers. In the United States, streamlining grant support for investigators in their thirties could buck the long-standing statistic that first-time recipients of NIH RO1 grants tend to be over 40 years old. Sadly, Kaplan-Meier retention curves reveal that many principal investigators stop receiving NIH funding after they receive their first year of R01 funding (*7*). Such a discouraging funding environment drives students and young scientists away from a field. Instead, the opportunity for groundbreaking discoveries in the cell biology of neurodegeneration should be a powerful global attractor for the next generation of scientists.

Cell biology requires a unique tool set, often centered around expensive microscopy, electrophysiological instrumentation, molecular probes, and image analysis. Therefore, research centers require dedicated watchdogs that are alert to cutting-edge technologies and are responsive to engineering needs through in-house tool-building capacity. Robust communication and data-sharing technologies are also essential and become even more important in centers that operate beyond institutional boundaries. Technologies for video conferencing and user-friendly platforms for data sharing and retrieval will contribute to a productive center. Posting prepublication draft papers online through life-sciences preprint servers would accelerate deposition of research results into the public domain. Massive data collections such as the Alzheimer's Disease Neuroimaging Initiative (*8*) need to grow as a platform with broader applications and accessibility, while maintaining protection for patient privacy. As metadata analyses and semantic-level searches improve for diverse types of data, in silico research will increasingly contribute to gaining new insights. The vast existing literature in neurodegeneration, including reported findings that are no longer considered accurate, makes entry into the field challenging. Informetric sciences and metadata extraction need development along with analyses of content that can capture research directions and knowledge gaps (*9*, *10*). Such analyses may also reveal investigator networks that foster collaborations.

"...the public must be engaged with evidence that well-executed discovery science is not only relevant but necessary..."

Economic and political shifts that have occurred since the "War on Cancer" have increased reliance of the research community on the private sector. Given the strong philanthropic history in the United States and the United Kingdom, philanthropists help shape the scientific trajectory of neurodegenerative disease research. Private partnerships with government and with academia are an effective strategy. Shared costs and greater freedom to operate in the private sector will allow a more nimble structure while avoiding the whimsical decisions that can tarnish donor-driven science. Private and academic institutions that have pioneered structures to accelerate discovery science in neurodegenerative disease include the Allen Institute for Cell Science, the Broad Institute, the Stowers Institute for Medical Research, the Whitehead Institute for Biomedical Research, and the Howard Hughes Medical Institute with its Janelia Research Campus. These institutes required enormous initial investments, but there are many structures through which smaller sums can make a difference. For example, the McDonnell-Pew Program in Cognitive Neuroscience is a lower-cost means to create an intellectual setting that attracts young scientists toward careers in neurodegeneration research. The Science Philanthropy Alliance helps philanthropists find a route to support basic scientific endeavors at any level.

A COMPREHENSIVE EFFORT

To sustain a basic science effort, the public must be engaged with evidence that well-executed discovery science is not only relwevant but necessary in the face of tempting promises of more short-term, high-risk treatments. Conquering neurodegenerative conditions requires a comprehensive effort that goes well beyond, but still begins with, basic cell science. A comprehensive effort cannot neglect improved clinical trial design, the economic burden of care delivery, and the discovery of new pharmaceuticals. Each of these endeavors is contributory to the overall effort: a cure for, or mode of prevention of, neurodegeneration. Our message is that a redoubled effort toward understanding the fundamental basis of neurodegeneration will ultimately have the highest impact on solving this affliction. ■

REFERENCES

1. F. X. Theillet *et al.*, *Nature* **530**, 45 (2016).
2. A. Molliex *et al.*, *Cell* **163**, 123 (2015).
3. B. Mollereau *et al.*, *Brain Res.* 10.1016/j.brainres.2016.02.033 (2016).
4. B. Bingol, M. Sheng, *Free Radic. Biol. Med.* 10.1016/j.freeradbiomed.2016.04.015 (2016).
5. *Back to Basics: A call for fundamental neuroscience research*; https://blog.ninds.nih.gov/2014/03/.
6. *Bypass Budget Proposal for Fiscal Year* 2017; www.nia.nih.gov/alzheimers/bypass-budget-fy2017.
7. S. Rockey, *Retention Rates for First-Time R01 Awardees*; https://nexus.od.nih.gov/all/2014/10/28/retention-of-first-time-r01-awardees/.
8. *Data & Samples*; http://adni.loni.usc.edu/data-samples/.
9. D. Lee, W. C. Kim, A. Charidimou, M. Song, *J. Alzheimers Dis.* **45**, 1207 (2015).
10. M. Song, G. E. Heo, D. Lee, *Scientometrics* **102**, 905 (2015).

SUPPLEMENTARY MATERIALS

www.sciencemag.org/content/353/6302/872/suppl/DC1

10.1126/science.aai7622

Downloaded from http://science.sciencemag.org/ on September 3, 2016

Published by AAAS

POLICY FORUM

GLOBAL HEALTH

Achieving global targets for antimicrobial resistance

The UN should promote targets, funding, and governance

By **Ramanan Laxminarayan,[1] Devi Sridhar,[2] Martin Blaser,[3] Minggui Wang,[4] Mark Woolhouse[2]***

After decades of neglect, antimicrobial resistance (AMR) has captured the attention and concern of the public health community and global leaders. In September 2016, a high-level meeting of the United Nations General Assembly (UNGA) will discuss how countries can cooperate to preserve global access to effective antimicrobials. This will be only the fourth health issue (and the first One Health issue, integrating human, animal, and environmental health) to bring together heads of state at the UNGA for a rare opportunity to set a global agenda to combat the crisis. We believe that (i) setting targets for reducing drug-resistant infections, (ii) adequate financing for global action, and (iii) defining the global health architecture to address AMR should be elements of a UN plan.

The costs of antibiotic treatment and mortality due to resistance are increasing worldwide (*1*). The greatest burden occurs in low- and middle-income countries (LMICs), especially among the young: An estimated 214,000 neonatal sepsis deaths are attributable to resistant pathogens each year (*2*). But high-income countries are not immune: An estimated 23,000 people in the United States and 25,000 in Europe die each year from resistant pathogens (*1*, *2*). That said, lack of access and delayed access to antibiotics kill more people than AMR. The challenges of expanding appropriate access to antimicrobials while restricting inappropriate access require changes to financing and delivering health care.

TARGETS AND SURVEILLANCE

Use of antibiotics is the most important driver of selection for resistance and loss of effectiveness. Use is increasing globally, driven by rising incomes and increasing access, and varies in human and animal sectors across countries, depending on prevailing medical, veterinary, and regulatory practices.

We propose that no country consume more than the current median global level [8.54 defined daily doses (DDDs) per capita per year] (see the figure). We estimate that this would lower overall human use by 17.5% globally [see (*3*); see supplementary materials (SM)]. Reducing use is accomplished by improving public health and sanitation. In low-income countries, antibiotics are used to compensate for the lack of public health infrastructure (e.g., vaccination coverage and infection control). A target linked to UN Sustainable Development Goals 3 (on health) and 6 (on water and sanitation) for public health would reduce reliance on antibiotics.

> ***"[Surveillance for AMR] is a global good and should be financed accordingly."***

Reductions could be achieved through public campaigns, aimed at physicians and patients, to discourage inappropriate antibiotic use (*4*), particularly in response to seasonal influenza (*3*). Although LMICs face a higher burden of infectious disease, per capita consumption of antimicrobials in most LMICs is well below our target, thus, it need not compromise legitimate uses.

There is potential for reducing consumption in the animal sector. We propose global phasing out of the use of antimicrobial growth promoters; a deadline of 5 years would be appropriate, given the urgency of the problem. This could avert much of the projected 67% increase in use for farm animals between 2010 and 2030 (*3*). Although this would incur some cost to agricultural sectors, even in China (the largest consumer of antibiotics in agriculture), that cost is likely on the order of $3 billion a year, a small fraction of the country's burden of AMR (*5*). The costs of improving biosafety and biosecurity in farming operations to phase out antimicrobial growth promoters would be largely offset by lowering the risk of infection and cost of antimicrobials. We envision a process similar to that in the European Union where there was declared intent to phase out subtherapeutic use, followed by regulatory changes. Globally, this could work through a multilateral process, as with global movements to phase out, e.g., asbestos or chlorofluorocarbons.

National-level restrictions on antibiotic effluents from pharmaceutical manufacturing, agricultural operations, and hospital waste that contribute to buildup of resistance genes in the soil and water are an urgent priority.

Targets for reductions in antibiotic consumption should be accompanied by targets to reduce levels of a drug-resistance index (e.g., the proportion of infections that are resistant), based on a weighted-average of resistance of the eight World Health Organization (WHO) priority pathogens to first-line antibiotics, nationally, regionally, and globally within 5 years (*6*). We do not specify the scale of reduction—the immediate priority is to prevent increases—but recommend review in 2021 to consider more stringent targets. The strategies chosen would reflect health system context and priorities of individual countries.

Existing surveillance programs for AMR can contribute to target monitoring at the national level (*7*), e.g., the Global Antimicrobial Resistance Surveillance System and ResistanceMap (*8*). Surveillance should involve the livestock sector and the wider environment and should track access and use, as well as indicators, such as water, sanitation, and vaccination coverage. Data on AMR must be translated into epidemiologically sound estimates of public health burden; such estimates require information on treatment rates and failures (*2*) not routinely collected.

Surveillance cannot be the sole responsibility of individual countries; it is a global good and should be financed accordingly. Initiatives such as the Fleming Fund and the Global Health Security Agenda provide opportunities to strengthen surveillance in countries with poor public health architecture. Not all surveillance elements need to be replicated at a national level; integrating local activities into multinational networks may be efficient, with appropriate structures for data-sharing, analysis, and communication.

GLOBAL FINANCING

Substantial funds have been committed in the United States and Europe to tackle AMR, but success will be limited without global-scale investments. The need to incentivize development of new vaccines, diagnostics, novel therapies, and stewardship methods, as

[1]Center for Disease Dynamics, Economics, and Policy, Washington, DC 20005, USA. [2]University of Edinburgh, Edinburgh EH8 9YL, UK. [3]New York University School of Medicine, New York, NY 10016, USA. [4]Fudan University, Shanghai 200433, China. *Email: mark.woolhouse@ed.ac.uk

Downloaded from http://science.sciencemag.org/ on September 3, 2016

Published by AAAS

Antimicrobial sales vary by country

Data from 75 countries. The five countries with highest total antibiotic sales for human use and the five with highest per capita sales are identified. See SM.

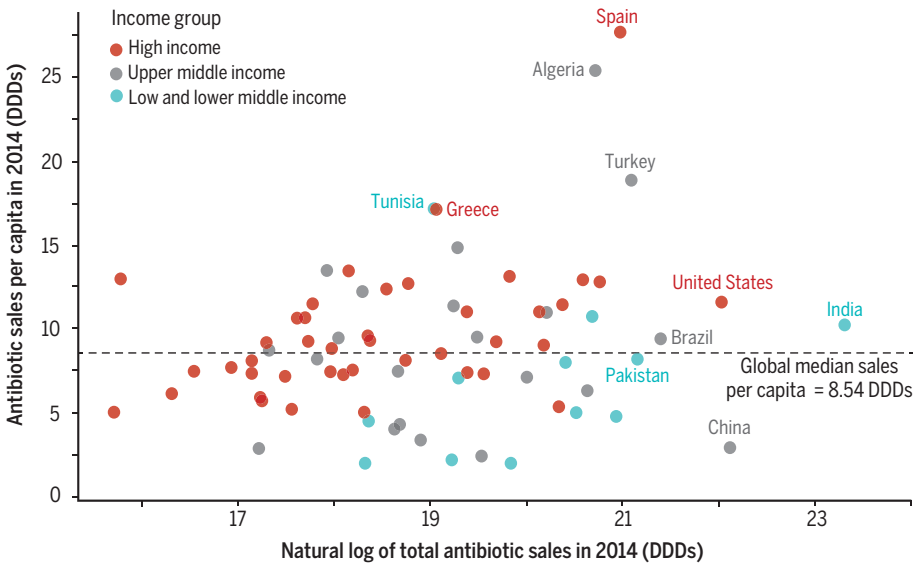

GRAPHIC: N. CARY/*SCIENCE*

well as traditional antibiotics, to ensure availability of the "antibiotic umbrella" has been recognized (*9*). Vaccines face high development costs and uncertain markets; however, the Gavi Vaccine Alliance financing mechanism has been successful in bringing new vaccines into wide use.

Development and deployment of diagnostics are more difficult. Knowledge of the underlying pathogen and its drug sensitivity would improve antibiotic use, but new diagnostics are needed. Diagnostics must be rapid and sufficiently inexpensive if they are to be used before the decision to begin antibiotic treatment. The Longitude, Horizon, and National Institute of Allergy and Infectious Diseases (NIH) prizes for innovative diagnostics stipulate that winners demonstrate the feasibility of deploying globally.

New alternatives to traditional antibiotics are needed. Multiple noncompound approaches that target bacteria or the host have been proposed (*10*). Antibiotics can interact to synergize, antagonize, or suppress each other's effects (*11*); interactions modify the evolution of resistance. Financial stimuli for antibiotic development must address the lack of incentives for appropriate use (*12*) and should enable sustainable access, when clinically appropriate. Initiatives are being implemented to improve the development pipeline for new antibiotics (e.g., the Generating Antibiotics Incentives Now in the United States and the Innovative Medicines Initiative in Europe) but cannot be long-term solutions because resistance develops quickly to new antibiotics. Initiatives like the Affordable Medicines Facility—Malaria, that aimed to conserve the effectiveness of antimalarial drugs, involved a high-level subsidy (aimed at manufacturers, not retailers) and were found to be successful at increasing sales of quality-assured artemisinin combinations and reducing the use of monotherapies that contribute to drug resistance (*13*, *14*). Scaling from the size of response relative to Gross Domestic Product in the European Union and United States (which allocates ~$1 billion annually to AMR), we anticipate that a global fund of at least $5 billion annually will be needed.

GLOBAL ARCHITECTURE

The global response to HIV/AIDS, effective in curtailing that epidemic, was accelerated by the 2001 UNGA on HIV/AIDS (*15*). A clear set of actions tied to targets, financing, institutional commitment to cross-sectoral coordination at the national level, international monitoring and accountability, and civil society participation should also now be reflected in a UNGA plan for AMR. A global architecture must transcend the individual animal and human domains (*16*). Proposed approaches include ones similar to the Intergovernmental Panel on Climate Change, or the Montreal Protocol (*17*).

The current tripartite arrangement among WHO, the Food and Agricultural Organization (FAO), and World Organization for Animal Health (OIE) offers promise but is unlikely to be sustainable given their other priorities. We recommend a new High-Level Coordinating Mechanism (HLCM) under the UN Secretary General because (i) access to effective antimicrobials transcends the remit of WHO, involving animal health and the environment; (ii) nonstate actors play an important role; and (iii) significant new funding is needed for research and development.

The HLCM, consisting of WHO, FAO, OIE, the World Bank, relevant UN agencies and other international organizations, major multisectoral stakeholders, and global experts, reports to the UN Secretary General and should coordinate support for development, implementation, and monitoring of national plans and relevant actions. It can raise awareness and financing if leadership is given seniority within the UN system. A new HLCM would allow a more inclusive governing body (e.g., with nonstate actor voting rights), and engagement with civil society, patient groups, and the private sector.

Financing would likely come through a replenishment process, such as used by the Global Fund and the Gavi Alliance through World Bank Trust Funds (*18*); an organization solicits multiyear donor commitments on a regular schedule (e.g., every 3 years), rather than every year. Buy-in of countries across the world, particularly the Group of 77, and funders, such as the Bill and Melinda Gates Foundation, would be essential.

Antibiotic resistance threatens decades of progress in medicine, food security, and public health. Global collective action rooted in national responses is needed. The UNGA high-level meeting could help shift world opinion, build consensus around core feasible goals, and integrate solutions into policy approaches by UN member states, international organizations, and philanthropies. ■

REFERENCES

1. R. Laxminarayan *et al.*, *Lancet Infect. Dis.* **13**, 1057 (2013).
2. R. Laxminarayan *et al.*, *Lancet* **387**, 168 (2016).
3. T. P. Van Boeckel *et al.*, *Lancet Infect. Dis.* **14**, 742 (2014).
4. B. Huttner, H. Goossens, T. Verheij, S. Harbarth; CHAMP Consortium, *Lancet Infect. Dis.* **10**, 17 (2010).
5. R. Laxminarayan, T. Van Boeckel, A. Teillant, "The economic costs of withdrawing antimicrobial growth promoters from the livestock sector" (OECD Food Agric.Fish. Papers no. 78. OECD Publishing, Paris, 2015).
6. R. Laxminarayan, K. P. Klugman, *BMJ Open* **1**, e000135 (2011).
7. WHO, "Antimicrobial resistance: Global report on surveillance 2014" (WHO, Geneva, 2014).
8. Center for Disease Dynamics, Economics, and Policy, "The State of the World's Antibiotics, 2015" (CDDEP, Washington, DC, 2015).
9. C. Årdal *et al.*, *Lancet* **387**, 296 (2016).
10. L. Czaplewski *et al.*, *Lancet Infect. Dis.* **16**, 239 (2016).
11. M. Baym *et al.*, *Science* **351**, aad3292 (2016).
12. R. Laxminarayan, *Science* **345**, 1299 (2014).
13. R. Laxminarayan *et al.*, *Science* **338**, 615 (2012).
14. S. Tougher *et al.*, *Lancet* **6736**, 1 (2012).
15. D. Sridhar, J. S. Morrison, P. Piot, "Getting the politics right for the September 2011 UN high-level meeting on noncommunicable diseases" (Center for Strategic and International Studies, Washington, DC, 2011).
16. M. Woolhouse, M. Ward, B. van Bunnik, J. Farrar, *Philos. Trans. R. Soc. Lond. B Biol. Sci.* **370**, 20140083 (2015).
17. M. Woolhouse, J. Farrar, *Nature* **509**, 555 (2014).
18. C. Clinton, D. Sridhar, *Governing Global Health: Who Runs the World and Why?* (Oxford Univ. Press, New York, 2016).

SUPPLEMENTARY MATERIALS

www.sciencemag.org/content/353/6302/874/suppl/DC1

Published online 18 August 2016

10.1126/science.aaf9286

Downloaded from http://science.sciencemag.org/ on September 3, 2016

Published by AAAS

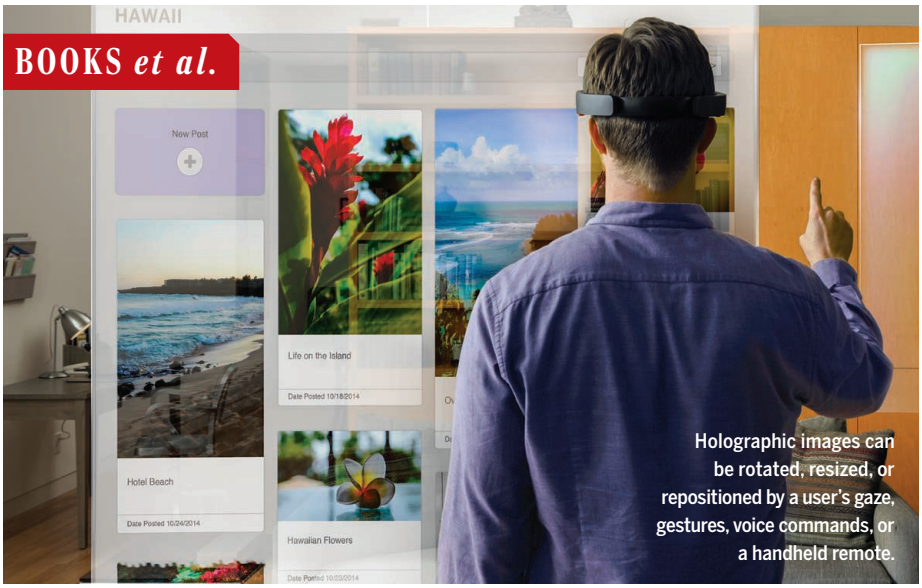

Holographic images can be rotated, resized, or repositioned by a user's gaze, gestures, voice commands, or a handheld remote.

Microsoft Hololens Development Edition
Microsoft Corporation
$3000

TECHNOLOGY

The future of three-dimensional thinking

A new holographic platform holds promise for enhancing education, research, and collaboration

By **Mark A Hoffman**

Most structures studied by science exist in three dimensions: molecules, organisms, ecosystems, galaxies. Flat-screen visualizations of these entities limit our understanding and experience of the objects and interactions that we study. Likewise, flat-screen–based video communication constrains our ability to interact with remote colleagues and collaborators. The Microsoft Hololens Development Edition, released on 30 March 2016, is a holographic platform that demonstrates the potential to enhance scientific understanding, education, and collaboration by transforming our interactions with three-dimensional representations and with one another.

ONLINE

See a demo of the Hololens's training potential at http://bit.ly/2bqutEO

Users of Hololens see and hear the augmented world through a visor, with holographic images and applications superimposed on their surroundings and high-definition sound projected above their ears. The gaze of the user, combined with gestures, voice commands, or a handheld clicker, allow him or her to rotate, resize, or reposition holograms.

Through surface mapping, Hololens avoids placing images in obstructed positions and generates an experience that is contextualized to the user's location. For example, browser-based applications appear as if they are attached to a wall. Unlike Google Glass or Oculus, Hololens is untethered; it accesses the Internet through Wi-Fi.

As a Windows 10 device, Hololens is integrated with Cortana, Microsoft's response to Apple's Siri. Speaking the command, "Hey, Cortana, display the periodic table of elements" invokes an Edge browser with an appropriate display floating in the user's view. Images and video captured by Hololens are stored to OneDrive, where they can then be viewed or downloaded.

The development edition of Hololens provides access to a set of early applications in the Windows Store. Although many are recreational, some demonstrate the scientific and educational potential of the device. For example, the preview version of an anatomy trainer developed by Case Western Reserve University projects a semitransparent human body. As the user works through examples, organ systems are highlighted. The user can walk around the body to learn the position of organs.

Another application, Galaxy Explorer, allows users to visualize astronomical structures. Through finger gestures, they can zoom in on features of a three-dimensional, semitransparent depiction of the Milky Way galaxy, including individual planets.

Small molecule structures can be imported into the free HoloStudio application. We have successfully used this approach to visualize aspirin. Importing more complex structures requires migrating the visualization through the Unity game engine platform and then Microsoft Visual Studio. I used this process to transfer the human leukocyte antigen molecule with the peptide-binding cleft emphasized and was able to view the molecule floating in our office suite. This has potential to improve our understanding of molecular docking, including drug-protein interactions.

Skype is integrated with Hololens and offers novel collaboration capabilities. Hololens wearers see the person that they are conversing with off to the side of their field of vision, while those on the call see the view from the visor. The wearer can walk around and annotate objects, seeking guidance and feedback from remote participants. One constraint is that holographic images are currently not visible during a Skype session.

There are several minor issues that I hope will be addressed before the device's full release. For example, the rectangular portion of the view dedicated to holograms does not cover the entire field of vision. Images must be carefully sized to fit.

Hololens is a more obvious device than Google Glass, so the privacy concerns associated with surreptitious recording are less important. However, this issue is still worthy of continued consideration, especially if future releases have a smaller format.

Three-dimensional thinking and communication are critical during this era of increasingly complex data. Hololens has the potential to transform scientific thinking, analysis, and communication by seamlessly integrating the virtual and the physical world. ■

The reviewer is at Children's Mercy Hospital and the Department of Biomedical and Health Informatics, University of Missouri–Kansas City, Kansas City, MO 64108, USA. Email: mhoffman@cmh.edu

10.1126/science.aah5394

Downloaded from http://science.sciencemag.org/ on September 3, 2016

PHOTO: USED WITH PERMISSION FROM MICROSOFT.

Published by AAAS

PROFESSIONAL DEVELOPMENT

Navigating today's job market

A step-by-step guide offers practical science career advice

By **Teegan A. Dellibovi-Ragheb**

According to data collected by the National Science Foundation, only 7% of life science Ph.D.s obtain tenure-track faculty positions within 5 years of completing their degrees. This statistic belies the widely held belief in academic culture that the "default" career path for such individuals is a professorship. The landscape of science career opportunities is changing, so-called "alternative" career paths are on the rise, and the personal career experiences of mentors are often not sufficient for the trainees they advise. There is a need for new resources, which are consistent with the rapidly changing job market and sensitive to the specific challenges of Ph.D. students and postdocs in the sciences.

Next Gen PhD: A Guide to Career Paths in Science is a practical and thorough manual for the entire career transition process, from defining personal interests and deciding on a career path all the way to day one of a new job. Written by experienced career counselor Melanie Sinche, it is geared toward postdocs and graduate students who may not have access to effective career counseling or mentorship or are not satisfied with what they have received thus far. Speaking in a positive and encouraging tone, Sinche is not only a valuable resource but also an advocate for early-career Ph.D.s. "The truth is that candidates who have successfully completed a PhD in science have myriad skills of value to employers of all kinds, from universities to research institutions, government agencies to nonprofits, start-ups to professional societies," she writes.

Sinche provides exercises to help new and prospective Ph.D.s identify their interests, skills, and values. She discusses different career options, lists potential job titles across various sectors, and includes survey data on the percentages of scientists that choose these routes, their reported levels of job satisfaction, the skills required, the work environment, and even salary ranges. She also breaks down the job search process into tangible goals.

To get the most out of graduate or postdoctoral training, it is important for both the trainee and his or her mentor to have clear goals and expectations for the training period, Sinche maintains. Career development activities may have to be balanced with laboratory work, and this requires communication with, and support from, one's principal investigator. Unfortunately, even if a mentor is supportive of a nontraditional career path, he or she may not have the experience to guide trainees in a substantive way. When this occurs, Sinche suggests developing relationships with additional mentors who can offer different perspectives and facilitate relevant networking opportunities.

Sinche also gives practical advice on informational interviewing and networking—two activities that are often among the most feared by frequently introverted scientists. Stressing the importance of these activities during one's job search, she explains, "Many job search methods exist, but *none* are as powerful as networking—and few work as well without networking." However she also offers the reassurance that "professionals from all occupations are typically delighted to hear from and engage with junior researchers."

Sinche recognizes that, despite being perhaps a decade out of college, many early-career scientists enter the job market with no concept of how it works. She carefully guides the reader through a typical job application process, from how to prepare for an interview to how to negotiate a job offer. The book is filled with examples of CVs, resumes, cover letters, interview questions, and more.

Finally, Sinche encourages early-career scientists to take charge of their own career paths. There are many options to choose from, and it is important to learn about each one and to assess one's unique talents and passions. It is easy to feel pressure from mentors, parents, or peers to follow a particular career trajectory, but the best career is the one that is the most suitable match for you. "Remember that you are the architect of your own career, and you, like the majority of Ph.D. scientists, *can* find satisfaction in your work," she writes. ■

10.1126/science.aah3463

The reviewer is at the National Heart, Lung, and Blood Institute, National Institutes of Health, Bethesda, MD 20892, USA. Email: teegan.dellibovi-ragheb@nih.gov

Next Gen PhD
A Guide to Career Paths in Science
Melanie V. Sinche
Harvard University Press, 2016, 272 pp.

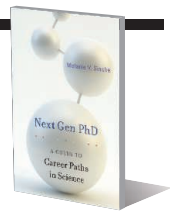

Building Star Trek
Mick Grogan
Yap Films for Smithsonian Channel and Discovery Canada, 2016
Premieres on Sunday, 4 September at 8:00 pm ET/PT

PHOTO: ERIC LONG/SMITHSONIAN'S NATIONAL AIR AND SPACE MUSEUM, COURTESY OF SMITHSONIAN CHANNEL © 2016

September 8, 2016, will mark the 50th anniversary of the first show of the television series *Star Trek*. To commemorate this, the Smithsonian Air and Space Museum is hosting the show's restored 11-foot USS Enterprise, and the Experience Music Project Museum in Seattle has built a re-creation of the ship's flight deck. In honor of these events, the Smithsonian channel will be airing a 2-hour special that describes the exhibits and looks at the effect *Star Trek* has had on science and technology. Like the television show, the documentary—to adult eyes—is occasionally cheesy, but there are more than enough episode details to delight the hard-core Trekkie (or Trekker, as many enthusiasts prefer to be called). More important, the program presents a lot of cool science that has been (and is still being) inspired by the franchise—from the invisibility cloak and the first real tractor beam, to the current XPRIZE challenge to create the first working tricorder. Uncountable numbers of young people have wanted to be like Kirk, Spock, Uhura, or McCoy, and the fostering of the excitement and mystery of scientific exploration may be *Star Trek*'s greatest achievement. – *Barbara Jasny*

10.1126/science.aai7464

Downloaded from http://science.sciencemag.org/ on September 3, 2016

Published by AAAS

In 2015, residents had to be evacuated from the Porter Ranch area of Los Angeles due to the natural gas leak from the Aliso Canyon storage facility.

Edited by **Jennifer Sills**

Reducing the risk of another Aliso Canyon

IN THEIR REPORT "Methane emissions from the 2015 Aliso Canyon blowout in Los Angeles, CA" (18 March, p. 1317), S. Conley *et al.* confirmed that the Aliso Canyon blowout was the largest ever methane leak from a U.S. underground storage facility. In the wake of this catastrophic accident, we should rethink the extent to which conventional underground storage is used in the U.S. gas infrastructure.

Extensive use of underground gas storage is energy inefficient: Gas must be produced, injected into a depleted reservoir for intermediate storage, and then withdrawn when needed. Injecting and withdrawing gas from reservoirs requires gas pressurization and transportation, and the associated fuel combustion, venting, and leakage cause substantial greenhouse gas emissions (*1*, *2*). As the Aliso Canyon gas leak demonstrates, underground storage facilities may also constitute a serious hazard for human health when located close to populated areas.

There may be a better option. Although the production technique has not yet been tested in practice, simulations suggest that fields with dry, mature shale-gas wells may alleviate the need for intermediate underground storage (*3*). Unlike the conventional strategy, in which gas is produced constantly and stored until it is needed, the characteristic geological shale-fracture system offers the possibility of wells that can produce gas or temporarily stop production, depending on demand. In shale-gas wells, pressure builds up quickly in the fracture network when a well is closed, allowing an unusually high production rate when production resumes. Because the high production rate compensates for lost production time, production can be stopped and resumed without incurring revenue losses from discounted value of the gas (*3*). This means that wells could operate by a per-demand policy, supplying gas directly from producer to end-user without the need for intermediate storage.

As a result of the shale-gas boom, and the steep and early decline in well productivity (*4*), a growing number of mature shale-gas wells are available, many of which are close to demand centers, with the pipeline infrastructure already in place. Using these existing resources as substitutes for current underground storage will decrease the need for intermediate storage reservoirs and reduce greenhouse gas emissions associated with the current storage practice. With fewer active underground storage facilities, the risk of disastrous gas leaks such as the Aliso Canyon blowout would also decrease.

Brage Rugstad Knudsen

Department of Engineering Cybernetics, Norwegian University of Science and Technology, 7491, Trondheim, Norway. Email: brage.knudsen@ntnu.no

REFERENCES

1. D. J. Zimmerle *et al.*, *Environ. Sci. Technol.* **49**, 9374 (2015).
2. J. Bradbury, Z. Clement, A. Down, "Greenhouse gas emissions and fuel use within the natural gas supply chain: Sankey diagram methodology," (Quadrennial Energy Review Analysis: U.S. Department of Energy, Office of Energy Policy and Systems Analysis, 2015).
3. B. R. Knudsen, C. H. Whitson, B. Foss, *Energy* **78**, 165 (2014).
4. J. D. Hughes, *Nature* **494**, 307 (2013).

10.1126/science.aah3833

NSF values mid-scale infrastructure

THE NATIONAL SCIENCE Foundation (NSF) recently unveiled 10 "Big ideas for future NSF investments" (*1*). One of those ideas targets mid-scale research infrastructure and greater flexibility to fund mid-scale projects. In his News In Depth story "Scientists cheer Senate bill" (1 July, p. 17), J. Mervis comments on the "mid-sized projects" referenced in the Senate bill, saying that NSF "has previously balked at the idea, although officials agree that NSF currently has no mechanism to fund unsolicited proposals in that price range." That statement mischaracterizes NSF's activities in mid-scale

PHOTO: SCOTT L./WIKIMEDIA COMMONS

Downloaded from http://science.sciencemag.org/ on September 3, 2016

Published by AAAS

infrastructure.

Far from balking at supporting mid-scale infrastructure, NSF Director France Córdova laid out goals and preliminary plans for this big idea at the May 2016 National Science Board meeting (*2*). In particular, lowering the threshold for Major Research Equipment and Facilities Construction expenditures would give the NSF-supported research community more opportunities to conduct excellent science and engineering. We have also discussed the importance of mid-scale research infrastructure during several other meetings of the National Science Board, in both open and closed sessions, including in 18–19 November 2015, 2–3 February 2016, and 9–10 August 2016 (*3*). Missing opportunities for mid-scale projects leaves essential science and engineering undone, and the long-term consequences of that neglect will be profound for science as well as for the economy, security, and competitiveness of the United States.

NSF has been able to support some smaller mid-scale projects from its Research and Related Activities budget in areas such as computing (*4*) and astronomy (*5*). However, we need to establish a mechanism that provides more flexibility and scope. Just a few examples of potential mid-scale projects are cyberinfrastructure, cosmic microwave background measurements, sensor networks, dark matter experiments, nuclear astrophysics measurements, and instruments for current major experiments or facilities.

As stewards of federal investments in critically important national research across all of science and engineering, we at NSF, together with our oversight body, the National Science Board, are continually looking to maximize the impact of our investments. Supporting mid-scale infrastructure is an important opportunity that we are actively considering.

Fleming Crim[1] and James Kurose[2]

[1]Assistant Director for Mathematical and Physical Sciences, National Science Foundation, Arlington, VA 22230, USA. [2]Assistant Director for Computer and Information Science and Engineering, National Science Foundation, Arlington, VA 22230, USA.

*Corresponding author. Email: jkurose@nsf.gov

REFERENCES AND NOTES

1. NSF, "10 big ideas for future NSF investments" (www.nsf.gov/about/congress/reports/nsf_big_ideas.pdf).
2. J. Mervis, "NSF director unveils big ideas, with an eye on the next president and congress," *Science*Insider (2016); www.sciencemag.org/news/2016/05/nsf-director-unveils-big-ideas-eye-next-president-and-congress.
3. National Science Board Meetings (http://nsf.gov/nsb/meetings/).
4. Global Environment for Network Innovations (GENI); www.geni.net/.
5. A search of NSF's awards database (www.nsf.gov/awardsearch/advancedSearch.jsp) for Active Awards in the Division of Astronomical Sciences (AST), Element Code 1257, with Original Award Dates between 1 April 2014 and 1 July 2015 yields five results.

10.1126/science.aah5056

ERRATA

Erratum for the Research Article "De novo design of protein homo-oligomers with modular hydrogen-bond network–mediated specificity" by S. E. Boyken *et al.*, *Science* **352**, aag1318 (2016). Published online 20 May 2016; 10.1126/science.aag1318

ONLINE BUZZ

Six-word stories

In the 1 July issue, we ran six-word stories by a variety of scientists about their experiences. Read them at http://science.sciencemag.org/content/353/6294/22.

On Twitter, we asked you to add your own six-word stories. Here are some of your responses:

So much data. Oh joy! More!
Osborne Transformer / @Osborne_Xfmr

#Gradschool is making everything from scratch.
Whitney F / @Wafers101

Had a nightmare, Neanderthals were back!
Danae Dodge / @DanaeDodge

Academia killed science with public relations.
André Esteves / @aifesteves

Our proposal got funded! NOW WHAT?!
Beck E. Strauss / @StraussBecky

My Twitter? It's networking, not procrastinating.
JW Stubbing Research / @StubbingScience

Have a six-word story to add? Post it on Twitter with hashtag #NextGenSci!

Published by AAAS

Downloaded from http://science.sciencemag.org/ on September 3, 2016

PHOTO: AAAS/COLELLA DIGITAL

Educators collaborate to optimize STEM teacher prep

AAAS 2016 Noyce Summit unites academics and practitioners to develop research agenda

By **Michaela Jarvis**

New Tech High School teacher Ben Woodford lives and breathes mathematics, and every day before class, he asks each of his students to send him a text. Their messages, however, may have nothing to do with equations or diagrams. Instead, they answer the question, what's going on that's most meaningful in your life?

Answers vary from the trivial to the tragic, the third-year teacher reported at the 2016 Noyce Summit education conference, but most importantly, the messages give Woodford an opportunity to know his students, to convey that he cares, to help out if he can, or at least to talk with a student facing a challenge. He said that his digital "daily check-in" is a crucial part of being an effective STEM (science, technology, engineering, and math) teacher in his high-need school district in Nipomo, California. "I don't know how I could do what I'm doing without it," said Woodford. "Being able to bond with students and create a trusting relationship helps us to overcome psychological hurdles that could prevent them from learning math."

Woodford's strategy is an example of a new current in education that advocates learning who your students are in order to teach them effectively. Presented at the 20 to 22 July summit, which was co-hosted by the AAAS Education and Human Resources Program and the National Science Foundation (NSF) Division of Undergraduate Education, the approach represented just one idea of potential value to the 500-plus attendees at the conference, among them, college and university faculty and researchers, students training to be teachers and researchers, and current K-12 teachers.

The NSF Robert Noyce Teacher Scholarship Program helps talented STEM majors and professionals to become K-12 science and math teachers. While building a community and giving teachers a venue where they can share ideas is among the important goals of the yearly Noyce Summit, this year's event also advanced a $3.7 million AAAS initiative, funded by NSF, to help stimulate research and foster evidence-based innovations in the preparation of STEM teachers for high-need schools.

"What we want to do is provide a guide for researchers who want to investigate STEM preservice education," said Yolanda George, deputy director of the AAAS Education and Human Resources Programs, adding that the resulting information would be disseminated "as widely as possible" throughout the education field.

Responding to this country's critical need for STEM teachers, and for teaching that supports students all the way to graduation and employment in ever-expanding STEM fields, education researchers and practitioners have fought hard to build effective approaches, and AAAS has helped to spearhead those efforts, said Rush Holt, AAAS CEO and executive publisher of the *Science* family of journals. "The STEM education reform movement—hands-on, inquiry-based, standards-based—grew out of AAAS activities, meetings we convened," said Holt, who spoke at the conference, adding that STEM education is important, not only to provide the workforce needed in the 21st century, but also to ensure that citizens understand the importance of basing policy decisions that determine our future on sound evidence.

"You're the centerpiece of the national effort to give America the STEM education that we need, so there's a lot riding on your shoulders," Holt told the Noyce Summit attendees. "I don't think it's an overstatement to say it's the most important challenge facing the country right now."

The challenge of training enough effective STEM teachers in this country is complicated by persistent problems. For decades, experts have referred to a "leaky pipeline" in STEM education. "Of every 100 people who walk in [to earn a bachelor's degree], we have about eight who stay through getting a bachelor's degree in STEM and actually working in STEM. And for minority students, it's even

Downloaded from http://science.sciencemag.org/ on September 3, 2016

Published by AAAS

Ben Woodford and teacher Sunshine Roque, of San Francisco's Lincoln High School, participated in a panel discussion.

worse. It really is dismal," said Roni Ellington, associate professor of mathematics education at Morgan State University.

The problem of recruiting STEM teachers is compounded by high attrition. Of every five new science teachers, one quits in the first year, said University of Pennsylvania Board of Overseers Professor of Education and Sociology Richard Ingersoll. That percentage can be dramatically improved, however, with preservice preparation such as coursework in teaching methods, practice teaching, instruction in selecting course materials, and child psychology classes, Ingersoll said.

Among the evidence provided at the conference of the need for improved outreach to potential STEM teachers was a graphic presented by Susan Singer, then director of the National Science Foundation's Division of Undergraduate Education. It showed that bachelor's degree attainment by age 24 in the highest quarter of the socioeconomic scale went from 40% to 77% between 1970 and 2013. For the lowest-income quartile, that percentage was 6% in 1970 and had only grown to 9% in 2013. "The gap has widened," said Singer, "and it represents a tremendous amount of untapped talent out there [among students who could be] future teachers." To cultivate that untapped talent, Singer said, educators have solid evidence of methods that work in STEM education—such as focusing on conceptual learning, problem-solving, and use of representations such as diagrams and evolution trees—but those methods are used in very few undergraduate classrooms where STEM teachers receive their training, Singer said.

Singer singled out active learning as an educational strategy that research shows is effective, demonstrating the example of a bicycle wheel that could be held by its axis while being spun. Students who spun the wheel and then tipped it to the side felt the vector of the resulting angular momentum. "Students who actually got to hold this bicycle wheel did much better—in a statistically significant way—when tested on angular momentum problems," Singer said. The same students did no better on other types of physics problems after spinning the wheel. "This could be very important," said Singer, "especially for the lab and field sciences as we think about what things are going to be really important to have our students do. The difference [in achievement] between classrooms with and without active learning is stunning."

Meanwhile, researchers are trying to weigh preliminary evidence related to skills students possess that are not easily measurable, such as being able to work in a team, communicating well, having academic tenacity, and "grit." Possessing such skills, according to Singer, has been correlated with success in college, specifically in STEM majors, but much more research is needed to know, for instance, whether it is possible to coach students in order to increase those skills.

Brent Duckor, associate professor in the Department of Teacher Education at San José State University, frames such "noncognitive" skills in a different way, putting the emphasis, not on whether a student inherently possesses tenacity, for instance, but on what seems to encourage perseverance and the contexts for learning that advance deeper student engagement. Duckor is a former high school teacher at a nationally recognized high school in East Harlem that pioneered Habits of Mind, which emphasizes interdisciplinary and project-based learning.

"We know that purpose and meaning matter for kids," said Duckor, who led brainstorming sessions at the summit on how to increase STEM teacher effectiveness. "If our students find purpose in what they do, they tend to stick with it. When kids have a voice and a sense of agency in their learning, then they tend to stick with the subject. Effective teachers and schools help students meet real scientists, mathematicians, engineers and technology specialists so they can engage more deeply with people in the outside world who are practitioners of STEM."

As researchers work to build "a deeper, richer evidence base" for the preparation of STEM teachers, they face the challenge of keeping the measures of educational research as uniform as possible, Singer said, emphasizing shared tools and clean data. "How are you going to make it interoperable?" she said. "How do we scale the great ideas?"

The Noyce networks of students, teachers, and researchers can help organize such research and the many approaches to a complex field, Singer said. "You're a beautiful example of connectivity in the departments of education and the colleges of arts and sciences," she said. "You're a wonderful model for where this should go."

Also expressing satisfaction with the cross-fertilization of the various communities represented at the Noyce Summit, Shirley Malcom, director for AAAS Education and Human Resources Programs, said that it is possible to experiment with new classroom methods and then to "backfill" according to what the research bears out in order to bolster and improve preservice education of STEM teachers, and STEM education itself, as quickly as possible.

Gabrielle Kristofich, an aspiring STEM teacher studying economics and elementary education at the University of Colorado, said that the Noyce Summit expanded her own network as she heads into her first year of teaching, and her awareness of new ideas in STEM education and the complex processes involved.

"It allowed me to reimagine what's possible," Kristofich said.

AAAS annual election: Preliminary announcement

The 2016 AAAS election of general and section officers is scheduled to begin in October. All members will receive a ballot for election of the president-elect, members of the Board of Directors, and members of the Committee on Nominations. Additionally, members registered in sections (up to three) will receive ballots for the specified section elections. Biographical information for the candidates will be provided along with ballots. The general election slate is listed below. The list of section candidates can be viewed at www.aaas.org/annual-election.

Names may be placed in nomination for any office by petition submitted to the Chief Executive Officer no later than 23 September 2016. Petitions nominating candidates for president-elect, members of the Board, or members of the Committee on Nominations must bear the signatures of at least seven members of the association. A petition to place an additional name in nomination for any office must additionally be accompanied by the nominee's curriculum vitae as well as a statement of acceptance of nomination.

General Election Slate

President-Elect

Margaret A. Hamburg, National Academy of Medicine; Douglas S. Massey, Princeton Univ.

Board of Directors

Mark C. Fishman, Harvard Medical School; S. James Gates Jr., Univ. of Maryland, College Park; Kaye Husbands Fealing, Georgia Institute of Technology; Thomas E. Lovejoy, George Mason Univ./ United Nations Foundation

Committee on Nominations

To be announced

Downloaded from http://science.sciencemag.org/ on September 3, 2016

Published by AAAS

RESEARCH

Coordination chemistry of berkelium

Silver et al., *p. 888*

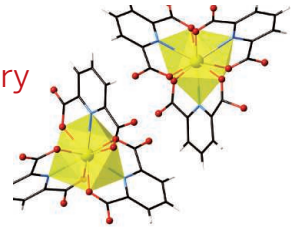

IN *SCIENCE* JOURNALS

Edited by **Nick Wigginton**

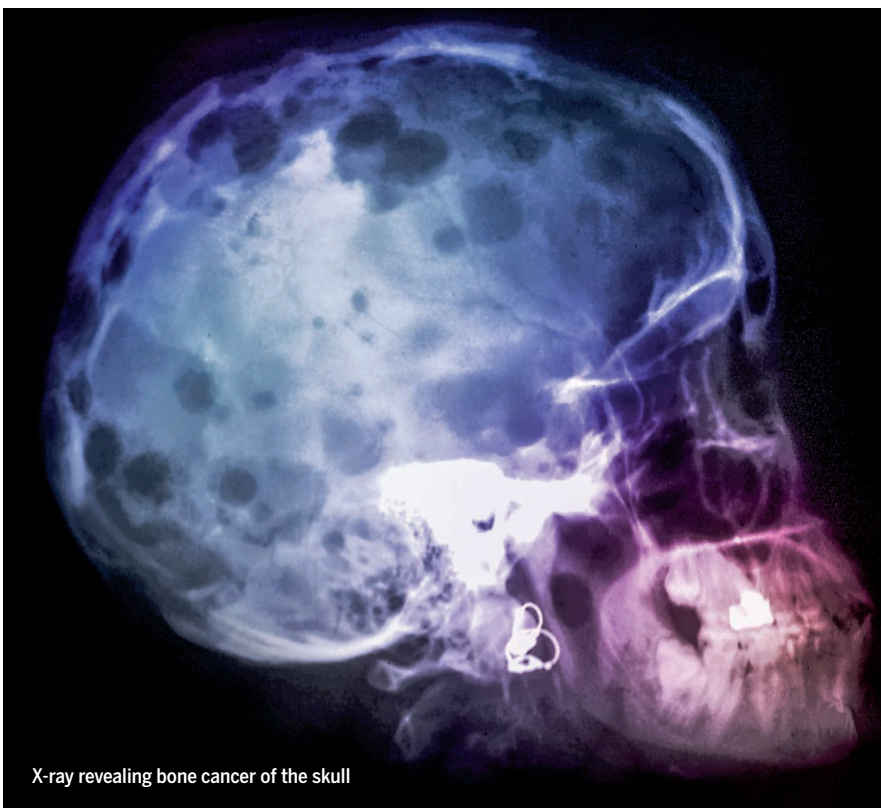

X-ray revealing bone cancer of the skull

CANCER METASTASIS

Myeloma enzyme makes way for metastasis

Bone tissue is built up by osteoblasts and broken down by osteoclasts in a balanced remodeling process. In metastatic cancer, however, the balance is tipped, leading to the formation of cancerous growths in the bone. Attempts to prevent metastasis have not been successful in the clinic, so Liu *et al.* set out in search of a new pathway to target. The authors found that an enzyme called thymidine phosphorylase (TP), which is produced by myeloma cells, suppressed osteoblast activity (new bone formation) and enhanced osteoclast activity (bone resorption). Inhibiting this enzyme reduced the incidence of myeloma-induced osteolytic bone lesions, suggesting a new target for translation to the clinic—especially given that certain TP inhibitors are already approved for human use. —MLF

Sci. Transl. Med. **8**, 353ra113 (2016).

STRUCTURAL BIOLOGY

How spliceosomes make the first cut

In eukaryotes, transcribed precursor mRNA includes noncoding sequences that must be spliced out. This is done by the spliceosome, a dynamic complex in which five small nuclear RNAs and several proteins go through a series of ordered interactions and conformational rearrangements to achieve splicing. Two protein structures provide a look at the first catalytic step in the pathway. Yan *et al*. report the structure of the activated spliceosome (the B^{act} complex) at 3.5 Å resolution, revealing how latency is maintained even though the complex is mostly primed for catalysis. Wan *et al*. report the structure of the catalytic step 1 spliceosome (the C complex) at 3.4 Å resolution; this complex forms after the first step of the splicing reaction. —VV

Science, this issue pp. 904 and 895

ULTRAFAST DYNAMICS

Shining a fast light on diamonds

Conceptually, the electronic structure of matter is a fixed scaffold of energy levels, which electrons climb with the help of light absorption. In reality, the light's electromagnetic field distorts the scaffold, a phenomenon that becomes increasingly evident with rising field intensity. Lucchini *et al*. studied a manifestation of this phenomenon, termed the dynamical Franz Keldysh effect, in diamond substrates exposed to sudden, moderately intense infrared fields. Using attosecond probe pulses and accompanying theoretical simulations, they resolved and accounted for the extremely rapid ensuing electron dynamics. —JSY

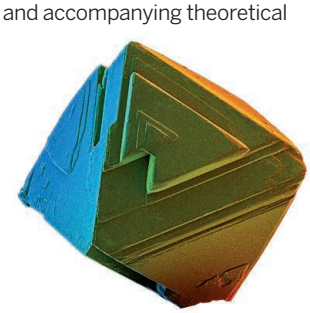

Microcrystalline diamonds are used to measure electron dynamics.

Science, this issue p. 916

TIME SERIES ANALYSIS

Harnessing complexity in ecology

Ecology concerns the behavior of complex, dynamic, interconnected systems of populations, communities, and ecosystems over time. Yet ecological time series can be relatively short, owing to practical limits on study duration. Ye and Sugihara introduce an analytical approach called multiview embedding, which harnesses the complexity

PHOTOS (FROM TOP): ZEPHYR/SCIENCE SOURCE; DAVID SCHARF/SCIENCE SOURCE

Published by AAAS

of short, noisy time series that are common in ecology and other disciplines such as economics. Using examples from published data sets, they show how this approach enhances the tractability of complex data from multiple interacting components and offers a way forward in ecological forecasting. —AMS

Science, this issue p. 922

SINGLE-CELL GENOMICS

Visualizing gene expression in nuclei

Gene expression can vary greatly within a single cell. Using techniques that they developed for sequencing single nuclei and labeling proliferating cells in vivo, Habib *et al*. performed RNA sequencing of 1402 single nuclei from the adult mouse hippocampus. Combining this approach with a clustering algorithm for single-cell and -nucleus RNA sequencing data delineated specific cell types during cell differentiation and development. By providing polyadenylated RNA from nuclei alone, as opposed to cytoplasmic RNA, these methods open the application of single-cell transcriptomics to tissues in which individual cells are difficult to isolate. —LMZ

Science, this issue p. 925

VIROLOGY

New insights into norovirus entry

There's no escaping norovirus when you have it—the symptoms from this gastroenteritis-causing virus, though brief, are often debilitating. Preventing infections will rely on improving our understanding of how norovirus enters host cells. Orchard *et al*. show that the entry of murine norovirus (MNoV) into host cells requires a protein called CD300lf. In cell culture, mouse cells needed to express CD300lf in order for MNoV binding, entry, and replication to occur. Deleting the gene encoding CD300lf in mice protected them against MNoV infection. Human cells expressing CD300lf allowed MNoV to break the species barrier, a finding that may lead to new insights into the infectivity of this virus. —KLM

Science, this issue p. 933

INNATE IMMUNITY

A new trick for IL-1β

One strategy to tame the symptoms of autoimmune diseases is to block the pain-causing inflammation. For rheumatoid arthritis, one such therapy is the interleukin-1β (IL-1β) receptor antagonist anakinra; however, patients who receive anakinra have increased susceptibility to group A *Streptococcus* (GAS) infections. LaRock *et al*. examined the mechanisms governing this effect and found that a microbial protease, SpeB, activates IL-1β by directly cleaving the prodomain that prevents IL-1β signaling. Blocking this inflammatory response with anakinra may account for the more frequent GAS infections in patients with rheumatoid arthritis, an effect that may also hold true for their increased susceptibility to infection by other microorganisms. —AB

Sci. Immunol. **1**, aah3539 (2016).

GEOPHYSICS

A seismic "weather bomb" detector

Seismic tomography is like an x-ray of Earth's interior, except that it uses earthquakes for the illumination. Earthquakes are imperfect illuminators because they are clustered on plate boundaries, leaving much of the interior in the shadows. Using a seismic array in Japan, Nishida and Takagi detected seismic waves that they attribute to a severe and distant North Atlantic storm called a "weather bomb" (see the Perspective by Gerstoft and Bromirski). The seismic energy traveling from weather bombs through the Earth appears to be capable of illuminating the many dark patches of Earth's interior. —BG

Science, this issue p. 919; see also p. 869

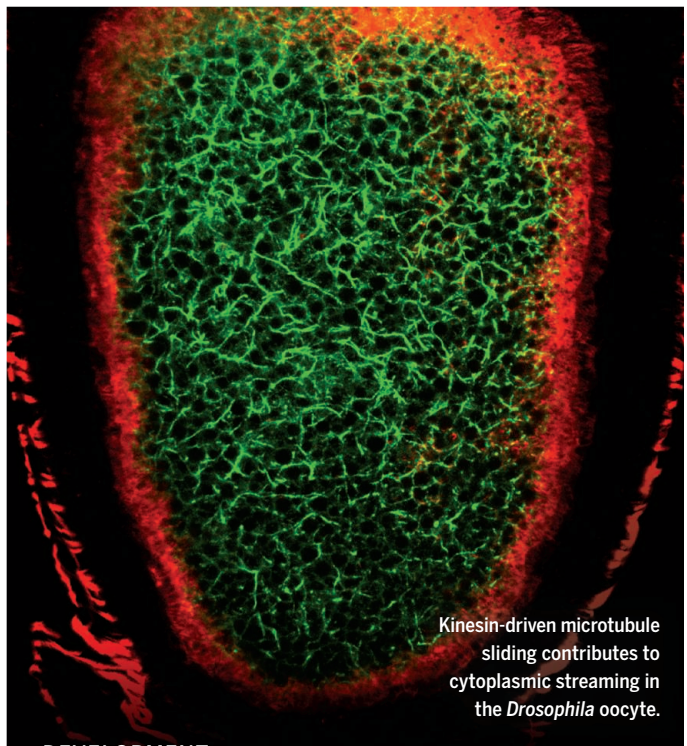

Kinesin-driven microtubule sliding contributes to cytoplasmic streaming in the *Drosophila* oocyte.

PHOTO: WEN LU, JOSHUA Z. RAPPOPORT AND VLADIMIR I. GELFAND (NORTHWESTERN UNIVERSITY)

DEVELOPMENT

Microtubule sliding during *Drosophila* development

The motor protein kinesin carries cargo to locations in the cell by moving along microtubules. Kinesin-1 can also move microtubules relative to each other. Winding *et al*. show that it does this by using its motor domain to move along one microtubule while using a second domain to bind another microtubule. They constructed a kinesin-1 mutant that was deficient in microtubule binding but able to bind and transport other cargo and a second mutant that was able to slide microtubules but could not transport cargo. Using these mutants, they demonstrated that microtubule sliding is important in axon and dendrite outgrowth during nervous system development. In addition, Lu *et al.* used the mutants to show that microtubule sliding contributes to cytoplasmic streaming, which is important in distributing RNA and proteins in *Drosophila* oocytes. —VV

Proc. Natl. Acad. Sci. U.S.A. 10.1073/pnas.1520244113 and 10.1073/pnas.1522424113 (2016).

OPTICS

An integrated route to frequency combs

A frequency comb is a light source that provides a spectrum of precisely spaced wavelengths, the range of which can sometimes span over an octave. Such a light source can find a broad range of applications in spectroscopy, sensing, metrology, and communication. There are considerable efforts under way to generate such combs "on chip" by using

Published by AAAS

ALSO IN *SCIENCE* JOURNALS

Edited by **Nick Wigginton**

MATERIALS SCIENCE

From quantum dot to quantum dot

A wide range of materials can now be synthesized into semiconducting quantum dots. Because these materials grow from solutions, there is scope to combine quantum dots into devices by using simple, low-cost manufacturing processes. Kagan *et al*. review recent progress in tailoring and combining quantum dots to build electronic and optoelectronic devices. Because it is possible to tune the size, shape, and connectivity of each of the quantum dots, there is potential for fabricating electronic materials with properties that are not available in traditional bulk semiconductors. —MSL

Science, this issue p. 885

STRUCTURAL BIOLOGY

A window into the cell for vitamin A

Vitamin A is an essential nutrient for mammals, and its metabolites affect diverse biological processes. It is carried in the bloodstream as retinol by retinol binding protein (RBP); a protein called STRA6 is implicated in facilitating retinol translocation across the cell membrane. Chen *et al*. determined the structure of zebrafish STRA6 to a resolution of 3.9 Å by electron microscopy. A lipophilic cleft is a likely binding site for RBP, and an opening in the cleft may allow retinol to diffuse into the membrane. Unexpectedly, the structure also includes bound calcium-modulated protein, but its function remains unclear. —VV

Science, this issue p. 887

ACTINIDE CHEMISTRY

Bonding to berkelium

A geographical theme prevailed in the recent naming of the heaviest chemical elements. The choices brought to mind berkelium (Bk) and californium (Cf), the names chosen for elements 97 and 98 over half a century ago. Silver *et al*. now revisit the chemistry of Bk, which has proven fiercely challenging to study over the years on account of its vigorous radioactive decay. Synthetic crystallized Bk borate and dipicolinate compounds structurally resembled Cf analogs in the solid state but manifested distinct electronic and magnetic characteristics stemming from spin-orbit coupling effects. —JSY

Science, this issue p. 888

HEALTH ECONOMICS

Delivering chlorine to those who use it

In developed countries, a consumer's valuation of a health product can be measured by his or her willingness to pay for it. But poorer individuals, especially those in developing countries, might want and need a product yet be unable to pay for it with money. Dupas *et al*. demonstrate that a nonprice voucher mechanism can be used to deliver chlorine for water treatment to people in Kenya who are too poor to pay for it, but who use it when they get it (see the Perspective by Olken). Having to redeem the vouchers screens out people who would accept the free chlorine solution but not use it. —GJC

Science, this issue p. 889; see also p. 864

ORGANIC SYNTHESIS

Rapid ryanodol route

The plant-derived compound ryanodine and its hydrolyzed cousin ryanodol are biochemically interesting for their calcium-regulating capacity and chemically interesting for their dense tangle of carbon rings brimming with oxygen appendages. Chuang *et al*. report an efficient 15-step asymmetric synthesis of ryanodol from the structurally much simpler terpene pulegone (see the Perspective by Verdaguer). Key steps include a Pauson-Khand cyclization of a tethered alkene and alkyne with carbon monoxide to set the ring motifs, followed by an oxidation using selenium dioxide that delivers three different oxygen substituents in tandem. –JSY

Science, this issue p. 912; see also p. 866

SIGNAL TRANSDUCTION

How hypoxia controls the kinase Akt

The protein kinase Akt controls cell survival and proliferation. In human cells in culture, Guo *et al*. found that Akt was modified by the prolyl hydroxylase EglN1 (see the Perspective by Voulgarelis and Tsichlis). Such prolyl hydroxylation suppressed enzymatic activity of Akt. EglN1 is sensitive to oxygen concentrations, and in cells experiencing hypoxia, EglN1 activity decreased and Akt became activated. This activation was associated with decreased binding of Akt to the pVHL tumor suppressor protein, which bound preferentially to prolyl-hydroxylated Akt and inhibited its activity. These effects could promote growth and survival of tumor cells exposed to hypoxia. —LBR

Science, this issue p. 929; see also p. 870

CONSERVATION

Harnessing expert knowledge

Complex conservation efforts can fail without effective communication between experts, policy-makers, and local people. For example, an attempt to use electric fences to prevent crop raiding by elephants in Kenya failed because the design did not fully account for the interests of different local groups. In a Perspective, Adams describes how experts' views of ecosystems may evolve under different scenarios, irrespective of their backgrounds. Transdisciplinarity, diversity, and transparency are crucial for groups of scientific experts to best contribute to effective conservation efforts. —JFU

Science, this issue p. 867

NEURONAL PLASTICITY

More responsive with epigenetics

Various neuropsychiatric and neurological diseases can change intrinsic membrane excitability, which affects how responsive neurons are to stimuli. Meadows *et al*. found that inhibiting the methylation of cytosines in DNA made cultured cortical neurons more responsive to stimuli. The increase in responsiveness was due to a decrease in the activity of a specific family of potassium channels, and inhibiting these channels enhanced intrinsic membrane excitability to a similar extent as inhibiting DNA cytosine methylation. Thus, epigenetic remodeling of DNA can control neuronal activity by altering the electrophysiological properties of the entire neuron. —NRG

Sci. Signal. **9**, ra83 (2016).

PHOTOSYNTHESIS

Sometimes, red light means grow

Some cyanobacteria are able to use the far-red end of the light spectrum by synthesizing chlorophyll f pigments. Introducing the protein responsible for chlorophyll f synthesis into crop plants could potentially expand the range of wavelengths that such plants use during photosynthesis and thereby increase their growth efficiency. Ho *et al*. identified chlorophyll f synthase

Published by AAAS

(ChlF) in two cyanobacteria that are acclimatized to grow using far-red light. Introducing the ChlF-encoding gene into a model cyanobacterium allowed the organism to synthesize chlorophyll f. Similarities between ChlF and a core protein of photosystem II suggest that they have a close evolutionary relationship, and ChlF may even represent a more primitive photochemical reaction center. —NW

Science, this issue p. 886

Published by AAAS

of short, noisy time series that are common in ecology and other disciplines such as economics. Using examples from published data sets, they show how this approach enhances the tractability of complex data from multiple interacting components and offers a way forward in ecological forecasting. —AMS

Science, this issue p. 922

SINGLE-CELL GENOMICS

Visualizing gene expression in nuclei

Gene expression can vary greatly within a single cell. Using techniques that they developed for sequencing single nuclei and labeling proliferating cells in vivo, Habib *et al*. performed RNA sequencing of 1402 single nuclei from the adult mouse hippocampus. Combining this approach with a clustering algorithm for single-cell and -nucleus RNA sequencing data delineated specific cell types during cell differentiation and development. By providing polyadenylated RNA from nuclei alone, as opposed to cytoplasmic RNA, these methods open the application of single-cell transcriptomics to tissues in which individual cells are difficult to isolate. —LMZ

Science, this issue p. 925

VIROLOGY

New insights into norovirus entry

There's no escaping norovirus when you have it—the symptoms from this gastroenteritis-causing virus, though brief, are often debilitating. Preventing infections will rely on improving our understanding of how norovirus enters host cells. Orchard *et al*. show that the entry of murine norovirus (MNoV) into host cells requires a protein called CD300lf. In cell culture, mouse cells needed to express CD300lf in order for MNoV binding, entry, and replication to occur. Deleting the gene encoding CD300lf in mice protected them against MNoV infection. Human cells expressing CD300lf allowed MNoV to break the species barrier, a finding that may lead to new insights into the infectivity of this virus. —KLM

Science, this issue p. 933

INNATE IMMUNITY

A new trick for IL-1β

One strategy to tame the symptoms of autoimmune diseases is to block the pain-causing inflammation. For rheumatoid arthritis, one such therapy is the interleukin-1β (IL-1β) receptor antagonist anakinra; however, patients who receive anakinra have increased susceptibility to group A *Streptococcus* (GAS) infections. LaRock *et al*. examined the mechanisms governing this effect and found that a microbial protease, SpeB, activates IL-1β by directly cleaving the prodomain that prevents IL-1β signaling. Blocking this inflammatory response with anakinra may account for the more frequent GAS infections in patients with rheumatoid arthritis, an effect that may also hold true for their increased susceptibility to infection by other microorganisms. —AB

Sci. Immunol. **1**, aah3539 (2016).

GEOPHYSICS

A seismic "weather bomb" detector

Seismic tomography is like an x-ray of Earth's interior, except that it uses earthquakes for the illumination. Earthquakes are imperfect illuminators because they are clustered on plate boundaries, leaving much of the interior in the shadows. Using a seismic array in Japan, Nishida and Takagi detected seismic waves that they attribute to a severe and distant North Atlantic storm called a "weather bomb" (see the Perspective by Gerstoft and Bromirski). The seismic energy traveling from weather bombs through the Earth appears to be capable of illuminating the many dark patches of Earth's interior. —BG

Science, this issue p. 919; see also p. 869

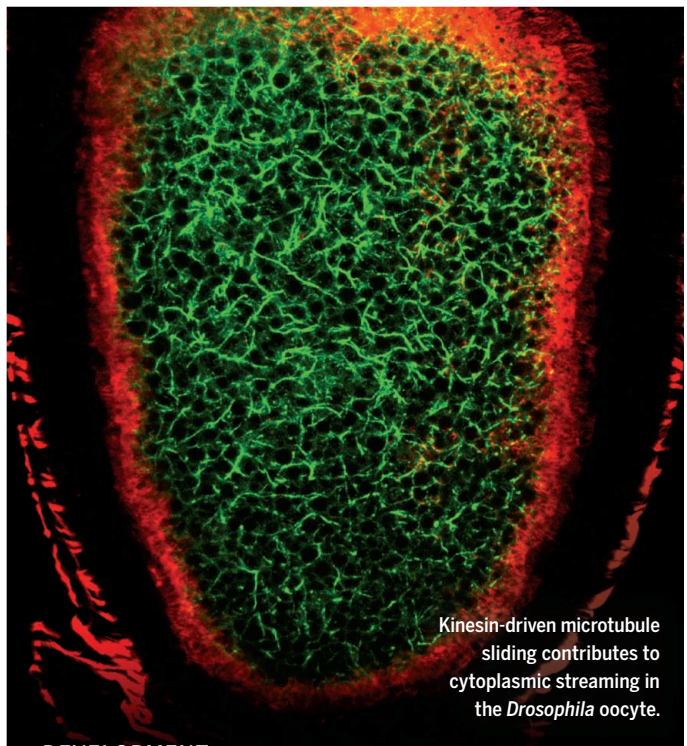

Kinesin-driven microtubule sliding contributes to cytoplasmic streaming in the *Drosophila* oocyte.

PHOTO: WEN LU, JOSHUA Z. RAPPOPORT AND VLADIMIR I. GELFAND (NORTHWESTERN UNIVERSITY)

DEVELOPMENT

Microtubule sliding during *Drosophila* development

The motor protein kinesin carries cargo to locations in the cell by moving along microtubules. Kinesin-1 can also move microtubules relative to each other. Winding *et al*. show that it does this by using its motor domain to move along one microtubule while using a second domain to bind another microtubule. They constructed a kinesin-1 mutant that was deficient in microtubule binding but able to bind and transport other cargo and a second mutant that was able to slide microtubules but could not transport cargo. Using these mutants, they demonstrated that microtubule sliding is important in axon and dendrite outgrowth during nervous system development. In addition, Lu *et al.* used the mutants to show that microtubule sliding contributes to cytoplasmic streaming, which is important in distributing RNA and proteins in *Drosophila* oocytes. —VV

Proc. Natl. Acad. Sci. U.S.A. 10.1073/pnas.1520244113 and 10.1073/pnas.1522424113 (2016).

OPTICS

An integrated route to frequency combs

A frequency comb is a light source that provides a spectrum of precisely spaced wavelengths, the range of which can sometimes span over an octave. Such a light source can find a broad range of applications in spectroscopy, sensing, metrology, and communication. There are considerable efforts under way to generate such combs "on chip" by using

Published by AAAS

PALEOECOLOGY

Climate change and megafaunal extinction

Woolly mammoths went extinct on the Asian and North American mainlands at the end of the last glaciation 13 to 14 thousand years ago. However, small relict populations are known to have survived for several thousand more years on the Beringian islands between the two continents. Graham *et al.* used a suite of paleoenvironmental proxy data to determine that the final extinction of mammoths on St. Paul Island occurred 5600 ± 100 years ago. There is no evidence of human occupation on St. Paul at that time, so hunting can be ruled out as a cause of the mammoths' disappearance from the island. Instead, their demise was caused by climate change and rising sea level acting synergistically to deplete freshwater resources. —AMS

Proc. Natl. Acad. Sci. USA 10.1073/pnas.1604903113 (2016).

Wooly mammoths survived on St. Paul Island in the Bering Sea for thousands of years after other populations went extinct.

microresonator cavities, thus providing the possibility of an integrated optics approach whereby the technology can be shrunk. Pu *et al*. report one such approach based on an AlGaAs-on-insulator platform. With the AlGaAs platform well developed in terms of processing and the material's optical properties well understood, the demonstration of such an approach could prove useful for the widespread commercialization of frequency comb technology. —ISO

Optica **3**, 823 (2016).

PSYCHOLOGY

Slow-motion state of mind

Memory is fallible and therefore a potentially unreliable source of information in a court of law. Much better would be video evidence of a crime. Caruso *et al.* show that this is not always so, however. Watching surveillance video of a shooting during an attempted robbery in slow-motion replay gave viewers a stronger impression that the shooter fired with the intent to kill, compared with watching it at regular-speed playback. This effect on perception of premeditation was reduced, though not eliminated, by viewing the video at both regular and slow-motion speed, but it was not mitigated simply by indicating elapsed time. —GR

Proc. Natl. Acad. Sci. U.S.A. 10.1073/pnas.1603865113 (2016).

Watching surveillance video in slow motion increases perception of an intent to kill.

PIEZOELECTRICS

Making vibration sensors noble

Piezoelectric materials produce an electrical current in response to mechanical stress, making them exceptional vibration sensors and actuators. Piezoelectric materials tend to be oxides, the most common example being quartz (SiO_2). Stenner *et al*. show that the nanoporous gold impregnated with electrolyte solution produces an exceptionally large electrical charge in response to stress. The electrical response to strain comes from the charge polarization of internal interfaces. The distinct mechanism for generating a charge from traditional piezoelectrics suggests that other nanoporous metals may also be useful for electromechanical coupling applications. —BG

Adv. Funct. Mater. 10.1002/adfm.201600938 (2016).

MATERIALS CHEMISTRY

A framework for drug delivery

Metal-organic frameworks (MOFs) are attractive candidates for drug delivery if they can be formed from low-toxicity materials. Levine *et al*. noted that olsalazine, a low-toxicity anti-inflammatory drug used in treatment of gastrointestinal diseases, is tolerated in multigram doses and structurally related to the ligands used to create M-MOF-74. One-dimensional hexagonal pore structures with diameters of 2.7 nm were formed from olsalazine and dications such as Mg^{2+} or Fe^{2+}. These materials not only displayed a high capacity for H_2 adsorption, but they could also be loaded with model drugs such as phenethylamine. Pressed pellets of the Mg-based material released 50% of the olsalazine and 95% of the phenethylamine after 3 hours in phosphate-buffered saline, suggesting applications for multidrug delivery. —PDS

J. Am. Chem. Soc. 10.1021/jacs.6b03523 (2016).

CREDITS (FROM TOP): FUNKMONK/WIKICOMMONS; HARRIS COUNTY SHERRIF'S OFFICE VIA HOUSTON CHRONICLE/ ASSOCIATED PRESS

Published by AAAS

REVIEW SUMMARY

MATERIALS SCIENCE

Building devices from colloidal quantum dots

Cherie R. Kagan,* Efrat Lifshitz,* Edward H. Sargent,* Dmitri V. Talapin*

BACKGROUND: The Information Age was founded on the semiconductor revolution, marked by the growth of high-purity semiconductor single crystals. The resultant design and fabrication of electronic devices exploit our ability to control the concentration, motion, and dynamics of charge carriers in the bulk semiconductor solid state.

Our desire to introduce electronics everywhere is fueled by opportunities to create intelligent and enabling devices for the information, communication, consumer product, health, and energy sectors. This demand for ubiquitous electronics is spurring the design of materials that exhibit engineered physical properties and that can enable new fabrication methods for low-cost, large-area, and flexible devices.

Semiconductors, which are at the heart of electronics and optoelectronics, come with high demands on chemical purity and structural perfection. Alternatives to silicon technology are expected to combine the electronic and optical properties of inorganic semiconductors (high charge carrier mobility, precise n- and p-type doping, and the ability to engineer the band gap energy) with the benefits of additive device manufacturing: low cost, large area, and the use of solution-based fabrication techniques. Along these lines, colloidal semiconductor quantum dots (QDs), which are nanoscale crystals of analogous bulk semiconductor crystals, offer a powerful platform for device engineers. Colloidal QDs may be tailored in size, shape, and composition and their surfaces functionalized with molecular ligands of diverse chemistry. At the nanoscale (typically 2 to 20 nm), quantum and dielectric confinement effects give rise to the prized size-, shape-, and composition-tunable electronic and optical properties of QDs. Surface ligands enable the stabilization of QDs in the form of colloids, allowing their bottom-up assembly into QD solids. The physical properties of QD solids can be designed by selecting the characteristics of the individual QD building blocks and by controlling the electronic communication between the QDs in the solid state. These QD solids can be engineered with application-specific electronic and optoelectronic properties for the large-area, solution-based assembly of devices.

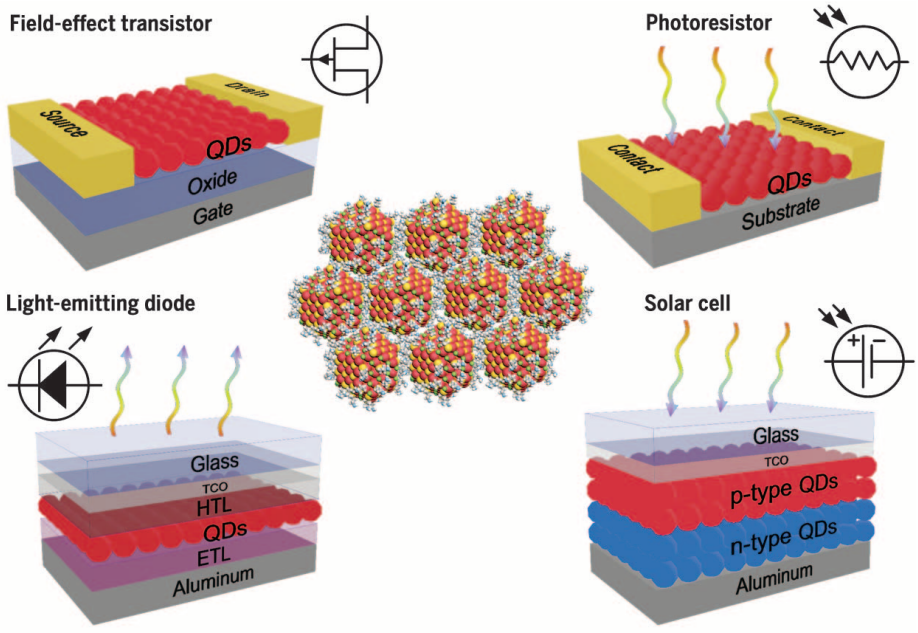

Colloidal quantum dot device architectures. Colloidal quantum dots (center) may be engineered in size, shape, and surface chemistry and deposited from solution to be integrated as thin-film solids in different electronic and optoelectronic devices that modulate and transmit charge and transduce light and electricity. [Figure courtesy of O. Voznyy and F. S. Stinner]

ADVANCES: The large surface-to-volume ratio of QDs places a substantial importance on the composition and structure of the surface in defining the physical properties that govern the concentration, motion, and dynamics of excitations and charge carriers in QD solids. Recent studies have shown pathways to passivate uncoordinated atoms at the QD surface that act to trap and scatter charge carriers. Surface atoms, ligands, and ions can serve as dopants to control the electron affinity of QD solids. Surface ligands and surrounding matrices control the barriers to electronic, excitonic, and thermal transport between QDs and between QDs and matrices. New ligand chemistries and matrix materials have been reported that provide freedom to control the dynamics of excitons and charge carriers and to design device interfaces. These advances in engineering the chemical and physical properties of the QD surface have been translated into recent achievements of high-mobility transistors and circuits, high-quantum-yield photodetectors and light-emitting devices, and high-efficiency photovoltaic devices.

ON OUR WEBSITE

Read the full article at http://dx.doi.org/10.1126/science.aac5523

OUTLOOK: The dominant role and dynamic nature of the QD surface, and the strong motive to build novel QD devices, will drive the exploration of new surface chemistries and matrix materials, processes for their assembly and integration with other materials in devices, and measurements and simulations with which to map the relationship between surface chemistry and materials and device properties. Challenges remain to achieve full control over the carrier type, concentration, and mobility in the QD channel and the barriers and traps at device interfaces that limit the gain and speed of QD electronics. Surface chemistries that allow for both long carrier lifetime and high carrier mobility and the freedom to engineer the bandgap and band alignment of QDs and other device layers are needed to exploit physics particular to QDs and to advance device architectures that contribute to improving the performance of QD optoelectronics. The importance of thermal transport in QD solids and their devices is an essential emerging topic that promises to become of greater importance as we develop QD devices.

The list of author affiliations is available in the full article online.
*Corresponding author. Email: kagan@seas.upenn.edu (C.R.K.); ssefrat@technion.ac.il (E.L.); ted.sargent@utoronto.ca (E.H.S.); dvtalapin@uchicago.edu (D.V.T.)
Cite this article as C. R. Kagan *et al.*, *Science* 353, aac5523 (2016). DOI: 10.1126/science.aac5523

Downloaded from http://science.sciencemag.org/ on September 3, 2016

REVIEW

MATERIALS SCIENCE

Building devices from colloidal quantum dots

Cherie R. Kagan,[1]* Efrat Lifshitz,[2]* Edward H. Sargent,[3]* Dmitri V. Talapin[4,5]*

The continued growth of mobile and interactive computing requires devices manufactured with low-cost processes, compatible with large-area and flexible form factors, and with additional functionality. We review recent advances in the design of electronic and optoelectronic devices that use colloidal semiconductor quantum dots (QDs). The properties of materials assembled of QDs may be tailored not only by the atomic composition but also by the size, shape, and surface functionalization of the individual QDs and by the communication among these QDs. The chemical and physical properties of QD surfaces and the interfaces in QD devices are of particular importance, and these enable the solution-based fabrication of low-cost, large-area, flexible, and functional devices. We discuss challenges that must be addressed in the move to solution-processed functional optoelectronic nanomaterials.

The development of modern electronics in the middle of the 20th century has changed the course of human society. Semiconductor crystals, typically of silicon, are used to build high-performance electronic circuits, solar cells, and light detectors. Today, electronics have become increasingly pervasive, and semiconductor devices are fabricated from a broader range of materials and introduced in more diverse forms, from microscopic sensors and implants to mobile devices to TVs, whose active components span meters in size. Solar farms use square miles of semiconductor panels to generate electricity at grid parity cost.

However, semiconductor fabrication processes, originally developed for small chips, become costly when applied to devices with a large form factor. Conventional semiconductor devices are also characteristically planar and rigid. In constrast, emerging applications often require ultracheap electronic devices and their integration on flexible and curved surfaces such as paper, fabric, and plastic.

In recent years, the "one crystal per device" concept has been challenged by the development of materials and processes that allow bottom-up fabrication, in which device parts are assembled from nanoscale components—such as semiconductor quantum dots (QDs), carbon nanotubes, and polymers—by using nontraditional techniques, such as solution-based and additive manufacturing. However, the shift from materials that are bulk single crystals to assemblies of many components introduces challenges, most notably the increased role of interfaces. Interfaces often introduce bottlenecks to charge transport and can also function as recombination sites that reduce carrier lifetime, leading to lower device performance.

Colloidal semiconductor QDs open up opportunities to integrate inorganic semiconductors, with a proven track record in electronic and optoelectronic devices, into high-performance and flexible devices by using low-temperature, large-area, solution-based methods instead of by costly, high-vacuum, high-temperature device manufacturing processes. Tuning of QD size, shape, or building heterostructures into each QD introduces tools for engineering electronic materials with properties not available in traditional bulk semiconductors.

From bulk crystals to QD arrays

Colloidal QDs are a subset of semiconductor nanocrystals (NCs), which at typical 2- to 20-nm diameters show effects of quantum confinement. Each QD contains hundreds to thousands of atoms (Fig. 1A). These colloidal QDs are commonly made of II-VI, III-V, and IV-VI semiconductors by means of inexpensive and scalable, wet-chemical synthetic procedures (*1*, *2*). The synthetic methodology for a wide range of technologically important semiconductors has been advanced to provide QD samples tunable in size and shape and with near-atomic-layer precision (*1*). The surface of as-synthesized QDs is coated with a layer of molecular ligands (Fig. 1A). These ligands stabilize colloidal QDs against precipitation (Fig. 1B), enabling QD inks that can be processed into thin-film electronic and optoelectronic devices through coating and printing techniques (*3*).

After evaporation of the carrier solvent, arrays of QDs form a solid material whose structure depends most notably on the size and shape uniformity of the individual QDs and the solvent characteristics and evaporation rate. A large dispersity in QD size or shape and a fast solvent evaporation rate tend to pack QDs in glassy solids with only short-range order (Fig. 1C, bottom). On the other hand, slow evaporation of the carrier solvent from a colloidal dispersion of QDs with tight size and shape distribution often leads to the formation of long-range ordered superlattices or supercrystals (Fig. 1C, top) (*1*). Either glassy or ordered QD arrays may also be assembled from two different types of QDs in order to form multicomponent QD arrays (*4*, *5*). Such superlattices should be considered supramolecular analogs of atomic crystals, whereas glassy QD films are the cousin of amorphous solids. These QD solids, ordered or amorphous, are used as active components of electronic and optoelectronic devices (*2*). A device can contain one or several QD layers, resembling a multilayer stack of active components in traditional semiconductor devices. Although this Review focuses on semiconductor QDs, colloidal NCs of various materials—including metal oxides, metals, dielectrics, and magnets—can be used in the solution-based fabrication of device components (*6*). The chemistry of surface ligands dictates the dispersability of QDs in different solvents, a topic that is particularly important for the fabrication of multilayered structures that require the deposition of QD colloids from mutually orthogonal solvents (such as polar dimethylformamide and nonpolar hexane).

The core and the surface of individual QDs

The electronic structure of semiconductor QDs differs fundamentally from that of the corresponding bulk material as a result of quantum and dielectric confinement effects. In bulk semiconductors, the large density (~10^{22} cm^{-3}) of covalently and/or ionically bonded atoms creates a high and broad density of conduction and valence band states. The conduction and valence bands are energetically separated by the band gap, which is empty of states (Fig. 2A). Instead of continuous valence and conduction bands, QDs develop discrete states whose energy and symmetry depend on QD size and shape (Fig. 2A). The energy gaps between the states decrease with increasing QD size, thus relating the energy gap between the highest occupied and lowest unoccupied states to the QD size (*7*, *8*).

The large surface-to-volume ratio of QDs introduces a substantial importance on the nature of the surface. A QD surface exposes different crystal facets and creates dangling bonds. Undercoordinated surface atoms often contribute electronic states with energies lying within the band gap of the QD core (Fig. 2B). These surface states alter the electronic and optical properties of QDs because low-energy states may serve as dopants, and deeper band-tail and mid-gap states may act

[1]Department of Electrical and Systems Engineering, Department of Materials Science and Engineering, and Department of Chemistry, University of Pennsylvania, 200 South 33rd Street, Philadelphia, PA 19104, USA. [2]Schulich Faculty of Chemistry, Solid State Institute and Russell Berrie Nanotechnology Institute, Technion, Haifa 32000, Israel. [3]Department of Electrical and Computer Engineering, 10 King's College Rd, Toronto ON M5S 3G4, Canada. [4]Department of Chemistry and James Franck Institute, University of Chicago, Chicago, IL 60637, USA. [5]Center for Nanoscale Materials, Argonne National Laboratory, Argonne, IL 60439, USA.
*Corresponding author. Email: kagan@seas.upenn.edu (C.R.K.); ssefrat@technion.ac.il (E.L.); ted.sargent@utoronto.ca (E.H.S.); dvtalapin@uchicago.edu (D.V.T.)

Downloaded from http://science.sciencemag.org/ on September 3, 2016

to trap charge carriers and provide a path for fast electron-hole recombination (*9*).

Dangling bonds can be satisfied by engaging surface atoms in strong chemical bonding with ligands. This pushes the energy of the occupied surface states below and the unoccupied surface states above the corresponding states of the QD core (Fig. 2C). For example, modifying the surface ligand chemistry for PbS QDs has been used to passivate electronic states, increasing the QD photoluminescence efficiency and the power conversion efficiency of QD solar cells (*10*, *11*).

The understanding of QD surfaces has dramatically improved in recent years (*12*). The combination of electronic, optical, and vibrational spectroscopies (*13*–*16*), nuclear magnetic resonance (*15*, *17*), x-ray and ultraviolet photoelectron spectroscopy (*18*), and high-resolution electron microscopy (*19*) has been used to reveal the arrangement of surface atoms in the QD core, the density and packing of the ligand molecules in the corona surrounding the QD core, and the influence of ligands on the QD electronic structure (*20*, *21*). The integration of experimental techniques and computational methods such as density functional theory and molecular dynamics provides complementary information on the interactions that govern surface structure and binding and enable the construction of compelling models of the QD-ligand interface (*22*, *23*).

The interactions between the QD core and ligand head-group can be rationalized by using the concepts originally developed for molecular coordination compounds and recently adapted to NC surfaces (*24*, *25*). Generally, electron-deficient metal ions at the QD surface interact with electron-rich nucleophilic ligands. These ligands can be either neutral molecules with lone electron pairs such as amines (RNH_2) and phosphines (R_3P) or ionic species such as carboxylate ($RCOO^-$) and various inorganic ions (for example, Cl^-, SnS_4^{4-}). The surface of metal chalcogenides and other compound QDs also exposes electron-rich sites that can interact with electrophilic species, such as $Cd(OOCR)_2$ or $PbCl_2$, that bind to the QD surface via empty orbitals on metal atoms (*25*). These bonding motifs are schematically shown in Fig. 2D. The requirement for QD charge neutrality as a whole constrains the composition of the inorganic core, depending on the type of surface ligands. The QD core can be either stoichiometric, if all ligands are neutral species, or deviate from the stoichiometry of the corresponding parent material, when ligands are charged. CdSe and PbSe QDs synthesized in the presence of carboxylate ligands show metal-to-selenium ratios significantly in excess of unity (*26*, *27*). Binding of small ions, such as OH^- and Cl^-, helps to match the density of ligand coating to the number of surface atoms and achieve more complete passivation of surface dangling bonds (*23*).

QDs may also be integrated in a matrix such as a conductive organic or inorganic host (such as polymers, chalcogenide glasses, oxides, or perovskites) (*12*). Early work in QD photovoltaics and photodetectors used semiconducting polymers, such as polythiophenes, to provide a charge-separating heterojunction (*28*, *29*). However, QD solids have progressed so rapidly in their charge carrier mobilities that the inclusion of a polymer phase typically leads to an undesired reduction in carrier mobility. In the area of light emission, the use of semiconducting polymers as a matrix material has had considerably more success (*30*). Infilling of QD solids through the atomic-layer deposition of oxides has been shown to increase the performance of QD electronics because the oxide matrix acts to passivate and stabilize QD surfaces (*31*, *32*). Recently, the organo-metal halide perovskite, a solution-processable semiconductor complementary to QDs, was successfully incorporated as a large band gap (type I) matrix (*33*) that produced a high degree of passivation of the incorporated QD phase. The perovskites, with their high mobilities, enabled efficient transport of photocharges to and capture across the hetero-interface with the QD inclusions.

QDs as tunable light absorbers and emitters

In bulk semiconductors, free carriers are generated by illumination with photons with energies above the band gap. The high dielectric constant of traditional bulk semiconductor leads to a small Coulomb binding energy of the electron and hole compared with thermal energy at room temperature. In contrast, quantum and dielectric confinement effects in semiconductor QDs give rise to strong optical absorption resonances associated with allowed transitions between discrete electronic states (Fig. 2A), producing electron-hole pairs with relatively large binding energies, thus creating single excitons (X) or multiple excitons [for example, biexcitons (BX)] at an amount depending on the QD absorption cross section at a given photon energy and the intensity of illumination (Fig. 3A, schemes for X and BX).

Electron-hole recombination in bulk crystals of direct band gap semiconductors typically occurs through radiative band-to-band transition. In direct band gap colloidal QDs, the band-to-band transitions have nearly monochromatic colors, with large oscillator strengths owing to the quantization of the electronic states (Fig. 3A). However, dangling bonds at the large-area surface create a high density of mid-gap trap states, introducing a competitive pathway to band-edge recombination. Ligand passivation can satisfy surface bonding and reduce the unintentional trap density and therefore the nonradiative, trap recombination. Another nonradiative route exists both in bulk and colloidal QDs: In the presence of high doping concentrations, recombination is typically dominated by the Auger process, involving the transfer of the electron-hole recombination energy to a neighboring third particle (electron or hole) and its ejection to a "hot" state. In QDs, the Auger process is more efficient with respect to the analogous process in the bulk because conservation of momentum is broken, strong spatial confinement of the carriers enhances multiple carrier Coulomb interactions (*34*), and proximal surface traps can accommodate ejected carriers (*35*). The Auger process leaves behind a charged QD that can interact with a subsequent excitation, forming a charged exciton (X^+) (an exemplary scheme for the Auger process is shown in Fig. 3A).

In addition to surface ligation, the QD surface may be engineered by synthesizing QDs in the

Downloaded from http://science.sciencemag.org/ on September 3, 2016

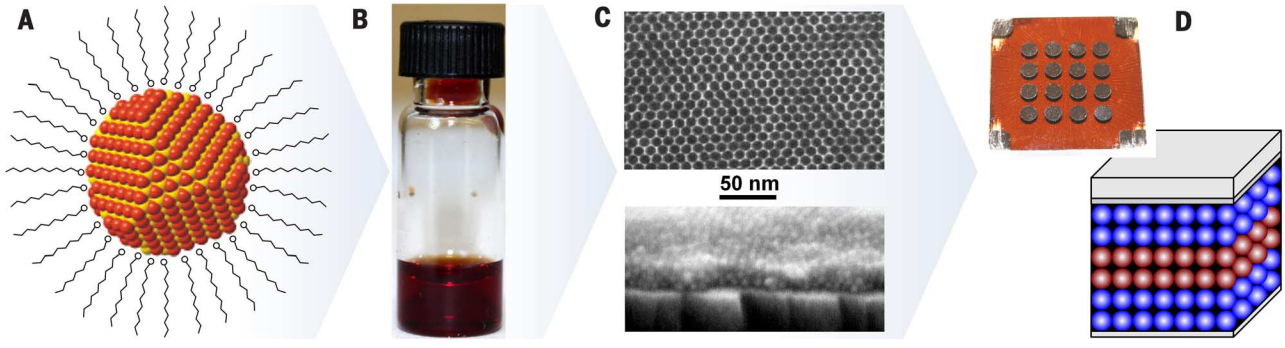

Fig. 1. Assembly of thin-film devices from colloidal QDs. (**A**) Schematic of an individual QD consisting of an inorganic semiconductor core surrounded by a layer of surface ligands. (**B**) The surface ligands stabilize the "QD ink," as seen by a photograph of a colloidal dispersion of QDs in a carrier solvent. (**C**) Colloidal dispersions of QDs can be cast or printed and form either glassy films with random packing of QDs (bottom) or long-range ordered QD superlattices (top), depending on the QD solvent evaporation rate and QD uniformity. (**D**) QD arrays are used as solution-deposited active components of electronic and optoelectronic devices such as transistors, light-emitting diodes, and solar cells (inset). Multiple QD layers can be stacked on top of each other by using chemically orthogonal solvents.

form of inorganic nano-heterostructures comprising a semiconductor core covered by another semiconductor as an epitaxial shell, forming type I and type II configurations. The band-offset in a type I core/shell heterostructure wraps the band edges of the core by that of the shell (Fig. 3B), confining the electron and hole into the core. In a type II or quasi–type II heterostructure, the core and shell band edges are staggered, permitting partial or complete extension of one carrier into the shell (Fig. 3B). This spatial separation of the electron and hole reduces exchange interactions and lowers radiative recombination rates. Thus, engineering the QD surface is a prerequisite for device design, in which type I core/shell QDs are beneficial for achieving high-photoluminescence quantum yields needed for efficient electroluminescence, whereas type II QDs provide charge separation beneficial for photovoltaic devices or photodetectors. Indeed, QDs with near unity luminescence efficiency and size-tunable emission colors are beginning to be exploited in today's technologies—for example, the size-dependent emission from core-shell InP/ZnS QDs is used to achieve vivid colors in Samsung televisions (*36*).

Multiple excitons (such as BX or triexciton) can be generated in individual QDs through the sequential absorption of multiple photons at high photoexcitation densities (*37*, *38*) or with multiple exciton generation (MEG) processes (Fig. 3A) (*39*–*42*) . MEG involves the excitation of a single electron-hole pair into a high-energy state (typically ≥2.7 times the band gap) to form the so-called "hot" exciton, followed by nonradiative relaxation (cooling) into band-edge states. The cooling process deposits sufficient energy to pump another electron-hole pair across the band gap. In other words, the primary "hot" exciton is converted into two (or more) excitons with the band-gap energy (Fig. 3A). MEG is a topic of major interest targeted toward multiplying the number of carriers in order to increase the efficiency of QD photovoltaic cells and photodetectors.

However, strongly interacting multiple excitons or multiple carriers occasionally lead to fluorescence intermittencies, also known as blinking. This phenomenon involves switching between bright luminescence, which is associated with the existence of neutral excitons (X or BX), and dark luminescence, which is associated with the formation of charged excitons (such as X^+) upon the occurrence of the Auger process (Fig. 3A). The blinking effect is a topic of a major concern because it limits the efficiency of optoelectronic devices. Therefore, nonblinking QDs are desired and have been synthesized in recent years by exploiting QD core/shell heterostructure design, making use of a giant shell (*43*), giant core (*44*), or alloying of the core-shell interface (*45*, *46*).

Connecting the dots

Arrays of solution-deposited colloidal QDs can be integrated in devices to modulate and transmit charge under bias and thereby produce and control an electrical current, convert an optical flux to electrical power, and use electrical current to generate light akin to bulk semiconductor devices. QD arrays provide added degrees of freedom for materials engineering because the electrical, optical, and thermal properties of a QD array are determined by the characteristics of and the communication between the individual QDs.

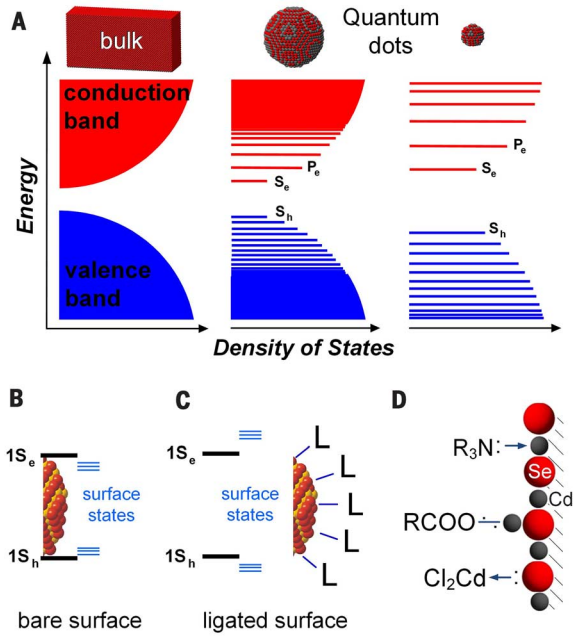

Fig. 2. The core and the surface of QDs. (**A**) Evolution of the electronic structure of inorganic semiconductors from bulk material to QDs of different size. (**B**) Broken chemical bonds at the QD surface introduce localized surface states inside the band gap. (**C**) Interaction of the QD surface atoms with ligand molecules alters the energy of the surface states, pushing them outside the band gap. (**D**) Diffrent types of chemical bonds between surface atoms and ligand molecules classified according to their chemical nature.

Electrical properties depend on the type, concentration, and mobility of charge carriers and the energy and density of states they occupy and through which they transport. In bulk semiconductor crystals, the carrier type and concentration are typically controlled by substitutional doping of electron donating or accepting impurity atoms in the lattice, and these carriers occupy and move with the mobility characteristic of the broad, high-density conduction and valence bands. In QD solids, the type and concentration of carriers may be similarly controlled by atoms in the QD core, but doping can be conveniently implemented by introducing atoms, ions, or ligands at the QD surface. These surface modifications may alter the observed carrier transport not only by acting as dopants, but also by shifting the QD energy levels and thereby the efficiency of carrier injection in devices (*18*, *47*). The efficiency of doping and the magnitude of the energy level shift depends on the type and oxidation state of the surface species and that of the QDs—and is an intriguing area only beginning to be explored. For example, nonstoichiometry created by the ligand type selected during synthesis (*26*), by means of surface atom stripping in solvents postsynthesis (*25*) or the physical or solution-based addition of atoms or ions (*48*–*50*), alter the polarity and magntiude of carrier transport (for example, arrays of PbSe QDs with excess Pb and excess Se show n- and p-type transport, respectively). Surface impurity atoms or ions and ligands can also serve as n- and p-dopants. For example, halide ligands have been shown to increase electron transport in PbS QD arrays (*51*). The additional carriers may occupy valence and conduction band states of the QDs or surface states, depending on the concentration of dopants in comparison with the mid-gap trap density.

In QD solids, the inorganic cores are separated by layers of surface ligands, creating relatively narrow, low-density conduction and valence band states (Fig. 3C). For charge to travel between the states of neighboring QDs, the carriers must transport through these interparticle layers with a tunneling rate $\Gamma \sim \exp\{-(2m^*\Delta E/\hbar^2)^{1/2}\Delta x\}$, where m^* is the electron effective mass, $\hbar$ is Planck's constant h divided by 2π, and ΔE and Δx are the height and width of the tunneling barrier defined by the ligands. The tunneling rate increases exponentially with decreasing separation between the QDs and is also very sensitive to the barrier height. The coupling between QDs is often expressed in terms of the coupling energy $\beta = \hbar\Gamma$, where $\hbar$ is Planck's constant and Γ is the tunneling rate described above. Here, we focus on the strong influence of the QD surface; however, charge transport in QD solids also depends on the size, size distribution, and organization of QDs in the arrays and has been reviewed elsewhere (*2*, *52*).

In a QD array, the effect of the intervening ligands that define energy barriers is multiplicative because of the large number of such barriers along the transport path of the charge carriers. In most cases, QD synthesis requires the use of long-chain organic ligands not suitable for electronic applications. Reducing Δx and ΔE by the proper design of the surface ligands increases the strength of electronic coupling between the QDs, and relatively small changes in ligand chemistry can dramatically alter the conductivity of the QD layer (*53*–*56*). The native ligands can be exchanged for shorter and conjugated organic molecules or compact inorganic compounds. The exponential increase in the mobility of charge carriers with

Downloaded from http://science.sciencemag.org/ on September 3, 2016

the shortening of organic ligand molecules is observed in films of PbSe QDs (*53*, *57*). The most mobile electron transport has been observed in arrays of QDs capped with inorganic ligands, represented by chalcogenidometallate (such as $Sn_2S_6^{4-}$, $In_2Se_4^{2-}$, and $CdTe_2^{2-}$) (*58*–*60*), halometallate ($PbCl_3^-$ and $InCl_4^-$) (*61*, *62*), chalcogenide (S^{2-}), halide (Cl^- and I^-), and pseudohalide (SCN^- and N_3^-) (*62*, *63*) ions. The combination of strong coupling by using compact ligand exchange and doping chemically, electrochemically (*64*), or electrostatically allows carriers to access higher-density and higher-mobility states. The recent introduction of high >10 $cm^2\ V^{-1}\ s^{-1}$ mobility QD solids (*48*, *60*, *65*, *66*) is enabling high-performance, solution-deposited QD electronics and fast carrier transport to outcompete multiple exciton quenching and carrier trapping and/or nonradiative Auger relaxation important for QD optoelectronics.

Inorganic shells in core/shell QDs can also contribute to the coupling strength among QDs. For type I heterostructures, the electronic states of the core material are substantially shielded within the QD and interact much less with their surroundings. This situation is favorable for high luminescence efficiency but not favorable for transport of electrons and holes between QDs. On the other hand, partial charge separation in type II heterostructures can enhance transport for one type of carrier (electrons or holes) while suppressing that of the other carrier (*65*).

Excitons can also be transferred between neighboring QDs (Fig. 3D). At interparticle separations of 0.5 to 10 nm, coupling through electromagnetic fields created by the transition dipoles of an excited QD (donor) and a ground-state QD (acceptor) lead to the radiationless transfer of excitons via Förster resonance energy transfer (FRET) (*67*). The efficiency of energy transfer is characterized by the Förster radius $R_o \propto \left(\frac{\phi_D}{n^4}\int_0^\infty F_D(\tilde{\nu})\varepsilon_A(\tilde{\nu})\frac{d\tilde{\nu}}{\tilde{\nu}^4}\right)^{1/6}$ in comparison with the physical center-to-center distance between donor and acceptor QDs, where ϕ_D is the donor QD emission quantum yield, $F_D(\tilde{\nu})$ the normalized spectrum of the excited donor QD emission, $\varepsilon_A(\tilde{\nu})$ is the molar extinction spectrum of the ground-state acceptor QD, and n is the refractive index of the QD array. FRET depends on the spectral overlap between QD donor emission and QD acceptor absorption, seen by the integrand, and therefore on the size and size distribution of the QDs and on the orientation of QDs in the solids. The surface chemistry of the QDs affects the efficiency of energy transfer through the emission quantum yield of the QDs, the refractive index of the array, and, as it increases, the center-to-center QD spacing, particularly as the ligand length or shell thickness become large compared with the QD diameter. At <0.5 nm interparticle distances, stronger exchange interactions lead to fast exciton diffusion.

FRET plays an important role in QD optoelectronic devices. In QD photovoltaics, energy transfer within the inhomogeneous distribution of QDs (*68*) leads to energy loss. In QD light-emitting devices, energy transfer in core-only QD arrays leads to undesirable self-quenching of the emission within the inhomogeneous distribution in QD states and to nonluminescent QDs, but energy transfer in core/shell QD arrays is believed to overcome poor charge injection, providing a route to QD excitation and to high-brightness QD devices (*69*).

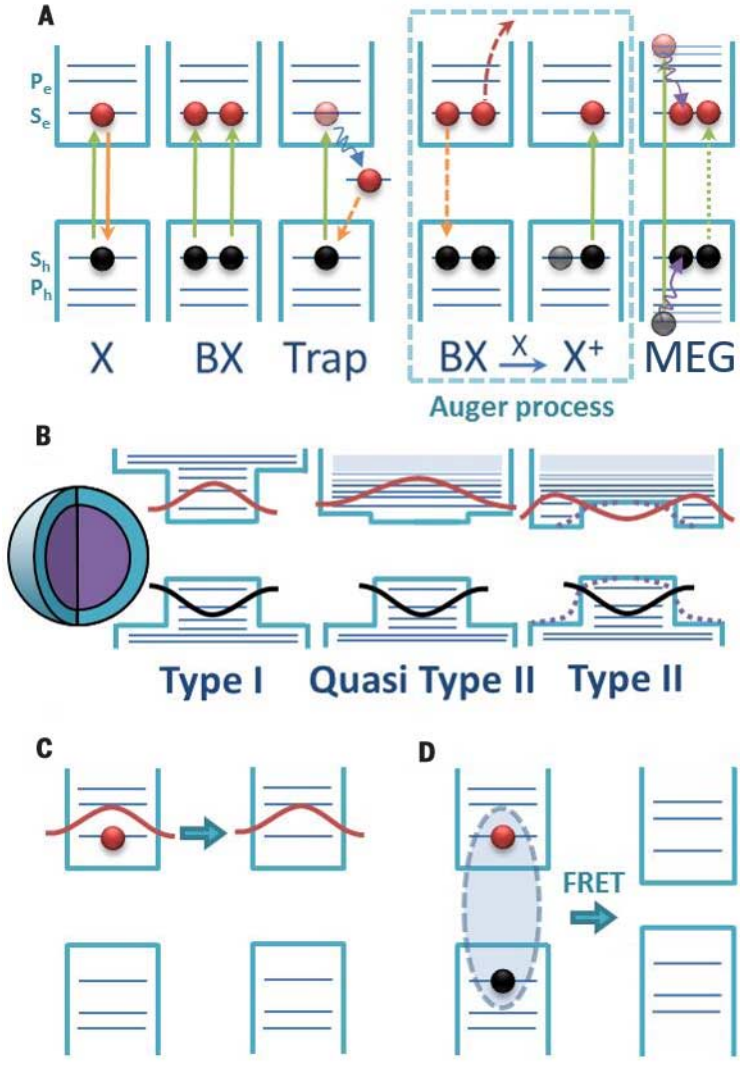

Fig. 3. Carrier dynamics and transport in QDs. (**A**) Schematic of absorption and emission processes in QDs. From left to right: band-edge absorption (green arrow) and emission (orange arrow) of a single exciton (X); sequential absorption of two photons in resonance with the band gap energy for the formation of a biexciton (BX); nonradiative decay of an electron (curled arrow) into a mid-gap trap state followed by trap-to-band recombination (dashed orange arrow); framed area: BX nonradiative Auger process, involving energy transfer from electron-hole recombination (dashed orange arrow) to a third carrier (such as an electron) and its ejection to a remote state (red dashed and curved arrow). The hole left behind (pale circle) becomes attached to a freshly formed exciton (X), creating a hole-hole-electron complex (trion, X^+); Multiple exciton generation (MEG) starts with the creation of an electron-hole pair with energy significantly above the band gap (pale circles), followed by nonradiative relaxation (cooling) into a band-edge state (curled arrows). The cooling energy enables the generation of additional electron-hole pair (or pairs) across the band-gap—the formation of multiple excitons. (**B**) Schematic of a core/shell heterostructure and (from left to right) type I, quasi-type II, and type-II core-to-shell band-edge alignments. Dashed lines in type II designate a smooth interface potential in the case of an alloyed boundary. (**C** and **D**) Schematics of (C) electron transfer between QDs via tunneling and (D) exciton transfer between QDs via FRET processes.

Understanding heat transport in QD arrays is another very important component of device engineering. For example, it has recently been shown that thermal runaway is the major obstacle to QD lasers (*70*). On the other hand, low thermal conductivity is naturally beneficial for thermoelectric applications. Unfortunately, little research effort has been devoted to this important subject. Several recent studies have revealed the key role of the QD surface in heat transport and to electron-phonon coupling strength (*71*). Reported values of the thermal conductivity of QD solids are in the range of 0.1 to 0.4 $Wm^{-1}\ K^{-1}$, which is about three orders of magnitude smaller

Downloaded from http://science.sciencemag.org/ on September 3, 2016

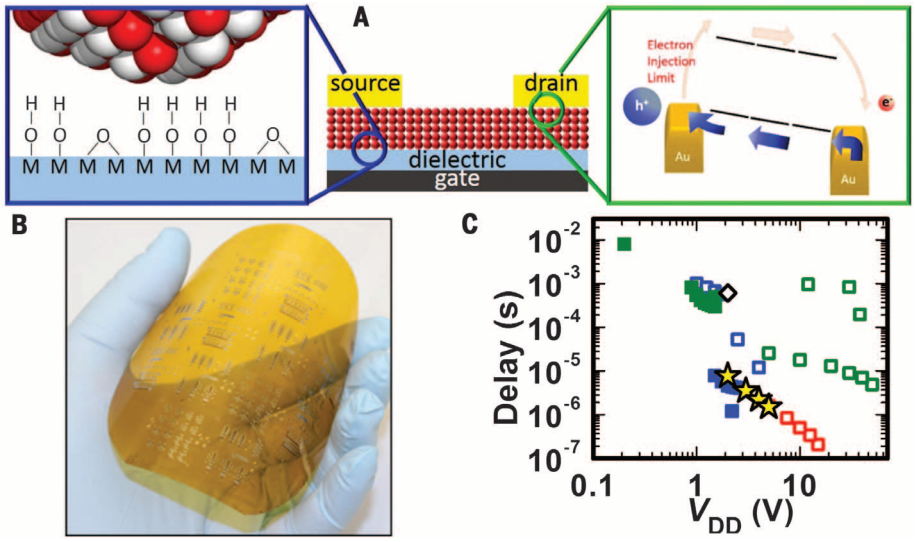

Fig. 4. QD electronics. (**A**) QD field-effect transistors highlighting the (left) semiconductor-gate dielectric interface, detailing the surface chemistry of commonly used oxides (*88*), and (right) metal-semiconductor interface, which introduces barriers to charge injection (*80*). (**B**) Large-area (40.64 cm^2) flexible QD electronic circuitry. (**C**) Comparison of the delay, a measure of the switching speed, as a function of supply voltage (V_{DD}) for flexible QD circuits (yellow stars) in comparison with rigid (solid symbols) and flexible (open symbols) solution-processable, semiconducting organic (green), carbon nanotube array (blue), sol-gel metal-oxide (red), and early QD channel layers (black) (*87*).

than the thermal conductivity of bulk Si (*72*). The analysis of QD solid thermal conductivity has used effective medium approximations (EMAs) that express the thermal conductivity of the composite in terms of the constituent volume fractions and thermal conductivities of the QDs and of the ligands. To achieve agreement with experiments, EMA must take into account thermal conductance across the interface between the QD core and the ligands, which depends on the overlap and coupling of the vibrational density of states for the QD core and the ligands (*72*, *73*). Available experimental observations and EMA modeling suggest that the ligand-ligand interface between neighboring QDs is critical to heat transfer and needs to be engineered to increase heat transport in QD solids.

Building devices from quantum dot solids

QD electronics

Colloidal QD solids have been incorporated as the semiconductor channel layer in thin-film field-effect transistors (FETs) (Fig. 4A). QD FETs provide a platform to probe carrier transport and as building blocks of low-cost, large-area, solution-processable, and flexible electronic technologies.

The FET uses the gate electrode to electrostatically shift the Fermi energy and modulate the majority carrier concentration and conductance of the QD thin-film channel spanning the source and drain electrodes and within the Debye length of the gate dielectric layer. The magnitude, voltage onset, and stability of the current and conductance modulation by the gate voltage are described by the metrics of mobility, current modulation, threshold (or turn-on) voltage, hysteresis, and subthreshold slope.

For electronic devices, the high carrier mobility (>10 $cm^2\ V^{-1}\ s^{-1}$) achieved through the combination of compact ligand exchange and surface passivation and doping (described above) is important to realizing high-performance circuitry. Synthetic methods that reduce the inhomogeneity in electronic structure of the QD building blocks and ligand exchange chemistries and processes that allow for compact ligand chemistries and yet the deposition of ordered QD assemblies promise increased mobilities, while retaining signatures of the quantum-confined building blocks (*52*). Alternatively, the compact chalcogenidometallate ligand chemistries have been shown to serve as a molecular "solder," allowing these QDs to provide a solution-processable precursor to bulk semiconductors with mobilities of >400 $cm^2\ V^{-1}\ s^{-1}$ (*60*). In addition to carrier mobility, FETs require a large gate-modulated current (I_{ON}/I_{OFF}) between the "ON" state and the "OFF" state. The current modulation is dominated by the gate-controlled change in carrier concentration. FETs constructed from QD solids with a high carrier concentration in the "OFF" state—such as that found in low-band-gap, high-intrinsic carrier concentration semiconductors (for example, IV-VI QD solids) or in highly doped QD solids—have undesirably limited current modulation. Current modulation >10^4 or even 10^5 are needed for analog and digital circuitry, and low pico-ampere "OFF" currents are required for display applications.

The construction of the FET introduces two interfaces with the semiconductor QD thin film solid that substantially affect device performance: One is with the gate dielectric layer, and the other is with the source and drain electrodes (Fig. 4A). The semiconductor–gate-dielectric interface typically introduces a density of trap states that tails from the conduction and valence band into the band gap and leads to an increase in carrier scattering and trapping. Selection of the gate dielectric material—such as replacing the SiO_2 layer with an Al_2O_3 or ZrO_2 layer (*66*, *74*, *75*) and/or tying up surface states with self-assembled monolayers—reduces the interface trap density from ~10^{13} cm^{-2} to 10^{12} cm^{-2}. The reduced interface trap density gives rise to an increase in FET mobility and subthreshold slope and a reduction in hysteresis. The higher dielectric constant of metal oxide gate dielectric materials allows for low-voltage operation. These strategies have similarly been used to improve the performance of one-dimensional (1D) nanowire and nanotube, 2D graphene, and organic semiconductor thin-film FETs (*76*–*79*).

The interface between metal source and drain electrodes and a semiconductor QD solid often introduces energetic barriers to charge injection (Fig. 4A) because metal electrodes create interface states that give rise to Fermi-level pinning. In weakly coupled QD solids, the high resistance of the channel layer dominates device performance. However, in the high-mobility, high-conductivity, strongly coupled QD solids of interest for electronics, complete or partial Fermi-level pinning may create more highly resistive electrical contacts, limiting charge injection and therefore controlling and ultimately determining FET polarity, mobility, and current level (*80*). As in the case of bulk semiconductor crystals, heavily doping the contact region by depositing a metal that also serves to dope the QD solid (*66*) provides a route to create Ohmic contacts.

The QD surface has been identified as a major culprit responsible for substantial device hysteresis; bias-stress instability, the degradation in device current under bias over time (*81*); and noise, the instantaneous fluctuations in the current (*82*, *83*). Infiltration and encapsulation of the FET QD thin-film solid with metal oxides grown by means of atomic layer deposition has been shown to reduce these instabilities (*32*, *83*). Continued advances and insight into the chemical species responsible for these instabilities will allow for a more targeted materials design to improve FET performance and therefore circuit operation.

To date, high-mobility colloidal QD FETs have been fabricated from II-VI, III-V, or IV-VI semiconductors. QD FETs from wider band gap II-VI and III-V semiconductors show high current modulation; however, only n-type FETs have been realized (*65*, *66*, *84*, *85*). In contrast, FETs from narrower bandgap IV-VI QDs show low current modulation yet can be doped n-type or p-type (*48*). Engineering the device interfaces (metal/semiconductor and semiconductor/gate dielectric) and metal oxide encapsulation has yielded low hysteresis and subthreshold swing and reduced bias stress and noise. These high-performance metrics of QD FETs are required to realize their operation, stability, and gain/speed in analog and digital circuits. These QD FETs were used as the

Downloaded from http://science.sciencemag.org/ on September 3, 2016

building blocks of integrated circuits, in which many transistors are connected on-chip (*86*, *87*). Multiple components of the FET device (semiconductor channel, metallic source and drain electrodes, and gate dielectric layer) can be constructed from colloidal nanoparticles, promising solution-phase circuit fabrication (*6*).

n-type II-VI QD FETs have been integrated to demonstrate all n-type circuits, referred to as NMOS (n-type metal oxide semiconductor) electronics, adopting the naming from conventional Si devices (Fig. 4B). These circuits include analog and digital topologies, namely inverters, negative-AND (NAND) and NOR logic gates, and ring oscillators for voltage amplification and switching (*87*). Methods to repair the QD surface after exposure to air and solvents have allowed QD circuit fabrication by using conventional clean room techniques (*88*). These techniques enable devices to be scaled down in dimension and scaled up in area so as to realize higher-bandwidth analog and higher-speed digital, large-area, QD integrated circuits. The low-temperature, solution processability of QD integrated circuits is compatible with fabrication of flexible circuitry, and their performance rivals that of other solution-processable semiconductors explored for flexible electronic devices. For example, solution-processable and flexible colloidal QD circuits show the highest switching speed at low voltages in comparison with solution-processable organic semiconductor (*89*, *90*), carbon nanotube array (*91*), and sol-gel metal oxide circuits (Fig. 4C) (*92*).

The demonstration of high-mobility QD-based semiconductors and further device scaling opens routes to continue to increase the speed of QD circuitry. However, NMOS circuitry is relatively limited in gain and speed and also has higher power dissipation than that of CMOS (complementary MOS) electronics constructed from a combination of n-type and p-type FETs. CMOS circuits—namely, two transistor inverters—have been fabricated from IV-VI QDs and show switching and higher gain (*80*, *93*), but these circuits are fundamentally limited by the narrow band gap of IV-VI QDs and therefore low current modulation. Design of high-mobility, high-current-modulation, and stable p-type QD FETs is needed to realize higher gain/higher speed CMOS QD circuitry. As an alternative, printable CMOS circuits can be constructed by combining n-type QDs with p-type organic electronic materials.

QD photoconductors

Absorption of photons may be used to control the conductivity of a QD solid, enabling application of these materials for light detection. The first generation of QD light detectors focused on photoconduction (*94*)—a light-sensing paradigm offering the advantage of signal amplification—and also leveraging rather than being limited by trap states, known in the photoconductor context as sensitizing centers (Fig. 5A). In the presence of such centers, photogeneration of an electron-hole pair is followed by capture of one carrier (we use electrons for illustration), whereas holes remain substantially free to travel. Symmetric contacting (Fig. 5A) can be used in this unipolar device. Photoholes are recirculated, and their photocurrent flows in proportion to their lifetime ratioed to their transit time. Photoconductive gain as large as 10^3 to 10^6 is possible as a result, and electron trapping—such as that enhanced by Auger-assisted ionization after multiple exciton generation (Fig. 2) (*95*)—favors the generation of additional signal.

The extended lifetimes of trapped photocarriers can be controlled via the QD surface chemistry, and early identification of surface oxides and sulfates was aided by studies that correlated QD surface composition with device response speed (*96*). Dark current is amplified via the same mechanism as that which provides photoconductive gain to photocharges, so within the classic resistive photoconductor, the ratio of light to dark current is increased only by minimizing dark free carrier density (*97*). The dark current has a lower bound defined by the intrinsic carrier density, and therefore photoconductors characteristically have undesirably high dark current density. Photodetectors based on QDs exploit tuning of the band-edge to a suitably chosen spectral cutoff energy, enabling dark current minimization for a given desired spectral response. Researchers have further overcome this limitation using gain-providing photo-field-effect transistors (*98*). The transistor introduces a threshold, so that turn-on occurs only after a certain photocarrier density (hence light level) is exceeded.

QD photodiodes and photovoltaics

QD photodiodes have been explored more recently in order to increase device speed and sensitivity, and QD photovoltaic devices (Fig. 5C) are of interest so as to harvest and convert solar energy and waste heat into electricity and, potentially, stored fuel (*99*). Compared with traditional silicon devices and organic semiconductors, QD solids are particularly suitable for efficiently capturing and detecting infrared photons, both in near- and mid-infrared regions (*100*, *101*).

Photodetectors and solar energy–harvesting devices should ideally achieve complete absorption above their band edge; as a result, they require thicknesses [or, when aided by photonic, plasmonic, or bulk heterojunction (*102*) techniques, an effective optical thicknesses] on the order of α^{-1}, where α is the absorption per unit length near the band edge. In QD solids, this is often assessed at the first excitonic peak, and the value of α^{-1} is ~ 500 to 1000 nm. Densifying the QD solid, first with high QD packing, is of interest, in order to increase the oscillator strength of absorbers, enhance the effective index of the medium, and maximize carrier capture. Superlattices achieve the highest packing, although the gap between random close packing (64%) and hexagonal/face-centered cubic close packing (74%) is not vast. Embedding dots in a high-index dielectric medium is of great interest, either via ligand design, the merging of shells, or epitaxial matrix growth (*33*).

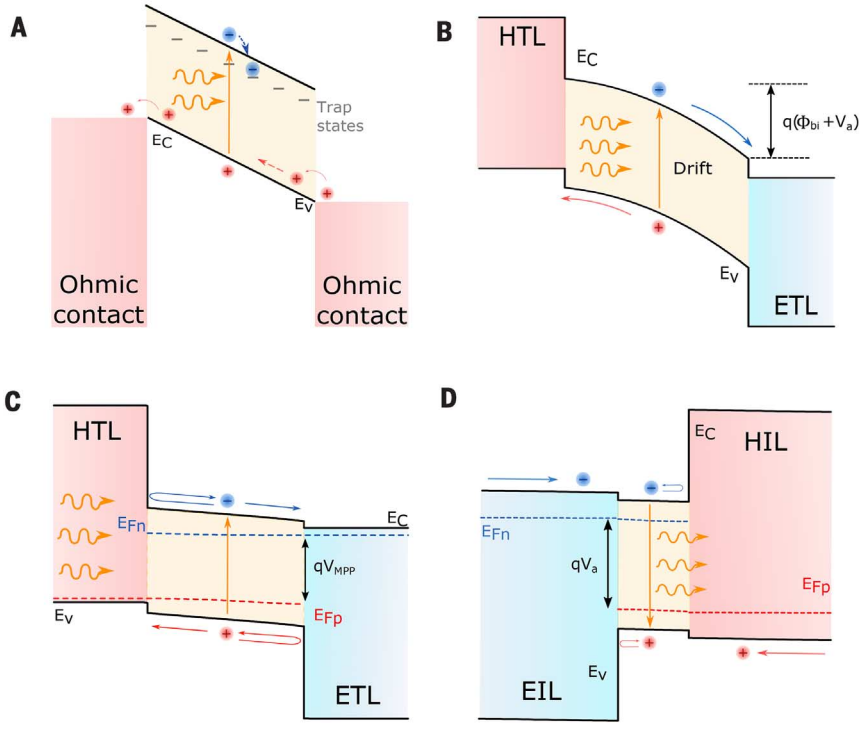

Fig. 5. QD optoelectronic devices. (**A**) Photoconductors, unipolar devices that include sensitizing centers to postpone recombination of one carrier class (electrons in the figure) while allowing the other carrier (holes in the figure) to flow. (**B**) Photodiodes that leverage the application of a voltage bias so as to achieve carrier separation and extraction. (**C**) Photovoltaics that must develop a photovoltage and rely on carrier diffusion, as well as on the use of selective contacts (an electron-accepting hole-blocker, and a hole-accepting electron blocker). (**D**) Light-emitting devices exploiting type-I heterojunctions.

Downloaded from http://science.sciencemag.org/ on September 3, 2016

Extracting photocarriers by using the built-in field in a photodiode (Fig. 5B, drift region) provides a ready path to achieving efficient photocurrent generation; when excited-state lifetimes are a typical ~100 ns, a built-in or applied potential on the order of 1 V can achieve a drift-based extraction time comparable with the excited lifetime when the lower of the electron or hole mobility exceeds 2×10^{-3} cm^2/Vs. Relative to the spectacular progress in QD FET mobilities, this is a modest requirement. QD photodetectors now reach bandwidths exceeding the megahertz frequencies (*100*); further progress into the gigahertz regime (relevant to centimeter-resolved time-of-flight sensing) will require mobilities exceeding 1 cm^2/Vs found in the strongly coupled QD solids.

In photodiodes, a reverse bias can be applied to supplement the built-in potential, and high internal quantum efficiency can be sustained even over thick active layers. A requirement of substantial applied potential does imply poor carrier diffusion in quasi-neutral material, and this may be a symptom of a high density of recombination-producing electronic trap states. In photodiodes, this does come with a disadvantage: States within the gap contribute to dark current generation, shrinking the effective band gap and enhancing thermal current generation. To produce photodiodes for highly sensitive detectors, it is desirable to satisfy the stringent conditions required of photovoltaic devices.

Solar cells must operate efficiently when transferring electric power to a load. This requires achieving high photocurrents while operating near the open-circuit (oc), hence flatband, condition (Fig. 5C). In the limit of approaching V_{oc}, at which point only recombination occurs, the separation of the quasi-Fermi levels in the active medium (which in turn provides an upper-bound on qV_{oc}) is desirably maximized. The requirements on efficient electroluminescent and photovoltaic devices are in fact one and the same: A maximal radiative efficiency is required of each (*103*).

From this perspective, QD solids have considerable room to improve. A first loss of V_{oc} comes from the Stokes shift that is inherent to individual QDs, which arises from the excitonic fine structure owing to the manifold of closely spaced optical transitions associated with the quasi-degenerate band edge states (*104*–*107*). Once QD films are formed, excitons and separated electron-hole pairs migrate among QDs and are funneled to the lowest-lying states in an inhomogeneously broadened ensemble. Light-emitting species present in QD solids—arising from QD aggregates or incorporated organic impurities—can potentially have a smaller photon emission energy and are capable in principle of additional undesired energy down-conversion (*108*).

Deep traps function as efficient recombination centers, impeding the generation of photocurrent in photovoltaic devices. It was recently found that present-day diffusion lengths in QD solids on the order of 100 nm can be accounted for by the one-part-per-10,000 density of deep trap recombination centers introduced by approximately one 5-nm, highly recombinative QD in a 100-nm cube of a QD solid (*109*). At present-day diffusion length values, increasing mobilities above 10^{-3} cm^2/Vs does not further benefit diffusion length because faster motion of carriers only leads to more efficient capture to traps (lifetime decreases as mobility increases). Carrier mobilities of 10^{-3} cm^2/Vs along with one-part-per-1000 deep trap state densities explain the best certified QD photovoltaic device power conversion efficiency (PCE) of 10.6% (*11*).

In order to approach the ultimate limit of solar cell performance by using QDs, the QD solid requires at least one of (i) minority carrier diffusion lengths exceeding the band-edge absorption length of ~ 1 μm; (ii) substantial densification of the QD solid to appreciably reduce the absorption length experienced by light near the band edge; or (iii) advanced photonic strategies to increase light absorption in an active medium having a single-pass absorbance. More modest progress along a few of these fronts would be sufficient to achieve substantial progress. The grand goal of a ~1 μm diffusion length should rely on part-per-10-million and lower deep trap state densities. This would entail QDs substantially free of bulk impurities, dislocations, and surface states, which lead to efficient recombination of excited photocarriers, and would rely on maintaining band gap integrity through avoidance of local aggregation and substantial loss of quantum confinement (*110*).

QDs-in-matrix (*33*, *60*) show promise, providing for the combination of increased dielectric constant for high absorption, epitaxial surface passivation for low-trap-state densities, and a smooth dielectric environment, which all work together in favor of increased minority carrier diffusion length and therefore solar cell efficiency.

QD electroluminescent devices

Light-emitting devices (Fig. 5D) based on QDs are of interest for displays in view of their spectrally narrow emission and size tunability, permitting a wide color gamut to be spanned. QDs also offer a qualitative benefit over organic and polymer materials because the emission of QD solids can extend into the near-infrared (NIR). This is of current interest for active illumination for gesture-recognition because the use of NIR light is invisible to the user and hence less intrusive than active visible-wavelength illumination. Many machine vision applications rely on active illumination of scenes by using structured light, ideally in the NIR.

External quantum efficiency (EQE) is a primary performance metric; it is the rate of emission into the final medium (such as free space) of photons, divided by the rate of injection of current expressed in electrons. Brightness translates into meeting a particular current density while keeping voltage efficiency high and ranges from milliamperes per square centimeter for displays and lighting to kiloamperes per square centimeter to enable lasing. An immediate first requirement for high EQE is high radiative efficiency within the QD active layer. Recent synthetic advances have produced excellent quantum yields (QYs) exceeding 97% in solution (*111*). Translating this into high luminescence efficiency in solid-state materials is an absolute requirement. The use of thick type I shells can keep the electron and hole wavefunction confined to the core, decreasing dependence on outer surface passivation; nevertheless, to achieve very high QYs a passivating ligand remains generally required. QDs in solids optimized for electroluminescent applications are therefore weakly interacting; exciton localization and efficient emission relative to nonradiative recombination outweigh the importance of carrier delocalization for transport. When high brightness is required, nonradiative processes such as the Auger process that arises under high-level injection conditions (Fig. 2A) must be forestalled—a topic of intense investigation in the QD synthesis community based on thick, graded, and type II shells (*112*–*114*).

The combination of the shells and ligands on the QD cores reduces carrier transport. Electroluminescent devices are fortunately not reliant on the very high electron and hole mobilities demanded of FETs. An effective QD electroluminescent device can be made on the basis of a single, light-emitting, QD monolayer and QD excitation via energy transfer of excitons or charge injection over only a few tens of nanometers in distance to form electron-hole pairs. Here, effective carrier injection and, crucially, effective blocking of carrier overflow are required. An electron-injection layer (Fig. 5D) is used to efficiently inject electrons into the light-emitting solid and block the egress of holes; the analogous qualities are desired of the hole injection layer. Translating quantitatively, very limited carrier mobilities of 10^{-6} cm^2/Vs (compatible with nanometer-thick shells and nanometer-long ligands) are adequate for tens of milliamperes per square centimeter of current to be injected into a QD-emitting monolayer at the modest price incurred in resistive overpotential (<0.1 V).

The result has been a rapid rate of progress in QD electroluminescent devices, reviewed elsewhere (*69*), leading to a recent 20.5% record EQE (*115*). Further frontiers for QD devices include increasing light extraction efficiencies via photonic and plasmonic structures, as has been achieved in organic LEDs (*116*), and exploiting QD matrix engineering for refractive index control so as to maximize light extraction. A further goal is to take QD electroluminescent devices beyond applications in displays and into the realm of lighting, projection, and lasing.

Summary and outlook

Unlike traditional bulk semiconductors whose electronic structure is locked in by their bonding at the atomic scale, semiconductor QDs introduce a new materials class from which to design solid-state electronic materials. Their properties may be rationally engineered in a one-at-a-time fashion by optimizing the largely independent degrees of freedom prized in individual QD building blocks and by engineering their surface chemistry to control the communication between

Downloaded from http://science.sciencemag.org/ on September 3, 2016

them. The chemical and physical properties of QD solids are being exploited in the low-cost, large-area, solution-based fabrication of QD electronic circuitry and optoelectronic light-emission, -sensing, and -harvesting devices and are now breaking through to find their introduction in technology.

The large-area surface of QDs and the many interconnections between QDs in solids present opportunities as well as a challenges. The dominant role of the surface and the wide range of materials chemistries that can be installed at the surface require continued advances in synthetic methods and their feedback with experimental probes and simulation to control the flow of charge, energy, and heat for specific device applications. In devices, the QD surface must be married with other materials, introducing interfaces that can govern device characteristics and performance. Engineering the interface between QD layers and other device components is in its infancy and promises to exploit new materials and methods in order to engineer the QD surface and optimize device performance.

REFERENCES AND NOTES

1. C. Murray, C. Kagan, M. G. Bawendi, Synthesis and characterization of monodisperse nanocrystals and close-packed nanocrystal assemblies. *Annu. Rev. Mater. Sci.* **30**, 545–610 (2000). doi: 10.1146/annurev.matsci.30.1.545
2. D. V. Talapin, J.-S. Lee, M. V. Kovalenko, E. V. Shevchenko, Prospects of colloidal nanocrystals for electronic and optoelectronic applications. *Chem. Rev.* **110**, 389–458 (2010). doi: 10.1021/cr900137k; pmid: 19958036
3. J. Yang, M. K. Choi, D.-H. Kim, T. Hyeon, Designed assembly and integration of colloidal nanocrystals for device applications. *Adv. Mater.* **28**, 1176–1207 (2016). doi: 10.1002/adma.201502851; pmid: 26707709
4. E. V. Shevchenko, D. V. Talapin, N. A. Kotov, S. O'Brien, C. B. Murray, Structural diversity in binary nanoparticle superlattices. *Nature* **439**, 55–59 (2006). doi: 10.1038/nature04414; pmid: 16397494
5. M. Cargnello *et al*., Substitutional doping in nanocrystal superlattices. *Nature* **524**, 450–453 (2015). doi: 10.1038/nature14872; pmid: 26310766
6. J.-H. Choi *et al*., Exploiting the colloidal nanocrystal library to construct electronic devices. *Science* **352**, 205–208 (2016). doi: 10.1126/science.aad0371; pmid: 27124455
7. L. E. Brus, Electron–electron and electron-hole interactions in small semiconductor crystallites: The size dependence of the lowest excited electronic state. *J. Chem. Phys.* **80**, 4403 (1984). doi: 10.1063/1.447218
8. A. I. Ekimov, A. L. Efros, A. A. Onushchenko, Quantum size effect in semiconductor microcrystals. *Solid State Commun.* **56**, 921–924 (1985). doi: 10.1016/S0038-1098(85)80025-9
9. L. Brus, Electronic wave functions in semiconductor clusters: Experiment and theory. *J. Phys. Chem.* **90**, 2555–2560 (1986). doi: 10.1021/j100403a003
10. A. H. Ip *et al*., Hybrid passivated colloidal quantum dot solids. *Nat. Nanotechnol.* **7**, 577–582 (2012). doi: 10.1038/nnano.2012.127; pmid: 22842552
11. X. Lan *et al*., Passivation using molecular halides increases quantum dot solar cell performance. *Adv. Mater.* **28**, 299–304 (2016). doi: 10.1002/adma.201503657; pmid: 26576685
12. M. A. Boles, D. Ling, T. Hyeon, D. V. Talapin, The surface science of nanocrystals. *Nat. Mater.* **15**, 141–153 (2016). doi: 10.1038/nmat4526; pmid: 26796733
13. A. Badia, L. Cuccia, L. Demers, F. Morin, R. B. Lennox, Structure and dynamics in alkanethiolate monolayers self-assembled on gold nanoparticles: A DSC, FT-IR, and deuterium NMR study. *J. Am. Chem. Soc.* **119**, 2682–2692 (1997). doi: 10.1021/ja963571t
14. A. Llordés, G. Garcia, J. Gazquez, D. J. Milliron, Tunable near-infrared and visible-light transmittance in nanocrystal-in-glass composites. *Nature* **500**, 323–326 (2013). doi: 10.1038/nature12398; pmid: 23955232
15. L. Protesescu *et al*., Atomistic description of thiostannate-capped CdSe nanocrystals: Retention of four-coordinate SnS4 motif and preservation of Cd-rich stoichiometry. *J. Am. Chem. Soc.* **137**, 1862–1874 (2015). doi: 10.1021/ja510862c; pmid: 25597625
16. D. Bozyigit, S. Volk, O. Yarema, V. Wood, Quantification of deep traps in nanocrystal solids, their electronic properties, and their influence on device behavior. *Nano Lett.* **13**, 5284–5288 (2013). doi: 10.1021/nl402803h; pmid: 24164600
17. Z. Hens, J. C. Martins, A Solution NMR Toolbox for characterizing the surface chemistry of colloidal nanocrystals. *Chem. Mater.* **25**, 1211–1221 (2013). doi: 10.1021/cm303361s
18. P. R. Brown *et al*., Energy level modification in lead sulfide quantum dot thin films through ligand exchange. *ACS Nano* **8**, 5863–5872 (2014). doi: 10.1021/nn500897c; pmid: 24824726
19. M. G. Panthani *et al*., Graphene-supported high-resolution TEM and STEM imaging of silicon nanocrystals and their capping ligands. *J. Phys. Chem. C* **116**, 22463–22468 (2012). doi: 10.1021/jp308545q
20. P. Guyot-Sionnest, B. Wehrenberg, D. Yu, Intraband relaxation in CdSe nanocrystals and the strong influence of the surface ligands. *J. Chem. Phys.* **123**, 074709 (2005). doi: 10.1063/1.2004818; pmid: 16229612
21. E. Lifshitz, Evidence in support of exciton to ligand vibrational coupling in colloidal quantum dots. *J. Phys. Chem. Lett.* **6**, 4336–4347 (2015).
22. P. Schapotschnikow, B. Hommersom, T. J. H. Vlugt, Adsorption and binding of ligands to CdSe nanocrystals. *J. Phys. Chem. C* **113**, 12690–12698 (2009). doi: 10.1021/jp903291d
23. D. Zherebetskyy *et al*., Hydroxylation of the surface of PbS nanocrystals passivated with oleic acid. *Science* **344**, 1380–1384 (2014). doi: 10.1126/science.1252727; pmid: 24876347
24. M. L. H. Green, A new approach to the formal classification of covalent compounds of the elements. *J. Organomet. Chem.* **500**, 127–148 (1995). doi: 10.1016/0022-328X(95)00508-N
25. N. C. Anderson, M. P. Hendricks, J. J. Choi, J. S. Owen, Ligand exchange and the stoichiometry of metal chalcogenide nanocrystals: Spectroscopic observation of facile metal-carboxylate displacement and binding. *J. Am. Chem. Soc.* **135**, 18536–18548 (2013). doi: 10.1021/ja4086758; pmid: 24199846
26. I. Moreels *et al*., Composition and size-dependent extinction coefficient of colloidal PbSe quantum dots. *Chem. Mater.* **19**, 6101–6106 (2007). doi: 10.1021/cm071410q
27. J. M. Luther, J. M. Pietryga, Stoichiometry control in quantum dots: A viable analog to impurity doping of bulk materials. *ACS Nano* **7**, 1845–1849 (2013). doi: 10.1021/nn401100n; pmid: 23527749
28. S. A. McDonald *et al*., Solution-processed PbS quantum dot infrared photodetectors and photovoltaics. *Nat. Mater.* **4**, 138–142 (2005). doi: 10.1038/nmat1299; pmid: 15640806
29. W. U. Huynh, J. J. Dittmer, A. P. Alivisatos, Hybrid nanorod-polymer solar cells. *Science* **295**, 2425–2427 (2002). doi: 10.1126/science.1069156; pmid: 11923531
30. G. J. Supran *et al*., QLEDs for displays and solid-state lighting. *MRS Bull.* **38**, 703–711 (2013). doi: 10.1557/mrs.2013.181
31. A. Pourret, P. Guyot-Sionnest, J. W. Elam, Atomic layer deposition of ZnO in quantum dot thin films. *Adv. Mater.* **21**, 232–235 (2009). doi: 10.1002/adma.200801313
32. Y. Liu *et al*., PbSe quantum dot field-effect transistors with air-stable electron mobilities above 7 cm2 V^{-1} s^{-1}. *Nano Lett.* **13**, 1578–1587 (2013). doi: 10.1021/nl304753n; pmid: 23452235
33. Z. Ning *et al*., Quantum-dot-in-perovskite solids. *Nature* **523**, 324–328 (2015). doi: 10.1038/nature14563; pmid: 26178963
34. D. Chepic *et al*., Auger ionization of semiconductor quantum drops in a glass matrix. *J. Lumin.* **47**, 113–127 (1990). doi: 10.1016/0022-2313(90)90007-X
35. J. Tang, R. A. Marcus, Mechanisms of fluorescence blinking in semiconductor nanocrystal quantum dots. *J. Chem. Phys.* **123**, 054704 (2005). doi: 10.1063/1.1993567; pmid: 16108682
36. E. Jang *et al*., White-light-emitting diodes with quantum dot color converters for display backlights. *Adv. Mater.* **22**, 3076–3080 (2010). doi: 10.1002/adma.201000525; pmid: 20517873
37. D. Oron, M. Kazes, I. Shweky, U. Banin, Multiexciton spectroscopy of semiconductor nanocrystals under quasi-continuous-wave optical pumping. *Phys. Rev. B* **74**, 115333 (2006). doi: 10.1103/PhysRevB.74.115333
38. R. Osovsky *et al*., Continuous-wave pumping of multiexciton bands in the photoluminescence spectrum of a single CdTe-CdSe core-shell colloidal quantum dot. *Phys. Rev. Lett.* **102**, 197401 (2009). doi: 10.1103/PhysRevLett.102.197401; pmid: 19518993
39. M. C. Beard *et al*., Multiple exciton generation in colloidal silicon nanocrystals. *Nano Lett.* **7**, 2506–2512 (2007). doi: 10.1021/nl071486l; pmid: 17645368
40. J. A. McGuire, J. Joo, J. M. Pietryga, R. D. Schaller, V. I. Klimov, New aspects of carrier multiplication in semiconductor nanocrystals. *Acc. Chem. Res.* **41**, 1810–1819 (2008). doi: 10.1021/ar800112v; pmid: 19006342
41. A. J. Nozik, Multiple exciton generation in semiconductor quantum dots. *Chem. Phys. Lett.* **457**, 3–11 (2008). doi: 10.1016/j.cplett.2008.03.094
42. A. Nozik, Quantum dot solar cells. *Phys. E Low-dimensional Syst. Nanostructures* **14**, 115–120 (2002). doi: 10.1016/S1386-9477(02)00374-0
43. Y. Chen *et al*., "Giant" multishell CdSe nanocrystal quantum dots with suppressed blinking. *J. Am. Chem. Soc.* **130**, 5026–5027 (2008). doi: 10.1021/ja711379k; pmid: 18355011
44. J. Tilchin *et al*., Quantum confinement regimes in CdTe nanocrystals probed by single dot spectroscopy: From strong confinement to the bulk limit. *ACS Nano* **9**, 7840–7845 (2015). doi: 10.1021/acsnano.5b02597; pmid: 26181051
45. M. Nasilowski, P. Spinicelli, G. Patriarche, B. Dubertret, Gradient CdSe/CdS quantum dots with room temperature biexciton unity quantum yield. *Nano Lett.* **15**, 3953–3958 (2015). doi: 10.1021/acs.nanolett.5b00838; pmid: 25990468
46. R. Vaxenburg, A. Rodina, E. Lifshitz, A. L Efros, Biexciton auger recombination in CdSe/CdS core/shell semiconductor nanocrystals. *Nano Lett.* **16**, 2503–2511 (2016). doi: 10.1021/acs.nanolett.6b00066; pmid: 26950398
47. A. M. Schimpf, K. E. Knowles, G. M. Carroll, D. R. Gamelin, Electronic doping and redox-potential tuning in colloidal semiconductor nanocrystals. *Acc. Chem. Res.* **48**, 1929–1937 (2015). doi: 10.1021/acs.accounts.5b00181; pmid: 26121552
48. S. J. Oh *et al*., Stoichiometric control of lead chalcogenide nanocrystal solids to enhance their electronic and optoelectronic device performance. *ACS Nano* **7**, 2413–2421 (2013). doi: 10.1021/nn3057356; pmid: 23368728
49. S. J. Oh *et al*., Designing high-performance PbS and PbSe nanocrystal electronic devices through stepwise, post-synthesis, colloidal atomic layer deposition. *Nano Lett.* **14**, 1559–1566 (2014). doi: 10.1021/nl404818z; pmid: 24499242
50. D. Kim, D.-H. Kim, J.-H. Lee, J. C. Grossman, Impact of stoichiometry on the electronic structure of PbS quantum dots. *Phys. Rev. Lett.* **110**, 196802 (2013). doi: 10.1103/PhysRevLett.110.196802; pmid: 23705733
51. Z. Ning *et al*., Air-stable n-type colloidal quantum dot solids. *Nat. Mater.* **13**, 822–828 (2014). doi: 10.1038/nmat4007; pmid: 24907929
52. C. R. Kagan, C. B. Murray, Charge transport in strongly coupled quantum dot solids. *Nat. Nanotechnol.* **10**, 1013–1026 (2015). doi: 10.1038/nnano.2015.247; pmid: 26551016
53. Y. Liu *et al*., Dependence of carrier mobility on nanocrystal size and ligand length in PbSe nanocrystal solids. *Nano Lett.* **10**, 1960–1969 (2010). doi: 10.1021/nl101284k; pmid: 20405957
54. D. V. Talapin, C. B. Murray, PbSe nanocrystal solids for n- and p-channel thin film field-effect transistors. *Science* **310**, 86–89 (2005). doi: 10.1126/science.1116703; pmid: 16210533
55. V. J. Porter, S. Geyer, J. E. Halpert, M. A. Kastner, M. G. Bawendi, Photoconduction in annealed and chemically treated CdSe/ZnS inorganic nanocrystal films. *J. Phys. Chem. C* **112**, 2308–2316 (2008). doi: 10.1021/jp710173q
56. N. C. Greenham, X. Peng, A. P. Alivisatos, Charge separation and transport in conjugated-polymer/semiconductor-nanocrystal composites studied by photoluminescence quenching and photoconductivity. *Phys. Rev. B Condens. Matter* **54**, 17628–17637 (1996). doi: 10.1103/PhysRevB.54.17628; pmid: 9985889
57. C. P. Collier, Reversible tuning of silver quantum dot monolayers through the metal-insulator transition. *Science* **277**, 1978–1981 (1997). doi: 10.1126/science.277.5334.1978
58. M. V. Kovalenko, M. I. Bodnarchuk, J. Zaumseil, J.-S. Lee, D. V. Talapin, Expanding the chemical versatility of colloidal

Downloaded from http://science.sciencemag.org/ on September 3, 2016

nanocrystals capped with molecular metal chalcogenide ligands. *J. Am. Chem. Soc.* **132**, 10085–10092 (2010). doi: 10.1021/ja1024832; pmid: 20593874
59. M. V. Kovalenko, M. Scheele, D. V. Talapin, Colloidal nanocrystals with molecular metal chalcogenide surface ligands. *Science* **324**, 1417–1420 (2009). doi: 10.1126/science.1170524; pmid: 19520953
60. D. S. Dolzhnikov *et al*., Composition-matched molecular "solders" for semiconductors. *Science* **347**, 425–428 (2015). doi: 10.1126/science.1260501; pmid: 25569110
61. D. N. Dirin *et al*., Lead halide perovskites and other metal halide complexes as inorganic capping ligands for colloidal nanocrystals. *J. Am. Chem. Soc.* **136**, 6550–6553 (2014). doi: 10.1021/ja5006288; pmid: 24746226
62. H. Zhang, J. Jang, W. Liu, D. V. Talapin, Colloidal nanocrystals with inorganic halide, pseudohalide, and halometallate ligands. *ACS Nano* **8**, 7359–7369 (2014). doi: 10.1021/nn502470v; pmid: 24988140
63. A. T. Fafarman *et al*., Thiocyanate-capped nanocrystal colloids: Vibrational reporter of surface chemistry and solution-based route to enhanced coupling in nanocrystal solids. *J. Am. Chem. Soc.* **133**, 15753–15761 (2011). doi: 10.1021/ja206303g; pmid: 21848336
64. M. Shim, P. Guyot-Sionnest, n-type colloidal semiconductor nanocrystals. *Nature* **407**, 981–983 (2000). doi: 10.1038/35039577; pmid: 11069172
65. J.-S. Lee, M. V. Kovalenko, J. Huang, D. S. Chung, D. V. Talapin, Band-like transport, high electron mobility and high photoconductivity in all-inorganic nanocrystal arrays. *Nat. Nanotechnol.* **6**, 348–352 (2011). doi: 10.1038/nnano.2011.46; pmid: 21516091
66. J. H. Choi *et al*., Bandlike transport in strongly coupled and doped quantum dot solids: A route to high-performance thin-film electronics. *Nano Lett.* **12**, 2631–2638 (2012). doi: 10.1021/nl301104z; pmid: 22509936
67. C. R. Kagan, C. B. Murray, M. Nirmal, M. G. Bawendi, Electronic energy transfer in CdSe quantum dot solids. *Phys. Rev. Lett.* **76**, 1517–1520 (1996). doi: 10.1103/PhysRevLett.76.1517; pmid: 10061743
68. C. R. Kagan, C. B. Murray, M. G. Bawendi, Long-range resonance transfer of electronic excitations in close-packed CdSe quantum-dot solids. *Phys. Rev. B Condens. Matter* **54**, 8633–8643 (1996). doi: 10.1103/PhysRevB.54.8633; pmid: 9984542
69. Y. Shirasaki, G. J. Supran, M. G. Bawendi, V. Bulović, Emergence of colloidal quantum-dot light-emitting technologies. *Nat. Photonics* **7**, 13–23 (2012). doi: 10.1038/nphoton.2012.328
70. M. M. Adachi *et al*., Microsecond-sustained lasing from colloidal quantum dot solids. *Nat. Commun.* **6**, 8694 (2015). doi: 10.1038/ncomms9694; pmid: 26493282
71. D. Bozyigit *et al*., Soft surfaces of nanomaterials enable strong phonon interactions. *Nature* **531**, 618–622 (2016). doi: 10.1038/nature16977; pmid: 26958836
72. W.-L. Ong, S. M. Rupich, D. V. Talapin, A. J. H. McGaughey, J. A. Malen, Surface chemistry mediates thermal transport in three-dimensional nanocrystal arrays. *Nat. Mater.* **12**, 410–415 (2013). doi: 10.1038/nmat3596; pmid: 23503009
73. M. Liu, Y. Ma, R. Y. Wang, Modifying thermal transport in colloidal nanocrystal solids with surface chemistry. *ACS Nano* **9**, 12079–12087 (2015). doi: 10.1021/acsnano.5b05085; pmid: 26553583
74. D. K. Kim, Y. Lai, T. R. Vemulkar, C. R. Kagan, Flexible, low-voltage, and low-hysteresis PbSe nanowire field-effect transistors. *ACS Nano* **5**, 10074–10083 (2011). doi: 10.1021/nn203948x; pmid: 22084980
75. D. S. Chung *et al*., Low voltage, hysteresis free, and high mobility transistors from all-inorganic colloidal nanocrystals. *Nano Lett.* **12**, 1813–1820 (2012). doi: 10.1021/nl203949n; pmid: 22385132
76. H. Klauk, U. Zschieschang, J. Pflaum, M. Halik, Ultralow-power organic complementary circuits. *Nature* **445**, 745–748 (2007). doi: 10.1038/nature05533; pmid: 17301788
77. W. Kim *et al*., Hysteresis caused by water molecules in carbon nanotube field-effect transistors. *Nano Lett.* **3**, 193–198 (2003). doi: 10.1021/nl0259232
78. C. M. Aguirre *et al*., The role of the oxygen/water redox couple in suppressing electron conduction in field-effect transistors. *Adv. Mater.* **21**, 3087–3091 (2009). doi: 10.1002/adma.200900550
79. J. Goldberger, D. J. Sirbuly, M. Law, P. Yang, ZnO nanowire transistors. *J. Phys. Chem. B* **109**, 9–14 (2005). doi: 10.1021/jp0452599; pmid: 16850973
80. S. J. Oh *et al*., Engineering charge injection and charge transport for high performance PbSe nanocrystal thin film devices and circuits. *Nano Lett.* **14**, 6210–6216 (2014). doi: 10.1021/nl502491d; pmid: 25298154
81. T. P. Osedach *et al*., Bias-stress effect in 1,2-ethanedithiol-treated PbS quantum dot field-effect transistors. *ACS Nano* **6**, 3121–3127 (2012). doi: 10.1021/nn3008788; pmid: 22480161
82. H. Liu, E. Lhuillier, P. Guyot-Sionnest, 1/f noise in semiconductor and metal nanocrystal solids. *J. Appl. Phys.* **115**, 154309 (2014). doi: 10.1063/1.4871682
83. Y. Lai *et al*., Low-frequency (1/f) noise in nanocrystal field-effect transistors. *ACS Nano* **8**, 9664–9672 (2014). doi: 10.1021/nn504303b; pmid: 25195975
84. W. Liu, J.-S. Lee, D. V. Talapin, III-V nanocrystals capped with molecular metal chalcogenide ligands: High electron mobility and ambipolar photoresponse. *J. Am. Chem. Soc.* **135**, 1349–1357 (2013). doi: 10.1021/ja308200f; pmid: 23267673
85. B. Sun, H. Sirringhaus, Solution-processed zinc oxide field-effect transistors based on self-assembly of colloidal nanorods. *Nano Lett.* **5**, 2408–2413 (2005). doi: 10.1021/nl051586w; pmid: 16351187
86. D. K. Kim, Y. Lai, B. T. Diroll, C. B. Murray, C. R. Kagan, Flexible and low-voltage integrated circuits constructed from high-performance nanocrystal transistors. *Nat. Commun.* **3**, 1216 (2012). doi: 10.1038/ncomms2218; pmid: 23169057
87. F. S. Stinner *et al*., Flexible, high-speed CdSe nanocrystal integrated circuits. *Nano Lett.* **15**, 7155–7160 (2015). doi: 10.1021/acs.nanolett.5b03363; pmid: 26407206
88. J.-H. Choi *et al*., In situ repair of high-performance, flexible nanocrystal electronics for large-area fabrication and operation in air. *ACS Nano* **7**, 8275–8283 (2013). doi: 10.1021/nn403752d; pmid: 23952742
89. H. Yan *et al*., Solution processed top-gate n-channel transistors and complementary circuits on plastics operating in ambient conditions. *Adv. Mater.* **20**, 3393–3398 (2008). doi: 10.1002/adma.200800629
90. L. Herlogsson, M. Cölle, S. Tierney, X. Crispin, M. Berggren, Low-voltage ring oscillators based on polyelectrolyte-gated polymer thin-film transistors. *Adv. Mater.* **22**, 72–76 (2010). doi: 10.1002/adma.200901850; pmid: 20217700
91. M. Ha *et al*., Aerosol jet printed, low voltage, electrolyte gated carbon nanotube ring oscillators with sub-5 μs stage delays. *Nano Lett.* **13**, 954–960 (2013). doi: 10.1021/nl3038773; pmid: 23394463
92. Y.-H. Kim *et al*., Flexible metal-oxide devices made by room-temperature photochemical activation of sol-gel films. *Nature* **489**, 128–132 (2012). doi: 10.1038/nature11434; pmid: 22955624
93. W. K. Koh, S. R. Saudari, A. T. Fafarman, C. R. Kagan, C. B. Murray, Thiocyanate-capped PbS nanocubes: Ambipolar transport enables quantum dot based circuits on a flexible substrate. *Nano Lett.* **11**, 4764–4767 (2011). doi: 10.1021/nl202578g; pmid: 22011060
94. G. Konstantatos *et al*., Ultrasensitive solution-cast quantum dot photodetectors. *Nature* **442**, 180–183 (2006). doi: 10.1038/nature04855; pmid: 16838017
95. V. Sukhovatkin, S. Hinds, L. Brzozowski, E. H. Sargent, Colloidal quantum-dot photodetectors exploiting multiexciton generation. *Science* **324**, 1542–1544 (2009). doi: 10.1126/science.1173812; pmid: 19541992
96. G. Konstantatos, L. Levina, A. Fischer, E. H. Sargent, Engineering the temporal response of photoconductive photodetectors via selective introduction of surface trap states. *Nano Lett.* **8**, 1446–1450 (2008). doi: 10.1021/nl080373e; pmid: 18399622
97. G. Konstantatos, J. Clifford, L. Levina, E. H. Sargent, Sensitive solution-processed visible-wavelength photodetectors. *Nat. Photonics* **1**, 531–534 (2007). doi: 10.1038/nphoton.2007.147
98. V. Adinolfi *et al*., Photojunction field-effect transistor based on a colloidal quantum dot absorber channel layer. *ACS Nano* **9**, 356–362 (2015). doi: 10.1021/nn5053537; pmid: 25558809
99. T. Abe *et al*., Molecular hydrogen evolution by organic p/n bilayer film of phthalocyanine/fullerene in the entire visible-light energy region. *J. Phys. Chem. C* **115**, 7701–7705 (2011). doi: 10.1021/jp1094992
100. J. P. Clifford *et al*., Fast, sensitive and spectrally tuneable colloidal-quantum-dot photodetectors. *Nat. Nanotechnol.* **4**, 40–44 (2009). doi: 10.1038/nnano.2008.313; pmid: 19119281
101. P. Guyot-Sionnest, J. A. Roberts, Background limited mid-infrared photodetection with photovoltaic HgTe colloidal quantum dots. *Appl. Phys. Lett.* **107**, 253104 (2015). doi: 10.1063/1.4938135
102. Z. Ren *et al*., Amorphous TiO_2 buffer layer boosts efficiency of quantum dot sensitized solar cells to over 9%. *Chem. Mater.* **27**, 8398–8405 (2015). doi: 10.1021/acs.chemmater.5b03864
103. O. D. Miller, E. Yablonovitch, S. R. Kurtz, Strong internal and external luminescence as solar cells approach the Shockley–Queisser limit. *IEEE J. Photovoltaics* **2**, 303–311 (2012). doi: 10.1109/JPHOTOV.2012.2198434
104. W. Yoon *et al*., Enhanced open-circuit voltage of PbS nanocrystal quantum dot solar cells. *Sci. Rep.* **3**, 2225 (2013). doi: 10.1038/srep02225; pmid: 23868514
105. C. Li *et al*., Large Stokes shift and high efficiency luminescent solar concentrator incorporated with CuInS2/ZnS quantum dots. *Sci. Rep.* **5**, 17777 (2015). doi: 10.1038/srep17777; pmid: 26642815
106. W. Ma, J. M. Luther, H. Zheng, Y. Wu, A. P. Alivisatos, Photovoltaic devices employing ternary PbS_xSe_{1-x} nanocrystals. *Nano Lett.* **9**, 1699–1703 (2009). doi: 10.1021/nl900388a; pmid: 19351196
107. J. M. An, A. Franceschetti, A. Zunger, The excitonic exchange splitting and radiative lifetime in PbSe quantum dots. *Nano Lett.* **7**, 2129–2135 (2007). doi: 10.1021/nl071219f
108. G. H. Carey, L. Levina, R. Comin, O. Voznyy, E. H. Sargent, Record charge carrier diffusion length in colloidal quantum dot solids via mutual dot-to-dot surface passivation. *Adv. Mater.* **27**, 3325–3330 (2015). doi: 10.1002/adma.201405782; pmid: 25899173
109. D. Zhitomirsky *et al*., Engineering colloidal quantum dot solids within and beyond the mobility-invariant regime. *Nat. Commun.* **5**, 3803 (2014). doi: 10.1038/ncomms4803; pmid: 24801435
110. A. H. Ip *et al*., Infrared colloidal quantum dot photovoltaics via coupling enhancement and agglomeration suppression. *ACS Nano* **9**, 8833–8842 (2015). doi: 10.1021/acsnano.5b02164; pmid: 26266671
111. O. Chen *et al*., Compact high-quality CdSe-CdS core-shell nanocrystals with narrow emission linewidths and suppressed blinking. *Nat. Mater.* **12**, 445–451 (2013). doi: 10.1038/nmat3539; pmid: 23377294
112. J. Lim *et al*., Influence of shell thickness on the performance of light-emitting devices based on $CdSe/Zn_{1-X}\ Cd_X\ S$ core/shell heterostructured quantum dots. *Adv. Mater.* **26**, 8034–8040 (2014). doi: 10.1002/adma.201403620; pmid: 25381683
113. B. N. Pal *et al*., 'Giant' CdSe/CdS core/shell nanocrystal quantum dots as efficient electroluminescent materials: Strong influence of shell thickness on light-emitting diode performance. *Nano Lett.* **12**, 331–336 (2012). doi: 10.1021/nl203620f; pmid: 22148981
114. S. A. Ivanov *et al*., Type-II core/shell CdS/ZnSe nanocrystals: Synthesis, electronic structures, and spectroscopic properties. *J. Am. Chem. Soc.* **129**, 11708–11719 (2007). doi: 10.1021/ja068351m; pmid: 17727285
115. X. Dai *et al*., Solution-processed, high-performance light-emitting diodes based on quantum dots. *Nature* **515**, 96–99 (2014). doi: 10.1038/nature13829; pmid: 25363773
116. S. Reineke *et al*., White organic light-emitting diodes with fluorescent tube efficiency. *Nature* **459**, 234–238 (2009). doi: 10.1038/nature08003; pmid: 19444212

ACKNOWLEDGMENTS

C.R.K. gratefully acknowledges the U.S. Department of Energy, Office of Basic Energy Sciences, Division of Materials Science and Engineering, under award DE-SC0002158 for support. E.L. thanks the Israel Council for High Education–Focal Area Technology (grant 872967), the Volkswagen Stiftung (grants 88116 and ZN2916), the Israel Science Foundation (grants 914/15 and 1508/14), and the Horizon2020 PHONSI project for their support. E.H.S. acknowledges award (KUS-11-009-21) from the King Abdullah University of Science and Technology (KAUST). D.V.T. acknowledges support by the U.S. Department of Defense (DOD) Office of Naval Research grant N00014-13-1-0490. C.R.K., E.H.S., and D.V.T. hold and have applied for several patents related to QD assemblies in devices. E.H.S. has a financial interest in and serves as Chief Technology Officer and director of InVisage Technologies.

10.1126/science.aac5523

Downloaded from http://science.sciencemag.org/ on September 3, 2016

RESEARCH ARTICLE SUMMARY

PHOTOSYNTHESIS

Light-dependent chlorophyll f synthase is a highly divergent paralog of PsbA of photosystem II

Ming-Yang Ho, Gaozhong Shen, Daniel P. Canniffe, Chi Zhao, Donald A. Bryant*

INTRODUCTION: Terrestrial cyanobacteria often occur in environments that receive strongly filtered light because of shading by plants or because of their associations with soil crusts, benthic mat communities, or dense cyanobacterial blooms. The light in such environments becomes highly enriched in far-red light (FRL) (wavelengths >700 nm). Cyanobacteria that are able to use FRL for photosynthesis have evolved a novel far-red light photoacclimation (FaRLiP) mechanism to gain a strong selective advantage over other cyanobacteria. The FaRLiP response involves extensive remodeling of photosystems I and II (PSI and PSII) and light-harvesting phycobilisome complexes. FaRLiP cells synthesize chlorophyll f (Chl f), Chl d, and FRL-absorbing phycobiliproteins under these conditions and thus can use FRL efficiently for oxygenic photosynthesis. A key element of the FaRLiP response is the FRL-specific expression of 17 genes that encode paralogs of core components of the three light-harvesting complexes produced during growth in white light.

RATIONALE: The ability to synthesize Chl f is a key element of the FaRLiP response, but the Chl f synthase had remained unknown. Transcription and phylogenetic profiling suggested that the gene(s) responsible for this activity were in the conserved FaRLiP gene cluster. This led us to focus on *psbA4*, a divergent member of the *psbA* gene family encoding so-called "super-rogue" PsbA, a paralog to the D1 core subunit of PSII. We used reverse genetics and heterologous expression to identify the Chl f synthase of two cyanobacteria capable of FaRLiP: *Chlorogloeopsis fritschii* PCC 9212 and *Synechococcus* sp. PCC 7335.

RESULTS: In both species, null mutants of *psbA4* no longer synthesized Chl f and lacked FRL absorption and long-wavelength fluorescence emission, the key spectroscopic properties associated with Chl f. Heterologous expression of the *psbA4* gene from *C. fritschii* PCC 9212 in the model non-FaRLiP cyanobacterium *Synechococcus* sp. PCC 7002 led to the synthesis of Chl f. These results showed that *psbA4* (renamed *chlF*) encodes the Chl f synthase. Growth experiments using intervals of FRL and darkness showed that Chl f synthesis is light-dependent, which implies that ChlF is a photo-oxidoreductase that oxidizes Chl a (or Chlide a) instead of water.

ON OUR WEBSITE

Read the full article at http://dx.doi.org/10.1126/science.aaf9178

CONCLUSION: ChlF may have evolved after gene duplication from PsbA of a water-oxidizing PSII complex by loss of the ligands for binding the $Mn_4Ca_1O_5$ cluster but by retaining catalytically useful chlorophylls, tyrosine Y_Z, and plastoquinone binding. Alternatively, PsbA may have arisen by gene duplication from ChlF and then by gaining the capacity to bind the $Mn_4Ca_1O_5$ cluster. Because ChlF seems likely to function as a simple homodimer and belongs to the earliest diverging clade of PsbA sequences in phylogenetic analyses, Chl f synthase may have been the antecedent of water-oxidizing PSII. This hypothesis provides a simple explanation for the occurrence of multiple reaction centers in an ancestral cyanobacterial cell. Thus, a Chl a photo-oxidoreductase that initially evolved for enhanced use of FRL may explain the origin of oxygen-evolving PSII. From an applied perspective, knowing the identity of ChlF may provide a tractable route for introducing the capacity for FRL use into crop plants, greatly expanding the wavelength range that they can use to conduct photosynthesis. ■

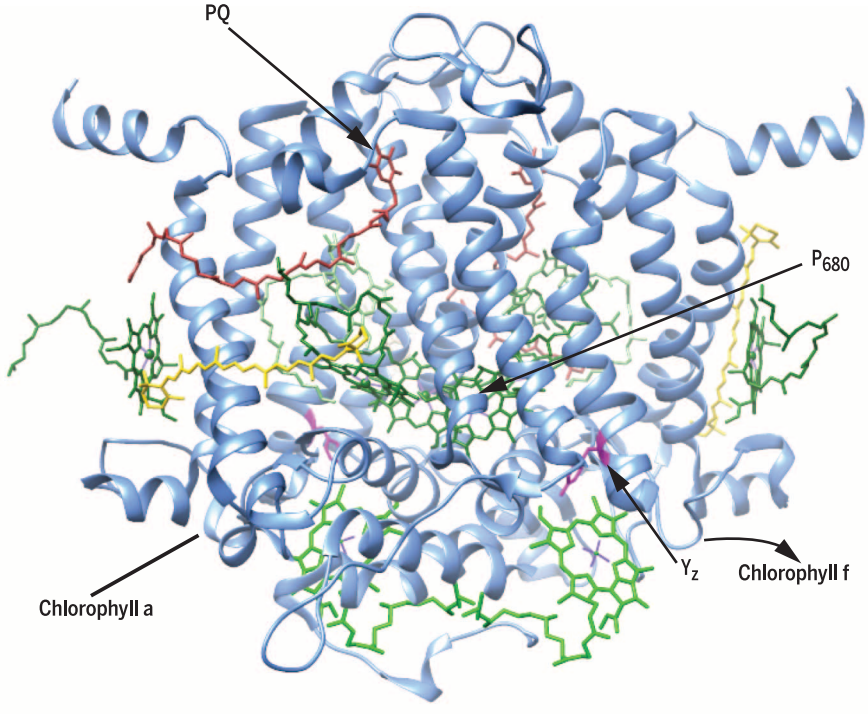

Structural model of ChlF homodimer based on PsbA of PSII. The PsbA4/ChlF homodimer polypeptides are shown as blue ribbon structures. Putative substrate chlorophyll (Chl) a molecules are shown in bright green at the bottom. Cofactors are Chl a (dark green), pheophytin a (pale green), plastoquinones (burgundy), β-carotenes (yellow), and tyrosine Y_Z (magenta).

The list of author affiliations is available in the full article online.
*Corresponding author. Email: dab14@psu.edu
Cite this article as M.-Y. Ho *et al.*, *Science* 353, aaf9178 (2016). DOI: 10.1126/science.aaf9178

Downloaded from http://science.sciencemag.org/ on September 3, 2016

RESEARCH ARTICLE

PHOTOSYNTHESIS

Light-dependent chlorophyll f synthase is a highly divergent paralog of PsbA of photosystem II

Ming-Yang Ho,[1,2] Gaozhong Shen,[1] Daniel P. Canniffe,[1] Chi Zhao,[1] Donald A. Bryant[1,2,3,4]*

Chlorophyll f (Chl f) permits some cyanobacteria to expand the spectral range for photosynthesis by absorbing far-red light. We used reverse genetics and heterologous expression to identify the enzyme for Chl f synthesis. Null mutants of "super-rogue" *psbA4* genes, divergent paralogs of *psbA* genes encoding the D1 core subunit of photosystem II, abolished Chl f synthesis in two cyanobacteria that grow in far-red light. Heterologous expression of the *psbA4* gene, which we rename *chlF*, enables Chl f biosynthesis in *Synechococcus* sp. PCC 7002. Because the reaction requires light, Chl f synthase is probably a photo-oxidoreductase that employs catalytically useful Chl a molecules, tyrosine Y_Z, and plastoquinone (as does photosystem II) but lacks a $Mn_4Ca_1O_5$ cluster. Introduction of Chl f biosynthesis into crop plants could expand their ability to use solar energy.

Terrestrial cyanobacteria are an underappreciated component of global primary productivity (GPP). About 55% of GPP is estimated to occur on land (*1*), and of the 45% of GPP that occurs in the oceans, oxygen-evolving *Prochlorococcus* and *Synechococcus* spp. are responsible for ~50% of the total (*2*, *3*). Given that the estimates for total marine and terrestrial cyanobacterial biomass are similar (*4*), terrestrial cyanobacteria could account for a substantial proportion of GPP and nitrogen fixation (*4*, *5*). Terrestrial cyanobacteria often occur in environments that receive strongly filtered light because of shading by plants or because of their associations with soil crusts, benthic mat communities, or dense cyanobacterial blooms (*6*). The light available in such environments becomes highly enriched in far-red light (FRL), specifically wavelengths greater than 700 nm (*6*). Therefore, cyanobacteria that are able to use FRL for photosynthesis gain a strong selective advantage over organisms that are unable to do so (*6*–*8*).

Cyanobacteria that grow in FRL undergo an extensive photoacclimation process known as far-red light photoacclimation (FaRLiP) (*7*). FaRLiP involves the FRL-dependent expression of a conserved cluster of 20 genes (fig. S1). Seventeen of these genes are paralogs of genes encoding core subunits of photosynthetic complexes that are expressed in white light (WL). The expression of the paralogous genes in FRL leads to extensive remodeling of the cores of the major light-absorbing complexes of cyanobacteria: phycobilisomes (*9*), photosystem I (PSI) (*10*), and PSII (*6*–*8*, *11*). About 10% of the chlorophyll a (Chl a) molecules are replaced by Chl f in the paralogous PSI and PSII complexes produced in FRL (*7*, *8*), and allophycocyanin B variants absorbing beyond 700 nm are also synthesized during FaRLiP (*7*, *8*, *12*, *13*). Together, these changes allow cells to make use of FRL for growth (*7*, *8*). The FaRLiP gene cluster also contains three regulatory genes—*rfpA*, *rfpB*, and *rfpC*—which form a signaling cascade that controls the expression of the FaRLiP genes (*14*). RfpA is a knotless red light (RL)/FRL–responsive phytochrome (RfpA) with a histidine kinase domain; RfpC is a small CheY-like response regulator that probably acts as a phosphate shuttle; and RfpB is a response regulator with a winged-helix DNA-binding domain and two CheY-like receiver domains (*7*, *14*). Null mutants for any one of these three *rfp* genes cannot grow in FRL, cannot express the genes in the FaRLiP gene cluster, and cannot synthesize Chl f (*14*).

Chl f (i.e., 2-formyl Chl a) was only recently discovered (*15*–*17*) and is synthesized when cells capable of FaRLiP are grown in FRL (*6*–*8*, *18*–*20*). Chl f absorbs maximally at ~707 nm in 100% methanol (*21*, *22*), and it is presumably made by reaction(s) extending from Chl a or chlorophyllide a, the immediate precursor of Chl a (Fig. 1) (*17*, *23*). Chl f could possibly be introduced into crop plants to extend their light harvesting into the far red (700 to 800 nm) and thereby improve their photosynthetic light use efficiency (*24*–*26*). However, the enzyme(s) responsible for Chl f synthesis have not been identified, and the complexity of Chl f synthesis remains unknown.

Identification of the gene encoding Chl f synthase by reverse genetics

To identify the Chl f synthase, the enzyme responsible for the synthesis of Chl f, we used reverse genetics in two cyanobacteria capable of FaRLiP—*Chlorogloeopsis fritschii* PCC 9212 and *Synechococcus* sp. PCC 7335—and heterologous gene expression in the model cyanobacterium *Synechococcus* sp. PCC 7002 (hereafter *Synechococcus* 7002). Several observations led us to focus on *psbA4*, which encodes a so-called "super-rogue" paralog (sr-PsbA) of PsbA, the D1 core subunit of PSII (*27*). A sr-*psbA4* gene is found in each FaRLiP gene cluster (fig. S1) (*7*, *8*), and *psbA4* expression is under the control of the RfpABC sensor kinase/response regulator system (*14*). Transcription profiling of FaRLiP strains [e.g., (*7*, *14*)] revealed striking increases in relative transcript abundance for hundreds of genes when cells were shifted from WL into FRL. However, phylogenetic profiling of ~600 genes whose relative transcript abundances more than doubled in FRL in *Leptolyngbya* sp. JSC-1 (*7*)—including monooxygenases, oxidoreductases, and other enzymes that might be logical candidates to be Chl f synthase—showed that only the genes of the FaRLiP cluster are universally present in cyanobacteria capable of performing FaRLiP. These observations strongly suggested that the gene(s) responsible for Chl f synthesis must be present in the FaRLiP gene cluster. sr-PsbA4 is predicted to be structurally similar to the PsbA core subunit of PSII reaction centers Fig. 2A, but sr-PsbA4 sequences collectively lack key residues required for binding the $Mn_4Ca_1O_5$ cluster for water oxidation (*27*, *28*) (Fig. 2, B and C, and fig. S2). Additionally, sr-PsbA4 has some important differences in the vicinity of its putative plastoquinone binding site (*8*, *27*, *28*) (fig. S2). However, sr-PsbA4 has retained tyrosine Y_Z and the ligands for binding Chl a (Fig. 2 and fig. S2). The structural and functional changes imposed by the inability to bind the $Mn_4Ca_1O_5$ cluster strongly suggested that sr-PsbA4 has a function other than being a core subunit of PSII.

Using a conjugation-based DNA transfer system (*14*), we constructed null mutants for *psbA4* genes in two cyanobacteria capable of FaRLiP (*8*): *C. fritschii* PCC 9212 and *Synechococcus* sp. PCC 7335 (fig. S3). Neither *psbA4* mutant was able to synthesize Chl f when the mutant cells were grown in FRL. The characteristic long-wavelength absorption at ~710 nm (Fig. 3A) and fluorescence emission at ~740 to 750 nm (Fig. 3B) associated with PS complexes containing Chl f was completely missing for the two *psbA4* mutants (Fig. 3, C and D, and fig. S4D). High-performance liquid chromatography (HPLC) analyses of pigments extracted from cells of the *psbA4* null mutants grown in FRL confirmed the absence of Chl f and showed that only Chl a and Chl d were synthesized (Fig. 4 and fig. S5). Reverse transcription polymerase chain reaction (RT-PCR) analyses showed that this was not due to a loss of transcriptional control by RfpABC. Transcripts of selected FaRLiP

[1]Department of Biochemistry and Molecular Biology, The Pennsylvania State University, University Park, PA 16802, USA. [2]Intercollege Graduate Degree Program in Plant Biology, The Pennsylvania State University, University Park, PA 16802, USA. [3]Department of Chemistry and Biochemistry, Montana State University, Bozeman, MT 59717, USA. [4]Singapore Centre for Environmental Life Sciences Engineering, Nanyang Technological University, Singapore.
*Corresponding author. Email: dab14@psu.edu

Downloaded from http://science.sciencemag.org/ on September 3, 2016

genes exhibited normal RL/FRL-dependent regulation (Fig. 5). PsaA2 and PsaB2 were detected at low levels in PSI trimers isolated from cells of the *psbA4* mutant of *C. fritschii* PCC 9212 grown in FRL by proteomic analysis (table S1). In the absence of Chl f in the *psbA4* mutant, it seems that FaRLiP subunits accumulate to much lower levels than in wild-type cells grown in FRL (table S1).

Heterologous expression of the sr-*psbA4* gene in *Synechococcus* 7002

To ascertain directly whether sr-PsbA4 is the Chl f synthase, we expressed the *C. fritschii* PCC 9212 *psbA4* gene heterologously under the control of the strong *Synechocystis* sp. PCC 6803 *cpcBA* promoter from plasmid pAQ1 in the model cyanobacterium *Synechococcus* 7002 (*29*). *Synechococcus* 7002 does not naturally synthesize Chl f and is unable to grow in FRL (*7*). Cells were grown at low irradiance in WL (15 μmol photons m^{-2} s^{-1}) at room temperature in hopes of minimizing sr-PsbA4 turnover and preventing photo-oxidation of any Chl f that might be formed, because no known Chl f–binding proteins are present in this heterologous system. Reversed-phase HPLC analysis of pigments extracted from wild-type *Synechococcus* 7002 cells showed only Chl a, as expected (Fig. 6A). However, HPLC analysis showed that pigments extracted from the *Synechococcus* 7002 strain expressing *psbA4* contained both Chl a and Chl f (Fig. 6A and fig. S6). Although only a small amount of Chl f was produced (~0.059% of total Chl), this pigment had the same retention time as Chl f from cells of *C. fritschii* PCC 9212 grown in FRL (fig. S6). Moreover, the in-line absorption spectrum of the pigment from the *Synechococcus* 7002 strain expressing *psbA4* was identical to those of Chl f from three FaRLiP strains (Fig. 6B). Finally, mass spectrometric analysis of the new pigment, after treatment with formic acid to produce the corresponding pheophytin, confirmed that this pigment had the expected mass/charge ratios (*m/z*) of 885.4 $[M+H]^+$, 902.4 $[M+NH_4^+]^+$, and 907.4 $[M+H]^+$ for pheophytin f or Chl f, respectively (fig. S7). Thus, expression of the *psbA4* gene is sufficient to direct the synthesis of Chl f in *Synechococcus* 7002. Collectively, the results show that the *psbA4* gene encodes Chl f synthase, and accordingly, we propose to rename this gene *chlF*.

Light dependence of Chl f synthase reaction

The discovery that a paralog of the D1 core subunit of PSII was responsible for Chl f synthesis was unexpected, because the implication was that this enzyme must be structurally and functionally related to core subunits of PSII. Interestingly, the oxidation of Chl a to Chl f (or Chlide a to Chlide f) is a four-electron oxidation, identical to the oxidation of water to produce dioxygen (*30*). We propose that ChlF is a photo-oxidoreductase that uses light to oxidize Chl a (or Chlide a) to produce Chl f (or Chlide f) while reducing bound plastoquinone (Figs. 1 and 2). If this hypothesis is correct, Chl f synthesis should be minimal if cells are allowed to express *chlF* but then shifted into darkness. To test this hypothesis, we grew wild-type *Synechococcus* 7002 cells expressing *chlF* in a medium containing 10 mM glycerol, a metabolizable carbon/energy source that supports heterotrophic growth (*31*), in continuous FRL, in continuous darkness, and in low-intensity WL (see materials and methods). There was a low level of Chl f in the cells at time zero (Fig. 7), and this level decreased slightly after 3 days in darkness, although the cells grew and their Chl a content increased. Similar amounts of Chl a were synthesized by cells grown for 3 days in continuous low-intensity WL or continuous FRL, and both synthesized identical amounts of Chl f (Fig. 7). The absorption spectrum of the pigment eluting at 14.5 min in Fig. 7 was identical to the spectra shown in Fig. 6B. (Note that retention times are different because an HPLC protocol was used that differed from that in Fig. 6A; see materials and methods for details.)

We also performed an alternative experiment designed to test whether light is required for the synthesis of Chl f (Fig. 8). Wild-type *C. fritschii* PCC 9212 was grown in continuous FRL or FRL interrupted by a dark period of 12 hours. At time zero, *C. fritschii* PCC 9212 wild-type cells that had been grown in a medium containing 5 mM fructose, a metabolizable carbon/energy source, were inoculated into two cultures, which were transferred to FRL for 24 hours to induce the expression of the FaRLiP gene cluster. One of the cultures was left in continuous FRL (Fig. 8A); the other was placed in darkness for 12 hours and then returned to FRL for another 12 hours (Fig. 8B). The Chl f content of the control cells, which could be detected by the increasing 740-nm low-temperature fluorescence emission from Chl f, increased throughout the FRL incubation. In the other sample, Chl f synthesis stopped when cells were placed in darkness, but Chl f synthesis resumed when cells were returned to FRL (Fig. 8B).

The data from both of these experimental approaches demonstrate that light is required for the synthesis of Chl f by ChlF/sr-PsbA4. Thus, we conclude that ChlF is a photo-oxidoreductase. Chl f synthase is the second light-dependent enzyme of Chl biosynthesis, the other being light-dependent protochlorophyllide oxidoreductase (POR) (*32*).

Implications of Chl f synthase (ChlF) for evolution of water oxidation and PSII

Within the context of PSII evolution, there are two ways to view the result that ChlF/PsbA4 is an enzyme that probably photo-oxidizes Chl a (or Chlide a) to produce Chl f (or Chlide f). In the first scenario, ChlF may have evolved from the PsbA (D1) subunit of a water-oxidizing PSII complex by loss of the ligands for binding the $Mn_4Ca_1O_5$ cluster but retention of catalytically useful chlorophylls, tyrosine Y_Z, and plastoquinone binding after gene duplication and divergence. Although this is certainly a reasonable possibility, phylogenetic analyses do not support this hypothesis

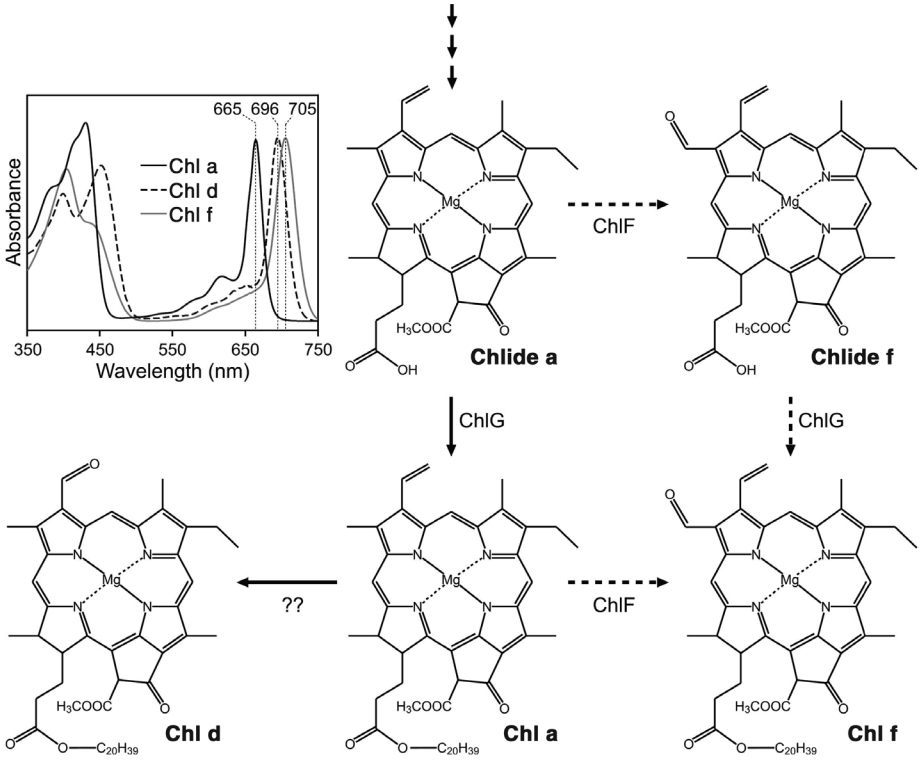

Fig. 1. Proposed biosynthetic pathways for Chl a, Chl d, and Chl f. The question marks indicate that the enzyme(s) that form Chl d from Chl a are not yet known, although this reaction pathway has been validated (*50*). ChlF converts either Chlide a or Chl a into Chlide f or Chl f. It is assumed that ChlG adds the esterifying alcohol, phytol, if Chlide f is formed as an intermediate. Upper left: In-line absorption spectra for Chl a, Chl d, and Chl f with Q_y absorption maxima at 665, 696, and 705 nm, respectively.

Downloaded from http://science.sciencemag.org/ on September 3, 2016

(*27*, *28*). An alternate possibility is perhaps more appealing: ChlF/PsbA4 could be ancestral to PsbA of PSII, and PsbA could have arisen by gene duplication and divergence to bind a $Mn_4Ca_1O_5$ cluster to catalyze water oxidation, thus providing an explanation for the origin of PSII (fig. S8) (*28*). Because the selection pressure to expand the wavelength range of photosynthesis is largely responsible for the many different Chls and antenna complexes extant today, this scheme provides an explanation for the origin of ChlF, for the reaction that it catalyzes, and for the occurrence of a presumably homodimeric type-2 reaction center in an ancestral cyanobacterium that may also have had a PSI-like reaction center (*33*, *34*).

Supporting this second possibility further, phylogenetic analyses show that ChlF/sr-PsbA, together with a highly unusual PsbA-like sequence from *Gloeobacter kilaueensis*, are the earliest diverging members of the PsbA family (fig. S8) (*8*, *27*, *28*). We hypothesize that ChlF functions as a homodimer, because introduction of *psbA4/chlF* into *Synechococcus* 7002 was sufficient to enable Chl f synthesis. All currently known photochemical reaction centers are either homodimers or heterodimers (*33*, *34*). Furthermore, because ChlF is apparently a photo-oxidoreductase and oxidation of the substrate probably occurs by a radical mechanism [assuming a one-photon, one-electron mechanism as in PSII (*30*)], dioxygen may not be required for the synthesis of Chl f. Thus, it is possible that Chl f synthase appeared before the atmosphere became oxic (i.e., before PSII had evolved). These implications could mean that ChlF is a long-sought transitional intermediate in the evolution of oxygenic photosynthesis: a simple, homodimeric, type 2 reaction center that might have first evolved in anoxygenic ancestors of modern cyanobacteria (fig. S8) (*28*, *34*, *35*). Subsequent gene duplication events [two are required to form the heterodimers found in PSII (*35*)], along with divergence to acquire the ligands to bind the $Mn_4Ca_1O_5$ cluster, could have ultimately led from an enzyme that could oxidize Chl (or Chlide) to an enzyme that could oxidize water.

In either case, the likely selective pressure for the synthesis of Chl f would have been to extend photosynthetic light harvesting into the far-red spectral region. The ability to use FRL or near-infrared light for photosynthesis provides a strong selective advantage to those organisms that can extend their light-harvesting range beyond the wavelengths absorbed by Chl a (*7*). Examples include the homodimeric type 1 reaction centers of *Chloracidobacterium thermophilum* (*36*) and green sulfur bacteria (*37*), both of which bind Chl a and bacteriochlorophyll a (BChl a). Similarly, the unusual cyanobacterium *Acaryochloris marina* has evolved to use Chl d, another FRL-absorbing Chl (see Fig. 1), together with Chl a to extend its photosynthetic light harvesting into the far-red region (*38*, *39*). It is increasingly clear that Chlide a is the central "hub" compound of Chl biosynthesis, and that the biosynthetic pathway repeatedly diverged away from this molecule (or from one of its precursors, 3,8-divinyl-protochlorophyllide) to extend light harvesting into the far red and near-infrared (*23*, *40*). These findings additionally provide strong support for the Granick hypothesis concerning the evolution of heme and Chl biosynthesis, namely that pathways evolved forward as organisms evolved [see discussion in (*40*)].

By using domain-swapping and site-directed mutagenesis methods, it may be possible to recapitulate evolution to determine which amino acid residues must be changed in PsbA to obtain a protein that no longer binds a $Mn_4Ca_1O_5$ cluster but can synthesize Chl f (or more interestingly, the

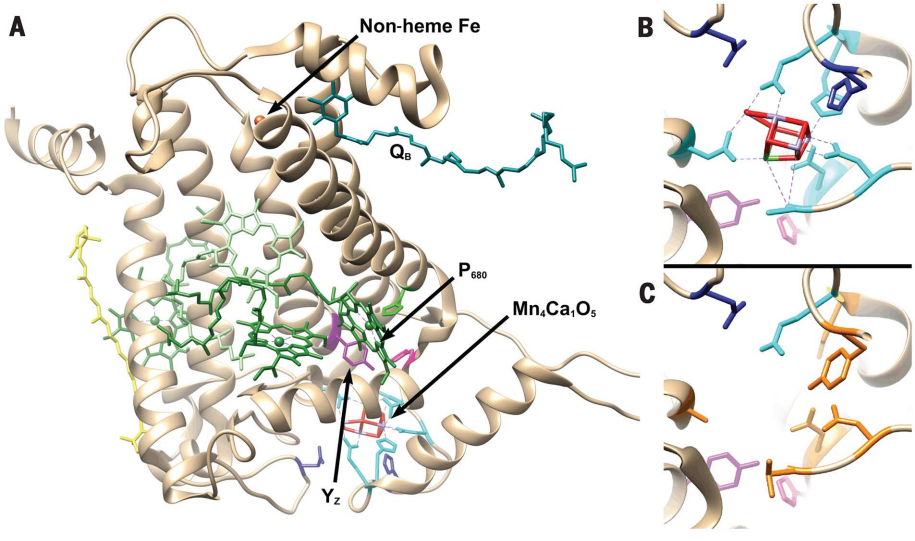

Fig. 2. Structural model of photosystem II core components from *Thermosynechococcus vulcanus* (PDB 3WU2). (**A**) PsbA (chain A) is shown in ribbon format in tan. Other components: green, three Chl a molecules and one pheophytin a molecule; teal, plastoquinone Q_B; orange, non-heme iron atom; magenta, tyrosine Y_Z; yellow, β-carotene; lilac, green, and red, the water-oxidizing $Mn_4Ca_1O_5$ cluster; aqua, amino acid side chain ligands to the $Mn_4Ca_1O_5$ cluster; blue, second-tier amino acids in the vicinity of the cluster. (**B**) Enlargement of the $Mn_4Ca_1O_5$ cluster that shows a histidine residue (pink) that may be involved in proton-coupled electron transfer in PSII. Components of the cluster: lilac, manganese atoms; green, calcium atom; red, bridging oxygen atoms; aqua, ligands to the $Mn_4Ca_1O_5$ cluster. (**C**) Model of the sr-PsbA4 $Mn_4Ca_1O_5$ cluster-binding site of *C. fritschii* PCC 9212. Only one ligand, a glutamate residue (aqua), and the C-terminal carboxyl group ligands of a nonconserved threonine residue are retained. Amino acids that replace the conserved ligands to the $Mn_4Ca_1O_5$ cluster are shown in orange. These include a second tyrosine residue found in 7 of 13 PsbA4 sequences. Note that tyrosine Y_Z and the associated histidine residue (magenta and pink, respectively) are conserved. The color coding used in this figure matches that in the multiple sequence alignment file shown in fig. S2. Images were created with the UCSF Chimera program (*51*); residues were substituted with conformations of highest probability using the Dunbrack backbone-dependent rotamer library (*52*).

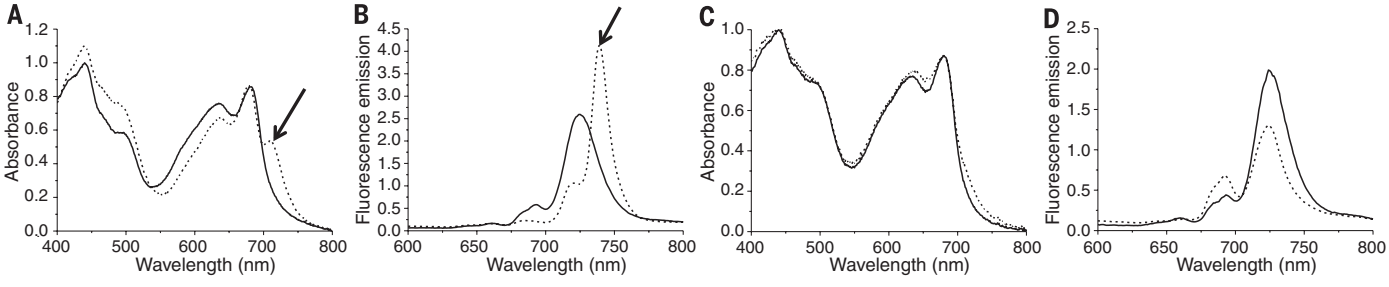

Fig. 3. The *psbA4* mutant of *C. fritschii* PCC 9212 lacks far-red absorbance and fluorescence emission. (**A** to **D**) Whole-cell absorption spectra [(A) and (C)] and low-temperature fluorescence emission spectra [(B) and (D)] of wild-type [(A) and (B)] and *psbA4* mutant cells [(C) and (D)] of *C. fritschii* PCC 9212 grown in WL (solid lines) or FRL (dashed lines). The arrows in (A) and (B) point to long-wavelength absorption and fluorescence features attributable to Chl f.

Downloaded from http://science.sciencemag.org/ on September 3, 2016

converse). Such approaches could provide an experimental framework for studying the origins of PSII, water oxidation, and thus oxygenic photosynthesis. Finally, because Chl f biosynthesis is the product of a single gene product, it may now be feasible to introduce the capacity for Chl f biosynthesis into plants to extend the wavelength range for their photosynthesis into the far-red region of the solar spectrum (*24*–*26*).

Materials and methods

Organisms and cultivation conditions

Cyanobacterial strains used in this study were obtained from the Pasteur Culture Collection (www.pasteur.fr/pcc_cyanobacteria) (*41*). *Synechococcus* 7002 was grown in medium A containing 10 mM nitrate (denoted as Medium A^+) (*42*). This cyanobacterium was routinely grown under "standard conditions" (*43*): 38°C, sparging with 1% CO_2 (v/v) in air, at 250 μmol photons m^{-2} s^{-1} provided by cool white fluorescent tubes. For some experiments, cells were grown at room temperature at an irradiance of ~15 μmol photons m^{-2} s^{-1}.

Synechococcus sp. PCC 7335 was cultured in ASN-III growth medium (*41*) to which vitamin B_{12} (final concentration 10 μg ml^{-1}) and Tris-HCl, pH 8.0 (final concentration 10 mM) were added. *C. fritschii* PCC 9212 was grown in the B-HEPES growth medium (*44*), a modified BG-11 medium containing 1.1 g $liter^{-1}$ HEPES (final concentration) with the pH adjusted to 8.0 with 2.0 M KOH. Cool white fluorescent bulbs provided continuous illumination at ~250 μmol photons m^{-2} s^{-1} (WL), and liquid cultures were sparged with 1% (v/v) CO_2 in air. *Synechococcus* sp. PCC 7335 was grown at a lower WL intensity of ~50 μmol photons m^{-2} s^{-1}. In some experiments, *C. fritschii* PCC 9212 was grown mixotrophically by adding 5 mM fructose to the growth media. Far-red light was provided by Epitex, L720-06AU LEDs (Marubeni, Santa Clara, CA) with emission centered at 720 nm (26 to 30 μmol photons m^{-2} s^{-1}), in combination with plastic filters as described (*7*, *14*). Light boards composed of 50 LEDs were assembled. Although all should nominally emit "720 nm" light, the peak emission ranges from 705 nm to 735 nm. Furthermore, the bandwidth characteristics for these LEDs is such that light from 660 nm to 760 nm is actually produced (see www.epitex.com/products/lpm/pdfs/L720-06AU.pdf). Growth of cells was monitored turbidometrically at 750 nm by using a GENESYS 10 spectrophotometer (ThermoSpectronic, Rochester, NY).

Media for the growth of mutants of *C. fritschii* PCC 9212 and *Synechococcus* sp. PCC 7335 and the *psbA4* overexpression strain of *Synechococcus* 7002 were amended with antibiotics as required: kanamycin (100 μg ml^{-1}), erythromycin (20 μg ml^{-1}), gentamicin (50 μg ml^{-1}).

Cultivation conditions to demonstrate the light requirement for Chl f synthase

To assess the requirement for light for Chl f biosynthesis in a strain of *Synechococcus* 7002 expressing *chlF/psbA4* from *C. fritschii*, a starter culture was grown in high light for 24 hours in medium A^+ containing 10 mM glycerol. This starter culture was used to inoculate duplicate cultures that were grown in the same medium under continuous FRL (28 μM photons m^{-2} s^{-1}), low WL (15 μM photons m^{-2} s^{-1}), and continuous darkness. The data shown in Fig. 7 indicate that only cells maintained in FRL or low-intensity WL could synthesize Chl f. However, cells grew under all three conditions. The $OD_{730\ nm}$ of the culture grown in darkness increased ~30%, but the $OD_{730\ nm}$ of cells grown in continuous FRL increased ~90% and that for cells grown in continuous WL ~60%. Importantly, the Chl a content of cells grown in darkness also increased during incubation in the dark, showing that these cells were capable of synthesizing Chl a but not Chl f (Fig. 7).

In a second experiment to test the requirement for light for Chl f biosynthesis, the wild-type strain of *C. fritschii* PCC 9212 was grown in continuous or interrupted FRL (Fig. 8). At time zero, wild-type cells grown in WL in a medium containing 5 mM fructose, which supports heterotrophic growth of *C. fritschii* PCC 9212 (*41*), were inoculated into two cultures, which were transferred to FRL for 24 hours. One of the cultures was left in continuous FRL (Fig. 8A), while the other was placed in darkness for 12 hours and then returned to FRL for another 12 hours (Fig. 8B). The control cells incubated in continuous FRL continuously synthesized Chl f, which could be detected by the increasing 740-nm fluorescence emission maximum from Chl f. Over the 48-hour duration of the experiment, the cell density under each growth condition increased by about 25%. Chl f synthesis stopped when cells were placed in darkness, but Chl f synthesis resumed when cells were returned to FRL (Fig. 8B). This experiment was repeated twice with essentially identical results for both trials. This experiment confirms that Chl f synthase requires light for its activity.

Construction of mutants and conjugation

J. Zhao (Peking University) provided the biparental conjugation system (*45*), and the method used was very similar to that described in (*14*). The donor *E. coli* strain HB101 contained the conjugal plasmid pRL443 and the helper plasmid pRL623 (*46*, *47*). Figure S3 shows maps of the scheme employed to delete the *psbA4* genes of *C. fritschii* PCC 9212 and *Synechococcus* sp. PCC 7335. The *psbA4* gene of *C. fritschii* was deleted and replaced by an *ermC* cassette conferring resistance to erythromycin, while the *psbA4* gene of *Synechococcus* sp. PCC 7335 was partly deleted and replaced by an *aphII* cassette, conferring resistance to kanamycin. Upstream and downstream DNA fragments for each target *psbA4* gene were cloned into the cargo plasmid pRL277 with an interposing DNA fragment encoding *ermC* or *aphII* to replace the target gene through a double-crossover recombination event. For each target gene, upstream and downstream DNA fragments with a size of ~2.5 to 3.0 kb were amplified by PCR using Phusion HF DNA polymerase (New England Biolabs). The primers for DNA fragment amplification of the upstream and downstream regions are listed in table S2.

Cargo plasmids were transformed into the donor *E. coli* HB101 cells containing the conjugal plasmid pRL443 and the helper plasmid pRL623. The resulting *E. coli* HB101 strains were grown in 5 to 20 ml of Luria-Bertani (LB) medium supplemented with appropriate antibiotics and cultured at 37°C

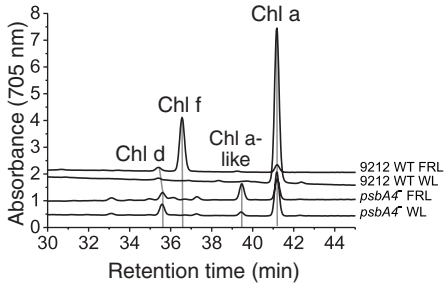

Fig. 4. The *psbA4* mutant of *C. fritschii* PCC 9212 is unable to synthesize Chl f but still produces Chl d and Chl a. The figure shows the elution profiles from reversed-phase HPLC analysis using method MY1 (see materials and methods) of pigment extracts from wild-type and *psbA4* mutant cells of *C. fritschii* PCC 9212 grown in WL or FRL. Note that Chl f is present in the wild-type pigments extracted from cells grown in FRL but not in *psbA4* mutant cells. The peak labeled "Chl a–like" had the absorption spectrum of Chl a but its retention time was different.

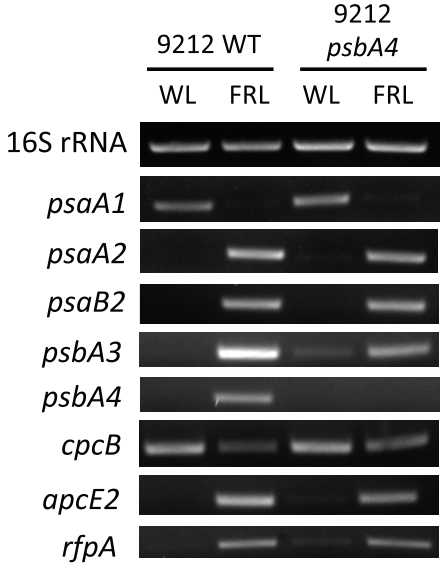

Fig. 5. Transcriptional regulation by the RfpABC system is not impaired in the *psbA4* mutant of *C. fritschii* PCC 9212. The figure shows electrophoretic analysis of amplicons derived from RT-PCR analysis of transcripts for selected genes from the FaRLiP gene cluster (*psaA2*, *psaB2*, *psbA3*, *psbA4*, *apcE2*, and *rfpA*) from wild-type and *psbA4* mutant cells of *C. fritschii* PCC 9212 grown in WL or FRL. Paralogous genes from elsewhere in the genome are more highly expressed in WL (*psaA1*, *cpcB*). Note that no *psbA4* transcripts are observed in the *psbA4* mutant grown in FRL.

Downloaded from http://science.sciencemag.org/ on September 3, 2016

overnight. The *E. coli* cells were harvested by centrifugation at low speed, washed with fresh LB medium three times, and resuspended in fresh LB, B-HEPES medium, or ASN-III medium (100 to 200 μl). Meanwhile, freshly grown wild-type *C. fritschii* 9212 or *Synechococcus* sp. PCC 7335 cells ($OD_{750\ nm}$ = 0.6 to 1.0; 500 μl to 2.0 ml) were centrifuged at low speed, washed with fresh B-HEPES or ASN-III medium three times, and finally resuspended in B-HEPES or ASN-III medium (100 to 200 μl). The *E. coli* and cyanobacterial cells were gently mixed in a sterile microcentrifuge tube and incubated at 30°C under low light for 4 to 6 hours, and the cell mixture was then spread onto a sterile nitrocellulose filter overlaid on a B-HEPES or ASN-III agar plate without antibiotics. The plate was incubated at 30°C under low light for another 18 to 36 hours, and then the filter was transferred to a B-HEPES agar plate containing 20 μg erythromycin ml^{-1} or an ASN-III agar plate containing 100 μg kanamycin ml^{-1}. Brown- or green-colored colonies appeared on the filter after about 4 weeks. Colonies were picked and streaked repeatedly on selective medium, and the purified transconjugant cells were ultimately transferred to liquid B-HEPES or ASN-III medium for analyses. Segregation of wild-type and mutant alleles of the target gene was analyzed by colony PCR.

Pigment extraction, HPLC analyses, and mass spectrometry

Two methods, denoted MY1 and MY2, were used for pigment extraction and HPLC analysis. Method MY1 was performed as previously described (*7*, *8*, *14*). Pigments were extracted with acetone/methanol (7:2, v/v) from cells and analyzed by reversed-phase HPLC on an Agilent 1100 HPLC system (Agilent Technologies) with an analytical Discovery C18 column (4.6 mm × 25 cm) (Supelco, Sigma-Aldrich). The gradient elution program [B, minutes] using Solvent A (methanol:acetonitrile:H_2O = 42:33:25) and Solvent B (methanol:acetonitrile:ethyl acetate = 50:20:30) was set as [30%, 0], [100%, 50], [100%, 58], [30%, 60] at a flow rate 1 ml min^{-1}. Elution of pigments was monitored at 705 nm, the absorbance maximum of Chl f.

Method MY2, adapted from Armenta *et al.* (*48*), was performed for both analytical and semipreparative purposes. Pigments were extracted using a previously published method (*49*) and separated with the same HPLC system using an analytical Discovery C18 column described above or a semipreparative Discovery C18 column (10 mm × 25 cm) (Supelco, Sigma-Aldrich). Solvents A and B were 88:10:2 methanol/ethyl acetate/H_2O (v/v/v) and 48:50:2 methanol/ethyl acetate/H_2O (v/v/v), respectively. After 10 min of washing with Solvent A, Chls were eluted with a linear gradient of 0% to 20% solvent B over 20 min, increasing to 100% to wash the column. The analytical program was performed at 1 ml min^{-1} and 3.5 ml min^{-1} for analytical and semipreparative purposes, respectively.

Mass spectrometric analysis of chlorophyll pigments collected by semipreparative method MY2 was performed on a Waters Q-TOF Premier quadrupole/time-of-flight (TOF) mass spectrometer [Waters Corporation (Micromass Ltd.), Manchester, UK]. Operation of the mass spectrometer was performed using MassLynx software Version 4.1 (www.waters.com). Samples were introduced into the mass spectrometer using a Waters 2695 HPLC system. The samples were analyzed using flow injection analysis (FIA), in which the sample is injected into the mobile phase flow and passed directly into the mass spectrometer, where the analytes are ionized and detected. The mobile phase used was 90% acetonitrile (LC-MS grade) and 10% aqueous 0.1% formic acid. The flow rate was 0.15 ml min^{-1}. The nitrogen drying gas temperature was set to 300°C at a flow of 6 liters min^{-1}, and the capillary voltage was 2.8 kV. The mass spectrometer was set to scan from 100 to 1000 *m/z* in positive ion mode, using electrospray ionization (ESI). The MS analysis of Chls and pheophytins was performed in the Proteomics and Mass Spectrometry Core Facility, Huck Institutes of the Life Sciences, Pennsylvania State University.

Absorption and fluorescence spectroscopy

Room-temperature absorption spectra were recorded with a GENESYS 10 spectrophotometer (ThermoFisher Scientific) or a Cary 14 UV-Vis-NIR spectrophotometer modified for computer-controlled operation by OLIS Inc. (Bogart, GA). Absorption spectra of whole cells of *Synechococcus* sp. PCC 7335 and mutants derived from it were recorded in growth medium ASN-III. The absorption spectra of *C. fritschii* PCC 9212 and mutant strains derived from it were recorded by homogenizing, resuspending, and diluting cells in B-HEPES medium with 60% w/v sucrose (1:10 dilution). Before recording the absorption spectra, whole cells were homogenized as necessary, and

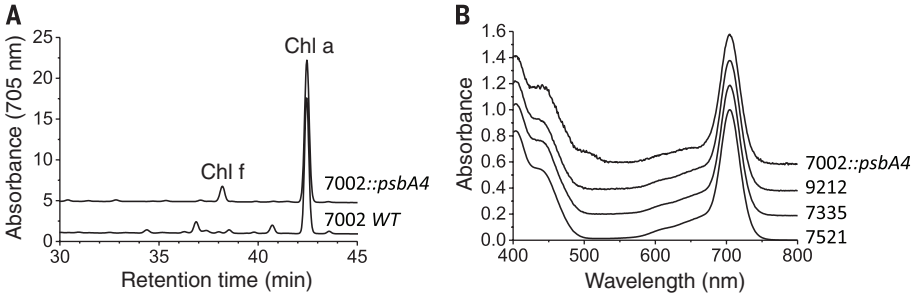

Fig. 6. Synthesis of Chl f in a *Synechococcus* 7002 strain expressing the *psbA4* gene of *C. fritschii* PCC 9212. (**A**) Reversed-phase HPLC elution profiles at 705 nm for pigments extracted from wild-type *Synechococcus* 7002 (7002 WT) and a strain expressing the *psbA4* gene from *C. fritschii* PCC 9212 (7002::*psbA4*). The pigments were analyzed using method MY1 (see materials and methods). Chl f was 0.059% of the total Chl in the cells. (**B**) In-line absorption spectra of Chl f from a *Synechococcus* 7002 strain expressing the *psbA4* gene from *C. fritschii* PCC 9212 (7002::*psbA4*). The absorption spectra of Chl f from *C. fritschii* PCC 9212 (9212), *Synechococcus* sp. PCC 7335 (7335), and *Fischerella thermalis* PCC 7521 (7521) were identical to that of Chl f from 7002::*psbA4*. Spectra were normalized to equal absorbance at 705 nm and were offset for clarity.

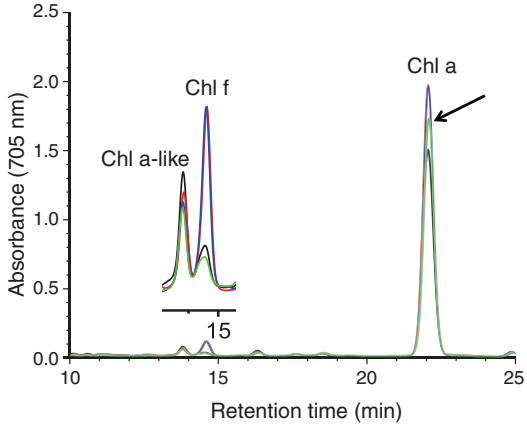

Fig. 7. Chl f synthesis, but not Chl a synthesis, requires light in *Synechococcus* 7002 expressing PsbA4/ChlF. The figure shows elution profiles from reversed-phase HPLC analysis pigments extracted from *Synechococcus* 7002 expressing *chlF/psbA4* using method MY2 (see materials and methods for details). The elution positions for an unidentified Chl a–like pigment, Chl f, and Chl a are indicated. Cells were grown in WL for 24 hours, which resulted in a basal level of Chl f synthesis (black line). These cells were used to inoculate cultures that were grown in medium A^+ containing 10 mM glycerol as a carbon/energy source. Cells were grown in darkness (green line), low-intensity WL (red line), or FRL (blue line). Cells grown in darkness for 3 days had a lower Chl f content than cells at time zero. However, cells incubated in the dark grew and synthesized new Chl a (arrow). Cells grown in FRL (blue line) and low WL (red line) also grew and synthesized more Chl a than cells grown in the dark. However, only cells grown in continuous FRL and low-intensity WL were able to synthesize Chl f (inset). This experiment was performed twice and identical results were obtained.

Downloaded from http://science.sciencemag.org/ on September 3, 2016

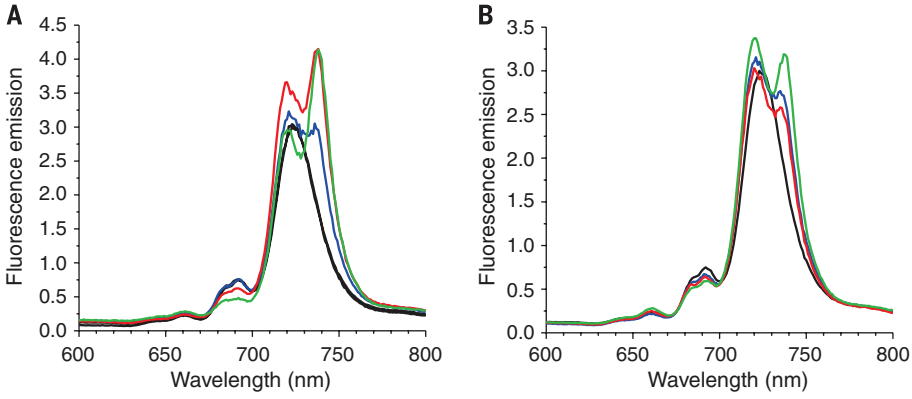

Fig. 8. Chl f synthesis in wild-type cells of *C. fritschii* PCC 9212 requires light. (**A**) A starter culture was grown in WL in a medium containing 5 mM fructose, and at time zero, these cells were used to inoculate two cultures in the same medium. One culture was grown in continuous FRL, and low-temperature fluorescence emission spectra were taken at time zero (black line), 24 hours (blue line), 36 hours (red line), and 48 hours (green line). (**B**) The second culture was incubated in FRL for 24 hours, shifted to darkness for 12 hours, and then returned to FRL for 12 hours. Low-temperature fluorescence emission spectra were taken at time zero (black line), after 24 hours in FRL (blue line), after 12 hours in the dark (36 hours; red line), and after an additional 12 hours of incubation in FRL (48 hours; green line). Chl f synthesis stopped during the 12-hour dark period but resumed when cells were returned to FRL.

spectra were recorded through the opal glass side of the cuvettes to allow correction for scattering. Fluorescence emission spectra of whole cells at 77 K were measured with an SLM 8000C spectrofluorometer, modified for computer-controlled operation by OLIS Inc. (Bogart, GA). Cells in exponential growth phase ($OD_{750\ nm}$ = ~0.6 to 0.7) were collected, homogenized, and resuspended in 50 mM Tris-HCl, pH 8.0 buffer. Glycerol was added to a final concentration of 60% (v/v). Cells were adjusted to a concentration of ~0.5 $OD_{750\ nm}$ and quickly frozen in liquid nitrogen. The excitation wavelength was set to 440 nm to excite Chls preferentially.

RNA isolation and RT-PCR

For gene expression analysis, total RNA was isolated from the wild-type and mutant strains grown to mid-exponential growth phase using a High Pure RNA isolation kit (Roche Diagnostics). To eliminate trace amounts of contaminating chromosomal DNAs, RNA samples were incubated with RNase-free DNase I (Promega) for 2 to 3 hours at 37°C. DNase-treated RNA samples were further purified using RNA purification cartridges. The absence of DNA in RNA samples was verified by PCR assays in which reverse transcriptase was omitted. The concentration of RNA was determined by NanoDrop measurements (Thermo Scientific).

RT-PCR analysis of total RNA isolated from wild-type and mutant strains was performed using a MyTaq One-Step RT-PCR kit (Bioline USA Inc., Taunton, MA). Primers were designed to amplify ~500-bp regions of specifically selected genes encoding major subunits of PSI, PSII, and phycobilisomes, as well as the 16*S* RNA gene as a control (see legend to Fig. 5). The resulting amplicons were analyzed by agarose gel electrophoresis.

Expression of the psbA4 *gene of* C. fritschii *PCC 9212 in* Synechococcus *7002*

To generate the expression vector for *psbA4*, a DNA fragment containing the *psbA4* gene was amplified by PCR from chromosomal DNA of *C. fritschii* PCC 9212 using Phusion HF DNA polymerase. The primers used were 9212 *psbA4* pAQ-1-1 (NcoINdeI) and 9212 *psbA4* pAQ-1-2 (BamHI) (table S2). After digestion with NdeI and BamHI, the *psbA4* gene amplicon was cloned into the pAQ1Ex-P_{cpcBA}/Gm shuttle vector (*29*). After verification by DNA sequencing, the *psbA4* expression construct [pAQ1Ex::9212_*psbA4* (Gm^R)] was transformed into the cells of *Synechococcus* 7002. Transformants were selected on agar plates made with A^+ medium amended with gentamicin. Transformants harboring the expression plasmid were confirmed by PCR analysis and DNA sequence analysis.

Isolation of PSI complexes and LC-MS/MS analysis

PSI complexes of the wild-type and *psbA4* mutant strains of *C. fritschii* PCC 9212 were isolated from cells grown under WL and FRL conditions following the procedures described previously (*7*). In-solution digestion of proteins with trypsin and LC-MS/MS analysis were performed at the PARC Mass Spectrometer Facility at Washington University in St. Louis. Peptide mass spectra (m/z range 380 to 1500) were acquired at high mass resolving power (70,000 for ions with m/z = 200) with a Fourier Transform (FT) Q Exactive Plus mass spectrometer (Thermo Fisher Scientific). The raw data from the LC-MS/MS analysis was directly loaded into PEAKS (v 7.0, Bioinformatics Solution Inc., Waterloo, Ontario, Canada) for performing database searches against the total proteome for *C. fritschii* PCC 9212, which was derived from the annotated genome sequence.

REFERENCES AND NOTES

1. P. G. Falkowski, J. A. Raven, *Aquatic Photosynthesis* (Princeton Univ. Press, 2013).
2. M. R. Speight, P. A. Henderson, *Marine Ecology: Concepts and Applications* (Wiley-Blackwell, 2010).
3. P. Flombaum *et al*., Present and future global distributions of the marine cyanobacteria *Prochlorococcus* and *Synechococcus*. *Proc. Natl. Acad. Sci. U.S.A.* **110**, 9824–9829 (2013). doi: 10.1073/pnas.1307701110; pmid: 23703908
4. F. Garcia-Pichel, J. Belnap, S. Neuer, F. Schanz, Estimates of global cyanobacterial biomass and its distribution. *Arch. Hydrobiol.* **148** (suppl.), 213–227 (2003). doi: 10.1127/1864-1318/2003/0109-0213
5. W. Elbert *et al*., Contribution of cryptogamic covers to the global cycles of carbon and nitrogen. *Nat. Geosci.* **5**, 459–462 (2012). doi: 10.1038/ngeo1486
6. F. Gan, D. A. Bryant, Adaptive and acclimative responses of cyanobacteria to far-red light. *Environ. Microbiol.* **17**, 3450–3465 (2015). doi: 10.1111/1462-2920.12992; pmid: 26234306
7. F. Gan *et al*., Extensive remodeling of a cyanobacterial photosynthetic apparatus in far-red light. *Science* **345**, 1312–1317 (2014). pmid: 25214622
8. F. Gan, G. Shen, D. A. Bryant, Occurrence of far-red light photoacclimation (FaRLiP) in diverse cyanobacteria. *Life* **5**, 4–24 (2015). doi: 10.3390/life5010004; pmid: 25551681
9. W. A. Sidler, Phycobilisome and phycobiliprotein structures. In *The Molecular Biology of Cyanobacteria*, Vol. 1 of *Advances in Photosynthesis and Respiration*, D. A. Bryant, Ed. (Kluwer Academic, 1994), pp. 139–216. doi: 10.1007/0-306-48205-3_7
10. I. Grotjohann, P. Fromme, Structure of cyanobacterial photosystem I. *Photosynth. Res.* **85**, 51–72 (2005). doi: 10.1007/s11120-005-1440-4; pmid: 15977059
11. Y. Umena, K. Kawakami, J.-R. Shen, N. Kamiya, Crystal structure of oxygen-evolving photosystem II at a resolution of 1.9 Å. *Nature* **473**, 55–60 (2011). doi: 10.1038/nature09913; pmid: 21499260
12. A. N. Glazer, D. A. Bryant, Allophycocyanin B (λ_{max} 671, 618 nm): A new cyanobacterial phycobiliprotein. *Arch. Microbiol.* **104**, 15–22 (1975). doi: 10.1007/BF00447294; pmid: 808186
13. Y. Li *et al*., Characterization of red-shifted phycobilisomes isolated from the chlorophyll *f*-containing cyanobacterium *Halomicronema hongdechloris*. *Biochim. Biophys. Acta* **1857**, 107–114 (2016). doi: 10.1016/j.bbabio.2015.10.009; pmid: 26514405
14. C. Zhao, F. Gan, G. Shen, D. A. Bryant, RfpA, RfpB, and RfpC are the master control elements of far-red light photoacclimation (FaRLiP). *Front. Microbiol.* **6**, 1303 (2015). doi: 10.3389/fmicb.2015.01303; pmid: 26635768
15. M. Chen *et al*., A red-shifted chlorophyll. *Science* **329**, 1318–1319 (2010). doi: 10.1126/science.1191127; pmid: 20724585
16. R. D. Willows, Y. Li, H. Scheer, M. Chen, Structure of chlorophyll *f*. *Org. Lett.* **15**, 1588–1590 (2013). doi: 10.1021/ol400327j; pmid: 23496297
17. M. Chen, Chlorophyll modifications and their spectral extension in oxygenic photosynthesis. *Annu. Rev. Biochem.* **83**, 317–340 (2014). doi: 10.1146/annurev-biochem-072711-162943; pmid: 24635479
18. Y. Li, Y. Lin, P. C. Loughlin, M. Chen, Optimization and effects of different culture conditions on growth of *Halomicronema hongdechloris* - a filamentous cyanobacterium containing chlorophyll *f*. *Front. Plant Sci.* **5**, 67 (2014). doi: 10.3389/fpls.2014.00067; pmid: 24616731
19. R. L. Airs *et al*., Chlorophyll *f* and chlorophyll *d* are produced in the cyanobacterium *Chlorogloeopsis fritschii* when cultured under natural light and near-infrared radiation. *FEBS Lett.* **588**, 3770–3777 (2014). doi: 10.1016/j.febslet.2014.08.026; pmid: 25176411
20. L. Behrendt *et al*., Chlorophyll *f*-driven photosynthesis in a cavernous cyanobacterium. *ISME J.* **9**, 2108–2111 (2015). doi: 10.1038/ismej.2015.14; pmid: 25668158
21. Y. Li, Z.-L. Cai, M. Chen, Spectroscopic properties of chlorophyll *f*. *J. Phys. Chem. B* **117**, 11309–11317 (2013). doi: 10.1021/jp402413d; pmid: 23614570
22. Y. Li, N. Scales, R. E. Blankenship, R. D. Willows, M. Chen, Extinction coefficient for red-shifted chlorophylls: Chlorophyll *d*

Downloaded from http://science.sciencemag.org/ on September 3, 2016

and chlorophyll *f*. *Biochim. Biophys. Acta* **1817**, 1292–1298 (2012). doi: 10.1016/j.bbabio.2012.02.026; pmid: 22395150
23. A. Gomez Maqueo Chew, D. A. Bryant, Chlorophyll biosynthesis in bacteria: The origins of structural and functional diversity. *Annu. Rev. Microbiol.* **61**, 113–129 (2007). doi: 10.1146/annurev.micro.61.080706.093242; pmid: 17506685
24. M. Chen, R. E. Blankenship, Expanding the solar spectrum used by photosynthesis. *Trends Plant Sci.* **16**, 427–431 (2011). doi: 10.1016/j.tplants.2011.03.011; pmid: 21493120
25. R. E. Blankenship, M. Chen, Spectral expansion and antenna reduction can enhance photosynthesis for energy production. *Curr. Opin. Chem. Biol.* **17**, 457–461 (2013). doi: 10.1016/j.cbpa.2013.03.031; pmid: 23602382
26. R. E. Blankenship *et al*., Comparing photosynthetic and photovoltaic efficiencies and recognizing the potential for improvement. *Science* **332**, 805–809 (2011). doi: 10.1126/science.1200165; pmid: 21566184
27. J. W. Murray, Sequence variation at the oxygen-evolving centre of photosystem II: A new class of 'rogue' cyanobacterial D1 proteins. *Photosynth. Res.* **110**, 177–184 (2012). doi: 10.1007/s11120-011-9714-5; pmid: 22187288
28. T. Cardona, J. W. Murray, A. W. Rutherford, Origin and evolution of water oxidation before the last common ancestor of the cyanobacteria. *Mol. Biol. Evol.* **32**, 1310–1328 (2015). doi: 10.1093/molbev/msv024; pmid: 25657330
29. Y. Xu *et al*., Expression of genes in cyanobacteria: Adaptation of endogenous plasmids as platforms for high-level gene expression in *Synechococcus* sp. PCC 7002. *Methods Mol. Biol.* **684**, 273–293 (2011). doi: 10.1007/978-1-60761-925-3_21; pmid: 20960136
30. J.-R. Shen, The structure of photosystem II and the mechanism of water oxidation in photosynthesis. *Annu. Rev. Plant Biol.* **66**, 23–48 (2015). doi: 10.1146/annurev-arplant-050312-120129; pmid: 25746448
31. D. H. Lambert, S. E. Stevens Jr., Photoheterotrophic growth of *Agmenellum quadruplicatum* PR-6. *J. Bacteriol.* **165**, 654–656 (1986). pmid: 3080411
32. M. Gabruk, B. Mysliwa-Kurdziel, Light-dependent protochlorophyllide oxidoreductase: Phylogeny, regulation, and catalytic properties. *Biochemistry* **54**, 5255–5262 (2015). doi: 10.1021/acs.biochem.5b00704; pmid: 26230427
33. M. F. Hohmann-Marriott, R. E. Blankenship, Evolution of photosynthesis. *Annu. Rev. Plant Biol.* **62**, 515–548 (2011). doi: 10.1146/annurev-arplant-042110-103811; pmid: 21438681
34. T. Cardona, A fresh look at the evolution and diversification of photochemical reaction centers. *Photosynth. Res.* **126**, 111–134 (2015). doi: 10.1007/s11120-014-0065-x; pmid: 25512103
35. T. Cardona, Reconstructing the origin of oxygenic photosynthesis: Do assembly and photoactivation recapitulate evolution? *Front. Plant Sci.* **7**, 257 (2016). doi: 10.3389/fpls.2016.00257; pmid: 26973693
36. Y. Tsukatani, S. P. Romberger, J. H. Golbeck, D. A. Bryant, Isolation and characterization of homodimeric type-I reaction center complex from *Candidatus* Chloracidobacterium thermophilum, an aerobic chlorophototroph. *J. Biol. Chem.* **287**, 5720–5732 (2012). doi: 10.1074/jbc.M111.323329; pmid: 22184116
37. G. Hauska, T. Schoedl, H. Remigy, G. Tsiotis, The reaction center of green sulfur bacteria. *Biochim. Biophys. Acta* **1507**, 260–277 (2001). doi: 10.1016/S0005-2728(01)00200-6; pmid: 11687219
38. H. Miyashita *et al*., Discovery of chlorophyll *d* in *Acaryochloris marina* and chlorophyll *f* in a unicellular cyanobacterium, strain KC1, isolated from Lake Biwa. *J. Phys. Chem. Biophys.* **4**, 149 (2014). doi: 10.4172/2161-0398.1000149
39. S. I. Allakhverdiev *et al*., Chlorophylls *d* and *f* and their role in primary photosynthetic processes of cyanobacteria. *Biochemistry (Moscow)* **81**, 201–212 (2016). doi: 10.1134/S0006297916030020; pmid: 27262189
40. D. A. Bryant, Z. Liu, Green bacteria: Insights into green bacterial evolution through genomic analyses. *Adv. Bot. Res.* **66**, 99–150 (2013). doi: 10.1016/B978-0-12-397923-0.00004-7
41. R. Rippka, J. Deruelles, J. B. Waterbury, M. Herdman, R. Y. Stanier, Generic assignments, strain histories and properties of pure cultures of cyanobacteria. *Microbiology* **111**, 1–61 (1979). doi: 10.1099/00221287-111-1-1
42. S. E. Stevens Jr., R. D. Porter, Transformation in *Agmenellum quadruplicatum*. *Proc. Natl. Acad. Sci. U.S.A.* **77**, 6052–6056 (1980). doi: 10.1073/pnas.77.10.6052; pmid: 16592896
43. M. Ludwig, D. A. Bryant, Transcription profiling of the model cyanobacterium *Synechococcus* sp. strain PCC 7002 by next-gen (SOLiD™) sequencing of cDNA. *Front. Microbiol.* **2**, 41 (2011). doi: 10.3389/fmicb.2011.00041; pmid: 21779275
44. J. M. Dubbs, D. A. Bryant, Molecular cloning and transcriptional analysis of the *cpeBA* operon of the cyanobacterium *Pseudanabaena* species PCC7409. *Mol. Microbiol.* **5**, 3073–3085 (1991). doi: 10.1111/j.1365-2958.1991.tb01867.x; pmid: 1809846
45. Y. Zhao *et al*., CcbP, a calcium-binding protein from *Anabaena* sp. PCC 7120, provides evidence that calcium ions regulate heterocyst differentiation. *Proc. Natl. Acad. Sci. U.S.A.* **102**, 5744–5748 (2005). doi: 10.1073/pnas.0501782102; pmid: 15811937
46. J. Elhai, C. P. Wolk, Conjugal transfer of DNA to cyanobacteria. *Methods Enzymol.* **167**, 747–754 (1988). doi: 10.1016/0076-6879(88)67086-8; pmid: 3148842
47. J. Elhai, A. Vepritskiy, A. M. Muro-Pastor, E. Flores, C. P. Wolk, Reduction of conjugal transfer efficiency by three restriction activities of *Anabaena* sp. strain PCC 7120. *J. Bacteriol.* **179**, 1998–2005 (1997). pmid: 9068647
48. R. E. Armenta, A. Burja, H. Radianingtyas, C. J. Barrow, Critical assessment of various techniques for the extraction of carotenoids and co-enzyme Q10 from the thraustochytrid strain ONC-T18. *J. Agric. Food Chem.* **54**, 9752–9758 (2006). doi: 10.1021/jf061260o; pmid: 17177497
49. D. P. Canniffe, P. J. Jackson, S. Hollingshead, M. J. Dickman, C. N. Hunter, Identification of an 8-vinyl reductase involved in bacteriochlorophyll biosynthesis in *Rhodobacter sphaeroides* and evidence for the existence of a third distinct class of the enzyme. *Biochem. J.* **450**, 397–405 (2013). doi: 10.1042/BJ20121723; pmid: 23252506
50. M. Schliep, B. Crossett, R. D. Willows, M. Chen, ^{18}O labeling of chlorophyll *d* in *Acaryochloris marina* reveals that chlorophyll *a* and molecular oxygen are precursors. *J. Biol. Chem.* **285**, 28450–28456 (2010). doi: 10.1074/jbc.M110.146753; pmid: 20610399
51. E. F. Pettersen *et al*., UCSF Chimera—a visualization system for exploratory research and analysis. *J. Comput. Chem.* **25**, 1605–1612 (2004). doi: 10.1002/jcc.20084; pmid: 15264254
52. R. L. Dunbrack Jr., Rotamer libraries in the 21st century. *Curr. Opin. Struct. Biol.* **12**, 431–440 (2002). doi: 10.1016/S0959-440X(02)00344-5; pmid: 12163064

ACKNOWLEDGMENTS

Supported by NSF grant MCB-1021725 (D.A.B.) and European Commission Marie Skłodowska-Curie Global Fellowship 660652 (D.P.C.). This research was also conducted under the auspices of the Photosynthetic Antenna Research Center (PARC), an Energy Frontier Research Center funded by the U.S. Department of Energy, Office of Science, Office of Basic Energy Sciences under award DE-SC 0001035. M.-Y.H., G.S., C.Z., and D.A.B. were partly supported by PARC and partly supported by NSF. We thank R. E. Blankenship, A. N. Glazer, J. H. Golbeck, C. N. Hunter, J. C. Lagarias, and J. T. J. Lecomte for reading, commenting, and offering suggestions to improve the draft manuscript; J. Miller for his expert assistance in performing and interpreting the mass spectral data for Chls and pheophytins; H. Zhang for assistance with the proteomic analyses; and W. Cui for assistance in depositing the proteomics data in the PRIDE database. All data are available in the supplementary materials. The mass spectrometry proteomics data have been deposited to the ProteomeXchange Consortium via the PRIDE [1] partner repository with the data set identifier PXD004458.

SUPPLEMENTARY MATERIALS

www.sciencemag.org/content/353/6302/aaf9178/suppl/DC1
Figs. S1 to S8
Tables S1 and S2

19 April 2016; accepted 22 June 2016
Published online 7 July 2016
10.1126/science.aaf9178

Downloaded from http://science.sciencemag.org/ on September 3, 2016

RESEARCH ARTICLE SUMMARY

STRUCTURAL BIOLOGY

Structure of the STRA6 receptor for retinol uptake

Yunting Chen,* Oliver B. Clarke,* Jonathan Kim, Sean Stowe, Youn-Kyung Kim, Zahra Assur, Michael Cavalier, Raquel Godoy-Ruiz, Desiree C. von Alpen, Chiara Manzini, William S. Blaner, Joachim Frank, Loredana Quadro, David J. Weber, Lawrence Shapiro, Wayne A. Hendrickson, Filippo Mancia†

INTRODUCTION: Vitamin A is an essential nutrient for all mammals, being vital for vision and for transcription of a wide array of genes. Retinol (vitamin A alcohol) is the predominant circulating retinoid. In the fasting state, retinol from liver stores is mobilized bound to retinol-binding protein (RBP), which transports this highly hydrophobic molecule in the bloodstream. How retinol is released from RBP and internalized by target cells has been the subject of intense debate. The RBP receptor, STRA6, was cloned in 2007. STRA6 was predicted to be a 75-kDa multipass transmembrane (TM) protein without sequence similarity to any known transporter, channel, or receptor. STRA6 is expressed widely, with particular abundance in the eye and placenta. Mutations in the human *STRA6* gene have been linked to Matthew-Wood syndrome, which presents with ocular abnormalities and developmental defects.

RATIONALE: Despite a wealth of biochemical work aimed at investigating how STRA6 mediates internalization of retinol from RBP, progress at the molecular level has been hindered by the absence of structural information. Purified STRA6 from zebrafish was a detergent-stable dimer in an unexpected association with calmodulin (CaM), forming a 180-kDa complex.

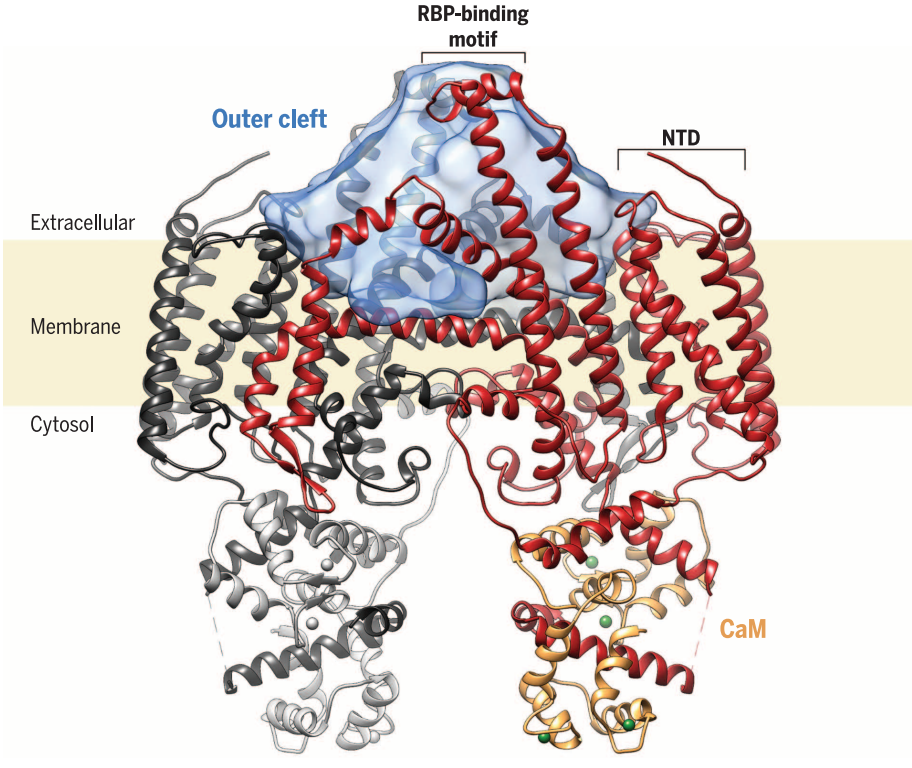

The structure of STRA6 in complex with CaM. The STRA6 dimer, drawn as a ribbon representation with one protomer in dark red and the other in black, is associated with two molecules of calmodulin, drawn in gray and gold. The internal volume of the outer cleft is represented as a semitransparent blue surface. Calcium ions are represented as green spheres.

RESULTS: Using cryo-electron microscopy, we determined the structure of zebrafish STRA6 in complex with CaM to 3.9 Å resolution. The protein is assembled as an intricate dimer with a topology that includes 18 TM helices (nine per protomer) and two long horizontal intramembrane (IM) helices interacting at the dimer core. Each STRA6 protomer comprises an N-terminal domain (NTD) of the first five TM helices, connected by a linker containing the first CaM-binding peptide to a central domain at the dimer interface that includes TMs 6 to 9 and the IM helices, and a cytoplasmic C-terminal segment that interacts with CaM through two additional helices. Each protomer is compactly associated with one molecule of CaM, adopting an unconventional arrangement in which it is bound to three helical regions of STRA6. We characterized the STRA6-CaM interaction biophysically by isothermal titration calorimetry, showing that the affinity of CaM for one STRA6 peptide alone is subnanomolar, and structurally by x-ray crystallography. We also demonstrated that the STRA6-CaM association is physiological by performing immunoprecipitation experiments on native zebrafish tissue. Both the extra- and intracellular surfaces of the NTD feature conserved polar pockets. The outer NTD pocket spans half the bilayer. The central domain of STRA6 defines a large ~20,000 $Å^3$ cleft on the extracellular side, which encompasses the space between previously characterized binding sites for RBP, ~25 Å above the membrane surface, and the IM helices located down at the mid-bilayer level. This outer cleft is hydrophobic, contains two ordered putative cholesterols, and is exposed to the membrane through two symmetry-related lateral windows defined by TMs 8 and 9 and the IM helices.

ON OUR WEBSITE

Read the full article at http://dx.doi.org/10.1126/science.aad8266

CONCLUSION: The structure of STRA6 suggests a mechanism for retinol release from RBP into the hydrophobic environment of the outer cleft and direct diffusion into the membrane through the lateral window. Our work also sets the basis for future experiments aimed at investigating how the system is regulated, whether STRA6 also has a role in signaling, and the functional relevance of its association with CaM. ■

The list of author affiliations is available in the full article online.
*These authors contributed equally to this work.
†Corresponding author. Email: fm123@cumc.columbia.edu
Cite this article as Y. Chen *et al.*, *Science* **353**, aad8266 (2016). DOI: 10.1126/science.aad8266

Downloaded from http://science.sciencemag.org/ on September 3, 2016

RESEARCH ARTICLE

STRUCTURAL BIOLOGY

Structure of the STRA6 receptor for retinol uptake

Yunting Chen,[1]* Oliver B. Clarke,[2]* Jonathan Kim,[1] Sean Stowe,[3] Youn-Kyung Kim,[4] Zahra Assur,[1] Michael Cavalier,[3] Raquel Godoy-Ruiz,[3] Desiree C. von Alpen,[5] Chiara Manzini,[5] William S. Blaner,[6] Joachim Frank,[2] Loredana Quadro,[4] David J. Weber,[3] Lawrence Shapiro,[2] Wayne A. Hendrickson,[1,2] Filippo Mancia[1]†

Vitamin A homeostasis is critical to normal cellular function. Retinol-binding protein (RBP) is the sole specific carrier in the bloodstream for hydrophobic retinol, the main form in which vitamin A is transported. The integral membrane receptor STRA6 mediates cellular uptake of vitamin A by recognizing RBP-retinol to trigger release and internalization of retinol. We present the structure of zebrafish STRA6 determined to 3.9-angstrom resolution by single-particle cryo-electron microscopy. STRA6 has one intramembrane and nine transmembrane helices in an intricate dimeric assembly. Unexpectedly, calmodulin is bound tightly to STRA6 in a noncanonical arrangement. Residues involved with RBP binding map to an archlike structure that covers a deep lipophilic cleft. This cleft is open to the membrane, suggesting a possible mode for internalization of retinol through direct diffusion into the lipid bilayer.

Vitamin A is an essential nutrient for all mammals. In its retinaldehyde (retinal) form, it is vital for vision (*1*); as retinoic acids (RAs), it provides ligands for RAR (retinoic acid receptor) and RXR (retinoid X receptor) nuclear receptor transcription factors (*2*). Consequently, retinoid metabolism affects diverse biological processes (*3*), with disease implications from blindness to cancer (*4*, *5*). Vitamin A deficiency is the third most common nutritional deficiency in the world, affecting millions of children and pregnant women (*6*).

Retinol (vitamin A alcohol) is the predominant circulating retinoid in the fasting state. In the absence of sufficient dietary vitamin A, retinol from liver stores is mobilized bound to retinol-binding protein (RBP, also called RBP4) (*7*), which solubilizes the hydrophobic retinol. In the bloodstream, retinol-RBP forms a complex with the transthyretin tetramer (14 kDa × 4) to prevent renal loss of RBP (21 kDa) (*8*). Once internalized into cells, retinol binds to cellular RBPs (CRBPs, notably CRBP1) (*9*, *10*).

A putative cellular receptor for RBP was identified and biochemically characterized (*11*) and subsequently shown to be required for the transfer of retinol from RBP to CRBP (*12*). In 2007, Kawaguchi *et al.* (*13*) cloned this RBP receptor, which proved to be the previously named protein STRA6 (stimulated by retinoic acid 6) (*14*). STRA6 was predicted to be a 75-kDa multipass transmembrane (TM) protein without sequence similarity to any known transporter, channel, or receptor, and it was later experimentally demonstrated to bear nine TM segments (*15*). STRA6 was shown to catalyze the release of retinol from RBP, where it is tightly bound (*16*), and to facilitate retinol translocation across the membrane and association with CRBP1 (*17*). Conversion of retinol to retinyl esters for storage by enzymes, such as lecithin retinol acyltransferase (LRAT) (*18*), increases the efficiency of this process by increasing the amount of available apo-CRBP1 (*13*). In in vitro experiments, STRA6 was also shown to catalyze the exchange of retinol between holo-RBP and apo-RBP, as well as the efflux of retinol from holo-CRBP1 to apo-RBP (*17*). Noy and colleagues have suggested a distinct and somewhat controversial (*19*, *20*) functional model for STRA6 (*21*), in which the movement of retinol is unidirectional from holo-RBP to CRBP1 and coupled to activation of a JAK-STAT (Janus kinase–signal transducers and activators of transcription) cascade, thus regulating gene expression (*21*, *22*).

STRA6 is expressed with particular abundance in the eye, where it localizes predominantly in the basolateral membrane of the retinal pigment epithelium, and in the female reproductive organs and placenta (*13*, *14*). Mutations in the human *STRA6* gene have been linked to Matthew-Wood syndrome (MWS), which presents with ocular defects ranging from mild microphthalmia to anophthalmia, as well as with an array of other developmental abnormalities including cardiac and pulmonary defects and cognitive deficits (*23*). Consistent with an important role of STRA6 in maintaining vitamin A homoeostasis in the eye, a zebrafish *stra6* gene knockdown model also exhibited severe ocular malformations during development (*24*). *Stra6* knockout mice have a less severe phenotype, exhibiting defects in the visual cycle (*25*, *26*) and impaired insulin signaling (*27*).

To gain insight into the mechanistic basis for STRA6 function, we determined the structure of STRA6 from zebrafish to 3.9 Å resolution by single-particle cryo-electron microscopy (cryo-EM). The protein is a dimer, and each protomer is associated at the cytoplasmic side with a molecule of calmodulin (CaM), which is unexpected given that there are no previous reports of CaM involvement with STRA6. The structure features a large lipophilic cleft on the extracellular side, to which RBP is expected to bind with induction of retinol release. Although additional pathways are possible, a window in the hydrophobic cleft is open to the bilayer, suggesting diffusion as a possible mechanism for translocation of retinol directly into the cell membrane, from which it may be internalized by CRBP1.

Structure determination by single-particle cryo-EM

We screened nine STRA6 orthologs from different species for expression and stability in nonionic detergents as green fluorescent protein (GFP) fusions in transiently transfected human embryonic kidney (HEK) 293 cells. Of these, the protein from zebrafish (75.4 kDa, 670 amino acids) performed best as judged by Western blot and fluorescence size exclusion chromatography (FSEC). We confirmed that recombinant zebrafish STRA6 is active with an HEK293 cell–based retinol uptake assay (*13*), which used recombinant zebrafish RBP in complex with retinol, and with cotransfection with species-matched CRBP1 and LRAT (Fig. 1A). Protein production was scaled up using baculovirus-infected Sf9 insect cells. Purified STRA6 failed to yield diffraction-quality crystals, despite the monodispersity of the sample (fig. S1A) and its thermal stability in detergents (fig. S1B).

SDS–polyacrylamide gel electrophoresis (PAGE) from purified STRA6 preparations always showed the presence of a lower-molecular-weight species (fig. S1C), identified as CaM by N-terminal sequencing, mass spectrometry, and immunoblotting from both mammalian cells, where STRA6 is functional for retinol uptake (Fig. 1, A and B), and insect cells, which were used to produce protein for structure determination (fig. S1D). The sequence of *Spodoptera frugiperda* CaM, the protein copurified from Sf9 cells, is not available; however, *S. littoralis* CaM (UniProt ID E3UJZ) is 98% identical to human and zebrafish CaM, which are 100% identical to one another. Removal of CaM was attempted by application of high concentrations of Ca^{2+} chelators and stringent high-ionic-strength washes of the isolated membrane fraction, but without success, which

[1]Department of Physiology and Cellular Biophysics, Columbia University, New York, NY 10032, USA. [2]Department of Biochemistry and Molecular Biophysics, Columbia University, New York, NY 10032, USA. [3]The Center for Biomolecular Therapeutics and Department of Biochemistry and Molecular Biology, University of Maryland School of Medicine, Baltimore, MD 21201, USA. [4]Department of Food Science and Rutgers Center for Lipid Research, Rutgers University, New Brunswick, NJ 08901, USA. [5]Department of Pharmacology and Physiology and Department of Integrative Systems Biology, George Washington University, Washington, DC 20037, USA. [6]Department of Medicine, Columbia University, New York, NY 10032, USA.
*These authors contributed equally to this work. †Corresponding author. Email: fm123@cumc.columbia.edu

Downloaded from http://science.sciencemag.org/ on September 3, 2016

is consistent with a specific, high-affinity interaction. A molecular weight estimate for the STRA6-CaM complex determined by SEC coupled to light-scattering and refractive index measurements (fig. S1F) indicated that the detergent-solubilized complex contained ~180 kDa of protein and thus was potentially within the tractable molecular weight range of cryo-EM. To this end, the complex was reconstituted in

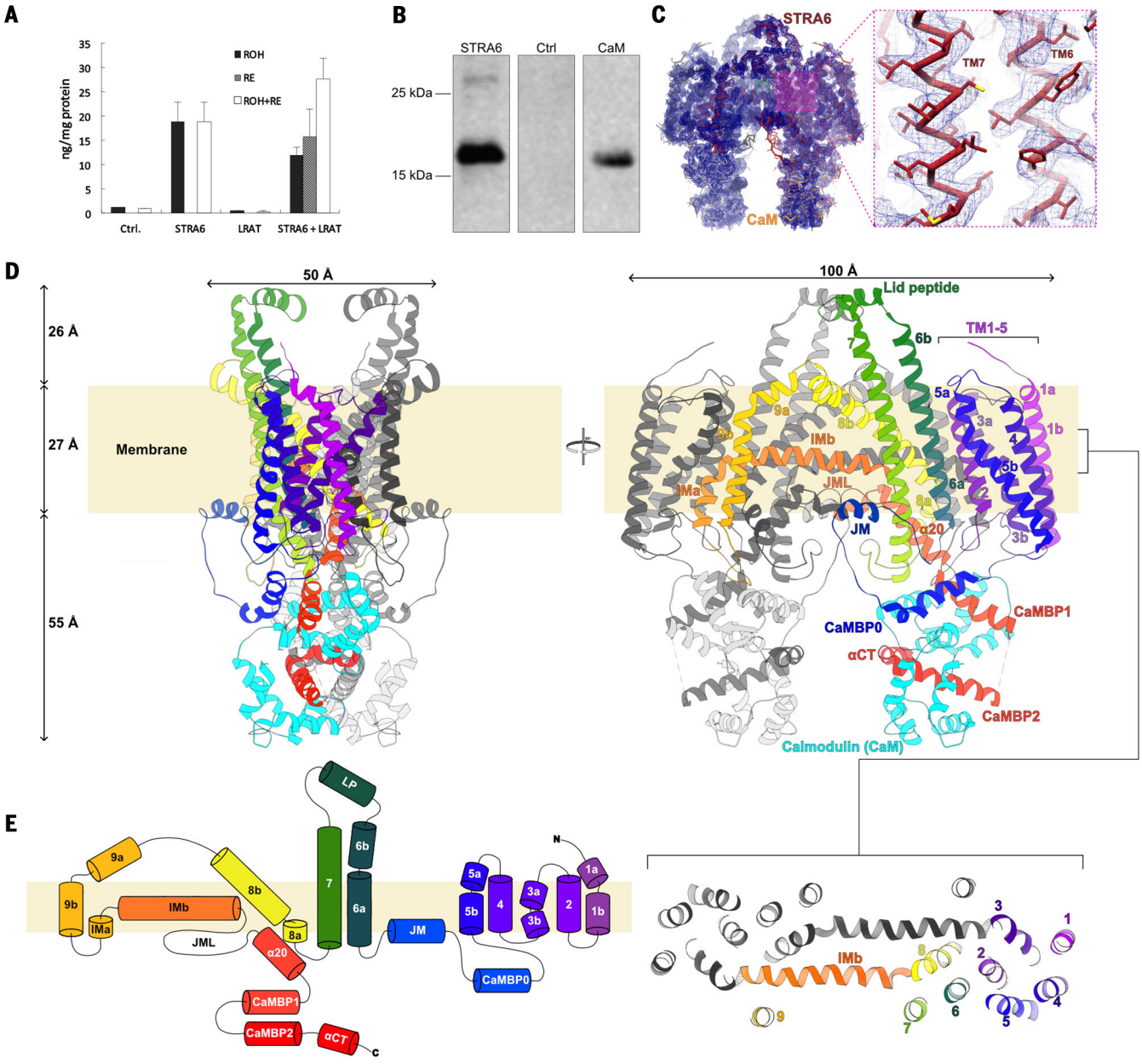

Fig. 1. Function and architecture of zebrafish STRA6 in complex with CaM. (**A**) Recombinant zebrafish STRA6 exhibits retinol uptake activity. The results of a cell-based retinol uptake assay are shown as a bar graph; the assay used HEK293T cells that either were stably expressing CRBP1 (Ctrl) or stably expressing CRBP1 and transiently transfected with expression constructs for STRA6, LRAT, or STRA6 and LRAT. The amount of retinol (black bars), the amount of retinyl esters (gray bars), and total retinoid content (white bars) were determined using high-performance liquid chromatography (HPLC). Error bars represent SEM. (**B**) Zebrafish STRA6 is associated with CaM in a functional context. Shown here is a Western blot probed with an antibody against human CaM on the results from a metal-affinity chromatography–based purification of polyhistidine-tagged zebrafish STRA6, expressed by transient transfection in HEK293T cells. The left lane shows the results of the purification, the middle lane shows purification results for the same cell line transfected with a control plasmid, and the right lane has purified recombinant human CaM loaded as a control. (**C**) A Cα trace of the STRA6-CaM complex is shown in the density map (blue mesh), contoured at 6x the root mean square. STRA6 is colored dark red and CaM is colored yellow. An inset shows the local quality of the density map in the TM6-TM7 region, with side chains in stick representation. (**D**) Structure of the STRA6 dimer in complex with CaM. A ribbon representation of the Cα trace of the STRA6 dimer associated with CaM is shown in orthogonal views from within the plane of the membrane. One STRA6 protomer is shown in spectral coloring from violet (N terminus) to red (C terminus). The associated CaM is in cyan. The approximate location of the membrane, estimated using the PPM server (*70*), is depicted as a cream-colored rectangle behind the proteins. The inset below the right panel depicts the arrangement of TM helices in STRA6 as a slab of the TM region. (**E**) Schematic representation of the connectivity and structural elements of STRA6, shown using the same color scheme as in (D). The start and end residue number of each helical element is marked. CaMBP0, CaMBP1, and CaMBP2 are the three helical segments of STRA6, which interact with CaM.

Downloaded from http://science.sciencemag.org/ on September 3, 2016

amphipol for structure determination by this technique.

Initial inspection of the two-dimensional (2D) class averages from cryo-EM images revealed a distinctly twofold symmetric assembly, with two "legs" protruding from an ellipsoidal TM region enveloped by an amphipol shell (fig. S2). After 3D classification (fig. S3), based on an initial reference volume generated by common-lines methods (*28*), the refinement of a set of 56,615 particles produced a cryo-EM density map with an overall resolution of 3.9 Å (fig. S2D and table S1). Inspection of the map allowed unambiguous determination of the TM topology and the location of the N and C lobes of CaM (Fig. 1C and fig. S4, A and B). The quality of the density (fig. S5) was sufficient to allow us to generate an atomic model for 581 of the 670 STRA6 residues (26 to 630; fig. S6) and 147 of the 151 CaM residues (fig. S7 and movie S1).

Architecture of the STRA6-CaM complex

The structure shows that STRA6 is a dimer and that it is associated with CaM, in agreement with our biochemical data (fig. S1, C to F). STRA6 is folded as an intricately associated symmetric dimer, comprising 18 TM helices (nine per protomer) plus two long horizontal intramembrane (IM) helices that interact at the central dimer interface (Movie 1; Fig. 1, D and E; and fig. S4C). The N terminus of STRA6 is extracellular, leading into the first five TM helices, which form an N-terminal helical bundle domain (NTD; Fig. 1, D and E, and fig. S4D). The NTD is separated from the rest of the molecule by a long intracellular loop that connects TM5 to TM6, which contains the first (CaMBP0) of three cytoplasmic helical segments that associate with CaM, as well as a juxtamembrane (JM) helix (Fig. 1, D and E). Two long TM helices (TM6 and TM7) follow centrally, extending more than 25 Å above the extracellular membrane surface in an archlike extension and connected by a short helix-containing loop (lid peptide) proximal to the twofold axis of dimer symmetry (Fig. 1, D and E).

TM8 spans the membrane at an angle and docks into the dimer-mate protomer in a TM helix–swapped arrangement that involves TM9 (Fig. 1, D and E). In total, 4811 Å^2 of surface area is buried at the dimer interface. Both TM8 and TM9 are kinked sharply after two helical turns. After TM9, the polypeptide chain returns to the body of its own protomer, first through a short vertical IM helix (IMa) and then through a long horizontal one (IMb) (Fig. 1). TM3a of the dimer mate interacts at the IMa-IMb boundary (Fig. 1D and fig. S4C). IMb helices are in antiparallel contact at the dimer interface, approximately at the level of the interface between membrane leaflets (Fig. 1, D and E).

The chain emerges into the cytoplasm after an irregular but well-ordered JM loop (JML) through inclined helix α20, which is intimately associated with the cytoplasmic extensions of TM6 and TM7. Two C-terminal CaM-binding helices (CaMBP1 and CaMBP2) follow, linked by a disordered segment (Fig. 1, D and E). A C-terminal helical extension (αCT) completes the chain after a proline-induced kink (P620). The two CaM molecules, one for each STRA6 protomer, constitute a large portion of the intracellular domain of the STRA6-CaM complex, with each STRA6-CaM interface burying 3124 Å^2. In the dimer, these cytoplasmic regions appear as two "legs" that protrude over 50 Å from the membrane surface into the cytoplasm (Fig. 1, C and D).

In essence, the STRA6-CaM architecture can be separated into three distinct regions (fig. S5): (i) the NTD plus the linker containing CaMBP0 and the JM helix; (ii) the central domain (CD), consisting of TMs 6 to 9, the IM, and α20; and (iii) the C-terminal tail, containing CaMBP1 and CaMBP2 and the associated CaM molecule.

STRA6-CaM interaction

CaM binds to the cytoplasmic side of STRA6 in an unconventional arrangement (Fig. 2A and

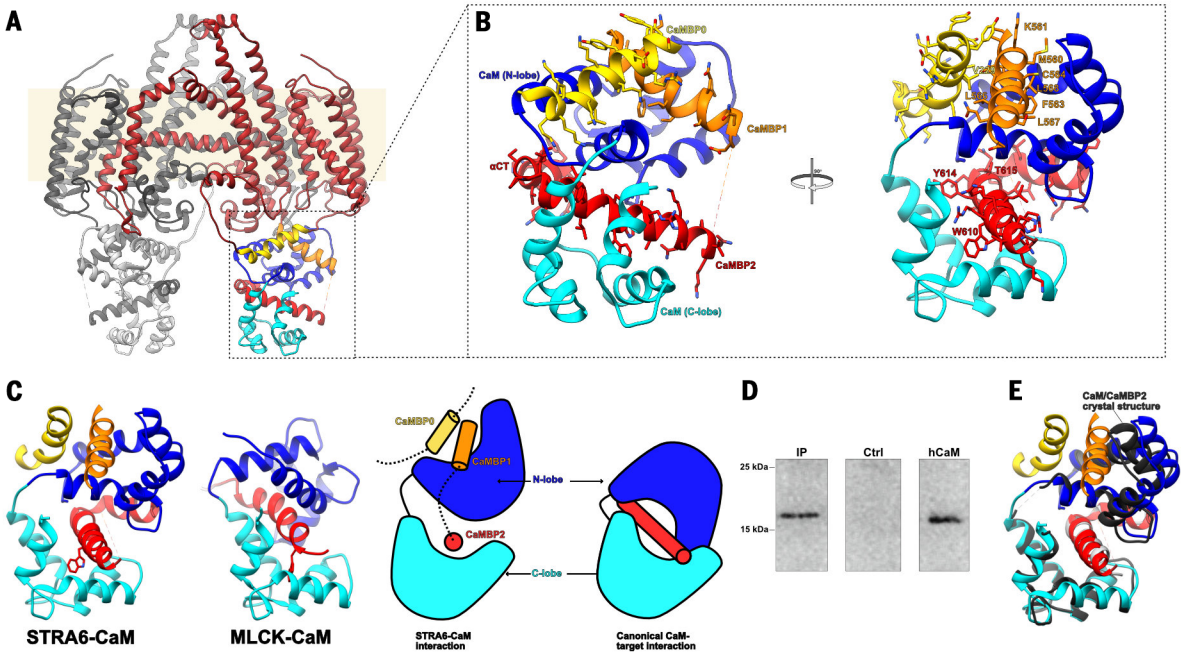

Fig. 2. The interactions between STRA6 and CaM. (**A**) View of the STRA6-CaM complex, shown as a Cα trace in ribbon representation, with STRA6 in dark red except for CaMBP0 (yellow), CaMBP1 (orange), and CaMBP2 (red). The N and C lobes of CaM are shown in dark blue and cyan, respectively. (**B**) A close-up view of the main interactions between STRA6 and CaM, represented and colored as in (A). All STRA6-CaM–interacting residues are depicted in stick representation and labeled. (**C**) Comparison between STRA6-CaM and MLCK-CaM (canonical) binding modes in ribbon representation (left) and as a schematic (right), using the same color scheme as in (A). (**D**) Endogenous zebrafish CaM can be immunoprecipitated using an antibody against zebrafish STRA6. Shown here is an immunoblot probed for CaM. The left lane shows immunoprecipitation from zebrafish tissue performed using the antibody against STRA6, the middle lane shows immunoprecipitation from zebrafish tissue performed using an antibody against an unrelated protein, and the right lane shows recombinant human CaM (10 ng). (**E**) Superposition of the structures of the Ca^{2+}–hCaM-CaMBP2 complex (black and gray) determined by x-ray crystallography, with the equivalent region from the STRA6-CaM complex, depicted as in (B). The side chains of CaMBP2 are depicted in stick representation. Single-letter abbreviations for the amino acid residues are as follows: A, Ala; C, Cys; D, Asp; E, Glu; F, Phe; G, Gly; H, His; I, Ile; K, Lys; L, Leu; M, Met; N, Asn; P, Pro; Q, Gln; R, Arg; S, Ser; T, Thr; V, Val; W, Trp; and Y, Tyr.

Downloaded from http://science.sciencemag.org/ on September 3, 2016

fig. S9). Overall, the intracellular region of each STRA6 protomer folds as a compact assembly in which CaM is intimately associated with three distinct STRA6 segments (Fig. 2B). The CaM structure that we observed suggests, on the basis of lobe-specific comparisons with previously solved structures of Ca^{2+}-CaM and apo-CaM (fig. S9), that Ca^{2+} is bound. Ca^{2+} binding to CaM results in conformational changes that expose two hydrophobic binding surfaces, one in the N lobe and the other in the C lobe (*29*). Typically, these wrap around a single amphipathic helix (Fig. 2C), although noncanonical CaM complexes have been reported (*30*). In STRA6, the CaMBP1 helix, which is part of the C-terminal extension, binds exclusively to the main hydrophobic cleft in the N lobe of CaM (Fig. 2, B and C; fig. S10; and movie S2). CaMBP0, which is part of the long TM5-TM6 loop, binds to the N lobe as well, at a surface position between CaM helices 1 and 4, and it interacts additionally with CaMBP1 in a helix-helix crossing mode (Fig. 2, B and C; fig. S10; and movie S2). CaMBP2 interacts with the hydrophobic groove of the CaM C lobe in a manner similar to the canonical 1-5 interaction of the myosin light-chain kinase (MLCK) peptide with the C lobe of CaM (*31*) (Fig. 2C and fig. S9B), and it links the two lobes of CaM together through interactions with the polar outer face of the CaM N lobe (Fig. 2, B and C; fig. S10; and movie S2).

To verify that the STRA6-CaM complex is formed under physiological conditions, we performed STRA6 immunoprecipitation experiments on zebrafish tissue by using a monoclonal antibody directed against recombinant zebrafish STRA6 (Fig. 2D and fig. S1E). Furthermore, we performed isothermal titration calorimetry experiments with synthetic CaMBP peptides and recombinant human CaM, which showed that the three main peptides are capable of binding to CaM in solution, with affinities ranging from low micromolar (CaMBP0) to subnanomolar (CaMBP2) (Table 1 and fig. S12). Lastly, to visualize the molecular details of the interaction, we determined the 1.7 Å crystal structure of human Ca^{2+}-loaded CaM in complex with a synthetic CaMBP2 peptide (table S2 and fig. S11). This structure is very similar to that of CaM as observed in the cryo-EM (Fig. 2E), confirming the sequence assignment in this region of the STRA6-CaM cryo-EM structure and providing additional high-resolution structural information for this part of the STRA6-CaM interface (fig. S11). The adoption of a noncanonical arrangement of CaM in the complex with CaMBP2 demonstrates that this segment alone is sufficient to specify the noncanonical conformation of CaM.

The cryo-EM analysis shows the STRA6-CaM complex to be rigid; no conformations differing substantially in the STRA6-CaM arrangement are identifiable by maximum-likelihood 3D classification of the data set (fig. S3). All STRA6 residues interacting with CaM, as well as residues forming the CaMBP1/CaMBP0 interface, are conserved across all species (fig. S7 and movie S2). The disordered CaMBP1-CaMBP2 linker is conserved in sequence for its central and acidic motif, EEGIQLV in zebrafish STRA6, with the Glu-Gly segment invariant across STRA6 orthologs (shown in bold in fig. S7). Lastly, two human STRA6 polymorphisms in CaMBP2, R655C and T644M (equivalent to R626 and T615 in zebrafish, respectively), are strongly associated with MWS (table S3) (*32*).

Surface features of the STRA6 dimer

The archlike TM6–lid peptide–TM7 extensions, together with outer portions of the TM8 and TM9 helices, define the sides of a large extracellular cleft (19,174 $Å^3$ in volume; Materials and methods), which we refer to as the outer cleft. This cleft is shaped like an arrowhead, and it extends from a "floor" of dyad-related IM helices at the mid-bilayer level to just under a "ceiling" of lid peptides ~25 Å above the membrane surface (Fig. 3A). The outer cleft is bounded along the short edges by the NTD, which protrudes only slightly above the membrane, defining large openings to the extracellular space at either side of the lid peptides. Toward the base of the outer cleft, TM8, TM9, and the IM helix define a triangular "lateral window" that is open to the lipid bilayer (Fig. 3B). Many of the residues lining the cleft are conserved (fig. S13A) and hydrophobic (Fig. 3, C and D). There is a clear shell of density corresponding to the polar part of the amphipol belt surrounding the TM region (Fig. 3C), as has been observed in other cryo-EM structures of membrane proteins (*33*, *34*). Specific to STRA6, however, a similar shell of density is also located at surfaces bounding the outer cleft (Fig. 3C),

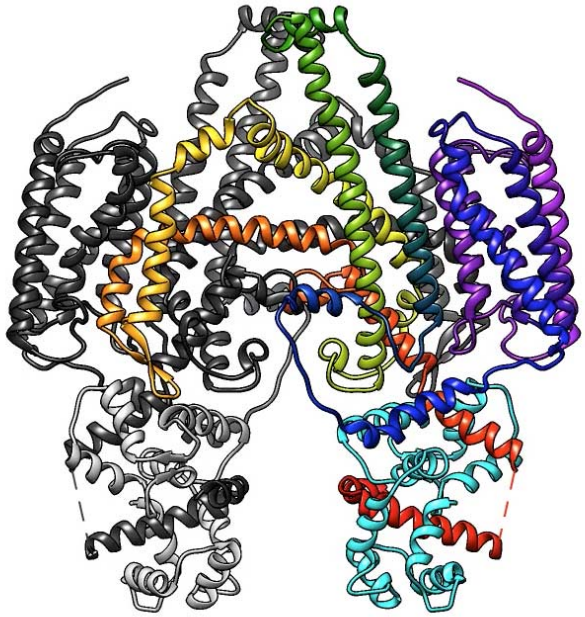

Movie 1. Architecture of STRA6 in complex with CaM. A ribbon representation of the Cα trace of the STRA6 dimer associated with CaM is shown from within the plane of the membrane, rotating about the dyad axis. One STRA6 protomer is shown in spectral coloring from violet (N terminus) to red (C terminus). The associated CaM is in cyan. The other protomers are shown in black and gray.

Table 1. Isothermal titration calorimetry analysis of the association of CaM with STRA6 peptides. *H*, enthalpy; *S*, entropy; *T*, absolute temperature (kelvin); *G*, Gibbs free energy; K_D, dissociation constant.

Peptide (site)	*N* (sites)	Δ*H* (kcal/mol)	*T*Δ*S* (kcal/mol)	Δ*G* (kcal/mol)	K_D (nM)
CaMBP0*	1.01 ± 0.07	−7.8 ± 0.8	0.02 ± 0.1	−7.8 ± 0.7	$2.56 \times 10^3 \pm 722$
CaMBP1*	0.99 ± 0.02	−7.3 ± 0.1	0.10 ± 0.02	−7.4 ± 0.1	$1.68 \times 10^3 \pm 140$
CaMBP2*	0.90 ± 0.02	−13.9 ± 0.2	−0.11 ± 0.03	−13.7 ± 0.1	0.9 ± 0.3
CaMBP1.2† (high)	0.88 ± 0.02	−39.4 ± 1.6	−3.34 ± 0.2	−36.1 ± 1.4	9.5 ± 1.2
CaMBP1.2† (low)	0.98 ± 0.09	−7.6 ± 1.0	0.06 ± 0.1	−7.6 ± 1.0	$1.93 \times 10^3 \pm 281$

*The STRA6 peptides were designed on the basis of the STRA6-CaM complex structure and are defined as follows: CaMBP0, residues 222 to 237; CaMBP1, residues 554 to 571; and CaMBP2, residues 600 to 626. Experiments were performed at 37°C in 20 mM HEPES (pH 7.4), 50 mM NaCl, 5 mM $MgCl_2$, and 0.5 mM TCEP, using 30 injections at 10 μl per injection. †This thermogram was fit using a two-site model (termed "high" and "low," referring to affinity) because of the endothermic region of the thermogram that was observed as the system approached saturation.

Downloaded from http://science.sciencemag.org/ on September 3, 2016

suggesting that the hydrophobic alkyl tails of the amphipol occupy the hydrophobic cleft of the purified protein, and that consequently this cleft would be lipid-filled in a native context.

Also on the extracellular side, but on the periphery of STRA6, a deep outer pocket (782 Å^3 in volume) is formed within the NTD (Fig. 3A). It is somewhat polar in nature (Fig. 3, C and D) and lined by two histidine residues (H41 and H160) along TM1 and TM4 and two tyrosine residues (Y130 and Y131) along TM3, all of which are conserved (fig. S13, B and C). A smaller pocket on the intracellular side of the NTD (Fig. 3A) is lined by histidine (H145 and H86) and tyrosine (Y150 and Y200) residues, although these are less conserved (fig. S13, B and D).

Molecular details of the outer cleft and pockets

The outer cleft is separated from the cytosol by a two-layer structure at the level of the cytoplasmic leaflet of the membrane (Figs. 3A and 4A). The top layer, corresponding to the floor of the outer cleft, is formed by the antiparallel dyad-related IM helices (Figs. 3A and 4A). The bottom layer is formed by the two JMLs, which interact symmetrically with one another and each with the IM helices of the apposed protomers (Figs. 3A and 4A). The two layers are connected by interactions between conserved residues R511 in the IM helix and D539 in the JML. Disruption of this salt bridge by mutation of an equivalent residue in human STRA6 (D560H) results in MWS (*35*).

The two IM helices form mostly hydrophobic contacts, except for a conserved asparagine (N519) and threonine (T515) pair, arranged around the twofold axis (Fig. 4A). The density maps show two lipid-like densities extending into the outer cleft from these polar residues (Fig. 4 and fig. S5). These densities are unlikely to correspond to retinol, given that no retinol was detectable in

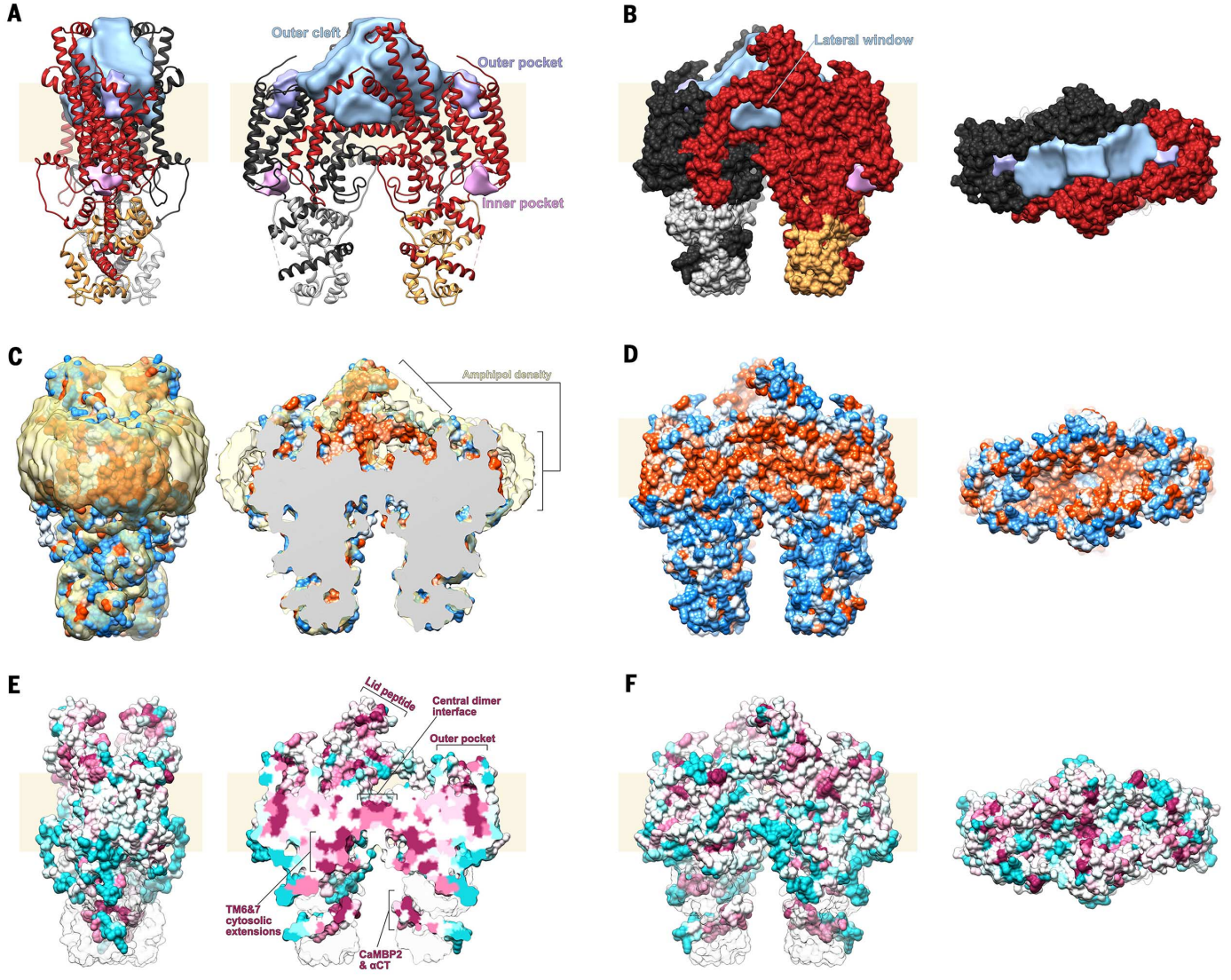

Fig. 3. Surface features of STRA6. (**A**) Ribbon representation of the STRA6-CaM complex in two orthogonal views along the plane of the membrane, with one STRA6 protomer shown in dark red and one CaM in gold; the other protomers are shown in black and gray. Surface features are labeled and shown in light blue (outer cleft), purple (outer pocket), and pink (inner pocket). Volumes were calculated using the Voss Volume Voxelator server (*63*) with an outer probe radius of 10 Å and an inner probe radius of 3 Å. (**B**) Spacefill representation of the STRA6-CaM complex in two views along (left) and from above (right) the plane of the membrane, colored as in (A). (**C**) Spacefill representation of the STRA6-CaM complex shown as in (A), colored by hydrophobicity according to the Kyte-Doolittle scale (*71*), ranging from blue (−4.5, most polar) to white (0.0) to orange (4.5, most hydrophobic). The amphipol layer surrounding the molecule is shown in yellow. The image on the right is a slice from the middle of the outer cleft. (**D**) Spacefill representation of the STRA6-CaM complex shown as in (B), colored by hydrophobicity as in (C). (**E**) Spacefill representation of the STRA6-CaM complex shown as in (C), colored by conservation from cyan (least conserved) to maroon (most conserved). (**F**) Spacefill representation of the STRA6-CaM complex shown as in (B) and (D) and colored as in (E).

Downloaded from http://science.sciencemag.org/ on September 3, 2016

the purified complex by spectroscopy. Although not conclusive, the shape of the density is consistent with cholesterol (Fig. 4), with each sterol oriented so that its hydroxyl group interacts with the N519-T515 pair. The two-layer structure is closed, and thus conformational changes effecting the separation of the symmetrically related IM helices and JMLs would be required to permit retinol transfer along this route. However, there is no obvious barrier to retinol diffusion from the outer cleft into the lipid bilayer via the lateral window (Figs. 3B and 4A).

Discussion

The unanticipated constitutive association of CaM with STRA6 occurs in vivo, as demonstrated by immunoprecipitation experiments performed at physiological concentrations (Fig. 2D and fig. S1E). CaM is a binding partner and functional regulator for diverse membrane protein families including ion channels, transporters, and enzymes (*30*). CaM adopts an unusual conformation in which it binds to three STRA6 helical segments (Fig. 2). There is one instance of an EF hand–containing protein with similarly disposed domains, namely, the activation domains of apicomplexan Ca^{2+}-activated, Ca^{2+}-dependent protein kinases (*36*) (fig. S9A). A comparable arrangement has not been observed for CaM itself, although distinct noncanonical CaM-target complexes have been characterized, such as, for example, the structure of the complex of CaM with the anthrax edema factor toxin (*37*). We determined the 1.7 Å–resolution crystal structure of Ca^{2+}-CaM in complex with CaMBP2 (Fig. 2E and fig. S11), the STRA6 peptide with the highest affinity (0.9 nM). Notably, CaMBP2 alone induces the same noncanonical conformation of Ca^{2+}-CaM as observed in the cryo-EM structure of STRA6-CaM. The seeming obligate nature of the CaM-STRA6 interaction explains previous observations that the C-terminal tail of the receptor is structurally and functionally indispensable (*15*). Several MWS mutations are located in this region (table S3), and random mutagenesis of STRA6 identified multiple mutations in the C-terminal tail that eliminate surface expression and prevent correct folding of the receptor (*38*). The role of CaM—and its regulation by Ca^{2+}—is enigmatic because no direct link between Ca^{2+} and retinol transport has been identified. Nevertheless, this interaction is conserved and structurally essential.

The CaM-interacting regions, as well as several other structural elements of STRA6, are conserved in RBPR2, a STRA6-like protein expressed primarily in the liver and intestine (*39*) (fig. S14), suggesting a similar architecture with potential functional differences in these specialized retinol storage and uptake tissues. In humans, the NTD of RBPR2 is expressed as a separate polypeptide (*39*), supporting our assignment of the NTD as a separable domain (fig. S5). More distantly related lipocalin receptors such as LMBR1 also have nine predicted TM helices and have been suggested to form dimers (*40*), and consequently we anticipate they may adopt a STRA6-like fold.

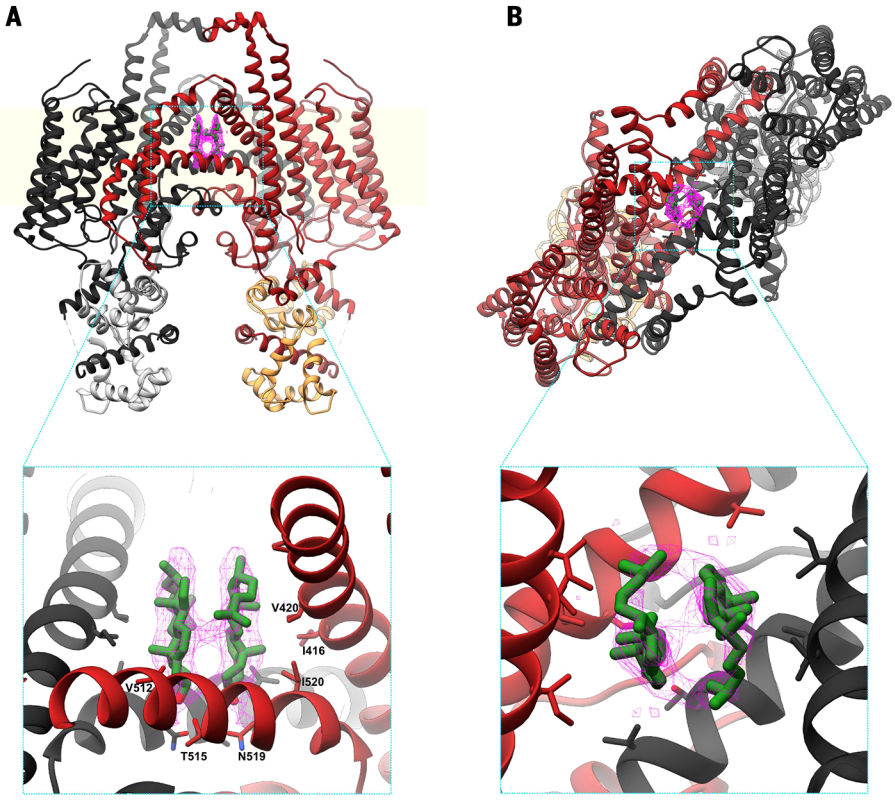

Fig. 4. Putative cholesterol binding sites in the STRA6 outer cleft. (**A**) Ribbon representation of the STRA6-CaM complex, shown along the plane of the membrane and colored as in Fig. 3A. Putative cholesterol molecules are shown in green, with the corresponding density in pink, as a mesh. (**B**) View from above the plane of the membrane, shown and colored as in (A). The two insets show molecular details of the interactions between the putative cholesterols and residues in the STRA6 outer cleft; key interacting residues are labeled.

The most notable feature of STRA6 is the large extracellular-facing hydrophobic cleft, which spans from the mid-bilayer to the lid peptides at the apex of the TM6–lid peptide–TM7 arch, 25 Å above the membrane surface (Fig. 3A). Human STRA6 residues that were implicated previously in RBP interactions (314 to 320, zebrafish numbering) by functional mutagenesis studies (*38*) all map to the lid peptide (Fig. 5A), thus putting constraints on the position of RBP in its interaction with STRA6. Furthermore, insertion of a Myc tag at the apex of the TM8-TM9 loop has been shown to impair RBP binding while not affecting surface expression of STRA6 (*15*). Mutants that disrupt a predicted C31-C171 disulfide bond within the NTD also show reduced RBP binding (*15*). The regions with impaired RBP binding, together with prior work on RBP itself that showed dependence on its CD loop for interaction with the lid peptide (*11*, *41*, *42*), allow us to place constraints on the location of the RBP-binding site (Fig. 5A). On the basis of this orientation and the hydrophobic nature of both retinol and the STRA6 outer cleft, it is reasonable to postulate that RBP binding to the lid peptide weakens RBP affinity for retinol, leading to deposition of retinol in the STRA6 outer cleft. It remains to be determined whether the catalysis of retinol release is primarily due to induced structural changes in the retinol exit pathway of RBP or to the enforced proximity of the retinol to the surface of the lipid bilayer.

The outer cleft is hydrophobic, it extends down about halfway through the bilayer, and it is exposed to the membrane via the lateral window (Fig. 3B). Furthermore, the outer cleft is covered by a shell of density, presumably from the polar backbone of the amphipol (Fig. 3C). These observations suggest that the outer cleft is occupied in vivo by bulk lipid rather than aqueous solvent. Such an environment could provide a low-energy pathway for retinol to partition into the lipid bilayer. The lipid composition within the outer cleft remains to be determined; however, broadly speaking, we envision two likely possibilities. In one, the content of the outer cleft could be similar to that of the surrounding membrane, namely, a distorted monolayer of phospholipids (Fig. 5B). Alternatively, it could be enriched in specific components such as cholesterol, perhaps similar to what is observed in lipid rafts (*43*).

Consistent with the above, we observed several distinct densities within this cleft, two of which we have tentatively assigned as cholesterol (Fig. 4). These could either originate from the expression host or represent hydrolysis products of the cholesteryl hemisuccinate used to

Downloaded from http://science.sciencemag.org/ on September 3, 2016

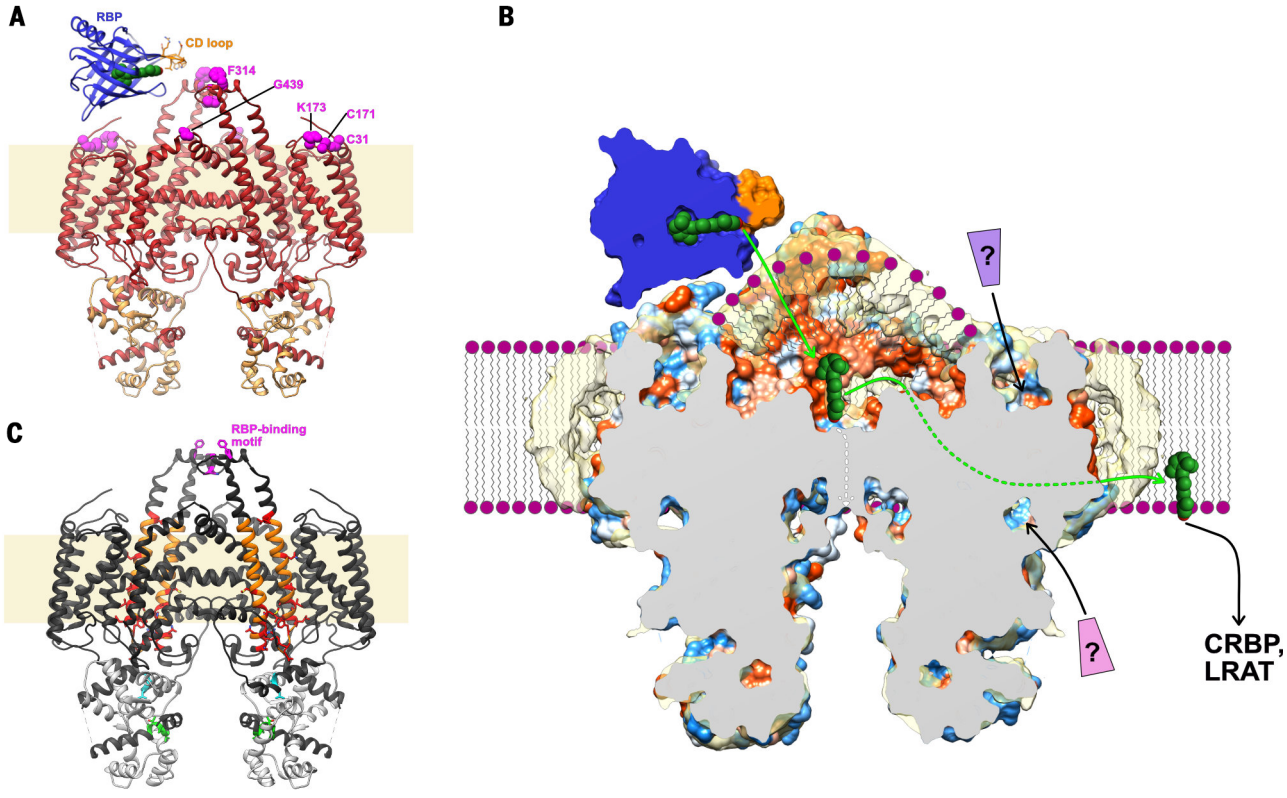

Fig. 5. Possible mechanism for STRA6-mediated retinol uptake. (**A**) Ribbon representation of the STRA6-CaM complex, viewed from the plane of the membrane, with STRA6 colored in red and CaM in gold. Residues previously shown to be important for RBP binding are shown as magenta spheres. Green spheres, retinol. (**B**) Schematic of STRA6-mediated retinol release from RBP into the outer cleft and translocation to the lipid bilayer (shown as purple spheres and wavy lines) through the lateral window. Question marks indicate putative ligands binding to the NTD; green and white arrows show two potential retinol exit pathways, via the lateral window and the central dimer interface, respectively; and coloring of the STRA6 surface is as in Fig. 3C (by hydrophobicity). (**C**) Previous work mapped onto the STRA6 structure, shown as follows: the RBP-binding motif in the lid peptide in magenta (*38*); the region probed by acute chemical modification of single cysteine point mutants (*48*) in orange, and residues in this region, modification of which severely affects retinol uptake from RBP, in red; the putative CRBP1 interacting motif (*45*), located in CaMBP0, in cyan; and the putative STAT5 binding motif (*22*), located in CaMBP2, in green.

stabilize the protein during purification (fig. S1B). The two putative cholesterol molecules are bound by their hydroxyl groups to the conserved T515-N519 site at the floor of the outer cleft. The fact that retinol, like cholesterol, is also hydrophobic with an apical hydroxyl group raises the possibility that the observed positions of the putative cholesterol molecules may also represent binding sites for retinol.

As noted in the previous section, the outer cleft is separated from the cytosol by a two-layer protein barrier at the level of the cytoplasmic leaflet of the membrane (Figs. 3 and 4). Because there is no evidence of a pore through which retinol could translocate via this central structure, a conformational change would be required. However, the structure suggests an alternative passageway for retinol by direct diffusion into the membrane through the lateral window (Fig. 5C). This hypothesis is consistent with the observation of (i) CRBP- and LRAT-independent STRA6-mediated retinol uptake from holo-RBP, (ii) STRA6-independent uptake of retinol from the membrane by CRBP1, and (iii) CRABP- and STRA6-dependent internalization of RA from a RA-RBP complex (*44*). Furthermore, retinol in the plasma membrane inhibits STRA6-dependent uptake of retinol from holo-RBP (*17*), raising the possibility of a mechanism of exchange between membrane- and RBP-bound retinol. The lateral window could provide a key element for such a mechanism.

The evidence for direct association of CRBP with STRA6 is ambiguous (*19*, *45*). Residues I232 and L233, which have been implicated in CRBP-binding (*45*), are located in our structure within CaMBP0, where they interact directly with CaM (Fig. 5C). Although the proposed mechanism of retinol uptake through the lateral window does not require direct binding of CRBP1 to STRA6, it does not preclude this interaction, which could also play a regulatory role. The STRA6 structure also suggests likely sites of interaction with other cytoplasmic partners. CaMBP1 and CaMBP2 are connected by a linker, that is disordered in the structure and that contains a conserved sequence motif (EEGIQLV; fig. S7) similar to the box2 motif of cytokine receptors, which is known to mediate recruitment of JAK family members through their FERM and SH2 domains (*46*, *47*). Furthermore, two residues (Y614 and T615) that have been implicated in JAK-dependent regulation of STRA6 (*45*, *48*) are located on CaMBP2 (Fig. 5D). These two residues are not solvent-accessible in our current structure, implying that a conformational change of either CaM or STRA6 would be required for their modification.

A previous study involving scanning cysteine mutagenesis of TM6 and TM7 identified a number of modifications that severely inhibited retinol uptake (*48*). Our structure shows that these residues are clustered near the cytoplasmic ends of these helices and that most are buried (Fig. 5D), precluding direct involvement in retinol translocation absent a substantial conformational change.

The N-terminal TM1-TM5 bundle may represent a regulatory module, which could potentially act as a sensor for an unidentified ligand. The NTD contains conserved polar pockets on both sides of the membrane (Fig. 3A and fig. S13), which could constitute ligand-binding sites. Free retinoids are known to stimulate RBP-dependent, STRA6-mediated retinol uptake activity (*49*), making them plausible candidates for such a role. Interestingly, TM3 packs against the IMa helix of the adjacent protomer. Because IMa is contiguous with the IMb helix that lines the outer cavity floor, it is conceivable that a ligand-induced change in NTD conformation could affect the efficiency of STRA6-mediated retinol release from holo-RBP and/or translocation.

Downloaded from http://science.sciencemag.org/ on September 3, 2016

Overall, the structure of STRA6 presented here is consistent with a model of retinol release from RBP into the lipid-filled outer cleft and its direct transfer into the membrane by diffusion through the lateral window (Fig. 5C). The release and transfer of ligands into specialized lipidic environments could represent a general mechanism for protein-mediated uptake of hydrophobic molecules.

Materials and methods

Expression constructs and small-scale expression screening

Nine STRA6 orthologs (human, mouse, chicken, zebrafish, dog, horse, bovine, rat, pig) were cloned into pFM1.2 (*50*) with a GFP and decahistidine tag engineered to express as a fusion at either and both the N- or C- terminus of the proteins. The constructs were transiently transfected into adherent HEK293T cells using lipofectamine (Invitrogen). The transfected cells were harvested after incubation for 72 hours at 37°C. The harvested cell pellets were lysed and solubilized for 1 hour on ice in a buffer containing n-dodecyl-β-D-maltopyranoside (βDDM). Samples were ultracentrifuged to remove debris, protein concentration determined by Bradford assay (BioRad) (*51*), and 20 µl of supernatant was loaded on a SDS-PAGE for Western blot, which was then probed with anti-GFP antibody (Invitrogen) and detected using Western Blot Luminol reagent (Santa Cruz). The expression levels and stability of the constructs were further assayed by FSEC. 10 ml of Freestyle 293-F cell culture (Invitrogen) was transiently transfected with each construct at a density of 1×10^6 cells per ml using polyethyleneimine (PEI) (Polysciences), grown in shaker flasks for 72 hours at 37°C and harvested by centrifugation. Cell pellets were treated following the same protocol as described above, and the supernatant was injected onto a Superdex 200 Increase 10/300 GL (GE Healthcare Life Sciences) SEC column connected to a Prominence UFLC system (Shimadzu) fitted with an RF-10AXL fluorescence detector (Shimadzu).

Large-scale protein expression and membrane preparation

STRA6 from zebrafish (*Danio rerio*) was cloned into pIEX/Bac-1 plasmid modified to include a C-terminal decahistidine tag and thrombin cleavage site and transfected together with baculovirus bacmid DNA (Sapphire Baculovirus DNA and Transfection kit, Allele Biotech) into *Spodoptera frugiperda* Sf9 cells for generation of recombinant baculovirus. The recombinant virus was amplified to high titer following standard procedures. Sf9 cells were infected at a density of 2×10^6 cells per ml with high titer virus at an approximate multiplicity of infection (MOI) of 1, grown in shaker flasks for 72 hours at 27°C and harvested by centrifugation. Cell pellets were resuspended in low salt buffer consisting of 10 mM HEPES pH 7.5, 10 mM KCl, 10 mM $MgCl_2$, 0.5 mM PMSF, EDTA-free complete protease inhibitor cocktail (Roche), DNase, and RNase and lysed by gentle homogenization in a glass homogenizer. Membrane fractions were isolated by ultracentrifugation, resuspended by homogenization and washed a minimum of two times, until the supernatant following ultracentrifugation was clear, in high salt buffer (10 mM HEPES pH 7.5, 10 mM KCl, 1 M NaCl, 10 mM $MgCl_2$, 0.5 mM PMSF, EDTA-free complete protease inhibitor tablet DNase, RNase). Extensively washed membranes were then resuspended again by homogenization in buffer containing 30 mM HEPES, pH 7.5, 200 mM NaCl, 0.5 mM PMSF, protease inhibitor cocktail III (Millipore) and stored at −80°C until use.

Protein purification

The membrane fraction was thawed on ice and solubilized by the addition of detergent—lauryl maltose neopentyl glycol (LMNG) or βDDM with or without cholesteryl hemisuccinate (CHS) in a 10 to 1 ratio—to a final concentration of 1% (w/v) detergent and 2 mg/ml protein, and gently agitated for 1.5 hours at 4°C. Insoluble matter was removed by ultracentrifugation, the supernatant was transferred to fresh tubes and imidazole added to a final concentration of 40 mM. The sample was then added to pre-equilibrated Ni^{2+}-NTA resin (Qiagen) and the mixture allowed to gently rotate overnight at 4°C. After transferring the mixture to a column, the resin was washed with 10 column volumes of buffer containing 60 mM imidazole, and the protein was eluted with buffer containing 200 mM imidazole. The eluted protein was loaded on a Superdex 200 Increase 10/300 GL SEC column (GE Healthcare Life Sciences) pre-equilibrated with buffer containing 20 mM HEPES pH 7.0, 150 mM NaCl, and detergent (LMNG or βDDM) at twice the critical micellar concentration (CMC). Typically, final yields ranged from 0.7 to 1mg purified protein per liter of Sf9 cells.

Light-scattering and refractive index measurements

Recombinant STRA6 was purified by metal affinity chromatography in buffer containing 20 mM HEPES, pH 7.0, 200 mM NaCl, 0.025% (w/v) βDDM, 0.0025% (w/v) CHS and subjected to SEC coupled to UV, dynamic light-scattering, and refractive index detectors to determine its molecular weight (*52*). SEC was performed on a FPLC (SEC-MALS) system attached to a DAWN HELEOS Multi Angle Light Scattering (MALS) detector (Wyatt technology). Light-scattering data were collected for multiple scans, and molecular masses and relative contributions to size were determined using ASTRA software (Wyatt technology).

Thermostability of STRA6 in detergent

STRA6 was extracted from purified membranes by addition of βDDM or LMNG with or without CHS. After an initial purification step by metal affinity chromatography, each sample was injected on a small-scale analytical SEC column (Superdex 200 5/150GL, GE Life Sciences) to determine conditions that yielded a sharp monodisperse peak. These optimized conditions were subsequently used for a thermostability assay (*53*). Partially purified protein was desalted using a PD miditrap G-25 column (GE Healthcare) and separate aliquots heated for 10 min over a range of temperatures from 25° to 70°C. After centrifugation to remove aggregated or precipitated protein, the supernatant was injected on an analytical SEC column in buffer containing 20 mM HEPES pH 7.0, 150 mM NaCl, and detergent with or without CHS. Thermal denaturation curves were constructed by measuring the height of the SEC peak measured from samples at each of the different temperatures (fig. S1D). The height of the SEC peak for sample maintained at 4°C was used as control for normalization. The thermal denaturation curves were fitted with a Boltzmann sigmoidal equation using SigmaPlot (SYSTAT Software).

Protein preparation for cryo-EM

STRA6 was purified in buffer containing LMNG and CHS in a 10:1 ratio (w/w). After elution from Ni^{2+}-NTA resin, the protein was desalted and reconstituted into amphipol A8-35 (Anatrace) at a ratio of 1:3 by weight. The mixture was incubated for 4 to 5 hours with gentle agitation at 4°C and the detergent was removed by the addition of Bio-Beads (Bio-Rad) and overnight incubation at 4°C. The reconstituted protein was then loaded on a Superdex 200 Increase 10/300 GL SEC column (GE Healthcare Life Sciences) equilibrated in buffer without detergent, to remove free amphipol and residual detergent. The eluted protein from the peak fractions (at ~0.6 mg/ml) was used without further concentration for cryo-electron microscopy as described below.

Zebrafish immunoprecipitations

Zebrafish heads (3 days post fertilization) were resuspended in lysis buffer consisting of 10 mM HEPES pH 7.5, 10 mM KCl, 10 mM MgCl2, 0.5 mM PMSF, EDTA-free complete protease inhibitor cocktail (Roche) and triturated using a syringe attached with a 25 gauge needle. Membranes were isolated by ultracentrifugation and solubilized at 1.5 mg/ml protein concentration in βDDM for 2 hours, and the insoluble material was cleared by ultracentrifugation. For each point, a volume corresponding to ~500 mg of solubilized protein was diluted to a final volume of 1 ml with 100 µl of supernatant from a hybridoma culture, 10 µl of a 50:50 pre-equilibrated mixture of protein A–coupled and protein G–coupled Sepharose resin (GE healthcare), and buffer containing 0.1% βDDM. Assays were incubated overnight at 4°C under gentle rotation, washed three times with 1 ml of 20 mM HEPES pH 7.5, 150 mM NaCl, 0.1% βDDM, and eluted with 50 µl of 100 mM glycine pH 2.5, 0.1% βDDM. 45 µl of the sample was recovered and the pH neutralized by transferring to a fresh tube containing 5 µl of 1.5 M Tris-HCl pH 8.8.

Grid preparation and data collection

3 µl of the central fraction of the peak (0.68 mg/ml) was applied to the surface of a holey gold grid, prepared in-house from Quantifoil R1.3 carbon

Downloaded from http://science.sciencemag.org/ on September 3, 2016

grids according to the procedure described by Russo and colleagues (*54*). The grid was blotted on both sides using Whatman ashless filter paper for 3.5 to 4 s at a blot force of 3 in a Vitrobot Mark IV (FEI) at 100% humidity and 4°C, then plunged in cooled liquid ethane after a wait time of 30 s. 2599 micrographs were collected, as dose fractionated stacks (71 frames with a total nominal dose of 100 $e^-/Å^2$) on a F30 Polara microscope (FEI) operated in electron counting mode, at a nominal magnification of 31000×, with a calibrated pixel size of 1.255 Å at the specimen plane. A single stack was collected from each hole (fig. S2G). Pixel size was calibrated by measuring real space correlation of a known crystal structure [Protein Data Bank (PDB) ID 2XOA; N-terminal 3 domains of RyR1] to maps calculated with a range of voxel sizes for a ryanodine receptor (RyR1) data set collected on the same microscope at the same nominal magnification. After gain correction, frame alignment and dose correction were performed in UNBLUR (*55*), and CTF estimation in CTFFIND4 (*56*) (fig. S2F). 2196 micrographs remained after screening based on visual inspection of the aligned averages and power spectra. 3000 particles were picked manually in RELION 1.3, extracted and subjected to 2D classification. Six classes representative of the most common views of the molecule were used (with application of a 30 Å lowpass filter) to generate templates for autopicking as implemented in relion_autopick (*57*). ~300,000 autopicked particles were subjected to extensive 2D classification to eliminate poor-quality particles and nonprotein contaminants. 20 high-quality 2D class averages were used to generate candidate initial models as references for refinement using EMAN2 (e2initialmodel.py) (*28*). After an initial trial refinement of the whole set of particles in RELION 1.3 without imposition of symmetry (in which secondary structural elements were clearly visible), 3D classification (K = 4, T = 4) was performed without the imposition of symmetry, and was used to identify a class of 70,000 particles with improved homogeneity (fig. S3), and with evident C_2 symmetry. Refinement of this class with application of C_2 symmetry yielded a map with final resolution of 4.18 Å according to the Fourier shell correlation criterion using the "gold standard" protocol (*58*). Inspection of the density map revealed features consistent with the estimated resolution, including clearly evident helical pitch throughout the map, and well-defined density for bulky side chains (fig. S5). At this point, it was evident that the reference model was of the wrong hand (the alpha helices were left-handed), and so the correct hand was obtained by reflecting the map about the *X-Y* plane using EMAN2 (e2proc3d.py). After the initial reconstruction, 3D classification was rerun with C_2 symmetry enforced (K = 4, T = 4), allowing identification of a further improved class of 56,614 particles, which were corrected for the motion of individual particles using alignmparts_lmbfgs with an estimated dose of 1.25 e^- per frame. Refinement of this improved set of polished particles using the 3D-auto-refine procedure of RELION 1.3 yielded a reconstruction with an estimated resolution of 3.9 Å. The mask used for Fourier shell correlation calculations was generated by creating a 10 Å low pass filtered map from the atomic model using the molmap command of UCSF Chimera, and using relion_mask_create to generate a soft-edged mask from this map. The map was low pass filtered at 3.5Å and a negative B-factor of –113.68 was applied to enhance visibility of high-resolution features using relion_ postprocess. Analysis of the orientational distribution of particles contributing to the final reconstruction demonstrates that STRA6 appears to adopt a preferred orientation under the conditions used for data collection, with the view parallel to the membrane so that both CaM "legs" are visible being the most common (fig. S2A).

Model building and refinement

Model building was initiated with the placement of the N and C lobes of CaM. Both apo-CaM and Ca^{2+}-bound CaM structures were tested; Ca^{2+}-bound CaM structures showed an excellent fit to the density map for both lobes, whereas no apo-CaM structure matched the density. Initial orientations of the N and C lobes (derived from the structure of human Ca^{2+}-CaM, PDB ID 1CDL, and mutated in silico to match the sequence of *Spodoptera littoralis* CaM, UniProt ID E3UJZ8) were obtained using the Jiggle-fit routine of COOT (*59*). Initial model building of STRA6 was informed by previous experimental studies of the transmembrane topology (*15*), computational predictions of secondary structure and disordered regions using the Xtalpred server (*60*), and the spacing of bulky hydrophobic residues in the sequence, which are especially recognizable in the density map. Model building was performed manually in COOT (*59*), alternating with cycles of automated real-space refinement in phenix.real_space_refine (*61*). All structural figures were prepared using UCSF Chimera (*62*). Analysis of clefts and pockets was performed using the Voss Volume Voxelator (3V) server with an outer probe radius of 10 Å and an inner probe radius of 3 Å (*63*). Sequence alignments were performed using MUSCLE (*64*) and all sequence alignment figures were prepared using Jalview (*65*).

Cross validation and model-map FSC calculations

Potential effects of overfitting in the final refined model were assessed by the following procedure. Two maps were calculated from random half sets of particles using *relion_reconstruct*; post-processing was performed with the same parameters as for the original full map using *relion_postprocess*. One of these maps (the "refine" half-map) was used to refine the final model, with all atoms randomly displaced by 0.2 Å (*phenix.pdbtools sites.shake=0.2*) to reduce the influence of overfitting on the initial model. The final model was used to generate a "model map" using *phenix.model_map*, which, after both maps (the model map and the test/refine/full maps) were masked using the same soft mask as used for resolution calculations, was used for FSC calculations performed with EMAN2.11 (*e2proc3d.py–calcfsc*). The FSC curves calculated thusly are presented in fig. S6B.

Mammalian cell culture and generation of stable lines

HEK293 cells were maintained at 37°C, in a humidified environment enriched with 5% CO_2. HEK293 cells were grown in DMEM (Gibco) supplemented with 10% FBS (Gibco), penicillin, streptomycin, and L-glutamine (Pen/Strep/L-Glu; Gibco). Zebrafish CRBP1 was cloned into pFM1.2 and RBP was cloned into pFM1.2R (*50*) with a hexahistidine tag appended to the C terminus. Each plasmid was mixed with plasmid carrying a puromycin resistance gene (1:5) before cotransfection using lipofectamine (Invitrogen) or PEI (Polysciences) into 293 GnTi$^-$ cells (*66*). Stable integrants were selected by addition of 5 μg/ml puromycin to the growth medium 24 hours after transfection. Production cell lines from fluorescent colonies were selected either by FACS sorting in Autoclone mode and subsequent visual inspection of the resulting colonies, to identify single, highly fluorescent colonies, or by manual picking of the most intense fluorescent colonies after antibiotic selection (*50*). Expression levels of selected colonies were checked by small-scale purification tests—performed by metal-affinity chromatography—to select the best lines for expansion.

Zebrafish RBP expression and purification

The stable mammalian cell line secreting RBP was maintained in DMEM supplemented with 10% FBS, Pen/Strep/L-Glu, and 5 μg/ml puromycin. Media was harvested from scaled-up cultures as monolayers in 225-cm^2 culture flasks (Costar) after 10 days. After centrifugation to remove cell debris, the media was adjusted to 30 mM HEPES, pH 7.5, 50 mM NaCl, and 5 mM imidazole for purification by metal affinity chromatography. After binding to equilibrated Ni^{2+}-NTA resin for 30 min, the slurry was transferred to a column, washed with 15 column volumes of buffer containing 10 mM imidazole, and the protein was eluted with buffer containing 200 mM imidazole. The eluted protein was desalted using PD MidiTrap G-25 (GE Healthcare) and purity was assessed by SDS-PAGE.

Holo-RBP preparation

Purified zebrafish RBP was precipitated in ice-chilled 100% ethanol to remove endogenous retinol. After ultracentrifugation, the precipitated RBP was resuspended in denaturing buffer (50 mM Tris pH 8.0, 6.6 M guanidine hydrochloride). After incubation at room temperature for 30 min, the sample (1 ml at 5 mg/ml) was slowly added drop-wise to a 10 ml ice-cold refolding buffer (0.4 M L-arginine, 20 mM HEPES pH 7.5, 100 mM NaCl) containing 0.1 mM all-trans retinol (Sigma). All the experimental steps were carried out in the dark and samples were protected from light at all times from this point onwards. The refolding mixture was gently agitated overnight at 4°C.

Downloaded from http://science.sciencemag.org/ on September 3, 2016

After centrifugation to remove aggregates, the sample was concentrated to 1 ml, loaded on a desalting column (PD MidiTrap G-25, GE Healthcare) and further purified by SEC (Superdex 200 10/300, AKTA, GE column) to remove free retinol. The concentration of eluted fractions was determined by Bradford assay (BioRad) (*51*). The success of retinol incorporation was assessed by measuring the absorption spectrum of the protein samples (Beckman Coulter DU730) at 260 to 400 nm and confirmed by HPLC (details described below in cell-based retinol uptake assay section).

Cell-based retinol uptake assay

Parental HEK293 cells or a cell line stably expressing zebrafish CRBP1 were seeded in six well plates at 0.5×10^6 cells per well the evening before the experiment and expression constructs transfected in triplicates. 72 hours after transfection, the media was replaced with serum free DMEM and incubated for an additional 16 hours in standard cell-maintenance conditions. Holo-RBP was added to a final concentration of 1 μM to the medium, and cells were maintained as such for 6 hours in standard cell-maintenance conditions. To detect retinol uptake, holo-RBP–containing media was removed from the cells, and these were gently washed three times with PBS and harvested by centrifugation at 800 × *g*. Cell pellets were resuspended with 300 μl of PBS, frozen on dry ice and stored at −70°C. Cells were lysed by repeated freeze-thaw cycles. 20 μl of the cell suspension was used to determine protein concentration by Bradford assay (*51*) (BioRad), and the remaining 280 μl was extracted with hexane followed by loading on HPLC run in reverse phase. Retinol and retinyl ester peaks were separated on a 4.6 × 250 mm Denali C18 column (Grace, Deerfield, IL) preceded by a C18 guard column (PerkinElmer, Waltham, MA) using acetonitrile, methanol, and methylene chloride (70:15:15, v/v) as the mobile phase flowing at 1.8 ml/min. Quantitative analysis was performed by comparing retention times and spectral data of experimental compounds with those of authentic standards.

Peptides

All peptides were synthesized and purchased from Bio-Synthesis. Peptide sequences corresponding to regions in zebrafish STRA6 were as follows: CaMBP0. residues 222 to 237 (EDLSSSYY RDYVKKILKKKK); CaMBP1, residues 554 to 571 (SQSHPVMKAFCGLLLQSS); CaMBP2, residues 600 to 626 (VSNAKRARAHWQLLYTLVNNPSLVGSR); CaMBP1_2, residues 554 to 571 and 601 to 626 separated by a flexible 8-resiude linker (SQSHPVMKAFCGLLLQSSGGGEGGGGSNAKRARAHWQLLYTLVNNPSLVGS R). The peptides were protected using N-terminal acetylation and C-terminal amidation, and purity was confirmed by HPLC and amino acid analysis.

Purification of human CaM

The vector for human CaM was generously supplied by L. M. Amzel at Johns Hopkins University in a pET24 plasmid without an affinity tag, which was transformed and expressed in *Escherichia coli* strain BL21(DE3) using 0.5 mM IPTG at 37°C. Bacterial cell pellets were resuspended in Buffer A (50 mM Tris, pH 7.5, 1 mM DTT) and lysed using a combination of lysozyme (0.1 mg/ml) and sonication. The lysate was clarified via centrifugation at 15,000 rpm. The resulting protein solution was extensively dialyzed against Buffer B [50 mM Tris, pH 7.5, 10 mM β-mercaptoethanol (β-ME)] and applied to a diethylaminoethanol (DEAE) sepharose column (Sigma-Aldrich) for initial purification. The protein was eluted from the DEAE column using a linear gradient of 10 to 35% Buffer C (50 mM Tris, pH 7.5, 10 mM β-ME, 1 M NaCl). After pooling the protein fractions, the sample was dialyzed extensively against Buffer D (10 mM Tris, pH 7.5, 500 mM NaCl, 10 mM $CaCl_2$, and 0.25 mM DTT) and applied to a Phenyl Sepharose column (Sigma-Aldrich). The protein was eluted from the column using a single step of 100% Buffer E (10 mM Tris, pH 7.5, 500 mM NaCl, 10 mM EDTA, and 0.25 mM DTT). As a final purification step, the pooled Phenyl Sepharose fractions were concentrated to <5 ml and loaded onto a Superdex 200 (S200-PG) SEC column (GE Healthcare) and eluted using Buffer F {20 mM HEPES, pH 7.4, 50 mM NaCl, 5 mM $MgCl_2$, 1 mM TCEP [tris(2-carboxyethyl)phosphine], and 0.02% NaN_3} as mobile phase. Throughout the purification process, the fractions containing the protein were identified using a combination of Bradford Assay and SDS-PAGE, and the final protein sample purity was assessed using SDS-PAGE and native PAGE (>99%). Pure protein was concentrated to 20 mg/ml, flash-frozen, and stored in 0.5 ml aliquots at −80°C.

Isothermal titration calorimetry

All isothermal titration calorimetry experiments were performed using a VP-ITC system obtained from MicroCal (Northampton, MA). Samples were extensively dialyzed against Buffer G (20 mM HEPES pH 7.4, 50 mM NaCl, 10 mM $CaCl_2$, 5 mM $MgCl_2$, and 0.5 mM TCEP), and experiments were performed at 37°C. Initial experiments had CaM in the syringe at a concentration of 150 to 500 μM with each STRA6 peptide at a concentration of 15 to 50 μM in the reaction cell. A series of 30 injections of 10 μl of protein solution was performed at 5-min intervals. The reverse titrations with CaM in the reaction cell at concentrations of 15 to 20 μM and peptide in the syringe at concentrations of 150 to 200 μM were also performed for confirmation of the initial results. The data were processed and analyzed with the MicroCal Origin 7 software and corrected by the heat of injection from the basal heat remaining after saturation and confirmed by titration into buffer only as a control. For CaMBP0 and CaMBP1, a one-site binding mode was used to fit the data, using a nonlinear least-squares algorithm, whereas CaMBP2 was fit using a two-site binding mode with a Levenberg-Marquardt nonlinear regression model, due to the endothermic interval before saturation (or initial binding interval in the reversed titration).

X-ray crystallography on CaM-CaMBP2

Crystallization experiments were performed using sitting-drop vapor diffusion methods as follows: CaM-CaMBP2 crystals were set in drops of 1.0 μl protein solution containing 20 mg/ml CaM, 1.2 mM CaMBP2, 20 mM HEPES pH 7.4, 50 mM NaCl, 10 mM $CaCl_2$, 5 mM $MgCl_2$, and 0.5 mM TCEP with 0.8% (v/v) DMSO with 1.0 μl mother liquor containing 0.1 M imidazole pH 5.5, 28% (v/v) polyethylene glycol monomethyl ether 550. Crystals formed over the course of 1 to 10 days at a temperature of 281 K before they were harvested. No additional cryo-protection was used before flash-cooling into liquid nitrogen. Diffraction data were collected remotely at the Northeastern Collaborative Access Team using beamline 24ID-E at the Advanced Photon Source (Argonne National Laboratory) at 100 K using an ADSC Q315 (315 mm × 315 mm) detector. A 1.74 Å data set was obtained at a wavelength of 0.97919 Å with 1.0° oscillation for each frame and processed then integrated using Mosflm (*67*) with a space group of C121. Diffraction statistics are summarized in table S2. Model building was started using molecular replacement with a search model derived from the CaM C lobe of a previously determined structure (PDB accession code 1ZUZ) using the PHENIX (*61*) AUTOMR (*68*) function. The models were completed via manual building within COOT (*59*) with peptide, ligands, and water incorporation guided by the m|Fo| - D|Fc| omit maps and iteratively refined with the PHENIX. REFINE (*69*) function. All structure refinement statistics can be found in table S2.

REFERENCES AND NOTES

1. K. Palczewski, Chemistry and biology of vision. *J. Biol. Chem.* **287**, 1612–1619 (2012). doi: 10.1074/jbc.R111.301150; pmid: 22074921
2. Z. Al Tanoury, A. Piskunov, C. Rochette-Egly, Vitamin A and retinoid signaling: Genomic and nongenomic effects. *J. Lipid Res.* **54**, 1761–1775 (2013). doi: 10.1194/jlr.R030833; pmid: 23440512
3. D. S. Goodman, Vitamin A and retinoids in health and disease. *N. Engl. J. Med.* **310**, 1023–1031 (1984). doi: 10.1056/NEJM198404193101605; pmid: 6369133
4. Y. Shirakami, S. A. Lee, R. D. Clugston, W. S. Blaner, Hepatic metabolism of retinoids and disease associations. *Biochim. Biophys. Acta* **1821**, 124–136 (2012). doi: 10.1016/j.bbalip.2011.06.023; pmid: 21763780
5. A. di Masi *et al*., Retinoic acid receptors: From molecular mechanisms to cancer therapy. *Mol. Aspects Med.* **41**, 1–115 (2015). doi: 10.1016/j.mam.2014.12.003; pmid: 25543955
6. K. P. West Jr., Extent of vitamin A deficiency among preschool children and women of reproductive age. *J. Nutr.* **132**, 2857S–2866S (2002). pmid: 12221262
7. D. R. Soprano, W. S. Blaner, in *The Retinoids: Biology, Chemistry, and Medicine*, M. B. Sporn, A. B. Roberts, D. S. Goodman, Eds. (Raven Press, 1994), pp. 257–282.
8. M. Vieira, M. J. Saraiva, Transthyretin: A multifaceted protein. *Biomol. Concepts* **5**, 45–54 (2014). doi: 10.1515/bmc-2013-0038; pmid: 25372741
9. A. C. Ross, Cellular metabolism and activation of retinoids: Roles of cellular retinoid-binding proteins. *FASEB J.* **7**, 317–327 (1993). pmid: 8440409
10. Y. Li, N. Wongsiriroj, W. S. Blaner, The multifaceted nature of retinoid transport and metabolism. *Hepatobiliary Surg. Nutr.* **3**, 126–139 (2014). pmid: 25019074
11. A. Sivaprasadarao, M. Boudjelal, J. B. Findlay, Solubilization and purification of the retinol-binding protein receptor from human placental membranes. *Biochem. J.* **302**, 245–251 (1994). doi: 10.1042/bj3020245; pmid: 8068012

Downloaded from http://science.sciencemag.org/ on September 3, 2016

12. M. Sundaram, A. Sivaprasadarao, M. M. DeSousa, J. B. Findlay, The transfer of retinol from serum retinol-binding protein to cellular retinol-binding protein is mediated by a membrane receptor. *J. Biol. Chem.* **273**, 3336–3342 (1998). doi: 10.1074/jbc.273.6.3336; pmid: 9452451
13. R. Kawaguchi *et al*., A membrane receptor for retinol binding protein mediates cellular uptake of vitamin A. *Science* **315**, 820–825 (2007). doi: 10.1126/science.1136244; pmid: 17255476
14. P. Bouillet *et al*., Developmental expression pattern of Stra6, a retinoic acid-responsive gene encoding a new type of membrane protein. *Mech. Dev.* **63**, 173–186 (1997). doi: 10.1016/S0925-4773(97)00039-7; pmid: 9203140
15. R. Kawaguchi, J. Yu, P. Wiita, M. Ter-Stepanian, H. Sun, Mapping the membrane topology and extracellular ligand binding domains of the retinol binding protein receptor. *Biochemistry* **47**, 5387–5395 (2008). doi: 10.1021/bi8002082; pmid: 18419130
16. U. Cogan, M. Kopelman, S. Mokady, M. Shinitzky, Binding affinities of retinol and related compounds to retinol binding proteins. *Eur. J. Biochem.* **65**, 71–78 (1976). doi: 10.1111/j.1432-1033.1976.tb10390.x; pmid: 945163
17. R. Kawaguchi, M. Zhong, M. Kassai, M. Ter-Stepanian, H. Sun, STRA6-catalyzed vitamin A influx, efflux, and exchange. *J. Membr. Biol.* **245**, 731–745 (2012). doi: 10.1007/s00232-012-9463-1; pmid: 22815070
18. A. Ruiz *et al*., Molecular and biochemical characterization of lecithin retinol acyltransferase. *J. Biol. Chem.* **274**, 3834–3841 (1999). doi: 10.1074/jbc.274.6.3834; pmid: 9920938
19. M. Zhong, R. Kawaguchi, M. Kassai, H. Sun, Apo-RBP, holo-RBP, and insulin resistance. *Mol. Cell. Biol.* **34**, 2105–2106 (2014). doi: 10.1128/MCB.01425-12; pmid: 24803600
20. N. Noy, Reply to "Apo-RBP, Holo-RBP, and insulin resistance". *Mol. Cell. Biol.* **34**, 2107 (2014). doi: 10.1128/MCB.01699-12; pmid: 24803601
21. N. Noy, Signaling by retinol and its serum binding protein. *Prostaglandins Leukot. Essent. Fatty Acids* **93**, 3–7 (2015). doi: 10.1016/j.plefa.2014.10.004; pmid: 25481334
22. D. C. Berry, H. Jin, A. Majumdar, N. Noy, Signaling by vitamin A and retinol-binding protein regulates gene expression to inhibit insulin responses. *Proc. Natl. Acad. Sci. U.S.A.* **108**, 4340–4345 (2011). doi: 10.1073/pnas.1011115108; pmid: 21368206
23. N. Chassaing *et al*., Phenotypic spectrum of STRA6 mutations: From Matthew-Wood syndrome to non-lethal anophthalmia. *Hum. Mutat.* **30**, E673–E681 (2009). doi: 10.1002/humu.21023; pmid: 19309693
24. A. Isken *et al*., RBP4 disrupts vitamin A uptake homeostasis in a STRA6-deficient animal model for Matthew-Wood syndrome. *Cell Metab.* **7**, 258–268 (2008). doi: 10.1016/j.cmet.2008.01.009; pmid: 18316031
25. J. Amengual *et al*., STRA6 is critical for cellular vitamin A uptake and homeostasis. *Hum. Mol. Genet.* **23**, 5402–5417 (2014). doi: 10.1093/hmg/ddu258; pmid: 24852372
26. A. Ruiz *et al*., Retinoid content, visual responses, and ocular morphology are compromised in the retinas of mice lacking the retinol-binding protein receptor, STRA6. *Invest. Ophthalmol. Vis. Sci.* **53**, 3027–3039 (2012). doi: 10.1167/iovs.11-8476; pmid: 22467576
27. D. C. Berry *et al*., The STRA6 receptor is essential for retinol-binding protein-induced insulin resistance but not for maintaining vitamin A homeostasis in tissues other than the eye. *J. Biol. Chem.* **288**, 24528–24539 (2013). doi: 10.1074/jbc.M113.484014; pmid: 23839944
28. G. Tang *et al*., EMAN2: An extensible image processing suite for electron microscopy. *J. Struct. Biol.* **157**, 38–46 (2007). doi: 10.1016/j.jsb.2006.05.009; pmid: 16859925
29. K. P. Hoeflich, M. Ikura, Calmodulin in action: Diversity in target recognition and activation mechanisms. *Cell* **108**, 739–742 (2002). doi: 10.1016/S0092-8674(02)00682-7; pmid: 11955428
30. H. Tidow, P. Nissen, Structural diversity of calmodulin binding to its target sites. *FEBS J.* **280**, 5551–5565 (2013). doi: 10.1111/febs.12296; pmid: 23601118
31. M. Ikura *et al*., Solution structure of a calmodulin-target peptide complex by multidimensional NMR. *Science* **256**, 632–638 (1992). doi: 10.1126/science.1585175; pmid: 1585175
32. F. Pasutto *et al*., Mutations in STRA6 cause a broad spectrum of malformations including anophthalmia, congenital heart defects, diaphragmatic hernia, alveolar capillary dysplasia, lung hypoplasia, and mental retardation. *Am. J. Hum. Genet.* **80**, 550–560 (2007). doi: 10.1086/512203; pmid: 17273977
33. M. Liao, E. Cao, D. Julius, Y. Cheng, Structure of the TRPV1 ion channel determined by electron cryo-microscopy. *Nature* **504**, 107–112 (2013). doi: 10.1038/nature12822; pmid: 24305160
34. P. Lu *et al*., Three-dimensional structure of human γ-secretase. *Nature* **512**, 166–170 (2014). doi: 10.1038/nature13567; pmid: 25043039
35. H. Van Esch, A. Jansen, M. Bauters, G. Froyen, J. P. Fryns, Encephalopathy and bilateral cataract in a boy with an interstitial deletion of Xp22 comprising the CDKL5 and NHS genes. *Am. J. Med. Genet. A.* **143A**, 364–369 (2007). doi: 10.1002/ajmg.a.31572; pmid: 17256798
36. A. K. Wernimont *et al*., Structures of parasitic CDPK domains point to a common mechanism of activation. *Proteins* **79**, 803–820 (2011). doi: 10.1002/prot.22919; pmid: 21287613
37. C. L. Drum *et al*., Structural basis for the activation of anthrax adenylyl cyclase exotoxin by calmodulin. *Nature* **415**, 396–402 (2002). doi: 10.1038/415396a; pmid: 11807546
38. R. Kawaguchi, J. Yu, P. Wiita, J. Honda, H. Sun, An essential ligand-binding domain in the membrane receptor for retinol-binding protein revealed by large-scale mutagenesis and a human polymorphism. *J. Biol. Chem.* **283**, 15160–15168 (2008). doi: 10.1074/jbc.M801060200 pmid: 18387951
39. P. Alapatt *et al*., Liver retinol transporter and receptor for serum retinol-binding protein (RBP4). *J. Biol. Chem.* **288**, 1250–1265 (2013). doi: 10.1074/jbc.M112.369132; pmid: 23105095
40. R. W. Hesselink, J. B. Findlay, Expression, characterization and ligand specificity of lipocalin-1 interacting membrane receptor (LIMR). *Mol. Membr. Biol.* **30**, 327–337 (2013). doi: 10.3109/09687688.2013.823018; pmid: 23964685
41. H. Melhus, C. O. Båvik, L. Rask, P. A. Peterson, U. Eriksson, Epitope mapping of a monoclonal antibody that blocks the binding of retinol-binding protein to its receptor. *Biochem. Biophys. Res. Commun.* **210**, 105–112 (1995). doi: 10.1006/bbrc.1995.1633; pmid: 7741728
42. C. Redondo, M. Vouropoulou, J. Evans, J. B. Findlay, Identification of the retinol-binding protein (RBP) interaction site and functional state of RBPs for the membrane receptor. *FASEB J.* **22**, 1043–1054 (2008). doi: 10.1096/fj.07-8939com; pmid: 17991731
43. M. Edidin, The state of lipid rafts: From model membranes to cells. *Annu. Rev. Biophys. Biomol. Struct.* **32**, 257–283 (2003). doi: 10.1146/annurev.biophys.32.110601.142439; pmid: 12543707
44. R. Kawaguchi *et al*., Receptor-mediated cellular uptake mechanism that couples to intracellular storage. *ACS Chem. Biol.* **6**, 1041–1051 (2011). doi: 10.1021/cb200178w; pmid: 21774515
45. D. C. Berry, S. M. O'Byrne, A. C. Vreeland, W. S. Blaner, N. Noy, Cross talk between signaling and vitamin A transport by the retinol-binding protein receptor STRA6. *Mol. Cell. Biol.* **32**, 3164–3175 (2012). doi: 10.1128/MCB.00505-12; pmid: 22665496
46. A. Usacheva *et al*., Contribution of the Box 1 and Box 2 motifs of cytokine receptors to Jak1 association and activation. *J. Biol. Chem.* **277**, 48220–48226 (2002). doi: 10.1074/jbc.M205757200; pmid: 12374810
47. H. J. Wallweber, C. Tam, Y. Franke, M. A. Starovasnik, P. J. Lupardus, Structural basis of recognition of interferon-α receptor by tyrosine kinase 2. *Nat. Struct. Mol. Biol.* **21**, 443–448 (2014). doi: 10.1038/nsmb.2807; pmid: 24704786
48. M. Zhong, R. Kawaguchi, M. Ter-Stepanian, M. Kassai H. Sun, Vitamin A transport and the transmembrane pore in the cell-surface receptor for plasma retinol binding protein. *PLOS ONE* **8**, e73838 (2013). doi: 10.1371/journal.pone.0073838; pmid: 24223695
49. R. Kawaguchi, M. Zhong, M. Kassai, M. Ter-Stepanian, H. Sun, Differential and isomer-specific modulation of vitamin A transport and the catalytic activities of the RBP receptor by retinoids. *J. Membr. Biol.* **246**, 647–660 (2013). doi: 10.1007/s00232-013-9578-z; pmid: 23811822
50. Z. Assur, W. A. Hendrickson, F. Mancia, Tools for coproducing multiple proteins in mammalian cells. *Methods Mol. Biol.* **801**, 173–187 (2011). doi: 10.1007/978-1-61779-352-3_12; pmid: 21987254
51. M. M. Bradford, A rapid and sensitive method for the quantitation of microgram quantities of protein utilizing the principle of protein-dye binding. *Anal. Biochem.* **72**, 248–254 (1976). doi: 10.1016/0003-2697(76)90527-3 pmid: 942051
52. B. S. Kendrick, B. A. Kerwin, B. S. Chang, J. S. Philo, Online size-exclusion high-performance liquid chromatography light scattering and differential refractometry methods to determine degree of polymer conjugation to proteins and protein-protein or protein-ligand association states. *Anal. Biochem.* **299**, 136–146 (2001). doi: 10.1006/abio.2001.5411; pmid: 11730335
53. R. Mancusso, N. K. Karpowich, B. K. Czyzewski, D. N. Wang, Simple screening method for improving membrane protein thermostability. *Methods* **55**, 324–329 (2011). doi: 10.1016/j.ymeth.2011.07.008; pmid: 21840396
54. C. J. Russo, L. A. Passmore, Ultrastable gold substrates for electron cryomicroscopy. *Science* **346**, 1377–1380 (2014). doi: 10.1126/science.1259530; pmid: 25504723
55. T. Grant, N. Grigorieff, Measuring the optimal exposure for single particle cryo-EM using a 2.6 Å reconstruction of rotavirus VP6. *eLife* **4**, e06980 (2015). doi: 10.7554/eLife.06980; pmid: 26023829
56. A. Rohou, N. Grigorieff, CTFFIND4: Fast and accurate defocus estimation from electron micrographs. *J. Struct. Biol.* **192**, 216–221 (2015). doi: 10.1016/j.jsb.2015.08.008; pmid: 26278980
57. S. H. Scheres, Semi-automated selection of cryo-EM particles in RELION-1.3. *J. Struct. Biol.* **189**, 114–122 (2015). doi: 10.1016/j.jsb.2014.11.010; pmid: 25486611
58. S. H. Scheres, S. Chen, Prevention of overfitting in cryo-EM structure determination. *Nat. Methods* **9**, 853–854 (2012). doi: 10.1038/nmeth.2115; pmid: 22842542
59. P. Emsley, B. Lohkamp, W. G. Scott, K. Cowtan, Features and development of Coot. *Acta Crystallogr. D Biol. Crystallogr.* **66**, 486–501 (2010). doi: 10.1107/S0907444910007493; pmid: 20383002
60. L. Slabinski *et al*., XtalPred: A web server for prediction of protein crystallizability. *Bioinformatics* **23**, 3403–3405 (2007). doi: 10.1093/bioinformatics/btm477 pmid: 17921170
61. P. D. Adams *et al*., PHENIX: A comprehensive Python-based system for macromolecular structure solution. *Acta Crystallogr. D Biol. Crystallogr.* **66**, 213–221 (2010). doi: 10.1107/S0907444909052925; pmid: 20124702
62. E. F. Pettersen *et al*., UCSF Chimera—A visualization system for exploratory research and analysis. *J. Comput. Chem.* **25**, 1605–1612 (2004). doi: 10.1002/jcc.20084; pmid: 15264254
63. N. R. Voss, M. Gerstein, 3V: cavity, channel and cleft volume calculator and extractor. *Nucleic Acids Res.* **38**, W555–W562 (2010). doi: 10.1093/nar/gkq395; pmid: 20478824
64. R. C. Edgar, MUSCLE: Multiple sequence alignment with high accuracy and high throughput. *Nucleic Acids Res.* **32**, 1792–1797 (2004). doi: 10.1093/nar/gkh340; pmid: 15034147
65. A. M. Waterhouse, J. B. Procter, D. M. Martin, M. Clamp, G. J. Barton, Jalview Version 2—a multiple sequence alignment editor and analysis workbench. *Bioinformatics* **25**, 1189–1191 (2009). doi: 10.1093/bioinformatics/btp033; pmid: 19151095
66. P. J. Reeves, N. Callewaert, R. Contreras, H. G. Khorana, Structure and function in rhodopsin: High-level expression of rhodopsin with restricted and homogeneous N-glycosylation by a tetracycline-inducible *N*-acetylglucosaminyltransferase I-negative HEK293S stable mammalian cell line. *Proc. Natl. Acad. Sci. U.S.A.* **99**, 13419–13424 (2002). doi: 10.1073/pnas.212519299; pmid: 12370423
67. T. G. Battye, L. Kontogiannis, O. Johnson, H. R. Powell, A. G. Leslie, iMOSFLM: A new graphical interface for diffraction-image processing with MOSFLM. *Acta Crystallogr. D Biol. Crystallogr.* **67**, 271–281 (2011). doi: 10.1107/S0907444910048675; pmid: 21460445
68. A. J. McCoy *et al*., Phaser crystallographic software. *J. Appl. Crystallogr.* **40**, 658–674 (2007). doi: 10.1107/S0021889807021206; pmid: 19461840

Downloaded from http://science.sciencemag.org/ on September 3, 2016

69. P. V. Afonine, R. W. Grosse-Kunstleve, P. D. Adams, A robust bulk-solvent correction and anisotropic scaling procedure. *Acta Crystallogr. D Biol. Crystallogr.* **61**, 850–855 (2005). doi: 10.1107/S0907444905007894; pmid: 15983406

70. M. A. Lomize, I. D. Pogozheva, H. Joo, H. I. Mosberg, A. L. Lomize, OPM database and PPM web server: Resources for positioning of proteins in membranes. *Nucleic Acids Res.* **40**, D370–D376 (2012). doi: 10.1093/nar/gkr703; pmid: 21890895

71. J. Kyte, R. F. Doolittle, A simple method for displaying the hydropathic character of a protein. *J. Mol. Biol.* **157**, 105–132 (1982). doi: 10.1016/0022-2836(82)90515-0; pmid: 7108955

ACKNOWLEDGMENTS

This work was supported by a NIH National Institute of General Medical Sciences initiative to the New York Consortium on Membrane Protein Structure (U54 GM095315). O.B.C. was supported by a Charles H. Revson Senior Fellowship. We thank G. Sciara and G. Ahlsen for sharing with us their expertise for the light-scattering experiments; F. Insaidoo, L. A. White, I. Ubarretxena, Y. Gomez, S. Brenner-Morton, and A. Nemes for their contributions during the initial stages of this work; B. Kloss, R. Bruni, and R. Kalathur from the New York Structural Biology Center for their many contributions to the project; R. Grassucci for assistance with data collection; A. des Georges, A. Marks, and R. Axel for advice and helpful discussions; and L. Hamberger for assistance with running the Mancia laboratory. The CaM-CaMBP2 structure has been deposited in the PDB under accession code 5K8Q. The STRA6-CaM coordinates have been deposited in the PDB under accession code 5SY1, and the map has been deposited in the Electron Microscopy Data Bank under accession code EMD-8315.

SUPPLEMENTARY MATERIALS

www.sciencemag.org/content/353/6302/aad8266/suppl/DC1
Figs. S1 to S14
Tables S1 to S3
Reference (*72*)
Movies S1 and S2

7 November 2015; accepted 16 June 2016
10.1126/science.aad8266

Downloaded from http://science.sciencemag.org/ on September 3, 2016

RESEARCH ARTICLE SUMMARY

ACTINIDE CHEMISTRY

Characterization of berkelium(III) dipicolinate and borate compounds in solution and the solid state

Mark A. Silver,* Samantha K. Cary,* Jason A. Johnson, Ryan E. Baumbach, Alexandra A. Arico, Morgan Luckey, Matthew Urban, Jamie C. Wang, Matthew J. Polinski, Alexander Chemey, Guokui Liu, Kuan-Wen Chen, Shelley M. Van Cleve, Matthew L. Marsh, Teresa M. Eaton, Lambertus J. van de Burgt, Ashley L. Gray, David E. Hobart, Kenneth Hanson, Laurent Maron, Frédéric Gendron, Jochen Autschbach, Manfred Speldrich, Paul Kögerler, Ping Yang, Jenifer Braley,† Thomas E. Albrecht-Schmitt†

INTRODUCTION: Developing the chemistry of late actinides is hindered by the lack of availability of isotopes, the need for specialized research facilities, and the nuclear instability of the elements. Berkelium represents one of the last elements that can be prepared on a milligram scale in nuclear reactors. However, its only available isotope, ^{249}Bk, has a half-life of only 320 days, which has greatly curtailed the expansion of its chemistry and fundamental exploration of how large relativistic and spin-orbit coupling effects alter its electronic structure. Furthermore, data gathered from Bk(III) in aqueous media suggest that its coordination may be different from that of earlier actinides. However, a single-crystal structure of a berkelium compound has remained elusive, leaving unanswered whether these structural changes occur in the solid state.

RATIONALE: This work focuses on characterizing two distinct berkelium compounds on the milligram scale. In particular, the goal was to obtain crystals of these compounds that could be used in structure determinations and physical property measurements. Two compounds were selected: a coordination complex of dipicolinate and a borate. Dipicolinate complexation occurs with most other lanthanides and actinides in the +3 oxidation state, facilitating comparisons across the series to discern periodic trends. In the borate family, the structural frameworks are hypersensitive to the nature of the bonding at the metal center and are rearranged accordingly. Modeling the experimental data using a variety of computational techniques allows us to deconvolute the role of covalent bonding and spin-orbit coupling in determining the electronic properties of berkelium.

RESULTS: Experiments with milligram quantities of ^{249}Bk were choreographed for 6 months before the arrival of the isotope because the total quantity used in the studies was 13 mg, which corresponds to a specific activity of 21 Ci. Although this isotope is a low-energy β emitter, it decays to ^{249}Cf at a rate of about 1.2% per week, and the latter produces hard γ radiation that represents a serious external hazard. In addition, the samples described in this work undergo about 10^{12} decays per second. This rapid decomposition necessitated the development of techniques for swiftly preparing and encapsulating samples and for collecting all structural and spectroscopic data within 24 hours of crystal formation. After this preparation, the single-crystal structures of Bk(III)tris(dipicolinate) and Bk(III) borate were determined. The latter compound has the same topology as that of californium(III) (Cf) and contains an eight-coordinate BkO_8 unit. This reduction in coordination number is consistent with previous solution-phase x-ray absorption measurements and indicates that a drop in coordination number in the actinide series from nine to eight begins at berkelium. The magnetic and optical properties of these samples were also measured. The red luminescence from Bk(III) was similar in nature to that of curium(III) and is primarily based on an *f-f* transition. The ingrowth of the broad green luminescence from Cf(III), which is caused by a ligand-to-metal charge transfer, was shown to be distinct in nature from that originating from Bk(III). Ligand-field, density functional theory, and wave-function calculations were used to understand the spectroscopic features and revealed that the single largest contributor to the unexpected electronic properties of Bk(III) is spin-orbit coupling. This effect mixes the first excited state with the ground state and causes a large deviation from a pure Russell-Saunders state. The reduction in the measured magnetic moment for these samples from that calculated for an f^8 electron configuration is primarily attributable to this multiconfigurational ground state.

ON OUR WEBSITE

Read the full article at http://dx.doi.org/10.1126/science.aaf3762

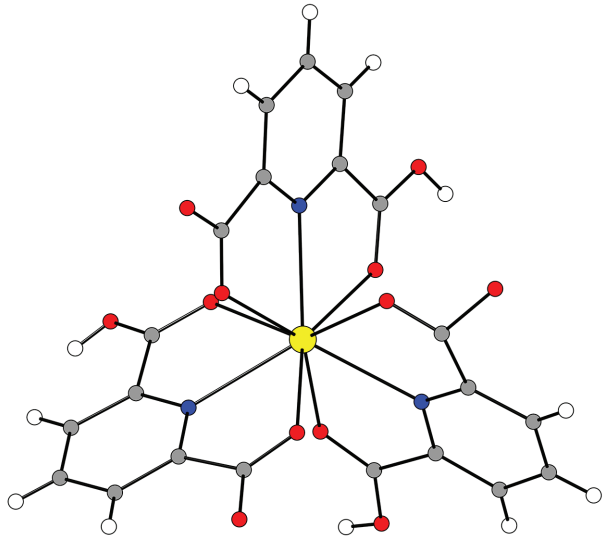

Crystal structure of a berkelium coordination compound. The central Bk(III) ion is coordinated by three monoprotonated dipicolinate ligands in tridentate O,N,O fashion. Bk, yellow; C, gray; N, blue; O, red; H, white.

CONCLUSION: The crystallographic data indicate that Bk(III) shares more structural similarities with Cf(III) than with Cm(III). However, ligand-field effects are more similar between Bk(III) and Cm(III). Terbium (Tb), in the lanthanide series, represents the closest analog of Bk because the trivalent cations possess $4f^8$ and $5f^8$ configurations, respectively. Spin-orbit coupling in Bk(III) creates mixing of the first excited state ($^5G_6$) with the ground state. In contrast, the ground state of the Tb(III)tris(dipicolinate) contains negligible contributions of this type. An overall conclusion from this study is that spin-orbit coupling plays a large role in determining the ground state of late actinide compounds. ■

The list of author affiliations is available in the full article online.
*These authors contributed equally to this work.
†Corresponding author. Email: jbraley@mines.edu (J.B.); albrecht-schmitt@chem.fsu.edu (T.E.A.-S.)
Cite this article as M. A. Silver *et al.*, *Science* **353**, aaf3762 (2016). DOI: 10.1126/science.aaf3762

Downloaded from http://science.sciencemag.org/ on September 3, 2016

RESEARCH ARTICLE

ACTINIDE CHEMISTRY

Characterization of berkelium(III) dipicolinate and borate compounds in solution and the solid state

Mark A. Silver,[1]* Samantha K. Cary,[1]* Jason A. Johnson,[2] Ryan E. Baumbach,[3] Alexandra A. Arico,[1] Morgan Luckey,[4] Matthew Urban,[4] Jamie C. Wang,[1] Matthew J. Polinski,[5] Alexander Chemey,[1] Guokui Liu,[6] Kuan-Wen Chen,[3] Shelley M. Van Cleve,[7] Matthew L. Marsh,[1] Teresa M. Eaton,[1] Lambertus J. van de Burgt,[1] Ashley L. Gray,[2] David E. Hobart,[1] Kenneth Hanson,[1] Laurent Maron,[8] Frédéric Gendron,[9] Jochen Autschbach,[9] Manfred Speldrich,[10] Paul Kögerler,[10] Ping Yang,[11] Jenifer Braley,[4]† Thomas E. Albrecht-Schmitt[1]†

Berkelium is positioned at a crucial location in the actinide series between the inherently stable half-filled $5f^7$ configuration of curium and the abrupt transition in chemical behavior created by the onset of a metastable divalent state that starts at californium. However, the mere 320-day half-life of berkelium's only available isotope, ^{249}Bk, has hindered in-depth studies of the element's coordination chemistry. Herein, we report the synthesis and detailed solid-state and solution-phase characterization of a berkelium coordination complex, Bk(III)tris(dipicolinate), as well as a chemically distinct Bk(III) borate material for comparison. We demonstrate that berkelium's complexation is analogous to that of californium. However, from a range of spectroscopic techniques and quantum mechanical calculations, it is clear that spin-orbit coupling contributes significantly to berkelium's multiconfigurational ground state.

Deep into the periodic table, the rising magnitudes of relativistic effects and spin-orbit coupling and the associated subtle rearrangement of orbital energies challenge our ability to predict and understand the chemical and physical properties of heavy elements. Recent experiments and computations have revealed that models based on monotonic changes in electronic structure across heavy element series are overly simplistic and that perhaps our current arrangement of the periodic table is subject to debate. A case in point is the recent determination that the outermost electron of lawrencium (Z = 103) lies in a p orbital rather than d as would have been predicted by extrapolating from earlier elements (*1*). Beyond the actinide series, the situation is no less complex with superheavy elements like seaborgium (Z = 106) exhibiting chemical behavior similar to the triad above (i.e., Cr, Mo, and W) (*2*), whereas reactivity of rutherfordium (Z = 104) and dubnium (Z = 105) can deviate significantly from expectations (*3*, *4*).

Although the exotic electronic structure of superheavy elements is now accepted, the validity of simple chemical principles to predict electron configuration, and thus chemical behavior, is questionable throughout the entire actinide series. Plutonium demonstrates these qualities best, and after seven decades of interrogation, only now do we understand that its electronic structure must be framed within the context of electronic states that are fluctuating on a subpicosecond time scale (*5*). Similarly, at californium (Z = 98) a metastable electronic state is observed near ambient conditions that also manifests in the spectroscopic features of complex molecules containing Cf(III) ions (*6*–*10*).

However, as is often true with heavy elements, our ability to probe chemical and physical properties is hampered by nuclear instability. This creates gaps that impede the feedback between experiment and theory. One such gap occurs just before californium at the element berkelium. Berkelium has no long-lived isotopes that can be isolated. The only accessible isotope is ^{249}Bk, with a half-life of only 320 days. Compounds that contain isotopes with half-lives of less than hundreds of thousands of years undergo rapid degradation because of the high energetics and ionization nature of nuclear decay processes that can be up to a million times larger than the strength of any chemical bond.

Although measurements and crystal-field modeling of the optical spectra of aqueous solutions of Bk(III), as well as solid-state samples doped with low levels of Bk(III) and Bk(IV), have been reported (*11*–*13*), single-crystal x-ray analysis of a berkelium compound proved elusive (*14*–*16*). Spectroelectrochemical measurements of berkelium's speciation in aqueous media have been accomplished using x-ray absorption spectroscopy and provided evidence that a break in the trend of complexation with actinides might begin at berkelium (*17*). This latter study points to the need for obtaining high-resolution structural data for berkelium compounds to investigate whether a transition also occurs in the solid state (*18*–*20*). Furthermore, the optical measurements obtained from hydrated Bk(III), $LnCl_3$:Bk (where Ln is generic for lanthanide), and CeF_4:Bk do not reveal the full range of the effects of ligation on the electronic properties of Bk(III) because water and chloride coordination induce relatively small electronic perturbations (*11*–*13*, *20*). Data fitting using early crystal-field models, based on electrostatic interactions between point

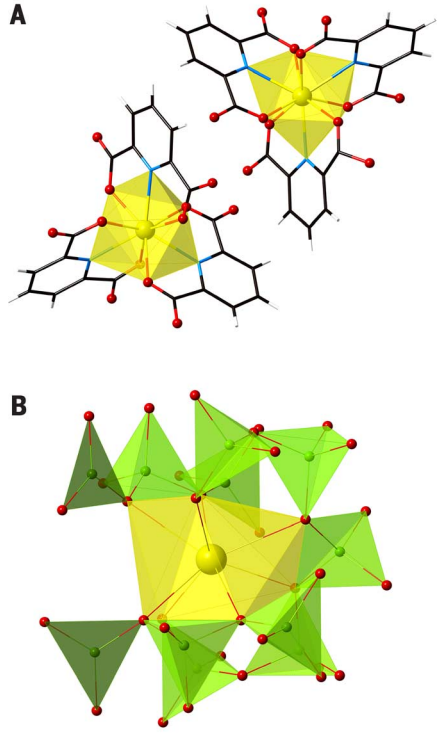

Fig. 1. Crystallography. (**A**) Views of the Λ (lower left) and Δ (upper right) enantiomers of Bk(HDPA)$_3$, showing the tricapped trigonal prismatic N_3O_6 coordination around Bk(III). (**B**) Depiction of the distorted square antiprismatic geometry of Bk(III) in Bk[$B_6O_8(OH)_5$].

[1]Department of Chemistry and Biochemistry, Florida State University, Tallahassee, FL 32306, USA. [2]Environmental Health and Safety, Florida State University, Tallahassee, FL 32306, USA. [3]National High Magnetic Field Laboratory, Tallahassee, FL 32310, USA. [4]Department of Chemistry and Geochemistry and Department of Nuclear Engineering, Colorado School of Mines, Golden, CO 80401, USA. [5]Department of Chemistry and Biochemistry, Bloomsburg University of Pennsylvania, Bloomsburg, PA 17815, USA. [6]Chemical Sciences and Engineering Division, Argonne National Laboratory, Argonne, IL 60439, USA. [7]Nuclear Materials Processing Group, Oak Ridge National Laboratory, One Bethel Valley Road, Oak Ridge, TN 37830, USA. [8]Laboratorie de Physique et Chimie des Nano-objets, Institut National des Sciences Appliquées, 31077 Toulouse Cedex 4, France. [9]Department of Chemistry, University at Buffalo, State University of New York, Buffalo, NY 14260, USA. [10]Institut für Anorganische Chemie, Rheinisch-Westfälische Technische Hochschule, Aachen University, D-52074 Aachen, Germany. [11]Theory Division, Los Alamos National Laboratory, Los Alamos, NM 87545, USA.
*These authors contributed equally to this work. †**Corresponding author. Email: jbraley@mines.edu (J.B.); albrecht-schmitt@chem.fsu.edu (T.E.A.-S.)**

Downloaded from http://science.sciencemag.org/ on September 3, 2016

charges, did not account for the possible involvement of the frontier orbitals in bonding (*21*).

For meaningful comparisons to be made between the chemistry of berkelium and other actinides, two divergent systems were selected for investigation. The first of these is an archetypal coordination complex that forms via the chelation of An^{3+} cations by 2,6-pyridinedicarboxylate [dipicolinate (DPA)] yielding $An(HDPA)_3{\cdot}nH_2O$ in the solid state (An is Pu, Am, Cm, Bk, or Cf) or $[An(DPA)]^+$, $[An(DPA)_2]^-$, and $[An(DPA)_3]^{3-}$ in solution (*6*, *19*, *22*–*24*). These complexes have a predictable coordination environment (a feature often absent in the *f* block), and serve as a benchmark for examining trends in bond distances, spectroscopy, and thermodynamics. The second system is one that has proven to be exquisitely sensitive to the nature of the actinide ions employed in the reaction. In this case, we have shown that polyborates form unique structural topologies with each of the different actinide ions from Pu(III) to Cf(III) (*7*–*9*, *25*).

Experiments with milligram quantities of ^{249}Bk were choreographed for 6 months before the arrival of the isotope because the total quantity used in the studies was 13 mg, which corresponds to a staggering activity of 21 Ci. Although this isotope is a low-energy β emitter, it decays to ^{249}Cf at a rate of ~1.2% per week, and the latter produces hard γ radiation that represents a serious external hazard. In addition, the samples described in this work undergo ~10^{12} decays per second. This rapid decomposition necessitated the development of techniques for swiftly preparing and encapsulating samples and collecting all structural and spectroscopic data within 24 hours of crystal formation. Crystals of these compounds underwent Coulombic explosions within 4 days, although they did not exhibit the color changes that often occur with high specific activity α emitters (*6*). With the exception of the magnetic susceptibility measurements, all of the data described below were acquired from isolated single crystals.

Synthesis

$^{249}BkCl_3{\cdot}nH_2O$, freshly prepared at the High Flux Isotope Reactor at Oak Ridge National Laboratory, was treated with a five-fold excess of dipicolinic acid in a 1:1 water:ethanol mixture. The initial solution was lime green and emitted faint green light as the result of electronic excitation from the high specific activity of ^{249}Bk (i.e., self-luminescence). The addition of DPA resulted in an immediate color change and precipitation of a golden-yellow crystalline product. Mild heating of the reaction mixture led to ripening of the microcrystals and formation of golden crystals of $Bk(HDPA)_3{\cdot}nH_2O$ with an approximate hexagonal prismatic shape (see fig. S1). Much like the reaction with Cf(III) (*6*), the precipitation of $Bk(HDPA)_3{\cdot}nH_2O$ was nearly quantitative, and little Bk(III) remained in solution at the end of the reaction. This sharply contrasts with curium(III), where a substantial portion of the ^{248}Cm remained in solution in the form of $[Cm(HDPA)(H_2DPA)(H_2O)_2Cl]^+$ (*20*).

Crystallography

Single-crystal x-ray diffraction studies revealed that $Bk(HDPA)_3{\cdot}nH_2O$ is isomorphous with the other members of the trivalent lanthanide and actinide series (table S1) (*6*). In short, the Bk(III) ions are complexed by three tridentate, monoprotonated dipicolinate ligands, constituting a nine-coordinate, tricapped, trigonal prismatic coordination environment with approximate D_3 symmetry. The nitrogen atoms from the pyridine rings are located in the capping positions, and the oxygen atoms from the carboxylate anions fill the six prismatic sites. Tris-chelate complexes, where the metal center is octahedral or nine-coordinate, are chiral. The two enantiomers are designated Δ and Λ, and unless stereoselective processes are involved, a racemic mixture of both enantiomers should be present in every system. $Bk(HDPA)_3{\cdot}nH_2O$ crystallizes in a centrosymmetric space group, indicating that a racemic mixture is present. In addition, a hydrogen-bonding network is present between the cocrystallized water molecules and the berkelium complexes. These interactions cause minor distortions of the local coordination around the Bk(III) centers. Each enantiomer is present in the structure in two distinct positions (see Δ and Δ′ in Table 1), one more distorted than the other because of these intermolecular interactions. A view of the Δ and Λ enantiomers is shown in Fig. 1A. Table 2 highlights bond distance changes in the tris(dipicolinate) series spanning Am(III) through Cf(III).

The preparation of Bk(III) borate followed the same procedure used for preparing all other An(III) borates (An is Pu, Am, Cm, or Cf) (*9*, *25*–*27*) and yielded golden tablets of $Bk[B_6O_8(OH)_5]$ (see fig. S2). The synthesis and crystal growth of $Bk[B_6O_8(OH)_5]$ required 10 days during which time nearly 2% of the ^{249}Bk converted to ^{249}Cf. We initially posited that this compound would remain stable under

Table 1. Selected bond lengths (Å) for $An(HDPA)_3$ (An is Am, Cm, Bk, or Cf) complexes.

	Am Δ	Cm Δ	Bk Δ	Cf Δ		Am Δ′	Cm Δ′	Bk Δ′	Cf Δ′
O13	2.472(3)	2.462(3)	2.457(3)	2.455(4)	**O1**	2.507(3)	2.496(3)	2.483(3)	2.476(4)
O14	2.491(3)	2.483(3)	2.455(3)	2.443(4)	**O2**	2.441(3)	2.433(3)	2.414(3)	2.413(4)
O15	2.430(3)	2.417(3)	2.410(3)	2.387(4)	**O3**	2.405(3)	2.389(3)	2.372(3)	2.363(3)
O16	2.468(3)	2.459(3)	2.440(3)	2.422(3)	**O4**	2.512(3)	2.501(3)	2.482(3)	2.476(3)
O17	2.516(3)	2.508(3)	2.497(3)	2.494(4)	**O5**	2.494(3)	2.480(3)	2.464(3)	2.441(3)
O18	2.499(3)	2.481(3)	2.433(3)	2.411(4)	**O6**	2.457(3)	2.448(3)	2.437(3)	2.417(4)
N1	2.550(4)	2.533(4)	2.512(4)	2.512(4)	**N2**	2.556(3)	2.520(4)	2.533(4)	2.518(4)
N3	2.551(4)	2.536(4)	2.518(4)	2.508(4)	**N4**	2.531(4)	2.535(4)	2.503(4)	2.506(4)
N5	2.591(3)	2.581(4)	2.558(4)	2.545(4)	**N6**	2.573(4)	2.569(4)	2.542(4)	2.526(4)

Table 2. Comparison of bond lengths (Å) between the Δ and Δ′ molecules of $An(HDPA)_3$ (An is Am, Cm, Bk, or Cf) complexes.

	Am Δ	Cm Δ	Bk Δ	Cf Δ	Am Δ′	Cm Δ′	Bk Δ′	Cf Δ′
Longest An-O	2.515(4)	2.509(4)	2.457(3)	2.494(4)	2.519(4)	2.501(4)	2.483(3)	2.477(4)
Shortest An-O	2.431(4)	2.416(4)	2.410(3)	2.386(4)	2.401(4)	2.388(4)	2.372(3)	2.363(4)
Average An-O	**2.482(4)**	**2.468(4)**	**2.449(3)**	**2.436(4)**	**2.468(4)**	**2.457(4)**	**2.442(3)**	**2.431(4)**
Longest An-N	2.589(4)	2.582(4)	2.558(4)	2.545(4)	2.573(4)	2.566(4)	2.542(4)	2.526(4)
Shortest An-N	2.551(4)	2.532(4)	2.512(4)	2.508(4)	2.532(4)	2.519(4)	2.503(4)	2.506(4)
Average An-N	**2.564(4)**	**2.550(4)**	**2.529(4)**	**2.522(4)**	**2.554(4)**	**2.540(4)**	**2.526(4)**	**2.517(4)**

Downloaded from http://science.sciencemag.org/ on September 3, 2016

steady β emission, but the buildup of positive charge in the crystals led to violent fracture within 4 days of isolation. Bk[$B_6O_8(OH)_5$] has the same formula but is not isomorphous with Cf [$B_6O_8(OH)_5$] (table S1), but distinct from all other actinide borates previously synthesized. The Bk(III) ions are present as eight-coordinate, distorted square antiprisms (Fig. 1B), in contrast to the nine- and ten-coordinate motifs in the Pu(III), Am(III), and Cm(III) borates (*9*, *25*–*27*).

Thermodynamics of complexation

The thermodynamics of Bk(III) complexation with dipicolinic acid are presented in Table 3, with the association constants presented in table S2. The Bk(III) β_{101} [$Bk(DPA)^+$], β_{102} [$Bk(DPA)_2^-$], and β_{103} [$Bk(DPA)_3^{3-}$] constants at 25°C and 1.0 M ionic strength are larger than values reported for Sm(III), Eu(III), or Gd(III). These lanthanides have ionic radii comparable to those proposed for Bk(III) (*28*). The enthalpic binding contribution for the berkelium 1:3 DPA complex is more exothermic than observed with any of the lanthanide dipicolinic acid complexes (*23*). The 1:1 and 1:2 complexes are comparable or slightly more exothermic than other lanthanide DPA complexes.

The correlation between coordination exothermicity and degree of bonding covalency is a subject of current debate. Comparisons of the interactions of aromatic nitrogen donors with Nd(III) and Am(III), using 2-amino-4,6-di-(pyridin-2-yl)-1,3,5-triazine (ADPTZ) have been assessed (*28*–*31*). The ADPTZ studies show the formation of the Am(III)-ADPTZ complex to be 9 kJ·mol^{-1} more exothermic than the Nd(III)-ADPTZ complex. When the thermodynamics of the 1:3 berkelium and samarium DPA complexes are considered, a $\Delta(\Delta H)_{Bk/Sm}$ for the 1:3 metal:dipicolinic acid complex of 9 kJ·mol^{-1} is observed.

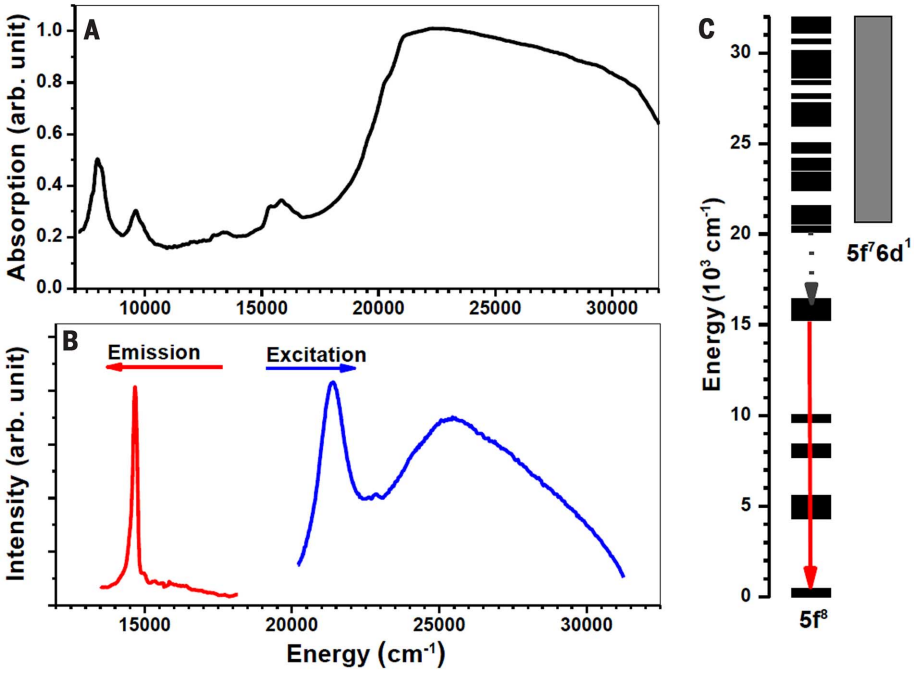

Fig. 2. Optical spectra of Bk(HDPA)$_3$·*n*H$_2$O obtained from a single crystal. (**A**) Room-temperature absorption. (**B**) Photoluminescence spectrum upon excitation at 420 nm (at 110 K) and excitation spectra monitored at 670 nm. (**C**) Predicted energy levels of 5f^8 and 5$f^7$6*d* states of Bk(III) in DPA and assignment of the 680-nm photoluminescence.

Table 3. Thermodynamic parameters for Bk(III)-dipicolinic acid complexation at 1.0 M ionic strength and various temperatures (in molality).

Temperature (°C)	Log β_{101}	Log β_{102}	Log β_{103}
5	9.30(9)	17.65(4)	23.90(2)
15	9.15(3)	17.50(2)	23.45(7)
25	9.07(7)	17.23(2)	23.14(1)
45	8.8(1)	16.85(6)	22.43(4)
ΔH (kJ mol^{-1})	−19(1)	−36(1)	−64(3)
ΔS (J mol^{-1} K^{-1})	108(5)	209(3)	230(10)

Experimental electronic structure analysis

The absence of the greenish self-luminescence of Bk(III) upon complexation by DPA is an indication of increased ion-ligand interactions that alter Bk(III) electronic structure and transition dynamics. Absorption, excitation, and photoluminescence spectra are shown in Fig. 2 and in figs. S3 and S4. The low-lying energy levels (<20,000 cm^{-1} or 2.5 eV) of the 5f^8 electronic states do not differ grossly from the corresponding states in the aquo complex (*11*), indicating relatively small changes in ligand-field splitting. Similar to the *5f* photoluminescence in Cm(HDPA)$_3$ (*6*, *20*), the narrowband emission near 14,700 cm^{-1} (680 nm) most likely arises from an intra-5f^8 transition. As shown in Fig. 2C, the 5000 cm^{-1} energy gap between the emitting state and the next 5f^8 state is critical for the red luminescence to be competitive with nonradiative phonon relaxation, whereas the smaller gap of ~35,000 cm^{-1} above the emitting state effectively eliminates green luminescence from the excited state near 20,000 cm^{-1} (*11*, *12*).

However, starting from 21,000 cm^{-1} in the blue and ultraviolet (UV) region, a broad band lacking *5f* characteristics appears in the absorption and excitation spectra. The *6d* levels of Bk(III) are much lower in energy than those of Am(III) or Cf(III) with the same ligands (*8*, *11*, *12*, *32*), and we attribute this transition in the Bk(III) spectra to 5f^8 to 5f^7 6*d* transitions. The narrow and intense peak at 21,350 cm^{-1} in the excitation spectrum has an energy and bandwidth consistent with the scheme of the 5f^8 states but an intensity on the same scale as the parity allowed *5f*-*6d* transitions. These observations are consistent with crystal-field induced coupling of the *5f* and *6d* orbitals, which is expected in a molecule with D_3 symmetry (*11*, *12*). The overlap of the 5f^8 and 5$f^7$6*d* states enhances this orbital hybridization. The low-lying *6d* states and the enhanced *5f*-*6d* hybridization contribute to Bk(III)-ligand bonding and coordination and therefore, put Bk(III) in a unique position in the heavy actinide group. These studies also provide a direct comparison between Bk(III) photoluminescence and the in-growth of Cf(III)-based luminescence. The latter is ligand-to-metal charge transfer–based and is therefore an allowed transition. In contrast, although the *5f*/*6d* mixing does provide some relaxation of the selection rules and hence greater intensity than a pure intra-*f* transition, the intensity from the Cf(III) is larger than that of the Bk(III) despite a sample composition of ~97% ^{249}Bk and only ~3% ^{249}Cf.

Magnetic properties

To further elucidate the ligand-field effects on Bk(III), as well as enhance our understanding of electronic structure, magnetic susceptibility data were measured in the 4 to 300 K temperature

Downloaded from http://science.sciencemag.org/ on September 3, 2016

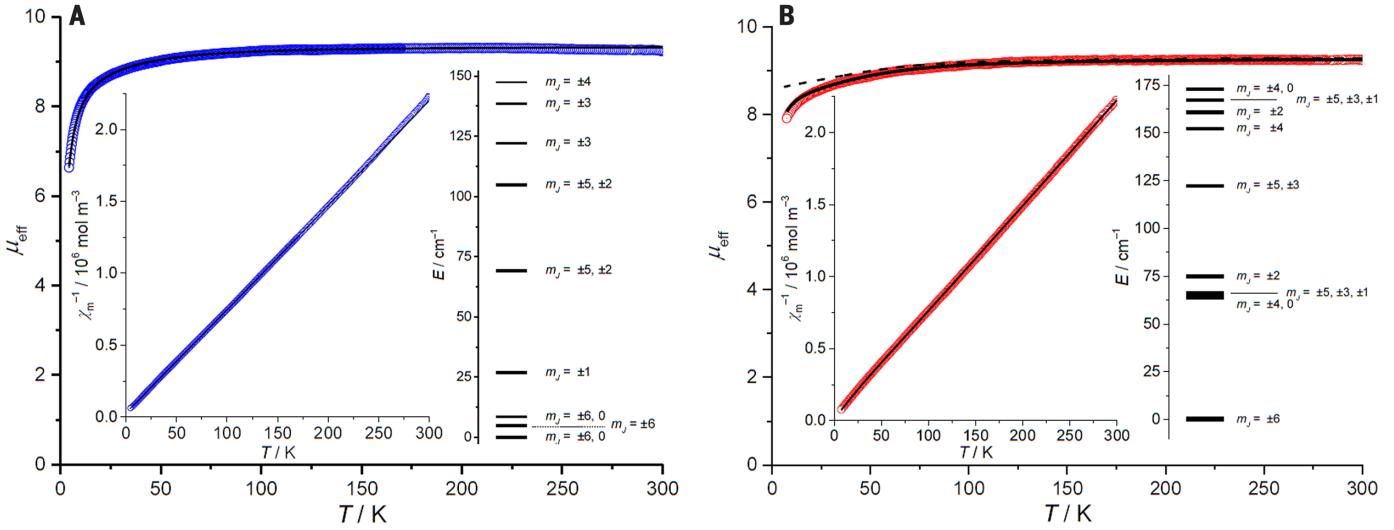

Fig. 3. Magnetic properties. Magnetic moment μ_{eff} versus T and inverse susceptibility versus T (inset) of polycrystalline samples of (**A**) Bk(HDPA)$_3$·nH$_2$O and (**B**) Bk[B$_6$O$_8$(OH)$_5$] at 1 kOe. Open circles, experimental data; solid black lines, least-squares fits to full model Hamiltonian. The energy-level diagrams display the splitting of the lowest multiplet states and their composition. The dashed black line represents the single-ion contribution of the Bk(III) centers in Bk[B$_6$O$_8$(OH)$_5$] in the absence of (antiferromagnetic) coupling interactions.

range for Bk(HDPA)$_3$·nH$_2$O and 7 to 300 K range for Bk[B$_6$O$_8$(OH)$_5$] under an applied field of 1 kOe (Fig. 3). The experimental μ_{eff} values of 9.24 μ_B {Bk[B$_6$O$_8$(OH)$_5$]} and 9.27 μ_B [Bk(HDPA)$_3$·nH$_2$O] at 300 K are close to the simulated value of 9.32 μ_B derived from spectroscopic data by Carnall (*12*). The susceptibility data were fitted to a full-model Hamiltonian (*33*), where the relevant spin-orbit coupling parameter (ζ = 3210 cm^{-1}) and Slater-Condon parameters (F^2 = 57,697 cm^{-1}, F^4 = 45,969 cm^{-1}, and F^6 = 32,876 cm^{-1}) were chosen on the basis of the optical spectra of BkCl$_3$ (*11*, *12*) and used as constants. To restrict the number of independent ligand-field parameters, a least-squares fit of the magnetic data for Bk(HDPA)$_3$·nH$_2$O requires assumption of an idealized C_{3v} symmetry for the BkN$_3$O$_6$ coordination sphere. Initial sets of most ligand-field (B^k_q) (Wybourne notation) parameters were again adopted from spectroscopically determined energy levels for BkCl$_3$; the Bk^{3+} site symmetry reduction from D_{3h} (BkCl$_3$) to C_{3v} mandates two additional ligand-field parameters (B^4_3 and B^6_3). The signs of the B^k_q values were assigned from point-charge electrostatic model calculations for a regular tricapped trigonal prism and fixed throughout the fitting procedure. This approach resulted in a near-perfect fit (quality of fit, SQ = 0.5%), yielding a ligand field characterized by B^2_0 = 59 cm^{-1}, B^4_0 = −870 cm^{-1}, B^4_3 = 150 cm^{-1}, B^6_0 = −2310 cm^{-1}, B^6_3 = −420 cm^{-1}, and B^6_6 = 800 cm^{-1}. The composition of the ground term [^7F (70%); ^5G (23%)] is in good agreement with CASSCF-SO results (vide infra). The total splitting of the J = 6 ground state into m_J substates amounts to 147.9 cm^{-1}, with a small energy gap of 4.9 cm^{-1} between the ground state and the first excited state. The observed temperature dependence of μ_{eff} ($\sim T^{1/2}$) below 15 K arises from the composition of the ground state (mixture of 50% m_J = 0 and 50% m_J = 6 states), not from exchange interactions.

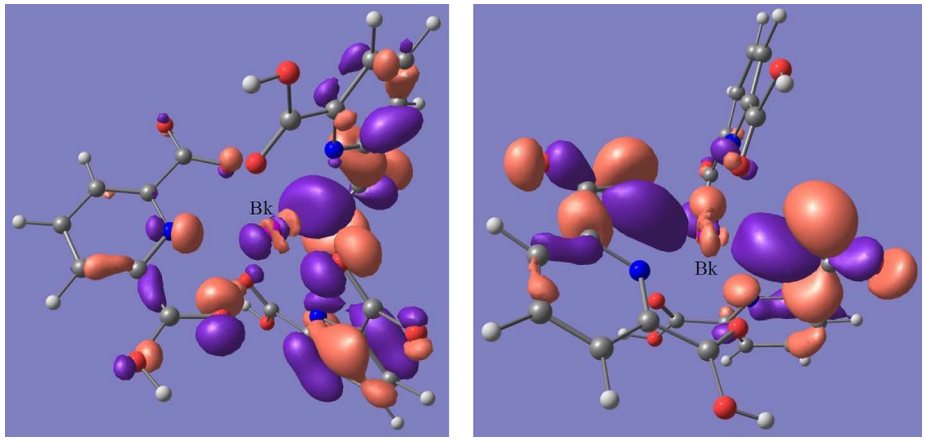

Fig. 4. Illustrations of some of the molecular orbitals involved in bonding in Bk(HDPA)$_3$. These orbitals are singly occupied molecular orbital (SOMO)−11 (left) and SOMO-12 (right). The involvement of the 5f_{z^3} orbital in SOMO-11 should be noted.

For Bk[B$_6$O$_8$(OH)$_5$], bridging borate anions provide exchange pathways between neighboring Bk^{3+} centers; therefore, 5*f*-5*f* coupling interactions were assumed to be significant and were accounted for in a molecular-field approach. Approximating the distorted square-antiprismatic geometry of the BkO$_8$ environments as C_4-symmetric, an analogous least-squares fit (SQ = 0.7%) then yielded B^2_0 = 140 cm^{-1}, B^4_0 = −910 cm^{-1}, B^4_4 = −550 cm^{-1}, B^6_0 = 460 cm^{-1}, B^6_4 = −860 cm^{-1}, and the molecular-field parameter λ_{mf} = −9400 mol m^{-3} (corresponding to a Weiss temperature of −1.3 K). In comparison to Bk(HDPA)$_3$·nH$_2$O, the composition of the ground term [^7F (73%); ^5G (24%)] is nearly identical; however, the ground state multiplet here is exclusively composed of the m_J = 6 states. The total splitting of the $^7F_6$ Russell-Saunders ground state amounts to 173 cm^{-1}, with a very low separation (0.4 cm^{-1}) between ground and first excited state (Fig. 3).

Theoretical electronic structure analysis

To further understand the bonding in Bk(HDPA)$_3$, the electronic structure was analyzed using a variety of computational approaches. At the density functional theory (DFT) level (B3PW91) (*34*, *35*), geometry optimizations were carried out separately on both independent molecules in the asymmetric unit (tables S3 and S4). The optimized structures are in good agreement with those observed crystallographically, affirming the capability of DFT to reproduce geometry and bond distances even for elements as heavy as berkelium. These calculations were also repeated with the Cm(III) and Cf(III) analogs, with the specific goal of examining trends in the bond distances. These data are provided in table S5. The bonding situation, although similar for both Δ and Δ′, was analyzed by scrutinizing the molecular orbitals with a focus on the berkelium atomic

Downloaded from http://science.sciencemag.org/ on September 3, 2016

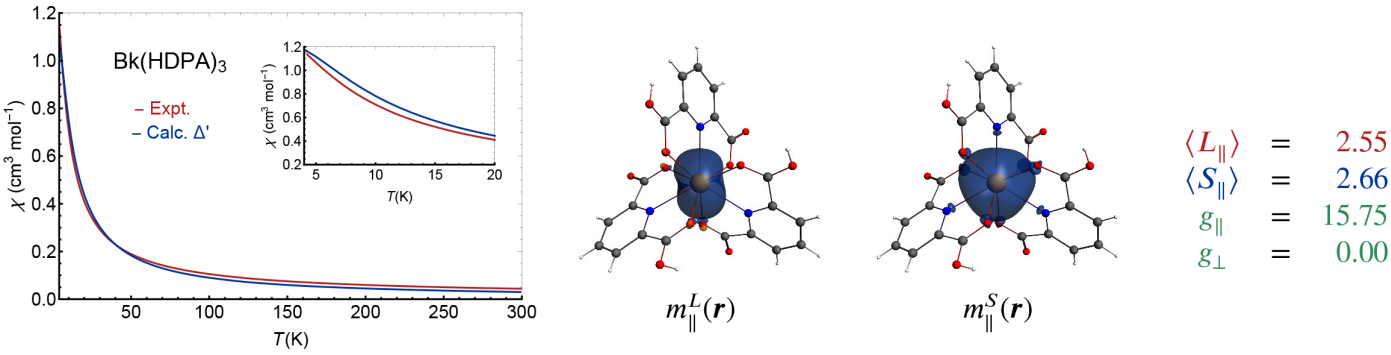

Fig. 5. Calculated magnetic susceptibility χ(*T*) for the Δ′ structure. CASSCF-SO calculations. Orbital ($m_{\|}^{L}$) and spin ($m_{\|}^{S}$) magnetization isosurfaces and *g* factors for the ground-state doublet, calculated using the method described in (*36*) from the septet states only. Doublet components with $\langle S_{\|} \rangle > 0$ along the easy magnetic axis.

orbitals involved in the bonding. Among others, the two highest bonding orbitals are depicted in Fig. 4. In particular, the $5f_{z^3}$ orbital is delocalized with a 2*p* orbital from a carboxylate oxygen atom. These orbitals involve hybrid 7*s*/6*d*/5*f* orbitals on berkelium and are consistent with the energetic availability of the 6*d* orbitals. Therefore, to probe the contribution of the 6*d* orbitals to bonding, an *f*-in-core calculation, as applied to lanthanides, was carried out. In this calculation, the $5f^8$ configuration is kept frozen in the core of the relativistic effective core potential (RECP) so that the 5*f* orbital cannot participate in bonding. In the latter calculation, the bonding situation is very similar to that described in Fig. 4 (see fig. S5), indicating that the 6*d* orbitals are crucial to describing the bonding in $Bk(HDPA)_3$, as is often true in actinide compounds.

The electronic structure and magnetic properties of $Bk(HDPA)_3$ were also probed using relativistic all-electron multireference wave-function theory, including spin-orbit (SO) coupling (see the supplementary materials). The lowest-energy level of the free Bk^{3+} ion is $^7F_6$, with $L = 3, S = 3$, and $J = L + S = 6$. An idealized D_3 symmetric ligand environment would split the 13-fold degeneracy $(2J + 1)$ into four non-Kramers doublets (*E*) and five singlets (*A*). The SO interaction mixes ion levels with the same $J = 6$. The calculated electronic states deriving from the $^7F_6$ level are characterized in Table 4 for the 100 K Δ′ structure. The ground state corresponds to a non-Kramers doublet that is slightly split due to the distorted D_3 geometry in the crystal. An admixture (~17%) of states from the excited $^5G_6$ level of the ion contributes to each entry in Table 4 (table S6 and fig. S7). The fact that these states derive mainly from the $^7F_6$ and $^5G_6$ levels indicates that for the 5*f* shell the ligand-field interactions are secondary to the SO coupling, in line with the 5*f*-in-core DFT results. The split Δ′ ground-state doublet can be described by a pseudo-spin ½ Hamiltonian with a large electronic *g* factor along the magnetic axis ($g_{\|} = 15.65$). As shown in Fig. 5, the calculated orbital (*L*) and spin (*S*) angular momentum are parallel, as expected, leading to a ground state with a large magnetic anisotropy. The calculated magnetic susceptibility $\chi(T)$ is in reasonable agreement with the experimental data (Fig. 5, inset). Due to the relatively small energetic spread of the states derived from the $^7F_6$ level (417 cm^{-1}) from the ligand field, χ reflects contributions from several electronic states even at relatively low *T*. See figs. S8 and S9 for comparative results of Δ structure.

Terbium represents the closest analog of berkelium because the trivalent cations possess $4f^8$ and $5f^8$ configurations, respectively. However, the distinct electronic properties of these elements is attributable to several factors. First, the $5f_{z^3}$ orbital of Bk(III) overlaps with the 2*p* orbital on the oxygen atoms in the dipicolinate ligands. This covalency is absent with the 4*f* orbitals of Tb(III). These ligand-field effects, however, are secondary to spin-orbit coupling in Bk(III) that creates mixing of the first excited state ($^5G_6$) with the ground state. In contrast, the ground state of $Tb(HDPA)_3$ contains negligible contributions of this type. Furthermore, although spin-orbit coupling also dominates the electronic structure of Cf(III), the magnitude of ligand-field splitting can be an order of magnitude larger in Cf(III) than in Bk(III). Ligand-field effects on berkelium are much more similar to that of curium. Hence, although the structural chemistry of berkelium is akin to that of californium, its electronic structure is more similar to that of earlier actinides.

Materials and methods

Syntheses

Caution! ^{249}Bk ($t_{1/2}$ = 320 d; specific activity = $1.6 \cdot 10^3$ Ci/g) β-decays to ^{249}Cf ($t_{1/2}$ = 351 y; activity = 4.1 Ci/g), which represents a serious external hazard because of its γ-emission (0.388 MeV). There is also a small α-decay branch for ^{249}Bk that yields ^{245}Am. While this does not contribute in a meaningful way to hazards, ^{245}Am β-decays to ^{245}Cm. Reports attributing luminescence near 600 nm to a second ^{249}Bk emission feature in the red are in error. This peak is from ^{245}Cm (*38*). All studies with transuranium elements were conducted in a laboratory dedicated to these studies. This laboratory is equipped with HEPA filtered hoods and negative pressure glove boxes that are ported directly into the hoods. A series of counters continually monitor radiation levels in the laboratory. The laboratory is licensed by the State of Florida (an NRC-compliant state). All experiments were carried out with approved safety operating procedures. All free-flowing solids were worked with in glove boxes, and products were only examined when coated with either water or Krytox oil. Thick lead sheets, respirators, and long lead vests were used as much as possible to shield researchers from radiation.

2,6-Pyridinedicarboxylic acid (99%, Sigma-Aldrich), ethanol (100%, Koptec), hydrobromic acid (ACS reagent 48%, Sigma-Aldrich), and berkelium (^{249}Bk) obtained from ORNL in the form of $BkCl_3$ were used without further purification. PTFE-lined Parr 4749 autoclaves with a 10 mL internal volume, and Millipore water were used in all of the following reactions. All solvents that were used in a glove box were sparged with argon.

$Bk(HDPA)_3 \cdot nH_2O$

Bk (4.33 mg, 0.0173 mmol) in the form of $BkCl_3$ was combined with an excess of DPA (17.2 mg, 0.1029 mmol) in 200 μL of a 1:1 mixture of ethanol and water. The reaction mixture was heated in a PTFE-lined Parr 4749 autoclave with a 10 mL internal volume for 4 hours at 150°C, and then slowly cooled to 40°C over a 22-hour period. The reaction was performed inside a negative-pressure glovebox that was surrounded by thick lead sheets. The reaction yielded gold-yellow crystals that had both hexagonal prismatic and columnar habits (see fig. S1).

$Bk[B_6O_8(OH)_5]$

Bk (4.33 mg, 0.0173 mmol) in the form of $BkCl_3$ was dissolved in deionized water (30 mL) and transferred to a PTFE-lined Parr 4749 autoclave with a 10 mL internal volume. Boric acid (69.6 mg, 1.125 mmol) was added to the autoclave, and the reaction mixture was heated to 240°C for seven days. The reaction was cooled slowly over the course of three days. The product was washed with deionized water to dissolve the excess flux and yield small, yellow-orange crystals with a tablet habit (see fig. S2).

Crystallographic studies

Single crystals of $Bk_2(HDPA)_6 \cdot 3H_2O$ and $Bk[B_6O_8(OH)_5]$ were glued to Mitegen mounts with epoxy and optically aligned on a Bruker D8 Quest x-ray diffractometer using a digital camera. Initial

Downloaded from http://science.sciencemag.org/ on September 3, 2016

Table 4. Calculated energetic splitting (cm^{-1}) of the low-energy electronic states of $Bk(HDPA)_3$ and characterization of the wave functions in terms of Bk^{3+} ion levels.

Δ′ Structure

State*	ΔE	$g_{\parallel}$†
E	0	15.65
	10	
A	74	
A	114	
A	126	
A	173	
A	185	
E	275	16.83
	278	
E	357	12.61
	368	
E	410	14.43
	417	

*The 13 SO states correspond here to an admixture of 82 and 17% of the states deriving from the ion $^7F_6$ and $^5G_6$ levels, respectively. †Electronic g factors for pseudospin $\tilde{S} = 1/2$ with $g_{\perp} = 0$, obtained with the approach of (*37*).

intensity measurements were performed using a IμS x-ray source (Mo$K\alpha$, λ = 0.71073 Å) with high-brilliance and high-performance focusing multilayered optics. APEXII software was used for determination of the unit cells and data collection control. The intensities of reflections of a sphere were collected by a combination of multiple sets of exposures (frames). Each set had a different φ angle for the crystal and each exposure covered a range of 0.5° in ω. Both data collections presented in this paper were taken using a set of standard hemispheres. Single crystals of each compound were run both at room temperature and 100 K. The SAINT software was used for data integration including Lorentz and polarization corrections. The structure was solved by direct methods and refined on F^2 by full-matrix least squares techniques using the program suite SHELX (tables S1 and S2). Parameters for Bk are not present in the SHELX software and have to be inputted manually. Solutions were checked for missed symmetry using PLATON (*39*).

UV–vis-NIR spectroscopy

Single crystals of each compound were placed on separate quartz slides under Krytox oil. The slide was kept inside a Linkam temperature control stage for an extra layer of containment throughout all the measurements. Using a Craic Technologies 20/20 microspectrophotometer the data were collected from 250 to 1700 nm (fig. S3). The exposure time was auto-optimized by the Craic software. Photoluminescence data were collected using the same microspectrophotometer with excitation wavelengths of 420 nm (fig. S4). The Linkam temperature control stage was used to control the temperature from room temperature down to 80 K.

Magnetic susceptibility measurements and magnetochemical modeling

Magnetism measurements were performed on polycrystalline samples using a Quantum Design VSM Magnetic Properties Measurement System under an applied field of 10 kOe for 4 K < 300 K, and for 0 < H < 70 kOe at T = 4 K and 50 K. The samples were sealed inside two different, custom-built Teflon capsules. The outermost capsule was also taped closed using Kapton. In order to extract the intrinsic magnetic behavior of the Bk-containing sample, we subtracted measurements of an empty capsule from those of the filled capsule. All magnetic parameters are given in SI units.

The dc-susceptibility data were analyzed with the program framework CONDON 2.0, employing a complete basis set (full f manifolds, i.e., 3,003 functions for Bk^{3+}) (*33*). Generally, a full model is required to accurately reproduce all magnetic aspects of $5f$ compounds, and CONDON accounts for all relevant single-ion effects, in particular the ligand-field effect (H_{lf}), interelectronic repulsion (H_{ee}), spin-orbit coupling (H_{so}), and the Zeeman effect of an applied field (H_{mag}). Whereas for $Bk(HDPA)_3{\cdot}nH_2O$, the nearest-neighbor Bk-Bk distances exceed 1.1 nm, which rules out significant coupling interactions, for $Bk[B_6O_8(OH)_5]$ exchange interactions between neighboring Bk^{3+} centers in the solid state are considered in the molecular field approximation

$$\chi_m^{-1} = \chi_m^{-1}(\zeta, F^2, F^4, F^6, B_q^k) - \lambda_{mf}$$

where χ_m is the single-center susceptibility and λ_{mf} is the molecular field parameter. Positive and negative values of λ_{mf} indicate dominant ferromagnetic and antiferromagnetic interactions, respectively.

As full model magnetic simulations of $5f^8$ systems had not been performed previously, we benchmarked the spin Hamiltonian implemented in CONDON against the more comprehensively parameterized model Hamiltonian used by Carnall for the interpretation of optical spectra of $TbCl_3$ ($4f^8$) and $BkCl_3$ ($5f^8$), where the M^{3+} ions reside in D_{3h}-symmetric ligand environments (*12*). Here, the ligand-field operator with reference to the threefold rotation axis for the angular part of the wave function reads

$$H_{lf}^{D3h} = \sum_{i=1}^{N} B_0^2 C_0^2(i) + \sum_{i=1}^{N} B_0^4 C_0^4(i) + \sum_{i=1}^{N} B_0^6 C_0^6(i) + \sum_{i=1}^{N} B_6^6 (C_{-6}^6(i) + C_6^6(i))$$

B^k_q parameter values from spectroscopically determined energy levels for $BkCl_3$ with D_{3h} symmetry were used as starting values in the magnetochemical fitting procedure. In order to highlight the differences between the $4f$ and $5f$ analogs, the $4/5f$ ions are first assumed as free ions, while both spin-orbit coupling and interelectronic repulsion are considered. This results in temperature-independent Bohr magneton numbers (μ_{eff}), where the lanthanide and actinide values clearly differ (fig. S6), with a simultaneous reduction of the main component in the Russell-Saunders ground term. The latter arises from an increase in spin-orbit coupling from $4f$ to $5f$ and admixture of excited terms into the ground term. Addition of the ligand-field effect then results in the characteristic temperature dependence of μ_{eff}. A critical implication is that a simple approximation like the Curie-Weiss law generally has no physical meaning for such actinide species: For both the free Bk^{3+} ion and the $BkCl_3$ simulation, the inverse molar susceptibility is linear in temperature (inset, fig. S6) over a broad temperature range, and the extrapolated plots do not pass through the origin. Note that a finite value of an apparent Weiss temperature θ in such cases cannot be interpreted as originating from exchange coupling. The Bk^{3+} multiplet energy levels resulting from the magnetic simulations match the energies derived from the crystal field analysis by Carnall with high accuracy (SQ = 2%), confirming that the full model spin Hamiltonian indeed reproduces the ligand-field splitting with the spectroscopically derived ligand-field parameterization.

Time-resolved emission, steady-state emission, and excitation spectra

Time-resolved emission, steady-state emission, and excitation spectra were collected at room temperature using an Edinburgh FLS980 spectrometer. The sample, between two microscope slide coverslips, was placed at a 45° angle relative to the excitation source and detector. For excitation and emission spectra, samples were excited using light output from a housed 450 W Xe lamp passed through a single grating (1800 l/mm, 250 nm blaze) Czerny-Turner monochromator. Emission from the sample was first passed through a 515 nm long-pass color filter, then a single grating (1800 l/mm, 500 nm blaze) Czerny-Turner monochromator and detected by a peltier-cooled Hamamatsu R928 photomultiplier tube. Time-resolved emission was monitored using the FLS980's time-correlated single-photon counting capability (1,024 channels; 5 μs window) with data collection for 10,000 counts. Excitation was provided by an Edinburgh EPL-445 picosecond pulsed diode laser (444.2 nm, 80 ps FWHM) operated at 200 kHz.

Acid association constants

The acid association constants of dipicolinic acid were assessed at appropriate temperatures to allow the calculation of free DPA^{2-} available for complexation. Titrations were performed manually using a Thermo/Ross semi-micro combination pH electrode. To allow work in $NaClO_4$ media, the filling solution of the electrode, originally potassium chloride (KCl) was replaced with 3.0 M sodium chloride (NaCl) to prevent potassium perchlorate ($KClO_4$) precipitation at the glass frit. Titrations were also maintained at 1.0 M ionic strength and were completed under a nitrogen atmosphere to prevent carbon dioxide

Downloaded from http://science.sciencemag.org/ on September 3, 2016

contamination. The measured mV data were converted to hydrogen ion concentrations using a mV versus pcH calibration curve generated in a strong acid-strong base titration of $HClO_4$ with NaOH at 1.0 M total ionic strength. All titrations were repeated in at least triplicate and data fitting was performed using the fitting program Hyperquad.

Extraction measurements

All complexation thermodynamics were assessed by using competitive solvent extraction investigations with bis-2-ethyl-hexyl-phosphoric acid (HDEHP) dissolved in *o*-xylene. The extraction constant (K_{Ex}) was assessed for berkelium at various temperatures. To assess β_{101}, β_{102}, and β_{103} metal-DPA stability constants, partitioning of berkelium and europium between the HDEHP/*o*-xylene organic phase and aqueous phase with increasing DPA concentration was measured. The ionic strength of the aqueous phase was maintained at 1.0 M using $NaClO_4$. All phases were pre-equilibrated with an appropriate aqueous or organic phase prior to use in the distribution study at the temperature of a given study. Pre-equilibration contact times were five minutes and contact times for thermodynamic measurements were fifteen minutes. The pcH of the aqueous phase was measured after contact by using a series of standardized acid solutions at 1 M $NaClO_4$. Conversions from molality were afforded by density determinations at 22°C. The partitioning of ^{249}Bk was monitored using a Packard 2500 Liquid Scintillation counter. All thermodynamic constants were fit in QtiPlot using nonlinear regression model weighting the distribution data (D values) using $w = 1/\sigma^2$ weighting. Metal K_{Ex} values were fitted assuming equilibria and mass balance relationships previously established in the literature (*24*).

DFT computational details

All the structures reported in this study were fully optimized with the Becke's three-parameter hybrid functional (*34*) combined with the non-local correlation functional provided by Perdew/Wang (denoted as B3PW91) (*35*). To represent the berkelium atom, a relativistic energy-consistent small-core pseudopotential obtained from the Stuttgart-Köln ECP library was used in combination with its adapted segmented basis set (*40*–*42*). For the *f*-in-core calculations in which the berkelium's oxidation state is fixed to +3, the corresponding 5*f*-in-large-core ECP (augmented by a *f* polarization function, $\alpha = 1.0$) was used (*43*). For the remaining atoms the 6-31G(d,p) basis set was used (*44*–*48*). In all computations, no constraints were imposed on the geometry. All stationary points have been identified as minima (number of imaginary frequencies $N_{imag} = 0$). The vibrational modes and the corresponding frequencies are based on a harmonic force field. Enthalpy energies were obtained at $T = 298.15$ K within the harmonic approximation. GAUSSIAN09 program suite was used in all calculations (*47*). Finally, for the 3D representation of the structures, the Chemcraft (*49*) program was used, as well as for the visualization of the molecular orbitals. For details regarding the CASSCF calculations, see the supplementary materials.

REFERENCES AND NOTES

1. T. K. Sato *et al*., Measurement of the first ionization potential of lawrencium, element 103. *Nature* **520**, 209–211 (2015). doi: 10.1038/nature14342; pmid: 25855457
2. J. Even *et al*., Synthesis and detection of a seaborgium carbonyl complex. *Science* **345**, 1491–1493 (2014). doi: 10.1126/science.1255720; pmid: 25237098
3. A. Bilewicz, S. Siekierski, Chemical studies of rutherfordium (Element 104): Part I. Thin film ferrocyanide surfaces for the study of the hydrolysis of rutherfordium. *Radiochim. Acta* **75**, 121–126 (1996). doi: 10.1524/ract.1996.75.3.121
4. N. J. Stoyer *et al*., Chemical identification of a long-lived isotope of dubnium, a descendent of element 115. *Nucl. Phys. A.* **787**, 388–395 (2007). doi: 10.1016/j.nuclphysa.2006.12.060
5. M. Janoschek *et al*., The valence-fluctuating ground state of plutonium. *Sci. Adv.* **1**, e1500188 (2015). doi: 10.1126/sciadv.1500188; pmid: 26601219
6. S. K. Cary *et al*., Emergence of californium as the second transitional element in the actinide series. *Nat. Commun.* **6**, 6827–6834 (2015). doi: 10.1038/ncomms7827; pmid: 25880116
7. T. Albrecht-Schmitt, Californium gleaming. *Nat. Chem.* **6**, 840 (2014). doi: 10.1038/nchem.2035; pmid: 25143222
8. G. Liu, S. K. Cary, T. E. Albrecht-Schmitt, Metastable charge-transfer state of californium(iii) compounds. *Phys. Chem. Chem. Phys.* **17**, 16151–16157 (2015). doi: 10.1039/C5CP01855B; pmid: 26032575
9. M. J. Polinski *et al*., Unusual structure, bonding and properties in a californium borate. *Nat. Chem.* **6**, 387–392 (2014). doi: 10.1038/nchem.1896; pmid: 24755589
10. S. Heathman, T. Le Bihan, S. Yagoubi, B. Johansson, R. Ahuja, Structural investigation of californium under pressure. *Phys. Rev. B* **87**, 214111–214118 (2013). doi: 10.1103/PhysRevB.87.214111
11. W. T. Carnall, J. V. Beitz, H. Crosswhite, Electronic energy level and intensity correlations in the spectra of the trivalent actinide aquo ions. III. Bk^{3+}. *J. Chem. Phys.* **80**, 2301–2308 (1984). doi: 10.1063/1.446980
12. W. T. Carnall, A systematic analysis of the spectra of trivalent actinide chlorides in D_{3h} site symmetry. *J. Chem. Phys.* **96**, 8713–8726 (1992). doi: 10.1063/1.462278
13. G. M. Jursich *et al*., Laser-induced fluorescence of $^{249}Bk^{4+}$ in CeF_4. *Inorg. Chim. Acta* **139**, 273–274 (1987). doi: 10.1016/S0020-1693(00)84093-1
14. J. H. Burns, J. R. Peterson, Crystal structures of americium trichloride hexahydrate and berkelium trichloride hexahydrate. *Inorg. Chem.* **10**, 147–151 (1971). doi: 10.1021/ic50095a029
15. P. G. Laubereau, J. H. Burns, Microchemical preparation of tricyclopentadienyl compounds of berkelium, californium, and some lanthanide elements. *Inorg. Chem.* **9**, 1091–1095 (1970). doi: 10.1021/ic50087a018
16. J. R. Peterson, J. P. Young, D. D. Ensor, R. G. Haire, Absorption spectrophotometric and x-ray diffraction studies of the trichlorides of berkelium-249 and californium-249. *Inorg. Chem.* **25**, 3779–3782 (1986). doi: 10.1021/ic00241a015
17. M. R. Antonio, C. W. Williams, L. Soderholm, Berkelium redox speciation. *Radiochim. Acta* **90**, 851–856 (2002). doi: 10.1524/ract.2002.90.12_2002.851
18. J. H. Burns, J. R. Peterson, R. D. Baybarz, Hexagonal and orthorhombic crystal structures of californium trichloride. *J. Inorg. Nucl. Chem.* **35**, 1171–1177 (1973). doi: 10.1016/0022-1902(73)80189-7
19. E. Galbis *et al*., Solving the hydration structure of the heaviest actinide aqua ion known: The californium(III) case. *Angew. Chem. Int. Ed.* **49**, 3811–3815 (2010). doi: 10.1002/anie.200906129; pmid: 20401881
20. S. K. Cary *et al*., Spontaneous partitioning of californium from curium: Curious cases from the crystallization of curium coordination complexes. *Inorg. Chem.* **54**, 11399–11404 (2015). doi: 10.1021/acs.inorgchem.5b02052; pmid: 26562586
21. M. L. Neidig, D. L. Clark, R. L. Martin, Covalency in f-element complexes. *Coord. Chem. Rev.* **257**, 394–406 (2013). doi: 10.1016/j.ccr.2012.04.029
22. B. Weaver, F. A. Kappelmann, TALSPEAK, A New Method of Separating Americium and Curium from the Lanthanides by Extraction from an Aqueous Solution of an Aminopolyacetic Acid Complex with a Monoacetic Organophosphate or Phosphonate; ORNL-3559, Oak Ridge National Laboratory: Oak Ridge, TN, 1964.
23. J. C. Braley, T. S. Grimes, K. L. Nash, Alternatives to HDEHP and DTPA for Simplified TALSPEAK Separations. *Ind. Eng. Chem. Res.* **51**, 629–638 (2012). doi: 10.1021/ie200285r
24. C. R. Heathman, K. L. Nash, Characterization of europium and americium dipicolinate complexes. *Sep. Sci. Technol.* **47**, 2029–2037 (2012).
25. M. J. Polinski *et al*., Differentiating between trivalent lanthanides and actinides. *J. Am. Chem. Soc.* **134**, 10682–10692 (2012). doi: 10.1021/ja303804r; pmid: 22642795
26. M. J. Polinski, S. Wang, E. V. Alekseev, W. Depmeier, T. E. Albrecht-Schmitt, Bonding changes in plutonium(III) and americium(III) borates. *Angew. Chem. Int. Ed.* **50**, 8891–8894 (2011). doi: 10.1002/anie.201103502; pmid: 21853508
27. M. J. Polinski *et al*., Curium(III) borate shows coordination environments of both plutonium(III) and americium(III) borates. *Angew. Chem. Int. Ed.* **51**, 1869–1872 (2012). doi: 10.1002/anie.201107956; pmid: 22246722
28. I. Grenthe, E. Jacobsen, E.-L. Syväoja, A. Alivaara, M. Trætteberg, Thermodynamic properties of rare earth complexes. II. Free energy, enthalpy, and entropy changes for the formation of rare earth diglycolate and dipicolinate complexes at 25.00 °C. *Acta Chem. Scand.* **17**, 2487–2498 (1963). doi: 10.3891/acta.chem.scand.17-2487
29. M. Miguirditchian *et al*., Thermodynamic study of the complexation of trivalent actinide and lanthanide cations by ADPTZ, a tridentate N-donor ligand. *Inorg. Chem.* **44**, 1404–1412 (2005). doi: 10.1021/ic0488785; pmid: 15732980
30. G. R. Choppin, Covalency in f-element bonds. *J. Alloys Compd.* **344**, 55–59 (2002). doi: 10.1016/S0925-8388(02)00305-5
31. J. A. Drader, M. Luckey, J. C. Braley, Thermodynamic considerations of covalency in trivalent actinide-(poly) aminopolycarboxylate interactions. *Solvent Extr. Ion Exch* **34**, 114–125 (2016). doi: 10.1080/07366299.2016.1140436
32. W. Wang, G. K. Liu, M. G. Brik, L. Seijo, D. Shi, 5f–6d Orbital hybridization of trivalent uranium in crystals of hexagonal symmetry: Effects on electronic energy levels and transition intensities. *Phys. Rev. B* **80**, 155120–155132 (2009). doi: 10.1103/PhysRevB.80.155120
33. J. van Leusen, M. Speldrich, H. Schilder, P. Kögerler, Comprehensive insight into molecular magnetism via CONDON: Full vs. effective models. *Coord. Chem. Rev.* **289-290**, 137–148 (2015). doi: 10.1016/j.ccr.2014.10.011
34. A. D. Becke, Density-functional thermochemistry. III. The role of exact exchange. *J. Chem. Phys.* **98**, 5648–5652 (1993). doi: 10.1063/1.464913
35. J. P. Perdew, Y. Wang, Accurate and simple analytic representation of the electron-gas correlation energy. *Phys. Rev. B Condens. Matter* **45**, 13244–13249 (1992). doi: 10.1103/PhysRevB.45.13244; pmid: 10001404
36. F. Gendron, B. Pritchard, H. Bolvin, J. Autschbach, Single-ion 4f element magnetism: An ab-initio look at $Ln(COT)_2^{(-)}$. *Dalton Trans.* **44**, 19886–19900 (2015). doi: 10.1039/C5DT02858B; pmid: 26510902
37. L. F. Chibotaru, L. Ungur, *Ab initio* calculation of anisotropic magnetic properties of complexes. I. Unique definition of pseudospin Hamiltonians and their derivation. *J. Chem. Phys.* **137**, 064112 (2012). doi: 10.1063/1.4739763; pmid: 22897260
38. I. Ahmad *et al*., α-Decay of $^{249}_{97}$Bk and levels in $^{245}_{95}$Am. *Phys. Rev. C Nucl. Phys.* **87**, 054328 (2013). doi: 10.1103/PhysRevC.87.054328
39. A. L. Spek, Single-crystal structure validation with the program PLATON. *J. Appl. Cryst.* **36**, 7–13 (2003). doi: 10.1107/S0021889802022112
40. W. Küchle, M. Dolg, H. Stoll, H. Preuß, Energy-adjusted pseudopotentials for the actinides. Parameter sets and test calculations for thorium and thorium monoxide. *J. Chem. Phys.* **100**, 7535–7543 (1994). doi: 10.1063/1.466847
41. X. Y. Cao, M. Dolg, H. Stoll, Valence basis sets for relativistic energy-consistent small-core actinide pseudopotentials. *J. Chem. Phys.* **118**, 487–497 (2003). doi: 10.1063/1.1521431
42. X. Cao, M. Dolg, Segmented contraction scheme for small-core actinide pseudopotential basis sets. *J. Mol. Struct. THEOCHEM* **673**, 203–209 (2004). doi: 10.1016/j.theochem.2003.12.015
43. A. Moritz, X. Y. Cao, M. Dolg, Quasirelativistic energy-consistent 5f-in-core pseudopotentials for divalent and tetravalent actinide elements. *Theor. Chem. Acc.* **118**, 845–854 (2007). doi: 10.1007/s00214-007-0330-6
44. W. J. Hehre, R. Ditchfield, J. A. Pople, Self—consistent molecular orbital methods. XII. Further extensions of gaussian—type basis sets for use in molecular orbital studies of organic molecules. *J. Chem. Phys.* **56**, 2257–2261 (1972). doi: 10.1063/1.1677527

Downloaded from http://science.sciencemag.org/ on September 3, 2016

45. P. C. Hariharan, J. A. Pople, The influence of polarization functions on molecular orbital hydrogenation energies. *Theor. Chim. Acta* **28**, 213–222 (1973). doi: 10.1007/BF00533485
46. J. S. Binkley, J. A. Pople, W. J. Hehre, Self-consistent molecular orbital methods. 21. Small split-valence basis sets for first-row elements. *J. Am. Chem. Soc.* **102**, 939–947 (1980). doi: 10.1021/ja00523a008
47. M. J. Frisch *et al.*, Gaussian 09, Revision A.02, Gaussian, Inc., Wallingford CT, (2009).
48. C. Lee, W. Yang, R. G. Parr, Development of the Colle-Salvetti correlation-energy formula into a functional of the electron density. *Phys. Rev. B Condens. Matter* **37**, 785–789 (1988). doi: 10.1103/PhysRevB.37.785; pmid: 9944570
49. G. A. Zhurko, D. A. Zhurko, ChemCraft Version 1.7. www.chemcraftprog.com (accessed May 2009).

ACKNOWLEDGMENTS

This material is based on work supported by the U.S. Department of Energy, Office of Science, Office of Basic Energy Sciences, Heavy Elements Chemistry Program under Award Number DE-FG02-13ER16414 (Florida State University) and DE-SC0012039 (Colorado School of Mines), and DE-SC0001136 (formerly DE-FG02-09ER16066) (F.G. and J.A.). M.S. and P.K. were supported by European Research Council StG 308051 MOLSPINTRON. The isotopes used in this research were supplied by the U.S. Department of Energy, Office of Science, by the Isotope Program in the Office of Nuclear Physics. The ^{249}Bk was provided to Florida State University and the Colorado School of Mines via the Isotope Development and Production for Research and Applications Program through the Radiochemical Engineering and Development Center at Oak Ridge National Laboratory. We are especially grateful for assistance and supervision by the Office of Environmental Health and Safety at Florida State University/Colorado School of Mines and the Office of Radiation Safety for their facilitation of these studies. Magnetization measurements using the vibrating sample magnetometer SQUID magnetic properties measurement system were performed at the National High Magnetic Field Laboratory, which is supported by National Science Foundation Cooperative Agreement no. DMR-1157490, the State of Florida, and the U.S. Department of Energy. We are indebted to the Office of Safety at the National High Magnetic Field Laboratory for helping to facilitate these studies as well. J.C.W. is supported by the National Science Foundation Graduate Research Fellowship under grant no. DGE-1449440. This research was support in part by an appointment to the CBFO Fellowship Program, sponsored by the U.S. Department of Energy and administered by the Oak Ridge Institute for Science and Education. Metrical parameters for the structures of $Bk(HDPA)_3{\cdot}nH_2O$ and $Bk[B_6O_8(OH)_5]$ are available free of charge from the Cambridge Crystallographic Data Centre under accession numbers CCDC-1451021 and 1490887, respectively.

SUPPLEMENTARY MATERIALS

www.sciencemag.org/content/353/6302/aaf3762/suppl/DC1
Figs. S1 to S9
Tables S1 to S6
References (*50*–*55*)

1 February 2016; accepted 29 June 2016
10.1126/science.aaf3762

Downloaded from http://science.sciencemag.org/ on September 3, 2016

RESEARCH ARTICLES

HEALTH ECONOMICS

Targeting health subsidies through a nonprice mechanism: A randomized controlled trial in Kenya

Pascaline Dupas,[1,2,3*] Vivian Hoffmann,[4*] Michael Kremer,[2,3,5*] Alix Peterson Zwane[6*]

Free provision of preventive health products can markedly increase access in low-income countries. A cost concern about free provision is that some recipients may not use the product, wasting resources (overinclusion). Yet, charging a price to screen out nonusers may screen out poor people who need and would use the product (overexclusion). We report on a randomized controlled trial of a screening mechanism that combines the free provision of chlorine solution for water treatment with a small nonmonetary cost (household vouchers that need to be redeemed monthly in order). Relative to a nonvoucher free distribution program, this mechanism reduces the quantity of chlorine procured by 60 percentage points, but reduces the share of households whose stored water tests positive for chlorine residual by only one percentage point, substantially improving the trade-off between overinclusion and overexclusion.

Policy-makers have long debated whether developing countries should charge for health products such as deworming medication, malaria medication, mosquito nets, water treatment solution, and latrines. Multiple studies have found that demand for preventive health goods is highly sensitive to price (*1*–*4*). For mosquito nets, usage appears as high among recipients who get them only when they are free or nearly free as among those able to pay a price of USD 1 or more (*2*, *5*–*8*). However, in the case of water treatment solution, Ashraf, Berry, and Shapiro (*9*) argue that households with lower willingness to pay for the product when a marketer comes to their doorstep are less likely to use it for its intended health purpose and more likely to use it for other purposes, such as washing clothes or cleaning toilets. Policy-makers may thus be concerned that free distribution of products that only part of the population values for their health purpose can generate wastage.

This study reports findings from a randomized controlled trial that compares three mechanisms for allocating dilute-chlorine water treatment solution: (i) charging a partially subsidized price; (ii) free provision during a clinic visit and a follow-up household visit (*10*); and (iii) combining free provision with a screening mechanism designed to make the water treatment solution available to those willing to expend a small effort (redemption of a month-specific voucher at a local shop) to obtain it. By testing households' stored water for chlorine residual, we assess actual use of the product and thus compare the extent to which each mechanism generates errors of inclusion (by providing the product to households that will not use it to treat water) or of exclusion (by preventing households that would use the product to treat water from obtaining the product.) We then examine how the optimal choice of mechanism for a policy-maker depends on these error rates, the cost of each mechanism, and policymakers' valuation of households' use of the water treatment solution.

We find that combining free provision with a voucher mechanism screens out 88% of those who would accept the product under free provision but not treat their water, thus markedly reducing errors of inclusion, while creating very few errors of exclusion relative to free provision. Rates of positive residual chlorine tests are almost identical when comparing free distribution and voucher provision. The proportion of households with water testing positive for residual chlorine was 32.9% in the group receiving vouchers and only 1 percentage point higher, at 33.9%, in the group with free distribution. The difference is not statistically significant. This suggests that the inconvenience of safekeeping and redeeming vouchers screened out very few of those who would have used chlorine solution if given it directly.

We also confirm previous findings that although errors of inclusion are low under cost sharing, cost sharing generates many errors of exclusion relative to free treatment. Only 12.4% of households in the cost-sharing group had chlorine in their water, many fewer than under either form of free treatment.

[1]Stanford University, Stanford, CA, USA. [2]National Bureau of Economic Research, Cambridge, MA, USA. [3]Cambridge, MA, USA. [4]International Food Policy Research Institute, Washington, DC, USA. [5]Harvard University, Cambridge, MA, USA. [6]Global Innovation Fund, Washington, DC, USA.
***Corresponding author. Email: pdupas@stanford.edu (P.D.); v.hoffmann@cgiar.org (V.H.); mkremer@fas.harvard.edu (M.K.); alix.zwane@globalinnovation.fund (A.P.Z.)**

Setting and background

Diarrhea is a major cause of child mortality (ages 1 to 59 months) globally and in Kenya (*11*). Water is a major channel for the transmission of diarrheal disease. Dilute chlorine solution kills many of the pathogens that cause diarrhea. Arnold and Colford (*12*) review 21 randomized controlled trials on the impact of point-of-use water treatment with dilute chlorine solution and find that access to point-of-use chlorination reduces reported child diarrhea by an average of 29% overall (*13*). Dilute chlorine solution is socially marketed in many countries by the nongovernmental organization (NGO) Population Services International (PSI), which receives donor support.

The study took place from November 2007 to September 2008 in western Kenya, a region with the second highest prevalence of child diarrhea in Kenya (*14*). In addition to free government provision during epidemics, the primary approach to distribution of water treatment solution in this area had been social marketing and sales to households through retail shops. PSI began marketing 150-ml bottles of dilute chlorine solution branded as "WaterGuard" in Kenya in May 2003. These bottles, expected to last a household 30 to 50 days (*15*–*17*), were sold at a price of 20 Kenyan shillings (Ksh) at the onset of this study, around US$ 0.30 at the exchange rate at that time (*18*, *19*). Although brand recognition for WaterGuard is high, as is reported understanding of the potential benefits of the technology, take-up of water chlorination in rural western Kenya is low. Kremer *et al.* (*20*) report that only 7% of rural households in this part of Kenya were using chlorine to treat their drinking water, a rate typical of many other rural African settings. Point-of-use water treatment requires repeated, proactive behavior on the part of households even when the technology is offered free of charge. Previous work in the region has found that the rate of verified water treatment is around 50% when chlorine solution is provided free, but encouragement and reminders are relatively infrequent (*20*, *21*). Limited use could be due to a number of factors, including aversion to the taste of chlorine, particularly if dosing is too high or water is consumed too soon after treatment.

Methods

Parents of children aged 6 to 12 months, an age group at high risk for mortality due to diarrheal disease, were recruited from the waiting rooms of four rural maternal and child health clinics in Busia District. Once enrolled, study participants were administered a baseline survey on basic demographics, current water treatment practices, knowledge about waterborne illness and diarrhea prevention, and child health. At the end of the survey, the 1118 participants in this study sample were randomly assigned to one of three experimental arms by choosing an envelope from a

Downloaded from http://science.sciencemag.org/ on September 3, 2016

bag full of identical envelopes, each containing a letter corresponding to one of these arms. Once the respondent selected an envelope and revealed the letter, the enumerator offered the corresponding treatment. The supplementary materials provide additional information on methods and sampling. Table S1 presents baseline characteristics of our study sample, as well as tests of balance across the treatment arms. Because the baseline survey was administered in waiting rooms of clinics and not at respondents' homes, no water test could be performed at baseline, and therefore we cannot test for baseline balance on the primary end point of interest (presence of chlorine in drinking water at home).

In each of these experimental treatments, participants were offered the opportunity to obtain sufficient water treatment solution to last them much beyond the time of the follow-up survey, which was conducted during a home visit 3 to 5 months later. Comparing take-up and usage at follow-up across these groups thus allows us to identify the targeting effects of varying the price and effort cost of obtaining the product. The three experimental treatments were as follows:

Cost sharing treatment

Water treatment solution was made available for immediate purchase at a 50% discount off the retail price. Participants could purchase up to five 150-ml bottles of the solution (enough to last approximately 5 to 8 months), at 10 Ksh per bottle.

Vouchers treatment

Twelve vouchers, each redeemable for one 150-ml bottle of water treatment solution at either a local shop or the clinic itself, were provided. Each voucher was marked for a specific month, for the next 12 consecutive months, and participants were given a calendar to track the expiration of vouchers.

Free delivery treatment

Two 500-ml bottles of water treatment solution were provided, one immediately and the second given during the follow-up survey conducted at the participant's home, 3 to 5 months later (*22*). At the time they received the first bottle, participants were informed that they would receive a second bottle later. This supply of 1000 ml of water treatment solution was expected to last approximately 7 to 11 months.

A follow-up was conducted at participants' homes 3 to 5 months after enrollment. Details on the methods and attrition at follow-up survey are provided in the supplementary materials and methods.

Results

Table 1 presents dilute chlorine procurement ("take-up") by treatment arm. Whereas take-up in the free delivery arm was nearly universal (everyone took the first bottle of water treatment solution offered at the clinic, and only about 1% of participants refused to accept the second bottle offered during the follow-up home visit), only 13.4% of the five bottles offered for sale were purchased in the cost sharing group [just over half (51.9%) of those in the group purchased a bottle, and few purchased more than one] (*23*).

Take-up in the vouchers group was higher, with 39.8% of the 12 monthly vouchers redeemed per household (85.3% of households redeemed at least one voucher). Analysis presented in table S2 indicates a positive relationship between household wealth and purchase of water treatment solution in the cost sharing group, but a negative association between wealth and procurement in the vouchers group.

Table 2 shows water treatment at follow-up by arm. The first row shows the unconditional proportions of participants in each treatment group, with a positive chlorine test among those with stored drinking water at the time of the survey, while the second row shows coefficients and standard errors from a regression of positive chlorine tests on treatment arm and baseline variables from table S1, stratification variables (clinic and survey wave indicator variables), and time since enrollment. The two sets of results are very similar. We focus our discussion and analysis on the specification conditional on controls.

Table 2 confirms the earlier literature showing that user fees create substantial exclusion errors relative to free delivery: The proportion of households with a positive chlorine test was only 12.4% in the cost sharing group, 21.5 percentage points lower than in the free delivery group.

Table 2 also presents the more novel finding that is the main result of this study: The rates of positive residual chlorine tests in the free delivery and vouchers groups are almost identical. In the vouchers group, 32.9% of households had water testing positive for residual chlorine. In the free delivery group, 33.9% tested positive, so the point estimate of the difference was only 1.0 percentage point (and this was not statistically significant). The 95% confidence intervals for the vouchers and free delivery groups are [25.3, 40.5] and [26.3, 41.5], respectively. Results are very similar and also do not differ statistically when restricting attention only to those households sampled at 3 or 4 months after enrollment, which collectively account for 80% of the sample: At 3 months, the difference between free delivery and vouchers groups was 1.4%; at 4 months the difference was 2.7% (see table S3). This indicates that results are not driven by households in the free delivery group running out of chlorine. The share of households that report running out in that group at the time of follow-up was 15.1% (13.6% for those surveyed after 3 months) (*24*).

Although we cannot directly test whether the same households that use the water treatment product under free delivery would also use it under the vouchers scheme, we can test whether confirmed users under the two schemes have similar characteristics. We do this in table S4, which shows, for the subsample of individuals in either the free delivery or vouchers groups, the coefficient estimates of a regression of confirmed water usage on baseline characteristics and interactions between baseline characteristics and the vouchers treatment. We cannot reject the null that users under the two schemes are selected along identical characteristics, which suggests that those who did not redeem vouchers would likely not have used them under free delivery.

Together, the results so far suggest that imposing the inconvenience of redeeming time-stamped vouchers does not substantially reduce water treatment relative to free distribution. Relative to free distribution, the voucher-allocation

Downloaded from http://science.sciencemag.org/ on September 3, 2016

Table 1. Take-up by treatment. Sources: Records from baseline survey (columns 1 to 3, 7); redemption data were collected from participating retailers (columns 4 to 6).

	1	2	3	4	5	6	7
	Cost sharing			Vouchers			Free delivery
	Purchased at least one bottle at clinic	Purchased at least two bottles	Proportion of five bottles purchased	Redeemed at least one voucher	Redeemed voucher month before follow-up	Proportion of 12 vouchers redeemed	Accepted water treatment solution at baseline
Mean	0.519	0.120	0.134	0.853	0.411	0.398	1.000
Observations	351	351	351	382	350	382	385

mechanism reduced errors of inclusion substantially (by 58 percentage points) and had almost no impact on errors of exclusion. Combining free provision with a voucher mechanism achieves most of the benefits of free treatment, while eliminating most of the downside of potential wastage due to errors of including people who would not use the product to treat water. As discussed more formally in the next section, our point estimates imply that unless a policy-maker is willing to accept almost 60 exclusion errors to avoid one inclusion error, the policy-maker will prefer a voucher screening mechanism to free delivery.

Although the effort required to redeem vouchers was not varied experimentally in this study, we can use variation in the location at which vouchers could be redeemed to generate a measure of the strength of the nonprice screen. Specifically, shops where the vouchers could be redeemed were in the nearest market center for 22% of respondents. Table 3, column 1, shows that participants who could redeem vouchers at the nearest market center were 15.3 percentage points more likely (adjusted *P*-value: 0.034) to have redeemed a voucher in the month before the follow-up interview than those who had to go further out of their way to do so, conditional on stratification variables (enrollment wave and clinic), time since enrollment, and baseline covariates. However, these participants were only 4.4 percentage points more likely (adjusted *P*-value: 0.532) to be using the solution to treat their water, according to chlorine test results (Table 3, column 2) (*25*). Distance to the redemption point was not randomly assigned, so it is possibly correlated with characteristics that were not measured at baseline and therefore not controlled for in the analysis. Future work could experimentally vary the location of voucher redemption to test the hypothesis that less onerous nonprice screening mechanisms generate higher take-up, but are less effective at screening out those who do not use a good for its intended purpose.

Optimal policy

To formally examine the optimal choice of mechanism for a policy-maker, let V denote the policy-maker's valuation of providing water treatment solution to a household that has children at risk of mortality from diarrheal disease and that will actually use the water treatment solution for its intended purpose. The policy-maker therefore seeks to maximize total value minus the total cost of the subsidy, or $VN_m - C_mT_m$, where the subscript m denotes the mechanism, N denotes the number of households using water treatment under mechanism m, C_m denotes the subsidy per household obtaining water treatment under mechanism m, and T_m denotes total take-up—i.e., the number of households that obtain chlorine solution under mechanism m. The policy-maker will prefer changing from delivery mechanism a to mechanism b that expands take-up relative to mechanism a, if and only if $V(N_b - N_a) > C_bT_b - C_aT_a$, which we can rewrite as

$$V(N_b - N_a) > C_b(T_b - T_a) + (C_b - C_a)T_a \quad (1)$$

The left-hand side of inequality (1) is the value to the policy-maker of additional chlorine usage, and the right-hand side is the cost to the policy-maker of achieving this change, which consists of the cost of reaching marginal consumers, $C_b(T_b - T_a)$, plus the cost of further subsidizing inframarginal consumers who would have obtained water treatment solution in any case, $(C_b - C_a)T_a$. In the special case in which the cost to the policy-maker per taker is the same under the two mechanisms ($C_b = C_a = C$), this expression simplifies and can be expressed as $(N_b - N_a)/(T_b - T_a) > C/V$, so that the ratio of new users to new recipients must be greater than the ratio of the subsidy per taker to the policy-maker's valuation of health. If the cost per user under method b (which achieves higher take-up) is greater, as will typically be the case, then this condition will be necessary (but not sufficient) for method b to be preferred.

Clearly, if policy-makers have a low enough valuation of a targeted household treating its water (any value less than the cost of the treatment and extending up to some range above this), they will want a positive price (either no subsidy or a subsidy that does not bring the price to zero). If policy-makers have a high enough valuation, they will prefer free household delivery. However, our estimates imply that it is possible to make a product available for free with little wastage, and hence that there will be a broad range of valuations over which they will prefer combining a full subsidy with a nonprice screening mechanism (*26*).

Table 4 summarizes the material cost of water treatment solution per additional user reached under the policy changes considered. The first column shows the change in chlorine usage for 100 subsidized doses, and columns 2 to 5 spell out the components of the two terms on the right-hand side of inequality (1). Column 6 indicates the total material cost per additional user, abstracting from differences in delivery costs. The first row of Table 4 illustrates the binary choice between cost sharing and free delivery, excluding the option of a voucher screening mechanism. Relative to cost sharing, delivering chlorine free of charge to users increases the proportion of households that obtain it by 86.6 percentage points, from 13.4 to 100% (columns 3

Table 2. Positive chlorine test at follow-up (3 to 5 months after intervention). Adjusted differences are computed from coefficients in a linear regression of the outcome (positive chlorine test at follow-up) on treatment indicators, controlling for clinic, recruitment wave, time since interview, and baseline controls shown in table S1. Standard errors are in parentheses.

	1	2	3
	Cost sharing	**Vouchers**	**Free delivery**
Raw means	0.124	0.345	0.344
	(0.019)	(0.026)	(0.026)
Adjusting for baseline controls	0.124	0.329	0.340
	(0.019)	(0.039)	(0.039)

Table 3. Take-up and usage by distance to redemption point. Standard errors are in parentheses. Data are from participants in the vouchers treatment whose chlorine use was observed at the follow-up interview (data on location of home is not available for attriters; chlorine test results not available for those without stored water at time of survey). Adjusted differences are computed from coefficients in a linear regression of each outcome on treatment indicators, controlling for clinic, enrollment wave, time since interview, and baseline controls shown in table S1.

	1	2
	Proportion redeemed voucher month of survey	**Proportion with positive chlorine test**
Vouchers redeemable at nearest market	0.507	0.368
	(0.060)	(0.059)
Observations	71	68
Not redeemable at nearest market	0.383	0.331
	(0.031)	(0.030)
Observations	253	248
Difference of means	0.124	0.037
P-value, unadjusted difference of means	0.062	0.569
Difference of adjusted means	0.153	0.044
P-value, difference of adjusted means	0.034	0.532

Downloaded from http://science.sciencemag.org/ on September 3, 2016

and 7 in Table 1), and increases the proportion of verified chlorine users by 21.5 percentage points, from 12.4 to 33.9% (columns 1 and 3, second row of Table 2). This implies that 4.03 additional doses of water treatment solution have to be delivered for every additional dose used (86.6/21.5) (*27*). Moreover, under free delivery the policy-maker fully subsidizes water treatment for the 13.4% of households that would purchase at the cost-sharing price (*28*). This adds a cost equivalent to 0.31 doses per additional user [(13.4 × 0.5 dose)/21.5 = 0.31], which brings the total cost to 4.34 doses for every new user (*29*). If a policy-maker has a high value of health, this could be a cost worth bearing to achieve high coverage, but a policy-maker with a lower value of health may choose a cost-sharing approach.

Once the possibility of a voucher screening mechanism is introduced, policy-makers with a broad range of valuations of health will prefer this approach to either cost sharing or full subsidy via free delivery (*30*).This result is shown in rows 2 and 3 of Table 4. Moving from cost sharing to a voucher-based screen implies that the policy-maker must provide 1.7 additional units of treatment solution for every additional chlorine-using household. To see this, it is apparent that in the vouchers treatment, 41.1% of recipients redeemed a voucher in the month before the follow-up visit, and 39.8% of total vouchers were redeemed over the 12-month span of their validity (columns 5 and 6, Table 1). Based on the prior-month redemption figure and the adjusted confirmed usage rate of 32.9% (Table 2, column 2) in this group, the proportion of households obtaining chlorine increases by 27.7 percentage points, relative to cost sharing, while the proportion of users increases by 20.5 percentage points, relative to cost sharing. Thus, moving from cost sharing to a voucher-based screen implies that the policy-maker must provide 27.7/20.5 = 1.35 additional units of treatment solution for every additional household with confirmed chlorine residual. Adding the cost of fully subsidizing those who would use under cost sharing, as calculated above, brings the full cost of the policy change to 1.68 units per new user.

If the additional value (beyond that of the household itself) that policy-makers place on a household treating its water is less than the cost of one dose, then they would not want to fully subsidize treatment. If they value it at between 1 and 1.68 times the cost of a dose, then the wastage associated with a voucher-based approach would lead them to reject such a program. If water treatment is valued above 1.68 times the cost of a dose, voucher programs are potentially attractive.

Moving from vouchers to universal free delivery, under which 33.9% of households were confirmed to be chlorinating at the follow-up visit, entails providing 58.9 additional units of treatment solution to reach one additional using household (100% take-up under free delivery minus 41.1% coupon redemption to achieve an increase of 1% in usage). If the value of reaching that one additional household is extremely high, a policy-maker might choose the free delivery mechanism. However, it is easy to see that for a wide range of values placed on the health of this 34th household, the voucher mechanism would be preferred to full subsidy via free delivery, as it is substantially cheaper.

We can be more specific about how policy-makers' decisions will depend on their valuation of averting a disability-adjusted life year (DALY) and their expectations about the number of DALYs saved per household chlorinating their water (*31*). For the purposes of illustration, we use the estimated impact of point-of-use chlorination on diarrheal disease reported by Arnold and Colford (*12*) and assume that the reduction in child deaths achieved through treatment of drinking water is roughly proportional to diarrhea cases averted. (If policy-makers believed that water treatment is half as effective as implied by these assumptions, they would simply require valuations twice as high as those reported here to make each decision.) Using estimates of the total under-5 mortality rate and under-5 diarrheal mortality rate in Kenya provided by the UN Inter-agency Group for Child Mortality Estimation (*32*) and Health Epidemiology Reference Group (*33*), respectively, a policy-maker would arrive at estimates of the material costs per DALY and life saved via water treatment shown in columns 7 and 8 of Table 4. Underlying data and assumptions are described in the supplementary materials and methods.

In this example, setting aside issues of differences in distribution costs between the options, policy-makers who value a DALY saved at between $70 and $2475 (or a statistical life at between $2134 and $74,921) will prefer the voucher screening approach to the other options. The range of valuations for which the voucher approach is preferred is very wide, encompassing values far below the very stringent standard of $246 per DALY corresponding to the current dollar value of the $150/DALY threshold implicitly suggested by the World Bank in the 1993 World Development Report (*34*, *35*) and extending above the more generous approach taken by the World Health Organization (WHO) (*36*, *37*) of considering interventions costing less than the gross domestic product per capita of the country (currently $1245 for Kenya) as highly cost effective. Policy-makers with valuations below $70/DALY would likely prefer cost sharing, whereas policy-makers with valuations above $2475/DALY would prefer free distribution.

This analysis considers only the cost of the water treatment itself. Administering a voucher

Table 4. Policy comparisons. Calculations reflect material cost of water treatment solution only; differences in delivery costs are not included. "Dose" refers to a yearly dose (12 bottles of 150 ml). At the time of writing, the exchange rate was Ksh 103 to USD 1; thus, a yearly dose costs (12 × 20)/103 = USD 2.33.

	1	2	3	4	5	6	7	8
	Additional verified users for 100 doses subsidized ($N_b - N_a$)	**Additional takers for 100 doses subsidized ($T_b - T_a$)**	**Doses fully subsidized per marginal user (col 1/col 2)**	**Full-dose equivalent for inframarginal users (Table 1 col 3 × 1/2)**	**Full-dose equivalent subsidy for inframarginal users, per marginal user (col 4/col 2)**	**Total additional doses provided per new user (col 3 + col 5)**	**Cost per additional DALY saved, USD***	**Cost per additional life saved, USD***
Policy change considered:								
1. Cost sharing to free delivery	21.5	86.6	4.03	6.70	0.31	4.34	182	5,520
2. Cost sharing to vouchers	20.5	27.7	1.35	6.70	0.33	1.68	70	2,134
3. Vouchers to free delivery	1.00	58.9	58.9	0	0	58.9	2,475	74,921

*See supplementary materials for assumptions used in calculations of costs per DALY and cost per life saved.

Downloaded from http://science.sciencemag.org/ on September 3, 2016

system could generate some additional costs relative to a partial subsidy system without vouchers; the magnitude of these costs is an important question when considering operationalizing such a program. Similarly, free household delivery would be substantially more expensive than a voucher system. Although delivering a 500-ml bottle at the clinic is relatively cheap, because children are vulnerable to diarrhea until age 5 and because dilute chlorine solution has a limited shelf life (18 months from the date of manufacture, so 6 to 12 months given distribution lags), additional bottles would have to be provided later on. Arranging for these to be delivered to households would be very expensive relative to vouchers (*38*). This suggests that only policymakers with a very high valuation of health would prefer free delivery to a voucher system.

Discussion

Ashraf *et al.* (*9*) report that use of a price mechanism to target a preventive health product—dilute chlorine solution for water treatment—disproportionately targets those who will use it, but also excludes many potential users. The results presented here suggest that combining free provision with a nonprice screening mechanism—requiring people to redeem vouchers—can also greatly reduce wastage but without a corresponding increase in the exclusion of those who would use treatment. This study makes several contributions. First, it extends a literature in economics on "ordeal mechanisms" as targeting mechanisms. Second, the findings demonstrate proof of concept for a novel approach to the distribution of water treatment solution.

An existing literature in economics discusses the effectiveness of "ordeal mechanisms," such as requiring work for welfare, in targeting redistributive transfers to the poor (*39*, *40*). For example, some food subsidy programs focus on coarser grains that richer households are less likely to consume to reduce errors of inclusion of richer households. This study takes the idea in a new direction, by examining the extent to which what might be termed "micro-ordeals" can target merit goods (goods for which the policy-maker values consumption beyond the value at which the household values consumption) to those who will use them as intended by the policy-maker. We provide evidence that time and money costs have different selection properties, and in particular that compared to free delivery, charging selects a richer group of households to obtain water treatment, whereas a voucher system selects a poorer group of households, consistent with a model in which richer households have a higher value of time. This differential pattern of selection suggests that price-based selection mechanisms are unlikely to be able to duplicate the pattern of selection created by the voucher redemption mechanism. To the extent that poorer households are more likely to experience mortality from diarrheal disease, the voucher system induces a pattern of selection that is likely to yield greater health benefits per person treating their water.

There are several possible reasons why, in our context, willingness to redeem vouchers predicted usage well, whereas willingness to pay a monetary cost led to many errors of exclusion of those who would use the water treatment solution. Perhaps households with a low valuation of time were more likely both to redeem vouchers and to use water treatment solution. Perhaps households that are motivated and organized enough to safekeep and redeem vouchers were also motivated and organized enough to treat their water, but labor market imperfections made it difficult for these households to convert their time to money that could be used to purchase the product.

Such micro-ordeal screens could potentially be used more broadly. For example, it might be the case that having to fill out application forms to apply for a college scholarship targets students who will later study diligently and thus use the college education most productively. As this example indicates, such judgments will have to be made on a case-by-case basis using the empirical evidence for that case. In some cases, a micro-ordeal might be insufficient to screen out people who would use a product in a way other than the policy-maker intended. For example, in the same area of Kenya, Cohen *et al.* (*41*) find that, conditional on having an episode of fever, willingness to pay the effort cost of visiting a local drug shop to redeem a voucher for highly subsidized antimalarial medication is poorly correlated with actual malaria status—specifically, 44% of those redeeming an antimalarial voucher do not have malaria (but think they do). This is due to poor access to accurate malaria diagnosis combined with the very high benefit of appropriately treating malaria when it truly is the underlying cause of the fever. Ma *et al.* (*42*) find that 90% of households in China redeem vouchers for free prescription eyeglasses for myopic children, even though less than half of the children end up wearing the eyeglasses regularly. This could be because for such a product, as in water chlorination, users need to try the product out to know the usage cost, and the option value of learning outweighs the redemption cost for most households. Unlike water chlorination, eyeglasses cannot be distributed in monthly doses, so the voucher mechanism cannot be used to screen out, over time, those who have learned that the usage costs are too high for them. In other cases, almost everyone who takes a product distributed for free may use it as intended, so there is no need for a micro-ordeal. [See, for example, (*6*) on antimalarial bed nets.]

Because many real-world free distribution programs do not involve in-person free delivery, but instead require those seeking a product to make some effort to obtain the product, our results suggest caution in extrapolating adoption rates from studies in which surveyors visit households and offer highly subsidized or free products, to predict the impact of scaled programs in which households must expend some effort to obtain a subsidized product. The very high uptake rate of dilute chlorine solution in the free delivery arm is consistent with the hypothesis that respondents who knew they were unlikely to use chlorine solution might have been reluctant to turn down the free gift because this might be perceived as rude or as signaling a lack of commitment to child health. To reduce the possibility of experimenter demand effects, it may be better to assess demand for products by examining whether households redeem coupons for products because this does not involve an enumerator directly observing the action of the survey respondent.

A voucher-based subsidy for water treatment solution seems potentially scalable. The NGO PATH and the U.S. Centers for Disease Control and Prevention have explored a similar approach of distributing dilute chlorine through antenatal clinics in Malawi (*43*), and the Tanzania National Voucher Scheme (*44*) provides a discount voucher for insecticide-treated mosquito nets to pregnant women and parents of young children through health centers. Vouchers could easily be bundled in safe birthing kits, which are an increasingly common intervention, and could also be implemented electronically using mobile phones.

There are several reasons that a voucher program could be appealing, in addition to avoiding wastage. One advantage of this approach is that it facilitates targeting subsidies to particular populations—in this case, households with young children at risk of diarrheal mortality and morbidity. Also, a voucher-based subsidy complements the existing system of social marketing by generating more business for shops that sell dilute chlorine solution, which may encourage shops to carry the product and avoid stockouts. To the extent that this approach leads households to continue using chlorine solution after their children have passed the age at which subsidies are provided, it may have broader benefits (*45*). As discussed further in the supplementary materials, vouchers also seem to target the poor, whereas richer households are more likely to adopt vouchers under cost sharing. Insofar as children from poor households may be at highest risk of diarrheal mortality and other outcomes such as stunting, this represents another advantage of free distribution through vouchers. Such a program, if implemented through the health care system (i.e., vouchers distributed during well-baby checkups), would also provide at least some increased incentive for households to bring children into clinics.

We note three limitations of this study. First, we do not report on health outcomes. Self-reported diarrhea in the context of a trial through which recipients were provided free water treatment solution may be subject to bias, and collection of observational data on this outcome was beyond the available budget. Second, the volume of water treatment solution offered to participants differed across treatments for logistical reasons. Although analysis of subgroups by time of follow-up data collection indicates that results were not driven by households differentially running out of water treatment solution across arms, it is possible that

Downloaded from http://science.sciencemag.org/ on September 3, 2016

larger quantities were interpreted as a signal of lower quality. However, this seems unlikely because all groups were given the same information on the importance of treating water with chlorine and on the potency of the product. Finally, although we show that screening with a voucher mechanism eliminates most of the wastage of water treatment solution associated with free delivery, with very little cost in terms of reduced water treatment, owing to budget constraints, we could not examine the full space of potential policies. Given our results, it would be of considerable intellectual interest for future work to examine a range of nonprice mechanisms, a range of prices, and the space combining price and nonprice mechanisms in various combinations (for example, by requiring households to both travel to a redemption center to redeem vouchers, and to make a payment), as well as the health consequences of the differential patterns of selection of different mechanisms. Because this space is extensive, fully exploring it would likely require multiple studies.

Future work could also formally examine a range of potential underlying mechanisms. For example, the finding that price and nonprice mechanisms have different patterns of heterogeneous effects with assets is consistent with the idea that liquidity constraints play a major role, as shown in previous work on mosquito nets (*46*). By examining a finer range of subsidy levels between 50 and 100% and by more fully examining heterogeneity among households with different levels of assets, it might be possible to test the hypothesis that a substantial fraction of households are severely credit constrained, with zero or extremely limited liquid assets but with access to labor that cannot easily be transformed into liquid assets, and thus that even if the price were as low as a single Kenyan shilling, rates of water treatment would be substantially lower than under free delivery, and thus that it would not be possible to replicate the pattern of selection induced by the nonprice mechanism. Future work could also examine hypotheses from psychology that households may seek to avoid the decision-making costs associated with making any choice to spend money or that there may be a discontinuity in behavior around a price of zero. Finally, future work could examine the hypothesis that differential social costs of refusing to accept water treatment solution during household visits, visits to clinics, and visits to shops induce different patterns of selection of those who will use water treatment solution.

REFERENCES AND NOTES

1. A. Holla, M. Kremer, "Pricing and Access: Lessons from Randomized Evaluations in Education and Health," Center for Global Development Working Paper 158, January 2009.
2. P. Dupas, *Annu. Rev. Econ.* **3**, 425–449 (2011).
3. M. Kremer, R. Glennerster, in *Handbook of Health Economics*, M. V. Pauly, T. G. McGuire, P. Pita Barros, Eds. (North Holland/Elsevier, 2012), vol. 2.
4. P. Dupas, *Science* **345**, 1279–1281 (2014).
5. P. Dupas, *Am. Econ. Rev.* **99**, 224–230 (2009).
6. P. Dupas, *Econometrica* **82**, 197–228 (2014).
7. V. Hoffmann, C. B. Barrett, D. R. Just, *World Dev.* **37**, 607–617 (2009).
8. J. Cohen, P. Dupas, *Q. J. Econ.* **125**, 1–45 (2010).
9. N. Ashraf, J. Berry, J. Shapiro, *Am. Econ. Rev.* **100**, 2383–2413 (2010).
10. Because chlorine is extremely reactive, the solution expires, so it is not possible to deliver enough chlorine to last through a child's period of mortality risk at one time.
11. L. Liu *et al*., *Lancet* **379**, 2151–2161 (2012).
12. B. F. Arnold, J. M. Colford Jr., *Am. J. Trop. Med. Hyg.* **76**, 354–364 (2007).
13. The average rates of verified chlorine use in these studies are around 75%, which implies a reduction of 39% among those with verified chlorine use.
14. Kenya National Bureau of Statistics (KNBS) and ICF Macro, Kenya Demographic and Health Survey 2008-09. Calverton, Maryland: KNBS and ICF Macro (2010).
15. Population Services International states that one 150-ml bottle protects a family of six for 1 month (*16*). However, Lantagne *et al*. (*17*) estimate, based on the assumption that a family of five to six uses 20 liters of high-quality water for drinking and cooking per day, that a bottle lasts 50 days.
16. PSI (Population Services International), Household water treatment, accessed 9 January 2015 at www.psi.org/program/household-water-treatment/.
17. D. Lantagne *et al*., *J. Environ. Eng.* **137**, 131–136 (2011).
18. This price is designed to cover the cost of the product and distribution, but not the social marketing, which is subsidized by donors (*19*).
19. US Centers for Disease Control and Prevention, "The Safe Water System Project: Social Marketing and Community Mobilization in Kenya," accessed 12 August 2016 at https://www.cdc.gov/safewater/pdf/sws-social-marketing-kenya.pdf.
20. M. Kremer, E. Miguel, S. Mullainathan, C. Null, A. P. Zwane, "Social engineering: Evidence from a suite of take-up experiments in Kenya," working paper, www.poverty-action.org/sites/default/files/publications/chlorinedispensers.pdf.
21. J. Luoto, D. Levine, J. Albert, S. Luby, *J. Dev. Econ.* **110**, 13–21 (2014).
22. We wanted to give respondents in the free delivery group water treatment solution in a non–easily divisible fashion. Given well-documented evidence of informal insurance and sharing in networks in the study area (and indeed we do see evidence of sharing in our study; see table S5), we were concerned that if people received 12 small bottles at once, they would be more likely to share them with others. The only available "big size" bottle was the 500-ml Aquaguard bottle, so we decided to give two of them over a year. The supply was given in the form of two separate 500-ml bottles, owing to concerns about chlorine degrading over time [see (*17*)]. Water treatment solution offered in 500-ml bottles is labeled as Aquaguard in the study area. This product is chemically equivalent to WaterGuard. We could have given three Aquguard bottles, and only 10 vouchers, to make the two quantities exactly match across groups, but because we planned to do the follow-up within 6 months anyway, we did not expect the total quantity to be a very important factor.
23. It is plausible that a substantial proportion of the population face liquidity constraints and that they might have bought more water treatment solution in steady state under a policy in which everyone knew in advance that the solution would be available to parents of young children at half price in clinics. However, a separate study conducted in fall 2006 in the study region provides suggestive evidence that take-up levels under the cost-sharing treatment would have been similar even if households could have purchased the water treatment solution over time. In that study, 210 households received 12 monthly coupons for a 50% subsidy on WaterGuard bottles redeemable at local shops (*20*). The authors report that ~10% of the 2520 coupons distributed were redeemed, a rate comparable to, if slightly lower than, the 13.4% purchase rate found in our study. Although the two samples were different [our study sampled parents of young children at clinics whereas Kremer *et al*. (*20*) had a representative sample], this nevertheless suggests that take-up is low even when households are given a month to find the money. This suggests that the cost sharing treatment yields estimates of take-up that are likely not very far from what would have been observed had this discount been offered over an extended period.
24. The follow-up survey recorded whether the initial Aquaguard bottle could be seen on the compound. It could be seen with Aquaguard in it in 72.6% of the compounds. Of recipients, 11.5% declared having given the bottle away to neighbors. See table S5.
25. The one clinic that served as a redemption point was not located in a market center, so all of the participants recruited at this clinic are included in the group unable to redeem at the nearest market. Omitting this subsample from the analysis does not affect the pattern or statistical significance of the results.
26. Policy-makers will not want to choose a negative price if households can freely and unobservably dispose of chlorine solution, because then people with no valuation of the water treatment solution will nonetheless obtain it to get the subsidy, but will simply throw it away.
27. We cannot rule out the possibility that some of these additional doses delivered were not "wasted" but were, for example, given to other households, or used after the period of water testing. However, because we assume that the policy-maker values water treatment in households with children in the age range at greatest risk of diarrheal mortality, and because dilute chlorine solution expires over time, we will treat the policy-maker as valuing verified water treatment.
28. We thus consider the problem of a health planner, who seeks to maximize health gains with a given fiscal expenditure and who does not value the implicit transfer involved in subsidies to inframarginal households. A social planner who valued household income would place at least some value on the implicit transfer to inframarginal households and would thus focus more on the figures that include only the cost of wastage. This slightly reduces the cost of moving from cost sharing to either of these policies, but does not alter the basic conclusions of this analysis.
29. This analysis considers only the cost of the water treatment solution, valued at 20 Kenyan shillings per 150 ml, the price at which WaterGuard is sold in Kenya. See below for a discussion of how the analysis might be affected by considering full delivery costs from implementing different policies at scale.
30. The time cost to recipients of redeeming vouchers is ignored in this analysis. Taking this cost into consideration reduces the cost-effectiveness of the voucher-based screening mechanism slightly; however, under reasonable assumptions on the value of time in this setting, the voucher policy remains preferred over a wide range of valuations on health.
31. The DALY is a metric commonly used by health economists to compare the cost-effectiveness of alternative interventions.
32. UN Inter-agency Group for Child Mortality Estimation, *CME Info database* (2015), www.childmortality.org/, accessed February 24, 2016.
33. R. E. Black *et al*., *Lancet* **375**, 1969–1987 (2010).
34. World Bank, *World Development Rreport 1993; Investing in Health* (Oxford Univ. Press, 1993).
35. This reflects the $150 benchmark, converted to 2016 dollars using the U.S. CPI. Taking into account real income growth would increase the threshold still further.
36. World Health Organization, *Report of the Commission on Macroeconomics and Health* (2002).
37. World Health Organization. *The World Health Report 2002: Reducing Risks, Promoting Healthy Life* (2002).
38. An alternative policy to either vouchers or free delivery would be to provide dilute chlorine solution to households when they visit clinics for other purposes. However, because households may not visit the clinic for other purposes at the times that their water treatment solution expires, coverage under this system might be substantially lower than under free delivery.
39. A. L. Nichols, *Am. Econ. Rev.* **72**, 372–377 (1982).
40. V. Alatas *et al*., *J. Polit. Econ.* **124**, 371–427 (2016).
41. J. Cohen, P. Dupas, S. Schaner, *Am. Econ. Rev.* **105**, 609–645 (2015).
42. X. Ma, S. Sylvia, M. Boswell, S. Rozelle, C.-Y. Cynthia Lin Lawell, "Ordeal Mechanisms, Information and the Cost-effectiveness of Subsidies: Evidence from Subsidized Eyeglasses in Rural China," Rural Education Action Project (REAP) Working Paper 266 (2014), https://reap.fsi.stanford.edu/sites/default/files/all6.ordeal_mechanisms_and_training_in_the_promotion_of_subsidized_products_in_developing_countries.pdf.
43. A. Loharikar *et al*., *Am. J. Trop. Med. Hyg.* **88**, 267–274 (2013).
44. J.-A. Mulligan, J. Yukich, K. Hanson, *Malar. J.* **7**, 32 (2008).

Downloaded from http://science.sciencemag.org/ on September 3, 2016

45. Such an effect of higher long-term demand following a temporary subsidy has been demonstrated for mosquito nets by Dupas (*6*).
46. A. Tarozzi *et al.*, *Am. Econ. Rev.* **104**, 1909–1941 (2014).

ACKNOWLEDGMENTS

We thank IPA Kenya for its collaboration; E. Chuang, K. Gatobu, B. Michel, S. Sylvia, A. Sebastian, N. Studer, and S. Ruiz for research assistance; and M. Baraza and his team for outstanding data collection. This study was funded by the Bill & Melinda Gates Foundation. P.D. gratefully acknowledges the support of NIH grant P01HD061315-01 and NSF grant 1254167. The research protocol for the study was approved by the ethical review committees of the Kenya Medical Research Institute (KEMRI), University of California at Berkeley, and Innovations for Poverty Action Kenya. The study is registered in the American Economic Association's registry for randomized controlled trials under ID AEARCTR-0001076. The data and code are publicly available on Dataverse (doi: 10.7910/DVN/PBLJXJ).

SUPPLEMENTARY MATERIALS

www.sciencemag.org/content/353/6302/889/suppl/DC1
Materials and Methods
Supplementary Text
Tables S1 to S5
References (*47*–*57*)

10 March 2016; accepted 11 July 2016
10.1126/science.aaf6288

STRUCTURAL BIOLOGY

Structure of a yeast catalytic step I spliceosome at 3.4 Å resolution

Ruixue Wan,* Chuangye Yan,* Rui Bai,* Gaoxingyu Huang,* Yigong Shi†

Each cycle of pre–messenger RNA splicing, carried out by the spliceosome, comprises two sequential transesterification reactions, which result in the removal of an intron and the joining of two exons. Here we report an atomic structure of a catalytic step I spliceosome (known as the C complex) from *Saccharomyces cerevisiae*, as determined by cryo–electron microscopy at an average resolution of 3.4 angstroms. In the structure, the 2′-OH of the invariant adenine nucleotide in the branch point sequence (BPS) is covalently joined to the phosphate at the 5′ end of the 5′ splice site (5′SS), forming an intron lariat. The freed 5′ exon remains anchored to loop I of U5 small nuclear RNA (snRNA), and the 5′SS and BPS of the intron form duplexes with conserved U6 and U2 snRNA sequences, respectively. Specific placement of these RNA elements at the catalytic cavity of Prp8 is stabilized by 15 protein components, including Snu114 and the splicing factors Cwc21, Cwc22, Cwc25, and Yju2. These features, representing the conformation of the spliceosome after the first-step reaction, predict structural changes that are needed for the execution of the second-step transesterification reaction.

Each cycle of pre-mRNA splicing results in the removal of an intron and the joining of two exons, through two sequential, S_N2-type transesterification reactions (*1*–*3*). In the first-step reaction, the 2′-OH of an invariant adenine nucleotide in the branch point sequence (BPS) of an intron serves as a nucleophile to attack the phosphorous atom of the guanine nucleotide at the 5′ end of the 5′ splice site (5′SS), forming an intron lariat–3′-exon intermediate and freeing the 5′ exon. In the second-step reaction, the 3′-OH of the RNA nucleotide at the 3′ end of the 5′ exon serves as a nucleophile to attack the phosphorous atom of the nucleotide at the 5′ end of the 3′ exon, joining the two exons and releasing the intron lariat (*2*). These two reactions are executed by a highly dynamic spliceosome that assumes at least six distinct states known as the B, B^{act}, B*, C, P, and ILS complexes (*4*).

The precatalytic spliceosome (B complex) contains all five small nuclear ribonucleoprotein particles (snRNPs): U1, U2, U4, U5, and U6. Dissociation of U1 and U4 snRNPs and recruitment of the nineteen complex (NTC) and NTC-related complex (NTR) trigger formation of the activated spliceosome (B^{act} complex). The B^{act} complex is converted to the catalytically activated spliceosome (B* complex), which executes the first-step reaction. The catalytic step I spliceosome, also known as the C complex, catalyzes the second-step transesterification with the help of a few splicing factors (*5*). The resulting P complex contains an intron lariat and a ligated exon, which is released in the ILS complex.

The spliceosome is a metalloribozyme (*6*–*8*), and conserved nucleotides in the intramolecular stem loop (ISL) of U6 snRNA coordinate the catalytic magnesium (Mg^{2+}) ions (*1*, *9*–*12*). During the first-step reaction, nucleotides at the 3′ end of the 5′ exon are anchored by loop I of U5 snRNA, whereas the 5′SS and BPS are recognized by U6 and U2 snRNA, respectively. The splicing active site, located in a catalytic cavity on the central spliceosomal component Prp8 (*13*), comprises the ISL of U6 snRNA, helix I of the U2/U6 duplex, loop I of U5 snRNA, and at least two Mg^{2+} ions (*11*, *12*).

Structures of individual spliceosomal components have been elucidated, primarily through x-ray crystallography (*14*–*21*). Investigations of the intact spliceosome, which is known for its conformational and compositional variability (*3*, *22*), have relied on electron microscopy (EM). Structures of various spliceosomal complexes over a wide range of resolution limits have been obtained (*11*, *12*, *23*–*42*). The 3.6 Å structure of the ILS complex from *Schizosaccharomyces pombe* unveils a detailed arrangement of U2, U5, and U6 snRNAs and specific interactions at the active site (*11*, *12*). More recently, the 3.5 Å structure of the B^{act} complex from *Saccharomyces cerevisiae* reveals how catalytic latency is maintained by the protein components surrounding the active site (*43*). Here we report the 3.4 Å structure of a spliceosomal C complex, which reveals the inner workings of the RNA elements together with their protein cofactors after the first-step transesterification reaction.

Beijing Advanced Innovation Center for Structural Biology, Tsinghua-Peking Joint Center for Life Sciences, School of Life Sciences, Tsinghua University, Beijing 100084, China.
*These authors contributed equally to this work. **†Corresponding author. Email: shi-lab@tsinghua.edu.cn**

Cryo-EM analysis

Using the NTC component Cef1 as an affinity-tagged protein, we purified a mixture of different spliceosomal complexes and used two-dimensional (2D) and 3D classifications to separate these distinct structural entities (*43*). Among the original set of 761,767 particles, 84,486 were used for reconstruction of the activated B^{act} complex at 3.52 Å resolution (*43*). The strategy of applying multiple simultaneous 3D classifications and merging all relevant classes proved to be important for the maximal inclusion of particles that represent the B^{act} complex. Starting from the same set of 761,767 particles, we applied the same strategy to identify those that represent the C complex (figs. S1 and S2A). After two rounds of 3D classification, 161,066 particles yielded a reconstruction at an average resolution of 3.95 Å, which, through particle polishing and autorefinement, was improved to 3.41 Å on the basis of the gold-standard Fourier shell correlation criteria (fig. S2B and tables S1 to S4).

The local resolutions vary greatly in the C complex (fig. S2C). The actual resolution in the central regions of the spliceosome reaches 2.9 to 3.5 Å, allowing atomic modeling. At the periphery, however, the EM density becomes contiguous only after being low-pass filtered to 10 Å (fig. S2D). To facilitate model building in the peripheral regions, we performed two more rounds of 3D classification, focusing on only the class that displays structural features in these regions (fig. S3). This effort generated two distinct reconstructions at 3.65 and 4.6 Å (fig. S4 and tables S1 to S4). In the central regions of the 3.41 Å density maps, most secondary structural elements are well defined, and a large proportion of amino acid side chains are identifiable (figs. S5 to S7). The RNA elements at the catalytic center and the surrounding protein components are marked by distinguishable features in the density maps (figs. S8 to S11), allowing atomic modeling of RNA nucleotides.

Overall structure

The refined model of the C complex from *S. cerevisiae* contains 8587 amino acids from 35 proteins, 377 nucleotides from three snRNAs,

Downloaded from http://science.sciencemag.org/ on September 3, 2016

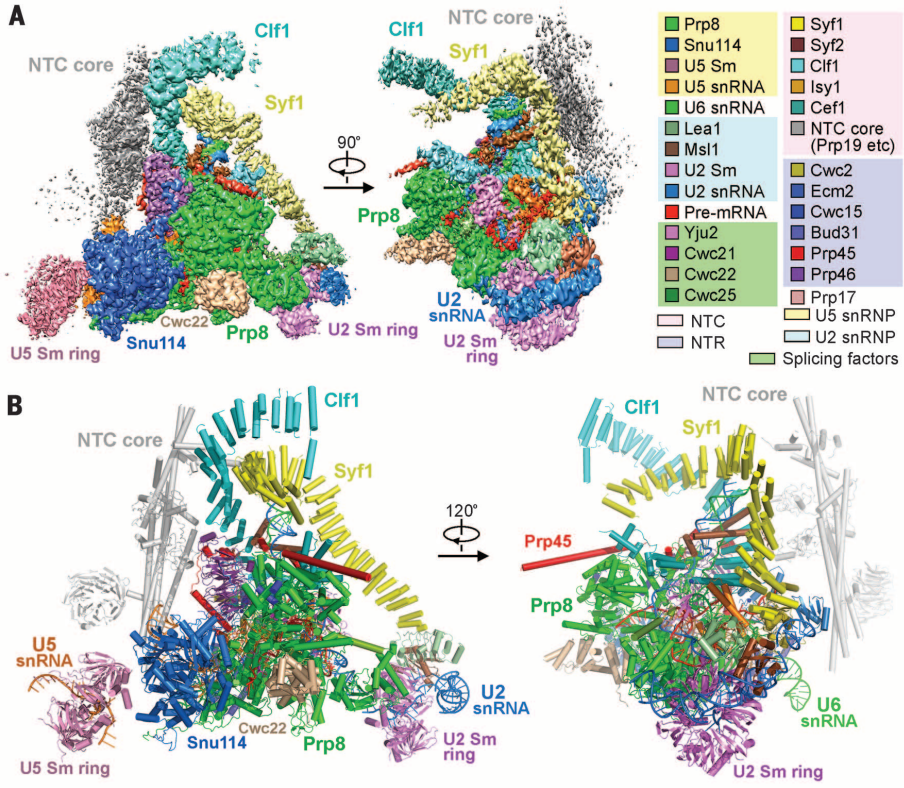

Fig. 1. Cryo-EM structure of the *S. cerevisiae* catalytic step I spliceosome (C complex) at 3.4 Å resolution. (**A**) EM density map of the C complex at an average resolution of 3.4 Å shown in two perpendicular views. The color-coded protein and RNA components are tabulated on the right. (**B**) Structure of the C complex. The cartoon representation shown in two views includes 35 proteins, three snRNAs, a free 13-nucleotide (nt) 5′ exon, and a 44-nt intron lariat, with a combined molecular weight of ~1.1 MDa. Among the modeled 8587 amino acids, 5040 have side chains. Figure 1A was prepared using CHIMERA (*72*). All other structural images were created using PyMol (*73*).

and 57 nucleotides from two pieces of the pre-mRNA molecule (Fig. 1A and tables S1 to S4), with a combined molecular mass of ~1.1 MDa. Among the modeled amino acids, 5040 have side chains and the remaining 3547 residues were built as poly-Ala. The poly-Ala sequences are mostly assigned to the NTC core (Prp19 tetramer, Snt309, and part of Cef1), U5 Sm ring, and the U2 snRNP components (Msl1, Lea1, and U2 Sm ring). The 35 protein components in the atomic model include nine from U5 snRNP, nine from U2 snRNP, seven from NTC, six from NTR, and four splicing factors (Cwc21, Cwc22, Cwc25, and Yju2). Notably, the adenosine triphosphatase (ATPase)/helicase Brr2 displays no discernable EM density, likely reflecting its dynamic nature in the C complex.

The C complex has an extended, triangular appearance, with the NTC core located on the back of the assembly (Fig. 1B). The three corners of the assembly are separated from one another by ~300 Å (fig. S12A). The center and bottom side of the triangular-shaped C complex are constituted by Prp8 and Snu114 of U5 snRNP, portions of the three snRNAs, pre-mRNA, at least 10 protein components from NTC and NTR, and four splicing factors (Fig. 1B). The splicing active site, located in the center of the C complex, and its adjacent RNA elements are sandwiched by two layers of protein components. One layer consists of the anchoring component Prp8, the guanosine triphosphatase Snu114, the NTR protein Bud31, and two splicing factors (Cwc21 and Cwc22) (fig. S12B); the other layer comprises four NTC components (Cef1, Isy1, Syf2, and a portion of Clf1), six NTR proteins (Bud31, Cwc2, Cwc15, Ecm2, Prp45, and Prp46), and the splicing factors Cwc25 and Yju2. Intermolecular interactions within these two layers are stabilized by the intrinsically disordered protein Prp45 and, to a lesser extent, by Cwc15.

The RNA map

The RNA elements display clear features in the density maps (fig. S8A). We assigned nucleotides 28 to 55 and 60 to 127 of U5 snRNA (fig. S8, B to D). In addition, 20 contiguous nucleotides at the 3′ end of U5 snRNA were docked into the density maps along with the heptameric Sm ring. Excluding nine nucleotides at the 3′ end, nucleotides 1 to 103 of U6 snRNA were identified in the maps (fig. S9). U2 snRNA in *S. cerevisiae* contains 1175 nucleotides, most of which are dispensable for pre-mRNA splicing (*44*). Virtually all functionally important sequences of U2 snRNA are visible in the maps, including 48 nucleotides at the 5′ end, which are responsible for forming duplexes with U6 snRNA (helix I and helix II) and with the BPS. The modeled U2 snRNA also includes the stem loop sequences and the binding sites for the U2 Sm ring and Msl1. Fifty-seven nucleotides are assigned to pre-mRNA, which consists of a free 5′ exon (13 nucleotides) and an intron lariat (44 nucleotides) (figs. S9C and S10).

The three snRNA elements are organized into an extended structure, and the pre-mRNA molecule is placed at the center of the RNA map through extensive base-pairing interactions with the snRNAs (Fig. 2A). Consistent with published evidence (*45*–*48*), the freed 5′ exon remains bound to loop I of U5 snRNA and is located close to the T-shaped junction of the intron lariat. Five contiguous nucleotides (UGUAU) of the intron, including three at the 3′ half of the 5′SS, are recognized by the U6 snRNA sequences (AUACA) through Watson-Crick base-pairing interactions (Fig. 2B). Nineteen contiguous nucleotides of the intron, including the BPS (UACUAAC), form a duplex with 17 conserved nucleotides of U2 snRNA, producing two single-nucleotide bulges in the pre-mRNA. One bulge is formed by the nucleophile-containing adenine nucleotide in the BPS. The base-pairing interactions between U2 and U6 snRNAs are consistent with published observations (*49*, *50*) and are nearly identical to those observed previously in the *S. cerevisiae* B^{act} complex (*43*) or the *S. pombe* ILS complex (*11*).

The active site

The active site of the C complex comprises the ISL of U6 snRNA, helix I of the U2/U6 duplex, loop I of U5 snRNA, and five metal ions that are probably magnesium (Mg^{2+}) (Fig. 3A). Three consecutive nucleotides at the 3′ end of the 5′ exon, modeled as AAG, form a short duplex with the nucleotides U96-U97-U98 in loop I of U5 snRNA. The phosphate group of the guanine nucleotide at the 5′ end of the 5′SS is already covalently bonded to the nucleophile (the 2′-oxygen atom of the invariant adenine nucleotide in the BPS). Three of the five putative Mg^{2+} ions are located away from the reaction center and likely stabilize the delicate fold of ISL by neutralizing the negative charges of the RNA backbone phosphates.

The other two Mg^{2+} ions may directly catalyze the two sequential transesterification reactions. The putative M2 ion, which is thought to activate the nucleophile during the first-step reaction (*1*, *6*), is coordinated by the phosphates of A59 and U80 of U6 snRNA (Fig. 3B). M2 is located ~6 Å away from the nucleophile, which likely reflects the postreaction state. During the second-step reaction, M2 is thought to stabilize the leaving group (the 3′-OH of the guanine nucleotide at the 3′ end of the intron) (*1*, *6*). The M1 ion, which stabilizes the leaving group during the first-step reaction (*1*), appears to be coordinated by four ligands in a planar fashion, with two ligands from the pre-mRNA and two from U6 snRNA (Fig. 3B). The coordinating ligands include the phosphate of the invariant adenine nucleotide in the BPS,

Downloaded from http://science.sciencemag.org/ on September 3, 2016

the 3′-OH of the nucleotide at the 3′ end of 5′ exon, and the phosphates of G78 and U80 of U6 snRNA.

Notably, the nucleophile for the second-step reaction—the 3′-OH of the nucleotide at the 3′ end of 5′ exon—is already coordinated and activated by M1, which is known to be responsible for the second-step nucleophile activation (*1*). Although the M1-activated nucleophile is poised to initiate nucleophilic attack, the scissile phosphodiester bond between the intron and 3′ exon is yet to be loaded into the active site. The placement of M2 away from the lariat junction in the C complex makes the reversal of the first-step reaction highly unlikely. Both steps of the pre-mRNA splicing reactions in vitro were shown to be reversible through alteration of the experimental conditions, particularly the identity and concentration of the cations (*51*).

Comparison of the snRNA elements

Structural analysis of the *S. cerevisiae* B^{act} complex supported the prediction that the overall conformation of the snRNA elements in the catalytic center is highly conserved in various spliceosomal complexes (*12*, *43*). Structural resolution of the *S. cerevisiae* C complex provides another opportunity to scrutinize this prediction. The U5 snRNA of the B^{act} complex aligns well with that of the C complex, with near-perfect registry for both the phosphodiester backbone and the base-pairing interactions (Fig. 4A and fig. S13A). Applying the same alignment matrix to the entire RNA map, the overall structures of U6 snRNA, the 5′ exon, and a portion of the intron at the 5′ end in the B^{act} complex superimpose well with those of the corresponding elements in the C complex (Fig. 4A and fig. S13B). A closer examination reveals minor shifts, mostly within ~3 Å, for nucleotides in the ISL of U6 snRNA (Fig. 4A, inset). Despite large conformational changes for the majority of the U2 snRNA sequences, nucleotides 1 to 30 adopt a nearly identical structure between these two complexes (Fig. 4A and fig. S13C). These sequences include helices I and II; the former contributes to formation of the active site. Notably, the U2 snRNA sequences (nucleotides 32 to 47) that form a duplex with BPS and the surrounding intron sequences are translocated by distances of 25 to 95 Å from the B^{act} to the C complex. This shift presumably occurs in the B* complex, which brings the nucleophile in the BPS in close proximity to the scissile phosphodiester bond for the first-step reaction (*52*).

Analogous to the comparison between the B^{act} and C complexes, U5 snRNA, U6 snRNA, and the 5′-end portion of U2 snRNA remain structurally similar between the *S. cerevisiae* C complex and the *S. pombe* ILS complex (*11*, *12*) (Fig. 4B and fig. S13, A to C). Unlike that in the *S. cerevisiae* B^{act} or C complex, the 5′ exon has been released from the ILS complex. The T-shaped junction of the intron lariat in the ILS complex is located in a different position compared with that in the C complex (Fig. 4C and fig. S13D). The guanine nucleotide at the 5′ end of the 5′SS and the invariant adenine nucleotide of the BPS in the ILS complex are separated from the corresponding nucleotides of the C complex by ~25 Å (Fig. 4D). Such translocation likely occurs before the second-step reaction so as to vacate the space for accommodation of the 3′ exon and the preceding intron sequences.

Prp8 and the RNaseH-like domain

Prp8 displays clear EM density for most sequences (fig. S5, A to G). The Jab1/MPN domain exhibits no density and is not modeled in our structure. Both the N domain and the core of Prp8 in the C complex align well with those in the B^{act} complex (*43*) (Fig. 5A). Consistent with a role in stabilizing the bound 5′ exon (*43*), the switch loops (residues 1402 to 1439) in these two complexes adopt an identical conformation. The ribonuclease H (RNaseH)–like domains, however, exhibit a large positional shift of up to 99 Å

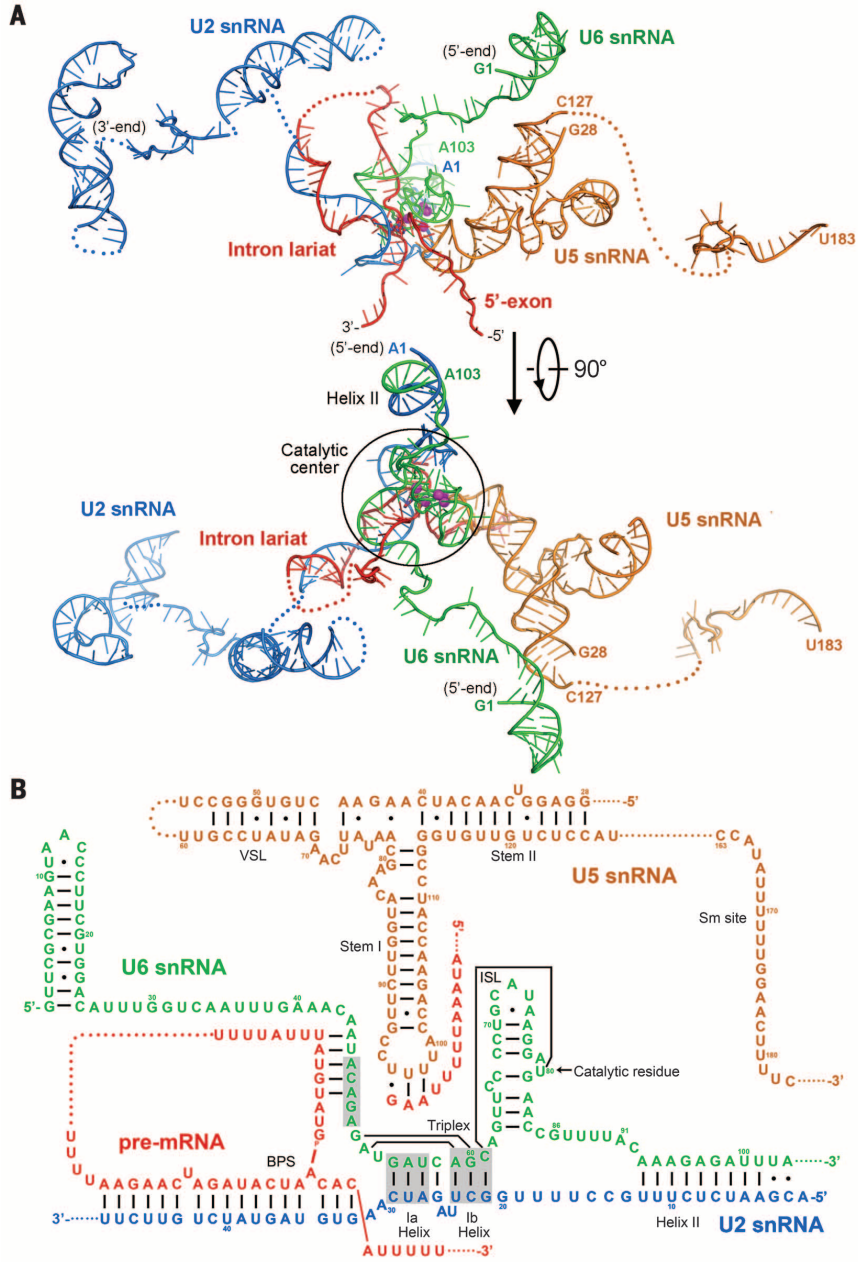

Fig. 2. Arrangement of the RNA elements in the *S. cerevisiae* C complex. (**A**) Overall cartoon representation of the RNA map displayed in two perpendicular views. The catalytic center comprises the ISL of U6 snRNA, helix I of the U2/U6 duplex, loop I of U5 snRNA, and the Mg^{2+} ions. After the first-step reaction, the freed 5′ exon remains anchored to loop I. The invariant adenine nucleotide from the BPS is covalently linked to the guanine nucleotide at the 5′ end of the 5′SS. The disordered RNA sequences are indicated by dotted lines. (**B**) Overall base-pairing interactions among U2 snRNA, U5 snRNA, U6 snRNA, the 5′ exon, and the intron lariat. Canonical Watson-Crick and noncanonical base-pairing interactions are identified by solid lines and dots, respectively.

Downloaded from http://science.sciencemag.org/ on September 3, 2016

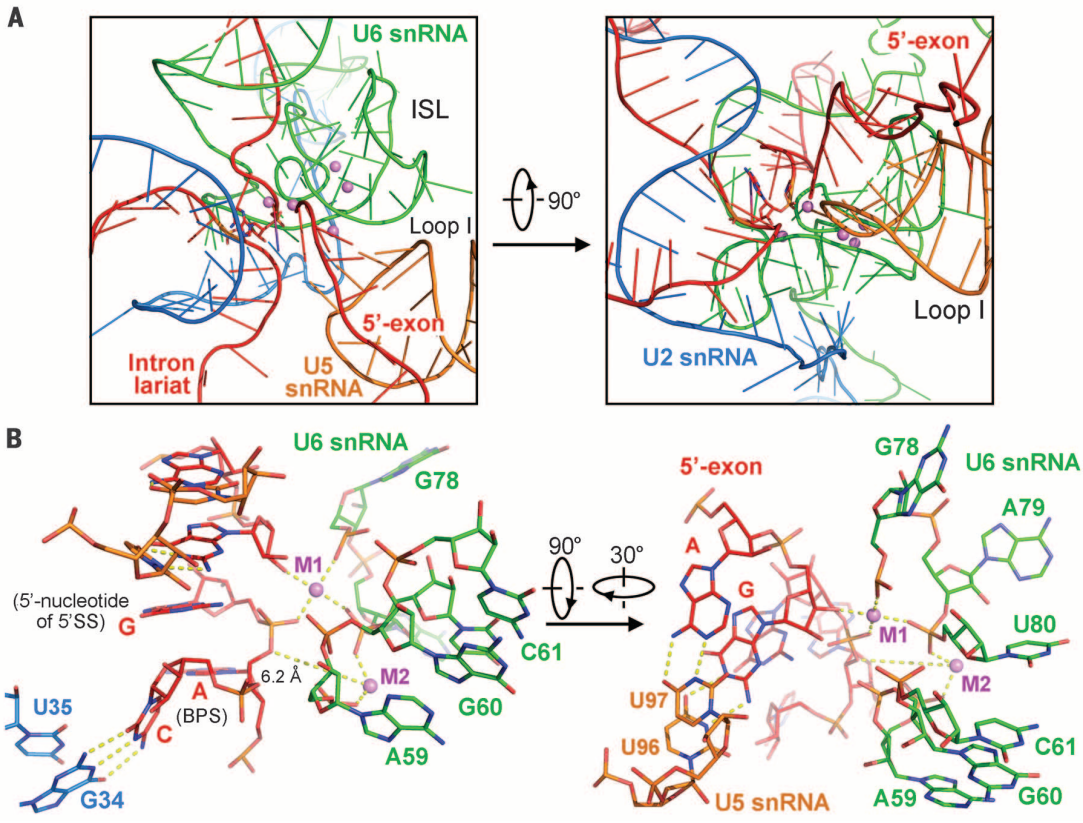

Fig. 3. Catalytic center and active site of the *S. cerevisiae* C complex. (**A**) Structure of the catalytic center is shown in two perpendicular views. Following the first transesterification reaction, the 2′-oxygen atom of the invariant adenine nucleotide in the BPS is covalently joined to the phosphorous atom of the guanine nucleotide at the 5′ end of the 5′SS. (**B**) Two close-up views of the active site. Among the two putative Mg^{2+} ions, M1 is coordinated by phosphate groups from G78 and U80 of U6 snRNA, and M2 is bound by phosphates from A59 and U80. In addition, M1 is bound to the phosphate of the guanine nucleotide at the 5′ end of the 5′SS and the 3′-OH of the nucleotide at the 3′ end of the 5′ exon. The M2 ion, which activates the nucleophile before the first transesterification reaction, is separated from the nucleophile (i.e., the 3′-OH of the invariant adenine nucleotide in the BPS) by ~6 Å.

between the B^{act} and C complexes. Prp8 of the *S. cerevisiae* C complex and Spp42 of the *S. pombe* ILS complex (*11*) also exhibit very similar conformations for their N domains and the cores (Fig. 5B). Conversely, the switch loop in Spp42 points in the opposite direction of that in Prp8 of the C complex, reflecting the 5′-exon released state in the ILS complex. The RNaseH-like domains in these two complexes adopt very different positions (Fig. 5B). Similar to that between the U4/U6.U5 tri-snRNP and the B^{act} complex (*43*), only the core of Prp8 from the tri-snRNP aligns well with that of the C complex (Fig. 5C). The N domains, switch loops, and RNaseH-like domains all display marked positional variations.

Despite their very different positions (Fig. 5D), the RNaseH-like domains in the three spliceosomal complexes align with each other to near-perfect registry (Fig. 5E). Thus, the RNaseH-like domain has a rigid conformation but serves as a highly mobile element in the various spliceosomal complexes. Structural analysis reveals a surprising role for the RNaseH-like domain in stabilizing a mobile RNA element during pre-mRNA splicing (fig. S14). In the U4/U6.U5 tri-snRNP (*41*, *42*), the RNaseH-like domain simultaneously interacts with Prp3, Prp6, and Prp31, whereas Prp3 and Prp31 directly recognize the U4/U6 duplex (fig. S14A). The RNaseH-like domain must be dislocated before Brr2 unwinds the U4/U6 duplex. In the B^{act} complex (*43*), the RNaseH-like domain associates with the scaffold protein Hsh155 and the splicing factor Cwc22 (fig. S14B). Because Hsh155 plays a major role in binding the BPS and intron sequences toward the 3′ end (*53*, *54*), the RNaseH-like domain would have to dissociate for the BPS to move to the catalytic center of the spliceosome. In the C complex, the RNaseH-like domain directly recognizes the intron-U2 snRNA duplex while interacting with the U2 Sm ring and the splicing factor Cwc25 (fig. S14C). In the *S. pombe* ILS complex (*11*), the RNaseH-like domain of Spp42 mainly interacts with Cwf19, which binds to the intron lariat and ISL of U6 snRNA while making close contacts with the core of Spp42 (fig. S14D). The dissociation of the intron lariat is likely preceded by the dislocation of the RNaseH-like domain.

Protein components at the center of the C complex

The RNA elements at the catalytic center are specifically recognized by a number of protein components (Fig. 6A). As previously observed (*11*), the splicing active site is anchored in a positively charged catalytic cavity formed between the N domain and the core of Prp8 (Fig. 6B). In addition to Prp8, at least 15 other proteins directly contact the RNA elements at the center of the C complex (Fig. 6C). These proteins and Prp8 also closely interact with one another to stabilize the conformation of the RNA elements.

The NTC components Cef1, Isy1, and Syf2

Cef1, the *S. cerevisiae* ortholog of Cdc5 in *S. pombe*, is essential for pre-mRNA splicing (*55*, *56*). The N-terminal sequences (residues 9 to 111) constitute a Myb domain of six α helices, followed by extended sequences that form four additional α helices (Fig. 6D). The N-terminal residues of helix α8 (residues 165 to 194) reach into the active site to contact the ISL, whereas the middle portion of α8 binds the NTC component Isy1. The C-terminal half of α8 and helices α9 and α10 of Cef1 interact with Ecm2 and the N-terminal helices of Clf1, and the intervening loop between α8 and α9 also binds the 5′ intron just downstream of the 5′SS. The N-terminal half of the Myb domain (α1 to α3) closely interacts with α7 to form a globular domain, which associates with helix I of the U2/U6 duplex, Prp45, Syf2, and the core of Prp8 (Fig. 6D).

Isy1 is thought to act together with U6 snRNA to promote a spliceosomal conformation favorable for the first-step reaction and also to interact with Prp16 to regulate the fidelity of pre-mRNA splicing (*57*). Isy1 (residues 2 to 96) consists of four α helices. Helices α1 and α2 reach into the lariat junction and interact with the surrounding intron sequences, the BPS-U2 duplex, one side of the 5′SS-U6 duplex, Cwc2, and the splicing factor Yju2 (Fig. 6E). A pair of antiparallel helices (α3 and α4) associates with the other side of the 5′SS-U6 duplex and helix α8 of Cef1. The NTC component Syf2 (residues 92 to 211), which is thought to modulate Syf1 function (*58*), wraps around helix II of the U2/U6 duplex while interacting with Prp45 and Clf1 (Fig. 6D).

The NTR components Cwc2, Ecm2, and Bud31

As an essential NTR component that contains a RRM motif and a zinc finger, Cwc2 is known to

Downloaded from http://science.sciencemag.org/ on September 3, 2016

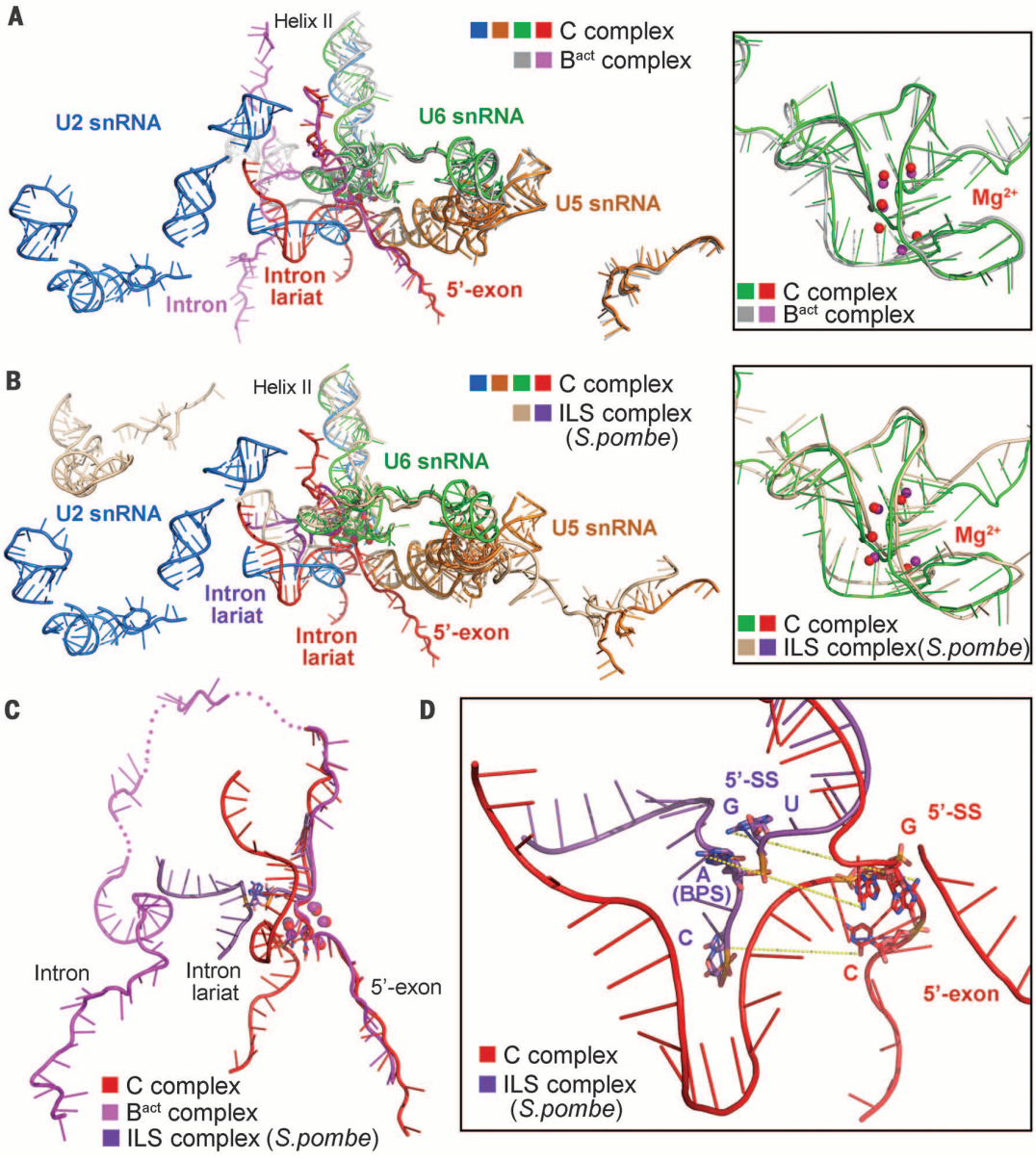

Fig. 4. Structural comparison of the RNA elements among the B^{act} and C complexes from *S. cerevisiae* and the ILS complex from *S. pombe*. (**A**) Structural comparison of the overall RNA maps between the B^{act} (*43*) and C complexes from *S. cerevisiae*. Comparison of the ISL is shown in the inset. U5, U6, and the 5′ portion of U2 snRNA remain largely the same between the two complexes. (**B**) Structural comparison of the overall RNA maps between the C complex from *S. cerevisiae* and the ILS complex from *S. pombe* (*12*). The ISL structure is similar between the two complexes (inset). (**C**) Structural comparison of the pre-mRNA molecules from the three complexes. (**D**) Close-up comparison of the lariat junction between the C complex from *S. cerevisiae* and the ILS complex from *S. pombe* (*12*). The T-shaped lariat junction in the ILS complex is separated from that in the C complex by 20 to 25 Å. The lariat junction in the C complex must be moved away before the second transesterification reaction can occur.

directly cross-link to U6 snRNA and pre-mRNA (*59*, *60*). In our structure, Cwc2 recognizes the intron sequences just downstream of the 5′SS and 11 nucleotides of U6 snRNA preceding the U6 sequences that base-pair with the 5′SS (Fig. 6E). Cwc2 also interacts with Ecm2, Bud31, and Isy1. Ecm2 is thought to facilitate the cooperative formation of helix II in the activation of yeast spliceosome (*61*). In our structure, Ecm2 consists of an N-terminal metal-binding domain (residues 3 to 125) and a C-terminal globular domain (residues 210 to 288) that comprises a four-stranded β sheet stacked against two α helices (Fig. 6F). These two domains are separated by and closely interact with Cwc2. The N-terminal domain of Ecm2 also binds Cef1, Prp45, and U6 nucleotides 29 to 32. The nonessential NTR component Bud31 is thought to stabilize the pre-mRNA–protein interactions (*62*). Bud31 associates with U6 nucleotides 25 to 29, stem II of U5 snRNA, and the N domain of Prp8 (Fig. 6E).

The splicing factors Cwc21, Cwc22, Cwc25, and Yju2

Cwc21 is the functional ortholog of SRm300, which is the only SR-related protein known to be located at the catalytic center of the human spliceosomes (*63*, *64*). In our structure, only residues 2 to 28 of Cwc21 are well characterized by the EM maps; these sequences are embedded in the center of the spliceosome, closely interacting with the 5′ exon (Fig. 6G). The N-terminal sequences of Cwc21 bind the Prp8 N domain, and a lone β strand of Cwc21 pairs with a short β strand from the switch loop. The sequences following the β strand of Cwc21 interact with Cwc22, whereas Cwc22 also associates with the core of Prp8 and directly contacts the switch loop.

Yju2 is thought to associate with the NTC and promotes the first-step reaction after the action of the ATPase Prp2 (*65*). The evolutionarily conserved N-terminal domain of Yju2 (residues 1 to 130) promoted the first transesterification reaction to ~75% of that by the full-length protein (*66*). The extended N-terminal sequences of Yju2 (residues 2 to 16) reach into a deep cleft at the active site, interacting with the 5′ exon, both the N domain and the core of Prp8, and a portion of U2 snRNA that recognizes BPS. An ensuing α helix (residues 17 to 31) intercalates between the BPS-U2 duplex and the α1 and α2 helices of Isy1 (Fig. 6H). A five-stranded β-sheet domain (residues 38 to 116) associates with the ISL, the phosphate backbone of the intron, and the splicing factor Cwc25. Cwc25 is a heat-stable step I factor containing a short coiled-coil motif and is required after Prp2 and Yju2 to facilitate the first-step

Downloaded from http://science.sciencemag.org/ on September 3, 2016

reaction (*52*, *67*). The extended N-terminal sequences of Cwc25 (residues 2 to 16) are inserted deeply into the active site, interacting with the ISL, the BPS-U2 duplex, helix I, and the β-sheet domain of Yju2 (Fig. 6H). An α helix (residues 17 to 42) of Cwc25 extends from the active site by ~37 Å to interact with the RNaseH-like domain of Prp8.

The NTR components Prp46, Cwc15, and Prp45

The WD40 protein Prp46 is a seven-bladed β propeller (*68*). The top face (*69*) of the Prp46 propeller interacts with Prp8, whereas the bottom face binds extended sequences of Prp45 (residues 51 to 99) (Fig. 6I). Prp46 also contacts Cwc15, Clf1, and stem I of U5 snRNA. The intrinsically disordered proteins Cwc15 and Prp45 appear to stabilize the catalytic center by simultaneously interacting with multiple components at the center of the spliceosome. Both Cwc15 and Prp45 directly contact all three snRNA elements.

RNA recognition by the splicing factors

The identified 16 protein components at the center of the spliceosome interact closely with one another and make numerous contacts to the four RNA elements. A detailed description of these interactions goes beyond the scope of this manuscript. Nonetheless, we wish to exemplify such interactions by focusing on the splicing factor Yju2. Yju2 and the surrounding proteins Cwc25, Isy1, and Cef1 together form a scaffold onto which the RNA elements are placed (Fig. 7A). The RNA elements closely follow the positively charged surface of the protein scaffold, where the basic amino acids play a key role in RNA recognition (Fig. 7B). Lys^{63} and Lys^{68} of Yju2 directly contact the phosphate groups of the BPS and U6 snRNA, respectively; Arg^{42} of Yju2 may recognize A51 of U6 snRNA through a base-specific hydrogen bond (H-bond) (Fig. 7C). Asn^{65} of Yju2 may also specifically recognize G50 of U6 snRNA. The N-terminal residue Arg^{3} of Isy1 likely donates a pair of H-bonds to the backbone phosphates of the BPS, whereas the N-terminal residue Gly^{2} of Cwc25 may make two H-bonds with the BPS and U6 snRNA. In addition, the side chain of Lys^{10} from Cwc25 donates a

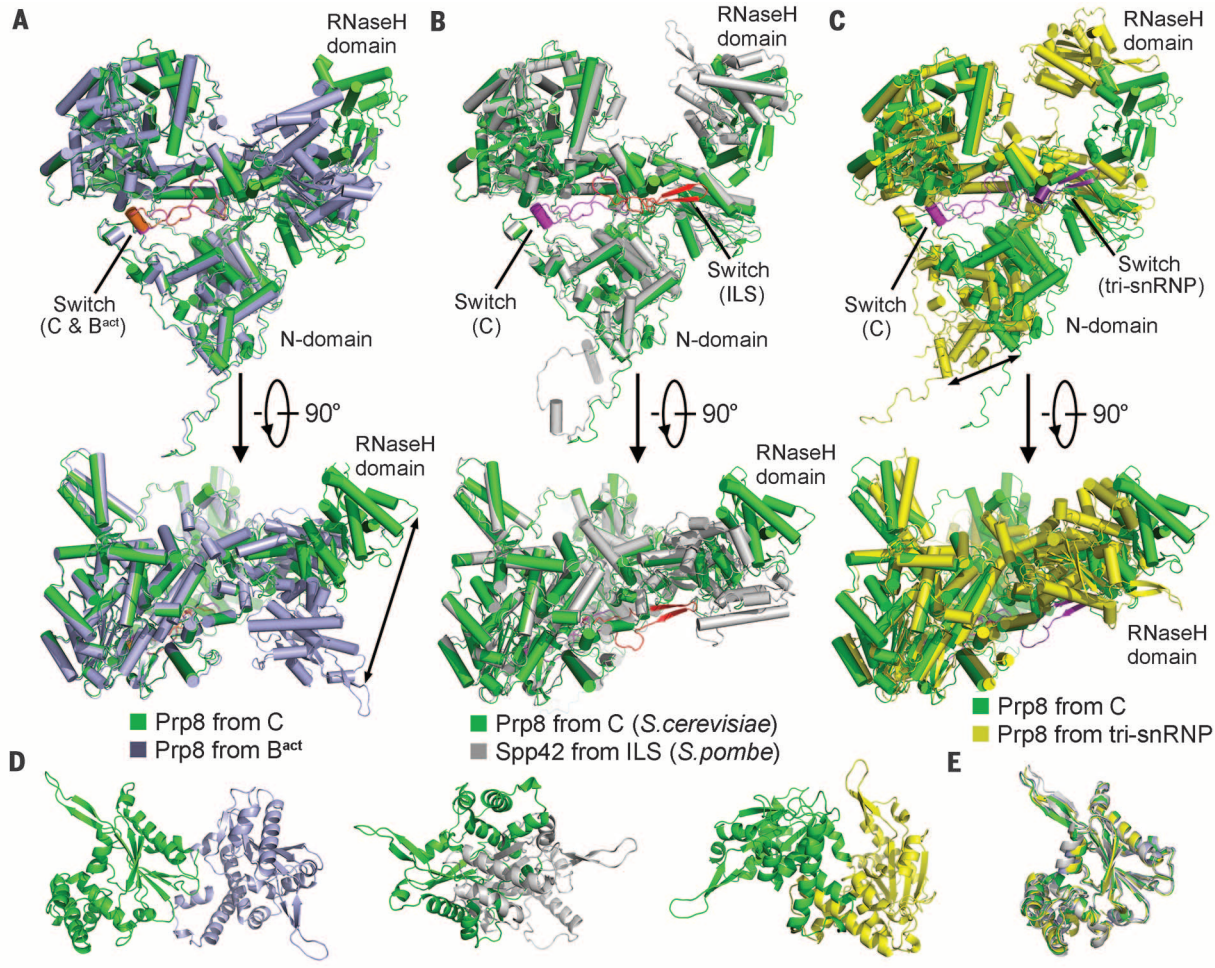

Fig. 5. Structural comparison of the central component Prp8 (Spp42 in *S. pombe*) among three spliceosomal complexes and the U4/U6.U5 tri-snRNP. (**A**) Structural comparison of Prp8 between the B^{act} (*43*) and C complexes from *S. cerevisiae*. Both the N domain and the core of Prp8 align well, including the switch loop (colored orange and magenta in the B^{act} and C complexes, respectively). In contrast, the RNaseH-like domain adopts two markedly different locations in the two complexes. (**B**) Structural comparison of Prp8 from the *S. cerevisiae* C complex and Spp42 from the *S. pombe* ILS complex (*11*). Compared with that in the C complex, the switch loop in the ILS complex (colored red) is flipped 180°. The RNaseH-like domains exhibit pronounced positional differences in the two complexes. (**C**) Structural comparison of Prp8 between the C complex and the U4/U6.U5 tri-snRNP from *S. cerevisiae* (*41*). The N domains, switch loops, and RNaseH-like domains all exhibit large differences. Similar to that in the ILS complex, the switch loop in the tri-snRNP points in the opposite direction of that in the C complex. (**D**) Three close-up views of the RNaseH-like domains. A pairwise comparison of the RNaseH-like domains is shown between the B^{act} (*43*) and C complexes from *S. cerevisiae* (left), between the *S. cerevisiae* C complex and the *S. pombe* ILS complex (*11*) (middle), and between the C complex and the tri-snRNP from *S. cerevisiae* (*41*) (right). (**E**) Superposition of the RNaseH-like domains from the four complexes. The smallest difference has a root mean square deviation (RMSD) of only 0.62 Å for 244 aligned Cα atoms between the B^{act} and C complexes. The largest variation has an RMSD of 1.52 Å for 228 aligned Cα atoms between the *S. cerevisiae* B^{act} complex and the *S. pombe* ILS complex.

Downloaded from http://science.sciencemag.org/ on September 3, 2016

candidate H-bond to the phosphate backbone of the BPS (Fig. 7C).

The other two splicing factors Cwc21 and Cwc22 cooperate to stabilize the 5′ exon (Fig. 7D). The extended sequences of Cwc21 are oriented by the switch loop of Prp8 and Cwc22 to recognize the 5′ exon. Four residues of Cwc21 (Ser[2], Lys[12], His[19], and Arg[22]) may make direct H-bonds to nucleotides of the 5′ exon (Fig. 7E). His[19] of Cwc21 may contact a base of the 5′ exon through cation-π interactions. The majority of these interactions are directed to the phosphates and the ribose of the 5′ exon, consistent with the highly variable nature of the 5′-exon sequences. In addition, the interactions between Cwc21 and the 5′ exon are of low-to-moderate intensity, which presumably would not impede dissociation of the joined exons after the second-step reaction.

Discussion

We previously reported atomic structures of the spliceosome, representing the beginning and ending states of the two transesterification reactions: the *S. cerevisiae* activated B^{act} complex

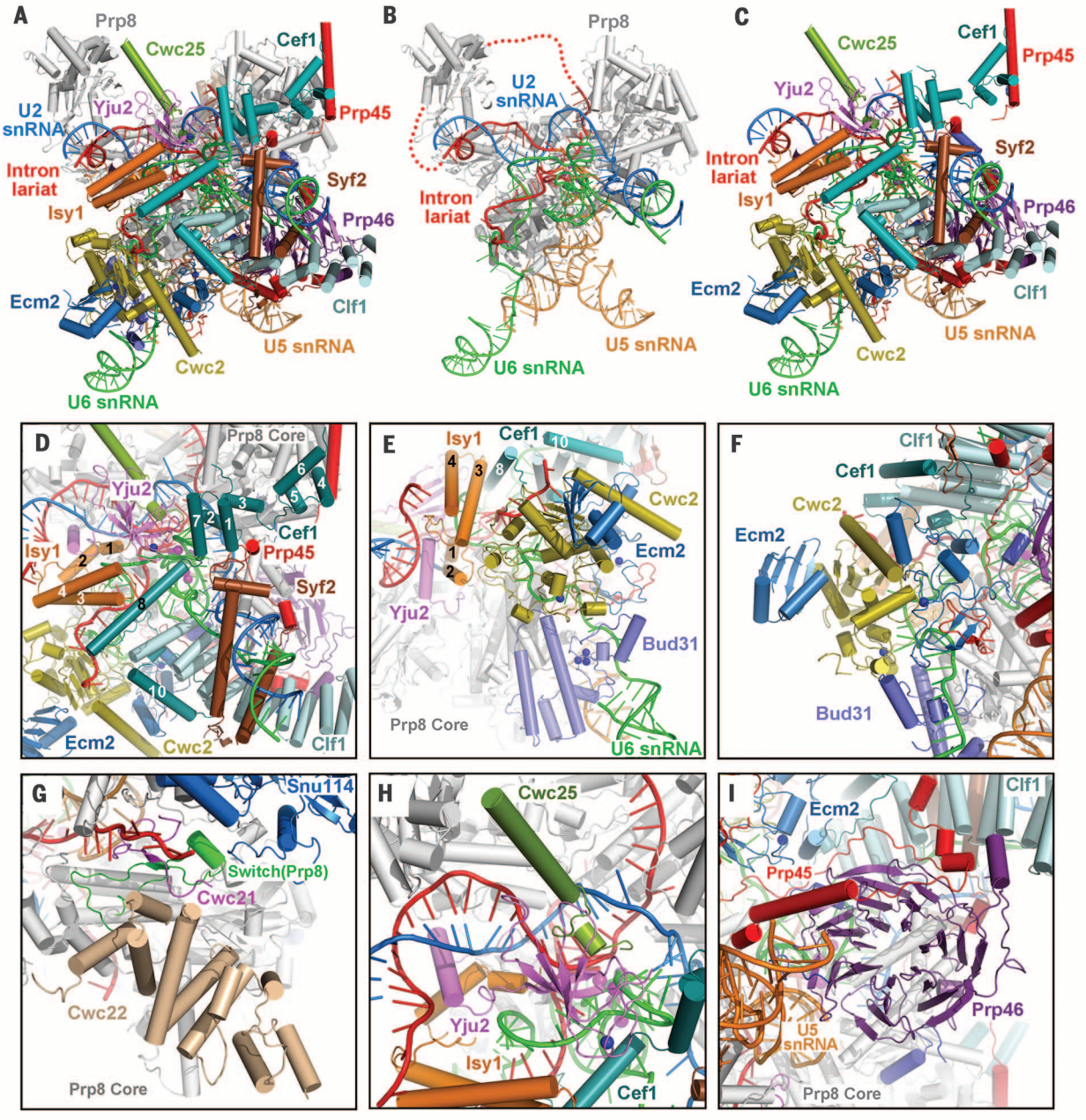

Fig. 6. Protein-protein and protein-RNA interactions at the center of the C complex. (**A**) Overall view on the center of the C complex. At least 16 protein components directly interact with the RNA elements at the catalytic center. (**B**) Prp8 anchors the RNA elements at the catalytic center. (**C**) Locations of 14 protein components relative to the central RNA elements. Prp8 and Snu114 are removed to allow improved viewing of the other proteins. (**D**) Close-up view of the NTC components Cef1 and Syf2. (**E**) Close-up view on the NTC component Isy1 and the NTR components Cwc2 and Bud31. The interactions and the compact fold of Cwc2 are stabilized by a zinc ion that is bound to $Cys^{73}/^{81}/^{87}$ and His^{91}. Bud31 contains a metal cluster of three zinc ions, each of which is tetrahedrally coordinated by four Cys residues ($Cys^{104}/^{105}/^{108}/^{148}$, $Cys^{104}/^{122}/^{150}/^{153}$, and $Cys^{108}/^{120}/^{122}/^{145}$). (**F**) Close-up view of the NTR component Ecm2. Two zinc ions in the N-terminal domain of Ecm2 are coordinated by $Cys^{13}/^{71}/^{73}/^{74}$ and $Cys^{34}/^{37}/^{61}/^{64}$. (**G**) Close-up view of the splicing factors Cwc21 and Cwc22. (**H**) Close-up view of the splicing factors Yju2 and Cwc25. A zinc ion is coordinated by $Cys^{51}/^{54}/^{88}/^{91}$ at the edge of the β sheet in Yju2. (**I**) Close-up view of the NTR component Prp46.

Downloaded from http://science.sciencemag.org/ on September 3, 2016

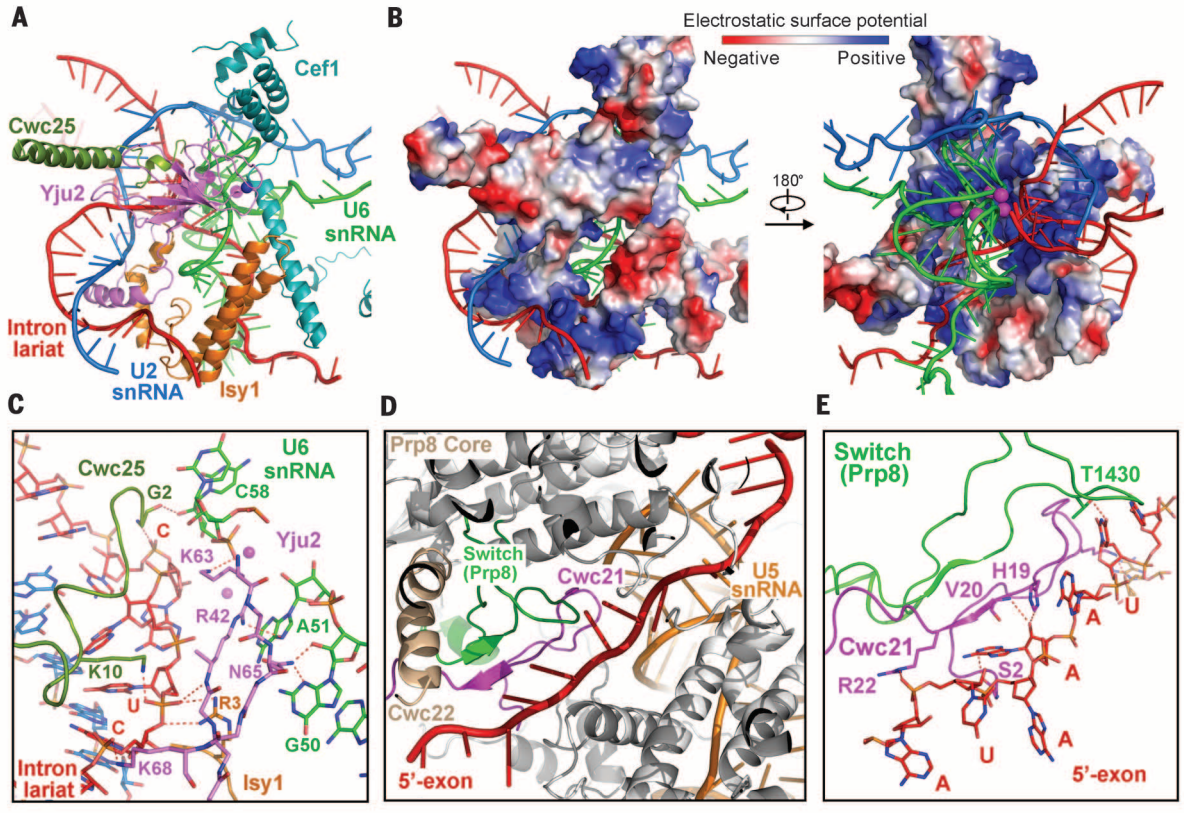

Fig. 7. RNA recognition at the catalytic center by the splicing factors Yju2, Cwc25, Cwc21, and Cwc22. (**A**) Recognition of the RNA elements at the catalytic center by Cef1, Cwc25, Isy1, and Yju2. Prp8 and other protein components are removed. (**B**) RNA elements mainly interact with the positively charged surface areas in the four proteins (Cef1, Cwc25, Isy1, and Yju2). Two views of the electrostatic surface potential are shown here. Proteins in the left panel display the same exact orientation as those in (A). (**C**) Close-up view of the detailed interactions involving the N terminus of Cwc25 and Yju2. A hydrogen bond (H-bond) is tentatively assigned when a H-donor and a H-acceptor are located within ~3.5 Å of each other. G, Gly; C, Cys; R, Arg; A, Ala; N, Asn; K, Lys. (**D**) Close-up view of Cwc21 and its interactions with 5′ exon and the switch loop (green). (**E**) Close-up view of the detailed interactions between Cwc21 and the 5′-exon sequences. T, Thr; H, His; V, Val; S, Ser.

(*43*) and the *S. pombe* intron-lariat ILS complex (*11*). In this manuscript, we report the cryo-EM structure of a crucial intermediate spliceosomal complex: the catalytic step I spliceosome. These three structures reveal detailed arrangements of the RNA map that begin to recapitulate the process of the pre-mRNA splicing reaction (Fig. 8A).

The structures of U5 and U6 snRNAs, along with their relative positions in the RNA map, remain largely unchanged in all three spliceosomal complexes (Fig. 8, A and B). Consequently, the U2 sequences that form duplexes with U6 snRNA (helices I and II) also remain relatively static among these spliceosomal complexes. Therefore, the 3′ half of the 5′SS and a few ensuing nucleotides of the intron, which are recognized by U6 snRNA, and the 5′ exon, which is anchored to loop I of U5 snRNA, should remain largely static throughout the two reactions. This conclusion has been corroborated by structures of the B^{act}, C, and ILS complexes (*11*, *12*, *43*). The mobile elements are the 5′ half of the 5′SS; the RNA sequences far downstream of the 5′SS, including the BPS and the 3′ exon; and some of the U2 snRNA sequences, particularly those that form duplexes with the BPS.

In the B^{act} complex, the nucleophile (i.e., the 2′-OH of the invariant adenine nucleotide of the BPS) is located ~50 Å away from the phosphorous atom of the guanine nucleotide at the 5′ end of the 5′SS (*43*). During the transition from the B^{act} to the B* complex, the BPS-U2 duplex must be moved into the active site to initiate the first transesterification reaction. Thus, the general features of the RNA map in the B* complex should be very similar to those of the C complex, except that the covalent linkage between the 5′SS and the 5′ exon in the B* complex is broken in the C complex and replaced by that between the 5′SS and the BPS (Fig. 8). In the C complex, the location to be occupied by the 3′ exon and its preceding intron sequences (the 3′SS, for example) is occupied by the T-shaped lariat junction and surrounding intron sequences. These structural elements must be moved away before the onset of the second transesterification reaction (*70*). In the P complex, the two ligated exons (the 5′ and 3′ exons) should remain bound at the catalytic center as a single chain, with the 5′ exon anchored to loop I of U5 snRNA (*45*, *48*) (Fig. 8). We speculate that the intron lariat in the P complex is bound at a similar position as that in the ILS complex (*11*, *12*), which leaves ample space for the accommodation of the 3′-exon sequences (Fig. 8). The spatial requirement for accommodation of the 3′ exon in the P complex is suggested by the structure of the ILS complex (*11*).

Three of the six distinct spliceosomal complexes (B^{act}, C, and ILS) that have been structurally characterized are interspersed by two missing conformations, B* and P, that are likely to be more transient. However, available information on the three structurally characterized complexes allows us to model the RNA maps of the B* and P complexes (Fig. 8A). The transition from the C to the P complex likely comprises two distinct steps. During the first step, the T-shaped lariat junction in the C complex is moved away from the active site, and the 3′ exon and its preceding intron sequences are translocated into the active site. The resulting complex, which perhaps should be named the step II catalytically activated spliceosome (or C* complex), is likely to be transient (Fig. 8B). The proposed C* complex just before the step II transesterification corresponds to the B* complex for the step I transesterification. During the second step, the step II transesterification occurs, and the released intron sequences preceding the 3′ exon are moved away from the active site, resulting in the P complex.

Because the conformation of the RNA elements in each spliceosomal complex is stabilized

Downloaded from http://science.sciencemag.org/ on September 3, 2016

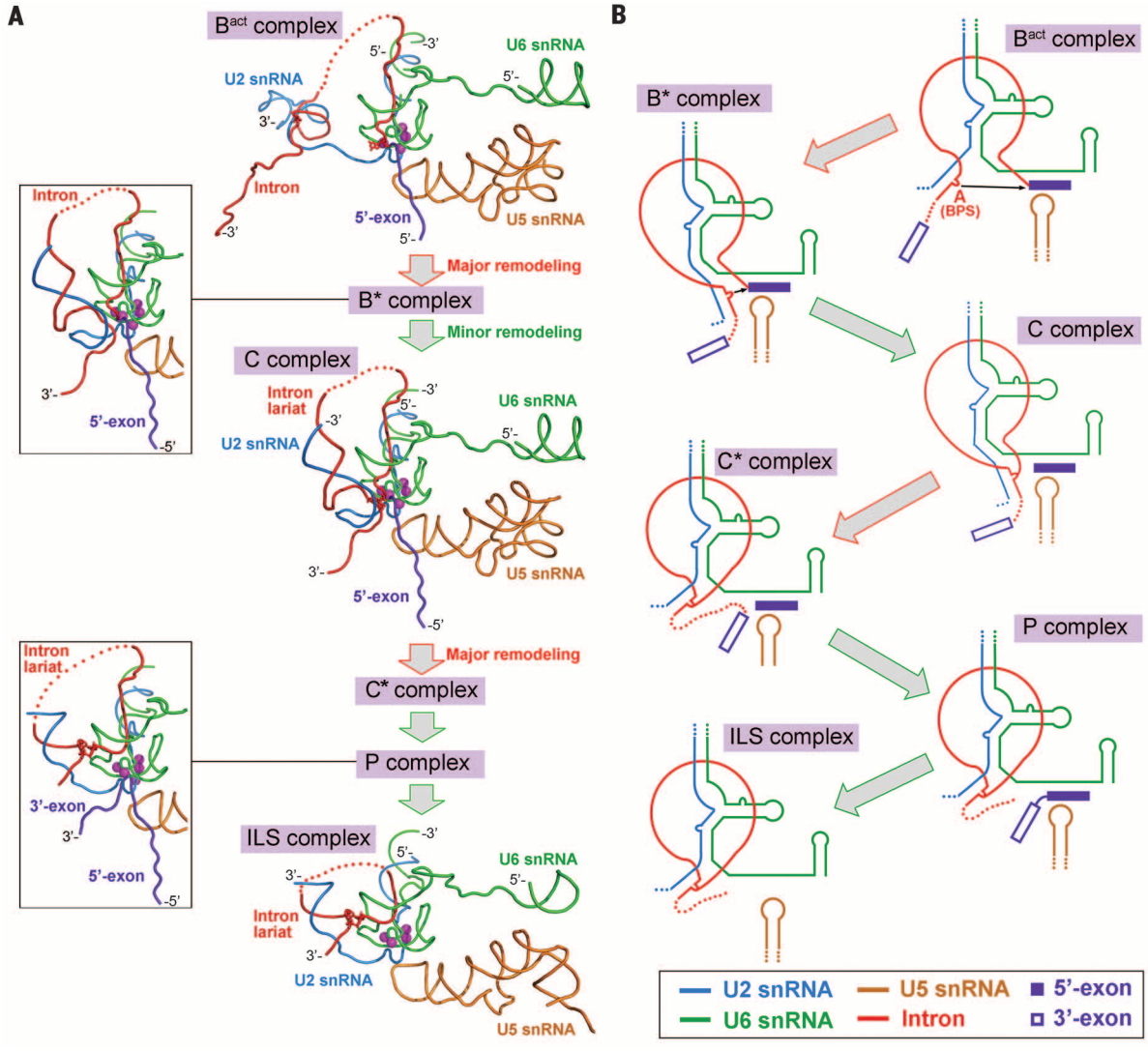

Fig. 8. Working model of pre-mRNA splicing at the level of RNA conformation. (**A**) Conformations of the RNA elements during the two transesterification reactions. In the B^{act} complex (*43*), the nucleophile-containing adenine nucleotide in the BPS is located ~50 Å away from the nucleotide at the 5′ end of the 5′SS. In the C complex, the 5′ exon is severed from the intron, but the lariat junction and the surrounding intron sequences occupy the same general location as that required for the 3′ exon and the preceding intron sequences. In the ILS complex (*11*, *12*), the lariat junction and the surrounding intron sequences are located more than 20 Å away from the catalytic Mg^{2+} ions. These structural observations allow us to model the yet-to-be-captured conformations of the RNA elements in the B* and P comlexes. The movement and placement of the RNA elements are driven by the protein components, the splicing factors, and the RNA-dependent ATPases/helicases. (**B**) A schematic representation of the pre-mRNA splicing pathway as proposed in (A). In the proposed C* complex (step II catalytically activated spliceosome), the lariat junction has moved away, and the 3′ exon and the preceding intron sequences are delivered into the active site.

by Prp8 and a distinct set of protein components, movement of the BPS-U2 duplex should be accompanied by dissociation of many proteins and association of many others. Such remodeling processes are driven by the highly conserved ATPase/helicases Prp2, Prp16, and Prp22. This has been experimentally observed for the transition from the B^{act} to the B* complex and then to the C complex, from the C to the P complex, and from the P to the ILS complex (*3*). Analysis of the RNA maps and associated protein components suggests that the remodeling processes may be particularly drastic for the transitions from B^{act} to B* and from C to C* (Fig. 8). For example, at least 12 structurally identified proteins in the B^{act} complex (*43*)—including three in the RES complex (Bud13, Pml1, and Snu17), seven in the SF3a/b complex (Rse1, Hsh155, Cus1, Hsh49, Rds3, Ysf3, and Prp11), and two splicing factors (Cwc24 and Cwc27)—are dissociated in the C complex. Simultaneously, at least three proteins that were absent in the catalytic center of the B^{act} complex now appear in the catalytic center of the C complex, including two splicing factors (Cwc25 and Yju2) and the NTC protein Isy1.

Limited by both the local resolution and the highly heterogeneous nature of the spliceosome, some of the cryo-EM density maps at the peripheral regions are poorly defined and the constituent proteins are yet to be identified. This is true for all three spliceosomal complexes (B^{act}, C, and ILS) and for the U4/U6.U5 tri-snRNP. Enhancement of the density maps, perhaps through acquisition of more spliceosomal particles and application of improved analysis software, will allow identification of more protein components and assignment of more RNA sequences. This practice will lead to more precise description of the splicing active site and the coordination of catalytic metal ions. Nonetheless, the local resolutions already reach 2.8 to 3.2 Å in the center of the three spliceosomal complexes, allowing unambiguous assignment of amino acid side chains. Such resolutions may facilitate identification of chemical components

Downloaded from http://science.sciencemag.org/ on September 3, 2016

that modulate the splicing reaction. After all, a sizable fraction of genetic disorders are caused by defects in pre-mRNA splicing (*77*).

REFERENCES AND NOTES

1. S. M. Fica *et al.*, *Nature* **503**, 229–234 (2013).
2. M. J. Moore, C. C. Query, P. A. Sharp, in *The RNA World*, R. F. Gesteland, J. F. Atkins, Eds. (Cold Spring Harbor Monograph Archive, Cold Spring Harbor Laboratory Press, 1993), pp. 303–357.
3. M. C. Wahl, C. L. Will, R. Lührmann, *Cell* **136**, 701–718 (2009).
4. C. L. Will, R. Lührmann, *Cold Spring Harb. Perspect. Biol.* **3**, a003707 (2011).
5. D. S. Horowitz, *Wiley Interdiscip. Rev. RNA* **3**, 331–350 (2012).
6. T. A. Steitz, J. A. Steitz, *Proc. Natl. Acad. Sci. U.S.A.* **90**, 6498–6502 (1993).
7. E. J. Sontheimer, S. Sun, J. A. Piccirilli, *Nature* **388**, 801–805 (1997).
8. P. M. Gordon, E. J. Sontheimer, J. A. Piccirilli, *RNA* **6**, 199–205 (2000).
9. S.-L. Yean, G. Wuenschell, J. Termini, R.-J. Lin, *Nature* **408**, 881–884 (2000).
10. P. Koodathingal, T. Novak, J. A. Piccirilli, J. P. Staley, *Mol. Cell* **39**, 385–395 (2010).
11. C. Yan *et al.*, *Science* **349**, 1182–1191 (2015).
12. J. Hang, R. Wan, C. Yan, Y. Shi, *Science* **349**, 1191–1198 (2015).
13. R. J. Grainger, J. D. Beggs, *RNA* **11**, 533–557 (2005).
14. W. P. Galej, C. Oubridge, A. J. Newman, K. Nagai, *Nature* **493**, 638–643 (2013).
15. S. Mozaffari-Jovin *et al.*, *Science* **341**, 80–84 (2013).
16. T. H. Nguyen *et al.*, *Structure* **21**, 910–919 (2013).
17. A. K. Leung, K. Nagai, J. Li, *Nature* **473**, 536–539 (2011).
18. L. Zhou *et al.*, *Nature* **506**, 116–120 (2014).
19. G. Weber, S. Trowitzsch, B. Kastner, R. Lührmann, M. C. Wahl, *EMBO J.* **29**, 4172–4184 (2010).
20. D. A. Pomeranz Krummel, C. Oubridge, A. K. Leung, J. Li, K. Nagai, *Nature* **458**, 475–480 (2009).
21. Y. Kondo, C. Oubridge, A. M. van Roon, K. Nagai, *eLife* **4**, e04986 (2015).
22. W. Chen, M. J. Moore, *Curr. Opin. Struct. Biol.* **24**, 141–149 (2014).
23. M. Azubel, S. G. Wolf, J. Sperling, R. Sperling, *Mol. Cell* **15**, 833–839 (2004).
24. N. Behzadnia *et al.*, *EMBO J.* **26**, 1737–1748 (2007).
25. S. Bessonov *et al.*, *RNA* **16**, 2384–2403 (2010).
26. D. Boehringer *et al.*, *Nat. Struct. Mol. Biol.* **11**, 463–468 (2004).
27. P. Fabrizio *et al.*, *Mol. Cell* **36**, 593–608 (2009).
28. M. M. Golas *et al.*, *Mol. Cell* **40**, 927–938 (2010).
29. M. Grote *et al.*, *Mol. Cell. Biol.* **30**, 2105–2119 (2010).
30. M. S. Jurica, D. Sousa, M. J. Moore, N. Grigorieff, *Nat. Struct. Mol. Biol.* **11**, 265–269 (2004).
31. M. D. Ohi, L. Ren, J. S. Wall, K. L. Gould, T. Walz, *Proc. Natl. Acad. Sci. U.S.A.* **104**, 3195–3200 (2007).
32. B. Sander *et al.*, *Mol. Cell* **24**, 267–278 (2006).
33. E. Wolf *et al.*, *EMBO J.* **28**, 2283–2292 (2009).
34. E. M. Makarov *et al.*, *Science* **298**, 2205–2208 (2002).
35. J. Deckert *et al.*, *Mol. Cell. Biol.* **26**, 5528–5543 (2006).
36. M. S. Jurica, L. J. Licklider, S. R. Gygi, N. Grigorieff, M. J. Moore, *RNA* **8**, 426–439 (2002).
37. J. O. Ilagan, R. J. Chalkley, A. L. Burlingame, M. S. Jurica, *RNA* **19**, 400–412 (2013).
38. W. Chen *et al.*, *RNA* **20**, 308–320 (2014).
39. T. H. Nguyen *et al.*, *Nature* **523**, 47–52 (2015).
40. D. E. Agafonov *et al.*, *Science* **351**, 1416–1420 (2016).
41. R. Wan *et al.*, *Science* **351**, 466–475 (2016).
42. T. H. Nguyen *et al.*, *Nature* **530**, 298–302 (2016).
43. C. Yan, R. Wan, R. Bai, G. Huang, Y. Shi, *Science* **353**, 904–911 (2016).
44. A. H. Igel, M. Ares Jr., *Nature* **334**, 450–453 (1988).
45. A. J. Newman, C. Norman, *Cell* **68**, 743–754 (1992).
46. J. R. Wyatt, E. J. Sontheimer, J. A. Steitz, *Genes Dev.* **6**, 2542–2553 (1992).
47. E. J. Sontheimer, J. A. Steitz, *Science* **262**, 1989–1996 (1993).
48. A. J. Newman, S. Teigelkamp, J. D. Beggs, *RNA* **1**, 968–980 (1995).
49. H. D. Madhani, C. Guthrie, *Cell* **71**, 803–817 (1992).
50. M. Anokhina *et al.*, *EMBO J.* **32**, 2804–2818 (2013).
51. C. K. Tseng, S. C. Cheng, *Science* **320**, 1782–1784 (2008).
52. Z. Warkocki *et al.*, *Nat. Struct. Mol. Biol.* **16**, 1237–1243 (2009).
53. D. S. McPheeters, P. Muhlenkamp, *Mol. Cell. Biol.* **23**, 4174–4186 (2003).
54. C. Schneider *et al.*, *PLOS Genet.* **11**, e1005539 (2015).
55. C. G. Burns, R. Ohi, A. R. Krainer, K. L. Gould, *Proc. Natl. Acad. Sci. U.S.A.* **96**, 13789–13794 (1999).
56. W. H. McDonald, R. Ohi, N. Smelkova, D. Frendewey, K. L. Gould, *Mol. Cell. Biol.* **19**, 5352–5362 (1999).
57. T. Villa, C. Guthrie, *Genes Dev.* **19**, 1894–1904 (2005).
58. C. H. Chen *et al.*, *Nucleic Acids Res.* **30**, 1029–1037 (2002).
59. J. C. McGrail, A. Krause, R. T. O'Keefe, *Nucleic Acids Res.* **37**, 4205–4217 (2009).
60. N. Rasche *et al.*, *EMBO J.* **31**, 1591–1604 (2012).
61. D. Xu, J. D. Friesen, *Mol. Cell. Biol.* **21**, 1011–1023 (2001).
62. D. Saha, P. Khandelia, R. T. O'Keefe, U. Vijayraghavan, *J. Biol. Chem.* **287**, 5390–5399 (2012).
63. R. J. Grainger, J. D. Barrass, A. Jacquier, J. C. Rain, J. D. Beggs, *RNA* **15**, 2161–2173 (2009).
64. M. Khanna *et al.*, *RNA* **15**, 2174–2185 (2009).
65. Y. C. Liu, H. C. Chen, N. Y. Wu, S. C. Cheng, *Mol. Cell. Biol.* **27**, 5403–5413 (2007).
66. T. W. Chiang, S. C. Cheng, *Mol. Cell. Biol.* **33**, 1746–1755 (2013).
67. Y. F. Chiu *et al.*, *Mol. Cell. Biol.* **29**, 5671–5678 (2009).
68. M. Albers, A. Diment, M. Muraru, C. S. Russell, J. D. Beggs, *RNA* **9**, 138–150 (2003).
69. M. A. Wall *et al.*, *Cell* **83**, 1047–1058 (1995).
70. M. M. Konarska, J. Vilardell, C. C. Query, *Mol. Cell* **21**, 543–553 (2006).
71. T. A. Cooper, L. Wan, G. Dreyfuss, *Cell* **136**, 777–793 (2009).
72. E. F. Pettersen *et al.*, *J. Comput. Chem.* **25**, 1605–1612 (2004).
73. W. L. DeLano, The PyMOL Molecular Graphics System (2002); www.pymol.org.

ACKNOWLEDGMENTS

We thank the Tsinghua University Branch of China National Center for Protein Sciences (Beijing) for providing facility support. The computation was completed on the "Explorer 100" cluster system of Tsinghua National Laboratory for Information Science and Technology. This work was supported by funds from the Ministry of Science and Technology (grant 2014ZX09507003006) and the National Natural Science Foundation of China (grants 31130002 and 31321062). For the C complex structure, the atomic coordinates have been deposited in the Protein Data Bank with accession code 5GMK, and the EM maps have been deposited in the Electron Microscopy Database with accession codes EMD-9525, EMD-9526, and EMD-9527. We declare no competing financial interests. Correspondence and requests for materials should be addressed to Y.S.

SUPPLEMENTARY MATERIALS

www.sciencemag.org/content/353/6302/895/suppl/DC1
Materials and Methods
Figs. S1 to S14
Tables S1 to S4
References (*74*–*93*)

25 May 2016; accepted 14 July 2016
Published online 21 July 2016
10.1126/science.aag2235

STRUCTURAL BIOLOGY

Structure of a yeast activated spliceosome at 3.5 Å resolution

Chuangye Yan,* Ruixue Wan,* Rui Bai,* Gaoxingyu Huang, Yigong Shi†

Pre–messenger RNA (pre-mRNA) splicing is carried out by the spliceosome, which undergoes an intricate assembly and activation process. Here, we report an atomic structure of an activated spliceosome (known as the B^{act} complex) from *Saccharomyces cerevisiae*, determined by cryo–electron microscopy at an average resolution of 3.52 angstroms. The final refined model contains U2 and U5 small nuclear ribonucleoprotein particles (snRNPs), U6 small nuclear RNA (snRNA), nineteen complex (NTC), NTC-related (NTR) protein, and a 71-nucleotide pre-mRNA molecule, which amount to 13,505 amino acids from 38 proteins and a combined molecular mass of about 1.6 megadaltons. The 5′ exon is anchored by loop I of U5 snRNA, whereas the 5′ splice site (5′SS) and the branch-point sequence (BPS) of the intron are specifically recognized by U6 and U2 snRNA, respectively. Except for coordination of the catalytic metal ions, the RNA elements at the catalytic cavity of Prp8 are mostly primed for catalysis. The catalytic latency is maintained by the SF3b complex, which encircles the BPS, and the splicing factors Cwc24 and Prp11, which shield the 5′ exon–5′SS junction. This structure, together with those determined earlier, outlines a molecular framework for the pre-mRNA splicing reaction.

Pre-mRNA splicing is a dynamic process that involves several distinct spliceosomal complexes (*1*–*3*). Association of the pre-spliceosomal A complex with the U4/U6.U5 tri-snRNP, formed from the U4, U5, and U6 small nuclear ribonucleoprotein particles (snRNPs), generates the precatalytic B complex. Dissociation of U1 and U4 snRNPs and recruitment of the nineteen complex (NTC) and NTC-related (NTR) protein trigger major structural rearrangement, resulting in formation of the activated B^{act} complex. The B^{act} complex is converted to the catalytically activated B* complex, in which an invariant adenine nucleotide of the branch-point sequence (BPS) initiates the first transesterification and generates a free 5′ exon and an intron–3′ exon lariat. The C complex catalyzes the second transesterification, which

Beijing Advanced Innovation Center for Structural Biology, Tsinghua-Peking Joint Center for Life Sciences, School of Life Sciences, Tsinghua University, Beijing 100084, China.
*These authors contributed equally to this work. **†Corresponding author. Email: shi-lab@tsinghua.edu.cn**

Downloaded from http://science.sciencemag.org/ on September 3, 2016

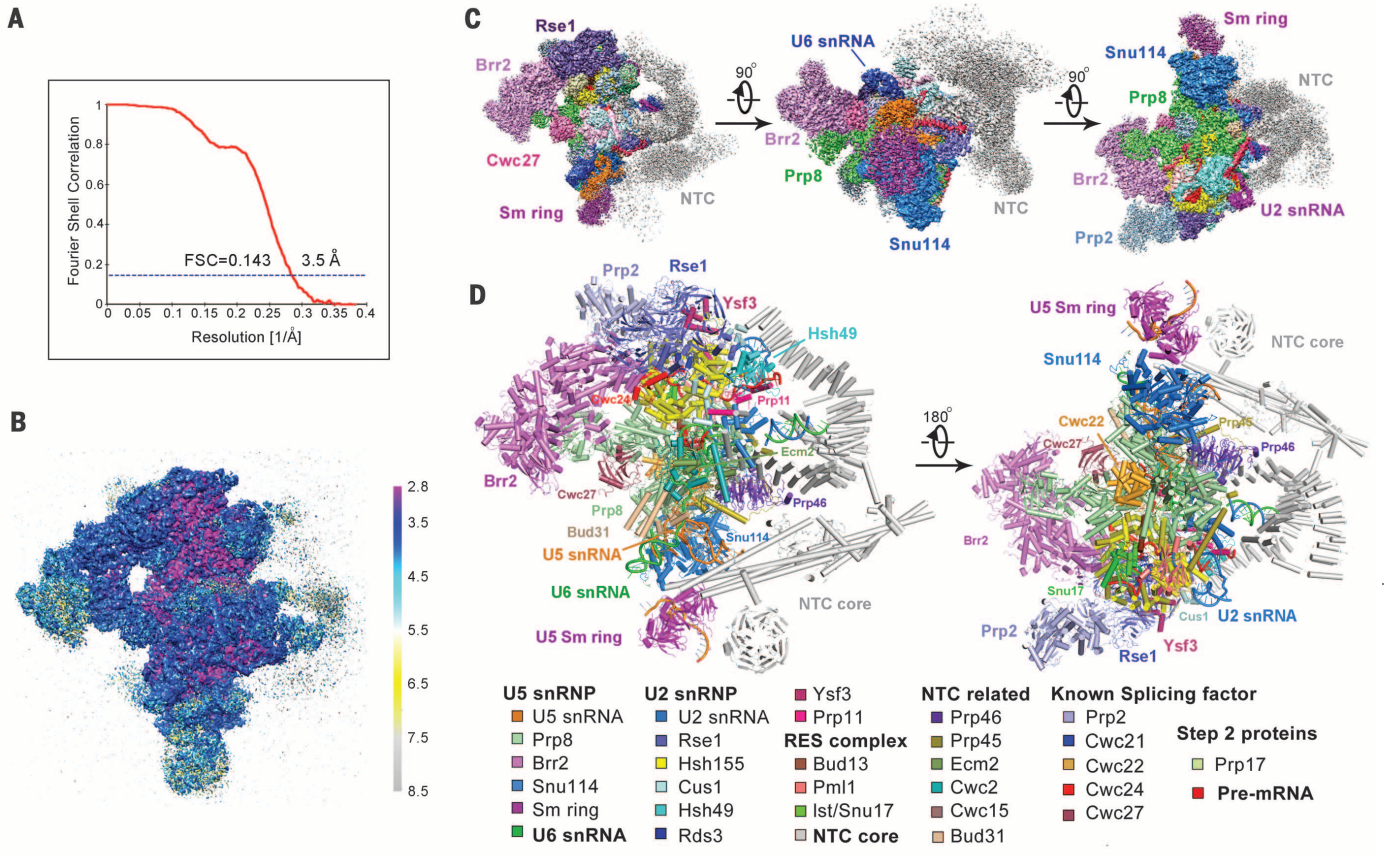

Fig. 1. Cryo-EM structure of an activated spliceosome (the B^{act} complex) from *S. cerevisiae*. (**A**) The overall resolution of the EM reconstruction is estimated to be 3.52 Å on the basis of gold-standard FSC criteria of 0.143. (**B**) An overall view of the EM density map for the B^{act} complex. The resolution is color coded for different regions of the B^{act} complex. The resolution goes to 2.8 to 3.5 Å for the majority of the B^{act} complex. (B) to (D) were prepared using CHIMERA (*61*). All other structural images were created using PyMol (*62*). (**C**) The EM density map of the *S. cerevisiae* B^{act} complex at an average resolution of 3.52 Å. Three mutually perpendicular views around the horizontal axis are shown. (**D**) A cartoon representative of the *S. cerevisiae* B^{act} complex. The color-coded protein and RNA components are listed below the images. This structure shown here includes 38 proteins, three snRNA elements, and one pre-mRNA molecule, with a combined molecular mass of ~1.6 MD. Among the modeled 13,505 amino acids, 10,050 have side chains. We tentatively assigned 357 RNA nucleotides, including 71 in the pre-mRNA molecule to the various structures listed.

ligates two exons. The ligated exons are released from the postcatalytic P complex, but the intron lariat remains bound to the intron-lariat spliceosomal (ILS) complex. Finally, the intron lariat is released, and the snRNPs are recycled.

The spliceosome is an RNA-directed metalloenzyme (*4*–*6*), and the intramolecular stem loop (ISL) of U6 small nuclear RNA (snRNA) coordinates the catalytic magnesium (Mg^{2+}) ions (*7*–*10*). During the first transesterification, the 3′ end nucleotides of the 5′ exon are anchored by loop I of U5 snRNA, whereas the 5′ splice site (5′ SS) and the BPS are recognized by U6 and U2 snRNAs, respectively. The active site, located in a catalytic cavity on the central component Prp8, comprises ISL of U6 snRNA, helix I of the U2/U6 duplex, loop I of U5 snRNA, and at least two catalytic Mg^{2+} ions (*9*, *10*).

Structural investigations of the various spliceosomal components have improved our knowledge of pre-mRNA splicing (*11*–*19*). Mechanistic understanding of spliceosome function requires atomic structures of the intact spliceosome at different stages of the splicing reaction. The large size and dynamic nature of the spliceosome represent formidable challenges for crystallization. Application of electron microscopy (EM) yielded structures of various spliceosomal complexes at low to medium resolutions that reveal a wealth of information on the architecture of the spliceosome but fall short of the requirement for atomic modeling (*20*–*37*). The 3.6 Å cryo-EM structure of an intact spliceosome from *Schizosaccharomyces pombe* (*S. pombe*) unveiled the spatial arrangement of U2, U5, and U6 snRNAs and specific determinants of the active site (*9*, *10*). More recently, structures of the U4/U6.U5 tri-snRNP from *Saccharomyces cerevisiae* were reported at 3.7 to 3.8 Å resolutions (*38*, *39*).

Here, we report the structure of an activated spliceosome (B^{act} complex) at an average resolution of 3.52 Å, which reveals the inner workings of the RNA elements together with their protein cofactors just before pre-mRNA splicing.

Spliceosome isolation and EM

The reported cryo-EM structure of the *S. pombe* spliceosome likely reflects that of the ILS complex, as judged by the lack of strong EM density for the 5′ exon (*9*). To isolate the early- to intermediate-stage spliceosomes, we screened a number of different proteins as targets of an affinity tag and eventually chose Cef1 on the basis of the yield and quality of the purified spliceosomes. Using tagged Cef1, we purified a mixture of spliceosomes at different stages of the splicing reaction (fig. S1, A to D). These different spliceosomes display distinct appearances in the EM images (fig. S1C) and can be differentiated by two-dimensional (2D) and 3D classifications. Thus, we decided not to further fractionate these spliceosomes and to rely on 2D and 3D classifications to sort the different particles. This strategy alleviated the dissociation

Downloaded from http://science.sciencemag.org/ on September 3, 2016

problem affiliated with excessive purification maneuvering and allowed determination of more than one spliceosome structure. In this article, we focus on the B^{act} complex.

The sample was imaged under cryo-conditions with a K2 direct electron detector mounted on a Titan Krios microscope. We collected 12,142 micrographs. A preliminary analysis of 841 micrographs was performed to generate an approximate reconstruction of the B^{act} complex and to determine the data-processing strategy (fig. S2). The chosen strategy was then applied to the whole data set, generating 761,767 particles for subsequent analysis (fig. S3). We then applied three rounds of 3D classifications to enrich the genuine B^{act} particles. At the end of the third round, 84,486 particles were auto-refined to produce a reconstruction at 3.9 Å resolution. Particle polishing and a final round of 3D classification improved the resolution to 3.52 Å on the basis of the gold-standard Fourier shell correlation (FSC) criteria (Fig. 1A and figs. S3 and S4). Two other spliceosomal complexes are well represented in the 3D classifications (figs. S2 and S3); these particles will be the subject of future investigations.

The actual resolution in the core regions of the B^{act} complex reaches 2.8 to 3.2 Å, allowing atomic modeling (Fig. 1, B and C). Throughout the spliceosome, most secondary structural elements are visible, and a large proportion of the amino acid side chains are defined by the density maps (figs. S5 to S12). Reflecting its dynamic nature, the B^{act} complex displays an overall appearance that is similar to the reported shape (*22*, *24*) but differs from that of the ILS complex

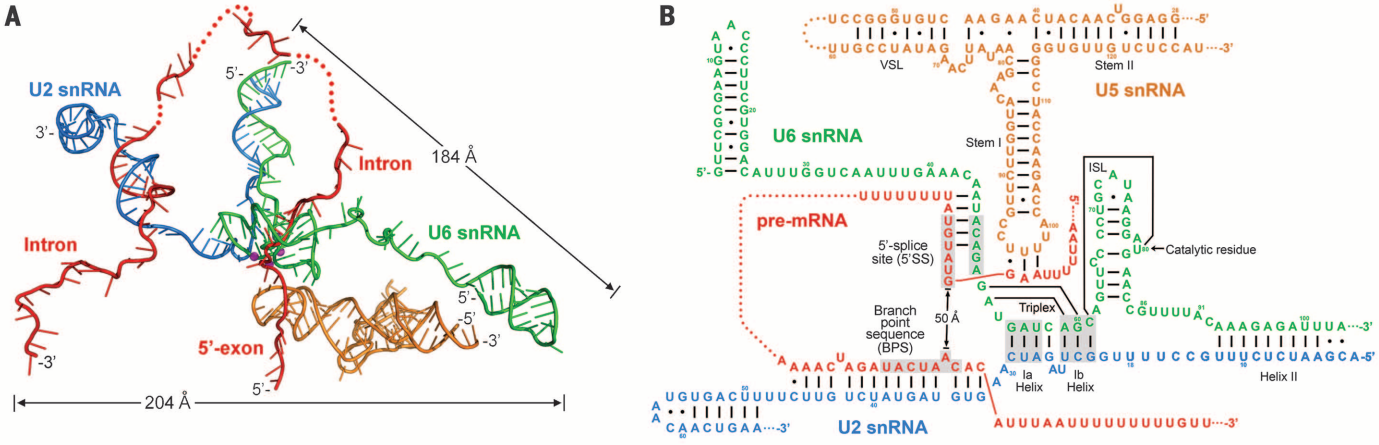

Fig. 2. Arrangement of the RNA components in the *S. cerevisiae* B^{act} complex. (**A**) An overall cartoon representation of the RNA map. The catalytic center comprises the ISL of U6 snRNA, helix I of the U2/U6 duplex, loop I of U5 snRNA, and the Mg^{2+} ions. The 5′ exon of pre-mRNA is anchored to loop I of U5 snRNA, whereas the 5′SS is recognized by the ACAGA box of U6 snRNA. The BPS forms a duplex with U2 snRNA and is located 40 to 50 Å away from the 5′SS. The disordered RNA sequences are indicated by dotted lines. (**B**) Overall base-pairing interactions among U2 snRNA, U5 snRNA, U6 snRNA, and pre-mRNA. Canonical Watson-Crick and noncanonical base-pairing interactions are identified by solid lines and black dots, respectively.

Fig. 3. The catalytic center and the active site of the *S. cerevisiae* B^{act} complex. (**A**) Structure of the catalytic center in the B^{act} complex. (Left) A close-up view of the RNA map in Fig. 2A. The scissile phosphodiester bond is located at the kink between the 5′ exon and 5′SS. The 5′ exon and 5′SS are recognized by U5 and U6 snRNA, respectively. The ISL of U6 snRNA is close to loop I of U5 snRNA. (Right) View rotated around the axis. (**B**) Two close-up views of the active site. Among the two Mg^{2+} ions shown, one is a structural metal and coordinated by the phosphate groups from C61 and G78 of U6 snRNA, and the other is likely a catalytic metal (M2) and bound by phosphates from A59 and G60. Note that A59, G60, and C61 are part of the RNA triplex. These two Mg^{2+} ions are separated by a distance of about 9.1 Å. (**C**) Comparison of the metal coordination between the *S. cerevisiae* B^{act} complex and the *S. pombe* ILS complex (*10*). Although the M2 metal is bound by A59 and G60 of U6 snRNA in the B^{act} complex, it is located away from the corresponding metal in the ILS complex. (**D**) Two close-up views of the base-pairing interactions between the 5′ exon and loop I of U5 snRNA and the interactions between U5 snRNA and U6 snRNA. H bonds are represented by red, dashed lines.

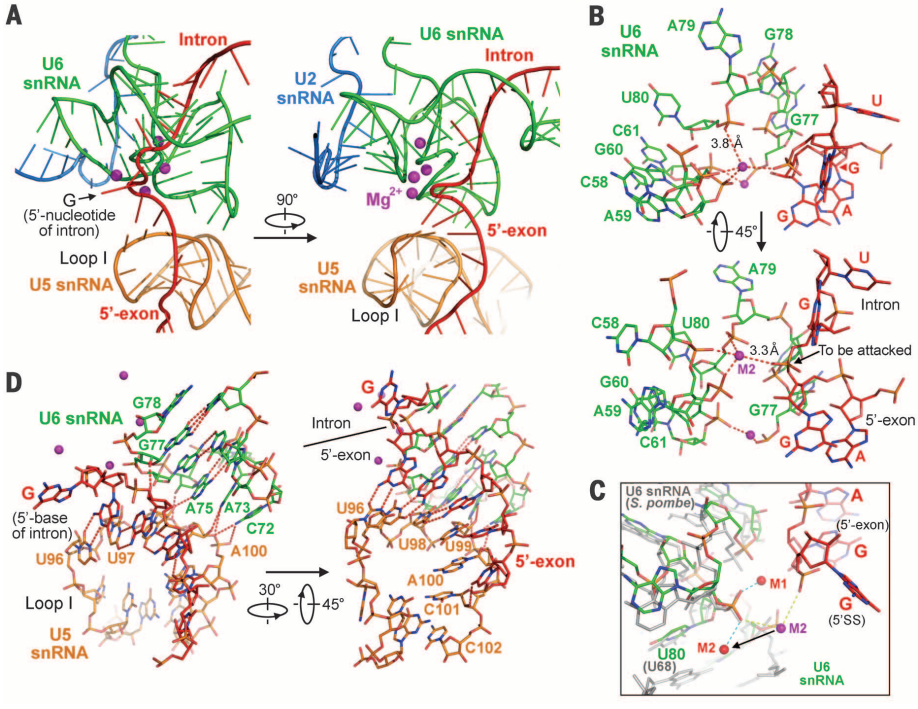

Downloaded from http://science.sciencemag.org/ on September 3, 2016

(*9*). The head group is no longer present, and arm II (mainly Prp19 and Cef1) and the two superhelical proteins Syf1 and the carboxyl-terminal half of Clf1 (Cwf4/Syf3 in *S. pombe*) exhibit weak EM density. In contrast, the triangular-shaped central body—which comprises U5 snRNP, the catalytic center, and a few other proteins—exhibits well-defined EM density (Fig. 1C). A sizable portion of the density connected to the central body is attributed to Brr2, U2 snRNP, and the precursor mRNA retention and splicing (RES) complex. The RNA elements and their surrounding proteins display characteristic features in the density maps (figs. S13 to S16) that allow assignment of the nucleotides.

Overall structure

The final refined model of the B^{act} complex contains 13,505 amino acids from 38 proteins and 357 nucleotides from three snRNAs and pre-mRNA (Fig. 1D and tables S1 to S4), with a combined molecular mass of ~1.6 MD. Among the modeled amino acids, 10,050 have side chains, and the remaining 3455 residues (mainly in NTC, U5 Sm ring, Prp2, and Hsh49) were built as poly(Ala). The 38 protein components in the atomic model include all 10 from U5 snRNP, 7 from U2 snRNP, 6 from NTC, 6 from NTR, 3 from the RES complex (Pml1, Bud13, and Snu17); four known splicing factors (Cwc21, Cwc22, Cwc24, and Cwc27); the adenosine triphosphatase (ATPase)/helicase Prp2; and the step 2 factor Prp17. Nearly complete atomic models are available for five large proteins: the central component Prp8 (residues 127 to 2398), the ATPase/helicase Brr2 (residues 113 to 2163), the only guanosine triphosphatase Snu114 (residues 67 to 975), and the SF3b proteins Rse1 (residues 56 to 1361) and Hsh155 (residues 16 to 971). The excellent EM maps also allow identification of the critical regions of several splicing factors, including Cwc21, Cwc24, and Prp11 near or at the active site.

On one side of the B^{act} complex, the tightly packed central body is connected to three extended spokes: one capped by the heptameric Sm ring that binds the 3′ end sequences of U5 snRNA and the other two terminated by Brr2 and Prp2 (Fig. 1 and fig. S17). On the other side of the B^{act} complex, the core NTC component Prp19 and the superhelical proteins Syf1 and Clf1 are flexibly connected to the central body. U2 snRNP stacks against U5 snRNP to form the core of the B^{act} complex (fig. S17). Components of the NTR closely interact with U5 snRNA and the RNA components at the catalytic center. The RES complex, stabilized by the NTR component Prp45, directly contacts both U2 snRNP and Prp8 of U5 snRNP.

The RNA map

The RNA elements are characterized by excellent electron density (fig. S13 to S16). U5 snRNA in *S. cerevisiae* has a long form (214 nucleotides) and a short form (179 nucleotides). Of the U5 snRNA nucleotides, 90, including most of the shared portion of the two forms, are defined by the density, particularly loop I and its interactions with the 5′ exon (fig. S13). Except for two short sequences toward the 3′ end, U6 snRNA is visible in its entirety in the density maps (fig. S14), totaling 103 nucleotides. In U2 snRNA, 66 nucleotides, including all functionally important regions, are identified by the density (fig. S15). Among the 357 modeled nucleotides, 71 are assigned to pre-mRNA (figs. S14 and S15). One stretch of the pre-mRNA contains 10 nucleotides from the 5′ exon and 15 nucleotides from the 5′SS, as well as the ensuing sequences of the intron; another stretch contains 36 nucleotides of the intron including the BPS.

These four RNA components are organized into an elaborate structure that spans a maximum distance of 204 Å (Fig. 2A). As previously noted (*10*), both the 5′ and 3′ ends of the three snRNA molecules are placed far away from the catalytic center, whereas the sequences important for pre-mRNA splicing are delivered to the center for assembly of a functional, active site (Fig. 2A). Three nucleotides at the 3′ end of the 5′ exon are recognized by loop I of U5 snRNA through base-pairing interactions (Fig. 2B and fig. S13C). At least five contiguous nucleotides of the intron, including three from the 5′SS, form a duplex with the ACAGA box and the ensuing sequences of U6 snRNA. Notably, the three nucleotides GUA at the 5′ end of the 5′SS are unpaired; this arrangement results in the protrusion of the phosphate group of the invariant guanine nucleotide. At least 14 nucleotides, including the BPS, form a long duplex with U2 snRNA. The intron-U2 duplex contains a bulge at the invariant adenine nucleotide of the BPS, where the nucleophile-containing ribose is flipped out of the duplex. Note that the invariant guanine nucleotide of the 5′SS is separated from the nucleophile-containing adenine nucleotide of the BPS by a distance of ~49 Å.

The active site

The active site in the B^{act} complex consists of ISL of U6 snRNA, helix I of the U2/U6 duplex, loop I of U5 snRNA, and four metal ions that are likely magnesium (Mg^{2+}) (Fig. 3A). Immediately after the 3′ end of the 5′ exon, the pre-mRNA is kinked around an Mg^{2+} ion, and the next three bases GUA of the 5′SS are unpaired. This kink in pre-mRNA is a direct result of the base-pairing interactions both preceding the kink (between 5′ exon and loop I) and following the kink (between part of the 5′SS and the ACAGA box).

Of the four putative Mg^{2+} ions at the active site, three mainly stabilize the delicate fold of ISL by neutralizing the negative charges of the phosphates. Two structural Mg^{2+} ions are bound by the phosphate group of the nucleotide G81 (fig. S14F). The third structural Mg^{2+} is coordinated by the phosphate groups of the nucleotides C61 and G77 from U6 snRNA (Fig. 3B). The only catalytic Mg^{2+} ion, which may correspond to the metal ion M2 (*8*), is located

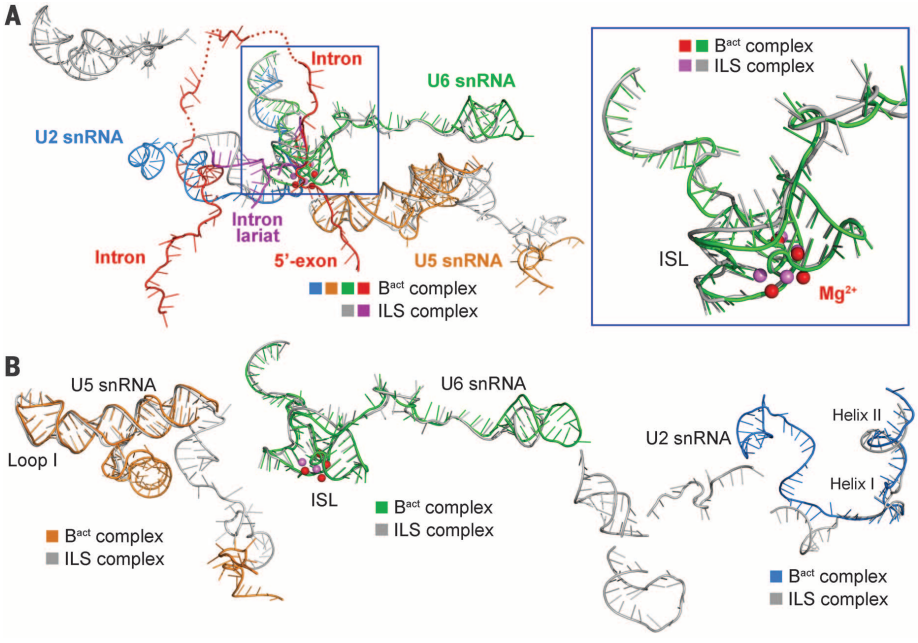

Fig. 4. Structural comparison of the RNA elements between the *S. cerevisiae* B^{act} complex and the *S. pombe* ILS complex. See (*9*, *10*) for previous work on the spliceosome and splicing. (**A**) Structural comparison of the overall RNA maps between the two spliceosomal complexes. Comparison with the ISL is shown in the inset. None of the RNA elements in the catalytic center exhibit marked difference between the two complexes. (**B**) Structural comparison of the individual RNA components between the two spliceosomal complexes. There are few differences in the core regions of U5 snRNA (left) or U6 snRNA (middle). Although the 3′ portion sequences of U2 snRNA adopt quite different positions between the two spliceosomal complexes (right), the sequences in the catalytic center and in helix II remain structurally similar.

Downloaded from http://science.sciencemag.org/ on September 3, 2016

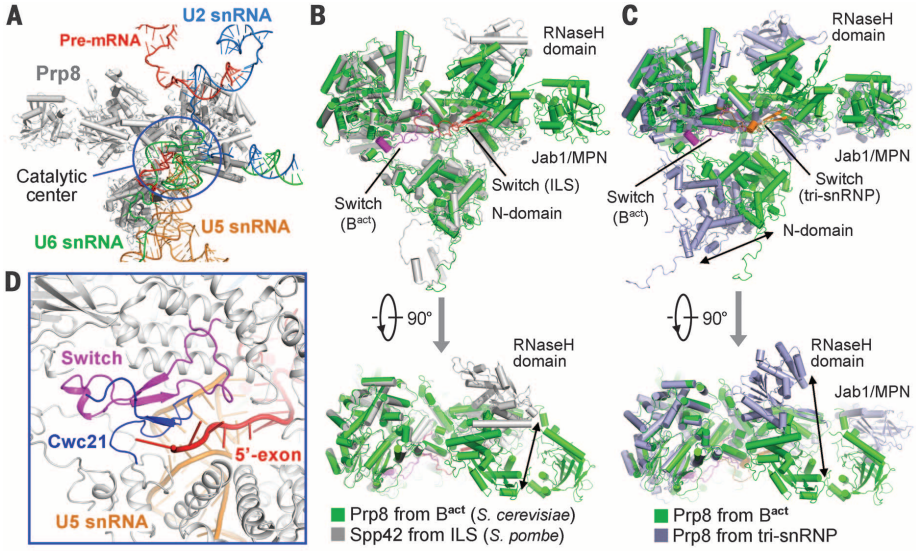

Fig. 5. Structure of the central spliceosomal component Prp8 (Spp42 in *S. pombe*) and identification of the switch loop. (**A**) Overall structure of Prp8 from the B^{act} complex. Prp8 is the only protein that interacts with all three snRNAs and pre-mRNA. The RNA components are shown, and the catalytic center is circled. (**B**) Structural comparison between Prp8 of the B^{act} complex and Spp42 of the ILS complex (*9*). Both the N-domain and the core of Prp8 are well aligned to those of Spp42. An extended loop sequence (residues 1402 to 1439), designated as the switch loop, is flipped 180° between these two proteins. The two ribonuclease H (RNase H) domains exhibit marked positional differences. (**C**) Structural comparison between Prp8 of the B^{act} complex and Prp8 of the U4/U6.U5 tri-snRNP (*38*). Only the cores are well aligned. The N-domains, RNase H domains, and the Jab1/MPN domains all exhibit large differences. Similar to that in the ILS complex (*9*), the switch loop of Prp8 in the tri-snRNP points in the opposite direction compared with that in the B^{act} complex. (**D**) The switch loop of Prp8 in the B^{act} complex closely interacts with the splicing factor Cwc21. Together, these two proteins bind the 5′ exon sequences preceding the bases that form base pairs with loop I of U5 snRNA. Such a location may allow the switch loop to play a role in 5′ exon loading and stabilization.

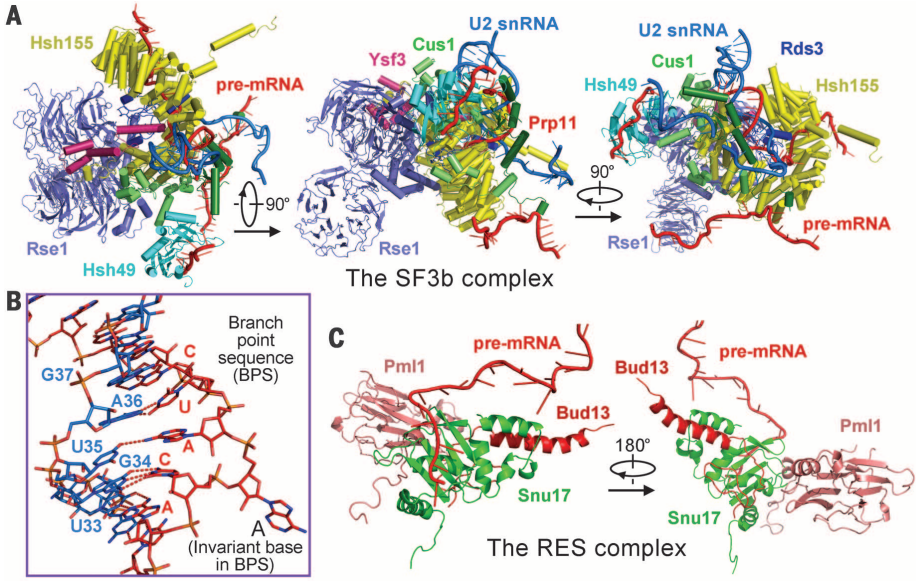

Fig. 6. Structures of the SF3b complex and the RES complex. (**A**) Structure of the SF3b complex in three perpendicular views. The SF3b complex comprises six proteins Cus1, Hsh49, Hsh155, Rds3, Rse1, and Ysf3 in yeast (*41*). These proteins closely interact with each other and with the SF3a protein Prp11, surrounding the duplex between the BPS and U2 snRNA. (**B**) A close-up view on the duplex between the BPS and U2 snRNA. Note that the invariant adenine nucleotide that harbors the nucleophile for the first-step reaction is flipped out of the duplex. (**C**) Structure of the RES complex with rotation on the axis to show the reverse side. Association of the three protein components of the RES complex is greatly facilitated by the NTR component Prp45. Of the three RES components, only Snu17 plays a major role in RNA binding by directly interacting with four RNA bases in the intron.

~3.3 Å away from the nearest oxygen atom of the scissile phosphodiester bond; this Mg^{2+} ion is coordinated by the phosphates of the nucleotides A59 and G60. Note that A59 and G60 are part of the RNA triplex at the active site.

These structural features demonstrate that the active site in the B^{act} complex is yet to be converted to a catalytically activated state (Fig. 3B). The second catalytic Mg^{2+} atom (M1) is yet to be loaded into the active site; G78, known to bind M1, remains unengaged. The distance between the catalytic nucleotide U80, which is known to coordinate both Mg^{2+} ions (*8*), and the nearest metal ion (M2) is 3.8 Å, is too far away for productive coordination (Fig. 3B). Although M2 is already recognized by A59 and G60 of U6 snRNA in the B^{act} complex, it is located away from the corresponding M2 metal in the *S. pombe* ILS complex (Fig. 3C). Thus, for the B^{act} complex to become catalytically activated, another catalytic Mg^{2+} ion needs to be incorporated into the active site, and the surrounding nucleotides of U6 snRNA must undergo minor configurational rearrangement.

Despite the latency of Mg^{2+} coordination, the 5′ exon is already anchored at the active site through base-pairing interactions with loop I of U5 snRNA (Fig. 3D). Three bases at the 3′ end of the 5′ exon make specific hydrogen bonds (H bonds) with U96-U97-U98 of U5 snRNA, whereas two preceding bases of the 5′ exon also contact bases of loop I. The conformation of loop I is stabilized by specific interactions with U6 snRNA (Fig. 3D).

Conservation of the active-site conformation

The overall conformation of the RNA elements in the catalytic center is thought to be conserved among the B^{act}, B*, C, P, and ILS complexes (*10*). Structural determination of the *S. cerevisiae* B^{act} complex allows assessment of this prediction. Because U5 snRNA, the N-domain of Prp8, and Snu114 represent a central scaffold conserved between tri-snRNP and the ILS complex (*38*), we initiated the comparison on U5 snRNA. U5 snRNA from the *S. pombe* ILS complex is superimposed very well on that from the *S. cerevisiae* B^{act} complex (Fig. 4, A and B); application of the same alignment matrix to the entire RNA elements resulted in an overall comparison between the two RNA maps (Fig. 4A). U6 snRNA molecules from the two spliceosomal complexes adopt a highly similar conformation throughout the sequences (Fig. 4B). Except minor shifts of the phosphodiester backbone and small configurational rearrangement, the ISL of U6 snRNA is well superimposed between these two complexes (Fig. 4A, inset). Although the conformation of U2 snRNA appears to be divergent, the U2 snRNA regions that are important for catalysis—helix I and helix II—remain unchanged in the two complexes (Fig. 4B).

Prp8 and the switch loop

The central component Prp8 binds to all four RNA elements and displays excellent density

Downloaded from http://science.sciencemag.org/ on September 3, 2016

(fig. S5). The RNA elements of the splicing active site are nestled in a catalytic cavity that is formed between the N-domain and the core of Prp8 (residues 749 to 1830) (Fig. 5A). Comparing Prp8 of the *S. cerevisiae* B^{act} complex and Spp42 of the *S. pombe* ILS complex (*9*) reveals a prominent surface loop (referred to as the switch loop) that adopts two very different positions (Fig. 5B and fig. S18). In the *S. cerevisiae* B^{act} complex, the switch loop (residues 1402 to 1439) points to the reverse transcriptase (RT) palm/finger domain and closely interacts with the N-domain, the RT palm/finger domain, and the thumb/X domain. In the *S. pombe* ILS complex (*9*), however, the switch loop (residues 1354 to 1391) is flipped 180°, pointing to the endonuclease domain and interacting with the linker and the endonuclease domain. Additional analysis reveals that the switch loop of Prp8 in the *S. cerevisiae* U4/U6.U5 tri-snRNP (*38*) also points in the opposite direction compared with that in the B^{act} complex (Fig. 5C and fig. S18).

The remarkable positional rearrangement of the switch loop likely reflects an important function. Close examination of the B^{act} complex reveals a close interaction of the switch loop with the splicing factor Cwc21 (Fig. 5D). Together, the switch loop and the splicing factor Cwc21 interact closely with the nucleotides of 5′ exon just before its base-pairing interactions with loop I of U5 snRNA. These otherwise free nucleotides are bound by Cwc21 and the switch loop; this binding stabilizes the interactions between the 3′ end nucleotides of the 5′ exon and loop I of U5 snRNA. Such interactions between Cwc21 and the 5′ exon sequences are likely preserved during both steps of the splicing reaction.

Reflecting different functional states of Prp8/Spp42, the ribonuclease H (RNase H) domains exhibit pronounced positional differences for Prp8 of the *S. cerevisiae* B^{act} complex and Spp42 of the *S. pombe* ILS complex (*38*) (Fig. 5B), as well as for the B^{act} complex and tri-snRNP in *S. cerevisiae* (*9*) (Fig. 5C). The Jab1/MPN domain of Prp8 also undergoes a marked positional shift from the tri-snRNP to the B^{act} complex in *S. cerevisiae*. Another important conformational difference between the tri-snRNP and the B^{act} complex is the position of the N-domain relative to the Prp8 core (Fig. 5C and fig. S18). Compared with that in the tri-snRNP, the Prp8 N-domain in the B^{act} complex is shifted 10 to 20 Å toward the RT palm/finger domain. A similar shift, observed in the comparison between Prp8 of the *S. cerevisiae* tri-snRNP and Spp42 of the *S. pombe* ILS complex, is thought to allow proper formation of the catalytic cavity in Prp8/Spp42 that hosts the splicing active site (*38*). Consistent with this analysis, the position of the N-domain relative to the Prp8 core in the *S. cerevisiae* B^{act} complex is preserved for Spp42 in the *S. pombe* ILS complex (Fig. 5B). Because the N-domain of Prp8, Snu114, and U5 snRNA together constitute a rigid entity (*38*), such a conformational shift aligns the active site conformation and likely occurs during spliceosome assembly and maturation.

The SF3b complex and the RES complex

The SF3b complex, as part of U2 snRNP, is mainly responsible for the recognition of the BPS and surrounding sequences in the intron (*40*). In yeast, SF3b comprises six protein components Rse1 (SF3b130 in human), Hsh155 (SF3b155), Cus1 (SF3b145), Rds3 (SF3b14b), Hsh49 (SF3b49), and Ysf3 (SF3b10) (*41*). These six proteins, unambiguously identified by the density maps (figs. S7 and S8), assemble into a compact structure (Fig. 6A).

As the central scaffold of the entire SF3b complex, Hsh155 consists of 20 HEAT repeats, each comprising a pair of antiparallel α helices. These repeats form a left-handed superhelical assembly (fig. S19A). Ysf3 interacts with the carboxyl-terminal α helices of Hsh155, whereas Cus1 in an extended conformation binds the six carboxyl-terminal HEAT repeats outside the superhelical assembly (fig. S19B). Rse1, comprising three β-propellers organized into a Y-shaped structure (fig. S19C), serves as another scaffold of the SF3b complex. Ysf3 together with a short α helix at the carboxyl terminus of Hsh155 are sandwiched between the first and third β-propellers of Rse1 (Fig. 6A and fig. S19D). This organization places the third β-propeller of Rse1 in close contact with one end of Cus1 and the ridges of the carboxyl-terminal HEAT repeats of Hsh155. Rds3 is bound in the hollow center of the Hsh155 superhelical assembly, making contact to the first β-propeller of Rse1. Hsh49 is defined by weak EM density and interacts with Cus1 from the outside (Fig. 6A).

The lateral opening of the Hsh155 superhelical assembly is bound by a duplex between BPS and U2 snRNA (fig. S15, A to C), which is defined by a large number of Watson-Crick H bonds (Fig. 6B). Nucleotide sequences following the 3′ end of the BPS zigzag through the hollow center of the Hsh155 superhelical assembly and exit from the other side of the spiral, interacting with residues from both Hsh155 and Rds3. The ensuing intron sequences

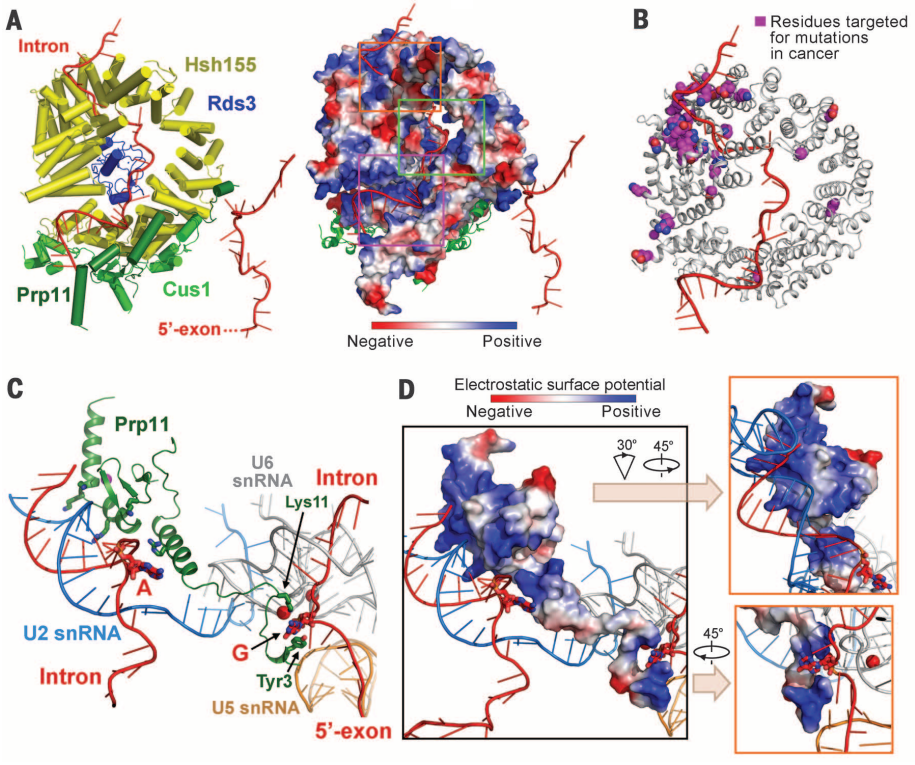

Fig. 7. Recognition of the intron sequences by the SF3b complex. (**A**) The BPS and surrounding sequences of the intron are recognized by Hsh155 and Rds3 of the SF3b complex. Cus1 and the SF3a protein Prp11 are shown as references in the cartoon representation (left). The fully extended pre-mRNA molecule follows the positively charged surface patches in Hsh155 and Rds3 (right). (**B**) Cancer-derived mutations target residues in Hsh155: 36 residues that are targeted for cancer-derived mutations are mapped onto the structure of Hsh155. A large majority of these residues are located in the HEAT repeats 4 to 7 of Hsh155 that bind the pyrimidine-rich sequences of the intron. (**C**) The SF3a protein Prp11 recognizes both the 5′SS and the duplex between the BPS and U2 snRNA. Prp11 has an extended conformation. Two residues, Tyr3 and Lys11, at the amino terminus of Prp11 help coordinate the 5′-guanine nucleotide of the 5′SS, whereas the carboxyl-terminal zinc finger domain and surrounding sequences of Prp11 recognize the BPS-U2 snRNA duplex. (**D**) The RNA-binding surface of Prp11 is highly positively charged. The electrostatic surface potential is shown for Prp11 (left), with close-up views shown for the two primary sites of RNA binding (right).

Downloaded from http://science.sciencemag.org/ on September 3, 2016

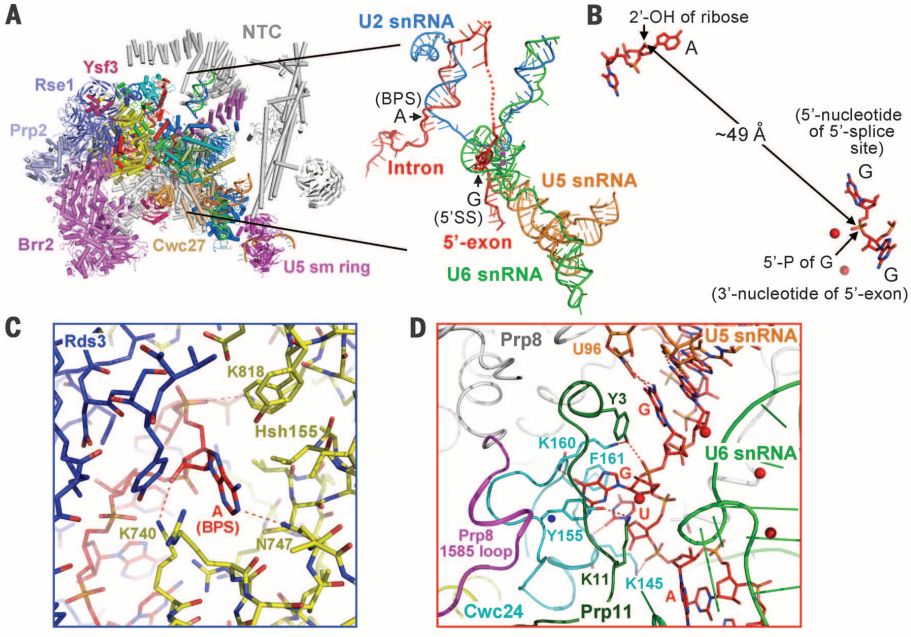

Fig. 8. Catalytic latency of the B^{act} complex. (**A**) Overall structure of the B^{act} complex (left) and the arrangement of the RNA elements (right). The spliceosomal components are color coded. (**B**) A close-up view on the two reacting moieties of the first-step reaction. The 2′-OH of the ribose of the invariant adenine nucleotide in the BPS—the nucleophile—is positioned ~49 Å away from the phosphorous atom of the 5′-guanine nucleotide in the 5′SS. (**C**) A close-up view on the invariant adenine nucleotide in the BPS. Compared with surrounding bases, the adenine base is flipped out of registry and interacts closely with surrounding residues from Hsh155. (**D**) A close-up view on the 5′-guanine nucleotide in the 5′SS. The guanine base interacts with residues from Cwc24 and Prp11. The 1585 loop of Prp8 (magenta) is located close to the 5′SS (*63*).

are recognized by the RES complex (fig. S15E). Note that the only SF3a protein, Prp11, binds to Cus1 and specifically recognizes the intron-U2 snRNA duplex (Fig. 6A).

The RES complex, which is important for RNA splicing and retention of the unspliced pre-mRNA, consists of Pml1, Snu17, and Bud13 (*42*). It closely stacks against the SF3b complex (fig. S15E). Formation of the RES complex appears to be stabilized by the NTR component Prp45 (residues 193 to 350), which wraps around Pml1 and Bud13 (fig. S9A) and places the RES complex between Hsh155 and the RT palm/finger region of Prp8. Bud13 binds Snu17, and an extended β sheet of Snu17 is involved in specific recognition of the 3′ end intron sequences (Fig. 6C).

Recognition of the intron

Specific recognition of conserved intron sequences is a prerequisite for faithful splicing of pre-mRNA. The negatively charged intron sequences track along the positively charged surface patches defined by Hsh155 and Rds3 (Fig. 7A). The canonical BPS contains seven nucleotides 5′-U1-A2-C3-U4-A5-A6-C7-3′. Except for the nucleophile-containing adenine nucleotide A6, the bases of all other six nucleotides form Watson-Crick H bonds with the corresponding bases in U2 snRNA. Notably, none of the seven bases is specifically recognized by an amino acid. In contrast, the phosphate groups in six of the seven nucleotides are recognized by H bonds. Altogether, the intron sequences are recognized by ~30 H bonds, of which about 70% are directed at the backbone phosphates.

Hsh155 is frequently mutated in various hematological malignancies (*43*). We mapped 36 residues that are targeted for cancer-derived mutations onto the structure of Hsh155 (Fig. 7B). A large majority of these residues map to the HEAT repeats 4 to 7 of Hsh155 that bind the pyrimidine-rich sequences to the 3′ end of the BPS. Presumably, these mutations may compromise the ability of Hsh155 to recognize the intron sequences and thus adversely affect splicing.

The SF3a protein Prp11 appears to play a key role in orienting the intron for the first transesterification (Fig. 7C). The amino-terminal residues Tyr^{3} and Lys^{11} of Prp11 are both involved in recognition of the 5′-guanine nucleotide of the 5′SS, whereas positively charged amino acids at the carboxyl terminus of Prp11 specifically contact the duplex between BPS and U2 snRNA. The highly positively charged electrostatic surface potential of these two regions of Prp11 likely facilitates binding of the pre-mRNA sequences (Fig. 7D).

The splicing factors

The ribonucleoprotein-particle remodeling ATPases/helicases and splicing factors play an essential role in the two-step splicing reaction by priming the appropriate spliceosomal complexes (*44*). Two ATPases/helicases (Brr2 and Prp2) and four splicing factors (Cwc21, Cwc22, Cwc24, and Cwc27) are identified in the B^{act} structure. The splicing factor Cwc21 encodes the functional ortholog of SRm300, the only serine-arginine–rich (SR)–related protein at the core of the human catalytic spliceosomes (*45*). A single β strand of Cwc21 forms a β sheet with a pair of antiparallel β strands in the switch loop of Prp8; residues from Cwc21 make close contacts to several nucleotides in the 5′ exon (fig. S20A). Cwc21 may play a role in the proper orientation of pre-mRNA toward the first-step reaction. In addition, Cwc21 and the MA3 domain of Cwc22 are located close to each other, both interacting with the core of Prp8 (fig. S20A). Cwc24 contains three zinc ions, two in the RING domain and one in a C3H-type zinc finger. The RING domain is bound to Rse1, whereas the C3H-type zinc finger is located at the active site and directly coordinates the bases GU in the 5′SS (fig. S20B). Cwc27, a peptidyl-prolyl *cis-trans* isomerase (*46*), simultaneously interacts with both the helix-loop-helix domain of Brr2 and the endonuclease domain of Prp8 (fig. S20C).

Brr2, which drives the transition from the B to B^{act} complex (*47*–*50*), simultaneously interacts with five proteins: two splicing factors Cwc24 and Cwc27, two SF3b scaffold proteins Rse1 and Hsh155, and the Jab1/MPN domain, as well as, to a lesser extent, the endonuclease domain of Prp8. Prp2, together with Spp2, is thought to facilitate the structural transition from the B^{act} to B* complex (*51*–*54*). This transition requires the departure of the SF3b complex and a number of splicing factors in the active site (*3*). Prp2 directly contacts the outside of the Hsh155 superhelical assembly and is located close to the RES complex and the 3′ end sequences of the intron (fig. S20D). The convenient location of Prp2 likely allows it to facilitate disassembly of the SF3b complex.

Discussion

The atomic structure of the B^{act} complex reveals a partially activated conformation of the spliceosome. With the help of the SF3b complex and other protein factors, the 5′SS and BPS are already recognized by U6 and U2 snRNAs, respectively (Figs. 2 and 8A). The 5′ exon is anchored to loop I of U5 snRNA with the help of Cwc21 and Prp11. Both the nucleophile-containing adenine nucleotide in the BPS and the 5′-guanine nucleotide of the 5′SS are already flipped out of registry from neighboring nucleotides, poised for the first transesterification (Fig. 8B). However, these two reactive moieties are separated by a distance of about 49 Å, each coated by specific protein factors (Fig. 8, C and D). The adenine nucleotide is nestled in a surface pocket of Hsh155, with its ribose 2′-OH, its adenine base, and the phosphate group each accepting a H bond from Lys^{740}, Asn^{747}, and Lys^{818}, respectively (Fig. 8C and fig. S16D). In addition, the adenine base is sandwiched by Val^{783} and Arg^{744} of Hsh155 (fig. S15D). In analogy to the adenine nucleotide of

Downloaded from http://science.sciencemag.org/ on September 3, 2016

BPS, the guanine nucleotide of the 5′SS is also recognized by three H bonds (Fig. 8D); the ribose, the base, and the phosphate are H bonded by Lys^{11} of Prp11, the amide group of Lys^{160} of Cwc24, and the Tyr^{3} of Prp11, respectively. The guanine base is sandwiched by Tyr^{155} and Phe^{161} of Cwc24 (fig. S16B). The 1585 loop of Prp8, which is thought to play an important role in pre-mRNA splicing (*55*), is located nearby (Fig. 8D and fig. S16A). The catalytic latency of the B^{act} complex is also manifested by the incompletely formed active site and the coordination of the Mg^{2+} ions (Fig. 3). Thus, the B^{act} complex must undergo an additional step of gross structural rearrangement before the splicing reaction can commence.

Structure of the B^{act} complex allows comparison of the RNA maps with the U4/U5.U6 tri-snRNP (fig. S21). In our tri-snRNP structure from *S. cerevisiae* (*38*), the pre-mRNA is already loaded, with its 5′ exon anchored by loop I and the 5′SS recognized by the ACAGA box. The unanticipated finding of pre-mRNA binding to the tri-snRNP is supported by published biochemical evidence (*56*, *57*). In the B^{act} complex, the 5′ exon sequences are similarly anchored by loop I; but U6 snRNA has undergone marked structural rearrangement (fig. S21). However, the 5′SS remains partially bound to the ACAGA box, and the duplex is placed in the same general location as that of the tri-snRNP. In another structure of the *S. cerevisiae* tri-snRNP (*39*), sequences at the 5′ end of U6 snRNA, as opposed to pre-mRNA in our structure (*38*), were assigned to form a duplex with loop I of U5 snRNA. These two contrasting structures may represent two different states of the tri-snRNP: one before pre-mRNA binding and one after. Before pre-mRNA binding, U6 snRNA may serve as a decoy to occupy the same general location.

The B^{act} complex is not catalytically activated yet and must undergo pronounced structural remodeling mediated by the RNA-dependent ATPase/helicase Prp2. Prp2 directly contacts Hsh155 of the SF3b complex and is located next to the 3′ end of the intron and close to the RES complex. Conceivably, ATP binding and hydrolysis may allow Prp2 to dissociate the SF3b and RES complex from the intron. These changes likely result in the exposure of the nucleophile in the BPS. But in order for the nucleophilic attack to occur, the protein components surrounding the guanine nucleotide of the 5′SS (such as Cwc24 and Prp11) need to be dissociated. Both the splicing factor Cwc24 and the SF3a protein Prp11 simultaneously interact with the SF3b complex and the active site in the B^{act} complex (Fig. 7C and fig. S20B). We speculate that perhaps these two proteins may sense the dissociation of the SF3b complex and help prime the nucleophile from BPS for the first-step reaction.

The findings reported in this manuscript represent a preliminary analysis of the intricate structure of the *S. cerevisiae* B^{act} complex. The functional importance of the numerous protein-protein and protein-RNA interfaces, along with myriad atomic interactions, remains to be scrutinized. This analysis applies equally to the *S. pombe* ILS complex (*9*, *10*). The RNA conformations and the active site specifics in the B^{act} complex are reminiscent of those in the self-splicing group IIC intron (*58*) (fig. S22). Notably, predictions for the active site of the spliceosome was first proposed on the basis of structural studies of the group II introns (*59*, *60*). In the current B^{act} complex, six proteins contains a total of at least 13 zinc ions (fig. S23); the functions of these zinc fingers await future experimental investigations. In summary, the detailed snapshots of the *S. cerevisiae* B^{act} complex, which acts before the first-step reaction, and the *S. pombe* ILS complex, which already has the ligated exon released (*9*, *10*), have outlined a molecular framework for mechanistic understanding of pre-mRNA splicing.

REFERENCES AND NOTES

1. C. B. Burge, T. Tuschl, P. A. Sharp, in *The RNA World: The Nature of Modern RNA Suggests a Prebiotic RNA World* (Cold Spring Harbor Laboratory, Cold Spring Harbor, NY, ed. 2, 1999).
2. D. A. Wassarman, J. A. Steitz, *Science* **257**, 1918–1925 (1992).
3. M. C. Wahl, C. L. Will, R. Lührmann, *Cell* **136**, 701–718 (2009).
4. T. A. Steitz, J. A. Steitz, *Proc. Natl. Acad. Sci. U.S.A.* **90**, 6498–6502 (1993).
5. E. J. Sontheimer, S. Sun, J. A. Piccirilli, *Nature* **388**, 801–805 (1997).
6. P. M. Gordon, E. J. Sontheimer, J. A. Piccirilli, *RNA* **6**, 199–205 (2000).
7. S.-L. Yean, G. Wuenschell, J. Termini, R.-J. Lin, *Nature* **408**, 881–884 (2000).
8. S. M. Fica *et al.*, *Nature* **503**, 229–234 (2013).
9. C. Yan *et al.*, *Science* **349**, 1182–1191 (2015).
10. J. Hang, R. Wan, C. Yan, Y. Shi, *Science* **349**, 1191–1198 (2015).
11. W. P. Galej, C. Oubridge, A. J. Newman, K. Nagai, *Nature* **493**, 638–643 (2013).
12. S. Mozaffari-Jovin *et al.*, *Science* **341**, 80–84 (2013).
13. T. H. Nguyen *et al.*, *Structure* **21**, 910–919 (2013).
14. A. K. Leung, K. Nagai, J. Li, *Nature* **473**, 536–539 (2011).
15. L. Zhou *et al.*, *Nature* **506**, 116–120 (2014).
16. G. Weber, S. Trowitzsch, B. Kastner, R. Lührmann, M. C. Wahl, *EMBO J.* **29**, 4172–4184 (2010).
17. D. A. Pomeranz Krummel, C. Oubridge, A. K. Leung, J. Li, K. Nagai, *Nature* **458**, 475–480 (2009).
18. Y. Kondo, C. Oubridge, A. M. van Roon, K. Nagai, *eLife* **4**, e04986 (2015).
19. P. C. Lin, R. M. Xu, *EMBO J.* **31**, 1579–1590 (2012).
20. M. Azubel, S. G. Wolf, J. Sperling, R. Sperling, *Mol. Cell* **15**, 833–839 (2004).
21. N. Behzadnia *et al.*, *EMBO J.* **26**, 1737–1748 (2007).
22. S. Bessonov *et al.*, *RNA* **16**, 2384–2403 (2010).
23. D. Boehringer *et al.*, *Nat. Struct. Mol. Biol.* **11**, 463–468 (2004).
24. P. Fabrizio *et al.*, *Mol. Cell* **36**, 593–608 (2009).
25. M. M. Golas *et al.*, *Mol. Cell* **40**, 927–938 (2010).
26. M. Grote *et al.*, *Mol. Cell. Biol.* **30**, 2105–2119 (2010).
27. M. S. Jurica, D. Sousa, M. J. Moore, N. Grigorieff, *Nat. Struct. Mol. Biol.* **11**, 265–269 (2004).
28. M. D. Ohi, L. Ren, J. S. Wall, K. L. Gould, T. Walz, *Proc. Natl. Acad. Sci. U.S.A.* **104**, 3195–3200 (2007).
29. B. Sander *et al.*, *Mol. Cell* **24**, 267–278 (2006).
30. E. Wolf *et al.*, *EMBO J.* **28**, 2283–2292 (2009).
31. E. M. Makarov *et al.*, *Science* **298**, 2205–2208 (2002).
32. J. Deckert *et al.*, *Mol. Cell. Biol.* **26**, 5528–5543 (2006).
33. M. S. Jurica, L. J. Licklider, S. R. Gygi, N. Grigorieff, M. J. Moore, *RNA* **8**, 426–439 (2002).
34. J. O. Ilagan, R. J. Chalkley, A. L. Burlingame, M. S. Jurica, *RNA* **19**, 400–412 (2013).
35. W. Chen *et al.*, *RNA* **20**, 308–320 (2014).
36. T. H. Nguyen *et al.*, *Nature* **523**, 47–52 (2015).
37. D. E. Agafonov *et al.*, *Science* **351**, 1416–1420 (2016).
38. R. Wan *et al.*, *Science* **351**, 466–475 (2016).
39. T. H. Nguyen *et al.*, *Nature* **530**, 298–302 (2016).
40. M. M. Golas, B. Sander, C. L. Will, R. Lührmann, H. Stark, *Science* **300**, 980–984 (2003).
41. A. Dziembowski *et al.*, *EMBO J.* **23**, 4847–4856 (2004).
42. M. D. Ohi *et al.*, *Mol. Cell. Biol.* **22**, 2011–2024 (2002).
43. C. N. Hahn, H. S. Scott, *Nat. Genet.* **44**, 9–10 (2012).
44. O. Cordin, J. D. Beggs, *RNA Biol.* **10**, 83–95 (2013).
45. R. J. Grainger, J. D. Barrass, A. Jacquier, J. C. Rain, J. D. Beggs, *RNA* **15**, 2161–2173 (2009).
46. A. Ulrich, M. C. Wahl, *Acta Crystallogr. D Biol. Crystallogr.* **70**, 3110–3123 (2014).
47. T. Achsel, K. Ahrens, H. Brahms, S. Teigelkamp, R. Lührmann, *Mol. Cell. Biol.* **18**, 6756–6766 (1998).
48. P. L. Raghunathan, C. Guthrie, *Curr. Biol.* **8**, 847–855 (1998).
49. D. H. Kim, J. J. Rossi, *RNA* **5**, 959–971 (1999).
50. D. Hahn, G. Kudla, D. Tollervey, J. D. Beggs, *Genes Dev.* **26**, 2408–2421 (2012).
51. S. H. Kim, R. J. Lin, *Mol. Cell. Biol.* **16**, 6810–6819 (1996).
52. Z. Warkocki *et al.*, *Genes Dev.* **29**, 94–107 (2015).
53. J. Roy, K. Kim, J. R. Maddock, J. G. Anthony, J. L. Woolford Jr., *RNA* **1**, 375–390 (1995).
54. E. J. Silverman *et al.*, *Mol. Cell. Biol.* **24**, 10101–10110 (2004).
55. W. P. Galej, T. H. Nguyen, A. J. Newman, K. Nagai, *Curr. Opin. Struct. Biol.* **25**, 57–66 (2014).
56. J. R. Wyatt, E. J. Sontheimer, J. A. Steitz, *Genes Dev.* **6** (12B), 2542–2553 (1992).
57. P. A. Maroney, C. M. Romfo, T. W. Nilsen, *Mol. Cell* **6**, 317–328 (2000).
58. R. T. Chan, A. R. Robart, K. R. Rajashankar, A. M. Pyle, N. Toor, *Nat. Struct. Mol. Biol.* **19**, 555–557 (2012).
59. K. S. Keating, N. Toor, P. S. Perlman, A. M. Pyle, *RNA* **16**, 1–9 (2010).
60. N. Toor, K. S. Keating, S. D. Taylor, A. M. Pyle, *Science* **320**, 77–82 (2008).
61. E. F. Pettersen *et al.*, *J. Comput. Chem.* **25**, 1605–1612 (2004).
62. W. L. DeLano, The PyMOL Molecular Graphics System (2002); www.pymol.org.
63. Single-letter abbreviations for the amino acid residues are as follows: A, Ala; C, Cys; D, Asp; E, Glu; F, Phe; G, Gly; H, His; I, Ile; K, Lys; L, Leu; M, Met; N, Asn; P, Pro; Q, Gln; R, Arg; S, Ser; T, Thr; V, Val; W, Trp; and Y, Tyr.

ACKNOWLEDGMENTS

We thank D. Wang for his generous support of our research and the Tsinghua University Branch of China National Center for Protein Sciences (Beijing) for the research facility. The computation was completed on the "Explorer 100" cluster system of Tsinghua National Laboratory for Information Science and Technology. This work was supported by funds from the Ministry of Science and Technology (2014ZX09507003006) and the National Natural Science Foundation of China (31130002 and 31321062). For the B^{act} complex, the atomic coordinates have been deposited in the Protein Data Bank with the accession code 5GM6, and the EM maps have been deposited in EMDB with the accession code EMD-9524. The authors declare no competing financial interests. Correspondence and requests for materials should be addressed to Y. Shi (shi-lab@tsinghua.edu.cn).

SUPPLEMENTARY MATERIALS

www.sciencemag.org/content/353/6302/904/suppl/DC1
Materials and Methods
Figs. S1 to S23
Tables S1 to S4
References (*64*–*95*)

2 May 2016; accepted 13 July 2016
Published online 21 July 2016
10.1126/science.aag0291

Downloaded from http://science.sciencemag.org/ on September 3, 2016

REPORTS

ORGANIC SYNTHESIS

A 15-step synthesis of (+)-ryanodol

Kangway V. Chuang,* Chen Xu,* Sarah E. Reisman†

(+)-Ryanodine and (+)-ryanodol are complex diterpenoids that modulate intracellular calcium-ion release at ryanodine receptors, ion channels critical for skeletal and cardiac muscle excitation-contraction coupling and synaptic transmission. Chemical derivatization of these diterpenoids has demonstrated that certain peripheral structural modifications can alter binding affinity and selectivity among ryanodine receptor isoforms. Here, we report a short chemical synthesis of (+)-ryanodol that proceeds in only 15 steps from the commercially available terpene (*S*)-pulegone. The efficiency of the synthesis derives from the use of a Pauson-Khand reaction to rapidly build the carbon framework and a SeO_2-mediated oxidation to install three oxygen atoms in a single step. This work highlights how strategic C–O bond constructions can streamline the synthesis of polyhydroxylated terpenes by minimizing protecting group and redox adjustments.

Terpenes are a large and structurally diverse family of natural products that range from simple hydrocarbons associated with flavors and fragrances, to complex, highly oxidized polycyclic molecules such as the antimalarial drug artemisinin, and the anticancer compounds ingenol and taxol (*1*). Although terpenes are isolated from natural sources, it can be challenging to translate their biological activity into a practical application (*2*). In some cases, the hurdle is low natural abundance; at other times, it is the difficulty encountered by chemists seeking to precisely edit a terpene's molecular structure to improve its drug-like properties or interrogate its role in modulating disease pathways. The development of concise chemical syntheses of terpenes can transform our ability to use these molecules and their synthetic derivatives as biological probes or as lead compounds for the development of new medicines (*3*–*5*). Furthermore, these scientific efforts often innovate chemical reactivity or synthetic design concepts (*6*).

The natural product ryanodine (**1**) (*7*, *8*) and its hydrolysis product ryanodol (**2**) (*8*, *9*) are among the most highly oxidized and synthetically challenging diterpenoids reported to date (Fig. 1A). Isolated from the tropical shrub *Ryania speciosa* Vahl in connection with its insecticidal properties (*7*), ryanodine is the namesake ligand of the ryanodine receptors (RyRs) (*10*), an important family of ion channels that regulate intracellular Ca^{2+} release and play a critical role in signal transduction (*11*). In mammalian cells, these receptors exist in multiple isoforms (RyR1, RyR2, and RyR3) that serve to mediate both movement and cognitive function. Mutations of RyRs are associated with genetic diseases such as malignant hyperthermia and central core disease (*12*), whereas altered expression of RyR2 and RyR3 has been associated with the pathogenesis of neurodegenerative disorders such as Alzheimer's disease (*13*). Ryanodine binds with high affinity to the conducting state of RyRs, exerting concentration-dependent modulation of Ca^{2+} release: At nanomolar concentrations, ryanodine locks RyRs in an open, subconductance state, whereas at higher concentrations, ryanodine causes closure of the channels (*14*). The deacylated compound ryanodol binds with lower affinity than **1** to mammalian RyRs; however, it still induces a subconductance state and has been reported as a reversible probe of RyR-mediated Ca^{2+} release in cells (*15*).

Since the initial reports describing the isolation of ryanodine from *Ryania*, a number of congeners (known as ryanoids) that vary in oxidation pattern have been isolated (*16*–*20*). Whereas ryanodol—the compound obtained by hydrolysis of ryanodine—has not yet been isolated directly from a natural source, the closely related compound C3-*epi*-ryanodol (**4**) was isolated by Gonzalez-Coloma from *Persea indica* (*18*). Indeed, owing to their structural similarities, C3-*epi*-ryanodol (**4**) was initially erroneously reported to be ryanodol (**2**); however, the structure of the Coloma-Gonzalez isolate (*21*) was recently reassigned through the synthetic efforts of Inoue (see below) (*22*). These subtle differences in structure exert a pronounced effect on RyR binding: C3-*epi*-ryanodine (**5**), prepared from **4**, binds to RyRs with an affinity 1/100th that of **1** (*23*).

Given the biological importance of the RyRs, the ryanoids have been the focus of both total synthesis and derivatization efforts. In 1979, Deslongchamps and co-workers disclosed a total synthesis of (+)-**2**, which hinged on a key Diels-Alder cycloaddition and a series of elegantly designed intramolecular aldol reactions to assemble the tetracyclic ABCD framework (Fig. 1B) (*24*–*28*). In a classic example of relay synthesis, the degradation product (+)-anhydroryanodol (**3**) was converted to (+)-ryanodol (**2**) in a final two-step sequence (*28*), providing the target molecule in 41 total steps (37 steps in its longest linear sequence). A more recent series of studies from Inoue and co-workers highlighted the utility of several radical-based C–O and C–C bond-forming reactions in a total synthesis that furnishes (±)-**2** (*29*) and (±)-**4** (*22*), each in 35 total steps. These studies allowed Inoue *et al.* to correctly reassign the structure of the natural product isolated from *P. indica* (*18*) as C3-*epi*-ryanodol (**4**). Inoue and co-workers subsequently reported that their synthesis could be rendered enantioselective through a catalytic asymmetric desymmetrization process and that an appropriately protected derivative of (+)-**2** could be elaborated to (+)-**1** in five synthetic steps (*30*, *31*). In addition to these total syntheses, several medicinal chemistry studies have focused on the derivatization of ryanodine and ryanodol (*32*–*34*). Here, we disclose a direct and concise strategy to access the central ryanoid ring system, which has enabled the chemical synthesis of (+)-ryanodol (**2**) in only 15 steps from commercially available starting materials. These studies provide a synthetic platform from which it will be possible to prepare previously inaccessible ryanoid derivatives.

Perhaps the most substantial synthetic challenge embedded within the structure of **2** is the highly oxidized five-membered A-ring, which bears an all-carbon quaternary center and four additional stereogenic carbons bonded to oxygen (Fig. 1A). A concise synthesis of **2** requires a carefully choreographed introduction of these moieties to minimize redox, protecting group, and functional group transformations. Guided by the landmark studies of Deslongchamps and co-workers (*28*), we identified the C1–C15 bond of ryanodol (**2**) as the most simplifying and strategic initial retrosynthetic disconnection (Fig. 1B). This analysis revealed the tetracyclic lactone anhydroryanodol (**3**) as our initial synthetic target (Fig. 1C), with the isopropyl group introduced at a late stage through a transition metal–catalyzed cross-coupling reaction of enol triflate **6**; this approach would also allow for versatile incorporation of alternative carbon-based fragments to facilitate long-term goals of preparing ryanoid derivatives. We anticipated that the requisite A-ring oxidation pattern could be accessed via chemo- and stereoselective functionalization of cyclopentenone **7**, whereby the enone would provide a functional group handle to install the critical C3, C4, and C12 alcohols of **2**. We envisioned preparing cyclopentenone **7** by an intramolecular Pauson-Khand reaction (*35*), a transformation that would be facilitated by the conformational rigidity of bicyclic lactone **8**. Lactone **8** could arise through a series of transformations from (*S*)-pulegone, a commercially available terpene. By this analysis, the oxygen atoms at C6, C10, and C11 would be incorporated early in the synthesis, whereas the oxygen atoms at C3, C4, and C12 would be introduced at a late stage. With the implementation of appropriate protecting groups, we anticipated that this strategy would minimize synthetic manipulations ancillary to the direct construction of the natural product.

Division of Chemistry and Chemical Engineering, California Institute of Technology, Pasadena, CA 91125, USA.
*These authors contributed equally to this work. †Corresponding author. Email: reisman@caltech.edu

Downloaded from http://science.sciencemag.org/ on September 3, 2016

We first investigated the stereoselective oxidation of (*S*)-pulegone (**10**) to install the C6 and C10 alcohols of the C-ring (Fig. 2), envisioning functionalization at both carbons via enolates accessed by γ- or α′-deprotonation of the ketone, respectively. Preliminary experiments confirmed that the C6-alcohol could be installed with 2.5:1 diastereomeric ratio (dr) through generation of the thermodynamic dienolate with potassium hexamethyldisilazide (KHMDS) followed by quenching with oxaziridine **11** (*36*). Noting that KHMDS did not appear to directly react with oxaziridine **11** at −78°C, we hypothesized that a one-step protocol involving excess KHMDS and **11** might simultaneously install both alcohols. Indeed, treatment of **10** with 2.5 equivalents (equiv.) of KHMDS at −78°C followed by dropwise addition of 2.4 equiv. of **11** provided α,α′-diol **12**, which could be isolated as a single diastereomer in 42% yield (120 mmol scale). Although the yield is modest, this single transformation converts a simple terpene to a valuable building block with the requisite ryanodol C-ring oxidation pattern. We improved the efficiency of this transformation to 50% yield by modification of the standard procedure on a smaller scale (10 mmol, see supplementary materials). However, given the operational simplicity of the former procedure on larger scales, this protocol was preferentially employed for increased material throughput.

Treatment of diol **12** with excess benzyl chloromethyl ether effected protection of both alcohols as benzyloxymethyl ethers to give **13**. At this stage, the D-ring was constructed by an efficient four-step sequence. First, addition of propynylmagnesium bromide to **13** at 0°C proceeded in 5:1 dr, providing the equatorially disposed alkyne in 81% isolated yield. Ozonolytic cleavage of the 1,1-disubstituted olefin proceeded in high yield to afford methyl ketone **14**. Although a *N*,*N*′-dicyclohexylcarbodiimide-mediated phosphonoacylation and intramolecular Horner–Wadsworth–Emmons lactone synthesis had proved moderately effective in model studies lacking C10 oxidation, the tertiary alkynol of **14** proved resistant to acylation under a number of conditions. Presumably, the increased steric encumbrance and inductively withdrawing C10-ether sharply decreases the nucleophilicity of the tertiary alkynol. Instead, ketone **14** was efficiently converted to α,β-unsaturated lactone **15** via 1,2-addition of ethoxyethynylmagnesium bromide followed by an Ag-catalyzed cyclization and elimination cascade (*37*).

With lactone **15** in hand, 1,4-addition of magnesium divinyl cuprate provided the corresponding enyne **16** as a single diastereomer in 84% yield, forging the critical all-carbon quaternary center at C5 while simultaneously setting the stage for a key Pauson-Khand cyclization. A number of Pauson-Khand procedures were screened for their ability to deliver **17** in both high yield and diastereoselectivity (Table 1). Although standard conditions (*38*, *39*) using stoichiometric amounts of $Co_2(CO)_8$ produced the desired product, separation of diastereomeric enone **17′** proved challenging and indicated that a more selective protocol was necessary. Monometallic

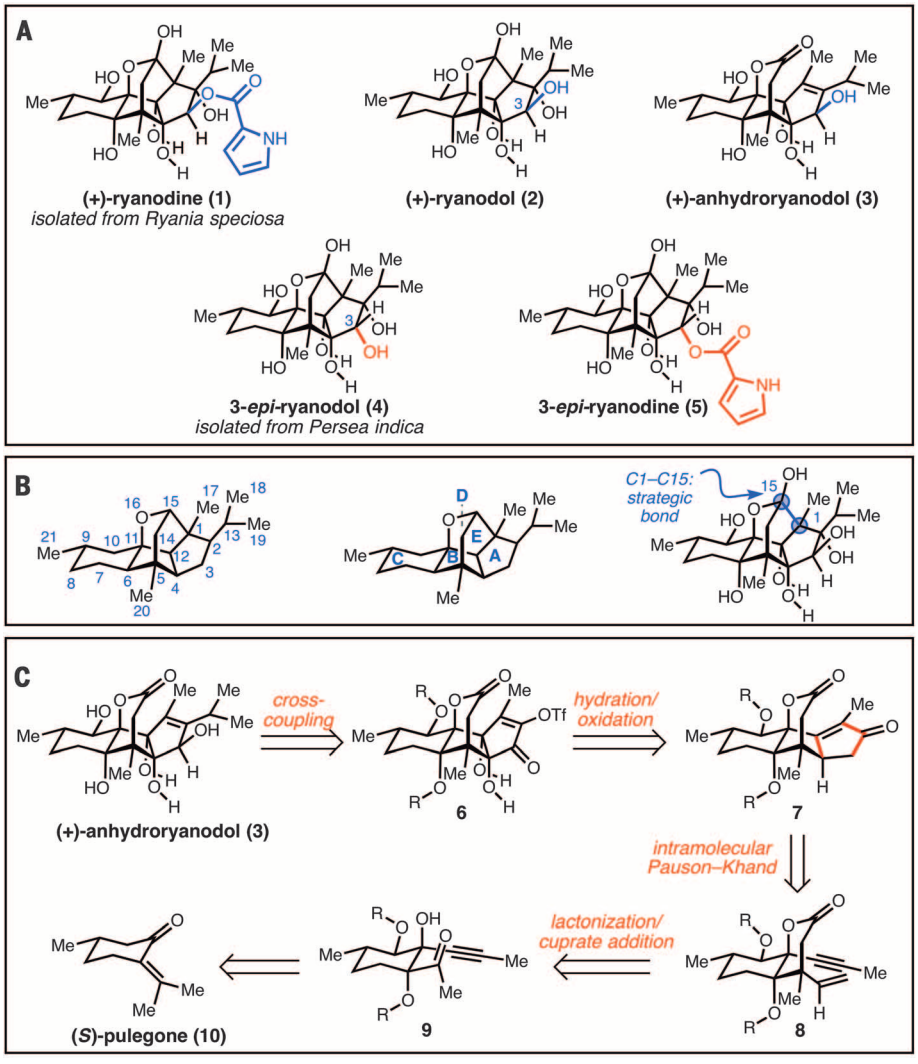

Fig. 1. Ryanodine and selected ryanoids. (**A**) Chemical structures of (+)-ryanodine (**1**), (+)-ryanodol (**2**), (+)-anhydroryanodol (**3**), 3-*epi*-ryanodol (**4**), and 3-*epi*-ryanodine (**5**). (**B**) Carbon numbering and ring system letter assignment. (**C**) Retrosynthetic analysis of anhydroryanodol.

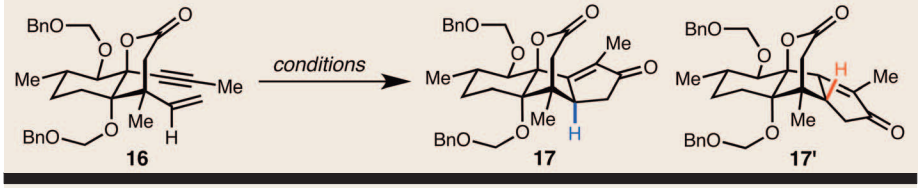

Table 1. Evaluation of Pauson-Khand reaction conditions.

Entry	Conditions*	dr†	Yield (%)‡
1	$Co_2(CO)_8$ (1.2 equiv.), THF, 12 hours; then DMSO, 65°C	2.2:1	46
2	$Co_2(CO)_8$ (1.2 equiv.), CH_2Cl_2, 9 hours; then NMO, 23°C	4.5:1	78
3	$Mo(CO)_6$ (1.2 equiv.), DMSO, PhMe, 110°C	–	Trace
4	$Mo(CO)_3(DMF)_3$ (1.1 equiv.), CH_2Cl_2, 23°C	>20:1	67
5	$[RhCl(CO)_2]_2$ (1 mol %), CO (1 atm), *m*-xylene, 110°C	>20:1	85

*Reactions conducted on 0.2 mmol scale. THF, tetrahydrofuran; DMSO, dimethylsulfoxide; NMO, *N*-methylmorpholine *N*-oxide; DMF, *N*,*N*-dimethylformamide. †Determined by ^{1}H-NMR spectroscopy. ‡Isolated yield after purification by silica gel chromatography.

Downloaded from http://science.sciencemag.org/ on September 3, 2016

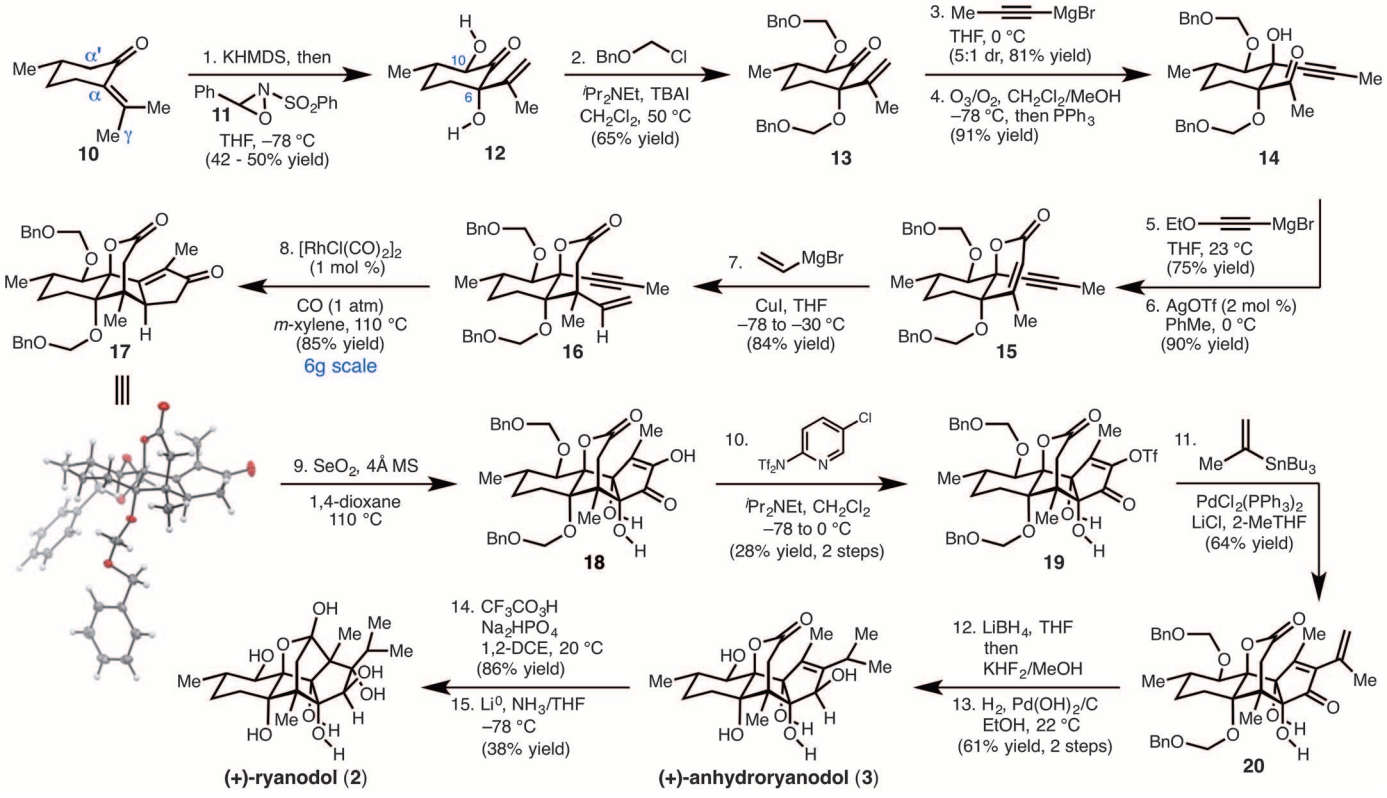

Fig. 2. Complete synthetic sequence for the chemical synthesis of (+)-anhydroryanodol and (+)-ryanodol. Reagents and conditions as follows: 1. potassium hexamethyldisilazide (2.5 equiv.), THF –78°C; then **11** (2.4 equiv.), 42 to 50% yield. 2. Benzyl chloromethyl ether (5.0 equiv.), $^{i}Pr_2NEt$ (8.0 equiv.), $^{n}Bu_4NI$ (2.0 equiv.), CH_2Cl_2, 50°C, 65% yield. 3. Propynylmagnesium bromide, THF, 0°C, 81% yield, 5:1 dr. 4. O_3/O_2, CH_2Cl_2/MeOH (4:1), –78°C; then PPh_3, 91% yield. 5. Ethoxyethynylmagnesium bromide (5.0 equiv.), THF, 0°C, 75% yield. 6. AgOTf (2 mol %), PhMe, 0°C, 90% yield. 7. CuI (3.0 equiv.), vinylmagnesium bromide (6.0 equiv.), THF, –78° to –30°C, 84% yield. 8. $[RhCl(CO)_2]_2$ (1 mol %), CO (1 atm), *m*-xylene, 110°C, 85% yield. 9. SeO_2 (10 equiv.), 4 Å MS, 1,4-dioxane, 110°C. 10. Comins' reagent, $^{i}Pr_2NEt$, CH_2Cl_2, –78° to 0°C, 28% yield, two steps. 11. $PdCl_2(PPh_3)_2$, tributyl(prop-1-en-2-yl)stannane, LiCl, 2-MeTHF, 85°C, 64% yield. 12. $LiBH_4$, THF, –15° to –10°C; then KHF_2/MeOH. 13. H_2, $Pd(OH)_2/C$, EtOH, 61% yield, two steps. 14. Trifluoroacetic anhydride, urea hydrogen peroxide, Na_2HPO_4, 86% yield. 15. Li^0 wire, NH_3/THF, –78°C, 38% yield.

mediators were found to improve the dr, with $Mo(CO)_3(DMF)_3$ (*40*) providing **17** as a single diastereomer in 67% yield. Despite the serviceable yield and scalability of this transformation, we sought a more efficient protocol that could obviate the need for stoichiometric metals and their attendant by-products. Treatment of **16** with 1 mol % $[RhCl(CO)_2]_2$ (*41*) under an atmosphere of carbon monoxide provided the desired product in 85% yield, again as a single diastereomer. This reaction has been conducted on a multigram scale, providing 5.7 g of enone **17** in a single pass. Single-crystal x-ray diffraction analysis of **17** confirmed both the absolute configuration and structural assignment of this key tetracyclic intermediate.

The successful realization of the Pauson-Khand cyclization led us to the next phase of our synthetic studies: chemo- and stereoselective functionalization of the A-ring through the introduction of the C3, C4, and C12-alcohols, as well as the C2-isopropyl unit. To this end, initial investigations were aimed at oxidation of the C4 allylic methine of **17**, but efforts in this vein were thwarted by undesired reactivity. For example, established methods for allylic oxidation via reactive radical species [e.g., $Pd(OH)_2/C$/*t*-BuOOH (*42*) or $Rh_2(cap)_4$/*t*-BuOOH (*43*)] were unfruitful owing to competitive functionalization of the C1–C12 olefin (i.e., epoxidation, 1,2-difunctionalization). Although we considered the possibility of advancing these unanticipated products further in the synthesis, it was unclear how to achieve efficient transposition to the requisite oxidation pattern.

Instead, we turned to C3-functionalization of **17** using SeO_2 (*44*), anticipating that the enone might be readily oxidized to the corresponding α-diketone (Fig. 3). We found that treatment of **17** with excess SeO_2 in wet 1,4-dioxane at 110°C not only effected C3-oxidation, but also the formal hydration of the enone, thereby installing the necessary C12-alcohol and providing diosphenol **21**. Hypothesizing that rigorous exclusion of water might promote C4-allylic hydroxylation before diketone formation, we subjected enone **17** to SeO_2 under anhydrous conditions in the presence of 4 Å molecular sieves (4 Å MS). Prolonged heating at 110°C in 1,4-dioxane provided a distinct product, which had incorporated an additional oxygen as determined by mass spectrometry analysis. Rigorous structural assignment of this compound revealed it to be the fully oxidized diosphenol **18**, a compound with the C4, C12 *syn*-vicinal diol of **2**. This single-step transformation installs the necessary oxygen atoms at C3, C4, and C12 while simultaneously providing a functional group handle for incorporation of the C2-isopropyl group.

Because C4-deoxy analog of ryanodine is itself a natural product, deoxyspiganthine (*20*), and could be of interest for future biological studies, we optimized procedures to prepare both **18** and **21** (Fig. 3). Given concerns that contamination by ^{1}H–nuclear magnetic resonance (^{1}H-NMR) silent, red selenium by-products resulted in artificially inflated isolated yields, our optimization efforts were guided by ^{1}H-NMR yields determined by integration versus an added standard. Isolated yields were determined after conversion to corresponding enol triflates **19** and **22**, which could be obtained as analytically pure compounds. Thus, subjection of tetracycle **17** to 10 equiv. of SeO_2 in wet 1,4-dioxane at 110°C for 1 hour provided **21** in 67 to 69% ^{1}H-NMR yield, and the corresponding vinyl triflate **22** in 56% isolated yield over two steps. Alternatively, treatment of **17** with 10 equiv. of SeO_2 in anhydrous 1,4-dioxane in the presence of freshly

Downloaded from http://science.sciencemag.org/ on September 3, 2016

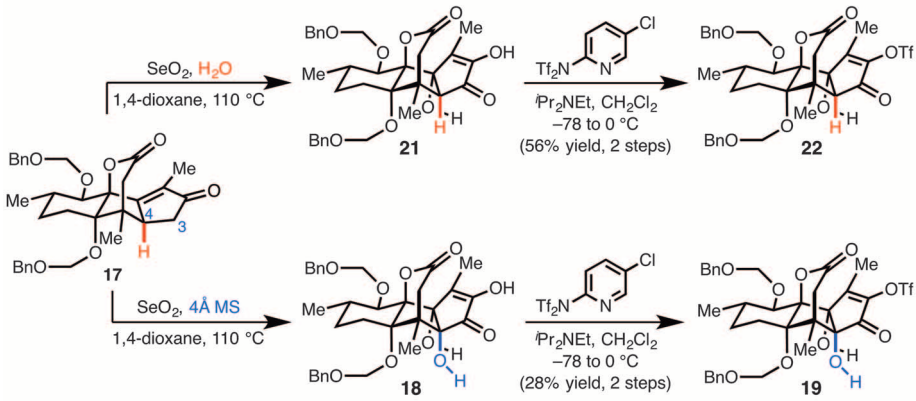

Fig. 3. Selenium dioxide-mediated A-ring oxidation. In the presence of water, SeO_2-mediated oxidation of enone **17** provides **21**. In the absence of water, further oxidation occurs to deliver **18**.

activated 4 Å MS at 110°C for 9 hours provided **18** in 33 to 35% ^{1}H-NMR yield, and vinyl triflate **19** in 28% isolated yield over two steps. Despite the modest yield, this sequence accomplishes the stereospecific incorporation of three oxygen atoms, proceeds with an average efficiency of ~70% yield per transformation, and fares well in comparison to conceivable multiple step protocols to achieve the same reactivity. Although the precise mechanism of the SeO_2-mediated oxidation remains unclear at this time, investigations are ongoing and should aid the development of a more efficient protocol.

In the final stages of the synthesis, advancement of **19** to (+)-anhydroryanodol was achieved by a three-step sequence. Palladium-catalyzed cross-coupling between **19** and tributyl(2-propenyl) stannane installed the final three carbons, delivering **20** in 64% yield. $LiBH_4$-mediated 1,2-reduction stereoselectively furnished the C3 alcohol, which was subjected to H_2 and $Pd(OH)_2$/C to simultaneously reduce the disubstituted olefin and remove the benzyloxymethyl groups, providing (+)-**3** in 61% yield over two steps. Using this route, we have prepared >400 mg of (+)- anhydroryanodol to date. Conversion of this material to (+)-ryanodol was achieved via a slight modification of Deslongchamps's two-step protocol (*28*). Treatment of **3** with trifluoroperacetic acid, freshly prepared from trifluoroacetic anhydride and urea hydrogen peroxide (in place of the originally reported concentrated hydrogen peroxide), cleanly afforded epianhydroryanodol epoxide in 86% yield. Subjection of this material to Li^0 in NH_3 (distilled from Na^0) at –78°C resulted in reductive cyclization to produce (+)-**2** in 38% yield (lit. 60% yield). In our hands, the reaction profile was highly dependent on the purity of the ammonia. Specifically, independent control reactions conducted with ammonia condensed directly from the gas cylinder, or using redistilled ammonia with either added H_2O (10 equiv.), or exogenous Fe-salts (*45*), revealed that these parameters all substantially affect the ratio of **2** to carbonyl-reduction products, as well as the formation of minor unidentified degradation products.

The concise synthesis of (+)-ryanodol described here proceeds in only 15 synthetic steps (0.42% overall yield) from (*S*)-pulegone (**10**), fewer than half the steps of the previously disclosed syntheses by Deslongchamps *et al.* (37 linear steps, 0.23% yield) and Inoue *et al.* (35 linear steps, 0.008% yield). The efficiency of our approach derives from the development of a direct and scalable route to key cyclopentenone **17**, which can be prepared on a multigram scale in only eight steps and rapidly elaborated to (+)-anhydroryanodol. The strategic use of C–O bond–forming reactions minimizes redox adjustments and the use of protecting groups. Indeed, the five alcohols found in (+)-***3*** are incorporated with just two transformations: the dihydroxylation of **10** and the SeO_2-mediated oxidation of enone **17**. Moreover, all but the C3-alcohol are introduced with the correct carbon oxidation level. We anticipate that the brevity of the synthesis will render feasible the design and preparation of ryanoid derivatives for studying RyR function.

REFERENCES AND NOTES

1. E. Breitmaier, *Terpenes: Flavors, Fragrances, Pharmaca, Pheromones* (Wiley, Weinheim, Germany, 2006).
2. F. E. Koehn, G. T. Carter, *Nat. Rev. Drug Discov.* **4**, 206–220 (2005).
3. L. Jørgensen *et al.*, *Science* **341**, 878–882 (2013).
4. S. Kawamura, H. Chu, J. Felding, P. S. Baran, *Nature* **532**, 90–93 (2016).
5. H.-H. Lu, M. D. Martinez, R. A. Shenvi, *Nat. Chem.* **7**, 604–607 (2015).
6. T. J. Maimone, P. S. Baran, *Nat. Chem. Biol.* **3**, 396–407 (2007).
7. E. F. Rogers, F. R. Koniuszy, J. Shavel Jr., K. Folkers, *J. Am. Chem. Soc.* **70**, 3086–3088 (1948).
8. K. Wiesner, Z. Valenta, J. A. Findlay, *Tetrahedron Lett.* **8**, 221–223 (1967).
9. S. N. Srivastava, M. Przybylska, *Can. J. Chem.* **46**, 795–797 (1968).
10. I. N. Pessah, A. L. Waterhouse, J. E. Casida, *Biochem. Biophys. Res. Commun.* **128**, 449–456 (1985).
11. J. T. Lanner, D. K. Georgiou, A. D. Joshi, S. L. Hamilton, *Cold Spring Harb. Perspect. Biol.* **2**, a003996 (2010).
12. T. V. McCarthy, K. A. Quane, P. J. Lynch, *Hum. Mutat.* **15**, 410–417 (2000).
13. M. Kelliher *et al.*, *Neuroscience* **92**, 499–513 (1999).
14. G. Meissner, *J. Biol. Chem.* **261**, 6300–6306 (1986).
15. J. Ramos-Franco *et al.*, *Pflugers Arch.* **460**, 767–776 (2010).
16. A. Isogai, S. Murakoshi, A. Suzuki, S. Tamura, *Agric. Biol. Chem.* **41**, 1779–1784 (1977).
17. T. Nohara, N. Tokubuchi, M. Kuroiwa, I. Nishioka, *Chem. Pharm. Bull.* (*Tokyo*) **28**, 2682–2686 (1980).
18. A. González-Coloma, M. G. Hernandez, A. Perales, B. M. Fraga, *J. Chem. Ecol.* **16**, 2723–2733 (1990).
19. A. González-Coloma, D. Terrero, A. Perales, P. Escoubas, B. M. Fraga, *J. Agric. Food Chem.* **44**, 296–300 (1996).
20. H. Achenbach, H. Hübner, W. Vierling, W. Brandt, M. Reiter, *J. Nat. Prod.* **58**, 1092–1096 (1995).
21. This compound has been referred to by Inoue *et al.* as "natural ryanodol." See (*22*).
22. M. Koshimizu, M. Nagatomo, M. Inoue, *Angew. Chem. Int. Ed. Engl.* **55**, 2493–2497 (2016).
23. W. Welch *et al.*, *Biochemistry* **36**, 2939–2950 (1997).
24. A. Bélanger *et al.*, *Can. J. Chem.* **57**, 3348–3354 (1979).
25. P. Deslongchamps *et al.*, *Can. J. Chem.* **68**, 115–126 (1990).
26. P. Deslongchamps *et al.*, *Can. J. Chem.* **68**, 127–152 (1990).
27. P. Deslongchamps *et al.*, *Can. J. Chem.* **68**, 153–185 (1990).
28. P. Deslongchamps *et al.*, *Can. J. Chem.* **68**, 186–192 (1990).
29. M. Nagatomo *et al.*, *J. Am. Chem. Soc.* **136**, 5916–5919 (2014).
30. M. Nagatomo *et al.*, *Chemistry* **22**, 222–229 (2016).
31. K. Masuda, M. Koshimizu, M. Nagatomo, M. Inoue, *Chemistry* **22**, 230–236 (2016).
32. A. L. Waterhouse, I. N. Pessah, A. O. Francini, J. E. Casida, *J. Med. Chem.* **30**, 710–716 (1987).
33. W. Welch *et al.*, *Biochemistry* **33**, 6074–6085 (1994).
34. J. L. Sutko, J. A. Airey, W. Welch, L. Ruest, *Pharmacol. Rev.* **49**, 53–98 (1997).
35. I. U. Khand, G. R. Knox, P. L. Pauson, W. E. Watts, M. I. Foreman, *J. Chem. Soc. Perkin Trans. I* **1973**, 977–981 (1973).
36. L. C. Vishwakarma, O. D. Stringer, F. A. Davis, *Org. Synth.* **66**, 203–207 (1988).
37. M. Egi *et al.*, *Org. Lett.* **15**, 4150–4153 (2013).
38. Y. K. Chung, B. Y. Lee, N. Jeong, M. Hudecek, P. L. Pauson, *Organometallics* **12**, 220–223 (1993).
39. S. Shambayani, W. E. Crowe, S. L. Schreiber, *Tetrahedron Lett.* **31**, 5289–5292 (1990).
40. M. R. Adrio, *Org. Lett.* **7**, 431–434 (2005).
41. Y. Koga, T. Kobayashi, K. Narasaka, *Chem. Lett.* **27**, 249–250 (1998).
42. J.-Q. Yu, E. J. Corey, *Org. Lett.* **4**, 2727–2730 (2002).
43. A. J. Catino, R. E. Forslund, M. P. Doyle, *J. Am. Chem. Soc.* **126**, 13622–13623 (2004).
44. R. Riley, J. F. Morley, N. A. C. Friend, *J. Chem. Soc.* **1932**, 1875–1883 (1932).
45. R. G. Harvey, K. Urberg, *J. Org. Chem.* **33**, 2570–2571 (1968).

ACKNOWLEDGMENTS

The California Institute of Technology Center for Catalysis and Chemical Synthesis is gratefully acknowledged for access to analytical equipment. We thank S. Virgil and J. Hofstra for assistance in obtaining x-ray–quality crystals and solving the structure of **15**, respectively. M. Takase and L. Henling are acknowledged for acquiring the x-ray diffraction data for **15** (CCDC deposition no. 1478621; the data are available free of charge from The Cambridge Crystallographic Data Centre). M. Kieffer is gratefully acknowledged for critical feedback and helpful suggestions. Fellowship support was provided by the National Science Foundation (graduate research fellowship to K.V.C., grant DGE-1144469) and the Shenzhen UV-ChemTech Inc. (postdoctoral fellowship to C.X.). S.E.R. is an American Cancer Society Research Scholar and Heritage Medical Research Institute investigator. Financial support from the NIH (National Institute of General Medical Sciences grant RGM097582-01), Eli Lilly, and Novartis is gratefully acknowledged. The California Institute of Technology has filed a provisional patent on this work (application no. 62/269,760).

SUPPLEMENTARY MATERIALS

www.sciencemag.org/content/353/6302/912/suppl/DC1
Materials and Methods
Schemes S1 and S2
Tables S1 to S9
References (*46*–*53*)
NMR Spectra

9 May 2016; accepted 25 July 2016
10.1126/science.aag1028

Downloaded from http://science.sciencemag.org/ on September 3, 2016

ULTRAFAST DYNAMICS

Attosecond dynamical Franz-Keldysh effect in polycrystalline diamond

M. Lucchini,[1]* S. A. Sato,[2] A. Ludwig,[1] J. Herrmann,[1] M. Volkov,[1] L. Kasmi,[1] Y. Shinohara,[3] K. Yabana,[2] L. Gallmann,[1,4] U. Keller[1]

Short, intense laser pulses can be used to access the transition regime between classical and quantum optical responses in dielectrics. In this regime, the relative roles of inter- and intraband light-driven electronic transitions remain uncertain. We applied attosecond transient absorption spectroscopy to investigate the interaction between polycrystalline diamond and a few-femtosecond infrared pulse with intensity below the critical intensity of optical breakdown. Ab initio time-dependent density functional theory calculations, in tandem with a two-band parabolic model, accounted for the experimental results in the framework of the dynamical Franz-Keldysh effect and identified infrared induction of intraband currents as the main physical mechanism responsible for the observations.

During the 1980s, rapid progress in picosecond and femtosecond ultrafast lasers started to bridge the gap between electronics and optics (*1*). The resulting synergy has since given rise to a wealth of new technologies and scientific insights, such as the optical generation of terahertz frequencies for the investigation of ever faster physical processes and device performance (*2*, *3*). The more recent progress in ultrafast laser sources, which now produce few-cycle femtosecond (*4*) and attosecond (*5*, *6*) pulses with full electric field control (*7*), extends these ideas into the petahertz frequency regime. Indeed, using measurement concepts similar to those developed for terahertz electric fields and femtosecond time resolution, we now can explore the speed limits of electronics at optical frequencies with methods such as attosecond transient absorption spectroscopy (ATAS) (*8*–*10*), which has recently been extended to solid-state materials (*11*–*13*). This has opened the possibilities of studying electron motion under the influence of a high-frequency electric field and of investigating the feasibility of petahertz electronic devices (*14*, *15*).

Here, we used ATAS to explore a regime where the electrons in a dielectric material are exposed to a relatively strong high-frequency optical field. In this case, the quiver energy (or ponderomotive energy U_p) of the electrons in the oscillating electrical field becomes comparable to the photon energy of the driving laser. The system transitions from a more quantum-mechanical (photon-driven) to a more classical (field-driven) regime (*16*). Although both limiting regimes have been extensively studied, the many phenomena occurring in the intermediate regime are still not well understood. In this intermediate regime, the material is described by coupled light-matter states, and effects such as band dressing (*17*), the dynamical Franz-Keldysh effect (*18*), and Wannier-Stark localization (*19*) coexist. Therefore, the total material response exhibits a complex behavior that often cannot be easily framed within only one of these effects. As a consequence, in this regime the role of intra- and interband transitions in determining the dynamical response of dielectrics also remains unclear (*20*, *21*).

A fundamental process related to the intraband motion of charges is the Franz-Keldysh effect. In a simple physical picture, a static external field applied to a dielectric bends the crystal potential and accelerates the electron-hole pair. Its wave function becomes an Airy function with an exponential tail that extends into the energy gap. As a result, photon-assisted tunneling through a distance that depends on the field strength can happen also for photon energies below the gap (*22*). When the static field is replaced by a time-dependent one, the response of the system is described by the dynamical Franz-Keldysh effect (DFKE) (*23*). In addition to the absorption within the band gap, one observes also an induced transparency above the band gap and the appearance of optical side bands (*18*). In contrast to resonant processes, the DFKE is an ultrafast nonresonant process in which no real carriers are created. It is therefore expected to be fast (*24*). To date, the DFKE has been observed only around the energy gap of dielectrics (*25*) and in the terahertz regime (i.e., picosecond time scales) where recent time-resolved studies have shown a nontrivial phase evolution (*23*). The observation of the DFKE at higher frequencies (i.e., femtosecond time scales) requires higher pump field strengths. At these field intensities, other effects such as multiphoton ionization will dominate the optical response of dielectrics around the band gap. The DFKE is expected to remain observable, but deeper in the conduction band (CB) at higher probing energies.

We used attosecond pulses with duration of ~250 as, centered at ~42 eV, to study field effects such as the DFKE in the high-energy part of the CB of polycrystalline diamond when exposed to a few-femtosecond intense infrared (IR) laser field (IR intensity in vacuum $I_{IR} \approx 1 \times 10^{12}$ W/cm^2). The transient absorption coefficient exhibits sub-femtosecond dynamics with a complex energy-dependent phase relation. Ab initio calculations performed by coupling time-dependent density functional theory (TDDFT) in real time with Maxwell's equations reproduce the experimental results. We used an orbital decomposition approach to disentangle the complexity of the numerical model and address independently the contribution of each electronic subband. With this approach, we can demonstrate that predominantly one valence band (VB) to CB transition determines the qualitative behavior of the optical response of diamond in the energy range under examination.

Figure 1A shows a schematic of the experimental setup (*26*, *27*). Extreme ultraviolet (XUV) single attosecond pulses and 5-fs phase-locked IR pulses (center energy $\hbar\omega_0 \approx 1.58$ eV) are focused on a double target composed of a gas jet and a solid sample. Both pulses are linearly polarized along the same axis. The few-cycle IR pulse acts as a pump, inducing dynamics that are then probed by the XUV pulse. The temporal properties of the pump and probe pulses are recorded simultaneously with the diamond transient absorption scan by acquiring a streaking trace from Ne atoms in a scheme similar to the one reported in (*11*) (Fig. 1B). In this way it is possible to unambiguously calibrate the pump-probe delay axis with respect to the pump electric field. The spectrum of the single attosecond pulses (SAPs) (Fig. 1C, black) spans from 30 to 55 eV and overlaps with the static absorbance for a 50-nm-thick polycrystalline diamond sample (Fig. 1C, blue). The smooth behavior of the absorbance reflects the absence of sharp resonant transitions in this spectral range. The XUV pulse can only excite electrons from the VB to the high part of the CB by single-photon absorption (Fig. 1, D and E). At our experimental intensities, the IR field is also expected to inject electrons into the CB by multiphoton ionization as suggested by a Keldysh parameter, $\gamma_K \approx 3$ (*27*, *28*). However, the IR pulse can efficiently inject electrons only from the top of the VB to the bottom of the CB. Therefore, even if the IR pulse populates the CB almost 1000 times as efficiently as the attosecond pulse, the contribution coming from direct charge injection by the IR pump pulse in the spectral region of the CB probed by the XUV pulse is negligible.

We investigated the dynamical optical response of the VB and CB of diamond by looking at the IR-induced absorbance, $\Delta Abs(E_{ph}, \tau)$, defined as the logarithm of the ratio of the transmitted XUV spectral intensities without and with the IR pump (*27*). Here, E_{ph} represents the XUV photon energy and τ the pump-probe delay. The experimental results for an IR intensity (in vacuum) of ~6.5×10^{12} W/cm^2 are shown in Fig. 2A. For small values of the delay τ, we observe the appearance of transient features that oscillate with $2\omega_0$ over almost all the bandwidth of the SAP. The main feature lies at an excitation energy of ~43 eV and corresponds to an absorption increment. Figure 2C shows the IR electric field $E_{IR}(t)$ extracted from a simultaneous streaking measurement together with the IR-induced absorbance averaged over three energy bands 2 eV wide and centered at 39, 43, and 48 eV. As can be observed, both the

[1]Department of Physics, ETH Zürich, 8093 Zürich, Switzerland. [2]Center for Computational Sciences, University of Tsukuba, 305-8577 Tsukuba, Japan. [3]Photon Science Center, University of Tokyo, 113-8656 Tokyo, Japan. [4]Institute of Applied Physics, University of Bern, 3012 Bern, Switzerland.
*Corresponding author. Email: mlucchini@phys.ethz.ch

Downloaded from http://science.sciencemag.org/ on September 3, 2016

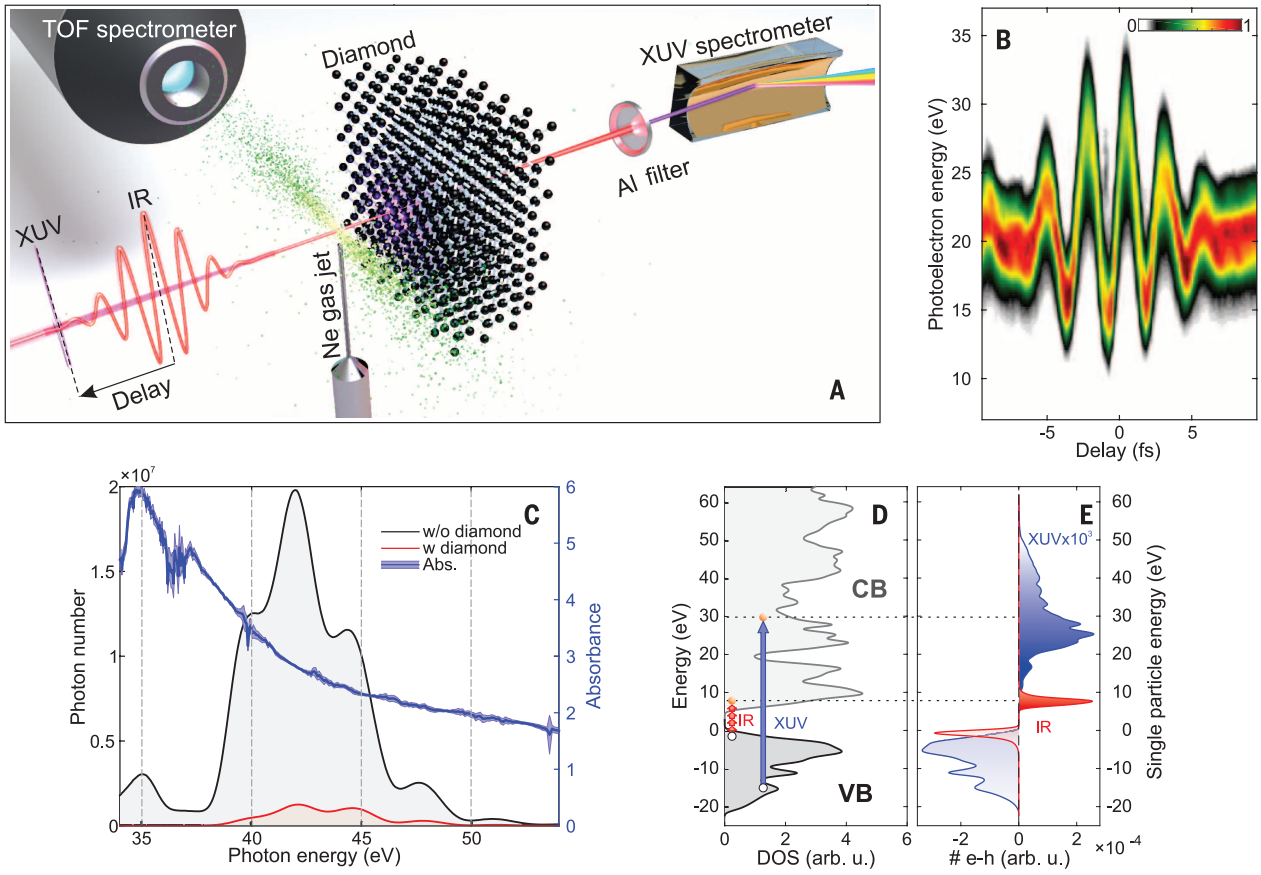

Fig. 1. Pulse and sample characterization. (**A**) Schematic of the experimental setup with the double-target for simultaneous detection of photons and electrons. (**B**) Example of a typical streaking trace used to characterize the single attosecond pulses (SAPs) and calibrate the pump-probe delay axis in a transient absorption measurement. (**C**) Spectrum of the SAP without (black line) and with (red line) transmission through a 50-nm polycrystalline diamond sample. The static absorbance measured with a broad harmonic spectrum (*27*) is shown in blue. The shaded light-blue area defines the statistical error bars assuming a Poisson distribution for the number of collected photons. (**D**) Density of states (DOS) of diamond calculated with density functional theory. The black and gray curves are the valence band (VB) and conduction band (CB), respectively. The zero of the energy axis coincides with top of the VB. (**E**) Number of electron-hole particles created by the XUV probe and the IR pump in blue and red, respectively.

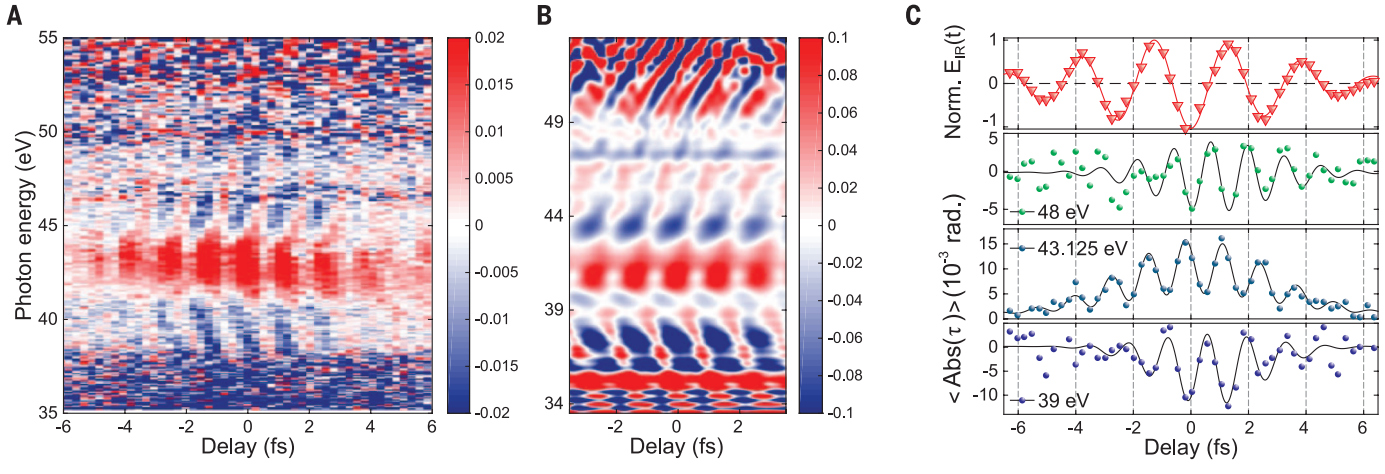

Fig. 2. Results obtained with single attosecond pulses. (**A** and **B**) Experimental (A) and calculated (B) IR-induced absorbance $\Delta Abs(E_{ph}, \tau)$. (**C**) Upper panel: IR electric field $E_{IR}(t)$ extracted from a streaking measurement acquired simultaneously with the trace in (A). Lower panels, from bottom to top: Average ΔAbs for three energy bands with a width of ~2 eV and centered at 39, 43.1, and 48 eV. In all panels, the markers represent the experimental data. The continuous lines are obtained by fitting the data with an oscillating function $f(\tau)$ (*27*). Calculation parameters: IR intensity in vacuum $I_{IR} = 5 \times 10^{12}$ W/cm^2, IR center energy $\hbar\omega_0 = 1.55$ eV, diamond thickness $L = 50$ nm.

Downloaded from http://science.sciencemag.org/ on September 3, 2016

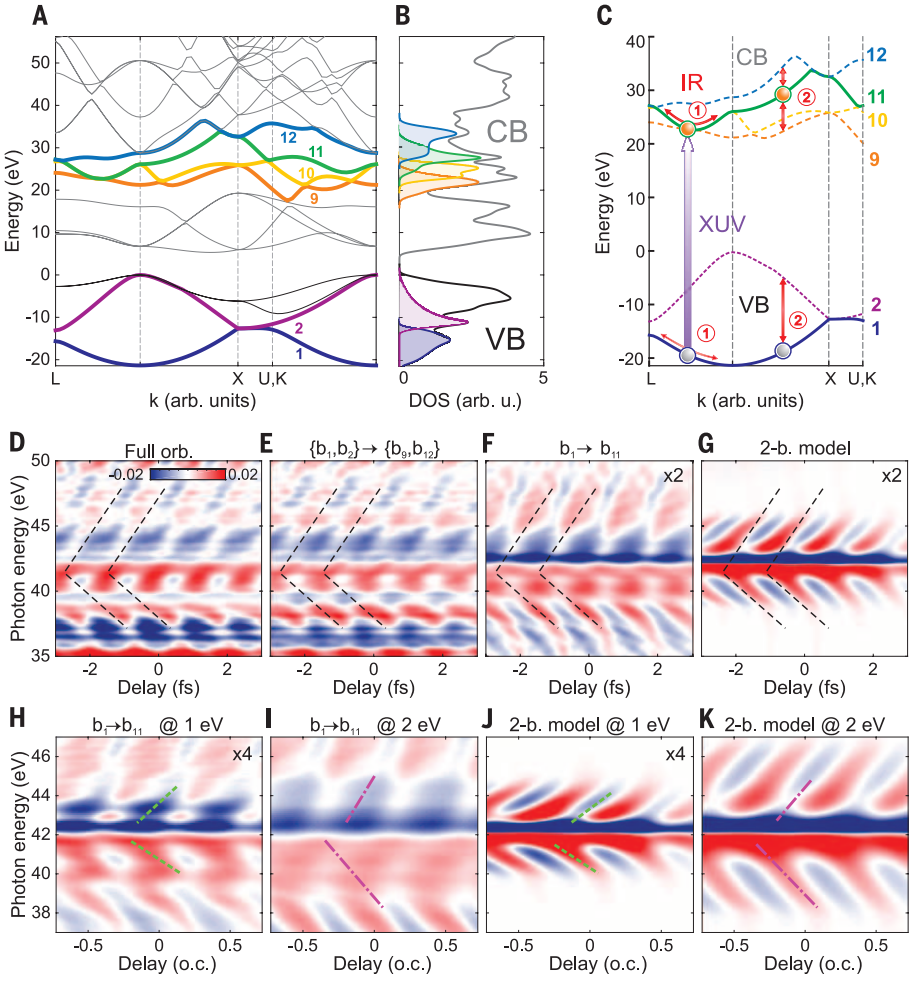

Fig. 3. Simulation results. (**A** and **B**) Diamond band structure and DOS, respectively. The main subbands dominating the diamond optical response are labeled with numbers and highlighted by a thicker colored line in (A); the same color code is used to mark the DOS of each subband in (B). (**C**) Cartoon of the two main physical mechanisms induced by the IR pump: (1) intraband motion, (2) interband coupling. (**D** to **G**) The 2D color plots show the calculated IR-induced changes in the imaginary part of the dielectric function $\varepsilon(\omega)$. The first row reports the results for the case of (D) full orbital expansion over the chosen 24 Houston states, (E) transitions between the bands highlighted in (A), (F) transition from b_1 to b_{11}, and (G) the two-band model. In all panels, the IR intensity inside the diamond is fixed to 3×10^{12} W/cm^2 (*27*). (**H** and **I**) The same results as (F), keeping the same adiabaticity parameter γ_a (*32*), but for a different IR center energy $\hbar\omega_0 = 1$ and 2 eV, respectively. (**J** and **K**) Same as (H) and (I) but obtained with the two-band model of (G).

position of the maximum of the interaction and the phase of the oscillations increase with increasing energy distance from the main feature at 43 eV. Therefore, the energy dispersion of the oscillating features assumes a V-shape with vertex at 43 eV, which does not follow the pump field adiabatically. The phase delay, extracted from eight independent measurements, between the square of the IR electric field $E^2_{IR}(t)$ and the main feature at 43 eV was found to be −235 ± 53 as.

We simulated the pump-probe experiment using TDDFT in real time (*29*, *30*). The results obtained for a single-crystal cell show that the IR pulse can indeed induce $2\omega_0$ oscillations in the imaginary part of the transient dielectric function $\varepsilon(\omega)$ and consequently in the absorbance of the material (*27*). Moreover, whereas the amplitude of the oscillations depends on the crystal orientation with respect to the light polarization axis, the phase does not change (fig. S8). This phenomenon explains why it is possible to experimentally observe the transient features in a polycrystalline sample. By coupling TDDFT with Maxwell's equations, it is possible to investigate the optical response of the target (*27*). The numerical results (Fig. 2B) show very good agreement with the experimental results. Both the oscillatory features and the V-shaped energy dispersion are reproduced. All the features in the calculations appear shifted down by almost 1.75 eV in photon energy (the main absorption feature lying at ~41 eV instead of 43 eV) because TDDFT fails to reproduce the energy gaps between the subbands in the CB with high accuracy.

To gain further insight into the physical mechanisms involved, we performed an orbital decomposition of the probe Hamiltonian into 24 Houston states (*31*), which, when the external IR field vanishes, correspond to the Bloch states depicted in the energy/momentum space of Fig. 3A (*27*). Figure 3, D and E, shows the pump-induced change in the dielectric function, $\Delta\varepsilon(\omega, \tau)$, under the same conditions as Fig. 2B except for a single unit cell of diamond (*27*). The main positive oscillating feature at ~41 eV and the V-shaped energy dispersion of the oscillations are still reproduced even when a smaller set of dressed subbands is taken into account, such as two subbands in the VB (b_1, b_2) and four in the CB (from b_9 to b_{12}). This result is in agreement with the decomposition of the static dielectric function $\varepsilon(\omega)$ (fig. S9). Furthermore, the main qualitative behavior of $\Delta\varepsilon(\omega, \tau)$ can be reproduced by the single transition between the bottom of the VB, b_1, and the seventh band in the CB, b_{11} (Fig. 3F). Given the definition of the Houston states used in the decomposition, this result suggests that IR-induced intraband motion, rather than interband transitions (Fig. 3C), is the main physical mechanism dominating the diamond response. To further validate our finding, we calculated $\Delta\varepsilon(\omega, \tau)$ using a parabolic two-band model employed in the DFKE (*32*). It is derived by parabolic fitting of the energy distance between b_1 and b_{11} in the crystallographic direction WL. The results (Fig. 3G) reproduce the main qualitative behavior of the TDDFT calculations in Fig. 3F. The main differences between the two models may come from the fact that the two-band model takes into account neither the anisotropy of diamond nor the anharmonic dispersion of its actual electronic bands. The complex dispersion of bands b_1 and b_{11} indeed suggests that more than a single parabolic fit might be needed to better describe the case of polycrystalline diamond with random orientation (fig. S12).

Finally, we investigated the dependence of $\Delta\varepsilon(\omega, \tau)$ on the IR frequency. The results are plotted in Fig. 3, H to K, for $\hbar\omega_0$ = 1 and 2 eV. The TDDFT calculations show a clear dependence of the tilt of the oscillating structures as a function of ω_0 (compare green dashed and violet dash-dotted lines in Fig. 3, H and I). This behavior is well reproduced by the two-band model, thus confirming the dominant role of the DFKE or, in other words, intraband transitions.

Our results demonstrate that attosecond transient absorption spectroscopy can be used to directly investigate the ultrafast electron dynamics in the valence and conduction bands of dielectrics in the intermediate regime of strong optical fields. For the particular case of diamond, the observed dynamics unfold on an attosecond time scale and fully recover after the interaction. A comparison with ab initio calculations and a parabolic two-band model allowed us to demonstrate the dominant role of intra- over intersubband transitions, thus moving another step toward a full understanding of optical manipulation of carriers in dielectrics in the petahertz regime. The field strength necessary to observe DFKE in the femtosecond regime is sufficient to inject a substantial number of electrons into the bottom of the CB via multiphoton excitation. Therefore, direct probing of the DFKE

Downloaded from http://science.sciencemag.org/ on September 3, 2016

around at the bottom of the CB with mid-IR or terahertz driving fields is impossible (*23*, *24*). Our results, however, prove that it is possible to observe the DFKE driven by femtosecond IR pulses at energies high above the band gap. We have also shown that the fine structure in the transient response of diamond deviates from the simplified parabolic model and thus encodes information about the particular band dispersion of the target.

REFERENCES AND NOTES

1. D. H. Auston, K. P. Cheung, J. A. Valdmanis, P. R. Smith, *Picosecond Electronics and Optoelectronics* (Springer-Verlag, 1985).
2. D. H. Auston, *Top. Appl. Phys.* **60**, 183 (1988).
3. D. Grischkowsky, S. Keiding, M. van Exter, C. Fattinger, *J. Opt. Soc. Am. B* **7**, 2006 (1990).
4. G. Steinmeyer, D. H. Sutter, L. Gallmann, N. Matuschek, U. Keller, *Science* **286**, 1507–1512 (1999).
5. P. M. Paul *et al.*, *Science* **292**, 1689–1692 (2001).
6. M. Hentschel *et al.*, *Nature* **414**, 509–513 (2001).
7. H. Telle *et al.*, *Appl. Phys. B* **69**, 327–332 (1999).
8. E. Goulielmakis *et al.*, *Nature* **466**, 739–743 (2010).
9. H. Wang *et al.*, *Phys. Rev. Lett.* **105**, 143002 (2010).
10. M. Holler, F. Schapper, L. Gallmann, U. Keller, *Phys. Rev. Lett.* **106**, 123601 (2011).
11. M. Schultze *et al.*, *Nature* **493**, 75–78 (2013).
12. M. Schultze *et al.*, *Science* **346**, 1348–1352 (2014).
13. H. Mashiko, K. Oguri, T. Yamaguchi, A. Suda, H. Gotoh, *Nat. Phys.* 10.1038/nphys3711 (2016).
14. F. Krausz, M. I. Stockman, *Nat. Photonics* **8**, 205–213 (2014).
15. H. J. Caulfield, S. Dolev, *Nat. Photonics* **4**, 261–263 (2010).
16. A. H. Chin, J. M. Bakker, J. Kono, *Phys. Rev. Lett.* **85**, 3293–3296 (2000).
17. Y. Mizumoto, Y. Kayanuma, A. Srivastava, J. Kono, A. H. Chin, *Phys. Rev. B* **74**, 045216 (2006).
18. A. P. Jauho, K. Johnsen, *Phys. Rev. Lett.* **76**, 4576–4579 (1996).
19. G. H. Wannier, *Elements of Solid State Theory* (Cambridge Univ. Press, 1960).
20. G. Vampa *et al.*, *Nature* **522**, 462–464 (2015).
21. T. T. Luu *et al.*, *Nature* **521**, 498–502 (2015).
22. P. Y. Yu, M. Cardona, *Fundamentals of Semiconductors* (Springer, ed. 4, 2010).
23. F. Novelli, D. Fausti, F. Giusti, F. Parmigiani, M. Hoffmann, *Sci. Rep.* **3**, 1227 (2013).
24. A. Srivastava, R. Srivastava, J. Wang, J. Kono, *Phys. Rev. Lett.* **93**, 157401 (2004).
25. K. B. Nordstrom *et al.*, *Phys. Rev. Lett.* **81**, 457–460 (1998).
26. R. Locher *et al.*, *Rev. Sci. Instrum.* **85**, 013113 (2014).
27. See supplementary materials on *Science* Online.
28. L. V. Keldysh, *Sov. Phys. J. Exp. Theor. Phys.* **20**, 1307 (1965).
29. S. A. Sato, K. Yabana, Y. Shinohara, T. Otobe, G. F. Bertsch, *Phys. Rev. B* **89**, 064304 (2014).
30. K. Yabana, T. Sugiyama, Y. Shinohara, T. Otobe, G. F. Bertsch, *Phys. Rev. B* **85**, 045134 (2012).
31. W. V. Houston, *Phys. Rev.* **57**, 184–186 (1940).
32. T. Otobe, Y. Shinohara, S. A. Sato, K. Yabana, *Phys. Rev. B* **93**, 045124 (2016).

ACKNOWLEDGMENTS

Supported by the National Center of Competence in Research Molecular Ultrafast Science and Technology (NCCR MUST) funded by the Swiss National Science Foundation, and by JSPS KAKENHI grants 15H03674 and 26-1511. This research used computational resources of the K computer provided by RIKEN AICS through the HPCI System Research project (Project ID hp150101), and was supported in part by MEXT as a priority issue theme 7 to be tackled by using Post K Computer.

SUPPLEMENTARY MATERIALS

www.sciencemag.org/content/353/6302/916/suppl/DC1
Materials and Methods
Figs. S1 to S13
References (*33*–*45*)

12 May 2016; accepted 27 July 2016
10.1126/science.aag1268

GEOPHYSICS

Teleseismic *S* wave microseisms

Kiwamu Nishida[1]* and Ryota Takagi[2]

Although observations of microseisms excited by ocean swells were firmly established in the 1940s, the source locations remain difficult to track. Delineation of the source locations and energy partition of the seismic wave components are key to understanding the excitation mechanisms. Using a seismic array in Japan, we observed both *P* and *S* wave microseisms excited by a severe distant storm in the Atlantic Ocean. Although nonlinear forcing of an ocean swell with a one-dimensional Earth model can explain *P* waves and vertically polarized *S* waves (*SV* waves), it cannot explain horizontally polarized *S* waves (*SH* waves). The precise source locations may provide a new catalog for exploring Earth's interior.

Microseisms are ambient seismic wavefields (*1*) that occur in the 0.05- to 0.5-Hz frequency range. Although they had been recognized as ambient noise for seismic observation, a new technique known as seismic interferometry turned them into signals for exploring Earth's interior (*2*). They can be categorized into two groups according to the typical frequencies. The first group is classified as primary microseisms ranging from 0.05 to 0.1 Hz, which corresponds to the typical frequency of ocean swells. The second is classified as secondary microseisms ranging from 0.1 to 0.5 Hz, which doubles the frequency of an ocean swell, indicating that the secondary microseisms are generated through nonlinear wave-wave interactions (*3*, *4*). They excite surface waves dominantly.

P wave microseisms from distant storms have been studied (*5*, *6*) by means of array analysis of dense seismic data. Source locations of the *P* wave provided a better spatial localization of the excitation source than that of surface waves. The estimated source distribution was consistent with a theoretical estimation that uses wave action models. Most studies, however, have focused only on *P* waves recorded as vertical components because of the larger amplitudes. Although *S* wave amplitudes are estimated to be one order of magnitude smaller than *P* wave amplitudes (*7*, *8*), the precise locations of *P* and *S* waves can help in understanding the excitation mechanism.

The energy partition between Love and Rayleigh waves is another key parameter for understanding the force system of excitation sources. The force system can be characterized by the surface pressure source and/or shear traction on the seafloor (*9*). The observed dominance of Love waves in primary microseisms suggests that they are generated by pressure loadings of an ocean swell acting on a sloping coast (*10*). However, the scattering of surface waves during propagation distorts the energy ratio at the source area. Because the teleseismic body waves are less scattered, the energy partition between *P* and *S* waves is more appropriate for understanding the source mechanism. However, the smaller body-wave amplitudes at a distance tend to be masked by the surface waves owing to local ocean swell activities (*8*, *11*, *12*).

For the detection of both *P* and *S* wave microseisms, we conducted an array analysis using 202 Hi-net stations operated by the National Research Institute for Earth Science and Disaster Prevention (NIED) in Chugoku district, where the crustal heterogeneity is weak in Japan (Fig. 1A). NIED deployed three-component velocity meters with a natural frequency of 1 Hz at the bottom of a borehole of each station. We deconvolved the instrumental response using the inverse filtering technique (*13*) after the reduction of common logger noise (*14*) so as to use low-frequency components below 1 Hz. We analyzed data of a rapidly deepening cyclonic low-pressure area known as a "weather bomb" (*15*), with a central pressure of ~940 hPa that developed in the Atlantic between Iceland and Greenland on 9–11 December 2014 (*16*). The system was a typical explosive cyclogenesis, with a reduction of 24 hPa in 24 hours on 9 December. We divided the records into 1024-s segments. After the exclusion of noisy data, we calculated two-dimensional (2D) frequency-slowness spectra (*9*) in the 0.1- to 0.2-Hz frequency window (Fig. 1B), assuming that signals at a station can be represented by a superposition of plane waves. The spectrum at a certain slowness vector represents the sum of all the records, with the predicted time delays. The spectra have local maxima in the slowness domain, where signals recorded at all the stations are in phase.

The spectra of the vertical and radial components displayed a clear teleseismic *P* wave. The slowness of ~0.05 s/km and the back azimuth of −5° were consistent with that of a *P* wave traveled from the Atlantic Ocean. The dominant *P* wave can be explained by the nonlinear forcing by ocean swell (*7*) according to Longuet-Higgins's theory (*3*), which can be equivalently represented by a vertical single force on the sea surface.

The spectrum of the radial component showed not only a *P* wave but also a rarely seen *SV* wave (*8*), with mean square (MS) amplitude of ~8% of the *P* wave amplitude. The observed slowness of the *SV* wave suggests that the source could be located in the same area of the *P* wave microseisms in the Atlantic Ocean. The simplest mechanism of the observed *S* wave excitation is the *P*-to-*SV* conversion on the sea bottom during multiple reflections within the ocean (*7*). Although the theoretical MS amplitude (*7*) of an *SV* wave is two orders smaller than

[1]Earthquake Research Institute, University of Tokyo, 1-1-1 Yayoi 1, Bunkyo-ku, Tokyo 113-0032, Japan. [2]Research Center for Prediction of Earthquakes and Volcanic Eruptions, Graduate School of Science, Tohoku University, 6-6 Aza-Aoba, Aramaki, Aoba-ku, Sendai 980-8578, Japan.
*Corresponding author. E-mail: knishida@eri.u-tokyo.ac.jp

Downloaded from http://science.sciencemag.org/ on September 3, 2016

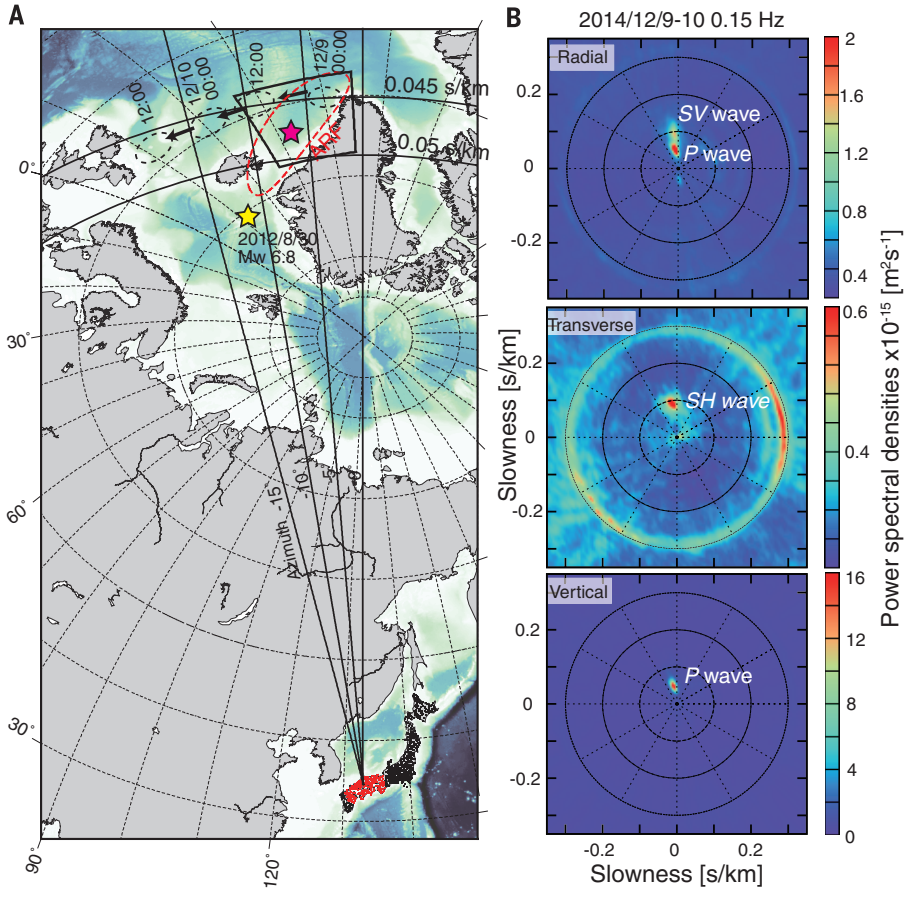

Fig. 1. Rough source location estimated by back-projection of the observed body-wave microseisms. (**A**) Station distribution and location of the weather bomb. Red points in Japan indicate the station locations used in the slowness-frequency analysis. Black and red dots indicate all the Hi-net station locations. The red dashed line represents 0.5 of the array response function for a point source at (−32.5, 63), indicated with the red star. The trapezoid region indicates the area shown in Fig. 2A. The location of the earthquake is indicated by the yellow star. (**B**) Frequency-slowness spectra of radial, transverse, and vertical components at 0.15 Hz. This figure shows the *P* wave traveling from the north direction with back azimuth of ~−7°. The slowness is ~0.048 s/km, which determined the distance between the source and the receivers as shown in (A).

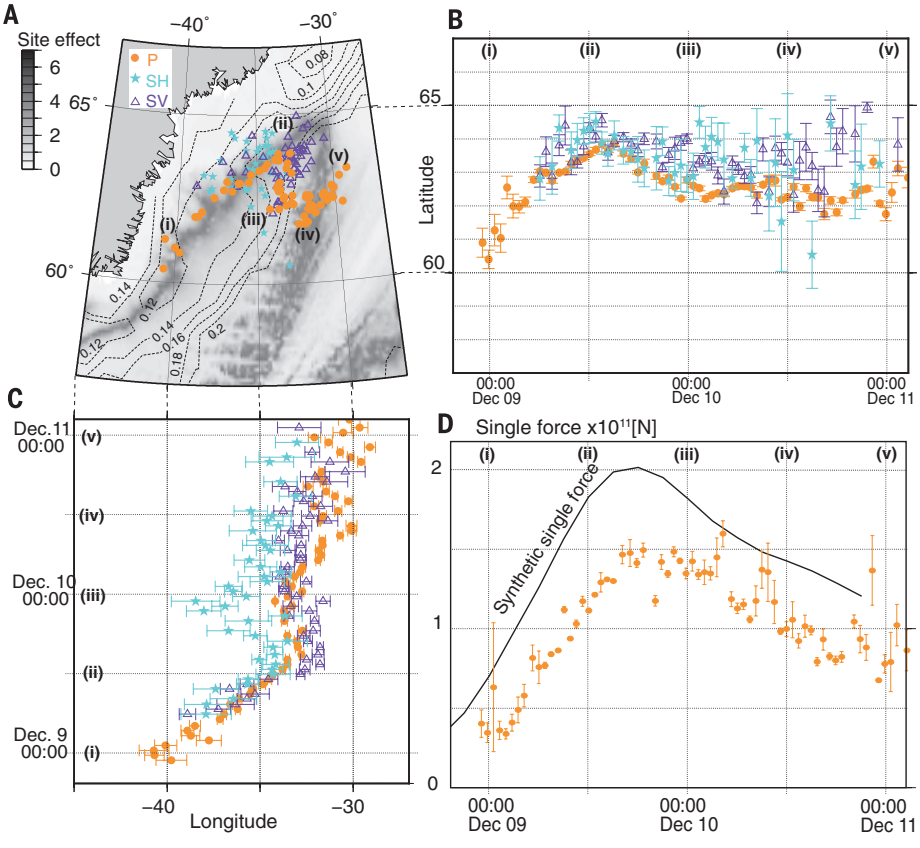

Fig. 2. Migration of precise centroid locations of *P*, *SV*, and *SH* waves. (**A**) Locations of the centroids with errors <1.5° in latitude and longitude. The error was estimated with the bootstrap method (*23*). Orange dots indicate the centroids of the *P* wave microseisms. Purple triangles indicate the *SV* waves. Blue stars indicate the *SH* wave. The background image shows the site effect of the ocean layer, whereas the contours show the resonant frequency of the sediment. The resonant frequency was estimated by means of a four-way travel time of multiple reflection of sediment-derived *S* waves in the vertical direction. (i) through (v) represent time labels every 12 hours, as shown in (B). (**B**) Latitude of centroids of *P*, *SH*, and *SV* waves with respect to time. (**C**) Longitude of the centroids with respect to time. This figure shows that source locations of *SH* wave at 0 hours on 10 December were west of the others. (**D**) Temporal variations of RMS amplitudes of the single force. The black line shows a synthetic vertical single force (*20*).

Downloaded from http://science.sciencemag.org/ on September 3, 2016

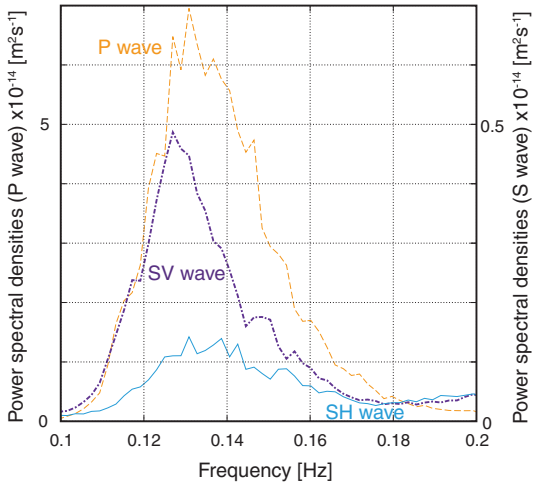

Fig. 3. Stacked power spectra of *P*, *SV*, and *SH* waves. Orange dashed line, *P* wave; purple dash-dotted line, *SV* wave; blue line, *SH* wave. They are power spectra of the seismograms of vertical (*P* wave), radial (*SV* wave), and transverse components (*SH* wave), with shift in time according to the corresponding travel times for the located centroids from 9 to 11 December 2014. The power spectral densities of the *SV* waves were 8% of the *P* wave. The *SH* waves consisted of one third of those for the *SV* waves. The peak frequencies of *P*, *SV*, and *SH* waves were ~0.13 Hz.

that of a *P* wave, the amplitude depends strongly on the incident angle. Within the possible range on the basis of different 1D seismic velocity models, our observation is consistent with the prediction.

Surprisingly, the spectrum of the transverse component also showed an *SH* wave microseism. A pressure source in the ocean cannot excite the *SH* waves in a spherically stratified Earth. Therefore, the shear traction acting on the sea-bottom horizon is required. This observation suggests that the steep topography beneath the source and thick sediments may affect the excitation. The smaller recorded amplitude of ~3% of the *P* wave MS amplitude suggests that this effect is secondary.

We inferred the centroid locations of *P* wave microseisms with a method that is similar to the GRiD MT (grid-based real-time determination of moment tensors) technique (*17*). We modeled the localized excitation source by approximating the source using a vertical single force at a surface point. We characterized the source by the centroid location and the root mean square (RMS) amplitude of the single force. We justify the point source approximation as the localized source area was on the order of 10^5 km^2, which we estimated by using the wave model WAVEWATCH III (fig. S1) (*18*, *19*) and which is smaller than the array response function (Fig. 1A). At an assumed grid point, we estimated RMS of the vertical single force by modeling the seismic wave fields using a ray-theory *P* wave Green's function (*20*) for a 1D Earth model (*21*). The variance reductions between the modeled wave field and the observations were calculated at assumed grid points every 0.1° by 0.1° in longitude and latitude. The maximum was selected as the centroid location for the vertical single force. We subtracted the station correction terms using a multichannel cross-correlation method (*22*) with an earthquake that occurred close to Iceland on 30 August 2012 (Fig. 1A) because 3D seismic structure biases the locations of the centroids. Without the station corrections, the centroid of the earthquake located by this method deviated ~300 km away from the original location. Orange dots in Fig. 2A represent the locations of the centroids inferred from the vertical components at 775 stations. RMSs of the centroid single force were on the order of 10^{11} N (Fig. 2D). They were consistent with the theoretical estimation of the wave model (fig. S2) and a previous study (*12*). The inferred centroid locations were consistent with a theoretical model (fig. S1). The centroids migrated along an area that contains a strong site effect (*7*) of the ocean layer. This can be described as the constructive interference of multiply reflected *P* waves in the ocean that are converted to *P* and *SV* waves at the sea bottom (*7*). The site effect becomes larger where the resonance frequency of the oceanic layer matches the *P* wave frequency. From time period (i) to (ii) shown in Fig. 2A, the centroids migrated along the strong site effect area. From (ii) to (iv), they were not in the area. From (iv) to (v), they migrated along the area again. We can explain this observation from (ii) to (iv) by the larger source area (fig. S1), including both the part from (i) to (ii) and that from (iv) to (v) in Fig. 2A with the strong site effects. This method determined the centroids of the distributed sources with weighting by the site effects.

We located centroids of the *SH* and *SV* waves by back-projecting the seismograms in the horizontal components with the station corrections (*24*). We did not estimate the equivalent single force because modeling is not practical, owing to the near source amplification from multiple reflections in the ocean and sedimentary layers. The centroid locations of the *SH* and *SV* waves are shown with a resonant frequency of the sediment (Fig. 2A) (*20*) that corresponds to the fundamental mode in a closed pipe system, based on CRUST1.0 (*25*). Our centroid locations of the *SV* waves were close to the *P* wave centroids. However, our centroid locations of the *SH* waves were to the west [in particular at around (iii), as shown in Fig. 2C], where the sediments have lower resonant frequencies closer to the *SH* wave frequency, as we observed (Fig. 2B). Our observation suggests *SH* waves trapped in the sedimentary layer. Moreover, the peak frequency of the *SH* wave at 0.13 Hz was similar to those of the *P* and *SV* waves (Fig. 3). We suggested the transfer of a large part of the *SV* wave energy into the sediments from the *P* wave to explain the frequency overlap, in which the sedimentary resonant frequency matched the dominant frequency of the *P* wave microseisms. During multiple reflections of the *SV* wave in the sediment, the polarization information was lost, and part of the *SV* wave energy was converted to the *SH* wave over time (*20*).

Body-wave microseisms provide information about Earth's deep interior beneath the stations via seismic interferometry (*26*), which extracts seismic-wave propagation between station pairs. We have characterized the excitation source by a centroid vertical single force (*3*, *4*, *7*). Hence, the seismic structure beneath a storm can be explored by using body-wave microseisms. Because the estimated vertical single force is consistent with a former study (*12*), we can expect similar potential events with amplitude on the order of 10^{11} N. A collection of precise locations of the centroid single force may provide a catalog for exploring Earth's interior. Such a catalog may open a different perspective from which to explore Earth's deep interior beneath a storm in the absence of seismic stations and earthquakes.

REFERENCES AND NOTES

1. B. Gutenberg, *J. Atmos. Sci.* **4**, 21 (1947).
2. R. Snieder, E. Larose, *Annu. Rev. Earth Planet. Sci.* **41**, 183–206 (2013).
3. M. S. Longuet-Higgins, *Phil. Trans. Roy. Soc. A* **243**, 1–35 (1950).
4. S. Kedar *et al.*, *Proc. R. Soc. London Ser. A* **464**, 777–793 (2008).
5. P. Gerstoft, M. C. Fehler, K. G. Sabra, *Geophys. Res. Lett.* **33**, L17308 (2006).
6. M. Landès, F. Hubans, N. M. Shapiro, A. Paul, M. Campillo, *J. Geophys. Res.* **115** (B5), B05302 (2010).
7. L. Gualtieri *et al.*, *Geophys. J. Int.* **197**, 1096–1106 (2014).
8. Q. Liu *et al.*, *Earth Planet. Sci. Lett.* **449**, 39–47 (2016).
9. K. Nishida, H. Kawakatsu, Y. Fukao, K. Obara, *Geophys. Res. Lett.* **35**, L16307 (2008).
10. F. Ardhuin, L. Gualtieri, E. Stutzmann, *Geophys. Res. Lett.* **42**, 765–772 (2015).
11. M. N. Toksöz, R. T. Lacoss, *Science* **159**, 872–873 (1968).
12. L. Vinnik, *Pure Appl. Geophys.* **103**, 282–289 (1973).
13. T. Maeda, K. Obara, T. Furumura, T. Saito, *J. Geophys. Res.* **116** (B10), B10303 (2011).
14. R. Takagi *et al.*, *Seismol. Res. Lett.* **86**, 901–907 (2015).
15. T. Matsuzawa, K. Obara, T. Maeda, Y. Asano, T. Saito, *Bull. Seismol. Soc. Am.* **102**, 1864–1871 (2012).
16. *Weather* **70**, 54 (2015).
17. H. Kawakatsu, *Bull. Earth. Res. Inst.* **73**, 267–274 (1998).
18. H. L. Tolman, *Ocean Model.* **25**, 35–47 (2008).
19. F. Ardhuin, E. Stutzmann, M. Schimmel, A. Mangeney, *J. Geophys. Res.* **116** (C9), 1–21 (2011).
20. Materials and methods are available as supplementary materials on *Science* Online.
21. B. L. N. Kennett, E. R. Engdahl, R. Buland, *Geophys. J. Int.* **122**, 108–124 (1995).
22. J. VanDecar, R. S. Crosson, B. Y. J. C. Vandecar, R. S. Crosson, *Bull. Seismol. Soc. Am.* **80**, 150–169 (1990).
23. B. Efron, *Ann. Stat.* **7**, 1–26 (1979).
24. M. Ishii, P. M. Shearer, H. Houston, J. E. Vidale, *Nature* **435**, 933–936 (2005).
25. G. Laske, G. Masters, Z. Ma, M. Pasyanos, Update on CRUST1.0—A 1-degree Global Model of Earth's Crust, *EGU General Assembly Conference Abstracts* (2013), vol. 15 of *EGU General Assembly Conference Abstracts*, pp. EGU2013–EGU2658.
26. P. Poli, M. Campillo, H. Pedersen, LAPNET Working Group, *Science* **338**, 1063–1065 (2012).

ACKNOWLEDGMENTS

We thank S. Kedar, an anonymous reviewer, and E. Stutzmann for constructive comments. Hi-net seismic records were provided by NIED at www.hinet.bosai.go.jp. This work was supported by Japan Society for the Promotion of Science KAKENHI grants 26400448 and 15J11322.

SUPPLEMENTARY MATERIALS

www.sciencemag.org/content/353/6302/919/suppl/DC1
Materials and Methods
Figs. S1 to S3
References (*27*–*31*)

25 March 2016; accepted 25 July 2016
10.1126/science.aaf7573

Downloaded from http://science.sciencemag.org/ on September 3, 2016

TIME SERIES ANALYSIS

Information leverage in interconnected ecosystems: Overcoming the curse of dimensionality

Hao Ye and George Sugihara*

In ecological analysis, complexity has been regarded as an obstacle to overcome. Here we present a straightforward approach for addressing complexity in dynamic interconnected systems. We show that complexity, in the form of multiple interacting components, can actually be an asset for studying natural systems from temporal data. The central idea is that multidimensional time series enable system dynamics to be reconstructed from multiple viewpoints, and these viewpoints can be combined into a single model. We show how our approach, multiview embedding (MVE), can improve forecasts for simulated ecosystems and a mesocosm experiment. By leveraging complexity, MVE is particularly effective for overcoming the limitations of short and noisy time series and should be highly relevant for many areas of science.

Complex interconnected systems pose a major challenge to scientific study in a variety of fields, including ecology, finance, neuroscience, and medicine (*1*–*4*). Although widely used, the common approach of reducing these systems to linearly independent components overlooks important interactions for the sake of computational tractability. Thus, many statistical frameworks (e.g., principal components analysis, generalized linear models, multivariate autoregressive models) assume that causal factors do not interact with each other and have independent or additive effects on a response variable. This simplification can lead to problems in identifying associations (*5*, *6*) or predicting out-of-sample behavior (*7*). Conversely, complex equation-based models that explicitly account for each interaction [e.g., end-to-end ecosystem models (*8*)] have great intuitive appeal but often have too many parameters to be precisely determined given the available data [the "curse of dimensionality" (*9*)], even assuming that the model structure is generally correct. These issues are particularly acute in biological fields where the relevant units (e.g., species or other variables) may not behave according to fundamental equations (*10*) and where data sets are often cross-sectionally wide (e.g., census many interacting species) but short in the time dimension (*11*, *12*).

One solution to the problem of uncertain model structure and unknown model equations is the framework of empirical dynamic modeling (EDM) (*13*–*15*), which uses attractor manifolds reconstructed from time series data to enable the study of systems [see brief introductory animation http://tinyurl.com/EDM-intro (*5*)]. If system behavior is governed by deterministic rules, then attractor manifolds exist and can be built from lags of a single variable (*16*) or multivariately from combinations of variables (*15*, *17*, *18*). However, because these manifolds are empirical, data limitations can be problematic, especially when time series are short and noisy. For example, with short time series, reconstructed attractors may be sparsely populated, which impedes accurate inference of dynamics from nearest neighbors. Furthermore, observational error will result in reduced precision; even when time series are long enough to densely populate the attractor, the nearest neighbors may not form a smooth map.

Here we introduce multiview embedding (MVE) as a general approach that exploits complexity to amplify information and address these issues. The basic idea is straightforward. In interconnected systems with multiple time series observations, many different variable combinations are possible (*16*–*18*) (Fig. 1A). Each reconstruction created from a particular combination of variables can be thought of as a caricature (view) of the system that contains distinctive information when constrained by finite and noisy data (*19*). For example, Fig. 1B show predictions for a three-species food-chain simulation (*20*) using models built on the same 25-point time interval. Here, predictions are produced from univariate models (views using lags of single variables x, y, or z), and each model view exhibits distinct errors. Even with valid embedding coordinates, 25 points may be too few to fully resolve the system behavior—that is, the manifold may be too sparse, especially with observation error. However, because each view is better at resolving different portions of the system, a more complete model should be possible through combination.

A simple and straightforward implementation to combine multiple views is as follows: In contrast to conventional simplex projection (*13*), where a forecast is based on the weighted average of the nearest neighbors in a single view (Fig. 2A), we examine the top k reconstructions, and use the single nearest neighbor from each (Fig. 2B). The MVE forecast (e.g., for variable y) is then defined as a simple average

$$\hat{y}_{t+1} = \frac{1}{k}\sum_{i=1}^{k} y_{nn^i(t)+1}$$

where $nn^i(t)$ is the time index of the nearest neighbor in the ith attractor. In essence, this approach is intended to mitigate prediction errors that occur when nearest neighbors are misidentified or inaccurately weighted based on distance (e.g., due to finite, noisy data). Instead, each of the k neighbors comes from a different view of the system; thus, each corresponding prediction $[y_{nn^i(t)+1}]$ is effectively weighted by how frequently it appears as a nearest neighbor among the top k reconstructions. This is a more robust indication of its true similarity to the target point. This simple implementation of MVE produces forecasts that are substantially better at covering the full range of system behavior than the individual univariate models (Fig. 1, B and C).

The information leverage of MVE follows from two results on dynamic systems arising from Takens' theorem (*16*): Causal effects are recorded in the time series of affected variables (*5*), and each combination of variables and lags is a valid embedding (*17*, *18*). These two properties mean that the interconnectedness of complex systems is actually a boon: Whenever variable x has an influence on some other variable y, information about x is recorded in y and can be recovered. Because each embedding filters this information in a different way, combining multiple models can be highly advantageous (Fig. 1C)—an advantage that increases as the system becomes more complex. In fact, the number of possible reconstructions grows combinatorially with the number of variables. Given l lags for each of n variables, the number of E-dimensional variable combinations is

$$m = \binom{nl}{E} - \binom{n(l-1)}{E}$$

For a simple system with 10 variables (and up to three lags each), the number of distinct three-dimensional combinations is nearly 3000. Although all variable combinations are valid embeddings, with limited data they will not resolve the system equally well. Therefore, we use only the top k reconstructions, as ranked by in-sample forecast accuracy (ρ, correlation between observations and predictions), and apply the heuristic of $k = \sqrt{m}$ (*21*–*23*).

To quantify performance, we compare the out-of-sample forecast skill of this multimodel approach with standard nonlinear methods: a univariate model using only lags of the variable being forecast and a multivariate model defined by the variable combination with the highest in-sample ρ. Figure 3 shows this comparison for three simple

Scripps Institution of Oceanography, University of California San Diego, 9500 Gilman Drive 0202, La Jolla, CA 92093-0202, USA.
*Corresponding author. Email: gsugihara@ucsd.edu

Downloaded from http://science.sciencemag.org/ on September 3, 2016

ecosystem simulations with 10% observational error [methodological details in (*24*)]: a three-species coupled logistic, a three-species food chain (*20*), and a three-stage flour beetle model (*25*). In nearly all conditions, MVE produces better forecasts (higher ρ) compared with the univariate and multivariate methods. Results were broadly similar when repeated with a more complex 12-species resource competition system (*26*) (figs. S1 and S2).

As a final test, we repeated the analysis using time series data from an 8-year mesocosm experiment of a plankton community isolated from the Baltic Sea (*27*, *28*). This experimental field system exhibits coupled oscillations between predator and prey species, providing a natural experiment for testing MVE. Here, we focus on a subsystem of two predators (rotifers and calanoid copepods) that consume two prey (picocyanobacteria and nanoflagellates) (Fig. 4A). A causality test (*5*) verifies that both prey affect both predators (Fig. 4B), indicating that prey abundances are informative for predicting predator abundances. Just as with the model systems, the multiview approach outperforms the other methods (Fig. 4C). In all cases, other metrics produce qualitatively identical results (figs. S3 to S6).

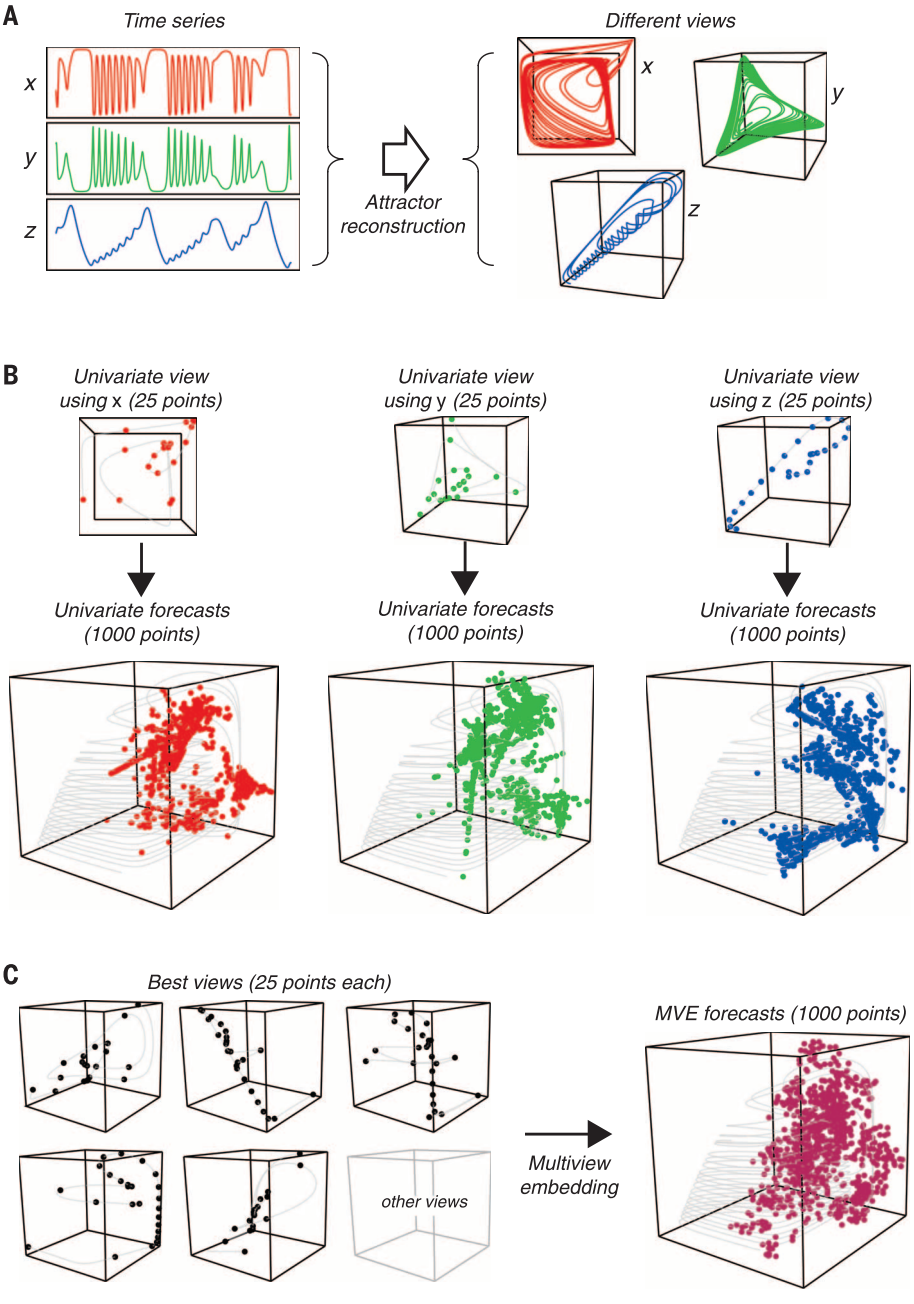

Fig. 1. Schematic for multiview embedding using the three-species food-chain model. (**A**) By combining multiple time series observations of the system, different attractor reconstructions (i.e., views of the system dynamics) are created. Here, the univariate reconstructions using lags of *x* (red), *y* (green), or *z* (blue) are depicted. (**B**) Forecasts based on univariate views of the system (from the same 25 time points of data) give incomplete coverage of the system attractor (gray lines) (*20*). Note that the 1000 predictions (solid points) from each univariate model occupy distinct subsets. (**C**) Combining information from multiple reconstructions [spanning the same 25 time points in (B)], the MVE model gives a clearer depiction of the actual dynamics, resulting in predictions that span more of the original system attractor.

An important concern with any modeling framework is how well it accommodates observational error. For EDM, noise in the data means that reconstructed states of the system are uncertain, affecting all calculations, including the computed distances between states, identification of nearest neighbors, and the final forecast. Depending on the system dynamics and the particular variable combination used for the reconstructed attractor, observational noise can cause large forecast errors (*19*). Our results indicate that as more observational noise is added, forecast skill for all three methods decreases (figs. S7 to S12). However, the use of multiple views in MVE can reduce the effects of noise. Thus, with particularly noisy data, the information advantage of combining multiple views can be more important than selecting a single best model (including the "true" multivariate model composed of the original state variables). This approach to noise reduction builds upon historical approaches in nonlinear state space reconstruction (*19*, *29*) and operates in a way that is fundamentally different from classical frameworks that seek to filter noise by using assumptions about the underlying dynamics and noise structure [e.g., Kalman filters (*30*)].

With longer time series, the single-view multivariate method (using native coordinates) should perform about as well as MVE. With sufficiently long time series, the performance of the two methods is nearly indistinguishable in the absence of observational error (figs. S13 and S14). However, even with small amounts of noise (i.e., 10% added variance), the multivariate approach produces less skillful forecasts than MVE (Fig. 3), suggesting that noise, rather than data length, is the limiting factor. Thus, given the practical constraints of collecting longer time series (true for many natural systems and particularly true for ecosystem studies constrained by short funding horizons), these results show how it can be highly beneficial to combine disparate data sets to leverage signal in synchronous observations.

Nevertheless, it is important that time series be long enough to sufficiently sample the system dynamics. The procedure of selecting the best views can be sensitive to short data segments that are nonrepresentative. For example, the best representation of the system behavior can change over time as dynamics pass through different regimes, such as in our 12-species resource competition model where different groups of species are active at different times (*26*). As a result, with very short temporal data, the multivariate and MVE methods (which rely on in-sample forecast

Downloaded from http://science.sciencemag.org/ on September 3, 2016

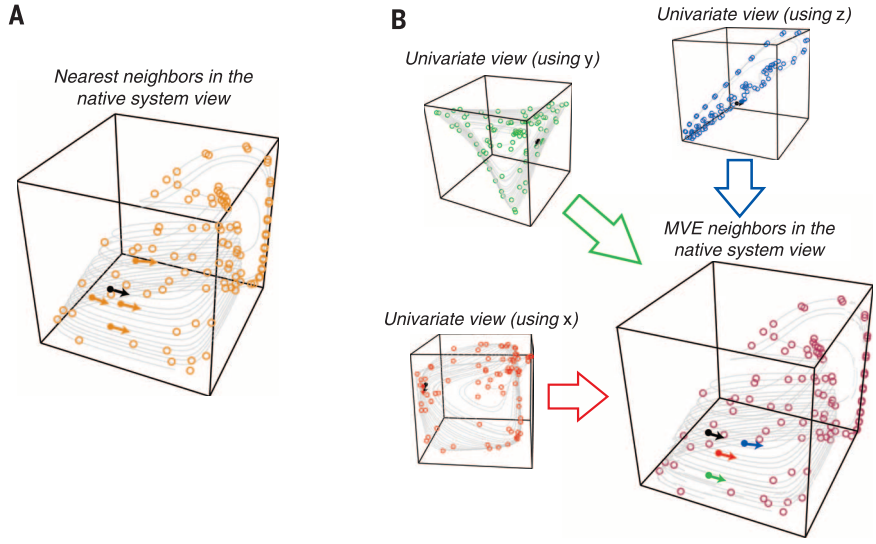

Fig. 2. Nearest-neighbor selection on attractor manifolds. (**A**) In the native system view, the nearest neighbors (solid orange points) to the target point (black) are used to predict the future trajectory. (**B**) MVE selects the single nearest neighbor in each of the different views to produce a more robust model. Here, the nearest neighbors (red, green, and blue) to the target point (black) from the three univariate views (based on lags of *x*, *y*, or *z*, respectively) are used to forecast the future behavior of the target.

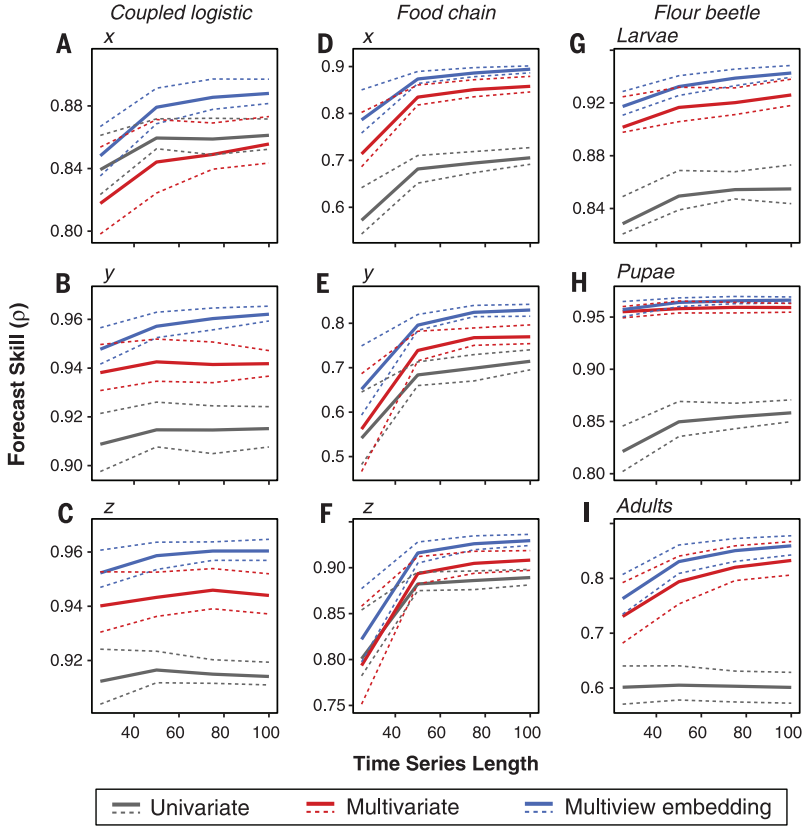

Fig. 3. Comparison of forecast skill for univariate, multivariate, and MVE methods on simulated data with 10% observational error. (**A** to **C**) Forecast skill (ρ, correlation between observations and predictions) versus library size for variables *x*, *y*, and *z* in the three-species coupled logistic. Solid lines indicate average values over 100 randomly sampled libraries; dashed lines denote upper and lower quartiles. (**D** to **F**) Same as (A) to (C) but for the three-species food-chain model (*20*). (**G** to **I**) Same as (A) to (C) but for the flour beetle model (*25*).

skill to select the best views) may show biases [e.g., for N_{11} with 25 data points (figs. S1 and S2)]. Even in simple systems, 25 time points may not provide full coverage of the system (gray areas in Fig. 1C), so it is to be expected that longer time series may be needed if the dynamics are more complex and pass through different regimes.

The example implementation of MVE given here is based on simple model averaging. Whereas this approach has the advantage of transparency and parsimony (involving few parameters), more sophisticated implementations should greatly enhance forecast skill. For example, rather than using the $k = \sqrt{m}$ heuristic (*21*), the optimal number of reconstructions can be tuned. In some cases, forecast skill may be maximized for small k, but in other cases, accuracy continues to increase

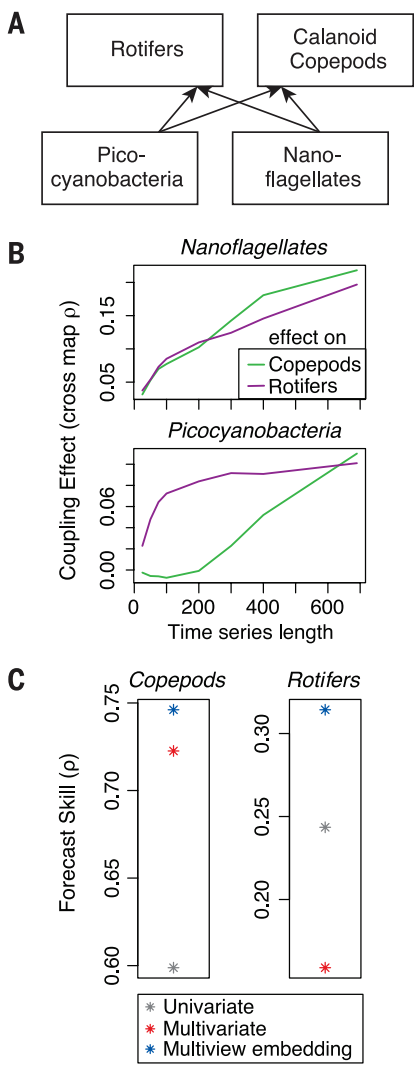

Fig. 4. Analysis of the long-term mesocosm experiment. (**A**) The subsystem examined in this work (*27*, *28*). (**B**) Cross mapping between grazers (calanoid copepods and rotifers) and prey (nanoflagellates and picocyanobacteria) indicates a causal influence of the prey on the grazers. (**C**) Forecast skill (ρ) is higher for MVE than for the univariate or multivariate methods.

Downloaded from http://science.sciencemag.org/ on September 3, 2016

until nearly all variable combinations are considered (figs. S15 to S20). Moreover, alternative criteria for selecting candidate views may be desirable to address specific objectives. For example, a more robust but less specifically predictive model could be constructed by selecting variable combinations that are maximally distinct. With enough data, it should even be possible to identify optimal weightings of the different views or have such weightings be state-dependent (e.g., to correct for the state-dependent biases of individual views). Regardless of details, the implementation of MVE demonstrated here is intended to be as simple as possible.

The main innovation of MVE is to leverage the interconnectedness (the shared information) of complex systems. As seen in Fig. 3, improvements in forecast skill can be especially evident for short time series (~25 time points). This result is especially promising given that many current ecological data sets are wide in scope, with many different variables being tracked, but shallow in terms of time series length. Furthermore, the noise-mitigating aspects of MVE are potentially useful for many other applications such as reconstructing historical behavior, signal processing (*31*), or nonlinear system control (*32*). Although the high-dimensionality of complex systems is typically perceived as an obstacle, such complexity is actually an advantage, leading to better clarity and prediction.

REFERENCES AND NOTES

1. R. M. May, S. A. Levin, G. Sugihara, *Nature* **451**, 893–895 (2008).
2. D. Boyd, K. Crawford, *Inf. Commun. Soc.* **15**, 662–679 (2012).
3. J. C. McBride *et al.*, *Neuroimage Clin.* **7**, 258–265 (2014).
4. M. G. M. Olde Rikkert *et al.*, *Crit. Care Med.* **44**, 601–606 (2016).
5. G. Sugihara *et al.*, *Science* **338**, 496–500 (2012).
6. J. Fan, F. Han, H. Liu, *Natl. Sci. Rev.* **1**, 293–314 (2014).
7. D. Lazer, R. Kennedy, G. King, A. Vespignani, *Science* **343**, 1203–1205 (2014).
8. E. A. Fulton, thesis, University of Tasmania (2001).
9. D. L. Donoho, "High-dimensional data analysis: The curses and blessings of dimensionality," presented at the American Mathematical Society Math Challenges of the 21st Century conference, Los Angeles, CA, 7 to 12 August 2000.
10. D. L. DeAngelis, S. Yurek, *Proc. Natl. Acad. Sci. U.S.A.* **112**, 3856–3857 (2015).
11. C.-H. Hsieh, C. Anderson, G. Sugihara, *Am. Nat.* **171**, 71–80 (2008).
12. T. Clark *et al.*, *Ecology* **96**, 1174–1181 (2015).
13. G. Sugihara, R. M. May, *Nature* **344**, 734–741 (1990).
14. G. Sugihara, *Philos. Trans. Phys. Sci. Eng.* **348**, 477–495 (1994).
15. P. A. Dixon, M. J. Milicich, G. Sugihara, *Science* **283**, 1528–1530 (1999).
16. F. Takens, *Dyn. Syst. Turbul. Lect. Notes Math.* **898**, 366–381 (1981).
17. T. Sauer, J. A. Yorke, M. Casdagli, *J. Stat. Phys.* **65**, 579–616 (1991).
18. E. R. Deyle, G. Sugihara, *PLOS ONE* **6**, e18295 (2011).
19. M. Casdagli, S. Eubank, J. D. Farmer, J. Gibson, *Physica D* **51**, 52–98 (1991).
20. A. Hastings, T. Powell, *Ecology* **72**, 896–903 (1991).
21. R. O. Duda, P. E. Hart, D. G. Stork, *Pattern Classification* (Wiley, 2012).
22. For nearest-neighbor methods, asymptotic convergence requires only that the selection of k satisfies Stone's consistency theorem (*23*). The square root was chosen for simplicity and for its use in the machine learning literature.
23. C. J. Stone, *Ann. Stat.* **5**, 595–620 (1977).
24. See supplementary materials on *Science* Online.
25. B. Dennis, R. A. Desharnais, J. M. Cushing, S. M. Henson, R. F. Costantino, *Ecol. Monogr.* **71**, 277–303 (2001).
26. J. Huisman, F. J. Weissing, *Nature* **402**, 407–410 (1999).
27. R. Heerkloss, G. Klinkenberg, *Verhandlungen - Int. Vereinigung für Theor. und Angew. Limnol.* **26**, 1952–1956 (1998).
28. E. Benincà, K. D. Jöhnk, R. Heerkloss, J. Huisman, *Ecol. Lett.* **12**, 1367–1378 (2009).
29. T. Sauer, *Physica D* **58**, 193–201 (1992).
30. R. E. Kalman, *J. Basic Eng.* **82**, 35–45 (1960).
31. T. L. Carroll, F. J. Rachford, *Chaos* **22**, 023107 (2012).
32. E. Ott, C. Grebogi, J. A. Yorke, *Phys. Rev. Lett.* **64**, 1196–1199 (1990).

ACKNOWLEDGMENTS

We thank S. Glaser, C. Hsieh, E. Deyle, and S. Munch for suggestions and feedback on early drafts of this work.

This work was supported by U.S. Department of Defense Strategic Environmental Research and Development Program 15 RC-2509, Lenfest Foundation award 00028335, NSF grant DEB-1020372, the McQuown Chair in the Natural Sciences, and the Sugihara Family Trust. Mesocosm data are available in the appendix of (*28*); model simulation data are available in Data S1.

SUPPLEMENTARY MATERIALS

www.sciencemag.org/content/353/6302/922/suppl/DC1
Materials and Methods
Figs. S1 to S20
References
Data S1

6 May 2016; accepted 1 August 2016
10.1126/science.aag0863

SINGLE-CELL GENOMICS

Div-Seq: Single-nucleus RNA-Seq reveals dynamics of rare adult newborn neurons

Naomi Habib,[1,2,3]* Yinqing Li,[1,2,3,4]* Matthias Heidenreich,[1,2,3] Lukasz Swiech,[1,2,3] Inbal Avraham-Davidi,[1] John J. Trombetta,[1] Cynthia Hession,[1] Feng Zhang,[1,2,3,5,6]† Aviv Regev[1,7]†

Single-cell RNA sequencing (RNA-Seq) provides rich information about cell types and states. However, it is difficult to capture rare dynamic processes, such as adult neurogenesis, because isolation of rare neurons from adult tissue is challenging and markers for each phase are limited. Here, we develop Div-Seq, which combines scalable single-nucleus RNA-Seq (sNuc-Seq) with pulse labeling of proliferating cells by 5-ethynyl-2′-deoxyuridine (EdU) to profile individual dividing cells. sNuc-Seq and Div-Seq can sensitively identify closely related hippocampal cell types and track transcriptional dynamics of newborn neurons within the adult hippocampal neurogenic niche, respectively. We also apply Div-Seq to identify and profile rare newborn neurons in the adult spinal cord, a noncanonical neurogenic region. sNuc-Seq and Div-Seq open the way for unbiased analysis of diverse complex tissues.

Single-cell RNA sequencing (scRNA-Seq) has extended our understanding of heterogeneous tissues, including the central nervous system (CNS) (*1*–*3*). However, dynamic processes, such as adult neurogenesis, remain challenging to study by scRNA-Seq. First, scRNA-Seq requires enzymatic tissue dissociation (Fig. 1A), which may compromise the integrity of neurons and their RNA content, skew data toward easily dissociated cell types, and is restricted to fetal or young animals (*1*). Second, it is difficult to capture rare cell types, such as adult newborn neurons (*4*), because of limitations in cell tagging and isolation at each phase of the dynamic process.

We therefore developed Div-Seq, a method for RNA-seq of individual, recently divided cells. Div-Seq relies on sNuc-Seq, a single-nucleus isolation and RNA-Seq method compatible with frozen or fixed tissue (Fig. 1A), which enables enrichment of rare labeled cell populations by fluorescence-activated cell sorting (FACS) (fig. S1). Div-Seq combines sNuc-Seq with pulse labeling of dividing cells by 5-ethynyl-2′-deoxyuridine (EdU) (*5*, *6*).

We validated that sNuc-Seq on population of nuclei faithfully represents tissue-level RNA

[1]Broad Institute of MIT and Harvard, 415 Main Street, Cambridge, MA 02142, USA. [2]Stanley Center for Psychiatric Research, 75 Ames Street, Cambridge, MA 02142, USA. [3]McGovern Institute of Brain Research, Massachusetts Institute of Technology, Cambridge, MA 02139, USA. [4]Department of Electrical Engineering and Computer Science, Massachusetts Institute of Technology, Cambridge, MA 02139, USA. [5]Department of Brain and Cognitive Sciences, Massachusetts Institute of Technology, Cambridge, MA 02139, USA. [6]Department of Biological Engineering, Massachusetts Institute of Technology, Cambridge, MA 02139, USA. [7]Howard Hughes Medical Institute, Koch Institute of Integrative Cancer Research, Department of Biology, Massachusetts Institute of Technology, Cambridge, MA 02139, USA.
*These authors contributed equally to this work.
†Corresponding author. Email: zhang@broadinstitute.org (F.Z.); aregev@broadinstitute.org (A.R.)

Downloaded from http://science.sciencemag.org/ on September 3, 2016

(7) (fig. S2, A and B), in agreement with earlier studies on the feasibility of single-nuclei sequencing (7, 8). Next, we analyzed 1367 single nuclei from hippocampal anatomical subregions [dorsal ganglion (DG), CA1, CA2, and CA3] from adult mice, including enrichment of genetically tagged low-abundance γ-aminobutyric acid–releasing (GABAergic) neurons (9) (fig. S1). sNuc-Seq robustly generated high-quality data across animal age groups (including 2-year-old mice; figs. S2, C to H, and S3), detecting 5100 expressed genes per nucleus on average, with complexity comparable

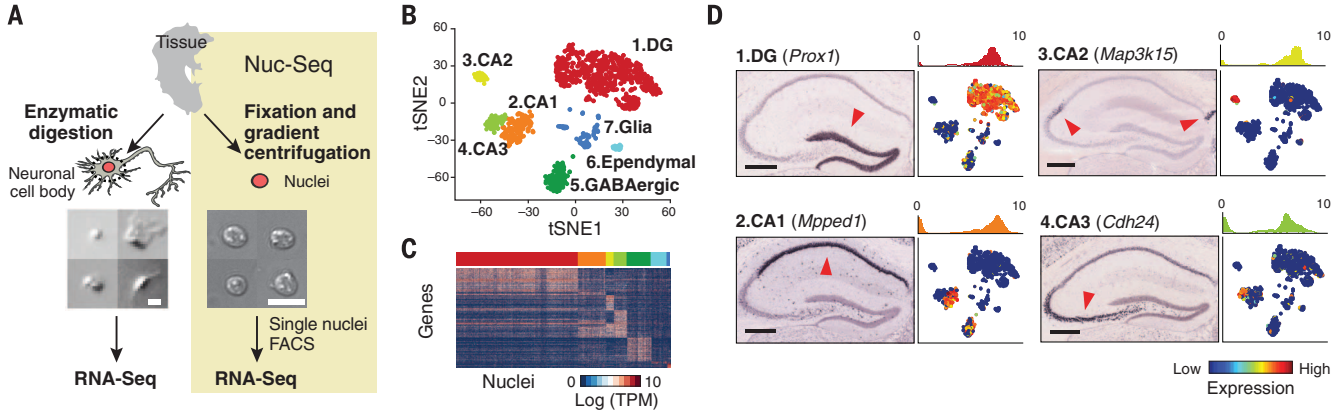

Fig. 1. sNuc-Seq identifies cell types in adult mouse brain. (**A**) Representative images of isolated nuclei are more uniform than images of dissociated neurons from adult brain. Scale bars, 10 μm. sNuc-Seq method (right): Single nuclei are isolated, FACS sorted, and profiled by modified Smart-Seq2 protocol (*21*). (**B**) Major cell types identified from sNuc-Seq data reflected by clusters, shown as two-dimensional (2D) tSNE embedding of 1188 nuclei from adult mouse hippocampus. Axes: 2D coordinates from tSNE algorithm. (**C**) Cluster-specific genes across single nuclei. Color bar matches cluster color in (B). TPM: transcripts per million. (**D**) Identification of DG granule cell, CA1, CA2, and CA3 pyramidal cell clusters by marker genes, shown as (i) ISH image in hippocampus section (*10*) (arrowhead: high expression; scale bar, 400 μm.); (ii) histogram quantifying expression in relevant cluster; and (iii) 2D embedding of nuclei [as in (B)] colored by relative expression.

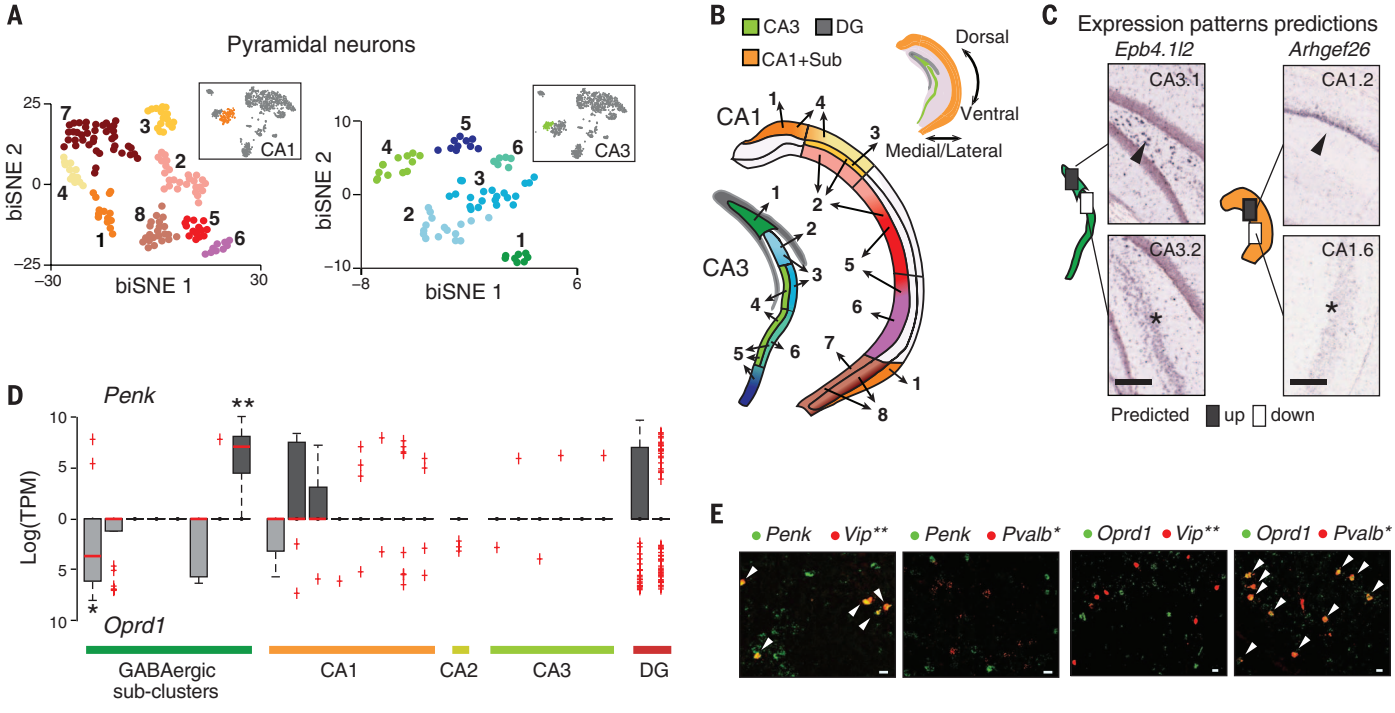

Fig. 2. sNuc-Seq and biSNE distinguish cell subtypes and spatial expression patterns. (**A**) Pyramidal CA1 and CA3 biSNE subclusters. Shown is a 2D embedding of the CA1 and CA3 pyramidal nuclei (colored by cluster). Insets: the CA1 cluster (orange) and CA3 cluster (green) within all other clusters from Fig. 1B. (**B**) Mapping of CA1 and CA3 pyramidal subclusters to subregions. Subcluster assignments are numbered and color coded as in (A). Top: hippocampus schematic. (**C**) Predictions by CA1 and CA3 subcluster spatial mapping match with Allen ISH data (*10*). Left illustrations: boxes: predicted differential expression regions; arrowhead: high expression; asterisk: low expression. (**D**) Mutually exclusive expression of *Penk* (facing up) and its receptor *Oprd1* (facing down) across neuronal subclusters. Red line: median; box: 75 and 25% quantile. Single and double asterisks: GABergic clusters associated with *Pvalb* or *Vip* markers, respectively. (**E**) Co-FISH of *Penk* or *Oprd* with markers of GABAergic subtypes [*Pvalb* and *Vip* as in (D)]. Arrowheads: coexpression. Scale bars, 20 μm.

Downloaded from http://science.sciencemag.org/ on September 3, 2016

to that of single-neuron RNA-Seq from young mice (*1*–*3*) (fig. S3, A to C).

Analysis of sNuc-Seq data revealed distinct nuclei clusters (Fig. 1, B to D; figs. S4, S5, and S6, A to C; and table S1) corresponding to known cell types and anatomical distinctions in the hippocampus. Analysis was consistent with microdissections, in situ hybridization [Allen Brain Atlas ISH (*10*), fig. S5], and bulk RNA-Seq (*11*) (fig. S6D). We captured finer distinctions between closely related cells using a new clustering algorithm, biSNE (biclustering on stochastic

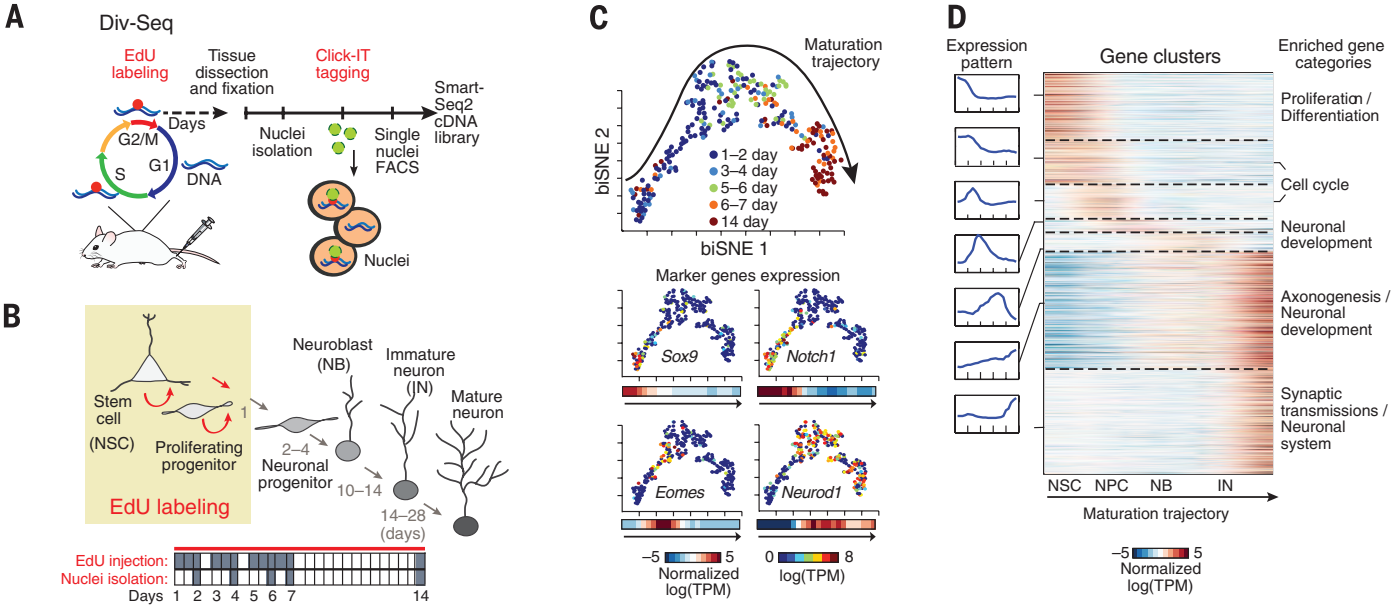

Fig. 3. Transcriptional dynamics of adult neurogenesis by Div-Seq. (**A**) Div-Seq method: EdU is injected into adult mice and incorporates into dividing cells (*5*). Isolated EdU-labeled nuclei are fluorescently tagged by click-IT chemistry and captured by FACS for sNuc-Seq. (**B**) Adult neurogenesis in the DG (*4*). Tan box: timing of EdU labeling. NSC: neuronal stem cell. Bottom panel: EdU labeling and tissue dissection (gray) time course. (**C**) A continuous trajectory of newborn cells in the DG. biSNE 2D embedding of neuronal lineage nuclei (n = 269). Arrow: direction of trajectory determined by labeling time and marker expression. Top: Colored by labeling time (1 to 14 days). Bottom: Expression of markers, shown as (i) average expression along the trajectory (left colorbar) and (ii) 2D embedding colored by the expression level (right colorbar). Markers (clockwise from top left): *Sox9* (NSC), *Notch1* (proliferation/differentiation), *Neurod1* (immature neurons), *Eomes/Tbr2* (neuronal precursor). (**D**) Expression waves along the trajectory. Left: average expression of cluster genes along the trajectory. Middle: heatmap of average expression of each gene along the trajectory and neurogenic stages [labeled as in (B)]. Right: representative enriched biological pathways.

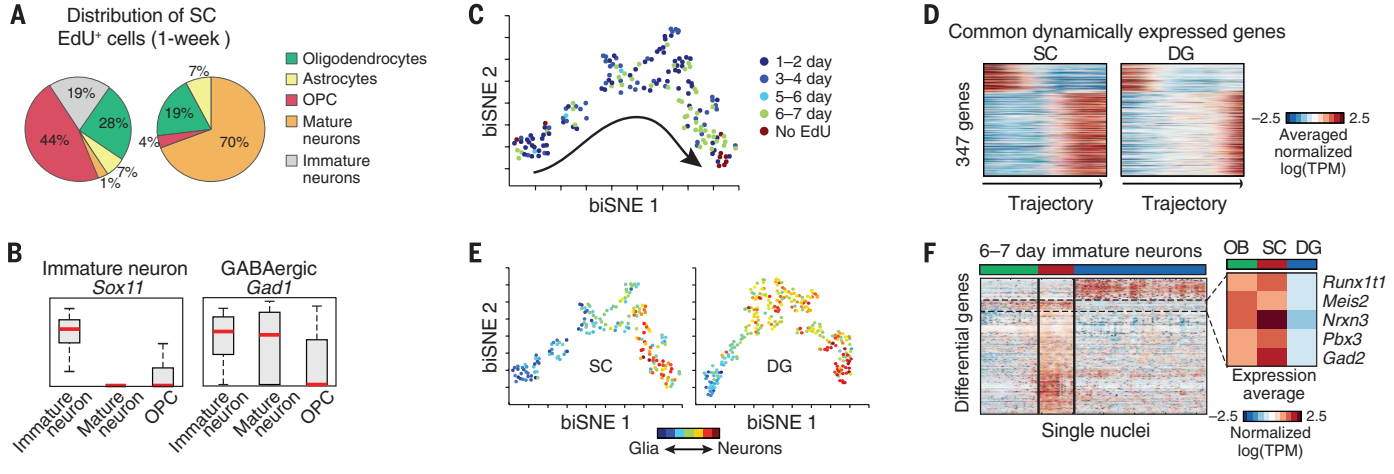

Fig. 4. Dynamics of adult newborn GABAergic neurons in SC. (**A**) Div-Seq in SC captures oligodendrocytes precursor cells (OPCs) and immature neurons. Distribution of cell types in non-EdU-labeled and 6 to 7 days EdU-labeled nuclei. (**B**) Div-Seq captured nuclei expressing marker genes of immature (*Sox11*) and GABAergic (*Gad1*) neurons. Box plots for immature neurons, mature neurons, and OPCs. Red: median; box: 75 and 25% quantiles. (**C**) Newborn cells in SC form a continuous trajectory. Two-dimensional embedding of 1 to 7 days EdU-labeled and nonlabeled nuclei (n = 184 neuronal lineage nuclei), colored by labeling time. Trajectory directionality is based on EdU labeling time and marker genes. (**D**) Dynamically expressed genes shared in SC and DG neurogenesis (347 genes from fig. S22B and Fig. 3D). (**E**) Gradual transition from a glia-like to neuronal state. Neuronal trajectories in the SC [as in (C)] and DG (as in Fig. 3C) colored by a glia-neuron RNA expression score. (**F**) Region-specific gene expression in immature neurons (6 to 7 days after EdU labeling). A total of 236 genes differentially expressed between SC and DG (t-test false discovery rate <0.05, log-ratio >1) in olfactory bulb (OB), SC, and DG. Box: average expression of example genes up-regulated in OB and SC compared to DG.

Downloaded from http://science.sciencemag.org/ on September 3, 2016

neighbor embedding) (fig. S7), which partitioned the GABAergic neurons into subclusters (fig. S8 and table S2) and associated each subcluster with combinations of canonical markers (fig. S8C). We validated selected markers using fluorescent RNA in situ hybridization (FISH) (fig. S9).

BiSNE also distinguished between spatial hippocampal subregions with divergent transcriptional profiles. BiSNE partitioned glutamatergic cells into subclusters (Fig. 2A and fig. S10), which were further mapped to hippocampal subregions, with ISH of spatial landmark genes (*10*) (Fig. 2B and figs. S11 to S13). We validated our mapping by confirming expression patterns using the Allen ISH data set (*10*) (Fig. 2C and fig. S14). Although some subregions were assigned to a single subcluster (e.g., dorsal lateral CA1, Fig. 2B), most subregions were assigned partially overlapping subclusters, suggesting a gradual transition of transcriptional profiles between neighboring subregions. This extends current anatomical resolutions of the hippocampus (fig. S15) and supports the notion that cellular diversity does not always partition into discrete subtypes (*12*).

We identified genes that are indicative of specific cell type or position (tables S1 to S3). For example, *Penk*, encoding an opioid neuropeptide (enkephalin), and its receptor *Oprd1* (*13*) were expressed in mutually exclusive subclusters of cells (Fig. 2D), which we validated by FISH and the Allen ISH data set (*10*) (Fig. 2E and fig. S16). These cell types and spatial positions may be involved in enkephalin signaling within the hippocampus.

Next, to study transcriptional dynamics during adult neurogenesis, we developed Div-Seq by combining sNuc-Seq with EdU labeling of dividing cells (Fig. 3A). Unlike genetic labeling (*2*, *14*), EdU tags proliferating cells at any time window, marking stem cells and their progeny with high temporal resolution. We applied Div-Seq in the DG, a canonical neurogenic niche (*4*), over multiple time points (1 to 14 days after cell division; Fig. 3B, fig. S17, and table S4). Div-Seq enriched for diverse newborn cell types and neurogenic stages (fig. S17, F and G), from proliferating stem cells to immature neurons (*4*).

BiSNE analysis of neuronal lineage nuclei placed the DG newborn neurons on a continuous trajectory. The order of nuclei along the trajectory matched the EdU labeling time (Fig. 3C), was independent of animal age (fig. S17H), and recapitulated known dynamics of neurogenesis markers (*2*, *3*, *15*) (fig. S18A), indicating that the trajectory indeed captured the neuronal maturation process.

To characterize the transcriptional program of adult neurogenesis, we identified and clustered genes with dynamic expression patterns along the trajectory (Fig. 3D and table S5). We found major coordinated transcriptional waves, involving hundreds of genes, and aligned with known transitions between neurogenic stages, with expression shifts from proliferation to neuronal differentiation [consistent with (*2*)], and then to neuronal integration and maturation (Fig. 3D). We identified genes with restricted expression in specific stages of neurogenesis (figs. S18 and S19), including transcription factors and chromatin regulators (fig. S18). We confirmed the early neurogenic stage-specific expression of the axon guidance molecule *Draxin* and the ribonucleotide reductase *Rrm2* by FISH (fig. S19).

Accumulating evidence suggests that adult neurogliogenesis occurs in multiple noncanonical regions (*16*), but traditional methods are limited for the characterization of rare newborn cells and can lead to less definitive findings, as in the spinal cord (SC) (*17*, *18*). We applied Div-Seq over multiple time points (1 to 7 days) in the SC (fig. S20). SC nuclei 6 to 7 days after labeling (Fig. 4, A and B) comprised a diverse population of newborn cells including oligodendrocyte precursor cells (OPCs, 44%) and immature neurons (19%), in contrast to 4% OPCs and no immature neurons in the non–EdU-labeled population. The SC newborn neurons expressed the GABAergic markers *Gad1* and *Gad2,* suggesting GABAergic neurogenesis [consistent with (*18*)] (Fig. 4B). Notably, we found a set of immature neuronal nuclei (10%) at 23 to 24 days after EdU labeling (fig. S21), suggesting survival of newborn neurons in the SC.

The full set of neuronal lineage nuclei (fig. S20A) map to a continuous trajectory (Fig. 4C) that matched labeling time and expression dynamics of known markers (fig. S20C). Comparison of dynamically expressed genes along the SC and DG trajectories (fig. S20B) identified 347 (28%) common neurogenesis genes (Fig. 4D and fig. S20C) but also revealed notable distinctions in the expression dynamics and branching along the DG and SC trajectories (Fig. 4, D and E) (*6*), which can result from differences in time scales, cell populations, or parallel gliogenesis and neurogenesis processes.

The immature neurons from SC and DG are composed of different neuronal types (GABAergic in SC, granule cells in DG). To identify candidate genes driving neuronal lineage specification, we first identified differentially expressed genes between SC and DG (*t* test) and then compared their expression patterns to those of newborn neurons in the olfactory bulb (OB), where GABAergic neurons are born (Fig. 4F). A set of SC-specific genes was also up-regulated in the OB relative to the DG, including the transcription factors *Pbx3* and *Meis2*. This is consistent with previous reports (*19*, *20*), and with immunohistochemistry of Pbx3 showing expression in newborn cells both in the OB and SC but not in the DG (figs. S22 to S24).

Application of Div-Seq to the adult CNS highlighted potential regulators and the neurogenic potential of the SC, though the functional roles of these SC newborn neurons remained to be elucidated. Future technology developments may increase the sensitivity, throughput, and cell types amenable to these methods. sNuc-Seq and Div-Seq open new avenues in the study of neuronal diversity and dynamic processes in the CNS and can be readily applied to diverse biological systems and human tissues.

REFERENCES AND NOTES

1. A. Zeisel *et al.*, *Science* **347**, 1138–1142 (2015).
2. J. Shin *et al.*, *Cell Stem Cell* **17**, 360–372 (2015).
3. B. Tasic *et al.*, *Nat. Neurosci.* **19**, 335–346 (2016).
4. G. L. Ming, H. Song, *Neuron* **70**, 687–702 (2011).
5. D. L. Moore, G. A. Pilz, M. J. Araúzo-Bravo, Y. Barral, S. Jessberger, *Science* **349**, 1334–1338 (2015).
6. Materials and methods are available as supplementary materials on *Science* Online.
7. B. Lacar *et al.*, *Nat. Commun.* **7**, 11022 (2016).
8. L. Swiech *et al.*, *Nat. Biotechnol.* **33**, 102–106 (2015).
9. H. Hu, J. Gan, P. Jonas, *Science* **345**, 1255263 (2014).
10. E. S. Lein *et al.*, *Nature* **445**, 168–176 (2007).
11. Y. Zhang *et al.*, *J. Neurosci.* **34**, 11929–11947 (2014).
12. M. S. Cembrowski *et al.*, *Neuron* **89**, 351–368 (2016).
13. B. P. Roques, M. C. Fournié-Zaluski, M. Wurm, *Nat. Rev. Drug Discov.* **11**, 292–310 (2012).
14. E. Llorens-Bobadilla *et al.*, *Cell Stem Cell* **17**, 329–340 (2015).
15. M. Schouten, M. R. Buijink, P. J. Lucassen, C. P. Fitzsimons, *Front. Neurosci.* **6**, 25 (2012).
16. D. M. Feliciano, A. Bordey, L. Bonfanti, *Cold Spring Harb. Perspect. Biol.* **7**, a018846 (2015).
17. P. J. Horner *et al.*, *J. Neurosci.* **20**, 2218–2228 (2000).
18. R. Shechter, Y. Ziv, M. Schwartz, *Stem Cells* **25**, 2277–2282 (2007).
19. Z. Agoston *et al.*, *Development* **141**, 28–38 (2014).
20. C. A. Rottkamp, K. J. Lobur, C. L. Wladyka, A. K. Lucky, S. O'Gorman, *Dev. Biol.* **314**, 23–39 (2008).
21. S. Picelli *et al.*, *Nat. Methods* **10**, 1096–1098 (2013).

ACKNOWLEDGMENTS

Raw data are deposited to the Gene Expression Omnibus with accession no. GSE84371; annotated data are available at https://portals.broadinstitute.org/single_cell, and software tools are available at https://github.com/yinqingl/nucseq_analysis. We thank N. Friedman, A. Shalek, D. Gennert, T. Blosser, S. Kadosch, O. Rosen, Z. Wang, P. Rogers, and L. Gaffeny for support and J. Campbell for dissociated neurons image. N.H. is a Howard Hughes Medical Institute Fellow of the Helen Hay Whitney Foundation. M.H. is supported by the Human Frontier Science Program. This work was supported by the Klarman Cell Observatory at the Broad Institute and National Institute of Mental Health (NIMH) grant U01MH105960 (F.Z., A.R.). F.Z. is supported by the NIH through NIMH (5DP1-MH100706 and 1R01-MH110049), NSF, the New York Stem Cell, Simons, Paul G. Allen Family, and Vallee Foundations; and James and Patricia Poitras, Robert Metcalfe, and David Cheng. A.R. is a Howard Hughes Medical Institute Investigator on the scientific advisory board of Syros Pharmaceuticals and Thermo Fisher and a consultant for Driver group. N.H., Y.L., A.R., and F.Z. are inventors on provisional patent application 62/311,129, applied for by the Broad Institute and MIT, that covers the methods described in this paper. All DNA constructs are available from Addgene subject to a material transfer agreement with Addgene.

SUPPLEMENTARY MATERIALS

www.sciencemag.org/content/353/6302/925/suppl/DC1
Materials and Methods
Supplementary Text
Figs. S1 to S24
Tables S1 to S7
References (*22*–*63*)

22 October 2015; accepted 19 July 2016
Published online 28 July 2016
10.1126/science.aad7038

Downloaded from http://science.sciencemag.org/ on September 3, 2016

SIGNAL TRANSDUCTION

pVHL suppresses kinase activity of Akt in a proline-hydroxylation–dependent manner

Jianping Guo,[1] Abhishek A. Chakraborty,[2] Pengda Liu,[1] Wenjian Gan,[1] Xingnan Zheng,[3] Hiroyuki Inuzuka,[1] Bin Wang,[1] Jinfang Zhang,[1] Linli Zhang,[1] Min Yuan,[4] Jesse Novak,[5] Jin Q. Cheng,[6] Alex Toker,[1] Sabina Signoretti,[5] Qing Zhang,[3] John M. Asara,[4] William G. Kaelin Jr.,[2,7] Wenyi Wei[1]*

Activation of the serine-threonine kinase Akt promotes the survival and proliferation of various cancers. Hypoxia promotes the resistance of tumor cells to specific therapies. We therefore explored a possible link between hypoxia and Akt activity. We found that Akt was prolyl-hydroxylated by the oxygen-dependent hydroxylase EglN1. The von Hippel–Lindau protein (pVHL) bound directly to hydroxylated Akt and inhibited Akt activity. In cells lacking oxygen or functional pVHL, Akt was activated to promote cell survival and tumorigenesis. We also identified cancer-associated Akt mutations that impair Akt hydroxylation and subsequent recognition by pVHL, thus leading to Akt hyperactivation. Our results show that microenvironmental changes, such as hypoxia, can affect tumor behaviors by altering Akt activation, which has a critical role in tumor growth and therapeutic resistance.

Inactivation of the *VHL* tumor suppressor gene is the gatekeeper event in most hereditary [von Hippel–Lindau (VHL) disease] and sporadic clear-cell renal carcinomas (ccRCCs) (*1*–*3*). Approved targeted therapies against advanced renal carcinomas include mechanistic target of rapamycin (mTOR) inhibitors (rapalogs) (*4*–*6*). Preclinical cancer models indicated that loss of *VHL* or *phosphatase and tensin homolog* (*PTEN*) increases rapalog sensitivity (*7*). Because Akt is frequently activated in *VHL*-defective renal carcinomas (*8*), we thus tested whether VHL protein (pVHL) might directly regulate Akt.

Cre-mediated deletion of *VHL* in conditional *VHL*-knockout mouse embryonic fibroblasts (MEFs) (*9*) increased Akt activity, as evidenced by increased phosphorylation at threonine 308 (pT308-Akt) and serine 473 (pS473-Akt) (Fig. 1A). Reintroducing pVHL in *VHL*-deficient renal carcinoma cells reduced pT308-Akt, and to a lesser extent pS473-Akt, in cells (Fig. 1B and fig. S1, A and B) and decreased Akt kinase activity in biochemical assays (fig. S1, C and D). Because phosphorylation of T308-Akt plays a more critical role in activating Akt than does phosphorylation of S473 (*10*), we focused on the regulation of the former by pVHL. (Single-letter abbreviations for the amino acid residues are as follows: A, Ala; C, Cys; D, Asp; E, Glu; F, Phe; G, Gly; H, His; I, Ile; K, Lys; L, Leu; M, Met; N, Asn; P, Pro; Q, Gln; R, Arg; S, Ser; T, Thr; V, Val; W, Trp; and Y, Tyr. In the mutants, other amino acids were substituted at certain locations; for example, P125N indicates that proline at position 125 was replaced by asparagine.)

To test whether the regulation of Akt by pVHL in our system was hypoxia-inducible factor (HIF)–dependent, we depleted *HIF1β* (*11*) in renal carcinoma cells, which did not decrease pT308-Akt (fig. S2, A and B). Similarly, silencing *HIF2α* in 786-O cells or ectopically expressing a non-degradable HIF2α-PA (*12*, *13*) in various cell lines did not alter pT308-Akt (fig. S2, C to F). Taken together, these results point to a HIF-independent link between pVHL and Akt activity.

Total Akt abundance was not affected by manipulating pVHL in different cell lines (Fig. 1, A and B). This left open the possibility that pVHL specifically polyubiquitylates phospho-Akt. However, depletion of *Cullin 2*, which is required for pVHL-dependent ubiquitylation and leads to stabilized HIF2α (*14*) as expected, did not affect Akt phosphorylation (fig. S2G). These data suggest that pVHL suppresses Akt kinase activity in an E3 ligase–independent manner.

Overexpressed pVHL bound to Akt1 and Akt2 but not to Akt3 (fig. S3, A to E). In contrast to the binding of HIF1α to pVHL (*15*, *16*), Akt

[1]Department of Pathology, Beth Israel Deaconess Medical Center, Harvard Medical School, Boston, MA 02215, USA. [2]Department of Medicine, Dana-Farber Cancer Institute and Brigham and Women's Hospital, Harvard Medical School, Boston, MA 02115, USA. [3]Department of Pathology and Laboratory Medicine, Lineberger Comprehensive Cancer Center, University of North Carolina School of Medicine, Chapel Hill, NC 27599, USA. [4]Division of Signal Transduction, Beth Israel Deaconess Medical Center and Department of Medicine, Harvard Medical School, Boston, MA 02115, USA. [5]Department of Pathology, Dana-Farber Cancer Institute and Brigham and Women's Hospital, Harvard Medical School, Boston, MA 02115, USA. [6]Department of Molecular Oncology, H. Lee Moffitt Cancer Center and Research Institute, Tampa, FL 33612, USA. [7]Howard Hughes Medical Institute, Chevy Chase, MD 20815, USA.
*Corresponding author. Email: wwei2@bidmc.harvard.edu

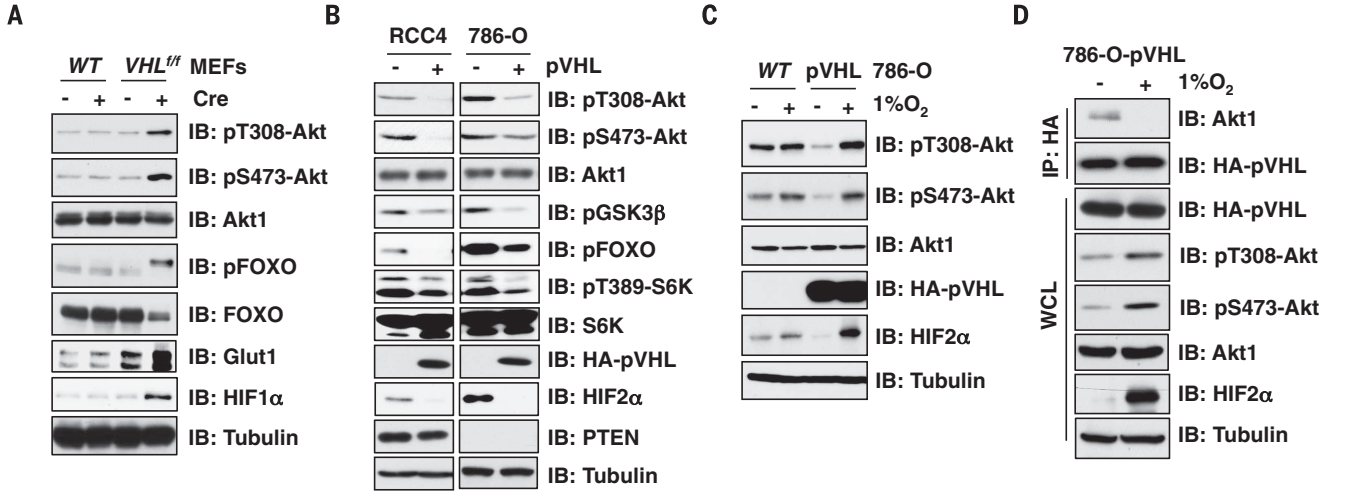

Fig. 1. pVHL suppresses Akt phosphorylation. (**A**) Immunoblot (IB) analysis of whole-cell lysates (WCL) derived from $VHL^{f/f}$ MEFs infected with Cre or control (EV) lentivirus. (**B**) IB analysis of WCL derived from RCC4 or 786-O cells infected with EV or *VHL* retrovirus. (**C** and **D**) 786-O cells were engineered via retroviral infection to stably express pVHL and harvested for hemagglutinin-immunoprecipitation (HA-IP) or IB analysis after culturing under normoxia or hypoxia (1% O_2) condition for 16 hours.

Downloaded from http://science.sciencemag.org/ on September 3, 2016

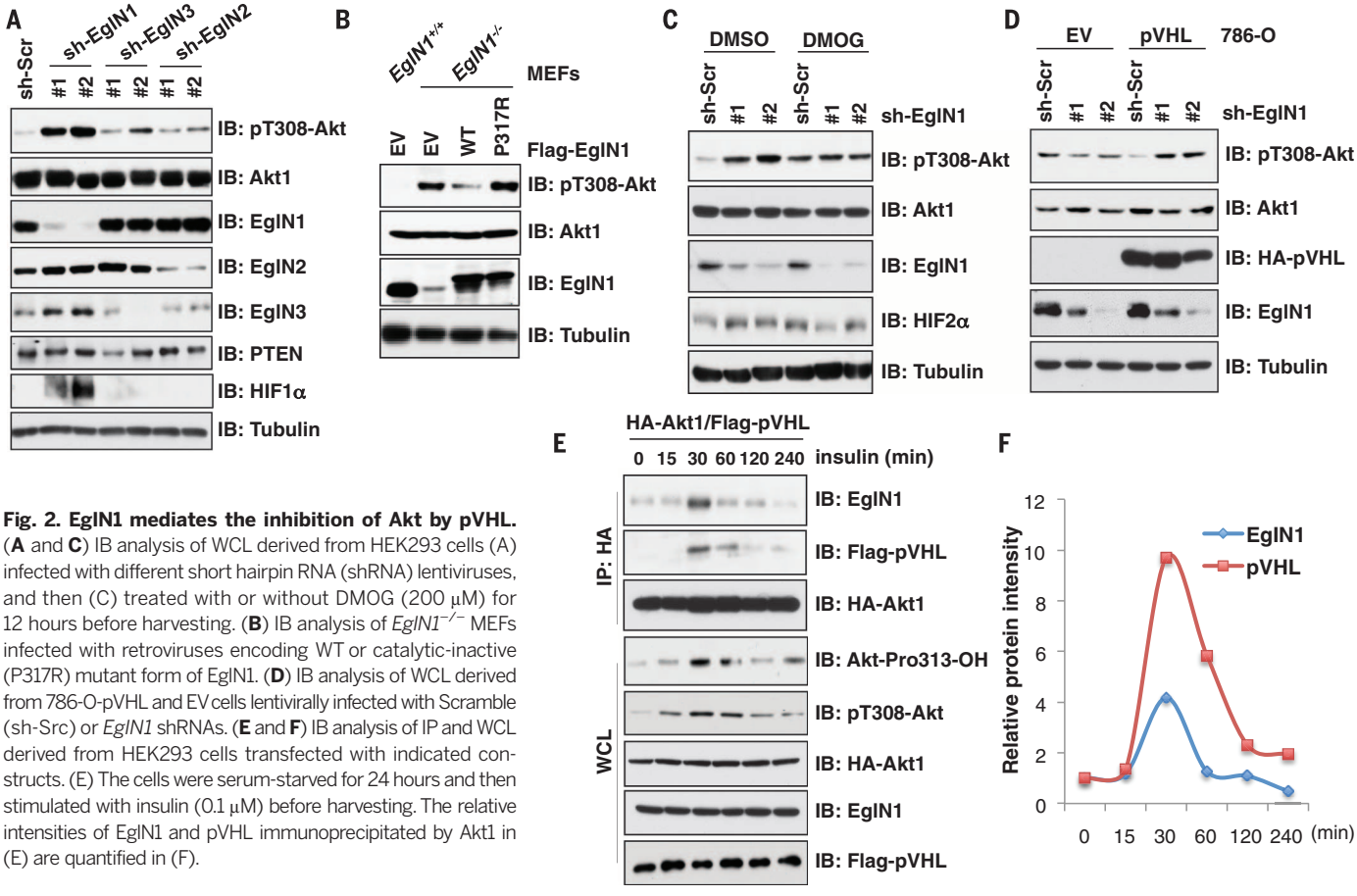

Fig. 2. EglN1 mediates the inhibition of Akt by pVHL. (**A** and **C**) IB analysis of WCL derived from HEK293 cells (A) infected with different short hairpin RNA (shRNA) lentiviruses, and then (C) treated with or without DMOG (200 μM) for 12 hours before harvesting. (**B**) IB analysis of *EglN1*$^{-/-}$ MEFs infected with retroviruses encoding WT or catalytic-inactive (P317R) mutant form of EglN1. (**D**) IB analysis of WCL derived from 786-O-pVHL and EV cells lentivirally infected with Scramble (sh-Src) or *EglN1* shRNAs. (**E** and **F**) IB analysis of IP and WCL derived from HEK293 cells transfected with indicated constructs. (E) The cells were serum-starved for 24 hours and then stimulated with insulin (0.1 μM) before harvesting. The relative intensities of EglN1 and pVHL immunoprecipitated by Akt1 in (E) are quantified in (F).

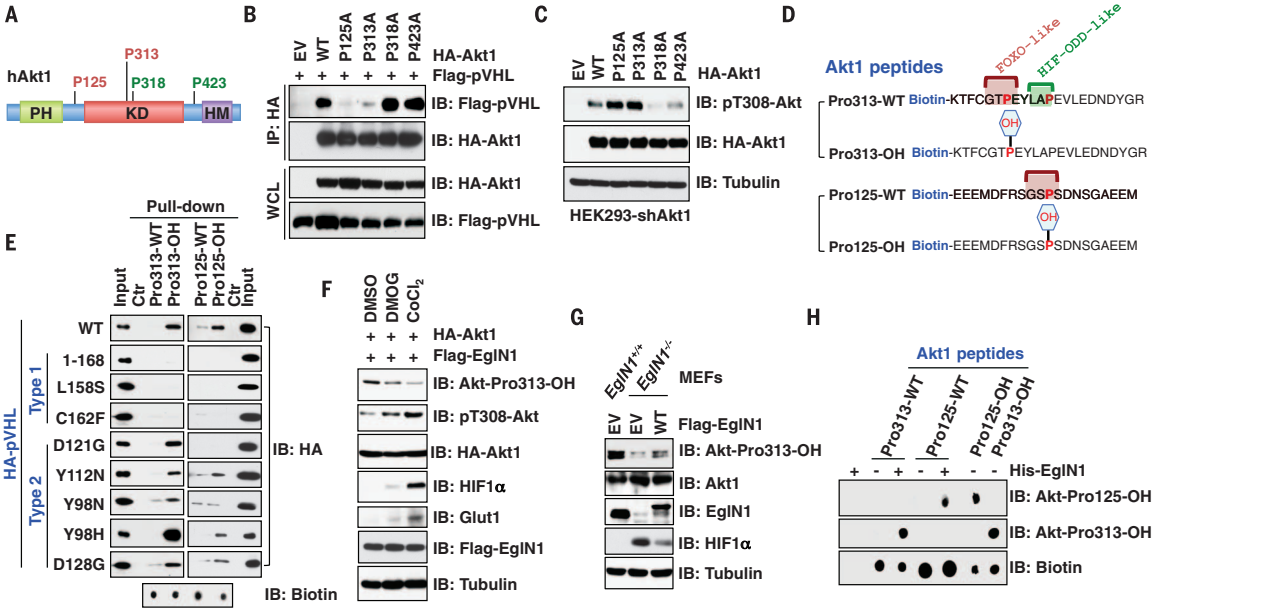

Fig. 3. EglN1 hydroxylates Akt1 at the Pro^{125} and Pro^{313} residues to trigger Akt1 interaction with pVHL. (**A**) A schematic illustration of Akt1 domain structures with four putative prolyl-hydroxylation residues identified by means of LC-MS/MS analysis. (**B** and **C**) IB analysis of co-immunoprecipitation and WCL derived from HEK293 cells transfected with Flag-pVHL and indicated HA-Akt1 constructs. (**D**) A schematic representation of the various biotinylated synthetic peptides used in this study. FOXO-like and HIF-ODD–like motifs were labeled in red and green, respectively. (**E**) Indicated peptides as denoted in (D) were incubated with WCL derived from HEK293 cells transfected with indicated constructs, and precipitated with streptavidin. (**F**) IB analysis of WCL derived from HEK293 cells transfected with indicated constructs. Where indicated, hypoxia mimetic reagents were used before harvesting for IB analysis. (**G**) IB analysis of WCL derived from WT or *EglN1*$^{-/-}$ MEFs infected with a retrovirus encoding Flag-tagged WT-EglN1. (**H**) In vitro hydroxylation assays with recombinant His-EglN1 and various Akt1 peptides were analyzed by means of dot immunoblot.

Downloaded from http://science.sciencemag.org/ on September 3, 2016

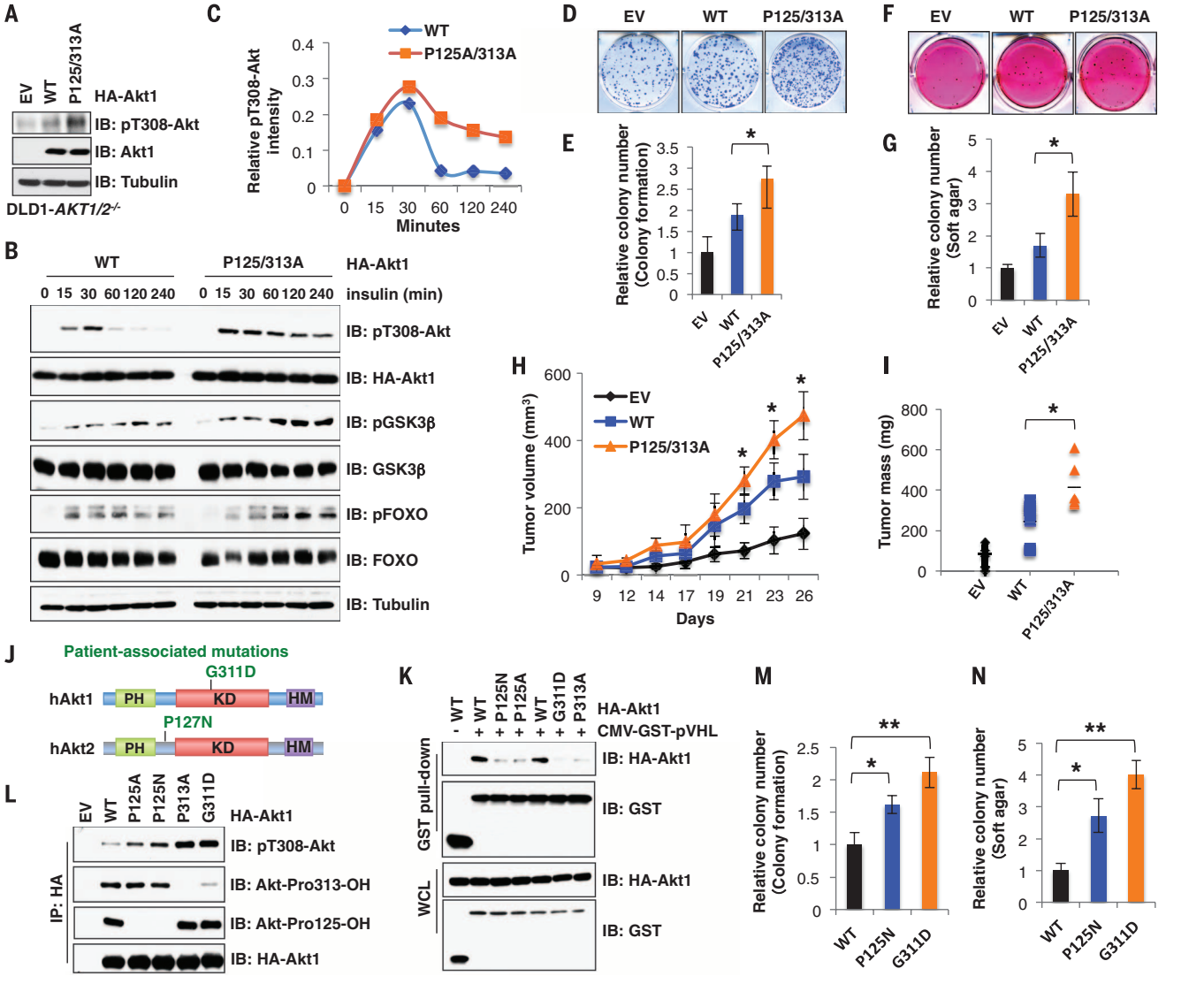

Fig. 4. Disruption of Akt proline-hydroxylation events leads to a sustained Akt kinase activation and increased colony formation and tumor growth. (**A** to **C**) IB analysis of WCL derived from DLD1-*AKT1/2*$^{-/-}$ cells (A) infected with lentiviruses encoding WT- or P125/313A-Akt1. (B) Cells were deprived of serum for 24 hours followed by stimulation with insulin (0.1 μM), and relative pT308-Akt intensity was quantified in (C). (**D** to **G**) Colony formation (D) and soft agar (F) assays were performed with DLD1-*AKT1/2*$^{-/-}$ cells generated in (A), and were quantified in (E) and (G) (mean ± SD, *n* = 3 wells per group). *$P < 0.05$ (Student's *t* test). (**H** and **I**) Mouse xenograft experiments were performed with the cells generated in (A). Tumor growth curve (H) and tumor weight (I) were calculated (mean ± SD, *n* = 6 mice per group). *$P < 0.05$ (one-way analysis of variance test). (**J**) A schematic representation of cancer patient-associated Akt mutations. (**K** and **L**) Glutathione *S*-transferase pull-down and IP analysis of WCL derived from HEK293 cells transfected with indicated constructs. (**M** and **N**) Relative colony numbers were quantified for colony formation (M) and soft agar (N) assays (mean ± SD, *n* = 3 wells per group). *$P < 0.05$, **$P < 0.01$ (Student's *t* test).

bound to wild type (WT) and most type 2 but not type 1 pVHL mutants (fig. S3, F to I) (*3*, *16*). Site-directed mutagenesis of critical residues within the hydroxyl-proline binding pocket of pVHL (*13*, *17*) revealed that pVHL residues critical for binding to Akt1 and HIF1α partially overlap but are not identical (fig. S3, J to M). Likewise, WT and most type 2 but not type 1 pVHL mutants inhibited pT308-Akt in 786-O cells (fig. S3N), suggesting that pVHL suppresses Akt through a direct physical association. Consistent with our findings in cell lines, pT308-Akt was increased in human *VHL* mutant ccRCC clinical samples relative to surrounding normal tissues (fig. S4, A to C).

HIFα must be prolyl-hydroxylated by the egg-laying defective nine (EglN) oxygen-sensitive enzymes to bind pVHL (*18*–*20*). To test whether inhibition of Akt by pVHL is likewise regulated by oxygen, we exposed cells to 1% O_2 or the EglN inhibitor dimethyloxaloylglycine (DMOG). Both treatments increased pT308-Akt in *VHL*-proficient but not *VHL*-deficient ccRCC cells (Fig. 1C and fig. S5A) in a HIF2α-independent manner (fig. S5B). Hypoxia and hypoxia-mimetics also disrupted the interaction of pVHL with Akt1 (Fig. 1D and fig. S5, C to G).

Depletion of *EglN1* (also termed *PHD2*), but not *EglN2* or *EglN3*, increased Akt kinase activity in various cell lines (Fig. 2A and fig. S6, A to E). Reactive oxygen species (ROS) can destabilize PTEN and thereby activate Akt (*21*, *22*). However, *EglN1* inactivation minimally induced cellular ROS levels and did not down-regulate PTEN (Fig. 2A and fig. S6, F to I). Akt hyperactivation was reversed by reintroducing wild-type but not catalytic-inactive EglN1 in *EglN1*$^{-/-}$ MEFs (Fig. 2B) or *EglN1*-depleted human embryonic kidney (HEK) 293 cells (fig. S6J). Furthermore, DMOG or hypoxia activated Akt in parental but not *EglN1*-depleted cells (Fig. 2C and fig. S6, K and L). Consistent with these findings, Akt1 bound to EglN1 but not EglN2 or EglN3, whereas both

Downloaded from http://science.sciencemag.org/ on September 3, 2016

pVHL and EglN1 bound to Akt1 and Akt2 but not Akt3 (fig. S7, A to K). Moreover, the interaction of pVHL with Akt1 was abolished in *EglN1*-depleted cells (fig. S8, A to C), and depleting *EglN1* resulted in increased pT308-Akt only in *VHL*-WT cells but not *VHL*-deficient cells (Fig. 2D and fig. S8, D and E). Hence, EglN1 is required for pVHL to suppress Akt.

Both EglN1 and pVHL preferentially bound the activated form of Akt1 (E17K variant or myristoylated-Akt) (fig. S9, A to H) (*23*). Moreover, binding of EglN1 to Akt1 correlated with the appearance of pT308-Akt in cells stimulated with insulin or epidermal growth factor (EGF) (Fig. 2, E and F, and fig. S10, A to H). Conversely, blocking Akt phosphorylation decreased the interaction of Akt1 with EglN1 (fig. S10, I to K). To test whether Akt can be hydroxylated by EglN1, we identified hydroxylation of multiple Akt1 prolyl-residues including Pro^{125}, Pro^{313}, Pro^{318}, and Pro^{423} by means of liquid chromatography-tandem mass spectrometry (LC-MS/MS) analysis (Fig. 3A and fig. S11, A to E). These prolyl-residues are highly conserved and can be divided into HIF oxygen-dependent-degradation (ODD)–like sites (Pro^{318} and Pro^{423}) (*12*, *13*, *24*) or Forkhead-Box-O3 (FOXO3)–like sites (Pro^{125} and Pro^{313}) (fig. S11F) (*25*). Mutating FOXO-like but not HIF-ODD–like sites reduced the interaction of Akt1 with pVHL (Fig. 3B), leading to increased pT308-Akt (Fig. 3C), arguing that these two residues are pivotal for the regulation of Akt by pVHL. Mutating FOXO-like sites to HIF-ODD motifs in Akt1 impaired its interaction with indicated type 2 pVHL mutants (fig. S12, A to F), again supporting that the pVHL residues used to bind hydroxylated HIFα and Akt are similar but not identical.

Mutations of Pro^{125} and Pro^{313} enhanced the interaction between Akt and its upstream kinase phosphoinositide-dependent kinase 1 (PDK1), leading to increased pT308-Akt that is insensitive to DMOG treatment (fig. S13, A to D). Moreover, hydroxylation-dependent recruitment of pVHL promoted the interaction of Akt1, but not Akt3, with the catalytic subunit of protein phosphatase 2A (PP2AC) (fig. S14, A to D) (*26*), which dephosphorylates pT308-Akt (*27*). The binding of PP2AC to Akt1, but not Akt3, was diminished in cells deficient in *EglN1* or *VHL* or by mutating the Akt1 FOXO-like motifs (fig. S14, E to I). Furthermore, recombinant pVHL promoted PP2A-mediated dephosphorylation of pT308-Akt in vitro (fig. S14, J to L). Collectively, these data suggest that EglN1-induced hydroxylation of Akt suppresses Akt activation, in part, by triggering pVHL-mediated PP2A-induced dephosphorylation of pT308-Akt (fig. S14M).

To test whether prolyl-hydroxylation might alter the recognition of Akt1 by pVHL, we performed in vitro binding assays with biotinylated Akt1-derived peptides. Peptides spanning the Akt1 FOXO-like sites bound to pVHL in a hydroxylation-dependent manner (Fig. 3, D and E). Furthermore, hydroxylated Akt1 peptides bound to WT and most type 2 but not type 1 pVHL mutants (Fig. 3E and fig. S15, A to E). Synthetic hydroxyl-peptides derived from HIF1α or Akt1 competed with one another for binding to pVHL (fig. S15, F and G). To study the Akt1 FOXO-like hydroxylation sites in cells, we generated and validated antibodies to Akt-Pro^{125}-OH or Akt-Pro^{313}-OH (fig. S16, A to F). In agreement with EglN1 as the major upstream hydroxylase for Akt, recognition of Akt1 by the Akt-Pro^{313}-OH antibody was diminished in *EglN1*-depleted cells and by hypoxic conditions (Fig. 3, F and G, and fig. S16, G to I). In multiple cell lines, Akt1 hydroxylation was triggered by growth factors (fig. S16, J to N). Using in vitro hydroxylation assays (fig. S17, A to C) (*25*, *28*) coupled with MS analysis, we identified both Pro^{125} and Pro^{313} residues as hydroxylation sites by EglN1 (Fig. 3H and fig. S17, D to K).

Given that aberrant Akt activation can alter cell survival and metabolism to favor tumorigenesis, we evaluated whether hydroxylation of Akt modulates Akt-oncogenic signaling. Reintroducing the FOXO-like hydroxylation-deficient mutants (P125A and/or P313A) of Akt1, but not the corresponding Akt3 variants, into DLD1-$AKT1^{-/-}/AKT2^{-/-}$ cells (denoted $AKT1/2^{-/-}$) led to increased pT308-Akt as compared with $AKT1/2^{-/-}$ cells expressing wild-type Akt (Fig. 4, A to C, and fig. S18, A to G). Moreover, P125A and/or P313A of Akt1, but not the corresponding mutation in Akt3, promoted colony formation and anchorage-independent growth in vitro, as well as enhanced tumor formation in vivo relative to wild-type Akt (Fig. 4, D to I, and fig. S18, H to R).

We also identified two cancer-associated Akt mutations, Akt1-G311D and Akt2-P127N (www.cbioportal.org) (Fig. 4J) (*29*). The corresponding Akt mutants displayed reduced Akt hydroxylation, associated with reduced interaction with pVHL and PP2AC (Fig. 4K and fig. S19, A to E), leading to increased pT308-Akt (Fig. 4L). Biologically, reintroducing either P125N or G311D mutant of Akt1 or P127N-Akt2 in $AKT1/2^{-/-}$ cells led to sustained activation of Akt oncogenic signaling (fig. S19, F to I), as well as increased oncogenic functions (Fig. 4, M and N, and fig. S19, J to O). These results indicate that these cancer-associated mutations in Akt exhibit increased oncogenic activity because of loss of proline-hydroxylation–dependent inhibition of Akt by pVHL (fig. S19P).

Therefore, our studies revealed that hypoxia and deficiencies in the VHL/EGLN tumor-suppressive pathway, in a HIF-independent and prolyl hydroxylation–dependent manner, lead to aberrant Akt activation, which in many models promotes apoptotic resistance. Conceivably, hypoxia-induced Akt activation promotes the survival of stem cells within hypoxia niches, regenerating cells within ischemic tissues and wounds, and cancer cells within hypoxic tumors. In a *VHL*-deficient ccRCC setting, accumulation of HIFα and activated Akt are likely to be integrated to promote renal carcinogenesis and metastasis (*30*). This view provides further support for targeting phosphatidylinositol 3-kinase and/or Akt to treat pVHL-defective kidney cancers specifically and as a way to chemosensitize hypoxic tumors generally.

REFERENCES AND NOTES

1. F. Chen *et al.*, *Hum. Mutat.* **5**, 66–75 (1995).
2. L. Gossage, T. Eisen, E. R. Maher, *Nat. Rev. Cancer* **15**, 55–64 (2015).
3. W. Y. Kim, W. G. Kaelin, *J. Clin. Oncol.* **22**, 4991–5004 (2004).
4. G. V. Thomas *et al.*, *Nat. Med.* **12**, 122–127 (2006).
5. G. Hudes *et al.*, *N. Engl. J. Med.* **356**, 2271–2281 (2007).
6. J. B. Brugarolas, F. Vazquez, A. Reddy, W. R. Sellers, W. G. Kaelin Jr., *Cancer Cell* **4**, 147–158 (2003).
7. M. Laplante, D. M. Sabatini, *Cell* **149**, 274–293 (2012).
8. M. Hager *et al.*, *J. Cell. Mol. Med.* **13** (8B), 2181–2188 (2009).
9. A. P. Young *et al.*, *Nat. Cell Biol.* **10**, 361–369 (2008).
10. M. Aoki, O. Batista, A. Bellacosa, P. Tsichlis, P. K. Vogt, *Proc. Natl. Acad. Sci. U.S.A.* **95**, 14950–14955 (1998).
11. E. Maltepe, J. V. Schmidt, D. Baunoch, C. A. Bradfield, M. C. Simon, *Nature* **386**, 403–407 (1997).
12. P. H. Maxwell *et al.*, *Nature* **399**, 271–275 (1999).
13. J. H. Min *et al.*, *Science* **296**, 1886–1889 (2002).
14. K. M. Lonergan *et al.*, *Mol. Cell. Biol.* **18**, 732–741 (1998).
15. M. Ohh *et al.*, *Nat. Cell Biol.* **2**, 423–427 (2000).
16. L. Li *et al.*, *Mol. Cell. Biol.* **27**, 5381–5392 (2007).
17. W. C. Hon *et al.*, *Nature* **417**, 975–978 (2002).
18. M. Ivan *et al.*, *Science* **292**, 464–468 (2001).
19. P. Jaakkola *et al.*, *Science* **292**, 468–472 (2001).
20. F. Yu, S. B. White, Q. Zhao, F. S. Lee, *Proc. Natl. Acad. Sci. U.S.A.* **98**, 9630–9635 (2001).
21. H. Zhang *et al.*, *Cancer Cell* **11**, 407–420 (2007).
22. D. Huang *et al.*, *Cell Reports* **8**, 1930–1942 (2014).
23. J. D. Carpten *et al.*, *Nature* **448**, 439–444 (2007).
24. W. Luo *et al.*, *Cell* **145**, 732–744 (2011).
25. X. Zheng *et al.*, *Genes Dev.* **28**, 1429–1444 (2014).
26. J. Li *et al.*, *Nature* **420**, 716–717 (2002).
27. T. A. Millward, S. Zolnierowicz, B. A. Hemmings, *Trends Biochem. Sci.* **24**, 186–191 (1999).
28. J. H. Zhang *et al.*, *Anal. Biochem.* **271**, 137–142 (1999).
29. E. Cerami *et al.*, *Cancer Discov.* **2**, 401–404 (2012).
30. B. Gan *et al.*, *Cancer Cell* **18**, 472–484 (2010).

ACKNOWLEDGMENTS

We thank B. North, L. Wan, and other Wei laboratory members for critical reading of the manuscript; W. Yu for his critical help in providing the triple mutant form of VHL to analyze the critical amino acids in proline-hydroxylation binding pocket of VHL that mediates its interaction with hydroxylated Akt1; as well as members of Kaelin, Zhang, Toker, and Cheng laboratories for helpful discussions. J.G. is an NRSA T32 trainee and supported by 5T32HL007893-17. W.W. is an ACS research scholar. This work was supported in part by NIH grants (W.W., GM094777; W.W. and A.T., CA177910; and J.A., 1S10OD010612, 5P01CA120964, and 5P30CA006516).

SUPPLEMENTARY MATERIALS

www.sciencemag.org/content/353/6302/929/suppl/DC1
Materials and Methods
Figs. S1 to S19
References (*31*–*38*)

20 October 2015; accepted 29 October 2015
10.1126/science.aad5755

Downloaded from http://science.sciencemag.org/ on September 3, 2016

VIROLOGY

Discovery of a proteinaceous cellular receptor for a norovirus

Robert C. Orchard,[1]* Craig B. Wilen,[1]* John G. Doench,[2] Megan T. Baldridge,[1] Broc T. McCune,[1] Ying-Chiang J. Lee,[1] Sanghyun Lee,[1] Shondra M. Pruett-Miller,[3] Christopher A. Nelson,[1] Daved H. Fremont,[1] Herbert W. Virgin[1]†

Noroviruses (NoVs) are a leading cause of gastroenteritis globally, yet the host factors required for NoV infection are poorly understood. We identified host molecules that are essential for murine NoV (MNoV)–induced cell death, including CD300lf as a proteinaceous receptor. We found that CD300lf is essential for MNoV binding and replication in cell lines and primary cells. Additionally, *Cd300lf*$^{-/-}$ mice are resistant to MNoV infection. Expression of CD300lf in human cells breaks the species barrier that would otherwise restrict MNoV replication. The crystal structure of the CD300lf ectodomain reveals a potential ligand-binding cleft composed of residues that are critical for MNoV infection. Therefore, the presence of a proteinaceous receptor is the primary determinant of MNoV species tropism, whereas other components of cellular machinery required for NoV replication are conserved between humans and mice.

Noroviruses (NoVs) are nonenveloped positive-sense RNA viruses (*1*, *2*). Because of the strict species tropism of viruses in the NoV genus and the lack of robust replication of human norovirus (HNoV) in animal models, murine norovirus (MNoV) has emerged as a model system to uncover basic mechanisms of NoV biology in vitro and in vivo (*1*, *3*–*8*). MNoV can establish persistent enteric infection, enabling studies of the interplay between viral persistence, resident enteric microorganisms, and the host immune system (*4*–*6*). The capacity of HNoV and MNoV to bind cells and the susceptibility of humans to HNoV have been linked to expression of cell-surface and secreted carbohydrates (*1*, *9*–*13*), whereas another member of the Caliciviridae family uses a proteinaceous receptor (*14*, *15*). Host factors, including receptors required for NoV infection and pathogenesis, have largely defied molecular identification; their discovery would aid in understanding mechanisms of NoV replication, vaccination, species tropism, and enteric viral persistence. To identify host molecules required for MNoV infection, we undertook an unbiased forward genetic approach (fig. S1).

MNoV replicates and induces cell death in murine macrophage-like cells, including the microglial BV2 cell line, allowing the identification of genes essential for MNoV replication by means of CRISPR-Cas9 technology. We introduced four independent genome-wide subpools of single-guide RNAs (sgRNAs) from the murine Asiago library into BV2 cells stably expressing Cas9 and then infected the cells with MNoV strains that either cause acute systemic infection (MNoV^{CW3}) or persistent enteric infection (MNoV^{CR6}) (*16*–*18*). sgRNA sequences from the surviving cells were sequenced and analyzed using the STARS gene-ranking algorithm (Fig. 1A) (*17*). sgRNAs targeting *Cd300lf* (CLM-1, CMRF35, MAIR-V, and LMIR3), a gene that encodes a cell-surface immunoglobulin (Ig) domain–containing molecule within a family of proteins involved in binding lipids, were most significantly enriched for both MNoV strains (Fig. 1A and tables S1 to S3) (*19*). We generated two independent BV2ΔCD300lf clones (where the delta signifies disruption of the *Cd300lf* gene); the growth of MNoV^{CW3} and MNoV^{CR6} was abolished in both clones, whereas the replication of other viruses was unaffected (Fig. 1B and fig. S2). We also validated the importance of several additional molecules that were predicted by our screen to play a role in MNoV-induced cell death (Fig. 1A and fig. S3). Taken together, these data provide a systematic overview of the molecules required for NoV replication in these cells.

We selected CD300lf for further analysis because of its cell-surface expression and the importance of viral receptors in conferring permissiveness for viral replication and species tropism. Transfection of MNoV^{CW3} RNA into BV2ΔCD300lf cells was sufficient to restore MNoV^{CW3} production, demonstrating that CD300lf is essential for viral entry (Fig. 2A). Preincubation of cells with a polyclonal antibody targeting CD300lf (α-CD300lf) blocked MNoV^{CW3}-induced cytopathic effects in BV2 cells (Fig. 2B). Similarly, incubating MNoV^{CW3} with recombinant CD300lf ectodomain (sCD300lf) neutralized MNoV^{CW3}-induced cytopathic effects, whereas annexin V or phosphoserine treatment had no effect (Fig. 2C and fig. S4). Similar results were obtained for infection of the B cell line M12, bone marrow–derived dendritic cells, and bone marrow–derived macrophages, indicating

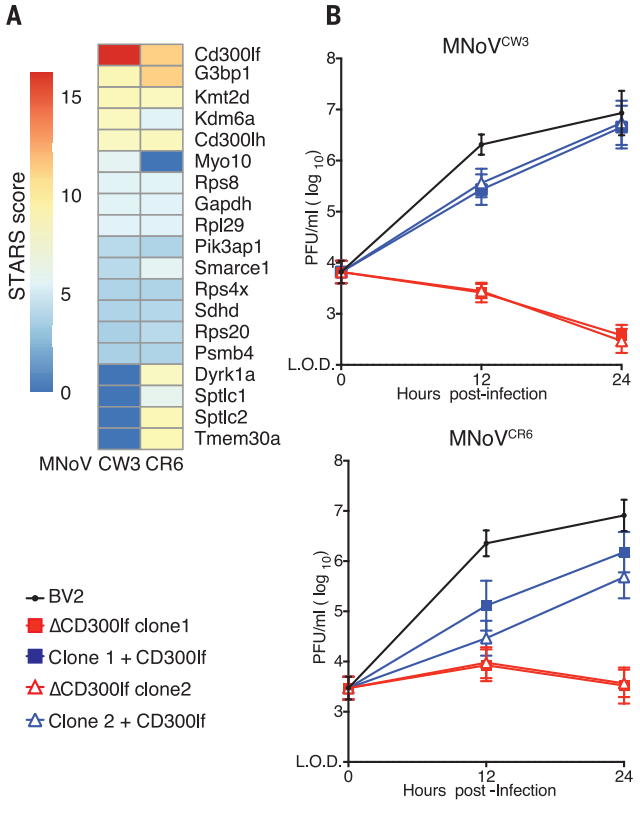

Fig. 1. CRISPR screen identifies CD300lf as necessary for MNoV infection. (**A**) A heat map showing enrichment of genes in the two indicated conditions. Genes are color-coded on the basis of their STARS score. (**B**) Wild-type BV2 cells and two independently derived CD300lf-deficient clones (clone 1 and clone 2) transduced with an empty vector or a vector expressing CD300lf were challenged with MNoV^{CW3} (top) or MNoV^{CR6} (bottom) at a multiplicity of infection (MOI) of 0.05. Viral production was assessed by plaque assay (PFU, plaque-forming unit). Shown are means ± SEM for data pooled from three independent experiments. L.O.D., limit of detection.

[1]Department of Pathology and Immunology, Washington University School of Medicine, St. Louis, MO 63110, USA. [2]Broad Institute of MIT and Harvard, Cambridge, MA 02142, USA. [3]Genome Engineering and iPSC Center, Department of Genetics, Washington University School of Medicine, St. Louis, MO 63110, USA.
*These authors contributed equally to this work. †Corresponding author. Email: virgin@wustl.edu

Downloaded from http://science.sciencemag.org/ on September 3, 2016

the essential role of CD300lf in multiple cell types (Fig. 2D). These data together indicate that interactions between MNoV and CD300lf are essential for MNoV infection.

To directly test whether CD300lf functions as a binding receptor for MNoV, we analyzed the attachment of MNoV^{CW3} to BV2 cells on ice. BV2ΔCD300lf cells were impaired in MNoV^{CW3} binding (Fig. 2E). Additionally, treating BV2 cells with α-CD300lf or preincubating virus with sCD300lf reduced MNoV binding (Fig. 2E). In BV2ΔCD300lf cells, binding of MNoV^{CW3} was

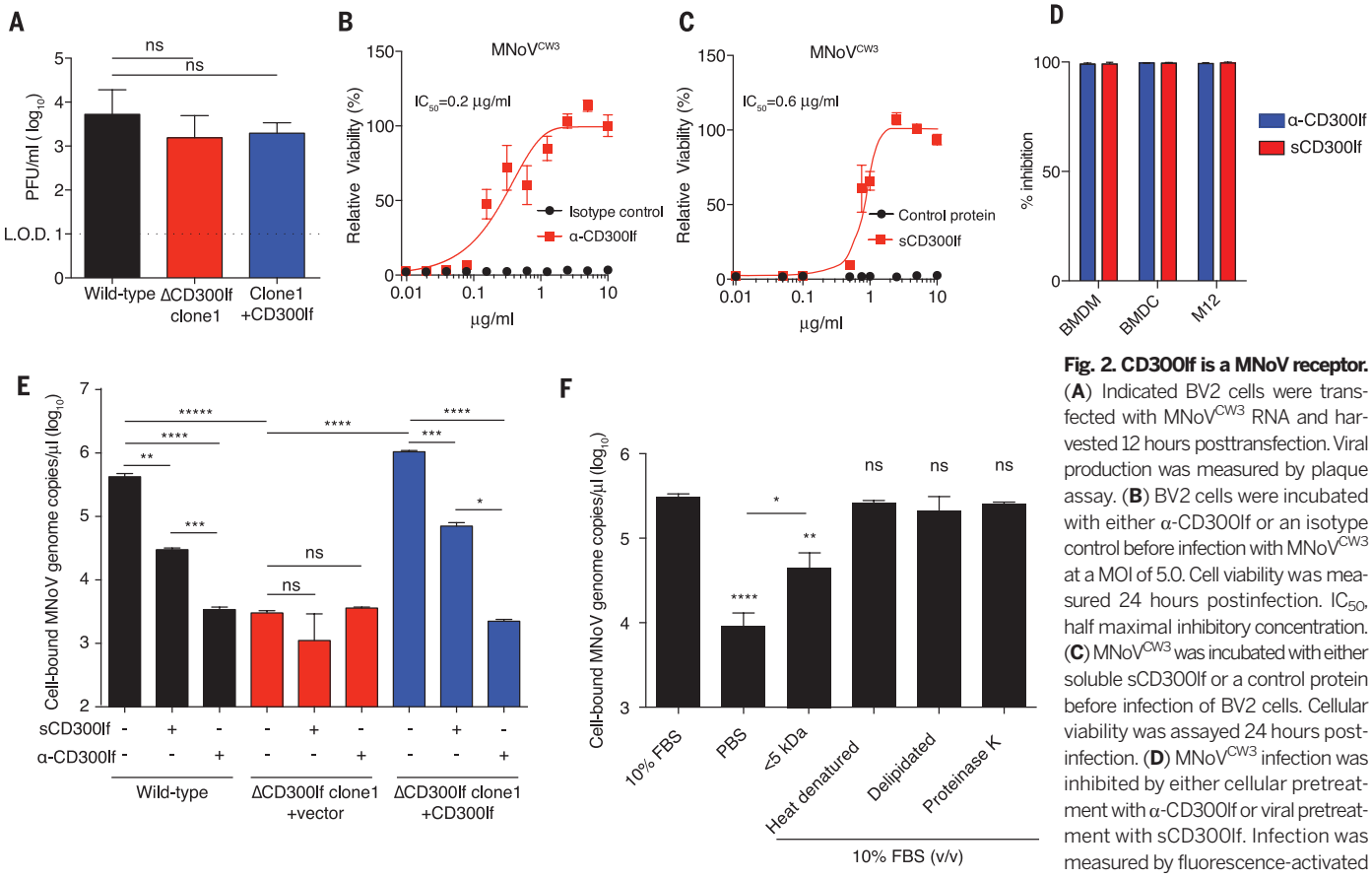

Fig. 2. CD300lf is a MNoV receptor. (**A**) Indicated BV2 cells were transfected with MNoV^{CW3} RNA and harvested 12 hours posttransfection. Viral production was measured by plaque assay. (**B**) BV2 cells were incubated with either α-CD300lf or an isotype control before infection with MNoV^{CW3} at a MOI of 5.0. Cell viability was measured 24 hours postinfection. IC_{50}, half maximal inhibitory concentration. (**C**) MNoV^{CW3} was incubated with either soluble sCD300lf or a control protein before infection of BV2 cells. Cellular viability was assayed 24 hours postinfection. (**D**) MNoV^{CW3} infection was inhibited by either cellular pretreatment with α-CD300lf or viral pretreatment with sCD300lf. Infection was measured by fluorescence-activated cell sorting for intracellular MNoV NS1/2 expression, and inhibition is relative to an isotype control (for α-CD300lf) or control protein (for sCD300lf). BMDM, bone marrow–derived macrophage; BMDC, bone marrow–derived cell. (**E**) A representative MNoV^{CW3} binding assay in complete media to indicated BV2 cell lines, as assayed by quantitative polymerase chain reaction. Binding assays were performed when cells or virus were preincubated with α-CD300lf or sCD300lf, respectively. Data were analyzed by one-way analysis of variance (ANOVA) with Tukey's multiple comparison test; three independent experiments were performed in triplicate. (**F**) MNoV^{CW3} binding assay performed in phosphate-buffered saline (PBS) plus 10% fetal bovine serum (FBS) or derivatives as indicated. Data were analyzed by one-way ANOVA with Tukey's multiple comparison test; three independent experiments were performed in triplicate. Throughout, results are shown as means ± SEM for data pooled from three independent experiments [except in (E), where results are shown from one representative experiment]. ns, not statistically significant; *$P < 0.05$; **$P < 0.01$; ***$P < 0.001$; ****$P < 0.0001$.

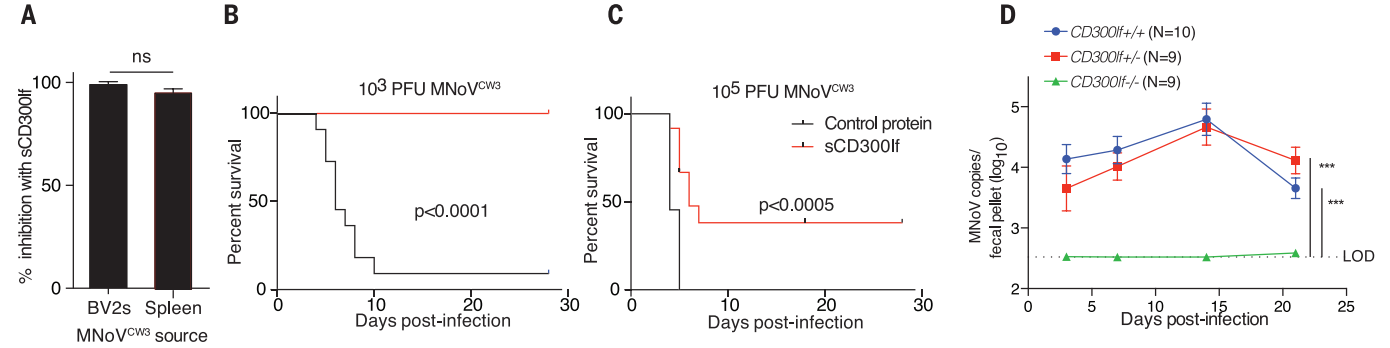

Fig. 3. CD300lf is a physiological MNoV receptor. (**A**) MNoV^{CW3} harvested from the spleens of BL6/J mice or derived from BV2 cells was preincubated with sCD300lf before plaque assay. Inhibition is relative to a control protein. Shown are means ± SEM for data pooled from three independent experiments. (**B** and **C**) Survival of *Stat1*$^{-/-}$ mice after challenge with (B) 10^3 PFU or (C) 10^5 PFU of MNoV^{CW3} preincubated with either sCD300lf or control protein. Data were analyzed by a log-rank test ($n = 11$ mice per cohort, combined from three independent experiments). (**D**) *Cd300lf*$^{-/-}$ and littermate control mice were challenged with 10^6 PFU of MNoV^{CR6} perorally. Fecal shedding of MNoV genomes was monitored for 21 days postchallenge. Data were analyzed by repeated measures ANOVA; shown are means ± SEM ($n = 9$ or 10 mice per cohort, combined from two independent experiments). ***$P < 0.001$.

Downloaded from http://science.sciencemag.org/ on September 3, 2016

not further inhibited by α-CD300lf or by premixing virus with sCD300lf (Fig. 2E). These results show that CD300lf mediates viral binding and is a functional receptor for MNoV.

Previous reports have suggested that carbohydrates facilitate the binding of MNoV and HNoV to host cells and control the susceptibility of humans to HNoV infection (*1*, *9*–*11*). Therefore, we assessed the relative contribution of carbohydrates to MNoV attachment and infection. Unexpectedly, mice deficient in *Fut2*, which controls histo-blood group antigen (HBGA) secretor status, had similar MNoV loads to those of wild-type littermate controls (fig. S5A). Also, treating cells with the mannosidase I inhibitor kifunensine significantly reduced cell-surface carbohydrates but did not significantly alter MNoV^{CW3} binding to cells (fig. S5, B and C). These data suggest that, within the sensitivity of these assays, MNoV binding and infection are dependent on CD300lf but not on protein-associated glycans or secretor status.

In addition to CD300lf, we discovered that efficient MNoV binding to cells requires a cofactor found in serum (Fig. 2F). The cofactor is present in delipidated serum and is resistant to proteinase K and heat denaturation (95°C; Fig. 2F). Size fractionation of serum indicates that the cofactor is present in fractions with an average molecular weight of less than 5000 Da (Fig. 2F). Thus, the serum cofactor is most likely a small nonproteinaceous heat-stable molecule that interacts with MNoV and/or CD300lf to facilitate cellular binding.

Next, we sought to assess the physiologic relevance of MNoV and CD300lf interactions. MNoV isolated from the spleens of MNoV^{CW3}-infected mice remained sensitive to sCD300lf inhibition, indicating that sCD300lf neutralizes MNoV regardless of the source of the virus (Fig. 3A). To test the role of CD300lf and MNoV interactions in vivo, we incubated MNoV^{CW3} with either sCD300lf or a control protein before infection of *Stat1*$^{-/-}$ mice, which succumb to MNoV^{CW3} infection. In a dose-dependent manner, sCD300lf preincubation was able to protect from MNoV-induced lethality (Fig. 3, B and C). Last, we generated *Cd300lf*$^{-/-}$ mice to test the in vivo role of CD300lf in MNoV infection. *Cd300lf*$^{-/-}$ mice were resistant to MNoV^{CR6} infection compared with littermate controls (Fig. 3D). These data demonstrate that CD300lf is the primary physiological receptor for MNoV in vivo.

MNoV replicates in murine dendritic cells, macrophages, and B cells, but not in epithelial cells or human cells because of a restriction at viral entry (*20*, *21*). Therefore, we tested whether expression of murine CD300lf was sufficient to confer susceptibility of HeLa cells to MNoV. As expected, HeLa cells transfected with a control plasmid were unable to support MNoV replication (Fig. 4A). In contrast, HeLa cells expressing

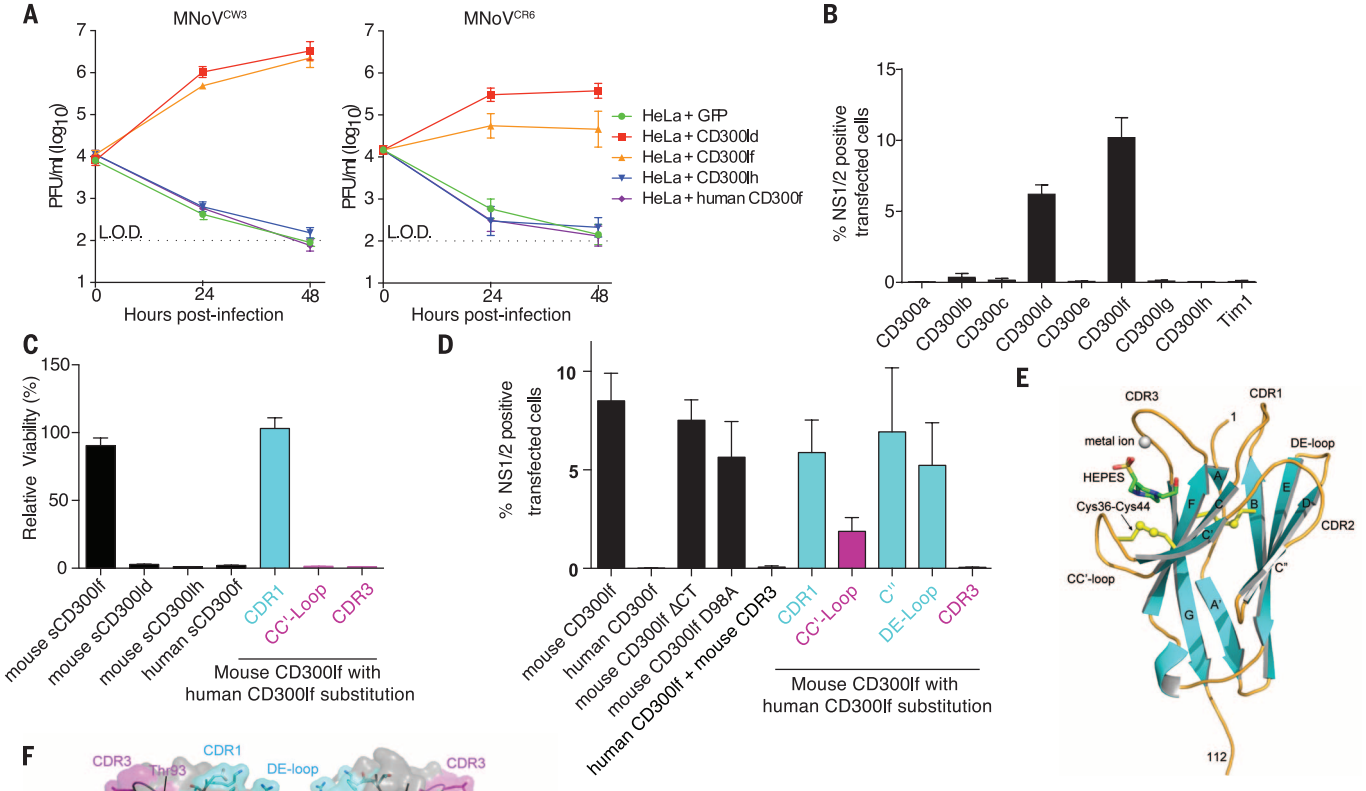

Fig. 4. Structure-guided mapping identifies the CC′ loop and CDR3 of CD300lf as critical for MNoV infection. (**A**) HeLa cells transiently transfected with indicated constructs were infected with either MNoV^{CW3} (left) or MNoV^{CR6} (right) at a MOI of 0.05. Viral production was measured by plaque assay at the indicated time points. GFP, green fluorescent protein. (**B**) HeLa cells transiently transfected with indicated CD300 constructs or TIM1 were infected with MNoV^{CW3} at a MOI of 5.0 and analyzed for expression of CD300 or TIM1 (FLAG) and MNoV NS1/2. (**C**) Recombinant ectodomains of indicated CD300 molecules (10 μg/ml) were preincubated with MNoV^{CW3} at a MOI of 5.0 before infection of BV2 cells. Cellular viability was assayed 24 hours postinfection. (**D**) HeLa cells transiently transfected with indicated CD300 constructs were infected with MNoV^{CW3} at a MOI of 5.0 and analyzed for expression of CD300 (FLAG) and MNoV NS1/2. CD300lfΔCT, CD300lf with truncation of cytoplasmic domain. In (A) to (D), results are shown as means ± SEM for data pooled from three independent experiments. (**E**) Ribbon diagram of murine CD300lf ectodomain with bound metal ion and Hepes. The β-sheets (cyan) are lettered as a canonical V-type Ig domain with the positions of the CDR-equivalent loops indicated. The disulfide bonds are shown in yellow. Numbers indicate amino acid positions. (**F**) Mapping of mutational results onto the CD300lf surface. Displayed in cyan are murine CD300lf residues replaced by human equivalent residues in CDR1, C″, and DE loop that had no effect on infection. The CC′ loop and CDR3 mutations that diminished viral infection are shown in magenta.

Downloaded from http://science.sciencemag.org/ on September 3, 2016

murine but not human CD300lf were susceptible to MNoV (Fig. 4A). These results indicate that CD300lf expression is sufficient for MNoV growth in human cells and suggest that differences between human and murine CD300lf could contribute to MNoV species restriction.

In mice, there are eight CD300 family members (*22*). Therefore, we sought to determine whether other CD300 molecules are capable of functioning as MNoV receptors. After transfection into HeLa cells, only CD300lf and CD300ld conferred susceptibility to MNoV, whereas the expression of other CD300 family members or of the unrelated phosphatidylserine binding protein TIM1 was unable to support MNoV infection (Fig. 4B and fig. S6) (*23*). We further confirmed that expression of CD300lf or CD300ld, but not CD300lh, was sufficient for viral replication in human cells (Fig. 4A). However, in contrast to murine CD300lf, the recombinant ectodomains of murine CD300ld, murine CD300lh, or human CD300lf failed to neutralize viral infection (Fig. 4C). Additionally, BV2ΔCD300ld cells are susceptible to MNoV infection, suggesting that CD300ld can act as a MNoV receptor when ectopically expressed, but it is not a universal requirement (fig. S7). However, we cannot exclude the possibility that CD300ld may play a role in viral tropism in some circumstances in vivo. Experiments in *Cd300lf*$^{-/-}$ mice indicate that this putative role is not essential for intestinal infection or shedding.

We next sought to define the mechanism for MNoV entry via CD300lf and to determine how MNoV discriminates between mouse and human CD300lf proteins. Importantly, the intracellular domain of CD300lf was not required to make HeLa cells susceptible, indicating that species tropism is determined by the ectodomain (Fig. 4D). We determined the crystal structure of the CD300lf ectodomain at 1.6 Å resolution (Fig. 4E and table S4). Densities corresponding to a bound Hepes molecule, which was present in the purification buffers, and a coordinated metal were visible in a surface cleft formed between the CDR3 loop and the β-hairpin turn that connects the C-C′ β-strands. CD300lf has been reported to mediate the phagocytosis of apoptotic cells through the calcium-dependent binding of lipids (*24*–*26*). Hepes has chemical resemblance to a phospholipid headgroup (fig. S8). Our structure also reveals a metal coordinated primarily by CD300lf Asp^{98} and two CDR3 loop carbonyl oxygens. Although mutation of murine CD300lf Asp^{98} has been shown to disrupt apoptotic cell-surface binding, this mutant still allows MNoV^{CW3} infection of HeLa cells, suggesting that viral entry can occur in the absence of bound metal (Fig. 4D and fig. S8) (*25*, *27*). The Ig domains of murine and human CD300lf share 59% sequence identity, and structurally the largest variation occurs in CDR3 and the CC′ loop (figs. S9 and S10) (*27*). Individual substitutions of human CC′ loop and CDR3 into murine CD300lf diminished and abolished MNoV^{CW3} infection of HeLa cells, respectively (Fig. 4, D and F). Additionally, purified recombinant proteins harboring CC′ loop and CDR3 human sequences failed to neutralize MNoV infection (Fig. 4C and fig. S11). However, the reciprocal CDR3 mutation (murine CDR3 into human CD300lf) was not sufficient for MNoV infection (Fig. 4D). Independently comparing murine CD300lf and CD300lh also indicated that the CD300lf CC′ loop and CDR3 sequences are necessary but not sufficient for receptor utilization by MNoV (fig. S12). These data provide a framework for understanding how MNoV discriminates between CD300 family members.

Our work establishes that CD300lf is a functional MNoV receptor that mediates binding to the cell surface and is both necessary and sufficient for viral entry and replication in vitro and in vivo. Because MNoV serves as a model system for understanding how viruses persist and shape the immune system, the modulation of receptor availability, either genetically or chemically, may foster understanding of immunomodulation, persistence, and tropism of MNoV. This work also enables the future study of MNoV replication in human cells, which may uncover novel mechanisms of viral replication and pathogenesis and allow a direct identification and mechanistic dissection of the cellular factors required for NoV replication across species. Additionally, our work has implications for understanding HNoV infections. HNoV binds to HBGA, and susceptibility to HNoV is correlated with host HBGA status; the studies that show this (*12*, *13*) are the foundation for the hypothesis that glycans are HNoV receptors (*9*). However, HBGA alone cannot explain species tropism or the entry barrier for HNoV. In contrast, our data indicate that murine CD300lf is sufficient to explain tropism for MNoV and more broadly suggest the possibility that other NoVs use proteinaceous receptors in addition to small molecule cofactors that are present in serum or other biological fluids. It is intriguing that CD300 molecules can bind a range of host lipids and bacterial products (*22*, *28*). It may therefore be that NoV cell and tissue tropism is determined in a combinatorial fashion by proteinaceous receptors interacting with permissiveness cofactors that are present at different sites.

REFERENCES AND NOTES

1. S. M. Karst, C. E. Wobus, I. G. Goodfellow, K. Y. Green, H. W. Virgin, *Cell Host Microbe* **15**, 668–680 (2014).
2. R. I. Glass, U. D. Parashar, M. K. Estes, *N. Engl. J. Med.* **361**, 1776–1785 (2009).
3. M. K. Jones *et al.*, *Science* **346**, 755–759 (2014).
4. E. Kernbauer, Y. Ding, K. Cadwell, *Nature* **516**, 94–98 (2014).
5. M. T. Baldridge *et al.*, *Science* **347**, 266–269 (2015).
6. T. J. Nice *et al.*, *Science* **347**, 269–273 (2015).
7. K. L. Newman, J. S. Leon, *Eur. J. Immunol.* **45**, 2742–2757 (2015).
8. S. Taube *et al.*, *MBio* **4**, e00450-13 (2013).
9. A. M. Hutson, R. L. Atmar, M. K. Estes, *Trends Microbiol.* **12**, 279–287 (2004).
10. A. M. Hutson, R. L. Atmar, D. Y. Graham, M. K. Estes, *J. Infect. Dis.* **185**, 1335–1337 (2002).
11. S. Taube *et al.*, *J. Virol.* **86**, 5584–5593 (2012).
12. L. Lindesmith *et al.*, *Nat. Med.* **9**, 548–553 (2003).
13. A. Kambhampati, D. C. Payne, V. Costantini, B. A. Lopman, *Clin. Infect. Dis.* **62**, 11–18 (2016).
14. R. J. Ossiboff, Y. Zhou, P. J. Lightfoot, B. V. Prasad, J. S. Parker, *J. Virol.* **84**, 5550–5564 (2010).
15. R. J. Ossiboff, J. S. Parker, *J. Virol.* **81**, 13608–13621 (2007).
16. D. W. Strong, L. B. Thackray, T. J. Smith, H. W. Virgin, *J. Virol.* **86**, 2950–2958 (2012).
17. J. G. Doench *et al.*, *Nat. Biotechnol.* **34**, 184–191 (2016).
18. T. J. Nice, D. W. Strong, B. T. McCune, C. S. Pohl, H. W. Virgin, *J. Virol.* **87**, 327–334 (2013).
19. D. H. Chung *et al.*, *J. Immunol.* **171**, 6541–6548 (2003).
20. C. E. Wobus *et al.*, *PLOS Biol.* **2**, e432 (2004).
21. V. K. Ward *et al.*, *Proc. Natl. Acad. Sci. U.S.A.* **104**, 11050–11055 (2007).
22. F. Borrego, *Blood* **121**, 1951–1960 (2013).
23. N. Kobayashi *et al.*, *Immunity* **27**, 927–940 (2007).
24. K. Izawa *et al.*, *Immunity* **37**, 827–839 (2012).
25. L. Tian *et al.*, *Nat. Commun.* **5**, 3146 (2014).
26. S. C. Choi *et al.*, *J. Immunol.* **187**, 3483–3487 (2011).
27. J. A. Márquez *et al.*, *J. Mol. Biol.* **367**, 310–318 (2007).
28. J. P. Cannon, M. O'Driscoll, G. W. Litman, *Immunogenetics* **64**, 39–47 (2012).

ACKNOWLEDGMENTS

We thank S. Karst and M. Diamond for providing valuable reagents and S. Handley and C. Desai for their helpful discussion and figure generation. We thank the Alvin J. Siteman Cancer Center at Washington University School of Medicine and Barnes-Jewish Hospital in St. Louis, Missouri, for the use of the Genome Engineering and iPSC Center. CD300 constructs, cell lines, and mice are available from H.W.V. under a material transfer agreement with Washington University. The data from this study are tabulated in the main paper and in the supplementary materials. H.W.V., D.H.F., R.C.O., C.B.W., and C.A.N. are inventors on a patent application submitted by Washington University entitled "Receptor for norovirus and uses thereof" (U.S. Provisional Application 62/301,965). The atomic coordinates are deposited in the Protein Data Bank under accession code 5FFL. The Siteman Cancer Center is supported in part by National Cancer Institute Cancer Center Support Grant P30 CA091842. This work was supported by NIH grants U19 AI109725 (H.W.V.), 1F31CA177194 (B.T.M.), and 5T32CA009547 (M.T.B.).

SUPPLEMENTARY MATERIALS

www.sciencemag.org/content/353/6302/933/suppl/DC1
Materials and Methods
Figs. S1 to S12
Tables S1 to S4
References (*29*–*39*)

19 December 2015; accepted 29 July 2016
Published online 18 August 2016
10.1126/science.aaf1220

Downloaded from http://science.sciencemag.org/ on September 3, 2016

REVEAL GREATER COVERAGE DEPTH IN WHOLE EXOME SEQUENCING

Achieve greater coverage depth from less sequencing through the enhanced coverage of the new **SeqCap EZ MedExome Target Enrichment Kit** for whole exome sequencing. Rely on a design developed to enrich the entire exome (Figure 1), but particularly optimized for analyzing regions of medical relevance (Figure 2) in research studies.

- **Focus on genomic regions that really matter**
  For disease-associated genes, 98% of bases are covered at ≥20X depth.
- **Call variants with confidence**
  Detect SNPs with 98% sensitivity and >99% specificity for SNP allele classification.
- **Gain greater efficiency at minimal cost**
  Reduce sequencing cost through uniform coverage (Figures 1 and 3) and fully supported multiplexing protocols.

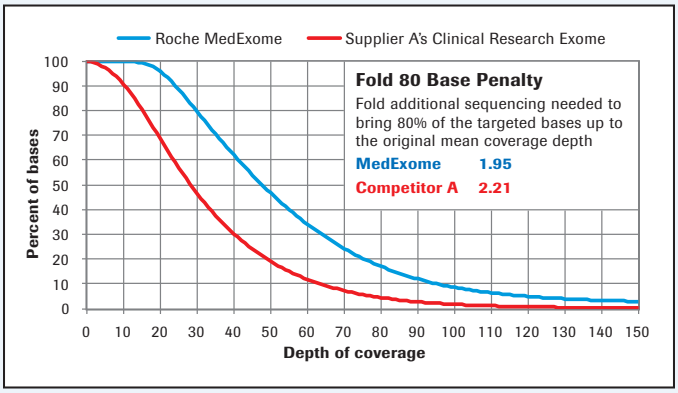

Figure 1. Roche's SeqCap EZ MedExome kit demonstrated sustained coverage at 100% and more uniform coverage than Supplier A's Clinical Research Exome. Fold 80 base penalty calculation shows more uniform capture for the SeqCap EZ MedExome Kit. This graph is of one representative sample from one 6-plex capture per product. For Supplier A's product, the targets are unpadded. SeqCap EZ MedExome kit target reflects empirical target across all metrics. All reads were subsampled to 60 million for assessment.*

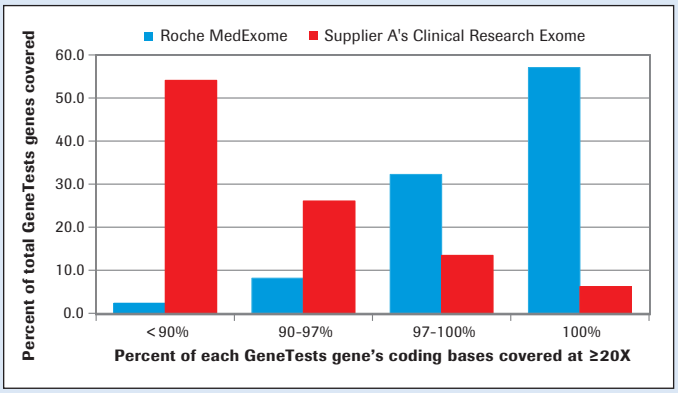

Figure 2. With SeqCap EZ MedExome, 53% of medically relevant genes are covered at 100% (≥20X coverage) vs. 6% by Supplier A's Clinical Research Exome. Percentage of bases covered at ≥20X for each consolidated target was determined using GATK (DepthOfCoverage), summarized by gene. Supplier A kit's data was generated by a third-party sequencing service provider, following Supplier A's protocol. All reads were subsampled to 60 million for assessment, then subjected to the same bioinformatics pipeline for analysis.*

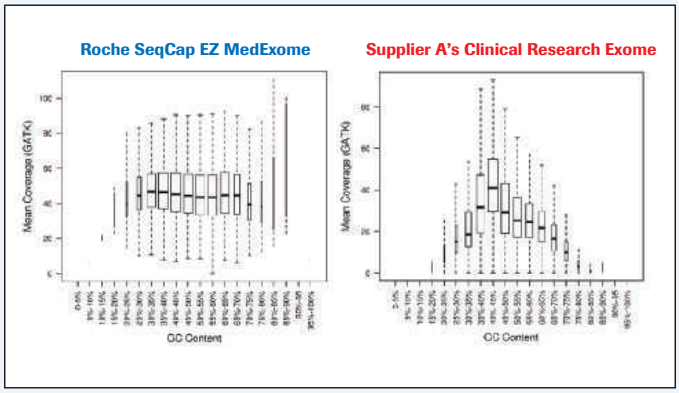

Figure 3. SeqCap EZ MedExome shows reduced GC bias in sequencing coverage with uniform coverage over a broad range of GC content. One-hundred nanograms of extracted NA12898 DNA was subjected to performance evaluation by both kits. Performance was determined post-enrichment following SeqCap EZ User's Guide v5.1. Supplier A's kit data was generated by a 3rd party service provider following vendor's protocol. All reads were subsampled to 60 million for assessment. Sequencing reads were subjected to the same bioinformatics pipeline for analysis. GC composition of all consolidated target regions (empirical target for MedExome, unpadded target for Supplier A) was determined and plotted against mean depth of coverage calculated by GATK DepthOfCoverage for all consolidated target regions.*

Reveal more about the exome

Learn more about how the **SeqCap EZ MedExome Target Enrichment Kit** can improve your whole exome sequencing. Visit ***sequencing.roche.com/medexome.html*** or call **800-262-4911**.

* Roche data on file.

For patent license limitations for individual products please refer to:
www.technical-support.roche.com

NIMBLEGEN and SEQCAP are trademarks of Roche.
All other product names and trademarks are the property of their respective owners.

© 2016 Roche PP-US-05710-0816

Roche Diagnostics Corporation
9115 Hague Road
Indianapolis, Indiana 46256

For life science research only.
Not for use in diagnostic procedures.

AMERICAN ASSOCIATION FOR THE ADVANCEMENT OF SCIENCE

BE THE CORE
MIND SPIRIT FACE
HEART REACH
CENTER VOICE
OF SCIENCE.

AAAS members harness the power of scientific thinking to help tackle complex, global challenges.

Join the community of scientists, engineers, and educators whose work impacts millions.

How will YOU make your mark in science?

Join AAAS today.
www.aaas.org/join

AAAS

Be Among the First to Publish in *Science Robotics*

Image: jim/AdobeStock

NOW ACCEPTING MANUSCRIPTS

ScienceRobotics.org

Science Robotics is a unique journal created to help advance the research and development of robotics for all environments. *Science Robotics* will provide a much-needed central forum to share the latest technological discoveries and to discuss the field's critical issues.

Join in the excitement for the Fall 2016 debut!

Science Robotics

AAAS

pH Electrodes

YSI showcases a strong set of pH measuring options for the lab. The IoLine electrodes host a unique iodine/iodide reference system with a patented three-chamber reservoir system. IoLine electrodes offer unbeatable stability, fast response times, and high accuracy at a higher speed compared to traditional silver/silver chloride (Ag/AgCl) reference systems. They have a 100% metal-ion-free reference system, and are ideal for Tris buffer solutions in complex biotech applications such as immunoassays. YSI TruLine Ion Selective Electrodes offer 15 refillable electrodes for 16 different parameters. Each electrode comes supplied with reference fill solution, an ionic strength adjustor, and a bottle of calibration standard, so the electrode can be used right away. Backed by a three-year warranty, TruLab and MultiLab meters are easy to use and come in single, dual, or triple channels. The MultiLab meters are available with Intelligent Digital Sensor technology, internal memory, and an optional built-in printer.

Xylem
For info: 978-778-1010
www.xylem.com

In-Vacuum Amplifier

The McPherson 671MX amplifier is a high-vacuum compatible, current-to-voltage converting amplifier developed specifically for use with vacuum ultraviolet (VUV) silicon photodiodes. With its integral socketed photodiode mount, the combination detector/amplifier hybrid can be used to measure small photogenerated currents with resolutions of 10 femptoampheres and dynamic ranges of four orders of magnitude. The 671MX consists of a very low-noise operation amplifier with a selectable feedback resistor. The feedback resistor is also socketed and may be changed to match the gain and dynamic range requirements of any experiment. McPherson VUV series photodiodes are used for the detection of UV, extreme UV, and X-ray (wavelength range 1,100 nm to .124 nm, energy range 1.13 eV to 1 keV) photons. All components are low tolerance, resulting in consistent current-to-voltage transfer characteristics with minimal offset voltage. It is sold without the photodiode and ±15-V power supply required for operation.

McPherson
For info: 978-256-4512
www.mcphersoninc.com

Milling Platform

The Fitzpatrick Company and Quadro Engineering Corp. have launched the Scalable Lab System (SLS), the latest incarnation of their lab-scale L1A FitzMill and U5 Comil combination package. The SLS includes five material processing and milling solutions: Fitzpatrick's FitzMill L1A Comminutor, and Quadro's U5 and U5 High Efficiency Comil, FlexSift S5, and H5 High Energy API Comil. Operators can alternate between multiple milling solutions in minutes, due to its innovative tri-clamp design. The equipment's head interchangeability makes it suitable for milling and/or wet material conditioning, as a stand-alone, or to complement lab-scale wet granulation systems. It enables operators to process samples as small as 5 g with minimal loss or product retention, and can achieve >50 kg/hr milling for certain products. The SLS utilizes "smart-detect"—a feature that automatically ensures the appropriate speed range is fixed by recognizing the head being installed—to ensure that scalability to production machines is maintained.

The Fitzpatrick Company
For info: 630-530-3333
www.fitzmill.com

Comet Assay Microplate

The new 96-well CometChip System enables reproducible and sensitive measurements of DNA damage in human cells and provides the necessary throughput for genotoxicity testing, drug development, epidemiological studies, and clinical assays. Instead of being randomly dispersed in agarose on a glass slide as in the traditional Comet Assay, cells in the CometChip are captured on an array of agarose microwells. Each well of the CometChip contains approximately 400 microwells of 30-micron diameter, displayed in a defined pattern and depth that causes the captured test cells to reside in a single plane. A single 96-well CometChip can produce 20,000 data points per chip, based on an average of 208 cells imaged per well. With a capacity for three CometChips per run, the output for just two runs per day is 120,000 data points. The Comet Analysis Software can analyze data from these 120,000 cells and generate a report in under 20 minutes.

AMS Biotechnology
For info: 44-(0)-1235-828200
www.amsbio.com

PTR-MS Autosampler

The real-time measuring capability of a proton transfer reaction-mass spectrometry (PTR-MS) trace gas analyzer is ideally suited for continuous volatile organic compound (VOC) monitoring, but also for rapid analysis of discrete samples within seconds. The new IONICON autosampler for PTR-MS enables automated screening of hundreds of sample vials. It can be loaded with multiple sample trays carrying up to 270 vials (20 mL) simultaneously, for liquid, solid, or gas samples. The benchtop autosampler allows for static and dynamic headspace measurements. A custom-made software controls the sampling process as well as the PTR-MS measurement for integrated and consistent data. Several preprogrammed sample treatment and analysis protocols can be further optimized for specific applications. This fully integrated, high-throughput system for VOC headspace analysis drastically reduces processing costs for larger batches of samples and provides high-quality data.

Ionicon
For info: +43-(0)-512-214-800
www.ionicon.com

Electronically submit your new product description or product literature information! Go to www.sciencemag.org/about/new-products-section for more information.

Newly offered instrumentation, apparatus, and laboratory materials of interest to researchers in all disciplines in academic, industrial, and governmental organizations are featured in this space. Emphasis is given to purpose, chief characteristics, and availability of products and materials. Endorsement by *Science* or AAAS of any products or materials mentioned is not implied. Additional information may be obtained from the manufacturer or supplier.

want new technologies?

antibodies
apoptosis
biomarkers
cancer
cytometry
data
diseases
DNA
epigenetics
genomics
immunotherapies
medicine
microbiomics
microfluidics
microscopy
neuroscience
proteomics
sequencing
toxicology
transcriptomics

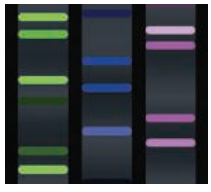

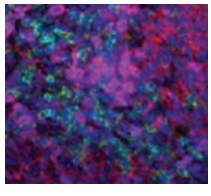

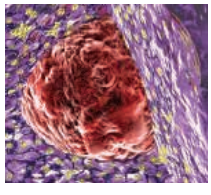

watch our webinars

Learn about the latest breakthroughs, new technologies, and ground-breaking research in a variety of fields. Our expert speakers explain their quality research to you and answer questions submitted by live viewers.

VIEW NOW!
webinar.sciencemag.org

Science
AAAS

Brought to you by the *Science*/AAAS Custom Publishing Office

@SciMagWebinars

Are your exosomes telling you everything they know?

Extracellular vesicles like exosomes can provide useful insights into cellular physiology and are a great source of circulating biomarkers. But are you getting all the information you can from them?

Let the experts at System Biosciences (SBI) help with our start-to-finish exosome profiling services:

Exo-NGS • Proteomics • Nanosight • Lipidomics

Just send us your samples, we'll take care of the rest.

Now offering new low pricing! Find out just how low—email us at services@systembio.com

SBI System Biosciences
Harnessing innovation to drive discoveries

There's only one Science

Science Careers Advertising

For full advertising details, go to ScienceCareers.org and click For Employers, or call one of our representatives.

Tracy Holmes
Worldwide Associate Director
Science Careers
Phone: +44 (0) 1223 326525

THE AMERICAS

E-mail: advertise@sciencecareers.org
Fax: +1 (202) 289 6742

Tina Burks
Phone: +1 (202) 326 6577

Nancy Toema
Phone: +1 (202) 326 6578

Online Job Posting Questions
Phone: +1 (202) 312 6375

EUROPE / INDIA / AUSTRALIA / NEW ZEALAND / REST OF WORLD

E-mail: ads@science-int.co.uk
Fax: +44 (0) 1223 326532

Sarah Lelarge
Phone: +44 (0) 1223 326527

Kelly Grace
Phone: +44 (0) 1223 326528

Online Job Posting Questions
Phone: +44 (0) 1223 326528

JAPAN

Katsuyoshi Fukamizu (Tokyo)
E-mail: kfukamizu@aaas.org
Phone: +81 3 3219 5777

Hiroyuki Mashiki (Kyoto)
E-mail: hmashiki@aaas.org
Phone: +81 75 823 1109

CHINA / KOREA / SINGAPORE / TAIWAN / THAILAND

Ruolei Wu
E-mail: rwu@aaas.org
Phone: +86 186 0082 9345

Danny Zhao
E-mail: dzhao@aaas.org
Phone: +86 131 4114 0012

All ads submitted for publication must comply with applicable U.S. and non-U.S. laws. *Science* reserves the right to refuse any advertisement at its sole discretion for any reason, including without limitation for offensive language or inappropriate content, and all advertising is subject to publisher approval. *Science* encourages our readers to alert us to any ads that they feel may be discriminatory or offensive.

ScienceCareers
FROM THE JOURNAL SCIENCE AAAS

ScienceCcareers.org

POSTDOCTORAL OPPORTUNITIES

MASTER OF BIOMEDICAL INFORMATICS, HARVARD MEDICAL SCHOOL

Program Description The program provides the intellectual framework for clinicians and biomedical scientists in the systematic and sound use of quantitative methods to increase agility with such methods in their respective domains. The program includes an intensive, hands-on quantitative boot camp, a range of foundational courses, and courses in emerging areas such as precision medicine, data science, and data visualization. All students are expected to complete a capstone research project and to participate in a longitudinal seminar series.

Who is this Program for? (1) Postdoctoral students who recognize the relevance of informatics to their research (2) MD's who are interested in qualifying for the subspecialty in clinical informatics 3)Medical students who would like to take a research year during their training to explore the importance of informatics in the practice of medicine Contact information to learn more about the program, please visit our website and email us with any questions through our 'Contact Us' page: **https://informaticstraining.hms.harvard.edu/**

Post-Doctoral Fellow, Research Technician, and Physician/Scientist Positions Available The Pathogenesis and Treatment of Microbial Sepsis

RESEARCH POSITIONS are open at the University of California, Santa Barbara for post-doctoral fellows, research technicians, and physician-scientists interested in studies of infectious disease and the complications of sepsis. The positions are with the laboratories of Drs. Jamey Marth and Michael Mahan, and are focused upon how protein glycosylation and glycoprotein remodeling control the aging and turnover of secreted proteins in modulating the coagulopathy and inflammation of microbial sepsis. Ideal candidates would have experience in infectious disease research, inflammatory biology, protein biochemistry, and proteomics. Training will be provided as necessary to include glycan linkage analyses. The project will include both mouse models and human patients involving collaborations between scientists and clinicians. Interested candidates should send their curriculum vitae and names of three personal references by email or regular mail to: **Katelyn Jerlinga, 9625 MCDB, University of California, Santa Barbara, CA 93106-9625. E-mail: kjerlinga@sbpdiscovery.org.**

University of California, Santa Barbara is an Equal Opportunity/Staff Affirmative Action Employer that values a diverse workforce.

POSTDOCTORAL RESEARCH FELLOW

The Center for Basic Research in Digestive Disease at the Mayo Clinic in Rochester, Minnesota - USA has positions available for a Postdoctoral Research Fellow within the Chris M. Carlos and Catharine Nicole Jockisch Carlos Endowment to Find a Cure for Primary Sclerosing Cholangitis (PSC). Applicants should have an M.D., Ph.D., or equivalent degree with experience in cellular and molecular biology immunology. An appointment for two–three years is envisioned. Candidates' work will focus on wet bench projects including in vitro, in vivo, and/or animal models with the goals of providing a better understanding of the pathogenesis of PSC and the identification of molecular targets that will lead to novel therapies for this disease. Applicants with expertise in macrophage biology will be given particular consideration. Interested candidates should provide two letters of recommendation and an updated curriculum vitae/bibliography to Jennifer Rud at e-mail: **rud.jennifer@mayo.edu.**

myIDP: A career plan customized for you, by you.

There's only one *Science*.

my IDP ScienceCareers

Recommended by leading professional societies and the NIH

Features in myIDP include:

- Exercises to help you examine your skills, interests, and values.
- A list of 20 scientific career paths with a prediction of which ones best fit your skills and interests.
- A tool for setting strategic goals for the coming year, with optional reminders to keep you on track.
- Articles and resources to guide you through the process.
- Options to save materials online and print them for further review and discussion.
- A certificate of completion for users that finish myIDP and more.

Start planning today!
myIDP.sciencecareers.org

In partnership with: Science Careers

advancing the life sciences 1912-2012 FASEB Federation of American Societies for Experimental Biology

Medical College of Wisconsin

UCSF University of California San Francisco

Burroughs Wellcome Fund

A career in big data is one of many alternative careers for postdocs

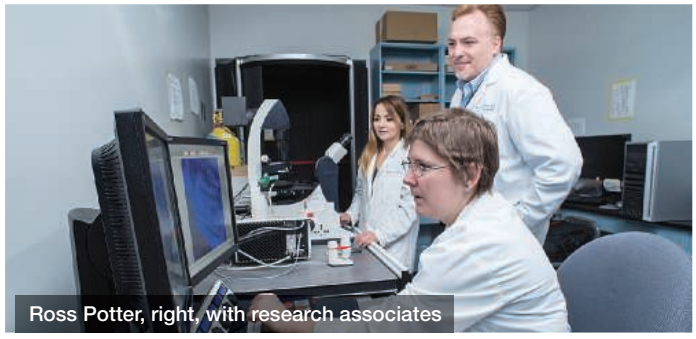
Ross Potter, right, with research associates

Alternatives to professorships in academia

If you're a Ph.D. scientist who loves academia but doesn't want to become a professor, don't fret—there are plenty of diverse and challenging career paths to be pursued in institutions of higher learning that don't require a faculty appointment.

By Alaina G. Levine

Like many Ph.D. scientists, **Latanya Scott** had made it her personal mission to help people through research. She envisioned a career as a faculty member to achieve this objective.

Scott pivoted slightly, thinking that working in Big Pharma might be more in tune with her nature. She pursued a postdoc at the Moffitt Cancer Center in Tampa, Florida, in cancer drug discovery. Yet, "I felt I wasn't realizing my purpose," she says. "Bench science can be very rewarding when you have a breakthrough, but a lot of times, experiments fail. It made me question whether I was making enough of an impact toward our mission to prevent and cure cancer. I wanted to find a way to help as many [therapeutic] strategies and technologies as possible get to the patients." Ultimately, she recognized that being a professor might not give her the opportunity to be as influential as she desired, so she started looking for other career avenues.

One of Scott's requirements for a new vocation was that she still had to be involved in the research enterprise in some manner. Bolstered by her principal investigator, she started exploring the profession of technology transfer. Informational interviews with staff in this field led to an internship in Moffitt's Office of Innovation and Industry Alliances, and ultimately a job offer as a licensing associate. Today, Scott continues to work toward her goal of advancing human health as the senior industry alliance development manager for the sprawling cancer research hospital. In the last 24 months, she has assisted in securing more than $35 million in research funding for Moffitt scientists by helping forge basic and translational research collaborations between clinicians, scientists, and industry. "I see the extraordinary value these preclinical projects and resulting technologies offer now and in the future," she says. "So I feel like I am helping make strides to finding cures someday. I'm playing a role in moving the science forward to benefit cancer patients everywhere."

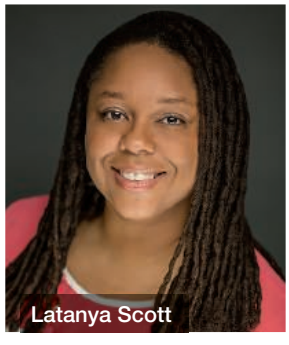
Latanya Scott

Those with doctorates naturally first look to the professoriate as their career choice. After all, they've seemingly spent eons in academia, have gotten to know—and in many cases love—the culture, and have been mentored their entire career by faculty. But what many Ph.D.s may not realize is that becoming a professor is simply one of the paths available in the academy. Indeed, universities and similar research institutions provide a fertile foundation for crafting multiple career paths, and offer diverse opportunities.

Catalyzing a new career

So what are the different career paths a Ph.D. scientist can pursue in academia? An obvious first choice is to serve as a scientist or technical professional in university departments. These positions can be based in disciplinary departments, such as physics. Alternatively, as is the case in some large research universities, they can be based in their own divisions, where Ph.D.s can serve as in-house consultants who help to solve scientific and technical problems for researchers.

As the use of big data becomes increasingly effective and popular, more universities are forming groups and subgroups that focus on big data problem solving, which in turn is spurring the creation of new employment opportunities for scientists with expertise in this arena. For example, **Nick Cross,** a staff scientist for the University of Edinburgh's Institute for Astronomy in the United Kingdom, develops software to process and archive imaging and other data from large astronomical surveys.

Big data jobs are often uncovered accidentally through networking, as **Jean Davidson** discovered. With a doctorate in molecular and cell biology, she originally came to Stanford University to pursue a postdoc. When her appointment came to a close, a colleague rolled his chair over to her one day and suggested her for a data scientist job with the Stanford-based Data Coordination Center of the ENCODE (Encyclopedia of DNA Elements) Consortium, an international collaboration of research groups funded by the cont.>

PHOTOS: (CLOCKWISE FROM TOP) © NICOELNINO/SHUTTERSTOCK.COM; MIDWESTERN UNIVERSITY; PURE EMOTIONS PHOTOGRAPHY

Upcoming Features

Faculty Careers—September 16 ■ *Faculty Careers—October 7* ■ *Focus on Wales—October 14*

"I love seeing all kinds of science and not just what I saw at the bench. I get a broader overview and perspective in a lot of different fields now."
—Christina Papke

National Human Genome Research Institute at the U.S. National Institutes of Health (NIH) in Bethesda, Maryland.

"I wasn't sure I was qualified, coming from a purely experimental biology background," says Davidson, "but luckily this team was looking for a more science-focused person to join the team to inform the data questions." Today, as a "data wrangler" (her official title), she collaborates with different labs around the country to "best capture and model the metadata of experiments, think about how the scientific community should access the data, and work to spread the utility and application of ENCODE." Knowledge gathering of this type involves developing databases, so she leverages skills in programming and knowledge of cloud-based computing, most of which she gained on the job. "This position is a great opportunity to stay in academic science, but in a different, nontenure track," she says.

Staying involved in research

Scientists who aspire to fuel the research engine find that pursuing a job managing core facilities (essentially the lab equipment and instrumentation) of a university is a smooth ride. Core facilities can be university-wide, or can be housed in a specific department. While at first glance these positions may seem to be focused only on operations, they still satisfy the drive many core facility managers have to be involved in research.

Ross Potter, laboratory manager in the department of physiology at Midwestern University in Glendale, Arizona, got his job because "they were interested in getting someone with an M.S. or a Ph.D. to build and expand the research program," he notes. But once they got wind of his expertise—he had done postdocs in immunology and receptor signaling at Vanderbilt University and at the Mayo Clinic in Scottsdale, Arizona, respectively—"they changed the job description a bit and made the offer to me to expand the position to manage the research building." Since his hiring in 2012, this dedicated health science university has increased its lab space and now has two research buildings, which Potter oversees. He manages all of the shared equipment, from confocal microscopes to freezers, and is responsible for maintaining and developing policies for using the facilities. He also serves as a liaison between the research staff and faculty/administration.

But like many core facility directors, Potter also has the chance to use the equipment to conduct research, a privilege also enjoyed by **Ralph J. Garippa,** director of the RNAi Core Facility at Memorial Sloan Kettering Cancer Center (MSKCC) in New York City. Garippa worked for over two decades in industry and was recruited by MSKCC to launch the core because of his expertise in high-throughput biological research techniques. He arrived in 2012 and now oversees a team of eight scientists (including two Ph.D.s and one M.D.) who support researchers with resources and tools related to RNA interference (RNAi) and CRISPR gene-editing technologies. Investigators engage his core facility with a research project in mind and a need to use equipment that is under his supervision, but "most of the time they want to compose the research with us and then have us do it, because we are experts in the assay development and automation-assisted techniques," notes Garippa. "We are also experts in troubleshooting and fine-tuning this specialized research." In some instances, he also has the chance to present at conferences about not only the techniques utilized but the research itself. Additionally, "our core chooses to spend a minimum of 20 percent of our time working on new technologies," he adds, which allows him to tap into his innate curiosity even more.

Grant management and writing and research development are other avenues that draw directly on doctorates and allow scientists to stay connected to the research enterprise. **Christina Papke,** Ph.D., a research development officer in the Research Development Services department at Texas A&M University (TAMU), revels in the fact that her job blends science with communications and strategic planning. She is able to dabble in the tasks she enjoys most, such as critiquing and editing NIH grant proposals, and providing training and related services on grant writing for TAMU investigators. Papke also facilitates the establishment of multidisciplinary research groups across the university, which contributes to TAMU's strategic plan to advance its grant portfolio. "Our goal is to promote a high level of collaboration across disciplines and increase competitiveness for larger, [more] complex interdisciplinary grant opportunities," she says. "I love seeing all kinds of science and not just what I saw at the bench. I get a broader overview and perspective in a lot of different fields now, and I really enjoy [the fact] that I still get to be involved with the research."

Keeping a toe in the professorial pool

For scientists who consider it a necessity to remain associated with the professoriate, there are several job paths that can be pursued in academia. You might not think a deanship is possible without a faculty appointment, but **Lisa M. Kozlowski** would argue otherwise.

She's the associate dean for student and postdoctoral affairs at Thomas Jefferson University in Philadelphia, Pennsylvania. Although she now has a joint appointment as a faculty member, she did not come into her deanship that way. Rather, she was hired for her knowledge of career development for early career scientists, which she honed as a leader in the postdoctoral association at her postdoc institution. It was only later that she renegotiated for a faculty post, something she advises others to do, preferably during the initial negotiations, for both the credence and benefits such as tenure.

For **Amy Replogle,** science core facility technician at the University of Puget Sound in Tacoma, Washington, keeping her toe in the professorial pool takes the form of teaching lab classes occasionally. Similarly, **Benjamin Porter's** staff title is Academic Program Officer II, but he unofficially serves as the assistant head of the Department of Bioengineering at the University of Texas at Dallas. "I'm not faculty, but I help run the department," he says. His portfolio of cont.>

Apply your scientific knowledge and technical skills to important societal challenges. Fellows serve in the executive, legislative, and judicial branches of the federal government.

"My fellowship was an amazing career catalyst. It broadened my horizons, connected me with remarkable individuals, and provided an exceptional platform for professional growth!"

Subhashree Mishra, Ph.D.,
Atmospheric Sciences Executive Branch Fellow at the Department of Energy

Current: Program Director, NCAR & Facilities at the National Science Foundation

Applications accepted May 1 – November 1.

To learn more and apply visit **go.stpf-aaas.org/Science2.html**

ScienceCareers online @sciencecareers.org
POSTDOCTORAL OPPORTUNITIES

FEATURED PARTICIPANTS

Division of Research, Texas A&M University
vpr.tamu.edu/researchdevelopment

Institute for Astronomy, The University of Edinburgh
www.roe.ac.uk/ifa

Midwestern University
www.midwestern.edu

Moffitt Cancer Center
www.moffitt.org

North Carolina Institute for Climate Studies, North Carolina State University
www.ncics.org

RNAi Core Facility, Memorial Sloan Kettering Cancer Center
www.mskcc.org/research-advantage/core-facilities/rnai-core

Stanford University
www.stanford.edu

Thomas Jefferson University
www.jefferson.edu/university

The University of Texas at Dallas
www.utdallas.edu

University of Puget Sound
www.pugetsound.edu

The University of Vermont
www.uvm.edu

"The recognition I get now is from the people I work with, that they like to work here, and that's recognition enough. You have to look for a different kind of reward."
—Benjamin Porter

responsibilities ranges from hiring and supervising staff and helping the department with accreditation, to event management, outreach, and even some media relations.

Leaning on research experience

Even though they do not serve as professors, researchers who pursue other academic paths note that their intensive training—in grad school, postdoc appointments, and other experiences—prepares them uniquely for the challenges of their new positions. "I lean a lot on my previous experience as a cancer researcher to review research protocols, conduct risk assessments, and add my 'oops, been there, done that!' to the trainings," says **Sonia Godoy-Tundidor,** assistant biosafety coordinator at the University of Vermont in Burlington. "I always bring out real-life examples of things I or someone else did wrong from the biosafety point of view when I worked at the bench. This usually impacts people and gets the message across."

Furthermore, the fact that these researchers received a Ph.D. gives them a certain level of currency in the academic marketplace. "My Ph.D. gives me confidence in speaking with faculty," says Papke. "[They know] I've done research, I've applied for grants. It does lend some credibility, especially since I was entering this [undertaking] without experience in this field."

However, a barrier still exists between faculty and nonfaculty at universities, as **Paula Hennon,** program manager for the North Carolina Institute for Climate Studies at North Carolina State University in Asheville, attests. As a Ph.D. atmospheric scientist (and an M.B.A.), "I've always had challenges being viewed as legitimate because I had a nonacademic plan," she shares. "As the deputy director of the technical support unit for the National Climate Assessment, I finally stopped questioning 'my worth' and second-guessing my path. Scientists need an advocate, a guide through the administrative quagmire, and a voice. They should prepare to hold on for the ride, as they will be the most misunderstood but potentially most valuable contributors to their scientific community or workplace."

Preparing for employment opportunities

One especially important feature of these nonfaculty jobs is their reliance on a diversity of skills, from management and communications to budgeting and planning. Yes, professors need to know how to write too, but unlike faculty, hiring decisions for nonfaculty academic posts are driven by the candidates' business and technical abilities.

So Kozlowski suggests that candidates should "get involved in things outside the lab, such as your institution's grad student or postdoc associations, where you can gain leadership and organizational skills." Porter helped launch the Washington, DC chapter of the Society for Neuroscience, which gave him excellent preparation for his current job.

Kozlowski also advises to do what you can to intimately learn the culture of academia—don't just rely on your experience in a lab in grad school. "As a member of the postdoctoral association at Johns Hopkins, one of the benefits I got was the ability to sit in on faculty senate meetings and hear about strategic plans for the coming years," she says. In doing so, she "got a feeling for how universities work."

Passing on the Nobel Prize

Ph.D. scientists in nonprofessorial positions are essential cogs in ensuring that universities remain successful and competitive. But that doesn't mean some who choose these professions don't mourn certain aspects that are tied to being a professor. "When you move out of research, you have to let go of the prestige of writing papers or getting the Nobel Prize, and that takes some getting used to," says Porter. "The recognition I get now is from the people I work with, that they like to work here, and that's recognition enough. You have to look for a different kind of reward."

Echoes Davidson: "You may feel you are giving up if you deviate from the [professorial] track, but there are still great careers out there [in academia] where you can be a scientist.... Although I miss being at the bench, I don't work many weekends and I have a better work–life balance. I didn't think I'd find a position like this that provided such balance and allowed me to contribute to science."

Alaina G. Levine is a freelance science writer based in Tucson, Arizona.

DOI: 10.1126/science.opms.r1600166

PHOTO: THE UNIVERSITY OF TEXAS AT DALLAS

Advance your career with expert advice from *Science* Careers.

Download Free Career Advice Booklets!

ScienceCareers.org/booklets

Featured Topics:

- Networking
- Industry or Academia
- Job Searching
- Non-Bench Careers
- And More

ScienceCareers

FROM THE JOURNAL SCIENCE AAAS

EMBL

The European Molecular Biology Laboratory (EMBL) is one of the highest ranked scientific research organisations in the world. EMBL offers a highly collaborative, uniquely international culture. It fosters top quality, interdisciplinary research by promoting a vibrant environment consisting of young, independent researchers with access to outstanding graduate students and postdoctoral fellows. Join our team as a

Group Leader in Structural Biology of Complexes

at EMBL Grenoble, France

The appointed Group Leader will be an ambitious structural biologist with an original multidisciplinary research programme oriented towards structure-function relationships of macromolecular complexes in eukaryotic systems. Current interests of Outstation groups are mainly focussed on protein-nucleic acid complexes involved in transcription, epigenetics, non-coding RNAs, RNA metabolism, RNA virus replication and host-pathogen interactions. He/she will benefit from the world-class environment offered by the inter-institutional Partnership for Structural Biology (EMBL, ESRF, ILL, IBS, **www.psb-grenoble.fr**) which gives access to state-of-the-art structural biology technologies including the ESRF synchrotron X-ray beamlines for MX and SAXS, cryo-EM (Polara/K2 at IBS, Titan Krios/K2 to be installed at the ESRF) as well as bacterial, insect and mammalian cell expression facilities, biophysical platform, confocal microscopy and high-throughput crystallisation platforms for soluble and membrane proteins.

Applicants should have a PhD, at least 3 years post-doctoral experience, a strong record of achievement in structural, molecular or cell biology and preferably research projects making use of both X-ray crystallography and electron microscopy.

Further information about this position can be obtained from the Head of EMBL Grenoble, Stephen Cusack (**cusack@embl.fr**). See also **www.embl.fr**.

Please apply online through **www.embl.org/jobs** and include a cover letter, CV and a concise description of research interests and future research plans. Please also arrange for 3 letters of recommendation to be emailed directly by your referees to **references@embl.de** at the latest by 27 September 2016.

Application closing date: 30 September 2016. Interviews are planned for end of October 2016.

EMBL is an inclusive, equal opportunity employer offering attractive conditions and benefits appropriate to an international research organisation with a very collegial and family friendly working environment. The remuneration package comprise a competitive salary, a comprehensive pension scheme, medical, educational and other social benefits, as well as financial support for relocation and installation, including your family. EMBL is committed to achieving gender balance and strongly encourages applications from women. Appointment will be based on merit alone. Further details on Group Leader appointments can be found under **www.embl.org/gl_faq**.

www.embl.org

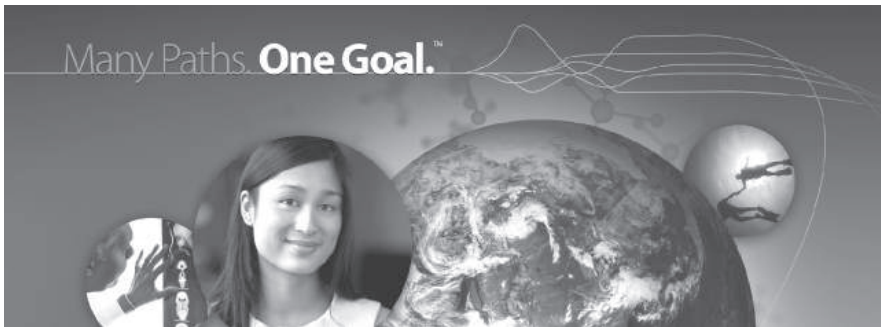

Pfizer Worldwide Research and Development Postdoctoral Program

At Pfizer, postdocs are trained in the art and science of drug discovery, and work side-by-side with scientists who are expert in cutting-edge biology, disease mechanisms, drug delivery and mechanisms of action, and the engineering of novel therapeutic proteins, vaccines, and nucleic acids. Areas of scientific focus include cardiovascular and metabolic diseases, clinical research, comparative medicine, drug safety, biotherapeutics/protein engineering, inflammation and immunology, human exploratory biology, medicinal chemistry, neuroscience and pain, oncology, pharmacology, and vaccines, among several others.

We recruit highly motivated Ph.D. recipients with an outstanding record of scientific productivity and a passion for ground-breaking, fast-paced research that facilitates the development of innovative therapies for human diseases. Our program promotes dissemination of research through publications and participation in scientific meetings, provides opportunities for collaboration with leading academic labs and industry consortia, and offers exceptional professional development training and networking opportunities.

To explore our program and research, visit us online at:
www.pfizercareers.com/student-programs/postdoc

Pfizer Working together for a healthier world®

www.pfizercareers.com

Does your postdoc deserve a MAJOR AWARD The largest of its kind in the world?

Nominate them for The Origins Project Postdoc Lectureship Award

This annual $10,000 international award, the largest of its kind in the world, will be given to an outstanding junior scholar chosen from any field of study relevant to the Origins Project mission. The winner will be hosted at ASU in Tempe, Arizona for one week, and will present 3 lectures on their research. In addition to the cash award, all travel and accommodation expenses will be covered by the Origins Project.

origins.asu.edu/postdocaward
Nomination deadline Nov. 1, 2016

ASU Origins PROJECT ARIZONA STATE UNIVERSITY

Our Next Breakthrough **IS YOU**
Lawrence Postdoctoral Fellowship
The Opportunity to Bring your Brightest Ideas to Life

The Lawrence Livermore National Laboratory (LLNL) has openings available in the Lawrence Fellowship Program. This highly competitive fellowship offers the freedom to conduct independent, self-directed, cutting-edge research in an area of the candidate's choice. Fellowships are awarded only to applicants with exceptional talent, credentials, leadership potential and track record of research accomplishments.

Successful candidates must propose and subsequently perform original research in a scientific area that is relevant to the mission and goals of LLNL. Broad topic areas include: Physics, Applied Mathematics, Computer Science, Chemistry, Material Science, Engineering, Environmental Science, Atmospheric Science, Geology, Energy, Lasers and Biology. Lawrence Fellows may participate in experimental or theoretical work at LLNL and will have access to LLNL's extensive computing facilities and specialized laboratory facilities. The duration of the Fellowship is up to three years. The salary is $8,887/mo.

Please refer to the following web page http://fellowship.llnl.gov for eligibility requirements and instructions on how to apply. When applying and prompted, please mention where you saw this ad. The deadline for applications is October 1, 2016. LLNL is operated by the Lawrence Livermore National Security, LLC for the U.S. Department of Energy, National Nuclear Security Administration. We are an equal opportunity employer with a commitment to workforce diversity.

Lawrence Livermore National Laboratory

http://fellowship.llnl.gov

EGL Charitable Foundation

The EGL Charitable Foundation
invites you to apply to the

Gruss Lipper Post-Doctoral Fellowship Program

Eligibility

- Israeli citizenship
- Candidates must have completed PhD and/or MD/PhD degrees in the Biomedical Sciences at an accredited Israeli University/Medical School or be in their final year of study
- Candidates must have been awarded a postdoctoral position in the U.S. host research institution.

Details regarding the fellowship are available at www.eglcf.org

NW210508R

DO YOUR RESEARCH HERE.

THE JACKSON LABORATORY

The Jackson Laboratory is actively recruiting highly qualified candidates for postdoctoral associate positions.

Accelerate your career at a world-class research institution with a legacy of innovation and discovery in genetic and genomic research.

Apply online at *www.jax.org/joinus*.

Opportunities are available to conduct cutting-edge research in diverse areas including aging, bioinformatics, cancer, computational biology, development, epigenetics, metabolism, immunology, infectious diseases, neurobiology, reproduction and systems genetics.

Join the search to discover tomorrow's cures.

Creating links that last a lifetime

at the International Centre for Fundamental Physics and its interfaces École normale supérieure, Paris (ENS-ICFP)

In 2016, the ENS-ICFP will hire four outstanding Junior Research Chairs at postdoctoral level for a two-year contract with a probable extension for a third year. Fellows are expected to develop new research projects within the Department of Physics at École normale supérieure.

What we offer :
- **Internationally competitive salary**
- **Attractive research funds and travel allowance**
- **Access to a cutting-edge scientific environment**
- **Complete integration into the Department of Physics through scientific exchange and teaching at the master level**

Application process and research themes can be found at http://phys.ens.fr/

Deadline to apply: October 30, 2016
Positions start in September 2017

One or two additional positions in Theoretical Physics will be made available by the Philippe Meyer Institute

The JRC positions are funded by the 10-year grant ENS-ICFP obtained through the French National Excellence initiative

PSL★ RESEARCH UNIVERSITY · UPMC SORBONNE UNIVERSITÉS · l'Observatoire de Paris · cnrs · ENS

W263339R

POSTDOCTORAL OPPORTUNITIES

The National Academies of
SCIENCES • ENGINEERING • MEDICINE

NRC Research Associateship Programs

Postdoctoral, Senior and Graduate Research Awards
offered for research at
U.S. federal laboratories

• Postdoctoral stipend $45,000 to $80,000 – higher for senior researchers •
• Relocation, professional travel, health insurance •
• Open to U.S. and non-U.S. citizens •

Annual application deadlines
• February 1 • May 1 • August 1 • November 1

Detailed program information can be found on the
NRC Research Associateship Programs website at:
www.nationalacademies.org/rap

Contact:
(202) 334-2760 or rap@nas.edu

*Qualified applicants will be reviewed without regard to race, religion, color, age, sex or national origin

COLUMBIA UNIVERSITY
College of Physicians and Surgeons

Assistant Professor – Research Scholar

Overlooking the Hudson River, the College of Physicians and Surgeons (P&S) is located two miles north of the Morningside Heights campus of Columbia University. P&S, along with the Mailman School of Public Health, the College of Dental Medicine, and the School of Nursing, comprise the 20-acre campus of the Columbia University Medical Center. With a budget of $1.5B, the College of Physicians and Surgeons employs more than 6,000 faculty and staff who provide world-class leadership in scientific research, medical education and patient care.

The College of Physicians and Surgeons is seeking one or more outstanding scientists in the Biomedical Sciences for appointment as the inaugural College of Physicians and Surgeons Research Scholar. These assistant professor positions are limited to MD, PhD or MD-PhD researchers who have, in general, 4 years or less of postdoctoral fellowship and who have demonstrated exceptional ability, creativity and productivity as reflected in first or senior author publications in leading scientific journals. Applicants who do not meet these criteria should not apply.

There is no limitation regarding the field of research and departmental affiliation will be decided after selection. Adequate start-up funds, space and mentorship will be provided. Priority will be given to applicants from outside Columbia University.

Applicants should provide 3 letters of recommendation and a proposed plan for their work over the next five years with the application. Please direct applications to: **Naomi Hornedo, Office of Research, College of Physicians and Surgeons, Columbia University.**

To apply: Please visit: **https://academicjobs.columbia.edu/applicants/Central?quickFind=62942 or search by requisition number 0006838**.

Columbia University is an Equal Opportunity/Affirmative Action Employer.

UT Southwestern Medical Center

Postdoctoral Training in Gene Regulation

Molecular Mechanisms, Computational Genomics, Mouse Genetic Models, Protein Structure, RNA Biology and Noncoding RNAs, Translational/Clinical

Dr. W. Lee Kraus is currently seeking applicants with a Ph.D. degree for postdoctoral training in the Laboratory of Signaling and Gene Regulation within the Cecil H. and Ida Green Center for Reproductive Biology Sciences.

The research in the Kraus lab covers a broad array of topics, including signaling, gene regulation, and genome function, especially in the areas of chromatin, transcription, epigenetics, RNA biology, and nuclear endpoints of cellular signaling pathways. We are interested in a wide variety of model systems and experimental approaches, including biochemistry, molecular biology, structural biology, animal models, genomics, proteomics, bioinformatics, and computational biology.

Projects in the lab are focused on signal-regulated transcription in the chromatin environment of the nucleus, with a focus on the estrogen and nuclear NAD^+ signaling pathways, PARPs, and non-coding RNAs in mammalian biological systems (e.g., hormone signaling, inflammation, ES cell biology, adipogenesis, and metabolism).

Candidates should submit a CV or resume, brief statement of interests and accomplishments, and a list of three references in one .pdf or .doc file by e-mail to **lee.kraus@utsouthwestern.edu**. Successful applicants will receive competitive pay and benefits commensurate with the applicant's level of experience.

UT Southwestern and the Green Center provide a dynamic, collaborative, and integrative research and training environment with state-of-the-art facilities.

See: **http://www.ncbi.nlm.nih.gov/pubmed/?term=kraus+wl**

UT Southwestern Medical Center is an Affirmative Action/Equal Opportunity Employer. Women, minorities, veterans and individuals with disabilities are encouraged to apply.

WILL YOUR RESEARCH LEAD TO BETTER LIVES FOR PATIENTS?

Gopinath Sutendra and Evangelos D. Michelakis, "Pulmonary Arterial Hypertension: Challenges in Translational. Research and a Vision for Change", *Sci. Transl. Med.* 5, 208sr5 (2013) Credit: *Science* Source

Science Translational Medicine | AAAS
INTEGRATING SCIENCE, ENGINEERING, AND MEDICINE

Find out more about the scope of the journal and submit your research today. **ScienceTranslationalMedicine.org**

D E Shaw Research

Postdoctoral Fellowships in Computational Chemistry, Biology, and Physics

D. E. Shaw Research is seeking postdoctoral fellows of exceptional ability to join our New York–based team. This is a unique opportunity to develop and work with transformative technology in a dynamic, interdisciplinary environment. Candidates should have expertise in computational, theoretical, or quantum chemistry, computational biophysics, structural biology, drug discovery, theoretical chemical physics, applied mathematics, or in a relevant area of computer science.

Relevant areas of experience might include direct application of molecular dynamics or other computational methods to drug discovery, investigation of allosteric interactions or other functionally important conformational changes in biological molecules, structure prediction or design for proteins or RNA, study of protein-protein or protein-nucleic acid interactions, force field improvement through detailed comparisons of simulation data with NMR measurements or other experimental data, development and implementation of new methodology, such as integrators or efficient approximations of long-range forces, methods for enhanced sampling or free-energy calculations, or tools to efficiently analyze large simulation datasets. Specific knowledge of any of these areas is less critical, however, than outstanding intellectual ability, unusually strong research skills, and a history of innovation and accomplishment. We are committed to fostering a stimulating, rewarding, and flexible work environment, and we offer above-market compensation to candidates of truly exceptional ability.

To submit an application, please email your CV to **ScienceCareers@DEShawResearch.com**.

D. E. Shaw Research is an independent research group that is pursuing an ambitious, long-term strategy aimed at fundamentally transforming the process of drug discovery. We have developed a special-purpose supercomputer capable of executing molecular dynamics (MD) simulations orders of magnitude faster than was previously possible. Our current projects include investigations of proteins and other biomedically relevant macromolecules as well as the development of computational chemistry methods to enable more accurate and effective MD simulations.

D. E. Shaw Research does not discriminate in employment matters on the basis of race, color, religion, gender, pregnancy, national origin, age, military service eligibility, veteran status, sexual orientation, marital status, disability, or any other protected class.

Max Planck Institute for Biophysical Chemistry

Research Group Leader Position

at the Max Planck Institute for Biophysical Chemistry

The Max Planck Institute for Biophysical Chemistry (Göttingen, Germany) seeks exceptional applicants for a research group leader position. We expect applicants to have a PhD, at least two years of successful post-doctoral experience and a track record in an area of ongoing research at the institute. Selection criteria include excellence in scholarship, creativity and originality in research.

A detailed description of the position as well as details about the application are available at:
www.mpibpc.mpg.de/en

Applications should be received no later than **September 20, 2016.**

The Max Planck Society is an equal opportunity employer. All qualified applicants will receive consideration for employment without regard to national origin, sex, age or status as qualified individuals with disabilities. We strongly encourage applications from women.

Neuroscience Post-doctoral Programme

Linköping University is one of Sweden's six large universities, currently enrolling 27,000 students. The Centre for Systems Neurobiology involves some 50 independent research groups, from the Faculty of Medicine and the Faculty of Science and Engineering, as well as the University Hospital.

The Centre for Systems Neurobiology is now seeking Postdoctoral Fellows (2+2 years) within several neuroscience research areas: Addiction, Animal Behavior, Electrophysiology and Circuits, Neuroimaging, Neurodegeneration, Neuroendocrinology, Neurodevelopment, Pain, Psychiatry, and Sensory Systems.

LINKÖPING UNIVERSITY

For more details regarding the Centre, the different research labs involved in the programme, and to submit a letter-of-intent please go to: liu.se/medfak/neuro. For information regarding the university and the region, please go to: liu.se/medfak, www.liu.se, www.eastsweden.com.

ScienceCareers online @sciencecareers.org

Georgia Institute of Technology

Tenure Track Faculty Position
Georgia Institute of Technology
School of Chemistry and Biochemistry
Atlanta, GA 30332-0400

THE **GEORGIA INSTITUTE OF TECHNOLOGY, SCHOOL OF CHEMISTRY AND BIOCHEMISTRY** seeks to fill one or more tenure-track faculty positions. Candidates from all areas will be considered, with opportunities for joint appointments in other departments of science and engineering to facilitate interdisciplinary research and scholarship. Exceptional candidates at **all levels** are encouraged to apply.

Candidates for appointment at the assistant professor level should submit an application letter, curriculum vitae, summary of research plans, description of teaching interests and philosophy, and arrange for submission of three letters of reference. Candidates at advanced levels should submit an application letter, curriculum vitae, and a brief description of research plans (particularly if future plans differ significantly from past efforts). All materials and requests for information should be submitted electronically, as per the instructions found at:

https://academicjobsonline.org/ajo/jobs/7626

The application deadline is **October 1, 2016** with application review continuing until the positions are filled.

Georgia Tech is an Equal Education/Employment Opportunity Institution.

TENURE-TRACK PROFESSOR
Harvard University
Faculty of Arts and Sciences
Cambridge, MA
Department of Chemistry and Chemical Biology

Position Description: Candidates are invited to apply for an open field tenure-track assistant professorship in the Department of Chemistry and Chemical Biology at Harvard University. The appointment is expected to begin on July 1, 2017. The tenure-track professor will be responsible for teaching at the undergraduate and graduate levels.

Basic Qualifications: Doctorate or terminal degree in chemistry or related discipline required by the time the appointment begins.

Additional Qualifications: Outstanding research record and a strong commitment to undergraduate and graduate teaching.

Special Instructions: Please submit the following materials through the ARIeS portal (**http://academicpositions.harvard.edu/postings/7065**). All applications and materials must be submitted no later than **October 15, 2016**.

1. Cover letter
2. Curriculum Vitae, including list of publications
3. Select Full Publications
4. Teaching statement (describing teaching approach and philosophy)
5. Future research plans
6. Names and contact information of 3-5 references (three letters of recommendation are required, and the application is complete only when all three letters have been submitted)

Contact Information: Helen Schwickrath, Search Administrator, Department of Chemistry and Chemical Biology, Harvard University, 12 Oxford St., Cambridge, MA 02138, Phone: 617-496-8190; helen@chemistry.harvard.edu

Harvard is an Equal Opportunity Employer and all qualified applicants will receive consideration for employment without regard to race, color, religion, sex, national origin, disability status, protected veteran status, or any other characteristic protected by law.

SCHOOL OF MEDICINE
CASE WESTERN RESERVE UNIVERSITY

Open Rank Protein Biophysics/Structural Biology Faculty Position
Department of Physiology and Biophysics

We invite outstanding individuals to apply for a faculty position at any rank in the area of Protein Biophysics and/or Structural Biology. Mid-career scientists with outstanding accomplishments at the level of Associate Professor or full Professor are especially encouraged to apply. We are particularly interested in applicants who are using interdisciplinary approaches to work on basic or translational aspects of human diseases. Visit our website at http://Biophysics.case.edu. The Department and School have excellent infrastructure, including x-ray crystallography, solution NMR spectroscopy, cryo EM and EPR spectroscopy. (see http://ccmsb.case.edu).

Applicants for a position as Assistant Professor should have a Ph.D. and/or M.D. degree, 3-5 years postdoctoral experience, and a strong record of scholarly activity. Competitive candidates for Associate Professor should have a strong publication record and an international reputation. Competitive candidates for Professor should have achieved records of leadership in the profession and have a substantial record of scholarly publications.

Applicants should submit a cover letter, a full *Curriculum Vitae*, including a record of prior/current funding, a brief description of their research, as well as the contact information for three professional references. Candidates at the Assistant Professor level should also submit a research plan. Please submit application materials with separate file attachments by email to: **Dr. Walter F. Boron, Chair, Department of Physiology and Biophysics, Case Western Reserve University, BiophysicsSearch@case.edu**

In employment, as in education, Case Western Reserve University is committed to Equal Opportunity and Diversity. Women, veterans, members of underrepresented minority groups, and individuals with disabilities are encouraged to apply. Case Western Reserve University provides reasonable accommodations to applicants with disabilities. Applicants requiring a reasonable accommodation for any part of the application and hiring process should contact the Office of Inclusion, Diversity and Equal Opportunity at 216-368-8877 to request a reasonable accommodation. Determinations as to granting reasonable accommodations for any applicant will be made on a case-by-case

Yale University
School of Medicine

FACULTY POSITION AT THE ASSISTANT PROFESSOR LEVEL

DEPARTMENT OF CELLULAR AND MOLECULAR PHYSIOLOGY

The Department of Cellular and Molecular Physiology is conducting a search for new faculty members at the assistant professor level.

The search seeks candidates whose research connects the properties of molecules to the properties of physiological systems.

Excellent opportunities are available for collaborative research, as well as for graduate and medical student teaching. Candidates must hold a Ph.D., M.D., or equivalent degree. Applicants should include a curriculum vitae, a statement of research interests and goals, and should arrange to have three letters of reference sent. Applicants should apply at the following website: **apply.interfolio.com/36676**

Application Deadline: **October 14, 2016**

Yale University is an Affirmative Action/Equal Opportunity Employer and welcomes applications from women, persons with disabilities, covered veterans, and members of minority groups.

ETH zürich

Assistant Professor (Tenure Track) of Ecology and Evolution in Forest Ecosystems

→ The Department of Environmental Systems Science (www.usys.ethz.ch) at ETH Zurich invites applications for the above-mentioned position.

→ The assistant professor develops and leads an internationally recognized research programme in "Ecology and Evolution in Forest Ecosystems" and is expected to integrate into research activities in related fields at ETH Zurich. He or she will use any relevant experimental, comparative and/or theoretical approaches to explore ecological and/or evolutionary processes that affect the composition, diversity, structure, dynamics and function of forest communities. The search is not limited to plant-based research, hence scientists working with non-plant forest components are encouraged to apply.

→ The new professor will teach in the Master of Environmental Sciences programme, offering subjects in Forest and Landscape Management that are also relevant to Ecology and Evolution. Undergraduate level courses are taught in German or English and graduate level courses in English.

→ Assistant professorships have been established to promote the careers of younger scientists. ETH Zurich implements a tenure track system equivalent to other top international universities.

→ **Please apply online at www.facultyaffairs.ethz.ch**

→ Applications should include a curriculum vitae, a list of publications, a statement of future research and teaching interests, the names and contact details of three referees, and three of your most important achievements. The letter of application should be addressed **to the President of ETH Zurich, Prof. Dr. Lino Guzzella. The closing date for applications is 31 October 2016**.
ETH Zurich is an equal opportunity and family friendly employer and is further responsive to the needs of dual career couples. We specifically encourage women to apply.

FACULTY POSITIONS AT THE ROCKEFELLER UNIVERSITY

The Rockefeller University seeks exceptional, interactive, and creative scientists to join its faculty. We invite applications from outstanding candidates for tenure-track positions.

The University has a laboratory-based organizational structure that fosters interdisciplinary research. We encourage applications in the following areas:

- **Chemical & Structural Biology**
- **Genetics & Genomics**
- **Immunology, Virology & Microbiology**
- **Medical Sciences, Systems Physiology & Human Genetics**
- **Molecular & Cell Biology**
- **Neurosciences & Behavior**
- **Organismal Biology & Evolution**
- **Physical, Mathematical & Computational Biology**
- **Stem Cells, Development, Regeneration & Aging**

The Rockefeller University provides strong support for the research work of its faculty, including competitive salary, a range of work-life employee benefits, start-up funds, renovated laboratory space and access to state of the art core facilities. There are extensive opportunities for collaboration both within the University and with neighboring institutions.

Visit **http://www.rockefeller.edu/facultysearch** to submit your application online and view further information about the positions.

The Rockefeller University 1901 — SCIENTIA · PRO · BONO · HUMANI · GENERIS

Application deadline is September 30, 2016.

If you have any questions regarding your application, please contact our Administrator at **facultysearch@rockefeller.edu.**

The Rockefeller University is an Equal Opportunity Employer that values diversity at all levels - Minorities/Women/Disabled/Veterans.

Keep your job search out of the cheap seats.

- Search thousands of job postings
- Create job alerts based on your criteria
- Get career advice from our Career Forum experts
- Download career advice articles and webinars
- Complete an individual development plan at "myIDP"

Target your job search using relevant resources on **ScienceCareers.org**.

ScienceCareers
FROM THE JOURNAL SCIENCE AAAS

Faculty Careers

September 16 issue book by August 30*

October 7 issue book by September 20*

There's only one *Science*.

Hiring Faculty? Whatever your timing, we've got two special features for your faculty ads this fall! The September 16 feature offers advice on how to develop skills for reviewing grants and papers. The October 7 feature covers business principles for researchers. Reach *Science* readers and share opportunities at your university.

Why choose these Faculty Features for your advertisement?

- Relevant ads lead off these career sections with a special Faculty banner
- October 7 issue will be distributed at the American Society of Human Genetics meeting, 18–22 October, Vancouver.

*Ads accepted until Sept 9 and Sept 30 if space allows.

Produced by the until *Science*/AAAS Custom Publishing Office.

ScienceCareers
FROM THE JOURNAL SCIENCE AAAS

SCIENCECAREERS.ORG

To book your ad: **advertise@sciencecareers.org**

The Americas
202 326 6582

Europe/RoW
+44(0)1223 326500

Japan
+81 3 3219 5777

China/Korea/Singapore/Taiwan
+86 186 0082 9345

MEDICAL SCHOOL
UNIVERSITY OF MICHIGAN

Faculty Director, Bioinformatics Core Biomedical Research Core Facilities & Department of Computational Medicine and Bioinformatics

The University of Michigan Medical School (UMMS) Biomedical Research Core Facilities (BRCF) and the Department of Computational Medicine and Bioinformatics (DCM&B) are seeking a Faculty Director for its well-established Bioinformatics Core. The Core's central mission is to provide bioinformatics support to investigators in the basic and clinical departments of UMMS and in other schools or colleges. The Core represents a vital connection between basic and translational research at the U-M.

The current focus of the Core is to develop and implement computational services to analyze high dimensional biological research data. Major Core functions include study consultation; genomics, multi-omics, and bioinformatics analysis; data storage and organization; data analysis and visualization; delivery of results, and performing related educational activities.

The Faculty Director will be appointed as a tenure-track or tenured instructional-track faculty in DCM&B. As a faculty member in DCMB, the Director will maintain an independently funded research program that contributes to the growth of high-throughput molecular data analysis. We believe that such active research is essential for maintaining the Core's long-term vision, ensuring close connection with cutting-edge methodological development, and upholding scientific rigor for all studies under Core support.

The Faculty Director is expected to create a strategy to initiate, optimize, and expand services needed by the researchers, both routine and custom. Supported by strong administrative staff of the BRCF, the Director will lead a team of professional bioinformaticians, developers, analysts, and IT specialists, to create and constantly update a robust service portfolio, which includes management and analysis of data from microarray, DNA and RNA sequencing, qRT-PCR, ChIP-seq, ATAC-seq and related epigenomic analyses. Such data are typically produced at the U-M DNA Sequencing Core. The Core will also engage with other units in BRCF to integratively analyze metabolomics, genome editing, microbiome, metagenomics, epigenomics and proteomics data. Extensive computational resources and database infrastructure are already in place.

Requirements:

- Established faculty record of publication and extramural funding.
- PhD in bioinformatics, biostatistics, epidemiology, computer science, engineering, or related field. Applicants with a biology or medicine background but extensive subsequent training in data-intensive quantitative research also qualify.
- Postdoctoral experience in statistical analysis of complex 'omics data, preferably in a biomedical research environment. Prior experience in multi-disciplinary collaboration or managing Core support is a plus.
- Demonstrated abilities in research, including technical knowledge, broad understanding of genomic application areas, and evidence of creativity and scientific vision.
- Extensive experience with high-throughput genomics data, including computing experience in a Unix/Linux environment; programming proficiency.
- Ability to communicate clearly, directly, and tactfully with faculty and staff in diverse fields.
- Organizational skills, especially in a multi-tasking environment.
- Demonstrated leadership experience with proven personnel and financial management.

Please send a letter of interest with Curriculum Vitae, statement of research interests, and contact information of three or more references to: **Search Committee, Department of Computational Medicine and Bioinformatics. Job Code 300, The University of Michigan, 2017 Palmer Commons, 100 Washtenaw Ave, Ann Arbor, MI. 48109-2218, email: ccmbrecruit@umich.edu. Applications will be reviewed September 2016 until the position is filled.**

http://www.ccmb.med.umich.edu; https://medicine.umich.edu/medschool/research/office-research/biomedical-research-core-facilities/bioinformatics

MEDICAL SCHOOL
UNIVERSITY OF MICHIGAN

Department of Computational Medicine and Bioinformatics Tenure-track positions (all ranks)

The Department of Computational Medicine and Bioinformatics (DCM&B) at the University of Michigan Medical School seeks outstanding applicants for tenure-track and tenured faculty positions in computational medicine and bioinformatics. DCM&B (http://www.ccmb.med.umich.edu/) has 13 primary, 13 joint, and 80 affiliate faculty, and is closely associated with the Michigan Institute for Data Science (MIDAS.umich.edu) as well as many basic science and clinical units and departments across the medical school and the university. DCM&B hosts the Bioinformatics Graduate Program which has ~60 PhD and >20 Master students, with 58 PhD alumni. DCM&B hosts NIGMS bioinformatics and NCI proteome informatics pre-doctoral T32 training grants. We have active national outreach for minority candidates, in partnership with the NIH Research Centers for Minority Institutions (RCMI) program. DCM&B has grown rapidly in both faculty publications and sponsored research, with >six-fold increase in grant funding in the past three years.

We are currently recruiting 1 senior and 3 junior to mid-career faculty members to establish independent research programs that address emerging challenges in analyzing large, complex datasets. Innovative researchers in the areas of bioinformatics, computational biology, and advanced methodological development as applied to biomedical research are encouraged to apply. Several areas of programmatic interest will receive special consideration:

- Cancer bioinformatics
- Translational bioinformatics as applied to studies of complex diseases
- Biomedical data science methodology, including, but not limited to, natural language processing, machine learning, and visualization.

Joint appointments may be considered with the Michigan Institute for Data Science (MIDAS), the Comprehensive Cancer Center, departments of Human Genetics, Learning Health Sciences, Biomedical Engineering, partnering clinical departments, Computer Science; Schools of Information and Public Health; and other appropriate units. There are extensive computational resources and data science infrastructure available. Opportunities exist for faculty leadership roles to influence institutional priorities in clinical and biomedical informatics.

Successful candidates will have a PhD and/or MD degree, or equivalent, with post-doctoral training, in areas such as (but not limited to) biomedical data mining and machine learning; multi-scale integrative omics analysis; systems biology; natural language processing and ontologies applied to biomedicine; informatics related to healthcare delivery and clinical decision support; precision medicine and pharmacogenomics. Publications, funding record, a detailed research plan, collaborative experience, and demonstrated interest in graduate and post-doctoral education will be essential components of the application.

Applicants should send a letter of interest with Curriculum Vitae, Research Plan, and a list of three or more references with current contact information to: **Search Committee, Department of Computational Medicine and Bioinformatics, Job Code 200. The University of Michigan, 2017 Palmer Commons, 100 Washtenaw Ave, Ann Arbor, MI. 48109-2218, email: ccmbrecruit@umich.edu. Applications are accepted in September 2016 – May 2017.**

Ann Arbor has a remarkable cultural and living environment. The University of Michigan is responsive to the needs of dual-career families, and is an Equal Opportunity Affirmative Action Employer committed to a diverse and inclusive faculty, staff and student body.

Science Careers online @sciencecareers.org

POSITIONS OPEN

ASSISTANT PROFESSORS

The Department of Chemistry and Biochemistry at the University of Oregon invites applications for either a tenure-track Biochemistry faculty or a tenure-track Chemical Biology faculty member, at the Assistant Professor level to begin in Fall 2017 or later. A Ph.D. is required.

ASSISTANT PROFESSOR - Biochemistry Biochemistry research at the University of Oregon takes place in context of the Institute of Molecular Biology (http://molbio.uoregon.edu) which promotes interdisciplinary interactions between life science researchers in the departments of Chemistry and Biochemistry, Biology and Physics. We seek applicants from all areas of molecular biology who are using advanced approaches to study mechanisms of cellular function, including topics in RNA and protein biochemistry. New faculty will join a rich and collaborative atmosphere with existing strengths in host-pathogen interactions, stem cell biology, organelle biogenesis, genome function, and cytoskeleton biochemistry.

ASSISTANT PROFESSOR - Chemical Biology We seek applicants with research interests focusing on the development and/or use of chemical tools and approaches to address fundamental questions in biology and medicine. Applicants are encouraged who are working in all areas of chemical biology, particularly in applications of synthetic chemistry to topics such as bio(in)organic chemistry, bioorthogonal chemistry, molecular sensing, metals in medicine, synthetic biology/directed evolution, and imaging. New faculty will join a rich and collaborative atmosphere between chemists, biologists, and physicists including interdisciplinary opportunities with the Institute of Molecular Biology (website: **http://molbio.uoregon.edu**) and the Materials Science Institute (website: **http://materialscience.uoregon.edu**), and complement strengths in organic synthesis, materials chemistry, and bio(in)organic chemistry within the department.

Successful candidates will have the potential for establishing an outstanding independent research program and excellence in teaching at the undergraduate and graduate levels. They will also support and enhance a diverse learning and working environment.

To assure full consideration, application materials should be received by **October 10, 2016**. Please apply at website: **https://academicjobsonline.org/ajo/jobs/7667** and upload a cover letter specifying your area of interest, Biochemistry or Chemical Biology, curriculum vitae, a statement of research plans and objectives, and a brief statement of teaching philosophy or interests. The candidate should also arrange for three letters of recommendation to be uploaded directly by the recommenders. Review of application materials will continue until the position is filled.

Of note, the University of Oregon Department of Chemistry and Biochemistry is also currently searching for faculty candidates in Physical Chemistry (website: **http://chemistry.uoregon.edu**).

The University of Oregon is an Equal Opportunity, Affirmative Action Institution committed to cultural diversity and compliance with the ADA. The University encourages all qualified individuals to apply, and does not discriminate on the basis of any protected status, including veteran and disability status.

ASSISTANT PROFESSOR

Hope College seeks applications for a **TENURE-TRACK POSITION** in Developmental Biology at the Assistant Professor level to begin August 2017. The successful candidate will have a Ph.D. and be expected to develop a vigorous, externally funded research program with active participation by undergraduate students. Hope College offers a competitive salary/benefit package, in addition to excellent start-up support. Please visit website: **www.hope.edu/employment/faculty** for a full job description and to apply. Applications received by October 1, 2016 will be assured full consideration.

POSITIONS OPEN

PHYSICAL CHEMISTRY FACULTY POSITION

UNIVERSITY OF OREGON Physical Chemistry Faculty Position. The Department of Chemistry and Biochemistry (website: **http://chemistry.uoregon.edu**) invites applications for a tenure-related position in experimental physical chemistry (broadly defined) beginning Fall 2017 at the anticipated rank of assistant professor. Exceptional candidates in theoretical chemistry or at advanced ranks may also be considered. A PhD is required and postdoctoral experience is preferred.

The potential for establishing a vigorous independent research program in physical chemistry and active participation and excellence in teaching at the undergraduate and graduate levels will be the most important criteria for selection. Candidates will also be evaluated on their ability to complement the existing physical chemistry program at the University of Oregon. Candidates who promote and enhance diversity are strongly desired. In addition to membership in the Department of Chemistry and Biochemistry, the successful candidate will have the opportunity to pursue research in a variety of interdisciplinary institutes (see website: **http://chemistry.uoregon.edu/research.html?institutes**).

To ensure consideration, please submit application materials by **October 15, 2016** at website: **https://academicjobsonline.org/ajo/jobs/7663** and upload a curriculum vitae, a statement of research plans and objectives (maximum 10 pages), and a brief statement of teaching philosophy or interests (1-2 pages). The candidate should also arrange for three letters of recommendation to be submitted directly by the recommenders via the preceding URL link. The position will remain open until filled.

The University of Oregon is an Equal Opportunity, Affirmative Action Institution committed to cultural diversity and compliance with the ADA. The University encourages all qualified individuals to apply, and does not discriminate on the basis of any protected status, including veteran and disability status.

CHEMICAL BIOLOGY FACULTY POSITION
Boston College Chemistry Department

The Chemistry Department of Boston College invites applications for a tenure track position to be effective in the fall of 2017. Applicants will be evaluated based on their potential to establish a prominent and well-funded research program and to excel in teaching at the graduate and undergraduate levels. Successful applicants will join a department of approximately 120 doctoral students, 30 postdoctoral fellows, 200 undergraduate majors, and an internationally recognized faculty.

Assistant Professor in the area of Chemical Biology requires a Ph.D. in Chemistry or related areas; postdoctoral experience is desirable but not required. The candidate is expected to have published in top refereed journals and demonstrated the ability to perform outstanding independent research.

Interested applicants must submit a cover letter (which includes the names of three references), a graphical executive summary of research plans (one page), curriculum vitae, a summary of research plans (eight pages maximum), a statement of teaching philosophy and arrange to have three letters of reference submitted via the online faculty application at website: **http://apply.interfolio.com/30499**.

All application materials must be submitted electronically on or prior to October 15, 2016.

Boston College, a university of eight schools and colleges, is an Equal Opportunity Employer and supports Affirmative Action.

Post Your Jobs
1.4 million candidates*
235,000 job applications*
Reach Scientists.
Fill Positions.
*Jan–Dec 2015
ScienceCareers
employers.sciencecareers.org

POSITIONS OPEN

ASSISTANT PROFESSOR OF CHEMISTRY OR BIOCHEMISTRY
CALIFORNIA STATE UNIVERSITY EAST BAY

The California State University, East Bay (CSUEB) Department of Chemistry and Biochemistry invites applications for a tenure track Assistant Professor position in any area of chemistry, including biochemistry (#17-18 CHEM-CHEMISTRY-TT). The successful candidate must have solid training in chemistry and a strong commitment to teaching. Applicants are expected to establish an externally funded research program appropriate for undergraduate and M.S. students pursuing a chemistry or biochemistry curriculum. Teaching responsibilities will include General Chemistry, both lecture and laboratory, and additional courses at the undergraduate and graduate level in the applicant's area of expertise. A Ph.D. is required; postdoctoral research and teaching experience in chemistry or biochemistry are preferred. Applications should include a letter of interest which addresses qualifications, a current curriculum vitae, a one-page statement of teaching philosophy, a brief research plan no longer than three pages, and scanned copies of undergraduate and graduate transcripts. Materials should be submitted electronically at website: **https://apply.interfolio.com/35591.** Three letters of recommendation are required and should be submitted electronically. Letters can be requested as instructed on the application website (+Add File under Confidential Letter). Review of applications will begin October 10, 2016 and continue until the position is filled. The start date is September 1, 2017. *CSUEB, an Equal Opportunity Employer, is committed to the principles of diversity in employment.*

PRINCETON UNIVERSITY
DEPARTMENT OF CHEMISTRY
ASSISTANT PROFESSOR

The Department of Chemistry at Princeton University invites applications for a **TENURE-TRACK ASSISTANT PROFESSOR** position in all areas of chemistry. We seek a faculty member who will create a climate that embraces excellence and diversity with a strong commitment to research and teaching that will enhance the work of the department and attract and retain a diverse student body. We strongly encourage applications from members of all underrepresented groups. Candidates are expected to have completed the Ph.D. in chemistry or a related field at the time of appointment. Applicants should submit a description of research interests, curriculum vitae, a list of publications, and contact information for three referees online at website **jobs.princeton.edu/applicants/Central?quickFind=67134**. The deadline for applications is October 15, 2015. *Princeton University is an Equal Opportunity Employer. All qualified applicants will receive consideration for employment without regard to race, color, religion, sex, national origin, disability status, protected veteran status, or any other characteristic protected by law. This position is subject to the University's background check policy.*

Post your jobs
Fast and Easy

ScienceCareers
employers.sciencecareers.org

2016 Annual
Top Employers in Biotech & Pharma

Special Career Feature:
October 28, 2016

Reserve your ad by October 11 to guarantee space.

Ads accepted until October 21 if space is still available.

For recruitment in science, there's only one **Science**

WHO IS NO. 1 THIS YEAR?

Science publishes the results of its 15th annual Top Employers Survey on October 28. *Science* has a long history of providing a forum for scientists to express their opinions about the biotech and pharma industry.

Recruit or brand your organization and reach both ACTIVE and PASSIVE job seekers.

Start building your pipeline today with *Science*.

SCIENCECAREERS.ORG

ScienceCareers
FROM THE JOURNAL SCIENCE AAAS

To book your ad:
advertise@sciencecareers.org

The Americas
202-326-6582

Japan
+81-3-3219-5777

Europe/RoW
+44 (0) 1223-326500

China/Korea/Singapore/Taiwan
+86-186-0082-9345

WASHINGTON STATE UNIVERSITY

Plant Community Ecology -- Assistant Professor
School of Biological Sciences, College of Arts and Sciences

The School of Biological Sciences at Washington State University, Pullman, Washington, invites applications for a full-time, permanent, tenure-track faculty position in plant community ecology. This position is to be filled at the Assistant Professor level and will begin in August of 2017.

Candidates should have research experience in plant community ecology. Areas of interest include, but are not limited to, the distribution and abundance of plants, species interactions, and/or the stability and assembly of biological communities. The ideal candidate will combine traditional and cutting edge approaches that shed light on ecological processes. Candidates with sophisticated quantitative skills and the ability to bridge both small and large spatial scales are especially encouraged to apply. Candidate research programs should consider pressing contemporary and future issues, with the potential to inform our understanding of local and global responses to global change.

Required qualifications include an earned doctorate at time of application, a record of research accomplishment in plant community ecology, evidence of a commitment to teaching excellence including the ability to teach undergraduate and graduate courses such as community ecology, effective communication skills, and demonstrated ability to collaborate with other scientists. Successful candidates will be expected to develop and maintain an active research program supported by extramural funding, train graduate and undergraduate students in research, participate in graduate and undergraduate teaching, participate in service needs, and advance our commitment to diversity and multiculturalism.

To apply, visit **www.wsujobs.com** to upload application materials. Applications must include a cover letter that addresses qualifications, a curriculum vitae, separate teaching and research statements, and up to three selected reprints of published or in press papers. Three (3) letters of recommendation that address the applicant's history of and potential for research, teaching, and communication excellence are required. The reference letters will be automatically requested and obtained from the reference provider through our online application system. Review of applications begins **October 24, 2016**.

For information on the position or the status of your application, candidates may contact **Dr. Jeremiah W. Busch** at **jwbusch@wsu.edu**. Full notice of vacancy can be viewed at **https://www.wsujobs.com**

EEO/AA/AD

MEDICAL SCHOOL
UNIVERSITY OF MICHIGAN

Faculty Positions in Cancer Pharmacology
Department of Pharmacology

The Department of Pharmacology at the University of Michigan Medical School is seeking applications for tenured/tenure-track positions at the **ASSISTANT**, **ASSOCIATE** or **PROFESSOR** level. We are seeking outstanding individuals with research experience and interests in **cancer pharmacology, oncology therapeutics, and precision medicine in oncology**. Qualifications include a Ph.D. in Pharmacology or a related discipline and/or a M.D. degree, and for those applying above the level of Assistant Professor, a strong record of nationally competitive external funding, a sustained record of excellent research productivity, and an outstanding national reputation in their field. Physician-Scientists are encouraged to apply, as joint appointments are available with clinical departments and the University of Michigan Comprehensive Cancer Center. Applicants will be expected to maintain extramural funding, participate in the teaching of medical, graduate, and undergraduate courses, and to support and mentor graduate students and postdoctoral fellows. An attractive startup package including excellent laboratory space and generous startup funds is available. Salary will be commensurate with experience.

The successful candidates will join a dynamic, diverse, and collaborative department with new leadership in a Top 10 Medical School in a university setting with superb opportunities for continuing career development. The quality of life in Ann Arbor is outstanding. The combination of a large, major research university with a diverse, safe, family-oriented community make Ann Arbor an ideal environment for work-life balance. Ann Arbor offers an outstanding combination of sports, recreation, and cultural events.

Applicants should send their *curriculum vitae*, a three-page summary of their research program and future research plans, and information related to past and current teaching experience as a single PDF file to jdani@umich.edu. Address all correspondence to: **Dr. John Traynor Chair, Pharmacology Faculty Search Committee, Department of Pharmacology, The University of Michigan Medical School, 1150 West Medical Center Dr., 2301 MSRB III, Ann Arbor, MI 48109-5632.** Review of applications will begin on **October 1, 2016**, and will continue on a rolling basis until positions are filled.

The University of Michigan is an Affirmative Action/Equal Opportunity Employer. Applications from qualified women, minorities and/or disabled individuals are encouraged.

ScienceCareers online @sciencecareers.org

By **Amit Kumar**

Adaptability in life and work

When I first arrived in Belgium to begin my Ph.D. studies, I wasn't sure how I would survive without my friends and family back in northern India. I had chosen to pursue my doctoral studies at Ghent University because of its unique biological engineering program, but I expected that living in a new country would be challenging. I was right. I had a hard time eating the unfamiliar food (on several occasions I didn't eat at all) and often struggled to overcome everyday obstacles, such as navigating public transportation and interacting with salespeople.

What I hadn't realized was how hard it would be on me emotionally. I felt extremely out of place and isolated. I was hesitant to explore anything unfamiliar, nervous that my ignorance of local norms would lead to embarrassment. A few times I reluctantly went dancing with friends, but I stuck to the sidelines because I didn't know how to salsa, cha-cha, or do any of the other dances everyone else seemed to know. For the most part, I did only what I had to do: I found a place to live and got started on my research project.

I felt discouraged at work, too. I wanted to be productive, but my personal struggles and the typical challenges of starting graduate school got in the way. I now realize that I was trying to rush things, but at the time, my lack of research progress made me feel even more discouraged about my decision to go to grad school abroad. Several times I felt like giving up and flying home.

But slowly, as I became friends with fellow graduate students from around the world, my outlook began to change. I saw how my friends from Italy and Spain threw themselves into the new culture without fear—happy to try new foods, learn about unfamiliar customs, and laugh and be laughed at. As I saw my friends take risks, I decided to take the leap and adopt their mindset. The next time we went dancing, I got out on the floor—even though I knew I would get some of the steps wrong—and I had a great time.

As my newfound confidence grew, I began to push further outside my comfort zone. I initiated conversations with strangers despite my relatively poor grasp of the language and accepted invitations for weekend group trips. I began to appreciate that there can be many "right" ways to think and behave, and that I could feel at home anywhere as long as I allowed myself to become part of the community.

"Being in an unfamiliar culture ... aided my research career."

At first, I didn't think about how this change in perspective might affect my work, but now I realize that many of the qualities I developed to deal with being in an unfamiliar culture—an openness to learning new things, an ability to appreciate and communicate with people from different backgrounds, and a greater comfort with uncertainty and change—have also aided my research career. Over the course of my training, I have followed my intellectual curiosity from environmental engineering to biological engineering to chemistry to applied microbiology to chemical engineering. I think I would have had a hard time successfully crossing these scientific borders if I hadn't had the experience of adapting to new settings in my personal life.

These qualities have also helped prepare me to take on leadership roles outside the lab, which are personally rewarding and hopefully will strengthen my applications for jobs in the future. Taking on responsibility as the energy and environment chair of the Massachusetts Institute of Technology Energy Club, for example, was somewhat intimidating at first, but by looking at it as another challenge to my adaptation skills, I have been able to dive in headfirst.

Even though going abroad for my degree was difficult at first, I'm so glad I did it. Since that time, I have studied in 11 more countries and visited 35 others. Together, these experiences have made me a better person, both personally and professionally, and that is a benefit I never expected when I first set foot in Belgium 12 years ago. ■

Amit Kumar is a chemical engineering postdoc at the Massachusetts Institute of Technology in Cambridge and an adjunct researcher at Harvard University. Send your career story to SciCareerEditor@aaas.org.

ILLUSTRATION: ROBERT NEUBECKER

Downloaded from http://science.sciencemag.org/ on September 3, 2016

Published by AAAS